Parametric and Nonparametric Identification of Nonlinearity in Structural Dynamics

by

Keith Worden

A thesis submitted for the degree of Doctor of Philosophy at Heriot-Watt University

Department of Mechanical Engineering

Edinburgh, November 1989

To my parents

CONTENTS

ABSTRACT

The work described in this thesis is concerned with procedures for the identification of nonlinearity in structural dynamics. It begins with a diagnostic method which uses the Hilbert transform for detecting nonlinearity and describes the neccessary conditions for obtaining a valid Hilbert transform. The transform is shown to be incapable of producing a model with predictive power. A method based on the identification of nonlinear restoring forces is adopted for extracting a nonlinear model. The method is critically examined; various caveats, modifications and improvements are obtained. The method is demonstrated on time data obtained from computer simulations. It is shown that a parameter estimation approach to restoring force identification based on direct least-squares estimation theory is a fast and accurate procedure. In addition, this approach allows one to obtain the equations of motion for a multi-degree-of-freedom system even if the system is only excited at one point.

The data processing methods for the restoring force identification including integration and differentiation of sampled time data are developed and discussed in some detail.

A comparitive study is made of several of the most well-known least-squares estimation procedures and the direct least-squares approach is applied to data from several experiments where it is shown to correctly identify nonlinearity in both single- and multi-degree-of-freedom systems.

Finally, using both simulated and experimental data, it is shown that the recursive least-squares algorithm modified by the inclusion of a data forgetting factor can be used to identify time-dependent structural parameters.

ACKNOWLEDGEMENTS

I would like to thank Professor Geoff Tomlinson, for introducing me to the subject of nonlinear dynamics and for his constant help and encouragement throughout the time this work was carried out.

Sincere thanks are due to all my colleagues in Edinburgh, Manchester and Sheffield for help and advice. I would particularly like to acknowledge Dr. Steve Billings, Dr. Steve Gifford, Mike Read, Khalid Mohammad, Dr. Jan Wright and Dr. Moufid Ajjan Al-Hadid who have all greatly improved my - still limited - understanding of nonlinear phenomena and basic engineering principles through innumerable helpful discussions.

Specific thanks are due to Khalid Mohammad, Paul Townsend and Phil Waters for their invaluable help in the dynamics laboratory at Manchester, and also to Steve Gifford for providing the majority of the graphics routines used in this work, particularly the three-dimensional plotting routine.

I would like to express my gratitude and love to my parents and Heather for all the support and encouragement they have given me throughout the course of this work.

This work was carried out with the financial support of the Science and Engineering Research Council and in collaboration with Dr. S.A.Billings of the Department of Control Engineering, Sheffield University.

INTRODUCTION

This work is concerned with reporting an attempt to develop a method of identifying an arbitrary nonlinear structural dynamical system using measured time data from the system. Before proceeding, some of the terms used above require explanation.

The term structural dynamical system or simply structural system shall be used throughout to refer to a system whose dynamics are governed by Newton's second law. In the case of a Single Degree–Of–Freedom (SDOF) system, this means that the dynamics are entirely captured by the equation of motion

$$m\ddot{y} + f(y,\dot{y}) = x(t)$$

Here, the system is one where the total mass m is concentrated at one point. This mass is always assumed to be independent of time. The mass moves in such a way that when an external force x(t) is applied the mass has acceleration $\ddot{y}(t)$, velocity $\dot{y}(t)$ and displacement y(t) at time t. These quantities are related via the equation above. The term $f(y,\dot{y})$, a function of velocity and displacement, is a generic internal or *restoring* force which returns the system to equilibrium when disturbed. If the function $f(y,\dot{y})$ is linear in it's arguments i.e.

$$f(y,\dot{y}) = c\dot{y} + ky$$

for some constants c and k, then the system is said to be linear. If $f(y,\dot{y})$ depends on any products of variables higher than first order the system is *nonlinear*. A multi degree–of–freedom system (MDOF) is specified by more than one equation of motion. A system which requires N equations

$$
\begin{aligned}
m_1 \cdot \ddot{y}_1 + f_1(y_1, \dot{y}_1, y_2, \dot{y}_2, \ldots, y_N, \dot{y}_N) &= x_1(t) \\
\cdot \qquad\qquad\qquad\qquad\qquad\qquad\qquad\qquad\qquad\qquad &\quad \cdot \\
\cdot \qquad\qquad\qquad\qquad\qquad\qquad\qquad\qquad\qquad\qquad &\quad \cdot \\
\cdot \qquad\qquad\qquad\qquad\qquad\qquad\qquad\qquad\qquad\qquad &\quad \cdot \\
m_N \cdot \ddot{y}_N + f_N(y_1, \dot{y}_1, y_2, \dot{y}_2, \ldots, y_N, \dot{y}_N) &= x_N(t)
\end{aligned}
$$

is said to have N degrees–of–freedom. As before, such a system is nonlinear if any products of variables higher than first order appear in the restoring force functions $f_1,\ldots,f_N$. In general, systems can have an infinite number of degrees of freedom. It is assumed in this work that any system can be accurately modelled by one with a finite number of degrees–of–freedom. The ultimate problem of *identification* is to determine the equations of motion of this model or equivalently the mass m_i and the restoring force functions f_i. A less ambitious problem is simply to determine if a system is linear or not.

The reason why one should be concerned about linearity, is that nonlinear systems can exhibit very complex behaviour which linear systems cannot. The most spectacular examples of this can be found in the literature relating to chaotic systems (1); in this case one can excite a system with a periodic external force x(t) and observe an apparently random response y(t). A linear system always responds to a periodic excitation with a periodic output at the same frequency. At a less exotic level, but no less important for that; the stability theory of linear systems is well understood, in direct contrast to that for nonlinear systems (2). Consequently if one is attemping to predict the behaviour of a nonlinear structure with a linear model, one might obtain results which are seriously in error.

Arguably the simplest test for linearity is to look for violations of the principle of superposition. This can be stated as follows; given that a system responds to an input $x_1(t)$ with an output $y_1(t)$, and to $x_2(t)$ with $y_2(t)$, superposition is observed if and only if the input $ax_1(t) + bx_2(t)$ provokes the response $ay_1(t) + by_2(t)$ for all contstants a and b (with appropriate initial conditions). If and only if superposition is observed for all possible inputs $x_1(t)$ and $x_2(t)$, can the system be defined as linear.

Clearly, this is of limited use experimentally, one can only carry out a finite number of experiments.

If one measures the Frequency Response Function (FRF) for a system one can make use of the fact that the form of the FRF has a well-known mathematical form which is independent of the level of excitation for a linear system. Attempts have been made to characterise nonlinearities from observations of how much the FRFs depart from this form as the level of forcing is increased ((3) and the references therein).

A more sophisticated diagnostic tool is provided by the Hilbert transform ((4) and references therein). This is essentially an analytic relationship between the real and imaginary parts of the FRF for a linear system which does not hold for most common nonlinear systems. The Hilbert transform approach extends naturally to MDOF systems and can allow one to associate the nonlinearity with particular modes of vibration of the system (5). Unfortunately, the procedure only gives qualitative information about the type of nonlinearity.

The Volterra/Wiener functional series approach to identification (6) is considerably more sophisticated. The curve-fitting procedures of classical modal analysis (7) where parameters are extracted from the linear FRF, can be extended to nonlinear systems by fitting surfaces or hypersurfaces to higher order frequency response functions (8). By this method one can extract the coefficients of nonlinear terms in the equations of motion. At the moment use of these methods is restricted by the fact that the higher order FRFs require a great deal of storage space and are difficult to interpret. Previous criticisms based on the computation time required have been answered by recent work which allows the higher order FRFs to be calculated very quickly using the NARMAX time-series methods (9) which themselves provide a very powerful identification technique as they allow one to construct a nonlinear difference equation model of a system.

Arguably the most general methods of identification are the restoring force methods

which, in principle, allow one to determine the form of the internal forces and hence the equations of motion of the system (or some appropriate finite order approximation). The raw material for the procedures are samples of measured time data x(t), ẏ(t), ẏ(t) and y(t) obtained from the system. The first appearance of an approach of this type is in the work of Masri and Caughey **(10)**. Their method allows one to represent the force f(y,ẏ) as a double expansion in Chebyshev polynomials in the variables y and ẏ which can be then plotted as a surface over the phase plane. This gives a direct visual representation of the type of nonlinearity present. In subsequent papers the authors and their collaborators extended the method to MDOF systems **(11)(12)** by expressing the forces f_1 to f_N as sets of double Chebyshev expansions. The expansion variables used were the normal coordinates for the system which meant that an estimate of the modal matrix $[\psi]$ was required. As in the SDOF case, the restoring force expansions can be plotted as surfaces. Very little experimental data was presented in support of their method, the majority of examples being computer simulations. In their earlier papers it is assumed that the mass matrix for the system is known, the more recent work is concerned with estimating the mass matrix from the measured time data **(13)**.

Essentially the same approach based on polynomial expansion rather than Chebyshev series was obtained independently by Crawley, O'Donnell and Aubert **(14)(15)** and christened the 'force–state mapping' technique. Direct least–squares techniques are used on the measured time data to determine the coefficients in the expansion. As before, the restoring force can be represented by a surface over the phase plane. Although their work is restricted to SDOF systems they do present extremely careful experimental verification of the utility of their procedure.

Yang and Ibrahim later used least–squares methods to identify MDOF systems **(16)**. By exploiting the symmetry of the system parameter matrices, they were able to determine the equations of motion for a single–input–multi–output (SIMO) system by using only the measured outputs together with an estimate of the total mass of the system. Only simulated systems were considered. Shye and Richardson **(17)** later made

use of symmetry in the same way. However, their work was based on measured freqency response functions and restricted to linear systems.

Recent work by Al-Hadid and Wright **(18)(19)** has concentrated on direct least-squares methods. They show using computer simulations that polynomial expansions are superior to Chebyshev expansions. A particular form for the system model is used which not only allows one to determine the type of nonlinearity present but also indicates the location of the nonlinear element within a lumped parameter model. An experimental study of a two degree-of-freedom system is presented. The thesis of Al-Hadid **(20)** presents a novel technique for determining the system mass matrix.

The restoring force surfaces are shown to be obtainable by an optimal control technique in the work of Lo, Hammond and Seager-Smith **(21)**. This paper is unique in it's consideration of the identification of a class of hysteretic systems. In the thesis of Lo **(22)**, the techniques are applied experimentally in a study of a class of vibration isolators. In their most recent work **(23)**, the optimal control approach appears to have been discarded in favour of a direct least-squares approach.

A group of researchers from Leuven, Mertens et.al. have presented a method of obtaining the damping or stiffness curves for a nonlinear SDOF system which they call the 'complex stiffness method' **(24)**. The method appears to be restricted to SDOF systems. Another limitation is that nonlinear cross-terms i.e. $y.\dot{y}$ cannot be accounted for.

The direct least-squares method has also been implemented in the frequency domain by Hunter et.al. **(25)**. An experimental study of a two degree-of-freedom system is presented.

The aim of the present work was to develop a practical identification procedure for nonlinear systems based on the restoring force methods. Chapter 1 introduces the Hilbert transform and describes how one can use it to diagnose nonlinearity as a first

step in any attempt to identify a system. It is shown that one must take the asymptotic behaviour of the FRF into account if one wishes to obtain unambiguous results. The Masri/Caughey procedure is introduced in Chapters 2 and 3. The restoring force surfaces are obtained using an improved interpolation scheme which can produce a differentiable surface. Various caveats, modifications and improvements are described. The use of the procedure is demonstated on a number of simulated systems both SDOF and MDOF. Chapters 4 and 5 develop the theory for direct least-squares identification of a general lumped-parameter nonlinear system. Again, the approach is demonstrated on a number of simulated systems. The problems of data processing and design of experiments are addressed in Chapters 6 and 7. In particular, as one would measure $\ddot{y}(t)$ in general, and integrate to obtain $\dot{y}(t)$ and $y(t)$, a comparitive study is made of various numerical differentiation and integration procedures. Chapters 8 and 9 contain experimental studies of both SDOF and MDOF nonlinear systems. Comparisons are made with theoretical estimates of the system parameters. Chapter 10 describes a method of determining system parameters which vary with time. The procedure is applied to a number of simulated systems with time-dependent stiffnesses and also to experimental data. Finally Chapter 11 presents conclusions and some suggestions for further work.

CHAPTER 1

THE HILBERT TRANSFORM AND ASYMPTOTIC BEHAVIOUR OF FREQUENCY RESPONSE FUNCTIONS

Before one attempts to identify a system in detail, it is useful to have a procedure which can simply determine if the system is linear or nonlinear. Given this information one can decide how to proceed and model the system. Such a diagnostic tool is provided by the Hilbert transform.

1.1. Background.

The Hilbert Transform is an integral transform defined by

$$\{H(F)\}(\omega) = \frac{-1}{i\pi} \int_{-\infty}^{+\infty} d\Omega \, \frac{F(\Omega)}{\Omega - \omega} \qquad (1)$$

which has been used for some time now as a diagnostic tool in the identification of nonlinear systems **(4)**. The transform is simply a map which carries one function into another. Unlike the Fourier transform which maps functions in the 'time-domain' to functions in the 'frequency-domain' and vice-versa, the image of a function under the Hilbert transform remains in the same domain. The map actually reduces to the identity on a particular subclass of functions. The reason for the utility of the Hilbert transform in dynamics lies in the fact that the Frequency Response Functions (FRFs) of linear systems fall inside this subclass.

The FRF for a system can be defined as follows; if one excites a system with a harmonic force $X.\cos(\omega t)$, one will observe in the response a component at the same frequency $Y.\cos(\omega t + \varphi)$. The response at any given forcing frequency is therefore

specified by the phase lag $\varphi(\omega)$ together with the amplitude gain factor $Y(\omega)/X(\omega) = Y(\omega)/X \geqslant 0$. The gain and phase can be regarded as the polar representation of a function taking values in the plane. One can equally well think of such a function as taking values in the Argand diagram. The response can therefore be specified by a complex function $H(\omega) = H_r(\omega) + iH_i(\omega)$ such that

$$H_r(\omega) = \{Y(\omega)/X\}.\cos\{\varphi(\omega)\}$$

$$H_i(\omega) = \{Y(\omega)/X\}.\sin\{\varphi(\omega)\}$$

It is not difficult to show that for a linear system, the FRF is the same function of frequency ω as the transfer function defined by

$$\text{Transfer function} = \frac{\text{Fourier transform of output signal}}{\text{Fourier transform of input signal}}$$

Now, because the Hilbert transform operator reduces to the identity if $F(\omega)$ is the FRF of a linear system,

$$\{H(F)\}(\omega) = F(\omega) = \frac{-1}{i\pi}\int_{-\infty}^{+\infty} d\Omega \, \frac{F(\Omega)}{\Omega - \omega} \qquad (2)$$

The reason for this result will be shown later. If $F(\omega)$ is the FRF of a nonlinear system, equation (2) need not hold, the Hilbert transform of $F(\omega)$ need not be the same function as $F(\omega)$. The usefulness of the transform is greatly increased by the fact that equation (2) does not appear to hold for systems containing the most commonly occuring types of nonlinearity encountered in structural dynamics. For example, systems with piecewise linear or polynomial stiffness, or systems with polynomial damping or Coulomb friction **(5)**.

A number of examples will serve to illustrate the sort of distortions which occur when one uses the Hilbert transform defined by equation (1) on the FRF of a nonlinear system. The method used to determine the transform in the examples is the so-called

frequency-domain method, where one simply discretises the integral (1) to obtain

$$\{H(F)\}(\omega_i) = \frac{-\Delta\omega}{i\pi} \sum_{j=-n}^{+n} \frac{F(\Omega j)}{\Omega_j - \omega_i} \qquad (3)$$

so the measurements of the FRF are required at a number of equally spaced frequency points ω_i where $i = -n,\ldots,+n$. Details of how one evaluates the integral including how one deals with the pole and how one removes the negative frequency part of the range are given in **(5)**.

The FRFs for the examples which follow are obtained by simulating the systems using a fourth-order Runge-Kutta procedure. For each frequency ω_i, the system is excited with a force $X.\sin(\omega_i t)$. The output from the simulation $Y.\sin(\omega_i t + \varphi)$ is examined and the amplitude $Y(\omega_i)$ and phase $\varphi(\omega_i)$ are obtained. The frequency response function amplitude and phase, $Y(\omega_i)/X$ and $\varphi(\omega_i)$ are now known at ω_i. Other methods of obtaining the FRF i.e from random excitation or impulse testing can be shown to be sub-optimal for carrying out the Hilbert transform test **(26)**.

Example (i). The FRF for the Single Degree-of-Freedom (SDOF) linear system governed by the equation of motion,

$$\ddot{y} + 20\dot{y} + 10^4 y = x(t)$$

was obtained. The FRF and it's Hilbert transform are displayed in Figure 1.1. The Nyquist plot i.e. the plot of the FRF in the Argand diagram, for the same data is shown in Figure 1.2. (In general, the Nyquist plot for the FRF of a linear system will be an ellipse. However, the following plots are all scaled so that they appear to be circular.) The two functions overlay almost perfectly. There is some difference at high frequencies; this is the result of approximating (1) by (3). The integral has an infinite range, the summation only considers data on the truncated range $-\omega_n$ to ω_n.

Example (ii). In this case a Duffing oscillator, with the equation of motion,

$$\ddot{y} + 20\dot{y} + 10^4 y + 5x10^9 y^3 = x(t)$$

was used. The system was excited with the amplitude X equal to 1.0. At lower levels of excitation the system essentially behaved as if it were linear. The FRF obtained is shown in Figure 1.3 together with it's Hilbert transform. The transform is shifted to the right of the FRF near the resonance. This shift is characteristic of systems with hardening stiffnesses. The distortion is shown most clearly in the Nyquist plane (Figure 1.4). The circle is rotated clockwise and is elongated to form an ellipse. One can see that the FRF itself suffers no distortion at this level of excitation, it still looks like that of a linear system. One concludes that the Hilbert transform is quite a sensitive indicator of nonlinearity. At higher levels of excitation, X = 5.0, the Duffing oscillator exhibits a jump phenomenon. This is illustrated in Figure 1.5 which shows the FRF and Hilbert transform at a high level of excitation. In this case one can deduce that the system is nonlinear from looking at the grossly distorted FRF. The Hilbert transform is still right–shifted. The characteristic clockwise rotation in the Nyquist plane is shown in Figure 1.6.

Example (iii). In this case the sign of the cubic term in the last example is changed so that the system now represents one with a softening stiffness nonlinearity i.e.

$$\ddot{y} + 20\dot{y} + 10^4 y - 5x10^9 y^3 = x(t)$$

This system becomes unstable at high levels of excitation when the cubic part of the restoring force becomes dominant and drives the system away from the equilibrium. A level was chosen which gave an indication of nonlinearity and also allowed the system output to remain bounded. The FRF obtained and it's Hilbert transform are shown in Figure 1.7. In this case the transform is left–shifted, this is characteristic of softening systems. Some distortion of the FRF is noticeable in this case. If one considers the Nyquist plot for the FRF (Figure 1.8) one observes that the transform of the FRF

'circle' is elongated as before, but rotated anti-clockwise this time.

Example (iv). The FRF Y_1/X_1 is obtained for the linear two degree-of-freedom system governed by the equations of motion,

$$\begin{bmatrix} \ddot{y}_1 \\ \ddot{y}_2 \end{bmatrix} + 20\begin{bmatrix} \dot{y}_1 \\ \dot{y}_2 \end{bmatrix} + 10^4\begin{bmatrix} 2 & -1 \\ -1 & 2 \end{bmatrix}\begin{bmatrix} y_1 \\ y_2 \end{bmatrix} = \begin{bmatrix} x_1 \\ 0 \end{bmatrix}$$

It is displayed in Figure 1.9, together with it's Hilbert transform. The Nyquist plot is given in Figure 1.10. As before, the overlay is nearly perfect. This is an illustration that the diagnostic method extends straightforwardly to MDOF systems.

These examples demonstrate the utility of the Hilbert transform as a diagnostic tool. It is unfortunate but the transform does not seem to be able to give more than gross qualitative information about the *type* of nonlinearity present. This appears to be because the transform is only sensitive to the position of the poles of the FRF in a fairly coarse way. It is also sensitive to the high-frequency behaviour of the FRF. These remarks will be justified in subsequent sections of this chapter as the basic theory is developed.

1.2. The Theory of the Hilbert Transform.

It can be argued that the Hilbert transform arises most naturally in the study of analytic functions of a complex variable. If one adopts this approach, the starting point is Cauchy's Theorem **(27)**, which states: given a function $F : \mathbb{C} \to \mathbb{C}$ and a simple closed contour C such that F is analytic on C and inside C, then

$$\frac{1}{2\pi i}\int_C d\Omega\ \frac{F(\Omega)}{\Omega - \omega} = 0 \qquad (4)$$

if and only if ω lies outside C. The basic derivation of the Hilbert transform is well known. However, it is included here as each step will be considered in reverse order

in section 6 when Fourier transform conventions are discussed. Before continuing, information is needed about the value of the integral in (4); (a) when ω is inside C, and (b) when ω is on C.

(a) ω inside C. In this case one can use the Residue Theorem (27) to find the value of the integral, i.e.

$$\frac{1}{2\pi i}\int_C d\Omega\ \frac{F(\Omega)}{\Omega - \omega} = \sum_{\text{Poles}} \text{Res}\left[\frac{F(\Omega)}{\Omega - \omega}\right]$$

where Res($A(z_i)$) is the residue of the function A(z) at the pole $z = z_i$. Now, if $F(\omega)$ is analytic inside C, the only pole in the integrand is the simple pole at $\Omega = \omega$.

As the pole is simple, the residue is given by

$$\lim_{\Omega \to \omega} (\Omega - \omega).\ \frac{F(\Omega)}{\Omega - \omega} = F(\omega)$$

$$\therefore \quad \frac{1}{2\pi i}\int_C d\Omega\ \frac{F(\Omega)}{\Omega - \omega} = F(\omega) \qquad \text{If } \omega \text{ is inside C.}$$

(b) ω on C. In all the arguments used in this work, only one sort of contour is needed, so for the sake of simplicity the results shown below are proved using that contour. The argument is lifted almost verbatim from (28).

Consider the contour in Figure 1.11. Initially $\omega = u - iv$ is below the real axis, the residue theorem gives

$$F(\omega) = F(u - iv) = \frac{1}{2\pi i}\int_{-R}^{+R} d\Omega\ \frac{F(\Omega)}{\Omega - u + iv} + I_C$$

where I_C is the integral over the semicircular part of the contour. If one now allows $R \to \infty$ and makes the additional assumption that $F(\Omega)/(\Omega - \omega)$ tends to zero as $\Omega \to \infty$ fast enough to make I_C vanish (for example supppose $F(\omega)$ is $O(R^{-1})$ as $R \to \infty$,

then the integrand is $O(R^{-2})$ and the integral is $\approx \pi R.O(R^{-2}) = O(R^{-1})$ and tends to zero as $R \to \infty$), one obtains

$$F(\omega) = F(u - iv) = \frac{1}{2\pi i} \int_{-\infty}^{+\infty} d\Omega \frac{F(\Omega)}{\Omega - u + iv} \qquad (5)$$

If one wishes to restrict the integrand in (5) to real values one must have $v \to 0$. i.e. $\omega \to u$. However, it is essential to the argument that ω should lie off the contour i.e. the real axis. One therefore defines a new section of contour C' which is deformed around $\Omega = u$, as shown in Figure 1.12.

Equation (5) becomes

$$2\pi i\, F(\omega) = 2\pi i \lim_{v \to 0} F(u - iv)$$

$$= \lim_{r \to 0} \left\{ \lim_{v \to 0} \int_{C'} d\Omega \frac{F(\Omega)}{\Omega - u + iv} \right\}$$

$$= \lim_{r \to 0} \left\{ \int_{+\infty}^{\omega+r} d\Omega \frac{F(\Omega)}{\Omega - \omega} + \int_{\omega-r}^{-\infty} d\Omega \frac{F(\Omega)}{\Omega - \omega} + \int_{0}^{\pi} \frac{r d(e^{i\theta})}{re^{i\theta}} F(\omega + re^{i\theta}) \right\}$$

$$= - PV \int_{-\infty}^{+\infty} d\Omega \frac{F(\Omega)}{\Omega - \omega} + i\pi F(\omega)$$

where PV is the Cauchy principal value. The final result is

$$\pi i\, F(\omega) = - PV \int_{-\infty}^{+\infty} d\Omega \frac{F(\Omega)}{\Omega - \omega} \qquad \omega, \Omega \in R \qquad (6)$$

Now,

$$\int_{-\infty}^{+\infty} d\Omega \frac{F(\Omega)}{\Omega - \omega} = \{H(F)\}(\omega)$$

where H(F) is the Hilbert transform of F, so one has the result.

$$-\pi i\ F(\omega) = \{H(F)\}(\omega) \qquad (7)$$

under the following assumptions:

(i) F is analytic in the area bounded by C, which is the lower half-plane in the limit $R \to \infty$.

(ii) $F(\omega)$ tends to zero fast enough as $R \to \infty$ for I_C to vanish.

It is convenient and also conventional to absorb the factor $-\pi i$ into the definition of the Hilbert transform. In this case, equation (7) becomes

$$\{H(F)\}(\omega) = F(\omega) \qquad (8)$$

If one now decomposes $F(\omega)$ into it's real and imaginary parts, the complex equation (8) splits into the two real equations

$$\text{Re } F(\omega) = -\frac{1}{\pi} PV \int_{-\infty}^{+\infty} d\Omega \frac{\text{Im } F(\Omega)}{\Omega - \omega} \qquad (9a)$$

$$\text{Im } F(\omega) = +\frac{1}{\pi} PV \int_{-\infty}^{+\infty} d\Omega \frac{\text{Re } F(\Omega)}{\Omega - \omega} \qquad (9b)$$

One can now see that under the conditions stated above, the real part of $F(\omega)$ uniquely fixes the imaginary part and vice versa. This is not an altogether surprising result if one recalls that simply assuming that $F(\omega)$ is differentiable allows one to relate the real and imaginary parts via the Cauchy–Riemann equations. The importance of condition (ii) will be made obvious in the following section.

1.3. Titchmarsh's Theorem.

The argument of the previous section is expressed rigorously by Titchmarsh's theorem which states (in the version taken from **(29)**)

Theorem If $F(\omega)$ is the Fourier transform of a function which vanishes for $t < 0$ and

$$\int_{-\infty}^{+\infty} d\omega \mid F(\omega) \mid^2 < \infty$$

then $F(\omega)$ is the boundary value of a function $F(\omega - i\gamma)$, $\gamma > 0$, which is analytic in the lower half-plane. Further

$$\int_{-\infty}^{+\infty} d\omega \mid F(\omega - i\gamma) \mid^2 < \infty$$

The last section indicated that the conditions (i) analycity in the lower half-plane, and (ii) fast fall-off of $F(\omega)$, are necessary for the Hilbert transform relations to hold. Titchmarsh's theorem states that they are sufficient and that $F(\omega)$ need only tend to zero as $\omega \to \infty$ fast enough to ensure the existence of $\int d\omega |F(\omega)|^2$.

The theorem is therefore concerned with Lesbegue square-integrable functions. Square-integrability is in any case a necessary condition for the existence of the Fourier transform of a function. If one assumes that all relevant transforms and inverses exist, one can express the theorem in a more straightforward form.

Theorem If one of (i),(ii) or (iii) is true, then so are the other two.

$F(\omega)$: (i) Satisfies Hilbert transform relations (9),

(ii) has a causal inverse Fourier transform

i.e. if $t < 0$, $f(t) = \{\mathcal{F}^{-1}(F)\}(t) = 0$,

(iii) is analytic in the lower half-plane.

The simple arguments of the previous section allowed the proof of (i) $\Leftrightarrow$ (iii). A fairly simple demonstration that (i) $\Leftrightarrow$ (ii) can be made, and this establishes the theorem.

(a) (i) $\Leftrightarrow$ (ii)

One assumes that $$F(\omega) = -\frac{1}{\pi i}\int_{-\infty}^{+\infty} d\Omega\ \frac{F(\Omega)}{\Omega - \omega}$$

(dropping the principal value PV). Then as

$$f(t) = \{F^{-1}(F)\}(t) = \frac{1}{2\pi}\int_{-\infty}^{+\infty} d\Omega\ e^{i\omega t}\ F(\omega)$$

One has

$$f(t) = -\frac{1}{2\pi}\int_{-\infty}^{+\infty} d\omega\ e^{i\omega t}\ \frac{1}{\pi i}\int_{-\infty}^{+\infty} d\Omega\ \frac{F(\Omega)}{\Omega - \omega}$$

Assuming that one can interchange the order of integration, one obtains,

$$f(t) = +\frac{1}{2\pi}\int_{-\infty}^{+\infty} d\Omega\ F(\Omega)\ \frac{1}{\pi i}\int_{-\infty}^{+\infty} d\omega\ \frac{e^{i\omega t}}{\omega - \Omega}$$

It is shown in appendix A that

$$\frac{1}{\pi i}\int_{-\infty}^{+\infty} d\omega\ \frac{e^{i\omega t}}{\omega - \Omega} = e^{i\Omega t}\cdot\varepsilon(t)$$

where $\varepsilon(t)$ is the sign function, $\varepsilon(t) = 1$ if $t > 0$, $\varepsilon(t) = -1$ if $t < 0$.

This implies that

$$f(t) = \frac{1}{2\pi}\int_{-\infty}^{+\infty} d\Omega\ F(\Omega)e^{i\Omega t} = f(t) \quad \text{if } t > 0$$

and

$$f(t) = \frac{-1}{2\pi}\int_{-\infty}^{+\infty} d\Omega\ F(\Omega)e^{i\Omega t} = -f(t) \quad \text{if } t < 0$$

which is only true if $f(t) = 0$ for all $t < 0$. Notice that one does not need to say anything about the value of $\varepsilon(t)$ at $t = 0$. This is because $\varepsilon(t)$ only appears under the integral sign and it's value at one point cannot affect the value of the integral.

(b) (ii) $\Leftrightarrow$ (i).

Suppose that $f(t) = \{\mathcal{F}^{-1}(F)\}(t) = 0$ if $t < 0$. Consider the object

$$\frac{-1}{\pi i}\int_{-\infty}^{+\infty} d\Omega\ \frac{F(\Omega)}{\Omega - \omega}$$

This is a convolution, equal to $F(\omega)*(2/i\omega)$

$$\therefore \quad \mathcal{F}^{-1}\left\{\frac{-1}{\pi i}\int_{-\infty}^{+\infty} d\Omega\ \frac{F(\Omega)}{\Omega - \omega}\right\} = \mathcal{F}^{-1}[F(\omega)] \times \mathcal{F}^{-1}(2/i\omega)$$

$$= f(t)\varepsilon(t)$$

and because $f(t)$ is causal

$$f(t)\varepsilon(t) = f(t)$$

so Fourier transforming the last equation gives

$$F(\omega) = \frac{-1}{\pi i}\int_{-\infty}^{+\infty} d\Omega\ \frac{F(\Omega)}{\Omega - \omega}$$

as required.

The last proof is useful because it provides a time-domain version of the Hilbert transform

$$\{H(F)\}(\omega) = \frac{-1}{i\pi}\int_{-\infty}^{+\infty} d\Omega\ \frac{F(\Omega)}{\Omega - \omega}$$

$$= F \circ \mathcal{F}^{-1}\left\{\frac{-1}{i\pi}\int_{-\infty}^{+\infty} d\Omega\ \frac{F(\Omega)}{\Omega - \omega}\right\}$$

$$= F[\ \epsilon(t)f(t)\ ]$$

The symbol $\circ$ above indicates the composition of functions, i.e. $(f \circ g)(t) = f(g(t))$. These two sections provide a discussion of the relationship between causality and the Hilbert transform relations (9). It is important to point out again that the previous theorem only holds if the technicalities of Titchmarsh's theorem are satisfied. The next section shows how one can apply the Hilbert transform relations to functions which do not satisfy the necessary conditions, and re-examines cases where confusion has arisen (30,31).

1.4. Correcting for Bad Asymptotic Behaviour.

The crucial point in Titchmarsh's theorem is that $F(\omega)$ should be square-integrable i.e. $\int d\omega |F(\omega)|^2 < \infty$. It happens that in many cases of physical interest this condition is not satisfied. There is however, a way of circumnavigating this problem.

The least troublesome function one can have which is not square-integrable is one which tends to a constant value at infinity, i.e.

$$F(\omega) \to F_\infty \quad \text{as} \quad \omega \to \infty.$$

A sufficiently general example for the purposes of this report is

$$F(\omega) = \frac{A(\omega)}{B(\omega)} = \frac{a_0 + a_1\omega + \ldots + a_n\omega^n}{b_0 + b_1\omega + \ldots + b_n\omega^n} \qquad (10)$$

i.e. $A(\omega)$ and $B(\omega)$ are polynomials of the same order n, and all the zeroes of $B(\omega)$ are in the upper half-plane. Clearly one has

$$\lim_{\omega \to \infty} F(\omega) = F(\infty) = \frac{a_n}{b_n}$$

If one were to carry out a long division on $F(\omega)$, the result would be

$$F(\omega) = (a_n/b_n) + \frac{A'(\omega)}{B(\omega)}$$

where $A'(\omega)$ is a polynomial of order $n - 1$. So

$$F(\omega) - F(\infty) = F(\omega) - a_n/b_n = \frac{A'(\omega)}{B(\omega)}$$

Now, $A'(\omega)/B(\omega) \sim O(\omega^{-1})$ as $\omega \to \infty$. This means that $A'(\omega)/B(\omega)$ is square-integrable and therefore satisfies the conditions required by Titchmarsh's theorem. Hence,

$$\frac{A'(\omega)}{B(\omega)} = \frac{-1}{i\pi} \int_{-\infty}^{+\infty} d\Omega \, \frac{A'(\Omega)}{B(\Omega)} \, \frac{1}{\Omega - \omega}$$

i.e.

$$F(\omega) - F(\infty) = \frac{-1}{i\pi} \int_{-\infty}^{+\infty} d\Omega \, \frac{(F(\Omega) - F(\infty))}{\Omega - \omega}$$

So if a function fails to satisfy the conditions required by Titchmarsh's theorem because it fails to be square-integrable, one can sometimes subtract the asymptotic behaviour which causes the problems. This leaves a function which does satisfy the requirements. Equations (9a) and (9b) become:

$$\text{Re } F(\omega) - \text{Re } F(\infty) = \frac{-1}{\pi} \int_{-\infty}^{+\infty} d\Omega \, \frac{(\text{Im } F(\Omega) - \text{Im } F(\infty))}{\Omega - \omega} \quad (11a)$$

$$\text{Im } F(\omega) - \text{Im } F(\infty) = \frac{+1}{\pi} \int_{-\infty}^{+\infty} d\Omega \, \frac{(\text{Re } F(\Omega) - \text{Re } F(\infty))}{\Omega - \omega} \quad (11b)$$

These equations are well known in elementary particle physics and optics. The first of the pair produces the Kramers-Kronig dispersion relation if one takes $F(\omega) = n(\omega)$ the complex refractive index of a material. The term dispersion refers to the phenomenon of variation of refractive index with the frequency of incident radiation.

One possible obstruction to the direct application of equations (11a) and (11b) is that

one usually measures $F(\omega)$ in some experiment. Clearly in this case one cannot obtain $F(\infty)$. However, one can make use of a 'subtraction' scheme as follows. Suppose for the sake of simplicity that the imaginary part of $F(\omega)$ tends to zero as the frequency tends to infinity and one has a measurement of $F(\omega)$ at $\omega = \alpha$. Equation (11a) yields

$$\text{Re } F(\omega) - \text{Re } F(\infty) = \frac{-1}{\pi} \int_{-\infty}^{+\infty} d\Omega \, \frac{\text{Im } F(\Omega)}{\Omega - \omega} \qquad (12)$$

At $\omega = \alpha$, one has

$$\text{Re } F(\alpha) - \text{Re } F(\infty) = \frac{-1}{\pi} \int_{-\infty}^{+\infty} d\Omega \, \frac{\text{Im } F(\Omega)}{\Omega - \alpha} \qquad (13)$$

so, subtracting (11) from (12) gives

$$\text{Re } F(\omega) - \text{Re } F(\alpha) = \frac{-1}{\pi} \int_{-\infty}^{+\infty} d\Omega \left\{ \frac{1}{\Omega - \omega} - \frac{1}{\Omega - \alpha} \right\} \text{Im } F(\Omega)$$

i.e.

$$\text{Re } F(\omega) - \text{Re } F(\alpha) = \frac{(\omega - \alpha)}{\pi} \int_{-\infty}^{+\infty} d\Omega \, \frac{\text{Im } F(\Omega)}{(\Omega - \omega)(\Omega - \alpha)} \qquad (14)$$

So one can compensate for one's lack of knowledge of $F(\infty)$. However, notice that in doing so, one is faced with a more complicated integral. In general if $F(\omega)$ goes as some polynomial as $\omega \to \infty$ one can subtract the bad asymptotic behaviour in much the same way as above. Unfortunately, every time one performs a subtraction the integral gets more complicated.

One can now use the theory outlined above to re-examine cases where confusion has arisen in structural dynamics concerning the applicability of the Hilbert transform.

(1) It is clear from the preceeding arguments that the Hilbert transform provides a means of detecting which functions $F(\omega)$ correspond to non-causal $f(t)$. If one measures the transfer function $H(\omega)$ of a linear system $\{F^{-1}(H)\}(t) = h(t)$ is the impulse response of the system and $h(t) = 0$ for all $t < 0$. This means that (

assuming all other neccessary conditions hold), $\{H(H)\}(\omega) = H(\omega)$. In general, if the frequency response function of a *nonlinear* system $H_{nl}(\omega)$ is measured using the stepped-sine input described earlier, $\{F^{-1}(H_{nl})\}(t) = g(t)$ will not necessarily be causal. In fact, for all the types of nonlinearity commonly encountered in structural dynamics the function g(t) is non-causal. So, failure of the Hilbert transform relations $\Rightarrow$ g(t) non-causal and one can take this as an *indication* that the system is nonlinear.

Rodeman in (30) states this correctly. However, in order to show that the Hilbert transform does not infallibly detect nonlinear systems he considers the following squaring system.

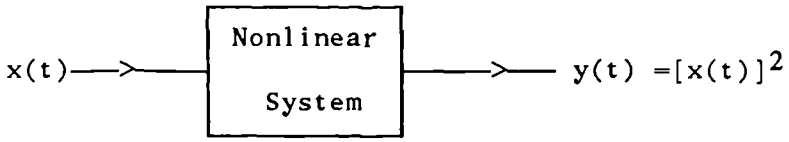

letting $x(t) = Ae^{-at} \quad t > 0, \quad a > 0$

$= 0 \quad t < 0$

(i.e. x(t) causal) one obtains the frequency response function

$$H_{nl}(\omega) = \frac{Y(\omega)}{X(\omega)} = \frac{A(\omega - ia)}{(\omega - 2ia)}$$

and

$$\text{Re } H_{nl}(\omega) = \frac{A(\omega^2 + 2a^2)}{\omega^2 + 4a^2}$$

$$\text{Im } H_{nl}(\omega) = \frac{Aa\omega}{\omega^2 + 4a^2}$$

He then argues that because $H_{nl}(\omega)$ is analytic in the lower half-plane, the real and imaginary parts of H_{nl} must form a Hilbert transform pair i.e. are related by the dispersion relations (9a) and (9b). This is <u>not</u> correct. If one evaluates the integrals one finds

$$\frac{1}{\pi}\int_{-\infty}^{+\infty} d\Omega \frac{\text{Re } H_{nl}(\Omega)}{\Omega - \omega} = \frac{Aa\omega}{\omega^2 + 4a^2} = \text{Im } H_{nl}(\omega)$$

as required. However,

$$\frac{-1}{\pi}\int_{-\infty}^{+\infty} d\Omega\ \frac{\text{Im } H_{n1}(\Omega)}{\Omega - \omega} = \frac{-2a^2A}{\omega^2 + 4a^2} \neq \text{Re } H_{n1}(\omega)$$

The reason for the error is that

$$\lim_{\omega \to \infty} H_{n1}(\omega) = A \neq 0$$

So $\int d\omega |H_{n1}(\omega)|^2$ does not exist and Titchmarsh's theorem does not hold. However, one observes that as Re $H_{n1}(\infty) = A$ and Im $H_{n1}(\infty) = 0$, the appropriate dispersion relation is (11a).

$$\text{Re } H_{n1}(\omega) - A = \frac{-1}{\pi}\int_{-\infty}^{+\infty} d\Omega\ \frac{\text{Im } H_{n1}(\Omega)}{\Omega - \omega}$$

i.e.

$$\text{Re } H_{n1}(\omega) = A - \frac{2a^2A}{\omega^2 + 4a^2}$$

$$= \frac{A(\omega^2 + 2a^2)}{\omega^2 + 4a^2}$$

as required. (In evaluating these integrals one obtains terms of the form $\int d\Omega/(\Omega - \omega)$ which are proportional to $\ln(-1)$. If one takes the principal sheet of the ln function one can disregard these terms.)

The problem shows up very clearly in the time domain. There, $H = F \circ X_\varepsilon \circ F^{-1}$ (where X_ε is pointwise multiplication by $\varepsilon(t)$). Now

$$\{F^{-1}(H_{n1})\}(t) = g(t) = \frac{1}{2\pi}\int_{-\infty}^{+\infty} d\omega\ e^{i\omega t}\left\{\frac{A(\omega - ia)}{(\omega - 2ia)}\right\}$$

$$= \frac{A}{2\pi}\int_{-\infty}^{+\infty} d\omega\ e^{i\omega t}\left\{1 + \frac{ia}{\omega - 2ia}\right\}$$

$$= \frac{A}{2\pi}\int_{-\infty}^{+\infty} d\omega\, e^{i\omega t} + \frac{iaA}{2\pi}\int_{-\infty}^{+\infty} d\omega\, \frac{e^{i\omega t}}{\omega - 2ia}$$

$$= A\delta(t) - g'(t).\theta(t)$$

so the 'impulse response' g(t) contains a Dirac δ-function together with a causal function.

, The removal of this δ-function is the time domain analogue of removing the bad asymptotic behaviour in the frequency domain.

This sort of behaviour will clearly occur for all cases where $F(\omega) = A(\omega)/B(\omega)$ as before. One needs to remove the δ-function $(a_n/b_n).\delta(t)$ from the 'impulse response'.

One concludes therefore that analycity in the lower half-plane is <u>not</u> a sufficient condition for the real and imaginary parts of a function to fprm a Hilbert transform pair.

In **(31)** Goyder illustrates the theory of the Hilbert transform with the linear system depicted in Figure 1.13. The system has the transfer function

$$H(\omega) = \frac{-i\omega}{c\omega - ik}$$

$$= \frac{k\omega}{c^2\omega^2 + k^2} - i\,\frac{c\omega^2}{c^2\omega^2 + k^2}$$

He correctly states that

$$\text{Re } H(\omega) = \frac{-1}{\pi}\int_{-\infty}^{+\infty} d\Omega\, \frac{\text{Im } H(\Omega)}{\Omega - \omega} = \frac{k\omega}{c^2\omega^2 + k^2}$$

However,

$$\lim_{\omega \to \infty} H(\omega) = \frac{-i}{c} \neq 0$$

so the appropriate dispersion relation for calculating Im $H(\omega)$ is

$$\text{Im } H(\omega) + \frac{1}{c} = \frac{1}{\pi} \int_{-\infty}^{+\infty} d\Omega \, \frac{\text{Re } H(\Omega)}{\Omega - \omega} = \frac{k^2}{c^3\omega^2 + ck^2}$$

$$\therefore \quad \text{Im } H(\omega) = \frac{k^2}{c^3\omega^2 + ck^2} - \frac{1}{c} = \frac{-c\omega^2}{c\omega^2 + k^2}$$

as required.

1.5. An Example of Engineering Interest.

If one measures the transfer function of a linear system defined by the equation of motion

$$m\ddot{y} + c\dot{y} + ky = x(t)$$

there are three forms it can take depending on the sort of output data one measures (7).

If one measures input force and output displacement one obtains the *receptance* form

$$H_r(\omega) = \frac{\{F(y)\}(\omega)}{\{F(x)\}(\omega)} = \frac{1}{-m\omega^2 + ic\omega + k}$$

and

$$\lim_{\omega \to \infty} H_r(\omega) = 0$$

Measuring the output velocity yields the *mobility* form

$$H_m(\omega) = \frac{\{F(\dot{y})\}(\omega)}{\{F(x)\}(\omega)} = \frac{i\omega}{-m\omega^2 + ic\omega + k}$$

and

$$\lim_{\omega \to \infty} H_m(\omega) = 0$$

Finally, if one measures output acceleration, one obtains the *inertance* form

$$H_i(\omega) = \frac{\{F(\ddot{y})\}(\omega)}{\{F(x)\}(\omega)} = \frac{-\omega^2}{-m\omega^2 + ic\omega + k}$$

and

$$\lim_{\omega \to \infty} H_i(\omega) = \frac{1}{m} \neq 0$$

This means that if one is testing for nonlinearity by applying the Hilbert transform to a transfer function, the appropriate Hilbert transform pair is (Re $H(\omega)$, Im $H(\omega)$) as expected, if the function is receptance or mobility type. However, if the function is of the inertance type the correct pair is (Re $H(\omega)$ − 1/m , Im $H(\omega)$) because the function has the form given in equation (10) i.e.

$$\text{Im } H_i(\omega) = \frac{1}{\pi} \int_{-\infty}^{+\infty} d\Omega \frac{(\text{Re } H_i(\Omega) - 1/m)}{\Omega - \omega}$$

$$= \frac{1}{\pi} \int_{-\infty}^{+\infty} d\Omega \frac{\text{Re } H_i(\Omega)}{\Omega - \omega}$$

after discarding the ln(−1) term. And

$$\text{Re } H_i(\omega) = \frac{-1}{\pi} \int_{-\infty}^{+\infty} d\Omega \frac{\text{Im } H_i(\Omega)}{\Omega - \omega} + \frac{1}{m}$$

Figure 1.14. shows the receptance transfer function and it's Hilbert transform for the linear system described by the equation,

$$\ddot{y} + 20\dot{y} + 10^4 y = x(t)$$

As one would expect, the overlay is perfect. Figure 1.15. shows the inertance transfer function and the uncorrected Hilbert transform. The Hilbert transform is shifted by −1/m as predicted. Overlay (apart from errors introduced by having to truncate the integral to allow for a finite frequency range,) could be obtained by using a subtraction, as in equation (14). A much simpler method is to convert the transfer function to receptance form using

$$H_r(\omega) = H_i(\omega)/(-\omega^2)$$

carry out the Hilbert transform and convert back to inertance. Figure 1.16. shows the result of carrying out this procedure.

In the case of a MDOF system (with proportional damping)

$$H_i(\omega) = \sum_{r=1}^{N} \frac{A_r\omega^2}{\omega_r^2 - \omega^2 + i\zeta_r\omega_r\omega}$$

The appropriate Hilbert transform pair is

$$\left(\text{Re } H_i(\omega) + \sum_{r=1}^{N} A_r \ , \ \text{Im } H_i(\omega) \right)$$

1.6. Fourier Transform Conventions.

Throughout this work the following conventions are used for the Fourier transform

$$F(\omega) = \{\mathcal{F}(f)\}(\omega) = \int_{-\infty}^{+\infty} dt \ e^{-i\omega t} \ f(t)$$

$$f(t) = \{\mathcal{F}^{-1}(F)\}(t) = \frac{1}{2\pi} \int_{-\infty}^{+\infty} d\omega \ e^{+i\omega t} \ F(\omega)$$

One could equally well choose the conventions,

$$F(\omega) = \int_{-\infty}^{+\infty} dt \ e^{+i\omega t} \ f(t)$$

$$f(t) = \frac{1}{2\pi} \int_{-\infty}^{+\infty} d\omega \ e^{-i\omega t} \ F(\omega)$$

These conventions shall be labelled F_- and F_+ respectively. Clearly, a continuous set of conventions are possible if one counts movements of the $(2\pi)^{-1}$ factor.

As one might expect, the Hilbert transform formulae depend critically on the convention used. The formulae for F_+ can be obtained as follows.

In the proof of (i) $\Leftrightarrow$ (ii) in section 3, the result

$$\frac{1}{i\pi}\int_{-\infty}^{+\infty} d\omega\ \frac{e^{i\omega t}}{\omega - \Omega} = e^{i\Omega t}\ \varepsilon(t) \qquad \text{(Appendix A.)}$$

was used. If F_+ conventions had been used, the term

$$\frac{1}{i\pi}\int_{-\infty}^{+\infty} d\omega\ \frac{e^{-i\omega t}}{\omega - \Omega} = -e^{-i\Omega t}\ \varepsilon(t)$$

would have been obtained. In order to cancel the negative sign generated, one would need the initial definition,

$$\{H(F)\}(\omega) = \frac{+1}{i\pi}\int_{-\infty}^{+\infty} d\Omega\ \frac{F(\Omega)}{\Omega - \omega}$$

To obtain this expression from the contour integration argument of the first section one would need the section of contour on the real line to go from $-\infty$ to $+\infty$. As one must move anticlockwise round the contour it needs to be completed in the upper half-plane. This means that the contour in Figure 1.17. is required. As a consequence of using this contour, one now requires analycity in the upper half-plane. The result of these arguments is the F_+ version of the second theorem of section 3. i.e. if one of (i)', (ii)' or (iii)' is true, then so are the other two.

$F(\omega)$: (i)' Satisfies Hilbert transform relations,

$$\mathrm{Re}\ F(\omega) = +\frac{1}{\pi}\int_{-\infty}^{+\infty} d\Omega\ \frac{\mathrm{Im}\ F(\Omega)}{\Omega - \omega}$$

$$\mathrm{Im}\ F(\omega) = -\frac{1}{\pi}\int_{-\infty}^{+\infty} d\Omega\ \frac{\mathrm{Re}\ F(\Omega)}{\Omega - \omega}$$

(ii)' has a causal inverse Fourier transform,

(iii)' is analytic in the upper half-plane.

The equations in (31) appear to be inconsistent in that equations (14) and (15) belong tp F_+ while all others belong to F_-.

Independently of convention, if one defines convolution by

$$F(\omega) * G(\omega) = \frac{1}{2\pi} \int_{-\infty}^{+\infty} d\Omega \; F(\Omega).G(\omega - \Omega)$$

one obtains the result

$$\{F^{-1}(F * G)\}(t) = f(t)g(t)$$

where $f(t) = \{F^{-1}(F)\}(t)$ and $g(t) = \{F^{-1}(G)\}(t)$. The statements about testing transfer functions for linearity made in section 4 apply to both F_+ and F_- . Suppose that a transfer function has poles in the upper half-plane in F_- . This means that the zeroes of the denominator

$$d_-(\omega) = -m\omega^2 + ic\omega + k$$

are in the upper half-plane. If one changes from F_- to F_+

$$d_-(\omega) \rightarrow d_+(\omega) = -m\omega^2 - ic\omega + k$$

i.e. the product of the roots remains the same while their sum changes sign. Clearly the roots of $d_+(\omega)$ are in the lower half-plane and one has analycity in the upper half-plane as required by the F_+ Titchmarsh theorem.

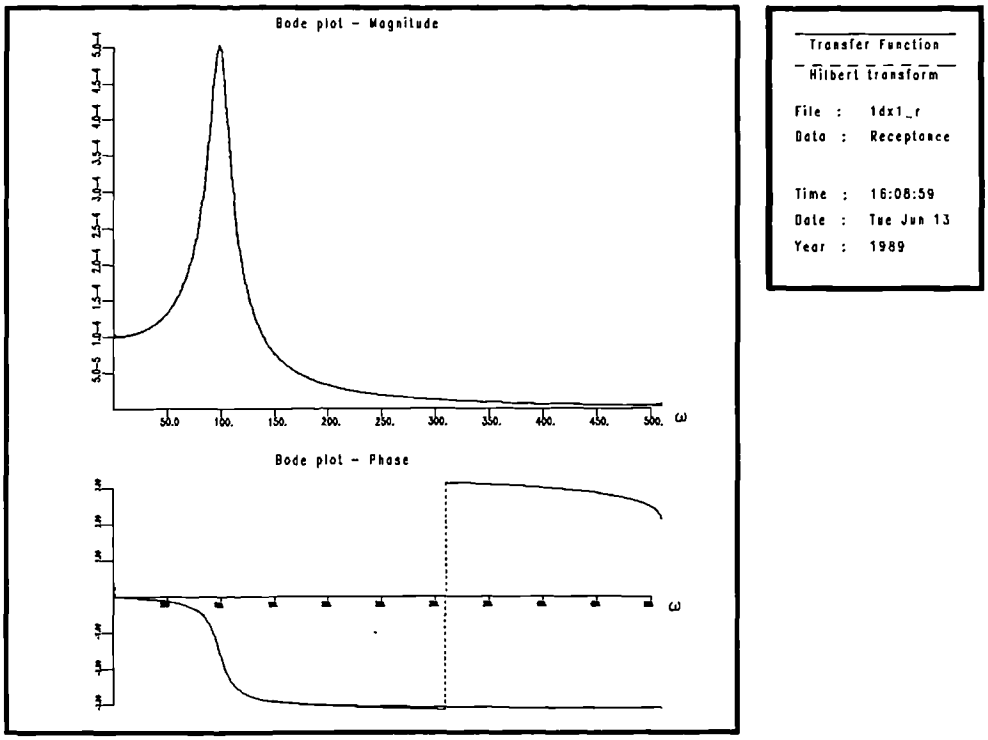

Figure 1.1 Bode plot of the FRF for the linear system of example (i) together with the Hilbert transform.

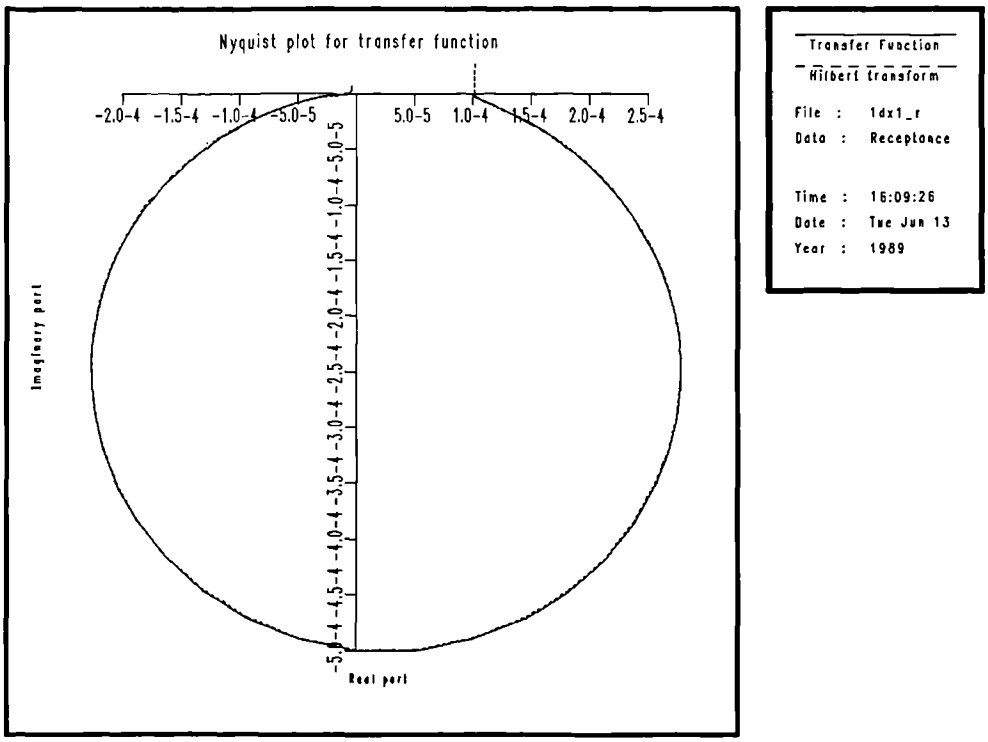

Figure 1.2 Nyquist plot and Hilbert transform for the FRF of the linear system of example (i).

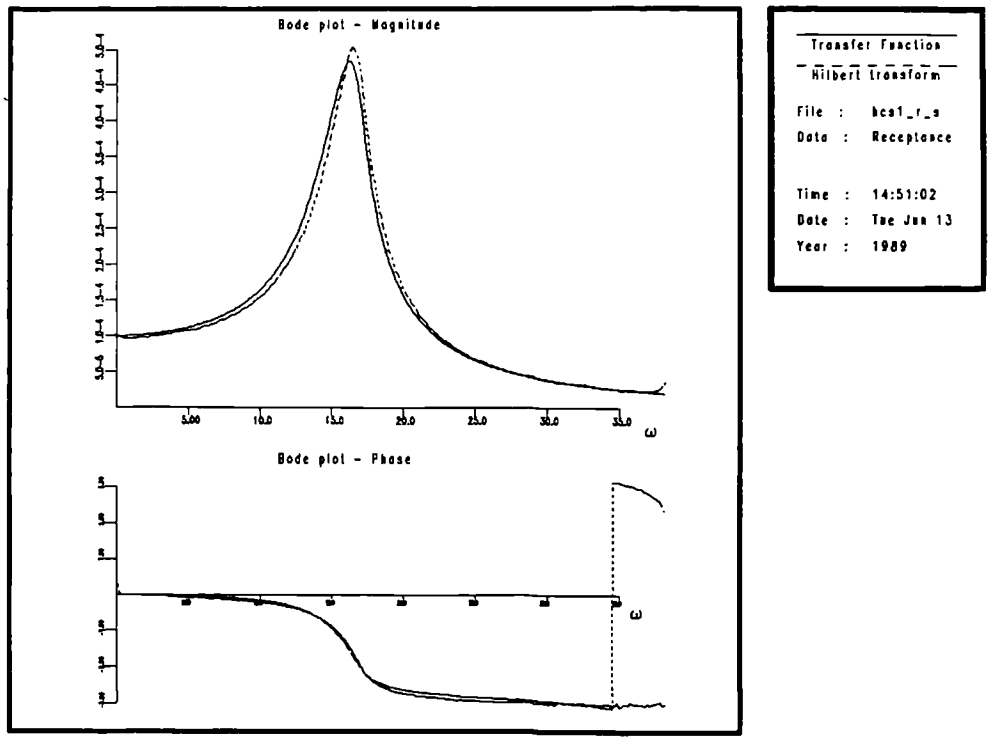

Figure 1.3. Bode plot and Hilbert transform for the FRF of the hardening cubic system of example (ii). Lower level of excitation.

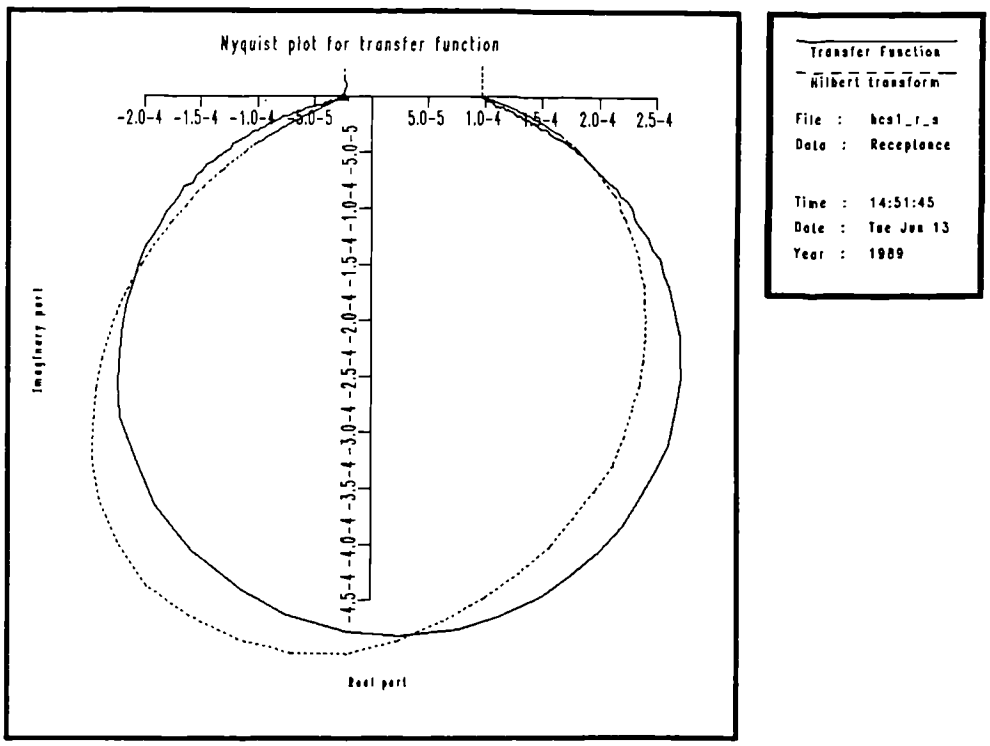

Figure 1.4. Nyquist plot and Hilbert transform for the FRF of the hardening cubic system of example (ii). Lower level of excitation.

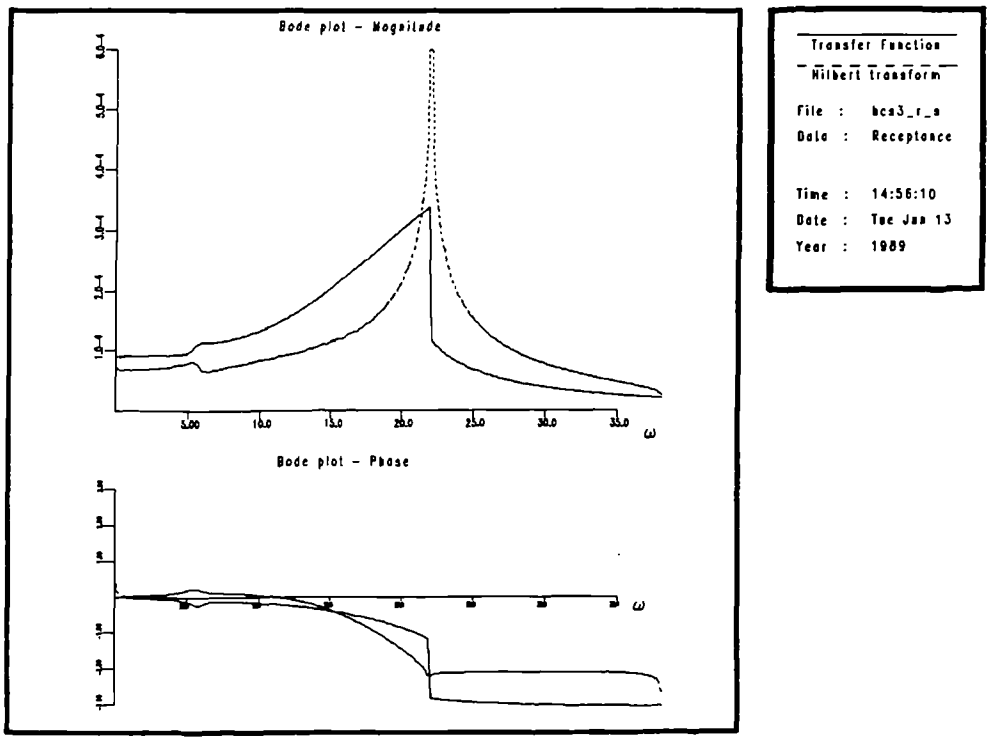

Figure 1.5. Bode plot and Hilbert transform for the FRF of the hardening cubic system of example (ii). Higher level of excitation.

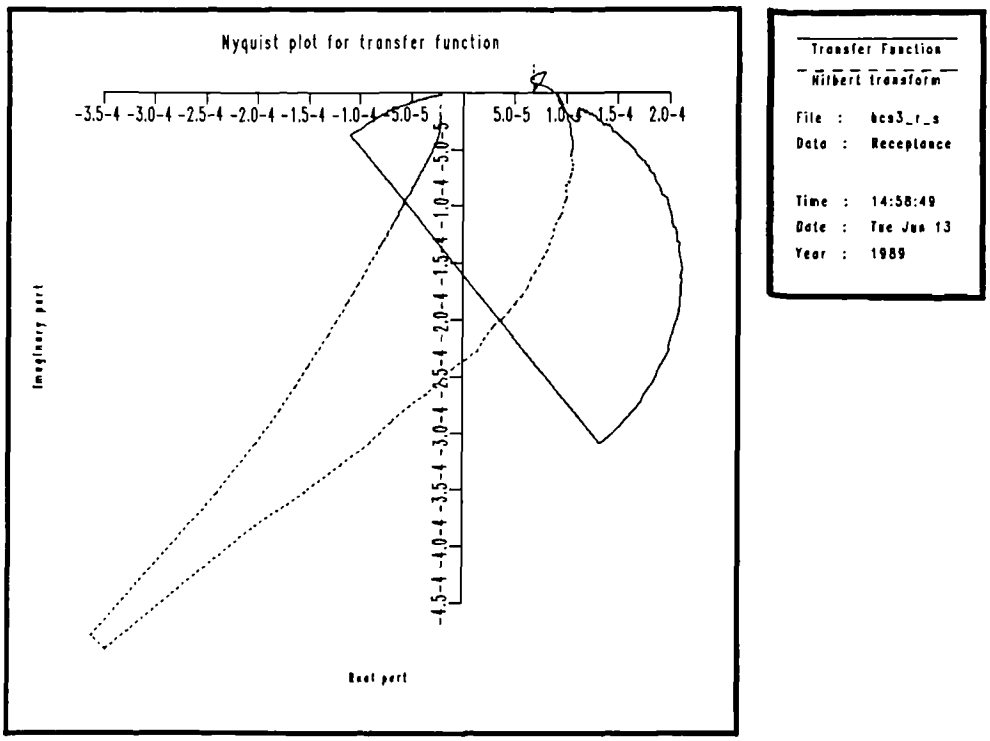

Figure 1.6. Nyquist plot and Hilbert transform for the FRF of the hardening cubic system of example (ii). Higher level of excitation.

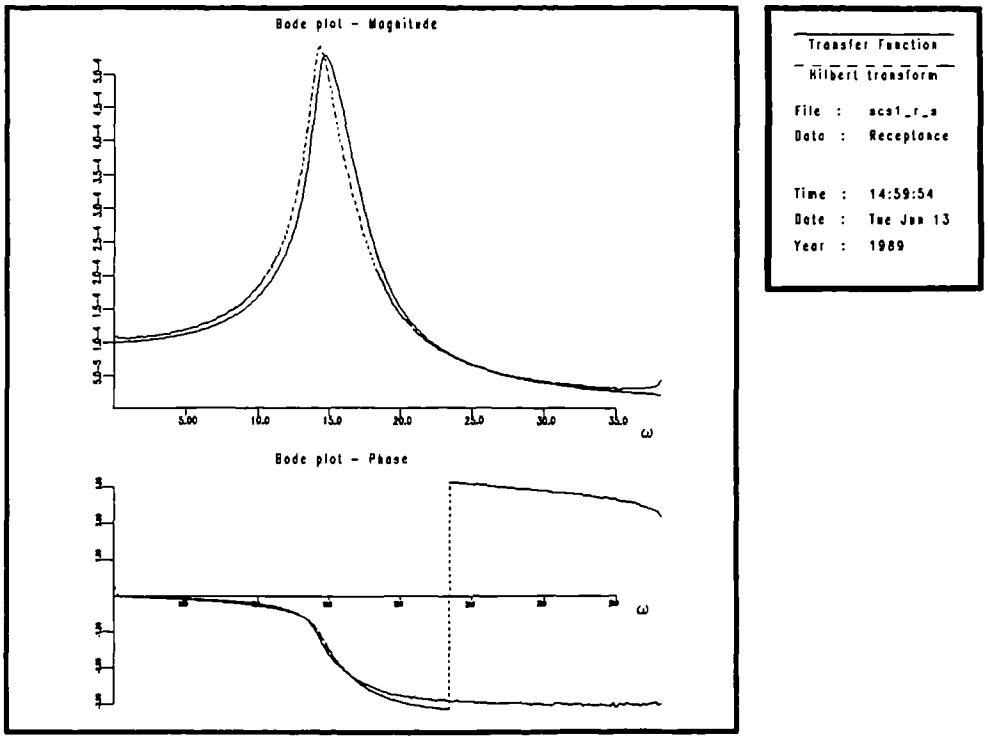

Figure 1.7. Bode plot and Hilbert transform for the FRF of the softening cubic system of example (iii).

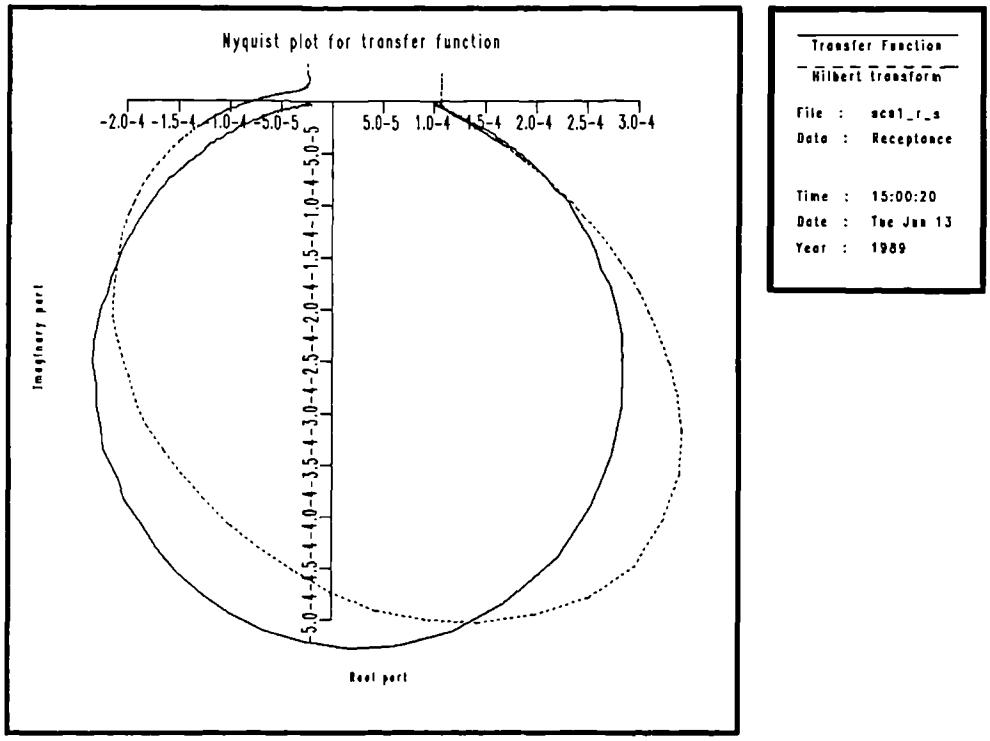

Figure 1.8. Nyquist plot and Hilbert transform for the FRF of the softening cubic system of example (iii).

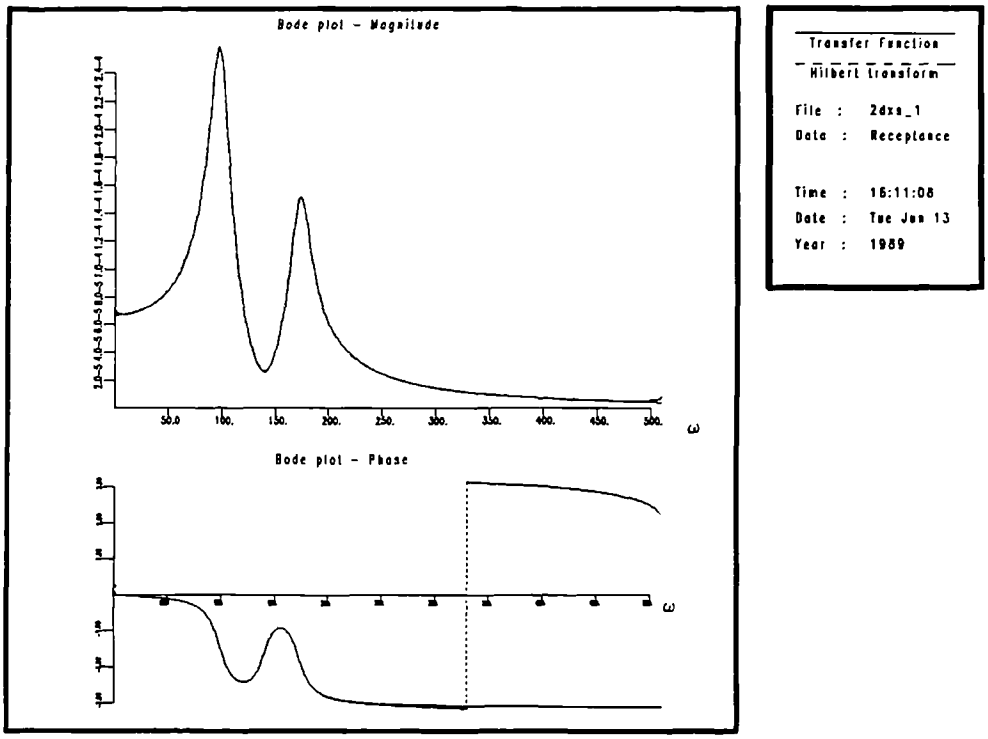

Figure 1.9. Bode plot and Hilbert transform for one of the FRFs of the linear two degree-of-freedom system of example (iv).

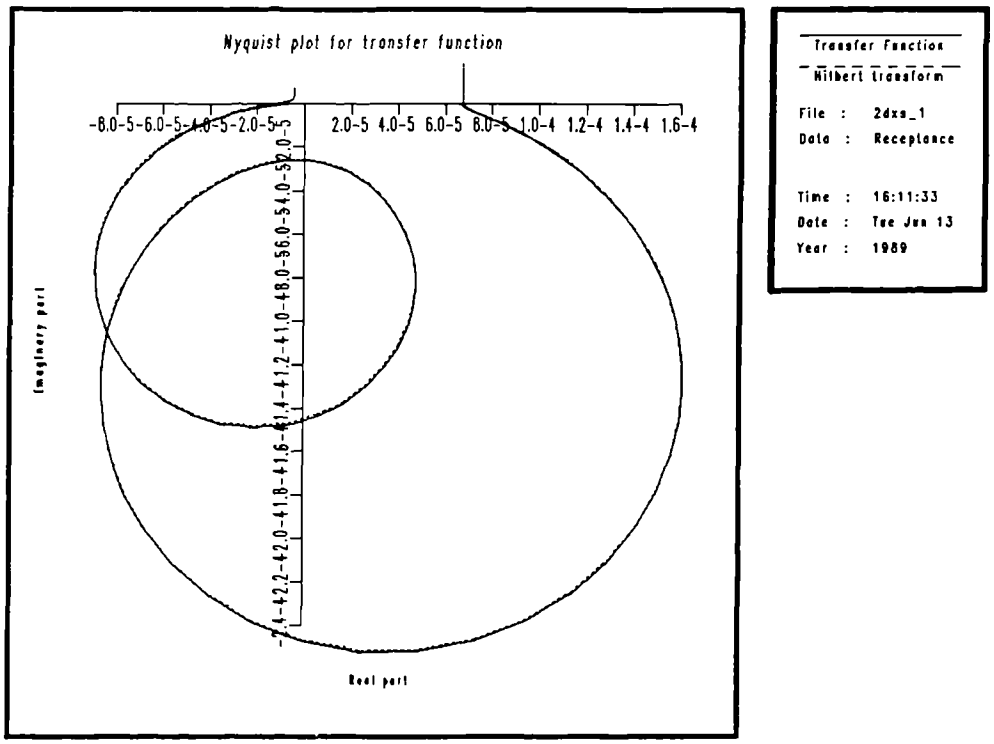

Figure 1.10. Nyquist plot and Hilbert transform for one of the FRFs of the linear two degree-of-freedom system of example (iv).

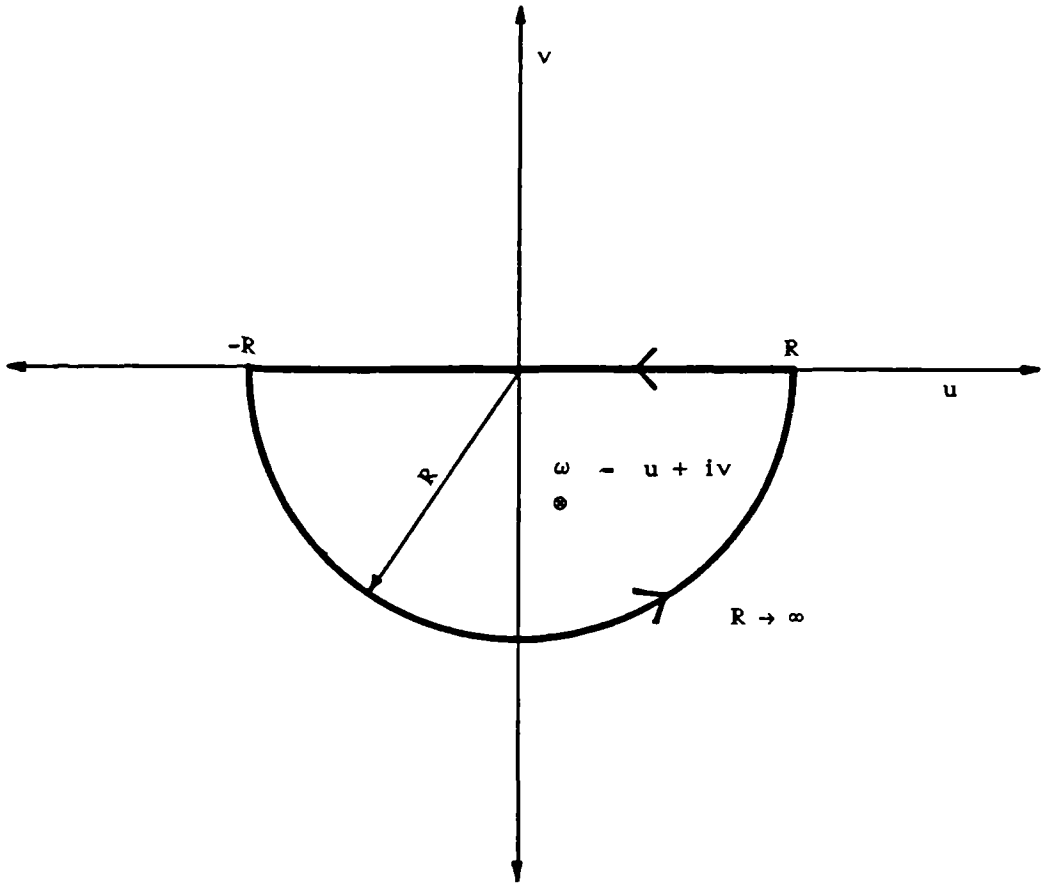

Figure 1.11. Contour in the complex plane used to obtain the Hilbert transform relations.

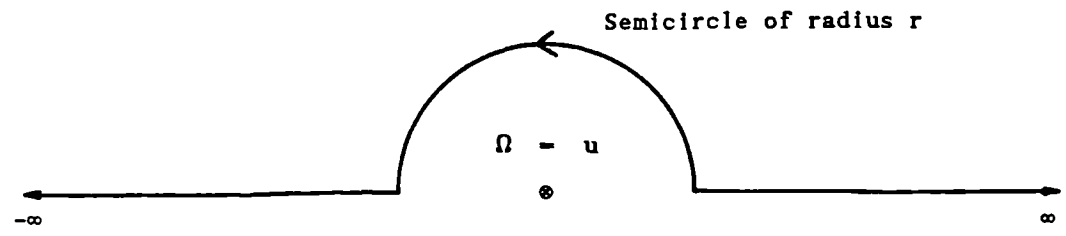

Figure 1.12. Deformation of the contour around the pole on the real axis.

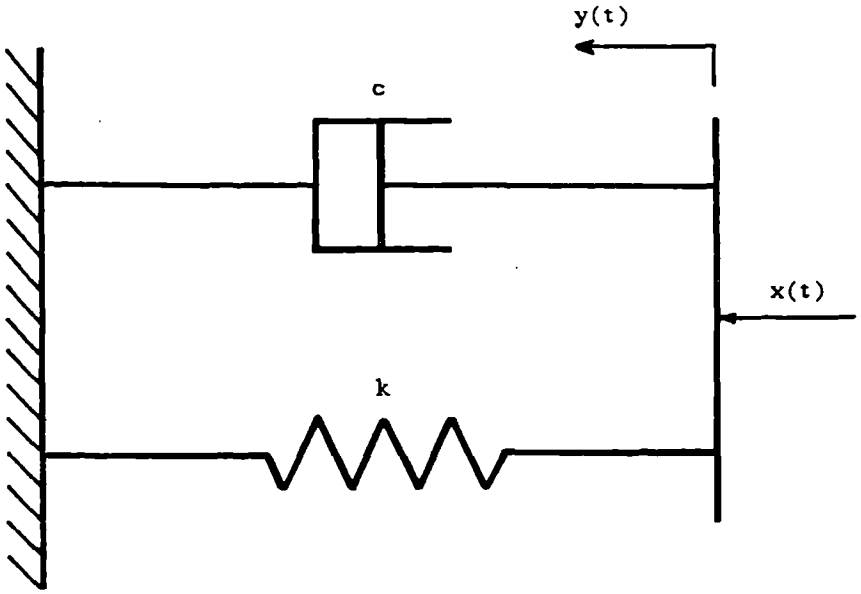

Figure 1.13. A first-order dynamical system.

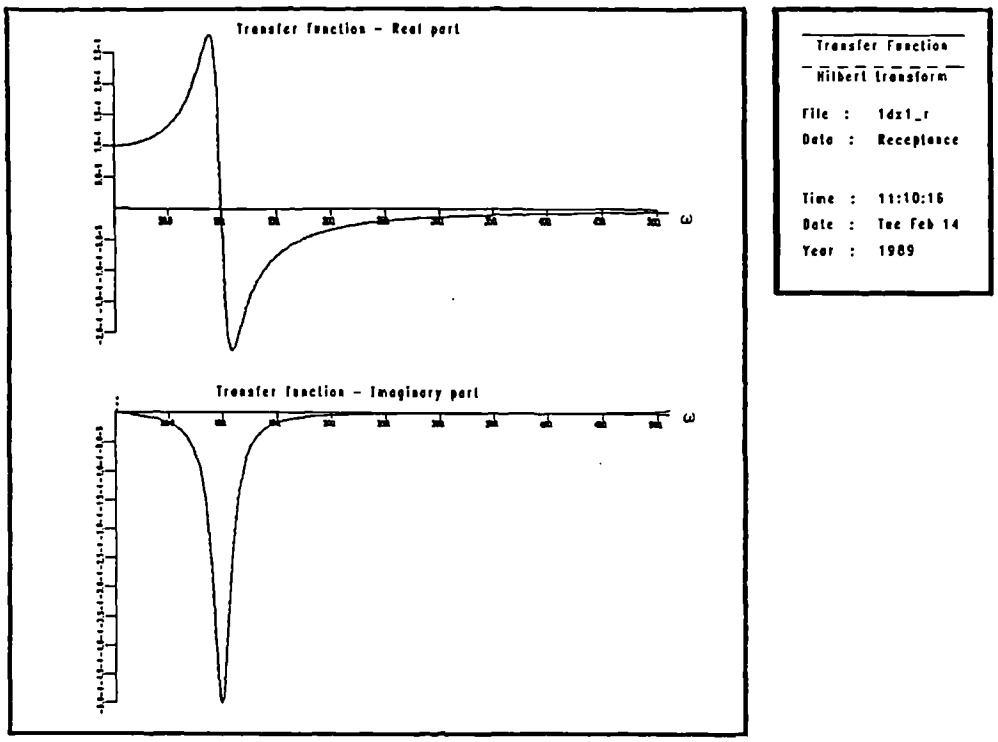

Figure 1.14. Receptance transfer function and Hilbert transform for the system $\ddot{y} + 20\dot{y} + 10^4 y = x(t)$.

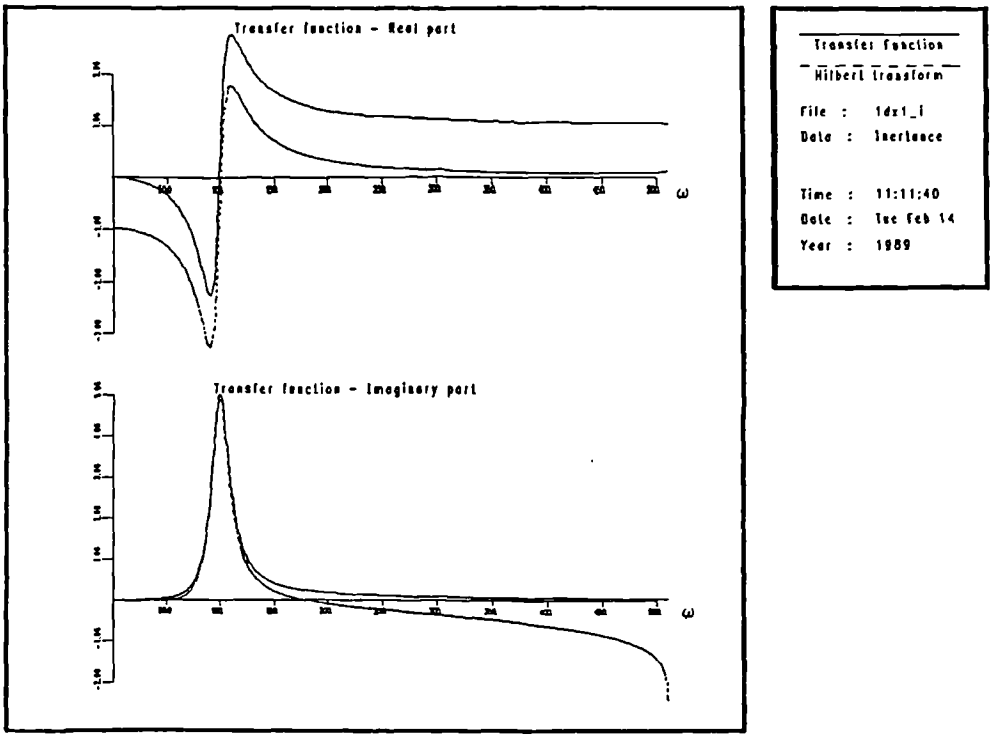

Figure 1.15. Inertance transfer function and Hilbert transform for the system $\ddot{y} + 20\dot{y} + 10^4 y = x(t)$ showing the shift in the real part of the transform.

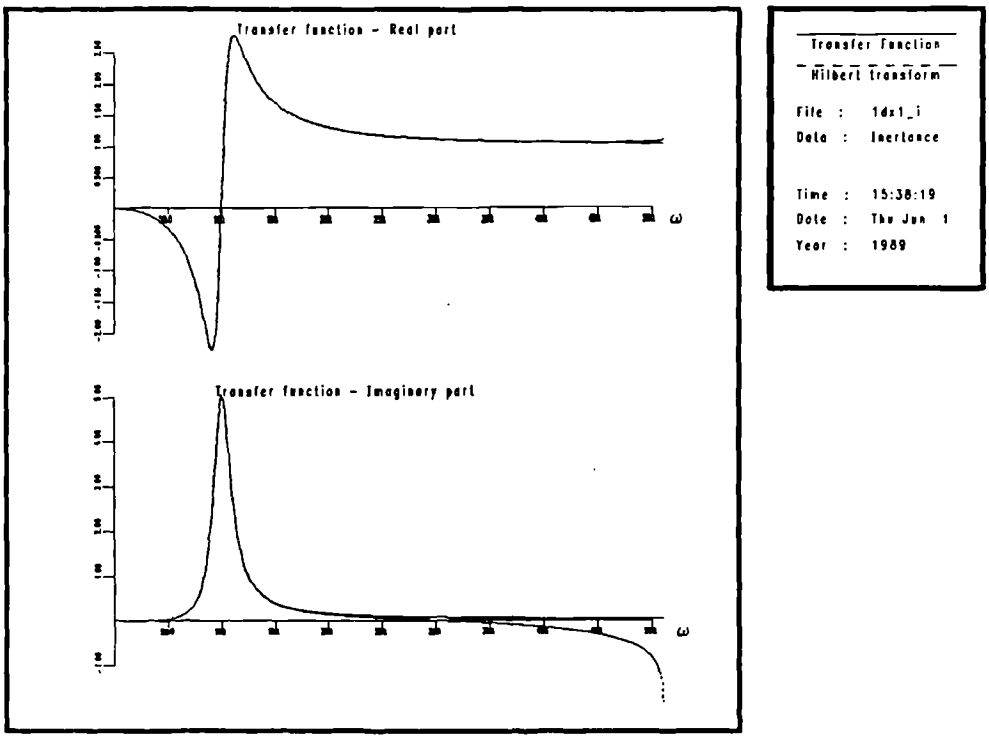

Figure 1.16. Inertance transfer function and Hilbert transform for the system $\ddot{y} + 20\dot{y} + 10^4 y = x(t)$. In this case the transform was obtained after converting the transfer function to receptance.

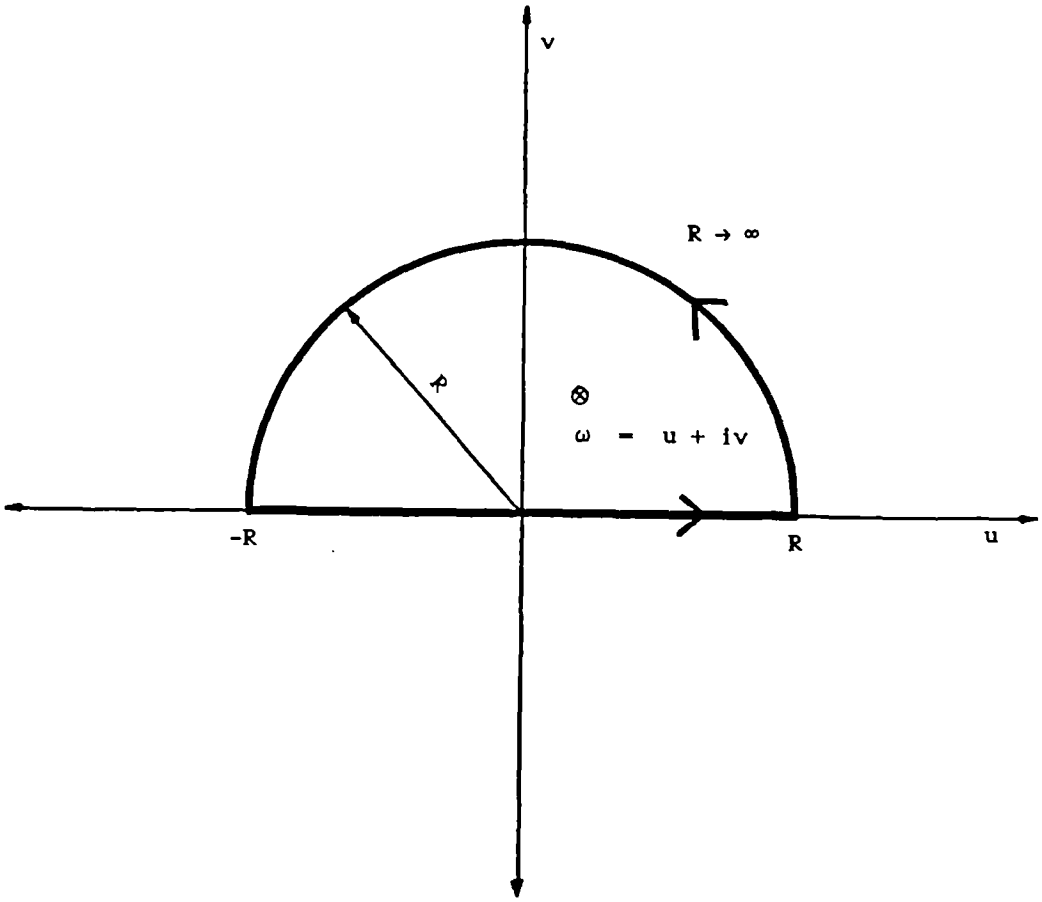

Figure 1.17. Contour used to obtain the Hilbert transform relations when the opposite Fourier transform conventions are used to those for Figure 1.1.

CHAPTER 2

THE MASRI/CAUGHEY PROCEDURE - SDOF SYSTEMS

The Hilbert transform procedure of the previous chapter is only able to provide very limited information about a system. One requires a method of extracting more useful information. Ideally, one would like to be able to determine the equations of motion of the system under study. Given that most systems will have a large (if not infinite) number of degrees of freedom one would be satisfied with the equations for a low order model. The procedure discussed in this chapter was proposed with these requirements in mind.

2.1. Basic Theory.

The purpose of this chapter is to describe the Masri/Caughey procedure for the identification of nonlinear systems **(10)**. In order to introduce the procedure in the simplest manner possible, the discussion is restricted to Single Degree–Of–Freedom (SDOF) systems. The extension to Multi–Degree–Of–Freedom (MDOF) systems is made in the next chapter.

The object of the method is the representation of the nonlinear restoring force in the system by a surface over the phase plane. Conceptually the method is very simple indeed. One begins with Newton's second law,

$$m\ddot{y} + f(y,\dot{y}) = x(t) \qquad (1)$$

where $f(y,\dot{y})$ is the internal restoring force of the system. For example, in a linear system $f(y,\dot{y})$ would be expressible as the linear function $c\dot{y} + ky$ for some constants c and k. In general it is assumed to be a nonlinear function of the displacement and

velocity responses $y(t)$ and $\dot{y}(t)$ but with no explicit time dependence. The mass m is also assumed to be constant. It is clear that $f(y,\dot{y})$ can be regarded as a surface over the phase plane. $x(t)$ is the externally applied force and $\ddot{y}(t)$ is the acceleration response. For the moment the mass m is assumed known. The time data $x(t)$ and $\ddot{y}(t)$ are sampled over a given period and the sampling interval need not be constant. If one now writes equation (1) as

$$f(y,\dot{y}) = x(t) - m\ddot{y}(t) \qquad (2)$$

the quantities on the right-hand side of this equation are all known at each sampling instant, so one can calculate $f(y,\dot{y})$ at each of these times. If the i^{th} sampling instant is denoted by t_i, and the sampled data by $x_i = x(t_i)$ and $\ddot{y}_i = \ddot{y}(t_i)$, then at t_i equation (2) becomes

$$f_i = f(y_i,\dot{y}_i) = x_i - m\ddot{y}_i \qquad (3)$$

Now, if one has somehow obtained $y_i = y(t_i)$ and $\dot{y}_i = \dot{y}(t_i)$, either from the experiment which produced the other responses or by numerically integrating the $\ddot{y}(t)$ data, then one has a sequence of triplets $(y_i,\dot{y}_i,f_i)$. This means that for each sampled point in the phase plane $(y_i,\dot{y}_i)$ the height of the restoring force surface f_i above that point is determined. If one is using numerical integration procedures or filtering it is neccessary for the sampling to be done at a constant frequency. As this is not an unreasonable restriction it is henceforth assumed to be the case. The sampling interval is denoted by Δt, so $t_i = (i-1)\Delta t$.

As the dependence of f_i on y_i and $\dot{y}_i$ is now known, one can attempt to fit a model of the form

$$f(y,\dot{y}) = \sum_{i=0}^{m} \sum_{j=0}^{n} C_{ij}\, T_i(y)\, T_j(\dot{y}) \qquad (3)$$

where $T_i(y)$ is the i^{th} Chebyshev polynomial in the variable y. The Chebyshev polynomials are useful for a number of reasons.

(i) They are orthogonal polynomials. This means that one can estimate coefficients for a double summation or series of order (m,n) and the truncation of the series to order (i,j) where $i \leqslant m$ and $j \leqslant n$ is the best approximation of order (i,j). This means that one need not re-estimate coefficients if a lower order model is required, as one would have to for a simple polynomial model. Similarly, if one estimates coefficients for an (m,n) order model and it is not accurate enough, one only needs to estimate the extra coefficients required, the lower order ones remain valid.

(ii) The estimation of the coefficients for an orthogonal polynomial approximation requires the evaluation of a number of integrals. In the case of the Chebyshev polynomials a change of variables exists which make the integrals fairly straightforward.

(iii) In the family of polynomials of a given order used to approximate a given function f(x) over a given interval there will be one which has the smallest maximum deviation from the true function over that interval. This approximating polynomial - the *minimax* polynomial is much sought after by numerical analysts. Unfortunately, the polynomial has proved difficult to find - it has so far eluded discovery. One of the nice properties of the Chebyshev polynomial is that it is very nearly the minimax polynomial. The reason for this is that the error in the Chebyshev approximation to a function oscillates between almost equal upper and lower bounds over the interval on which the approximation is made. This property is sometimes called the 'equal-ripple' property.

The various properties of Chebyshev polynomials used in this work are collected for convenience in Appendix B. A comprehensive reference is **(32)**. Reference (33) contains a number of useful routines and algorithms relating to Chebyshev approximation.

The first problem one encounters in forming a model of the form (3) relates to the normalisation of y and $\dot{y}$ i.e. their overall scale. To obtain the coefficients C_{ij} one can see from the arguments of Appendix A that the orthogonality properties of the polynomials are needed. The polynomials $T_n(x)$ are orthogonal on the interval $[-1,1]$ as follows

$$\int_{-1}^{+1} dx\ \omega(x)\ T_i(x)\ T_j(x) \;=\; \pi.\delta_{ij} \;-\; \frac{\pi}{2}.\delta_{i0}.\delta_{j0} \qquad (4)$$

where δ_{ij} is the Kronecker delta i.e. $\delta_{ij} = 1$ if $i = j$ and $\delta_{ij} = 0$ otherwise. The weighting factor for orthogonality $\omega(x)$ is given by

$$\omega(x) \;=\; (\ 1 - x^2\ )^{-\frac{1}{2}}$$

Using the relation (4) one can show that

$$C_{ij} \;=\; X(i)X(j) \int_{-1}^{+1}\int_{-1}^{+1} dxdy\ \omega(x)\omega(y)T_i(x)T_j(y)f(x,y)$$

where $X(i) = (1 + \delta_{i0})/\pi$ (Appendix B). The problem is that the data is actually contained in the rectangle $[y_{min},y_{max}]x[\dot{y}_{min},\dot{y}_{max}]$ in the phase plane where y_{max} is the maximum sampled displacement etc. However, the orthogonality relations only hold on the square region $[-1,1]x[-1,1]$. This means that if $y_{max} > 1$ very little of the data can be used for the integral and there will be a consequent loss in accuracy. If $y_{max} < 1$ the data will only cover a small area in the centre of $[-1,1]x[-1,1]$ and one cannot estimate the integral at all. The solution is fairly straightforward; one transfers the data from $[y_{min},y_{max}]x[\dot{y}_{min},\dot{y}_{max}]$ to $[-1,1]x[-1,1]$ using the maps

$$\xi(y_i) \;=\; \bar{y} \;=\; \frac{y_i - \frac{1}{2}(y_{max} + y_{min})}{\frac{1}{2}(y_{max} - y_{min})} \qquad (5a)$$

$$\dot{\xi}(\dot{y}_i) \;=\; \bar{\dot{y}} \;=\; \frac{\dot{y}_i - \frac{1}{2}(\dot{y}_{max} + \dot{y}_{min})}{\frac{1}{2}(\dot{y}_{max} - \dot{y}_{min})} \qquad (5b)$$

In this case $\dot{\zeta}$ does not mean $d\zeta/dt$. So one actually estimates the model

$$f(y,\dot{y}) = \bar{f}(\bar{y},\dot{\bar{y}})$$

$$= \sum_{i=0}^{m} \sum_{j=0}^{n} C^{\zeta}_{ij}\, T_i(\bar{y})\, T_j(\dot{\bar{y}})$$

$$= \sum_{i=0}^{m} \sum_{j=0}^{n} C^{\zeta}_{ij}\, T_i[\,\zeta(y)]\, T_j[\,\dot{\zeta}(\dot{y})]$$

The first of these three equations is simply the transformation law for a scalar function under a change of coordinates. It is clear now that the coefficients for the model will be sample-dependent. The coefficients are now obtained from

$$C^{\zeta}_{ij} = X(i)X(j) \int_{-1}^{+1}\int_{-1}^{+1} dxdy\ \omega(x)\omega(y)T_i(x)T_j(y)\bar{f}(x,y) \qquad (6)$$

and $\bar{f}(x,y) = f(\zeta^{-1}(x), \dot{\zeta}^{-1}(y))$. If one now makes a change of variables or coordinates to

$$\theta = \cos^{-1}(x)$$

$$\psi = \cos^{-1}(y)$$

The integral becomes

$$C^{\zeta}_{ij} = X(i)X(j) \int_{0}^{\pi}\int_{0}^{\pi} d\theta d\psi\ \cos(i\theta)\cos(j\psi).$$
$$.\bar{f}(\cos(\theta),\cos(\psi)) \qquad (7)$$

If the θ-range $(0,\pi)$ is divided into n_θ intervals of length $\Delta\theta = \pi/n_\theta$ and the ψ-range into n_ψ of length π/n_ψ, The integral can be approximated by the summation

$$C^{\zeta}_{ij} = X(i)X(j) \sum_{k=1}^{n_\theta} \sum_{m=1}^{n_\psi} \Delta\theta\Delta\psi\ \bar{f}(\cos(\theta_k),\cos(\psi_m)).$$
$$.\cos(i\theta_k)\cos(j\psi_m)$$

where $\theta_k = (k-1).\Delta\theta$ and $\psi_m = (m-1).\Delta\psi$.

It is clear from this analysis that some sort of interpolation scheme is required to evaluate the function $\bar{f}$ at the points $(\cos(\theta_k),\cos(\psi_m))$. The interpolation procedure is the subject of the next section.

The model finally obtained is of the form

$$f(y,\dot{y}) = \sum_{i=0}^{m} \sum_{j=0}^{n} C^{\zeta}_{ij}\, T_i[\,\zeta(y)]\, T_j[\,\dot{\zeta}(\dot{y})]$$

This is valid on the rectangle $[y_{min},y_{max}]x[\dot{y}_{min},\dot{y}_{max}]$. As long as the force $f(y,\dot{y})$ is a multinomial in y and $\dot{y}$, and x(t) the excitation used is high enough to excite the highest order terms, this approximation will extend to all the phase plane. If $f(y,\dot{y})$ is a more complicated function e.g. piecewise linear in y, the approximation will only be valid on the rectangle containing the sample data. This means that in the latter case the model sample-dependence is actually input-dependence and it may well lose it's predictive power if a different input to the system generates phase trajectories which pass through different areas in the phase plane than those of the identification data.

2.2. The Interpolation Procedure.

The problem of interpolating a continuous surface from values specified on a regular grid is well documented (33), In this case it is a straightforward matter to obtain an interpolated value or *interpolant* which can be differentiated many times. However, if the data is randomly or irregularly spaced the problem becomes considerably more difficult. Discussions of various approaches can be found in references (34) and (35). One method in particular - Sibson's Natural Neighbour method is not only capable of producing a continuous interpolation, it can produce a differentiable interpolation. The method is rather complicated as it requires the construction of a triangulation of the phase plane, for this reason a discussion of the theory is postponed until Appendix C. Fortunately a software package TILE4 is available from Professor Sibson which carries out the procedure. The software is in the form of approximately 7000 lines of

FORTRAN code. The user can build programs specific to his requirements from the subroutines provided. Figure 2.1 - reproduced from (36) illustrates the suitability of the method for the problem.

In the discussion that follows, the term C^0 is used to indicate an interpolant or surface which is continuous. To say that the method produces a C^0 surface is equivalent to the statement that the procedure is exact for a linear function f(x,y) i.e.

$$f(x,y) = \alpha + \beta x + \gamma y \qquad (8)$$

A surface which is not only continuous but differentiable is designated C^1. The C^1 surface produced by the Natural Neighbour method is constructed so that it is exact for all 'spherical' quadratic functions

$$f(x,y) = \alpha + \beta x + \gamma y + x^2 + y^2 \qquad (9)$$

This is a slight restriction, to specify a general second order function, one needs the form

$$f(x,y) = \alpha + \beta x + \gamma y + \varepsilon x^2 + \eta xy + \sigma y^2$$

In order to evaluate the integrals described in the previous section, one needs to find interpolants for the restoring force over a regular grid in the (θ,ψ) plane. In order to display the surface one needs interpolants over a grid in the $(y,\dot{y})$ plane. The TILE4 package can take quite a long time to produce the required data - up to 25 minutes per surface if a 100x100 grid is obtained from 10000 sample points. For this reason, estimating both surfaces from the package is considered too time-consuming. It was decided that being able to display the force surface was the more basic requirement, so the interpolation onto a regular grid is carried out for $(y,\dot{y})$ space. The (θ,ψ) data is obtained from this by a simple bilinear interpolation (3) as described below

Given arrays y(i) and $\dot{y}$(i) containing the y and $\dot{y}$ values which specify the grid, and f(i,j) containing the force values estimated at points on the grid, one can obtain a bilinear interpolant at the general point $(y,\dot{y})$ quite simply. If

$$y(j) \leq y \leq y(j+1) \qquad \text{and}$$

$$\dot{y}(k) \leq \dot{y} \leq \dot{y}(k+1)$$

if one defines

$$f_1 = f(j,k)$$

$$f_2 = f(j+1,k)$$

$$f_3 = f(j+1,k+1)$$

$$f_4 = f(j,k+1)$$

and

$$t = (y - y(j))/(y(j+1) - y(j)) \quad \epsilon \quad [0,1]$$

$$u = (\dot{y} - \dot{y}(k))/(\dot{y}(k+1) - \dot{y}(k)) \quad \epsilon \quad [0,1]$$

then the interpolant is given by

$$f(y,\dot{y}) = (1-t)(1-u)f_1 + t(1-u)f_2 + tuf_3 + u(1-t)f_4$$

Now the values of the function over a grid in the (θ,ψ) plane can be obtained very simply i.e. the force at the point (θ_k,ψ_m) is given by $\bar{f}(\cos(\theta_k),\cos(\psi_m))$.

In order to estimate the coefficients accurately a 100x100 grid was used. It was found that with such a fine grid, the errors produced by making the (θ,ψ) grid of secondary importance, were negligible.

A further problem which may occur is as a result of singularities in the restoring force. A singularity in this sense being a point at which a derivative of some order does not exist. For example, a piecewise linear function is quite singular in that the first derivative does not exist. In the case of Coulomb friction the function itself is not continuous. This problem is considered in greater detail when a number of basic SDOF systems are considered at the end of this chapter.

2.3. The Extrapolation Problem.

The most serious problem associated with obtaining the force surface is caused by the irregular density distribution of sample points in the phase plane. If one considers Figure 2.2 which shows the distribution in the phase plane of 10000 simulated data points for a linear SDOF system excited by a Gaussian noise sequence, one can see that the data is mainly concentrated in a circular region centred on the origin in phase space. (In the physical coordinates $(y,\dot{y})$, the area is elliptical. The scaling transformation to the $(\bar{y},\bar{\dot{y}})$ maps the region into a circle.) There is no data near the corners of the square $[-1,1]x[-1,1]$. The situation shown in Figure 2.3 is even worse. In this case the variables are (y_1,y_3) the first and third displacement responses from a three degree-of-freedom system. Because y_1 and y_3 are strongly anti-correlated, the data is confined to a narrow elliptical region within the square. The problem is that the interpolation procedure cannot *extrapolate*. In the case of the C^0 procedure the interpolant can only grow linearly as one moves away from the data. This is clearly inadequate to describe a nonlinear system. The situation is slightly improved if one uses the C^1 option which can grow as a quadratic away from the data. However, one of the simplest types of structural nonlinearity of interest is a cubic (and some are not polynomial at all) so even the C^1 procedure is inadequate. In fact it is shown later that in most cases one loses the option of forming a C^1 interpolant. This means that one has to have some way of dealing with regions of the phase plane which have a low density of points.

The method used in **(10)** to try and circumnavigate this problem is fairly simple. In the regions where there is a high density of points an unspecified interpolation procedure is used. Over the areas where there is little or no data the restoring force is assumed to take the form

$$f(y,\dot{y}) = f_s(y) + f_d(\dot{y})$$

so one can model $f(y,\dot{y})$ with an expression of the form

$$f(y,\dot{y}) = \sum_{i=0}^{m} a^{\zeta}{}_i T_i[\zeta(y)] + \sum_{i=0}^{n} b^{\zeta}{}_i T_i[\dot{\zeta}(\dot{y})] \qquad (10)$$

To evaluate the $a^{\zeta}{}_i$'s for example, one assumes that

$$\bar{f}_s(\bar{y}) = \bar{f}(\bar{y},0) = \sum_{i=0}^{m} a^{\zeta}{}_i T_i(\bar{y})$$

As before, the expansions only make sense in the $(\bar{y},\dot{\bar{y}})$ plane. In order to estimate the coefficients one takes all the data from the plane contained in some small band about the $\bar{y}$ axis i.e such that $|\dot{\bar{y}}| < \epsilon$ for some small ϵ. This procedure is illustrated in Figure 2.4. If one associates the force values $\bar{f}(\bar{y},\dot{\bar{y}})$ now with the $\bar{y}$ value for each point, one obtains a rather noisy graph of $\bar{f}_s(\bar{y})$. If this irregularly spaced data is now interpolated to give values at regularly spaced values, one can obtain the coefficients by the same means as the previous section i.e. one evaluates the integral

$$a^{\zeta}{}_i = X(i) \int_{-1}^{+1} d\bar{y}\ \omega(\bar{y})\ T_i(\bar{y})\ \bar{f}(\bar{y},0)$$

by changing variables to $\theta = \cos^{-1}(\bar{y})$, discretising the integral and summing

$$a^{\zeta}{}_i = X(i) \sum_{k=1}^{n_\theta} \Delta\theta\ \cos(i\theta_k)\ \bar{f}(\cos(\theta_k),0)$$

Clearly in this case the interpolation procedure should actually find values at regularly spaced θ points. As before the coefficents are sample-dependent, from now on this is accepted to be the case and the ζ superscript is dropped. The same procedure can be used to evaluate the coefficients for the damping force $\bar{f}_d(\dot{\bar{y}})$. Having obtained the model in equation (10), it is used in (10) to estimate the value of the restoring force over regions where there is little data.

This method has a serious drawback. It cannot account for cross-product terms of the

form $y^m\dot{y}^n$ in the restoring force. This type of term will contribute most when the y and $\dot{y}$ values are equally large i.e. along the lines $y \pm \dot{y} = 0$. From figure 2.2, one can see that these are precisely the areas where there is no data. In Figure 2.3. the distortions caused by the correlation of the variables mean there is more data along the line $y_1 - y_3 = 0$, but less along $y_1 + y_3 = 0$. This means that equation (10) is not a good approximation to the function whether the expansion variables are correlated or not. Consider the restoring force function for the Van der Pol oscillator

$$f(y,\dot{y}) = \epsilon(1 - y^2)\dot{y} + y$$

then

$$f(y,0) = y$$
$$f(0,\dot{y}) = \epsilon\dot{y}$$

and the procedure in **(10)** produces a linear extrapolation over areas where the force is actually third-order.

The approach taken in the present work is much more straightforward. Rather than try to extrapolate, one displays the data and then chooses a rectangular sub-region of the phase plane which is well covered by data. This produces a reduced data set which is then mapped onto the square $[-1,1]x[-1,1]$. The rectangle indicated by the dotted lines specifying the reduced set is shown in Figures 2.2 and 2.3. The interpolation and Chebyshev expansion procedures are then carried out. The main drawback of this method is that one discards the data which corresponds to the largest displacements and velocities measured. Because of this one must take care. If the system under test is only just showing signs of nonlinearity, this procedure may concentrate attention on a region of the phase plane over which the restoring force is nominally linear. In this case it will be impossible to accurately identify the higher order Chebyshev coefficients for the model. One must take care in choosing the level of the excitation used, it must be high enough for the reduced data set to still show signs of nonlinearity. If it is too high, estimation of the lower order terms will suffer

as the higher terms will dominate. If the model is to be of any use for prediction at lower excitations, the linear and constant terms must be identified accurately. In particular, if C_{00} is incorrect one will observe the wrong position of equilibrium in the predicted output.

Theoretically there is another possible way of obtaining a surface without discarding data or extrapolating. One could change to a non-Cartesian coordinate system which maps the data region onto a square. The situation is simplest when the expansion variables are uncorrelated as in Figure 2.2. The data is confined within a roughly circular region; this suggests that one could try polar coordinates (r,φ) such that $y = r\cos(\varphi)$ and $\dot{y} = r\sin(\varphi)$. If the data shown in Figure 2.2 is mapped to

$$r_i = y_i^2 + \dot{y}_i^2$$
$$\varphi_i = \tan^{-1}(\dot{y}_i/y_i)$$

The resulting distribution of data in the (r,φ) plane is shown in Figure 2.5. Because there is little data at large values of y and $\dot{y}$, there is correspondingly little data at large r. However, because the y and $\dot{y}$ values are uncorrelated, the density distribution of points is independent of φ. The surface interpolated from this data is shown in Figure 2.6. Because the restoring force function is highly nonlinear in the (r,φ) coordinates i.e.

$$f'(r,\varphi) = cr\sin(\varphi) + kr\cos(\varphi)$$

(c being the damping constant for the system, and k the stiffness), even the C^1 routine is inadequate to estimate the surface in areas where there is not much data. This accounts for the distortions in the surface at large r. If the smaller region indicated by a dashed line in Figure 2.5 is used for interpolation, one obtains a much better distribution of points (Figure 2.7), and a correspondingly better surface (Figure 2.8). However, this is after discarding data again which rather defeats the object of the exercise. The problem is that in gaining a better distribution of points in the new coordinate system, the interpolation has lost accuracy because the force surface expressed in the new coordinates is highly nonlinear. Even so, this procedure could

still be of use if the expansion variables are highly correlated as in Figure 2.3. One can map the data onto a square by using the sequence of transformations illustrated in Figure 2.9. Of these transformations only the last, the change to polars, is nonlinear. In carrying out this sequence one is essentially choosing an elliptical polar representation. Unfortunately, this idea has other problems, the surface obtained (Figure 2.8) gives no indication that the system is linear. To plot the surface in a recognisable form one would need to change coordinates back to the cartesian $(y,\dot{y})$, carrying the force surface back by using an interpolation. This either introduces a further source of error if one uses the bilinear method, or takes an unnacceptably long time if one uses TILE4 to form the surface from the basic data. For this reason, nonlinear coordinate systems are not recommended.

In most cases, one has some control over the test and can adjust the level of excitation to the system in order to give significant nonlinear contributions to the restoring force over the reduced data set.

2.4. Simulated SDOF Nonlinear Systems.

In order to test the identification procedure described above, a number of sets of data corresponding to different types of SDOF nonlinear systems were simulated. A fourth-order Runge-Kutta procedure was used to generate displacement, velocity and acceleration response data by integrating over regular intervals the general differential equation of motion for a SDOF system.

$$m\ddot{y} + f(y,\dot{y}) = x(t)$$

In all the simulations except for the Van der Pol oscillator, the excitation is a Gaussian white noise sequence with zero-mean. The Gaussian random numbers are generated using the routines RAN1 and GASDEV from reference (33). Because the Runge-Kutta routine is unstable for high frequencies, the excitation signal is filtered

using a low-pass Butterworth filter which is designed to cut-off at one-fifth of the sampling frequency, the sampling frequency being the inverse of the time-step used in the integration procedure. For the sake of simplicity x(t) is held constant between sampling instants even though the Runge-Kutta procedure needs to know the values at mid-interval times. This is perfectly adequate for simulation studies. Later, when experimental data is considered, a more sophisticated integration routine is introduced.

The first example considered is a linear system. The equation of motion used was

$$\ddot{y} + 40\dot{y} + 10^4 y = x(t) \qquad (11)$$

and x(t) was a Gaussian sequence with mean zero and variance (RMS) 10.0. The time-step for the simulation was 0.001 seconds, giving a sampling frequency of 1.0 kHz. The filter produced a band-limited signal in the range 0 - 200 Hz. The undamped natural frequency of the system is 100 rad/s or 15.92 Hz.

10000 points of displacement, velocity and acceleration data were accumulated. The distribution of the points in the phase plane is shown in Figure 2.10. The dashed rectangle in the figure indicates the reduced data set which was chosen for the interpolation stage. The reduced set shown in Figure 2.11 contains 9486 points. The number of points discarded is small. However, one observes that the reduced set contains only those points with displacements up to about 5/8 of the maximum.

The data was then used to construct a C^1 interpolation using the TILE4 package, the tesselation and associated triangulation are shown in Figure 2.12. The TILE package proved able to cope with interpolations based on up to 10000 points without difficulty. The C^1 surface obtained is shown in Figure 2.13; the linearity of the system is very clearly indicated. The restoring force surface shown has been constructed over a 100x100 grid, this grid size was used for all the systems studied. The surface data was then used to calculate coefficients for a Chebyshev polynomial model. A (3,3) model was determined i.e. third-order in displacement and third-order in velocity. Because

of the orthogonality properties mentioned earlier, all models of order (i,j), $i \leq 3$, $j \leq 3$ have also been determined. This means that for each model one can calculate the force surface values at each point on the grid, and the relative error between the interpolated surface and the model surface can be estimated. The measure of difference adopted is the normalised mean-square error, or MSE, defined by

$$MSE(f) = \frac{100}{N\sigma_f 2} \sum_{i=1}^{N} (f_i - \hat{f}_i)^2 \qquad (12)$$

where f_i is the surface value at a grid point labelled i, and N = 10000 is the number of grid points. $\hat{f}_i$ is the estimated force from the model (throughout this work carets denote estimated quantities). σ_f is the standard deviation of the force values and the summation is over all grid points. The normalisation factor is chosen such that, if a (0,0) model (simply the mean-level of the forces) is used to predict the force values the MSE value will be 100. This is sometimes written as a percentage to reflect the fact that the MSE above is the mean-square difference expressed as a percentage of the variance of the measured data. A comparison was made between the interpolated surface and an exact surface calculated from the analytic expression for $f(y,\dot{y})$ in the equations of motion. The comparison is shown in Figure 2.14 and produced an MSE of 6.7×10^{-5} indicating excellent agreement.

The coefficients for the models of order up to (3,3) are shown in Table 2.1. The MSE for each model is shown in Table 2.2 There is a marked drop in the error for the (1,1) model and then no significant decrease as the model order is increased further; in fact, the model error is a minimum for the (1,1) model. This clearly indicates that the system is linear. By tabulating the various model errors in this way it is hopefully possible to determine the actual order of the system. The surface generated from this model is compared with the interpolated surface in Figure 2.15 and the MSE of 0.186% shows how close the agreement is. The residual surface plotted in Fig. 2.15 is not important at the moment, it will become so when the extension to MDOF systems is made in the next chapter. The exact Chebyshev

coefficients for this data were calculated by the method described in Appendix B. Comparison with the estimated coefficients produced the following results.

	Exact	Estimated	% error
C_{00}	-0.352031	-0.239064	-32.09
C_{01}	3.052770	3.056534	0.12
C_{10}	8.240615	8.242984	0.03
C_{11}	0.0	-0.226003	∞

Using these results to produce an ordinary multinomial in y and $\dot{y}$ gave

$$\hat{f}(y,\dot{y}) = 40.05\dot{y} + 10002.9y$$

if one neglects the cross term and the constant. The results are very accurate indeed. A further measure of the model accuracy can now be made. By using the estimated force in the Runge-Kutta procedure, one can predict the displacement output from the model system under the excitation x(t). This can then be compared with the actual or 'measured' displacement. The comparison for this system is shown in Figure 2.16. The MSE is defined as in equation 12, the only difference being that the summation is made over sampling instants rather than grid points.

$$MSE(y) = \frac{100}{N\sigma_y^2} \sum_{i=1}^{N} (y_i - \hat{y}_i)^2$$

This type of MSE is used throughout the present work whenever two records of time data are to be compared. For this case, the MSE of 0.106 indicates an excellent fit.

Included in (10) is a study of the linear system

$$\ddot{y} + 0.1\dot{y} + y = x(t)$$

The much lower resonant frequency of this system (1 rad/s) reflects the fact that Masri and Caughey are interested in Civil Engineering systems. They do not compare their coefficients with the exact ones. However, they provide enough information for the calculation to be made, the results are

	Exact	Estimated	% error
C_{00}	-0.070	-0.22	209.9
C_{01}	0.793	0.65	18.0
C_{10}	7.745	7.64	0.07
C_{11}	0.0	0.003	∞

The results of the present study are better than those of (10) for this particular case. This indicates that the extrapolation problem can be dealt with adequately by reducing the data set.

The second example considered is of a nonlinear system with cubic stiffness. The Duffing oscillator system with equation of motion

$$\ddot{y} + 20\dot{y} + 10^4 y + 5\times10^9 y^3 = x(t)$$

was simulated. This type of nonlinearity is important because it represents the first level of approximation to any odd nonlinearity. x(t) was a noise sequence as before, with variance 50.0. The time–step for the simulation was 0.001 seconds. giving the same frequency range for the filtered x(t) as the previous example

10000 points of time data were obtained. The resulting distribution of sample points is shown in Figure 2.17. The dashed rectangle indicates the chosen reduced data set which contained 8694 points in this case. The force surface was obtained using the C^1 procedure and the results are displayed in Figure 2.18. A comparison between this and the exact surface is shown in Figure 2.19, the MSE of 0.196 verifies that the agreement is excellent. The cubic stiffness is shown very clearly in the surface i.e.

there is curvature in the direction of increasing displacement but none in the direction of increasing velocity.

The Chebyshev coefficients for models up to order (5,3) were obtained, and are shown in Table 2.3. The MSEs for the various models are displayed in Table 2.4. There is a significant drop in the error for the (3,1) model as expected, in fact this error is a minimum. This is reassuring, the true order of the system is indicated correctly. The surface generated from the (3,1) model is compared with the interpolated surface in Figure 2.20. The MSE of 0.19 signals that the fit is very good. The coefficients for the chosen model compare with the exact results as follows

	Exact	Estimated	% error
C_{00}	-1.616901	-0.637758	-60.5
C_{01}	8.967750	8.966823	0.0008
C_{10}	72.370255	72.302673	-0.093
C_{11}	0.0	-1.638723	∞
C_{20}	-0.750752	-2.313370	208.14
C_{21}	0.0	0.033068	∞
C_{30}	16.277388	16.213997	-0.3894
C_{31}	0.0	-0.510824	∞

The procedure has badly overestimated the size of the C_{20} coefficient. This is possibly due to a slight problem with the coefficient estimation which could occur, small deviations from the correct curvature in the interpolated surface could be modelled well by the inclusion of spurious terms, even though the other estimates may not be affected much.

Converting back to a multinomial model for $f(y,\dot{y})$ produces the result

$$f(y,\dot{y}) = 1.99 + 20.0002.\dot{y} + 10057.y - 8.35\times10^{5}.y^{2} + 4.98\times10^{9}.y^{3}$$

after removing those terms which are insignificant. The quadratic term and the

constant are an unavoidable nuisance, the rest of the estimation is very accurate. Comparing the 'measured' displacements with those predicted by the (3,1) model produced the results shown in Figure 2.21. The MSE of 19.4 is quite high. Deleting the C_{20} coefficient produces the comparison in Figure 2.22 with a more acceptable MSE of 6.80. Systematic deletion of the coefficients followed by this sort of comparison can sometimes allow one to judge the significance and utility of each of the terms. However, this is time-consuming and can sometimes be misleading. For example, deleting C_{00} and comparing is not a good way to estimate the significance of a constant term as the constant is actually distributed throughout all terms of (even,even) order.

The cubic system

$$\ddot{y} + 0.04\dot{y} + y + 0.003y^3 = x(t)$$

is considered in **(10)** and the following results are obtained for a (3,1) Chebyshev model

	Exact	Estimated	% error
C_{00}	0.2	0.06	300.0
C_{01}	3.1	3.6	16.13
C_{10}	196.07	193.00	1.57
C_{11}	0.0	-0.09	∞
C_{20}	0.0	0.13	∞
C_{21}	0.0	0.27	∞
C_{30}	51.64	51.0	1.54
C_{31}	0.0	0.13	∞

Apart from the overestimated quadratic term the results of the present study are better. It is interesting to note why there is no quadratic term in their results. This is because $|y_{max}| = |y_{min}|$ for their simulated data set, so the ζ-transformation (5) on the data is simply a rescaling, no quadratic is introduced. By insisting that the boundary of the reduced set is symmetric about the origin in the phase plane, the

Υ-mappings can be reduced to simple scalings. However, this was considered too restrictive, if a system has an even nonlinearity the data may be concentrated away from the origin.

Next, a system with nonlinear damping is considered. The equation of motion used was

$$\ddot{y} + 20\dot{y} + 100\dot{y}|\dot{y}| + 10^4 y = x(t)$$

The excitation was a noise signal as before with RMS 100.0. The same time-step was used. This example is interesting because it is the first with a singular nonlinear function. It is a fairly mild example, the second derivative of the damping function does not exist along the line $\dot{y} = 0$ in the phase plane. This means that it cannot have an exact polynomial representation. However, according to the Weierstrass representation theorem it can be approximated arbitrarily accurately over a given interval by an appropriately high-order polynomial. This allows the identification to proceed as before, bearing in mind that the approximation found will be dependent on the sample.

As before, 10000 points of the data were obtained, the distribution in the phase plane is shown in Figure 2.23 along with the boundary for the reduced data set. The reduced set contains 9272 points. The C^1 interpolation produced from this data is shown in Figure 2.24. The comparison with the exact restoring force surface is displayed in Figure 2.25, the MSE of 7.2×10^{-5} indicates almost perfect agreement.

Chebyshev coefficients were estimated for models up to order (2,8). The coefficients are shown in Table 2.5 and the MSE values in Table 2.6. The MSE's have a minimum for the (1,3) model. This indicates that for this level of excitation, the system damping is adequately represented by a cubic term. At high levels of excitation (1,5) or (1,7) models would be required. The comparison between the

model-generated surface and the interpolated surface is shown in Figure 2.26. The MSE of 0.18 indicates a good fit. The (1,3) model is

$$\begin{aligned}\bar{f}(\bar{y},\dot{\bar{y}}) = {} & -4.7419 + 38.68\dot{\bar{y}} + 59.13\bar{y} - 1.94\bar{y}.\dot{\bar{y}} \\ & -0.722T_2(\dot{\bar{y}}) + 5.49T_3(\dot{\bar{y}}) + 0.02T_2(\dot{\bar{y}}).\bar{y} \\ & -4.27T_3(\dot{\bar{y}}).\bar{y}\end{aligned}$$

The comparison between the actual displacement and the predicted displacement from the model is shown in Figure 2.27. The agreement is excellent. One should bear in mind that the system has not stricly been identified, an approximation has been obtained valid on a fixed interval. It is only with the benefit of prior knowledge that one can avoid concluding that the system has a cubic damping nonlinearity.

A Van der Pol oscillator system is the subject of the next study. Following Reference **(10)** in this case, the equation of motion used was,

$$\ddot{y} - 0.2(1 - y^2)\dot{y} + y = x(t)$$

In this case the linear resonance is at 1 rad/s. A sampling interval of 0.1 seconds was used, which gives a sampling frequency of 10 Hz. The excitation used was a 'chirp' signal of the form $x(t) = 10\sin(t^2/200)$. 10000 points were accumulated, giving a sweep range for the signal of 0 to 5 rad/s. The phase trajectory for the first 3000 samples is shown in Figure 2.28. At this stage the behaviour of the system is very regular. However, as the phase trajectory spirals inwards, it eventually passes into the region where the damping force is negative. Around this point, there appears to be a transition to chaotic behaviour. This transition is shown very clearly shown in Figure 2.29. This behaviour will be important later when a comparison is made between the actual and predicted displacements. The distribution of the 10000 points sampled is shown in Figure 2.30. The complex shape of the region covered by the data means that the extrapolation problem will be particularly severe unless a reduced data set is taken. The reduced set is shown and contains 7913 points. This example allows one

to demonstrate very well how extrapolation can lead to serious errors. Here, the data is irregularly distributed and the nonlinearity is third-order so even the C^1 interpolation cannot represent the surface away from the data.

First, the force surface is obtained from a C^1 interpolation over all the data, this is shown in Figure 2.31 and the comparison with the exact surface is shown in Figure 2.32. The MSE for the comparison is 33.5% which is extremely high. Next, the surface is obtained from a C^1 interpolation over the reduced data set (Figure 2.33) and compared with the exact surface (Figure 2.34). The MSE for the comparison is reduced to 0.0056 which is more than acceptable.

The Chebyshev fit is made to the second interpolation, models up to order (4,4) were estimated. The coefficients are displayed in Table 2.7, the associated errors in Table 2.8. As one would expect, the minimum error is for the (2,1) model. Comparison of the model-generated surface with the interpolation gave an MSE of 0.116. The comparison is shown in Figure 2.35. The exact Chebyshev coefficients were calculated and comparison with those estimated produced the results

	Exact	Estimated	% error
C_{00}	0.359706	0.422658	17.5
C_{01}	3.428425	3.417381	-0.32
C_{10}	3.186125	3.182658	-0.11
C_{11}	0.999160	0.994759	-0.44
C_{20}	0.219377	0.149419	-31.9
C_{21}	4.267792	4.198861	-1.62

Comparing the 'measured' displacements to those predicted by the model produces interesting results. The overall MSE for a comparison over 10000 points is 7.85%. Yet, the first part of the comparison, shown in Figure 2.36 is excellent. The high MSE is due to the fact that the predicted output makes the transition to 'chaos' earlier because of the slight differences in the coefficients. This is entirely consistent with the behaviour of chaotic systems. Figure 2.37 shows a comparison over the

region of transition.

The results in **(10)** for this system are

	Exact	Estimated	% error
C_{00}	0.035	0.44	1157.0
C_{01}	37.34	3.58	90.4
C_{10}	6.185	8.48	37.1
C_{11}	0.892	-0.27	130.3
C_{20}	0.0	0.09	∞
C_{21}	39.4	-1.30	103.3

The results are terrible, this is because Masri and Caughey use a (7,7) model and only the (2,1) subsection is shown here. In their case the higher order terms are needed to improve the fit. In their model, the largest coefficients are C_{03}, C_{30} and C_{34}. This is to be expected as their extrapolation procedure simply cannot cope with cross terms. In this case using a reduced data set produces significantly more accurate results and the correct nonlinear order of the system is identified.

The next system considered is a piecewise linear system. Between $y = \pm 0.001$ the equation of motion is given by

$$\ddot{y} + 20\dot{y} + 10^4 y = x(t)$$

outside of this interval the stiffness force is 11 times larger. Once again, the restoring force can only be approximated by a polynomial. In this case the first derivative of the stiffness force does not exist along the lines $y = \pm 0.001$. This is a more severe form of singularity than the nonlinear damping example. Because of this it will be more difficult to approximate the force by a polynomial.

The input excitation x(t) was a noise sequence with RMS 50.0. The time-step used was 10^{-4} seconds corresponding to a sampling frequency of 10 kHz. The Runge-Kutta filter band-limited the input into the range 0 to 2000 Hz. As usual, 10000 samples of

data were obtained, their distribution in the phase plane is shown in Figure 2.38. The reduced data set is also shown, it contains 8815 points in this case.

The C^1 surface obtained from TILE4 is displayed in Figure 2.39. The comparison with the exact surface (Figure 2.40) yields a MSE of 4.6×10^{-4} which indicates near perfect agreement.

The Chebyshev coefficients up to order (9,2) were estimated and the results are given in Table 2.9. The associated error table is given also (Table 2.10). The error has a minimum for the (9,1) model, which is the highest estimable odd-order model. The surface generated from this is compared with the TILE surface in Figure 2.41. The MSE of 0.66 is good. However, it is still clear from the comparison that a 9^{th} order model is inadequate to model this stiffness behaviour.

The comparison between the exact and estimated displacements produces terrible results. The two streams of data diverge and the MSE overflows. The reason for this is simple. In fitting a polynomial to the piecewise linear function, to obtain close agreement it may be neccessary for the coefficients to be nonphysical i.e the higher order stiffness coefficients may be negative. When one estimates the displacements from the model, this is done on the entire data set rather than the reduced set. On this extended area it is then possible to obtain negative stiffness *forces* from the model and the system will quickly become unstable. This phenomenon can occur for any non-polynomial restoring force. It is a consequence of the approximation procedure, the model is only valid on the reduced data set.

A system with Coulomb friction is the subject of the next study. The equation of motion for the system used is

$$\ddot{y} + 20\dot{y} + 10\,\mathrm{sgn}(\dot{y}) + 10^4 y = x(t)$$

x(t) is a noise sequence with RMS 50.0. The sampling frequency used was 1 kHz. The Runge–Kutta filter limited the signal to the range 0 – 200 Hz. Of the examples considered in this section, this is the most singular. There is a discontinuity in the restoring force surface along the line $\dot{y} = 0$. This force will be the most difficult to model with a polynomial.

10000 points of data were accumulated. They are shown in Figure 2.43 together with the boundary of the reduced data set which contains 9258 points. Initially, the TILE package was used to provide a C^1 interpolation. This is shown in Figure 2.44. A problem arises here. One can see spikes in the surface. This is because the algorithm for a C^1 surface needs to estimate the gradient of the surface at each sample point. If the routine considers two points very close together but separated by the discontinuity it will drastically overestimate the gradients at these points. In fact, the gradient at points *on* the discontinuity is infinite. The interpolant is constructed from the force values and estimated gradients in a similar way to forming a Taylor series, if the gradients are too high, the estimated interpolant will be too high. If the C^0 interpolation scheme is used, this problem does not occur (Figure 2.45). However, in this case the surface is not as good along the boundary of the data region. In order to obtain the best possible estimate of the surface, one can form a hybrid by taking the C^1 surface as the basic one and then replacing the neighbourhood of the singularity by that from the C^0 surface. This procedure is illustrated in Figure 2.46. The resulting hybrid surface is displayed in Figure 2.47. Comparing the hybrid C^1/C^0 surface with the exact one gives a MSE value of 0.0097, this result is excellent. The comparison is shown in Figure 2.48. The regions of surface used in the transplant are chosen by considering contour maps of the surfaces. The singular regions show up as areas with densely packed contours.

Using the hybrid surface, Chebyshev coefficients for models up to order (1,9) were estimated. The coefficients are given in Table 2.11 and the associated errors in Table 2.12. The minimum MSE of 1.57% occurs for the (1,9) model. The Chebyshev surface generated from this model is shown in Figure 2.49. The model surface clearly

does not represent the force surface very well at all. Even a 9^{th} order model is inadequate to model the nonlinear damping force. As one would expect, comparing the measured and predicted displacements does not produce very good results (Figure 2.50). The MSE is 6.87%.

Finally a hysteretic system is considered. Hysteretic systems or systems with memory cause particular problems for this method because the restoring force has an explicit time-dependence and as a consequence the force surface will be multi-valued. (It would be single-valued if displayed as an appropriate Riemann surface. However it is not obvious how one can make use of this remark.) There are a number of useful models of hysteretic systems, the one chosen here is the Bouc-Wen model (37) which can simulate systems with widely varying hysteresis loop areas and envelopes. The parameters used in this example were taken from the paper of Hammond et.al. (21). The equations of motion are

$$\ddot{y} + 15.08\dot{y} + 5684.89y + z = x(t)$$

$$\dot{z} = 1000\dot{y} - 1.5|\dot{y}|.z.|z| + 1.5\dot{y}|z|^2$$

Naively integrating the second of these equations with respect to time and substituting the z obtained into the first equation, shows that the $1000\dot{y}$ term is actually a linear stiffness term. This gives a linear resonance for the system at 13Hz. As before, x(t) was a Gaussian noise sequence. In order to produce noticeable nonlinear effects an RMS of 200.0 was used for the input. The sampling frequency was 1 kHz, giving the same frequency limits for x(t) as the previous example. The distribution of 10000 sampled points is shown in Figure 2.51. The reduced data set shown contains 8199 points. As with the previous example a problem occurs when the C^1 option is used for the interpolation. Because the surface is multi-valued, two arbitrarily close points in the phase plane can have a finite difference between the force values above them. This causes the overestimation of gradients and the resulting surface will contain spikes. This is clear from a comparison of Figure 2.52 with Figure 2.53. The former shows the C^1 surface and the latter, the C^0 surface, the second of these is

considerably more regular. Both the surfaces are essentially linear. Because there are a large number of spikes and their distribution is irregular, it is impractical to form a hybrid surface. For this reason the C^1 option can not be used for systems with memory.

The Chebyshev coefficents are estimated form the C^0 surface (Table 2.13). The associated MSE values are given in Table 2.14. The error is a minimum for the (1,1) model. This is because the effects of the multivaluedness average out over the 10000 points to give a linear surface. The comparison between the model-generated surface and the TILE surface is given in Figure 2.54. The MSE of 0.19% indicates that the system is well modelled over this range by linear forces. If the Chebyshev model is converted to a simple polynomial model, the results are

$$f(y,\dot{y}) = -5.51 + 18.32\dot{y} + 6666y + 4.6y.\dot{y}$$

The effective linear stiffness approximates to 5684.89 + 1000.0 as expected. Also, the estimation has modelled the hysteresis by an effective viscous damping term equal to $(18.32-15.08)\dot{y} = 3.24\dot{y}$. In order to check that this is the correct interpretation and not simply an error in the damping estimate, a comparison was made between the actual displacements and those generated from the model above. The comparison is shown in Figure 2.55, a MSE of 0.87 was obtained. The damping in the model was then changed to the 'correct' value 15.08, and the comparison was repeated. This time the MSE was 3.13. This indicates that the estimation has compensated for the energy loss through hysteresis by adding extra viscous damping.

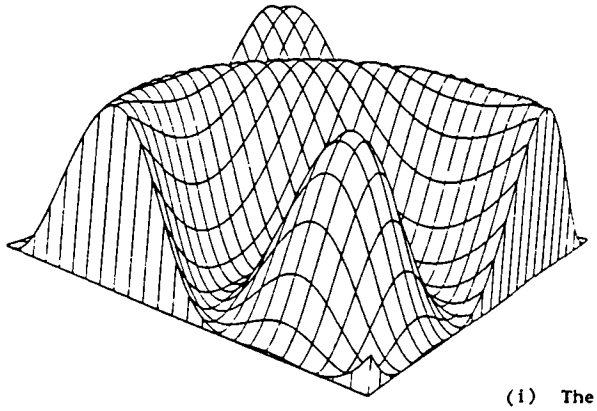

(i) The function
$f(x,y) = \cos\{ [(x - \frac{1}{2})^2 + (y - \frac{1}{2})^2]^{\frac{1}{2}} \}$
on the unit square $[0,1]x[0,1]$.

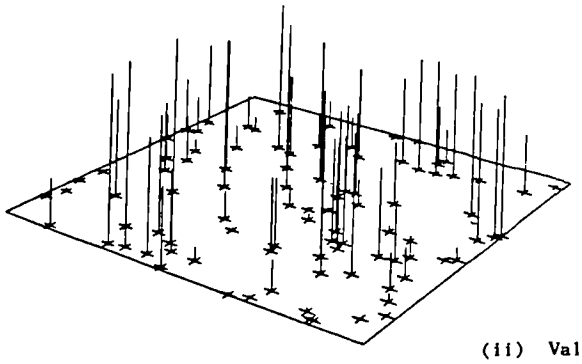

(ii) Values of the above function at data sites in the unit square.

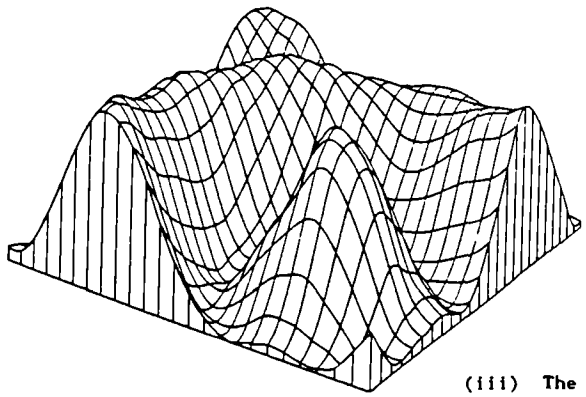

(iii) The reconstruction of the function by the C^1 natural neighbour method.

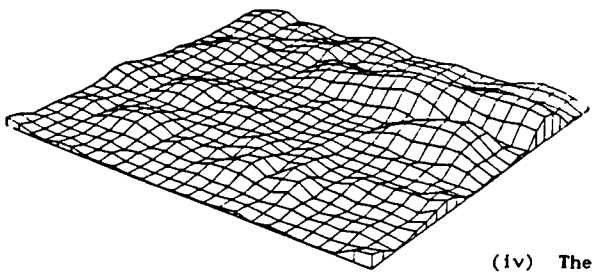

(iv) The absolute error in the interpolation.

Figure 2.1. Natural neighbour interpolation for a function on the unit square (reproduced from (36).)

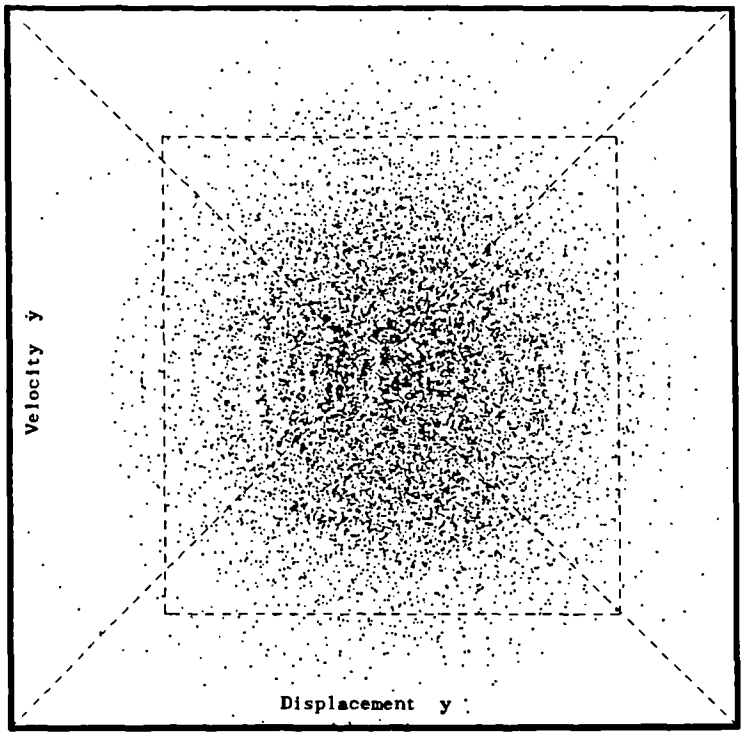

Figure 2.2. Distribution in the phase plane of 10000 data points $(y,\dot{y})$ for a randomly excited linear SDOF system.

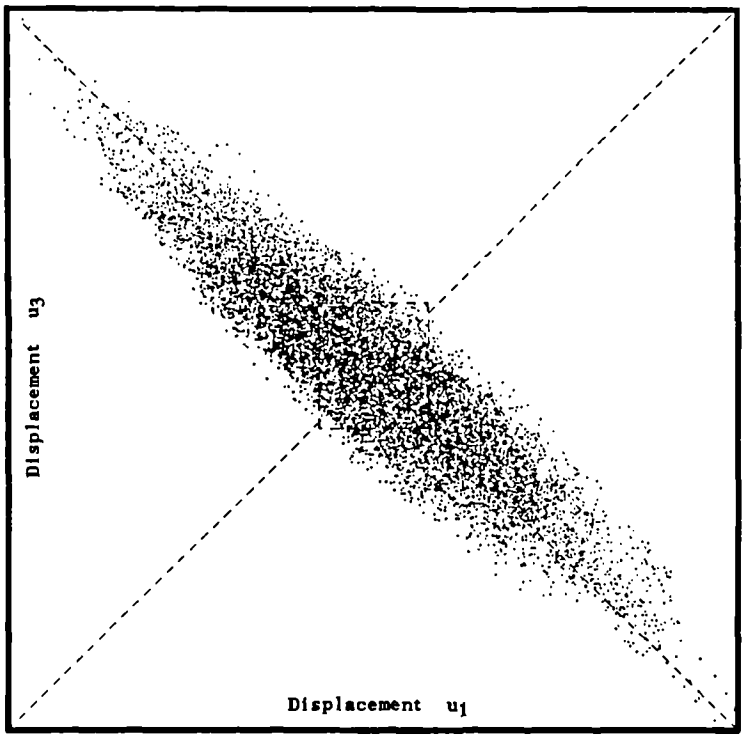

Figure 2.3. Distribution of 10000 data points (u_1,u_3) for a randomly excited nonlinear MDOF system.

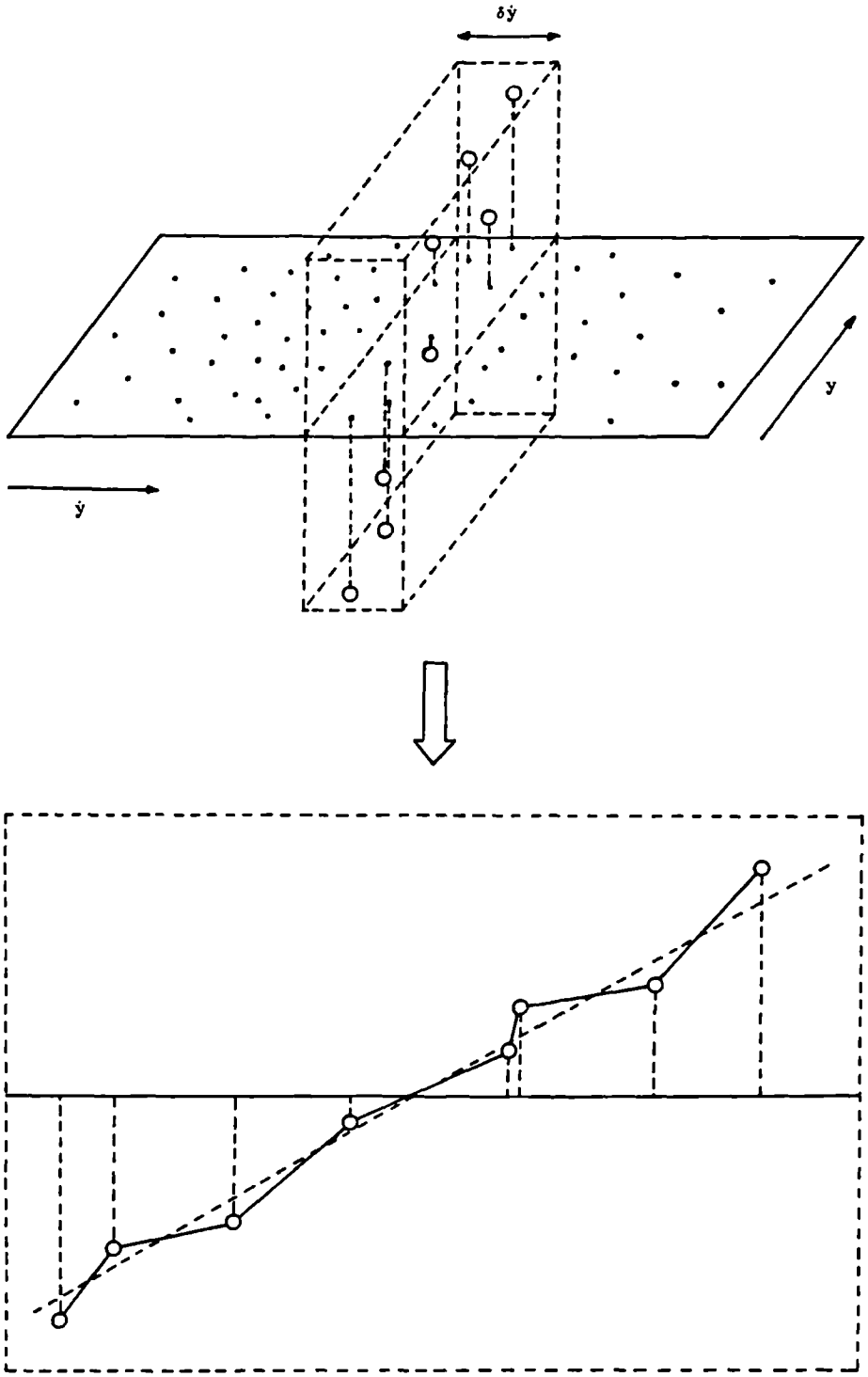

Figure 2.4. The collection of points close to the line $\dot{y} = 0$ in the phase plane.

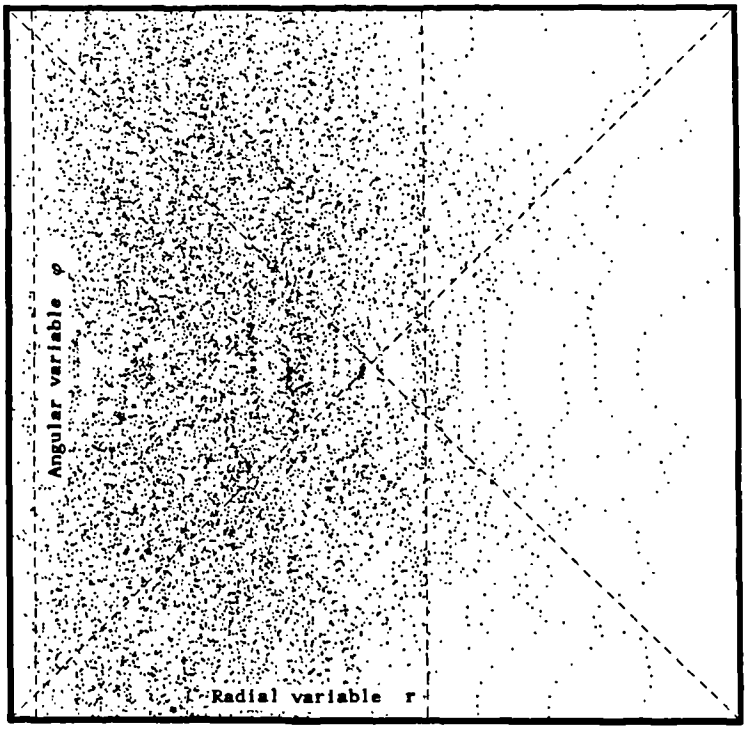

Figure 2.5. Distribution of 10000 points of data for the system of Figure 2.1 shown in polar coordinates (r,φ).

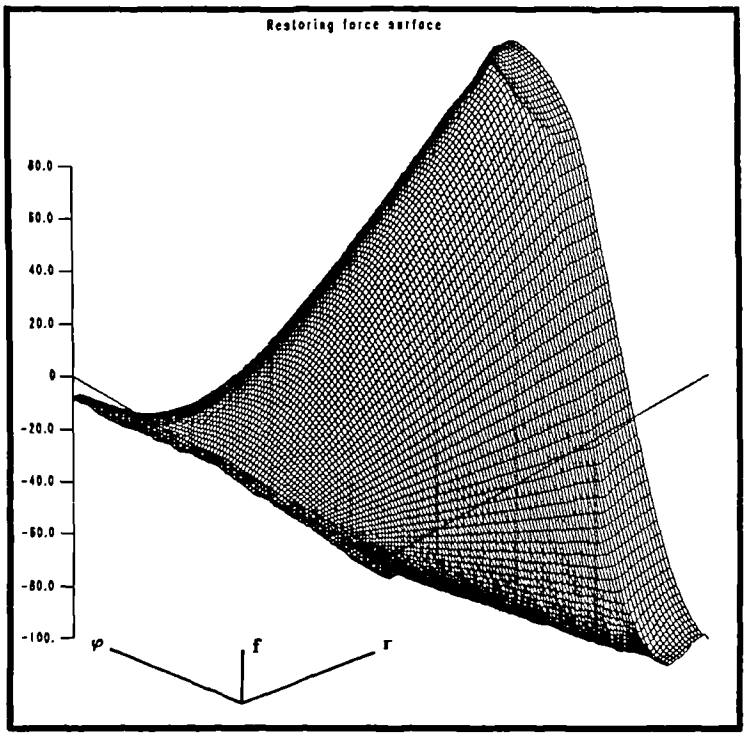

Figure 2.6. The C^1 TILE restoring force surface above the (r,φ) plane for the data shown in Figure 2.5.

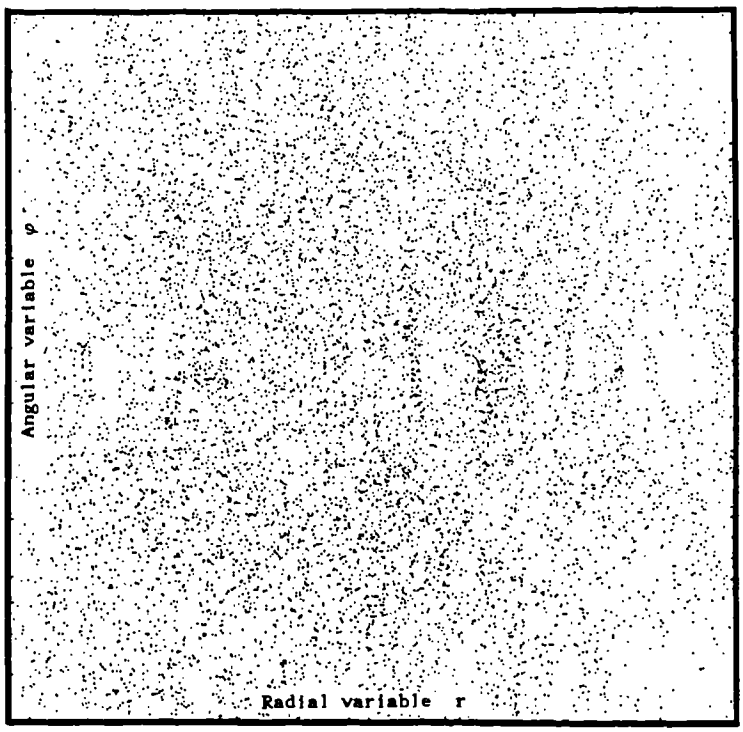

Figure 2.7. Reduced data set in the (r,φ) plane.

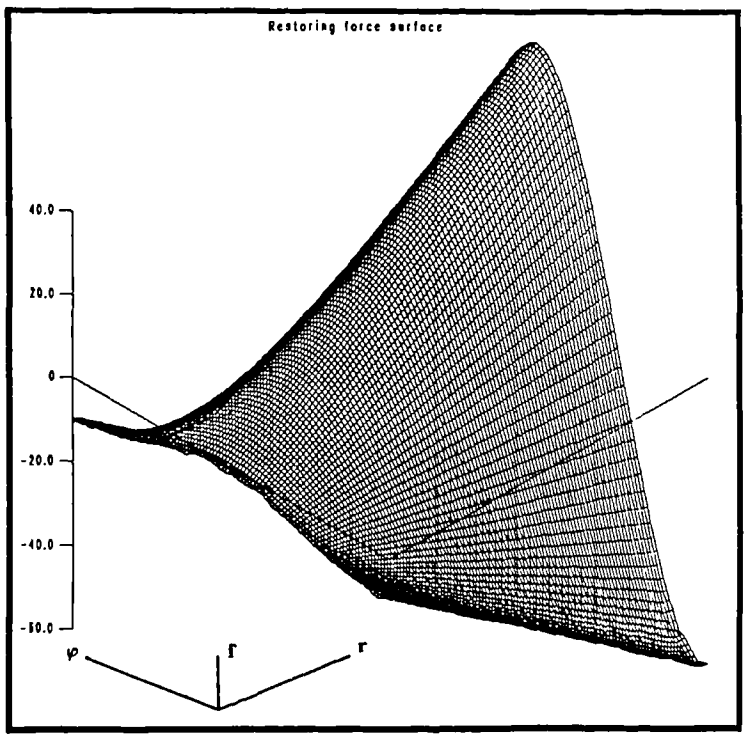

Figure 2.8. C^1 force surface above the reduced data set in the (r,φ) plane.

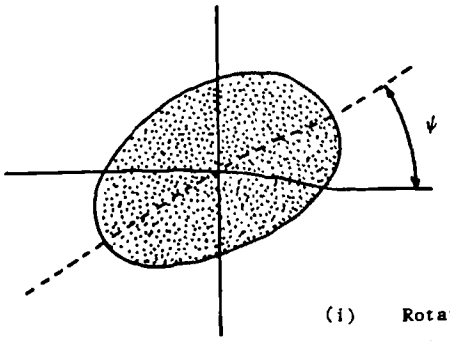

(i) Rotate so that the major axis of the ellipse coincides with a coordinate axis.

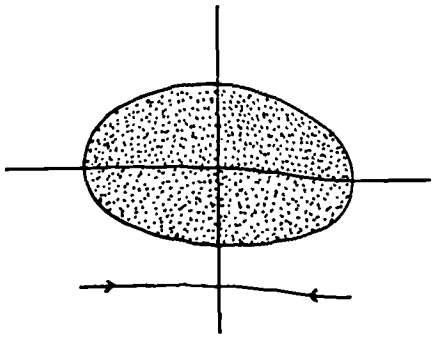

(ii) Scale the coordinates along the major axis to give a circular data region.

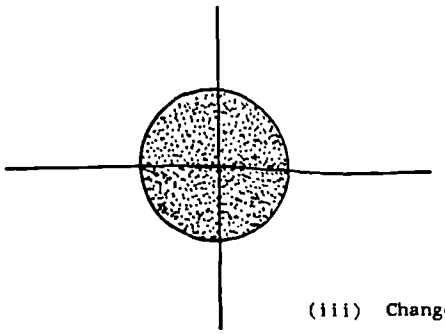

(iii) Change to polar coordinates.

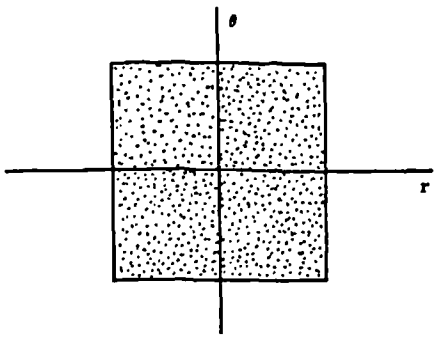

Figure 2.9. The sequence of operations required to map an elliptical region onto a square region

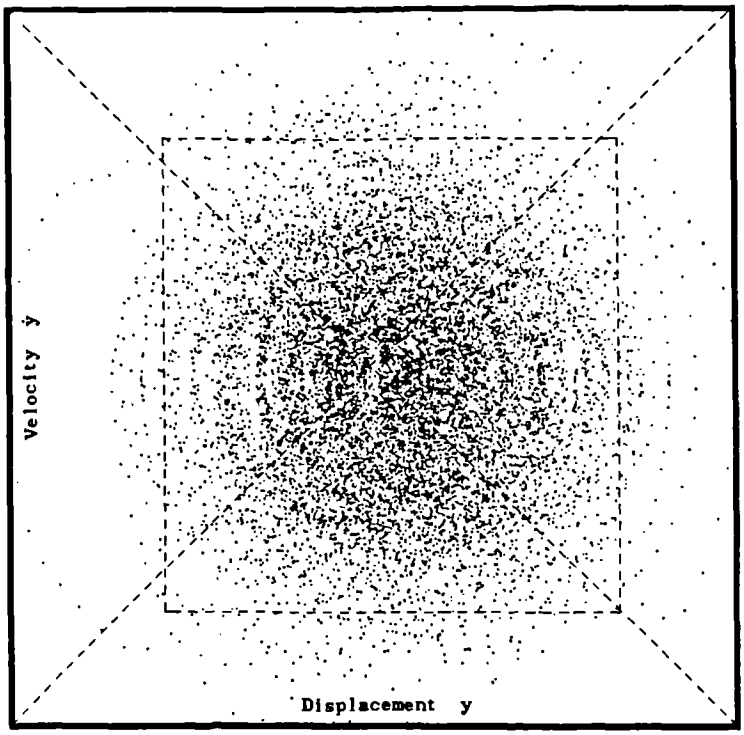

Figure 2.10. Distribution in the phase plane of 10000 points of data from the simulated linear system given in the examples in the text.

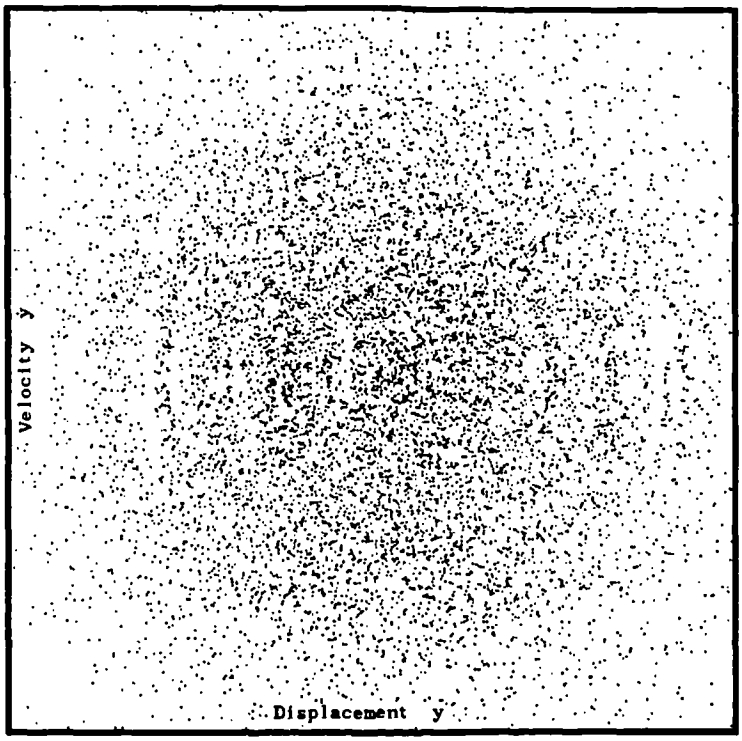

Figure 2.11. Reduced data set for the linear system. i.e. the data contained in the dotted rectangle in the previous figure.

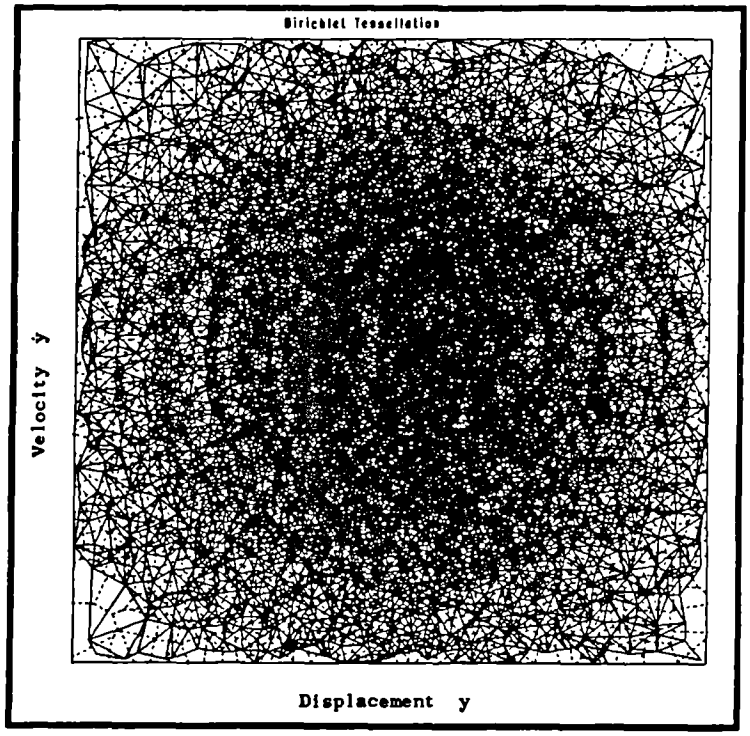

Figure 2.12. Tesselation and triangulation over the reduced data region for the linear system.

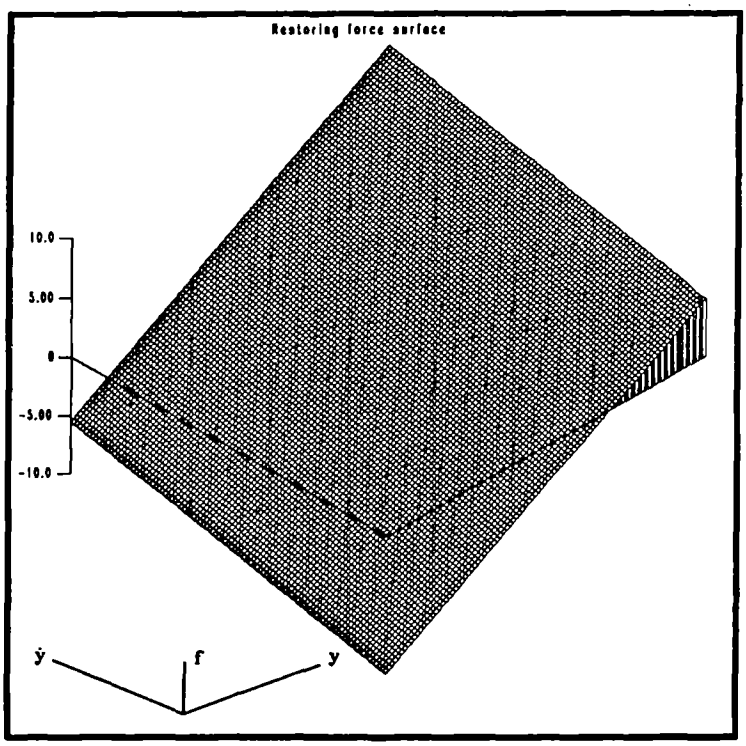

Figure 2.13. C^1 restoring force surface for the linear system.

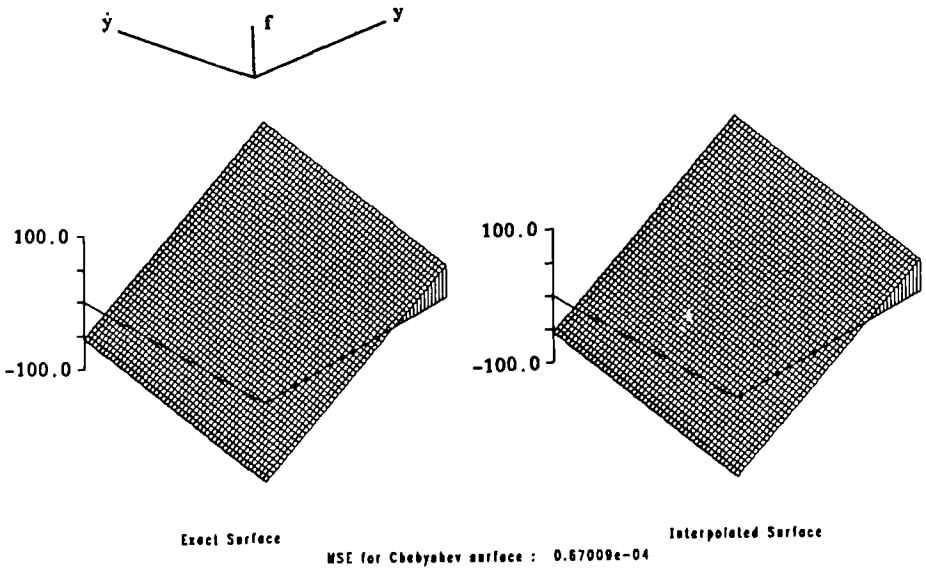

Figure 2.14. Comparison of the interpolated surface with the exact surface for the linear system.

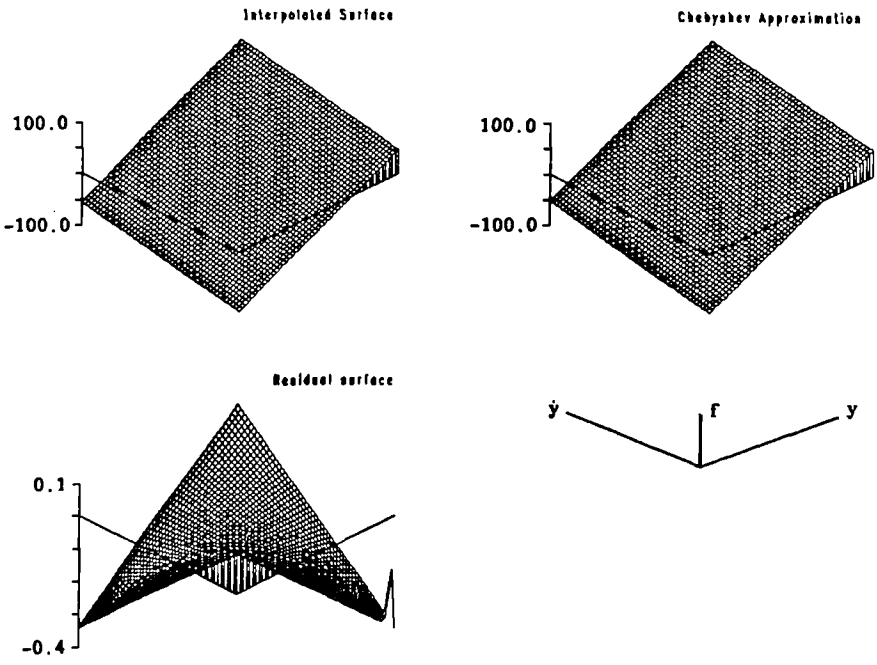

Figure 2.15. Comparison of the (1,1) Chebyshev model surface with the interpolated surface for the linear system.

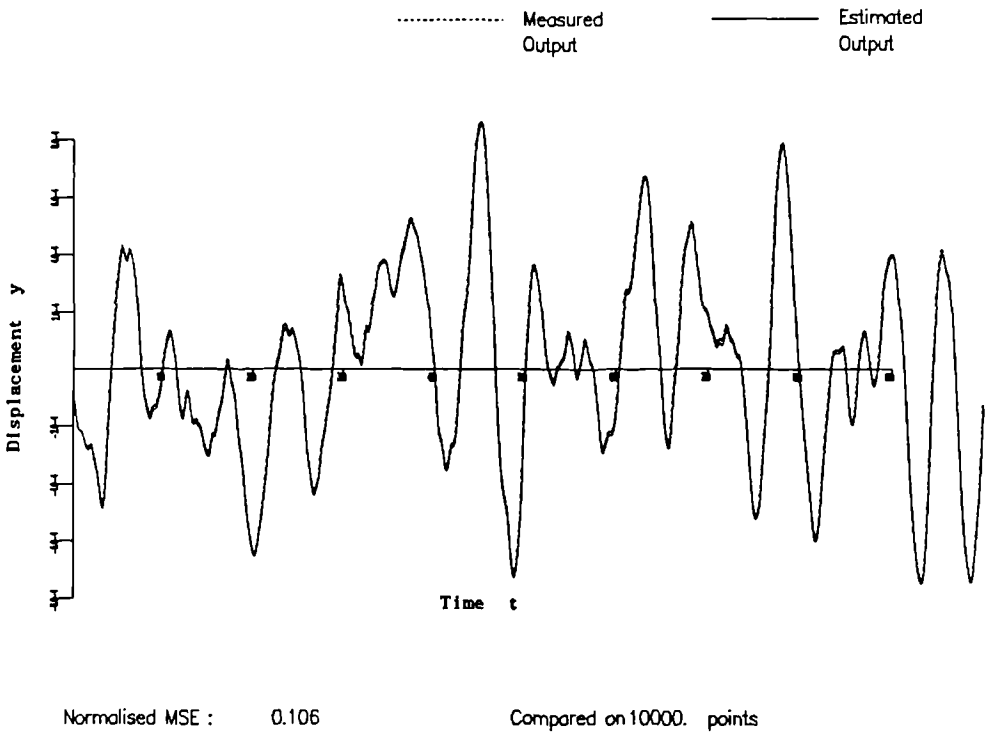

Figure 2.16. Comparison of the (1,1) Chebyshev model displacement data with the exact displacement for the linear system.

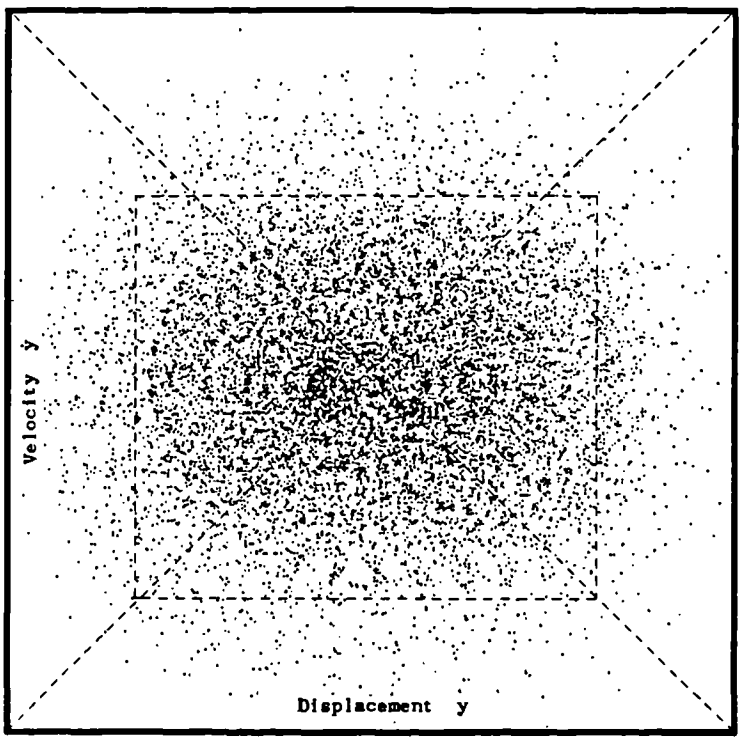

Figure 2.17. Distribution in the phase plane of 10000 data points for the simulated system with a cubic stiffness given in the text.

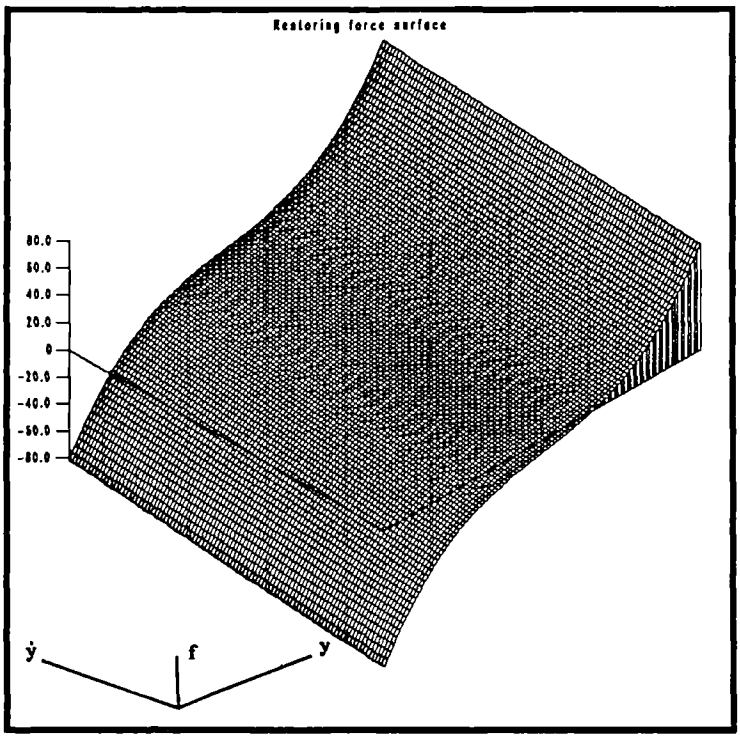

Figure 2.18. C^1 restoring force surface for the system with a cubic stiffness term.

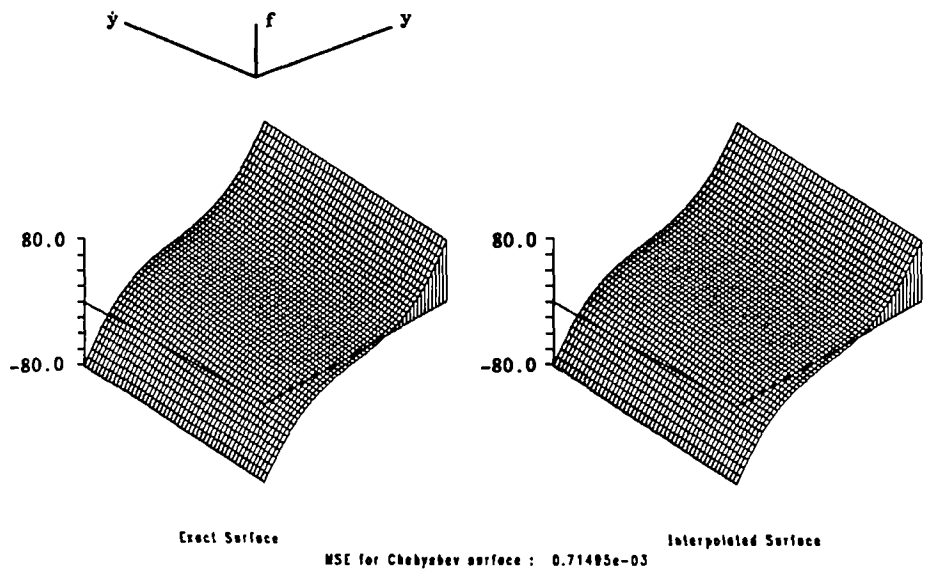

Figure 2.19. Comparison of the interpolated surface with the exact surface for the cubic stiffness system.

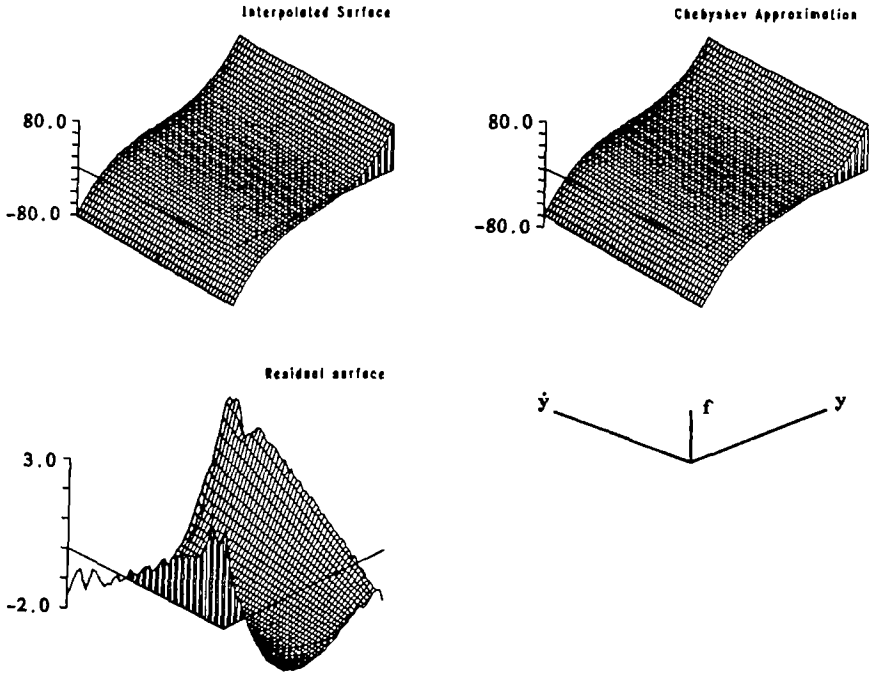

Figure 2.20. Comparison of the (3,1) Chebyshev model surface with the interpolated surface for the cubic stiffness system.

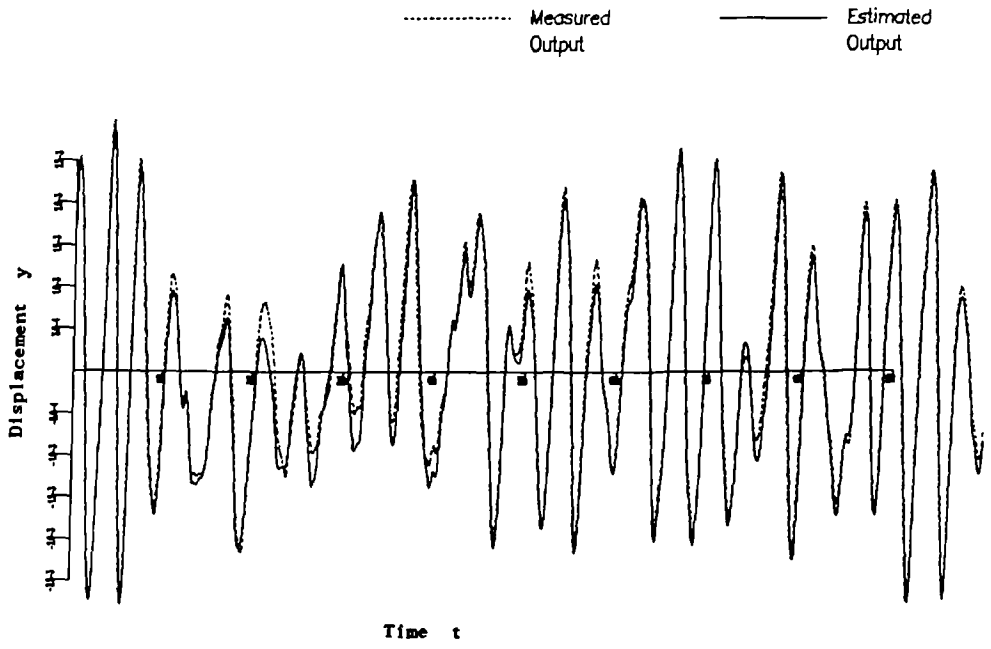

Normalised MSE : 19.4 Compared on 10000. points

Figure 2.21. Comparison of the Chebyshev model displacement data with the true displacement data for the cubic stiffness system.

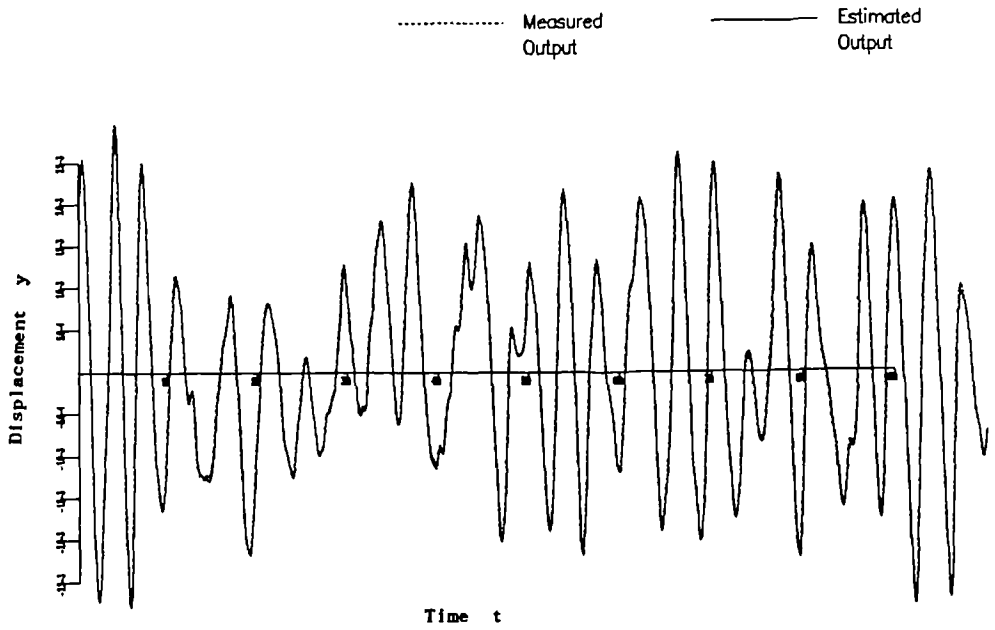

Figure 2.22. The same comparison as in the previous figure except that the y^2 term has been deleted from the model.

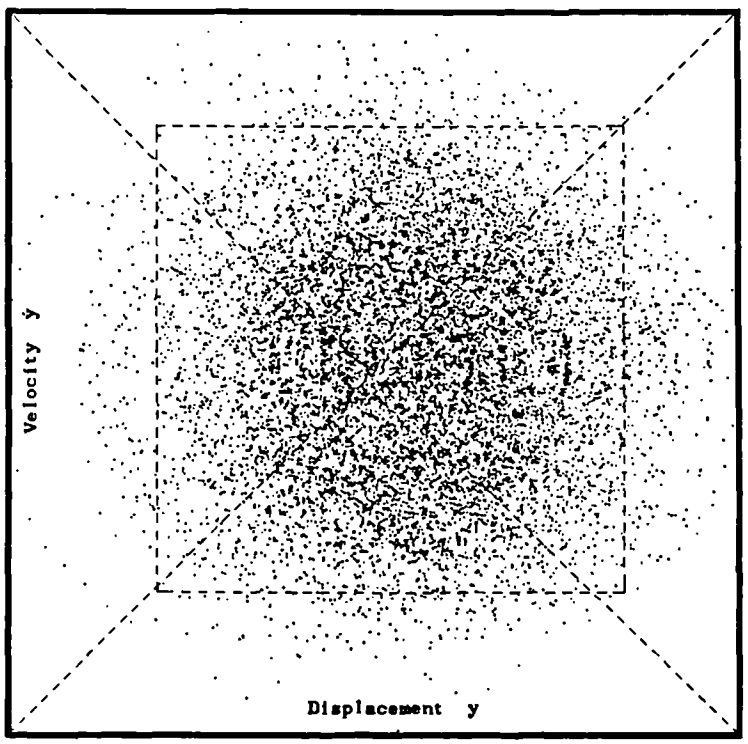

Figure 2.23. Distribution in the phase plane of 10000 points of data for the simulated system in the text with a quadratic damping term.

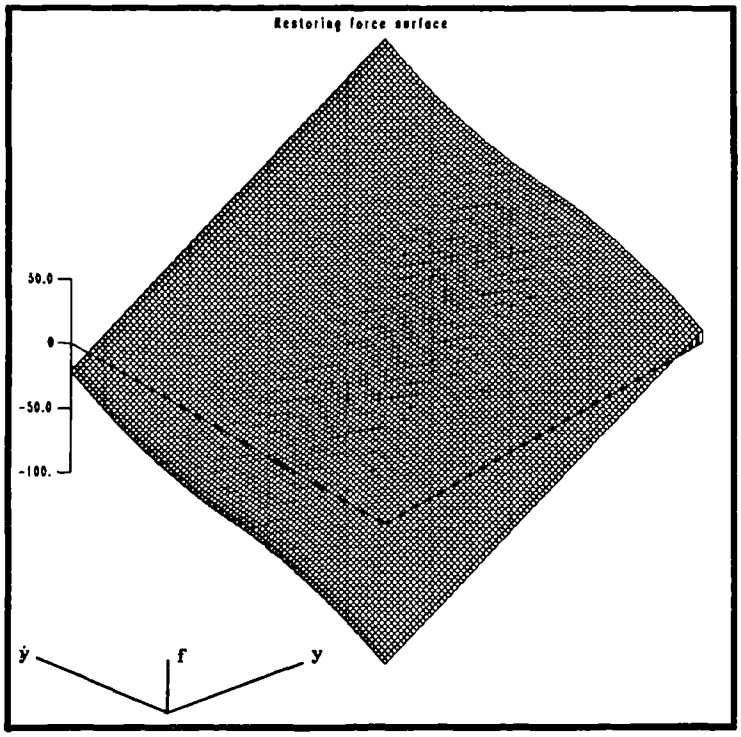

Figure 2.24. C^1 interpolated force surface for the system with quadratic damping.

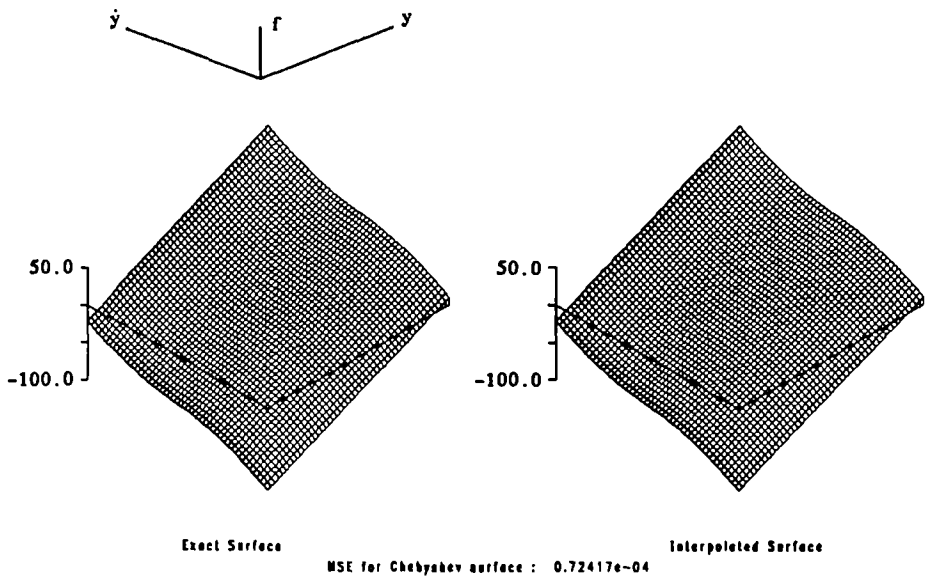

Figure 2.25. Comparison of the interpolated force surface with the exact surface for the system with quadratic damping.

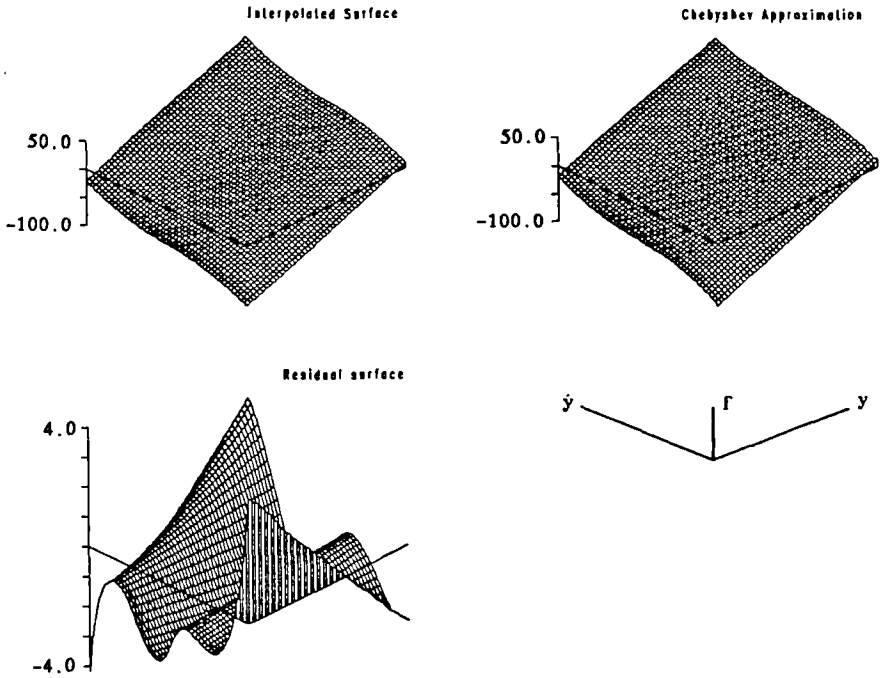

Figure 2.26. Comparison of the Chebyshev model surface with the interpolated surface for the system with quadratic damping

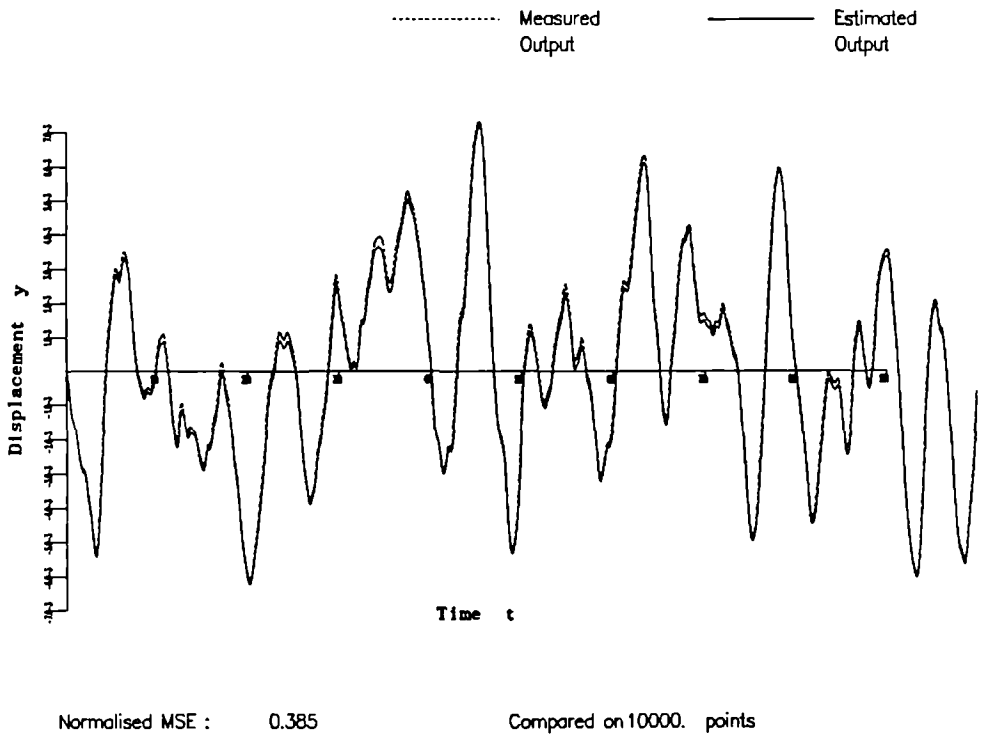

Normalised MSE : 0.385 Compared on 10000. points

Figure 2.27. Comparison of the model displacement data with the true displacement data for the system with quadratic damping.

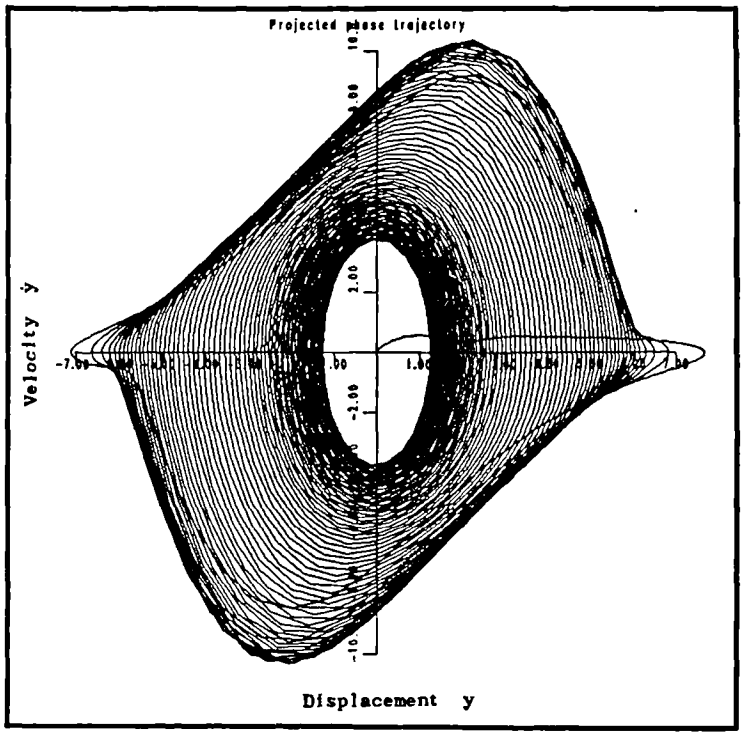

Figure 2.28. 3000 points of the phase trajectory for the Van der Pol oscillator system described in the text.

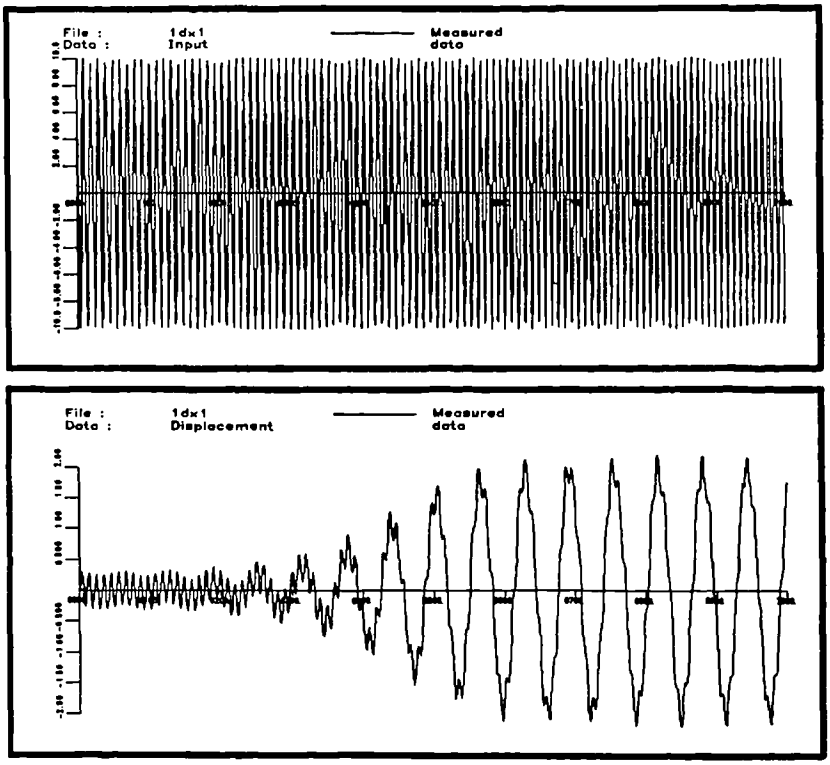

Figure 2.29. 1000 sample points of the input force and displacement response for the simulated Van der Pol oscillator system showing the transition to chaos.

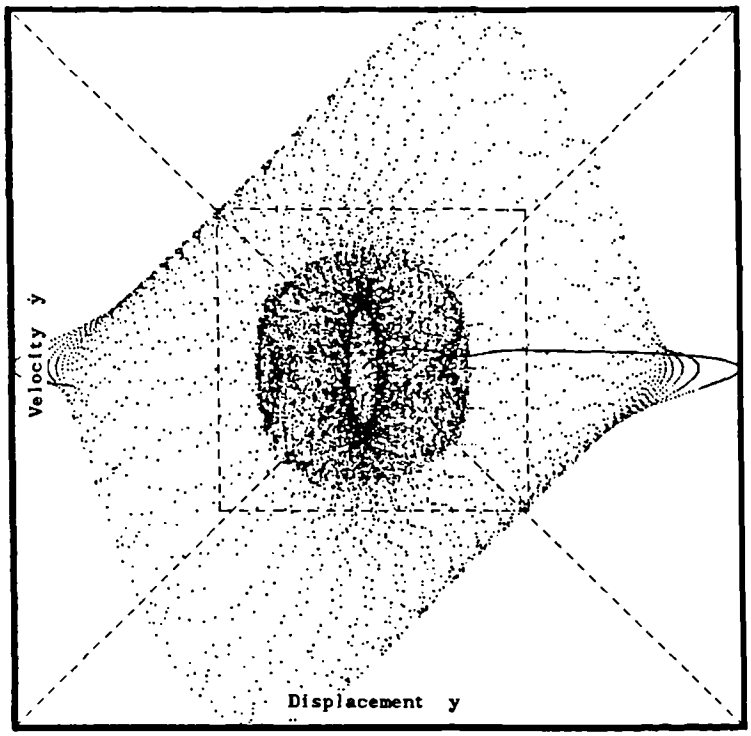

Figure 2.30. Distribution in the phase plane of 10000 points of data for the simulated Van der Pol oscillator system.

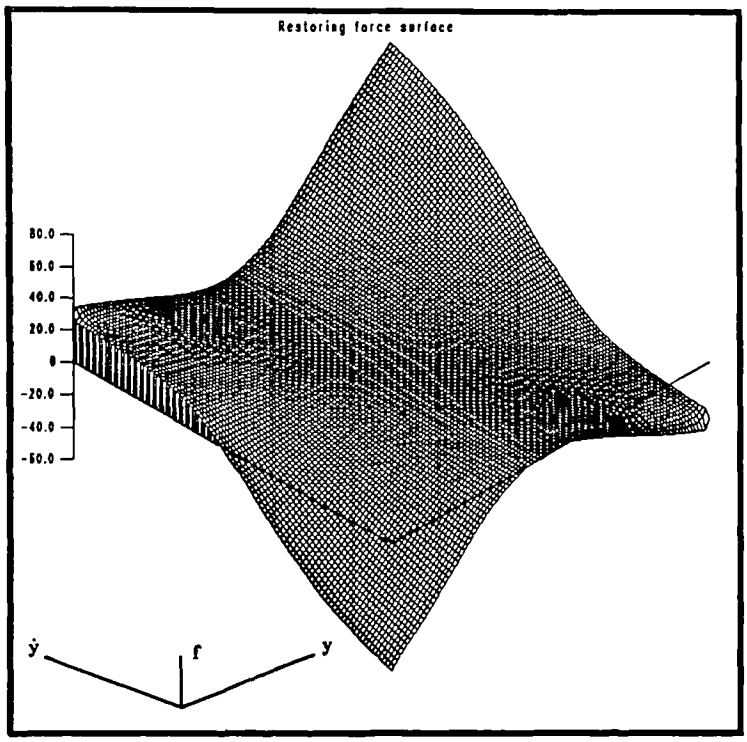

Figure 2.31. C^0 interpolated force surface for the Van der Pol oscillator.

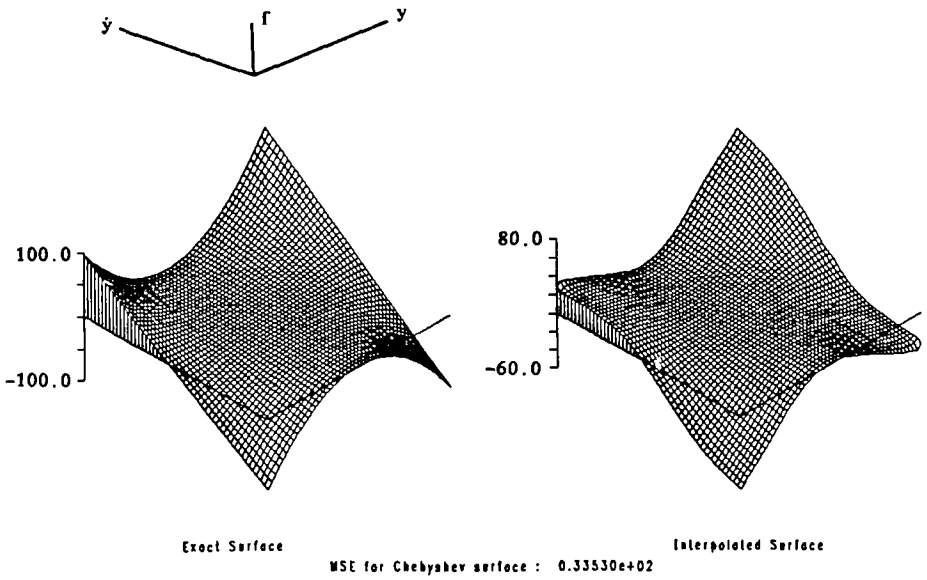

Figure 2.32. Comparison of the C^0 interpolated surface with the exact surface for the Van der Pol oscillator.

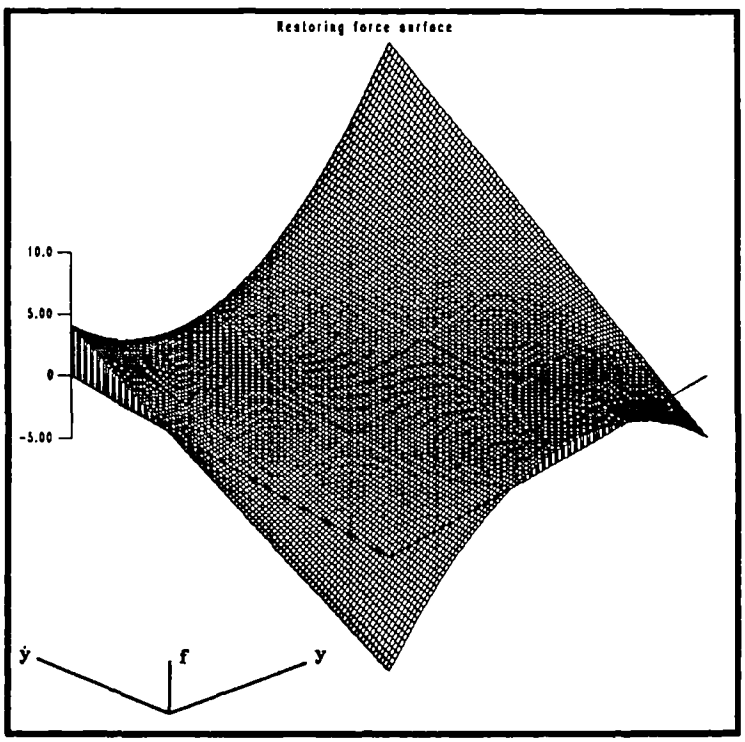

Figure 2.33. C^1 interpolated force surface for the Van der Pol oscillator.

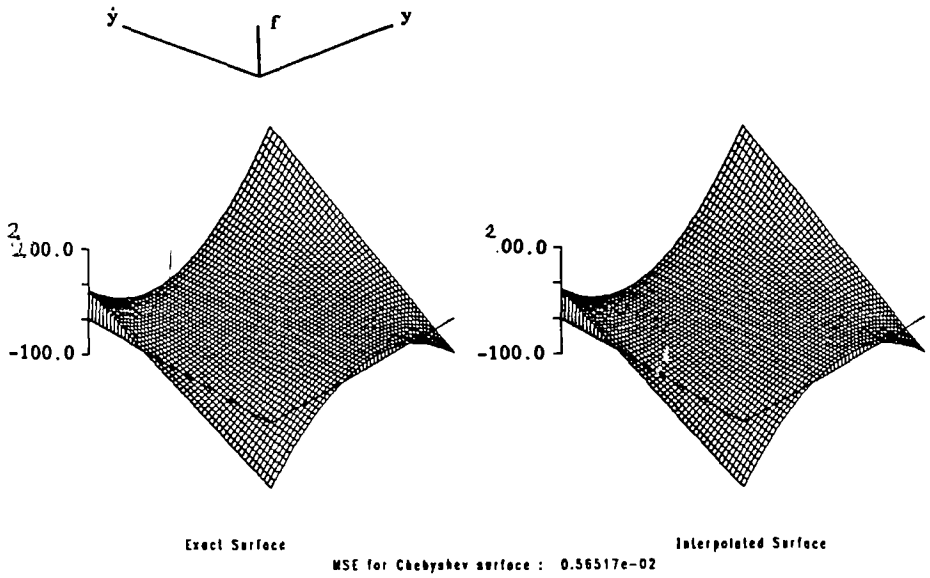

Figure 2.34. Comparison of the C^1 interpolated surface with the exact surface for the Van der Pol oscillator.

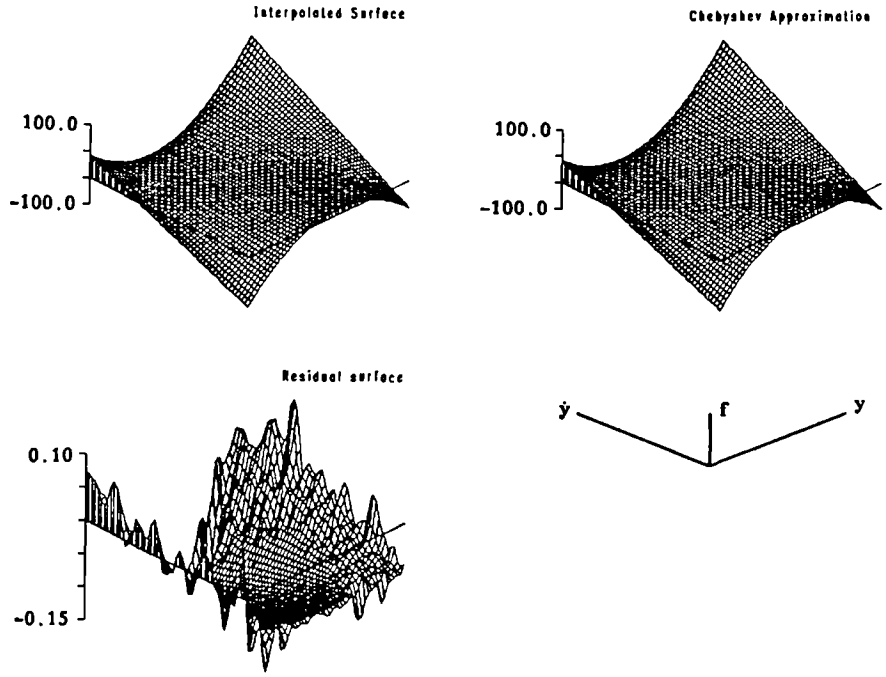

Figure 2.35. Comparison of the (2,1) Chebyshev model surface with the exact surface for the Van der Pol oscillator.

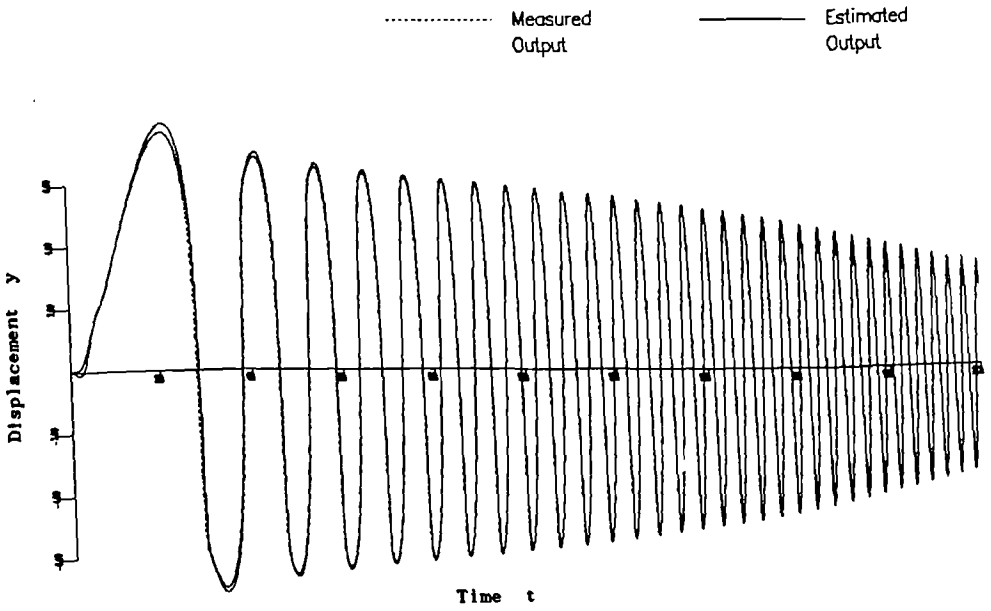

Normalised MSE : 7.85

Figure 2.36. Comparison of the model displacement data with the true displacement data for the Van der Pol oscillator showing the data before the transition to chaos.

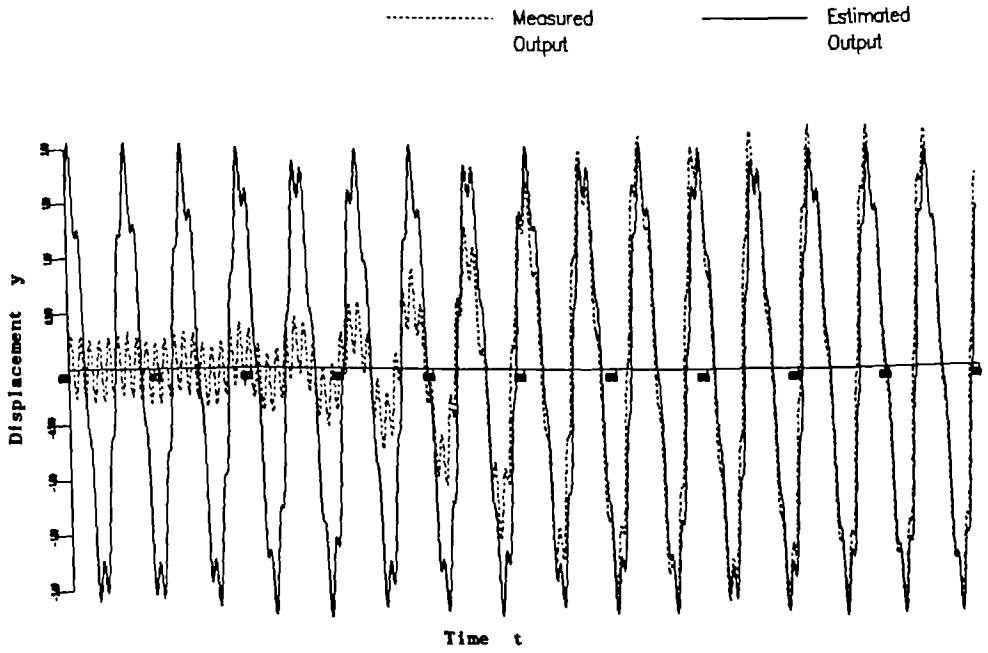

Normalised MSE : 7.85

Figure 2.37. The same comparison as the previous figure except that the transition to chaos is shown for the true data.

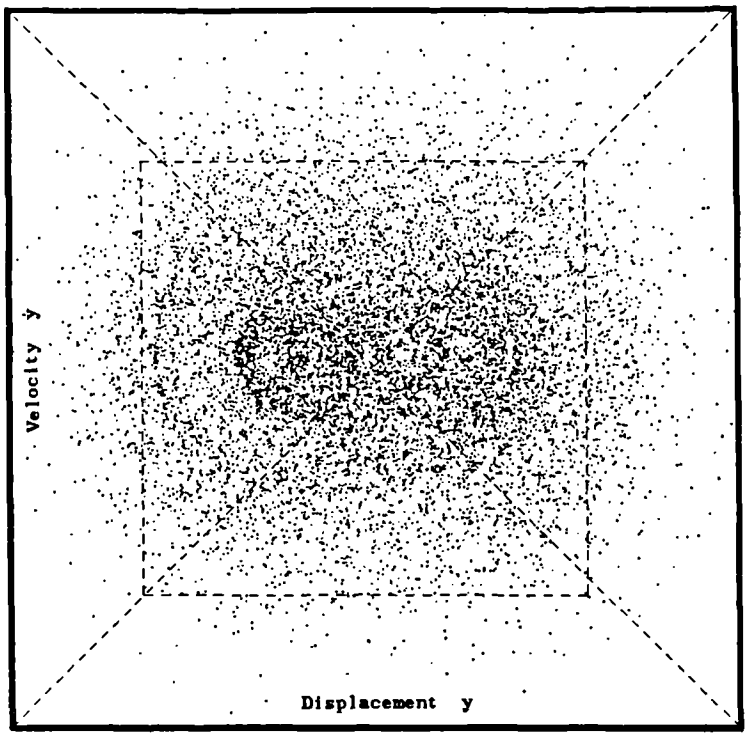

Figure 2.38. Distribution in the phase plane of 10000 data points for the simulated piecewise-linear system described in the text.

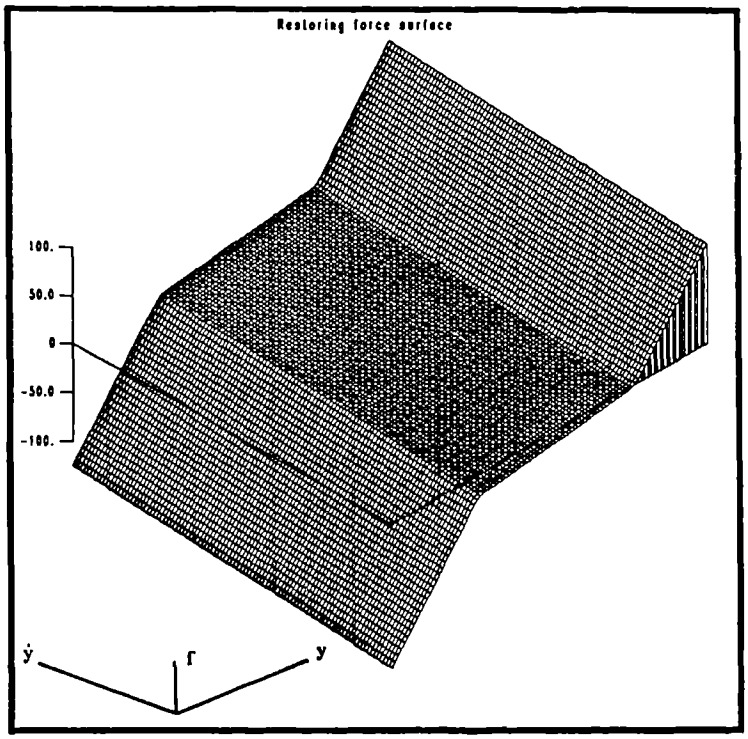

Figure 2.39. C^1 interpolated force surface for the piecewise-linear system.

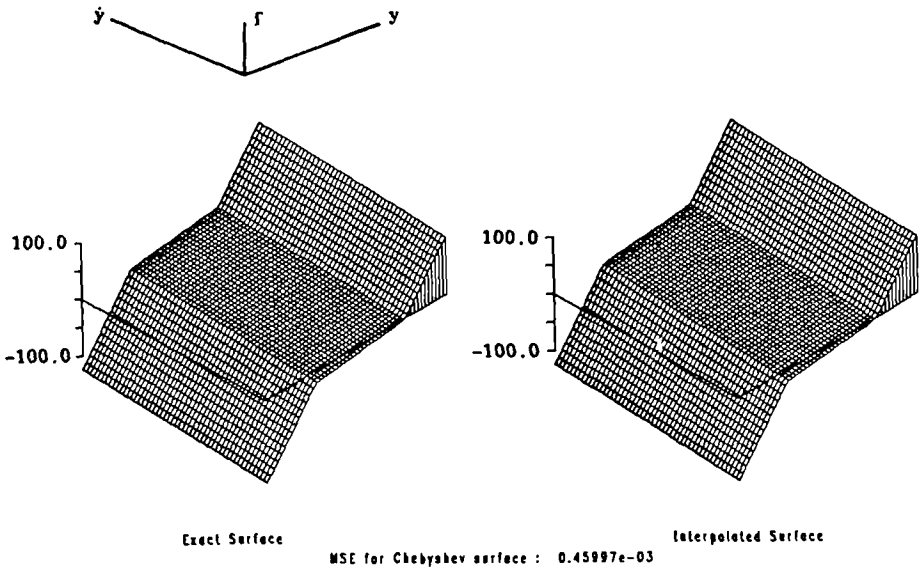

Figure 2.40. Comparison of the interpolated force surface with the exact force surface for the piecewise-linear system.

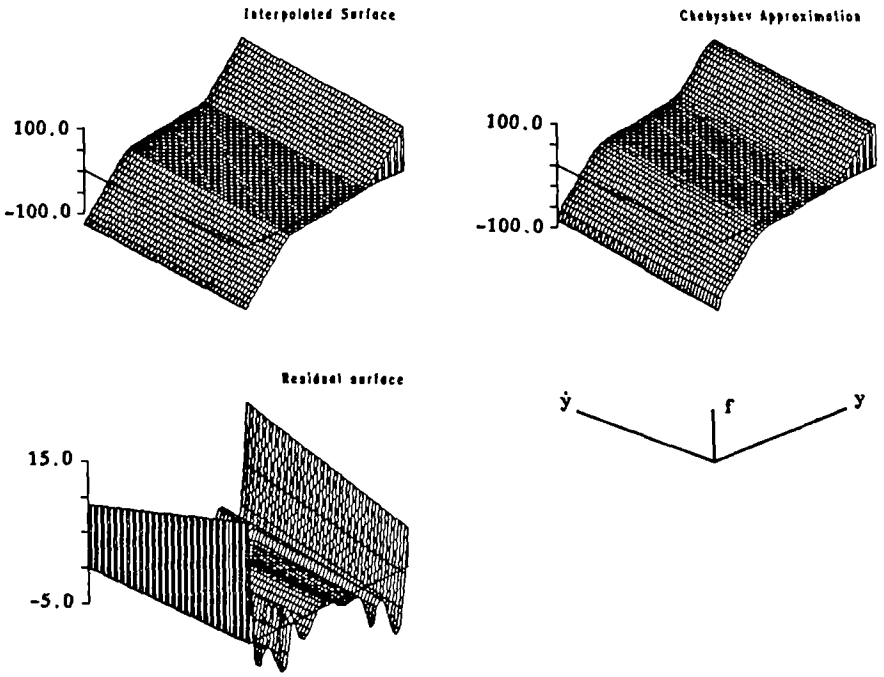

Figure 2.41. Comparison of the (9,1) Chebyshev model surface with the interpolated surface for the piecewise-linear system.

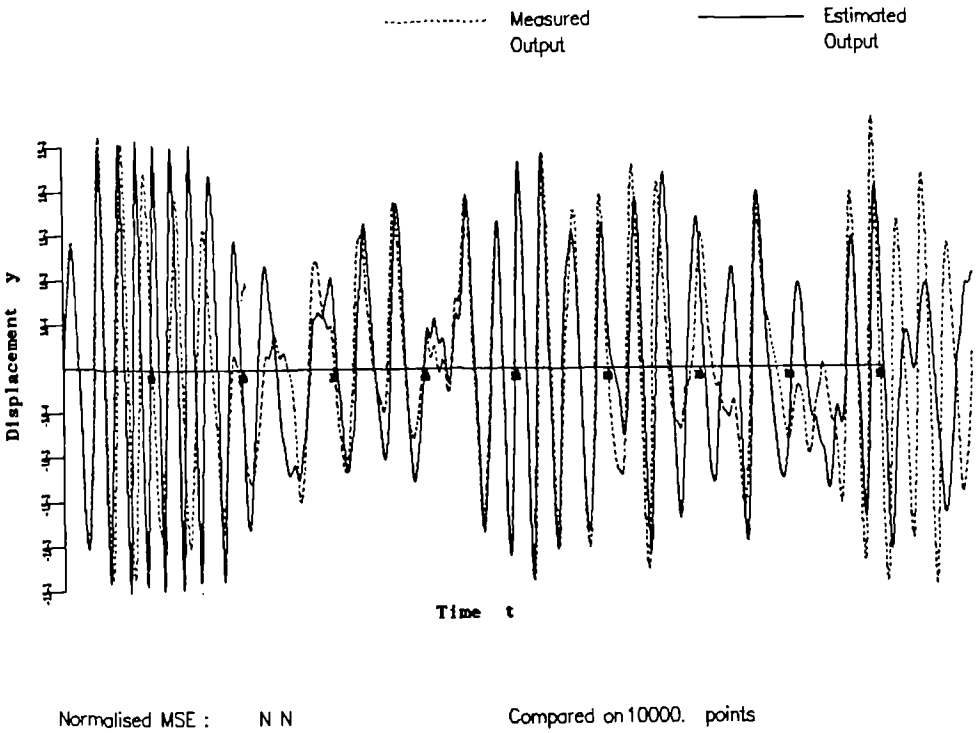

Figure 2.42. Comparison of the model displacement data with the true displacement data for the piecewise-linear system.

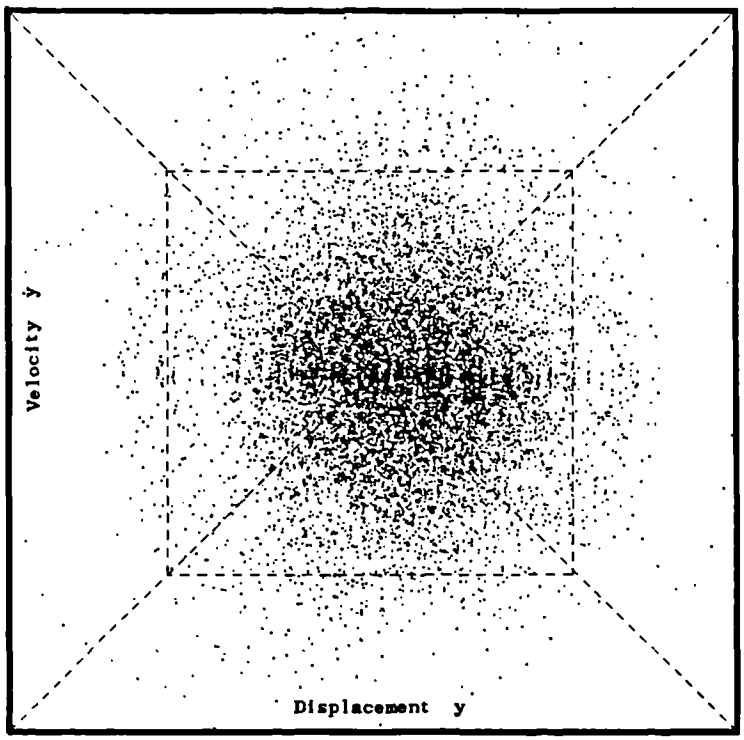

Figure 2.43. Distribution in the phase plane of 10000 data points for the simulated system with Coulomb friction described in the text.

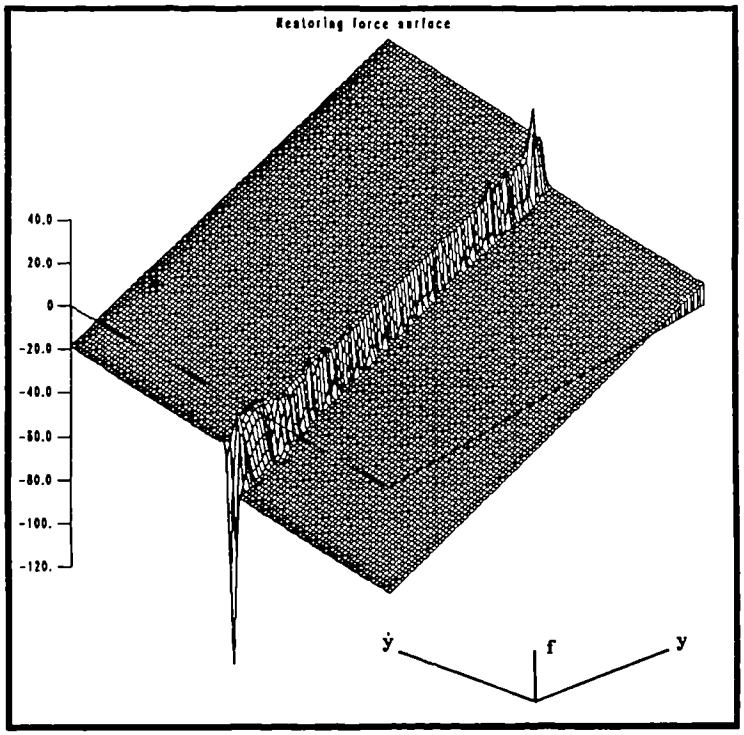

Figure 2.44. C^1 interpolated force surface for the system with Coulomb friction.

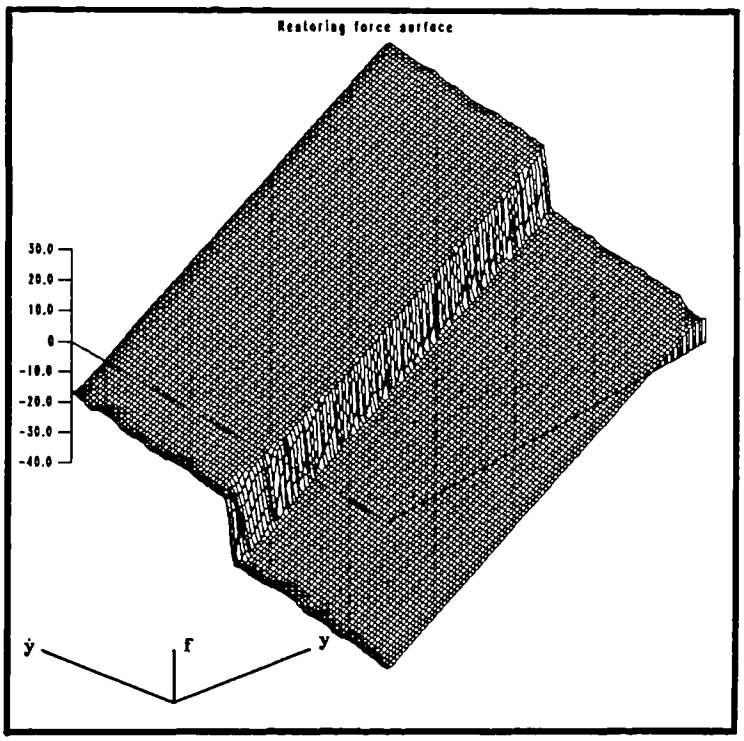

Figure 2.45. C^0 interpolated force surface for the system with Coulomb friction.

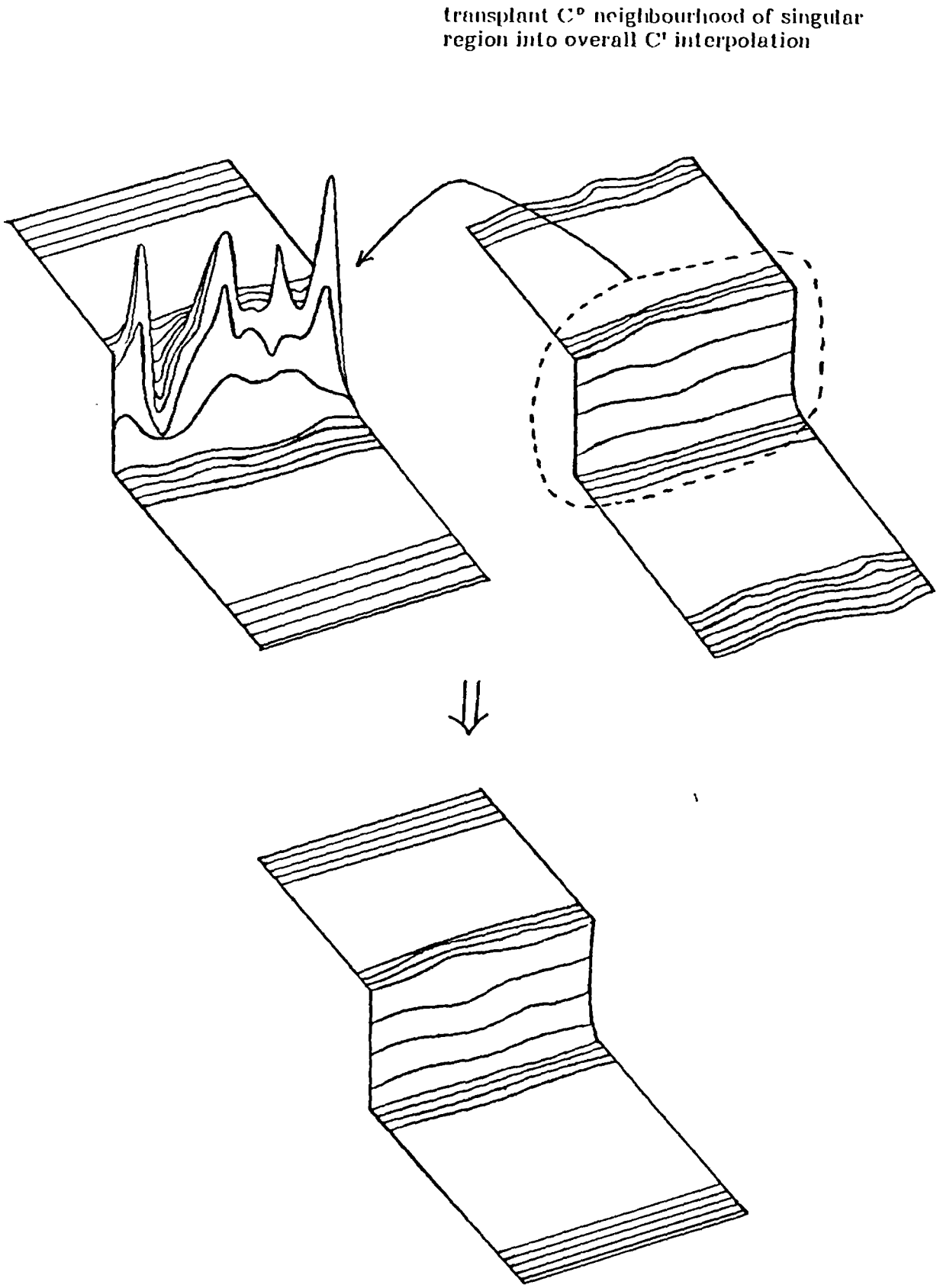

Figure 2.46. The formation of the C^1/C^0 hybrid surface.

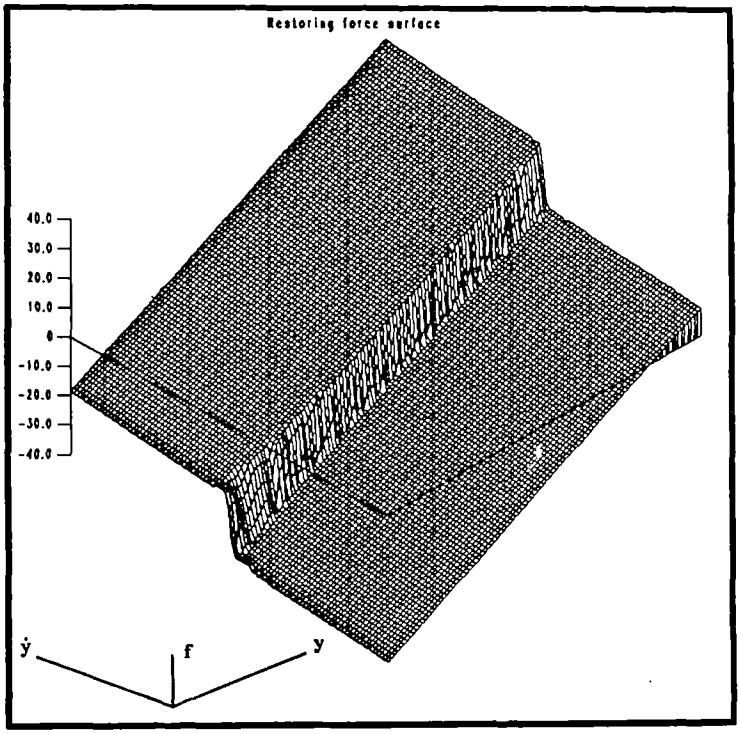

Figure 2.47. C^1/C^0 hybrid force surface for the system with Coulomb friction.

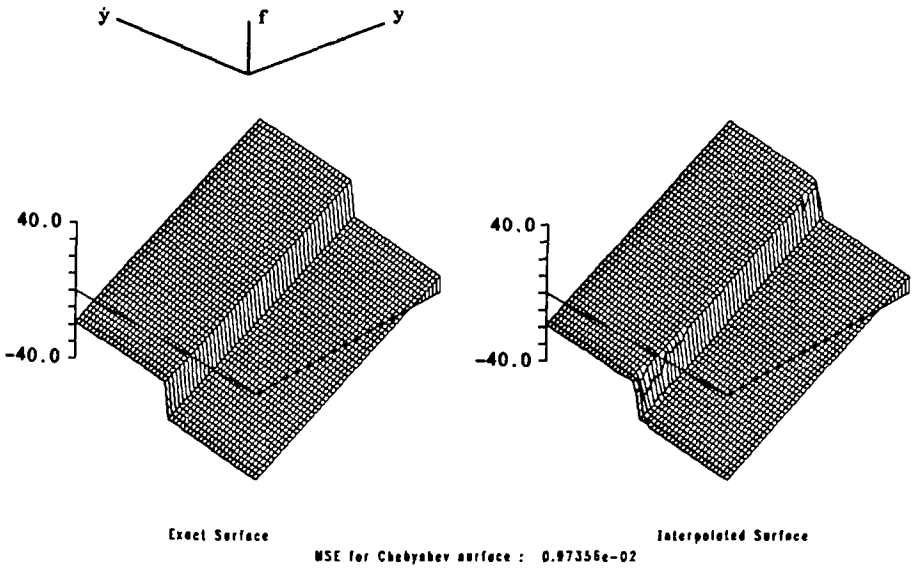

Figure 2.48. Comparison of the hybrid interpolated force surface with the exact force surface for the system with Coulomb friction.

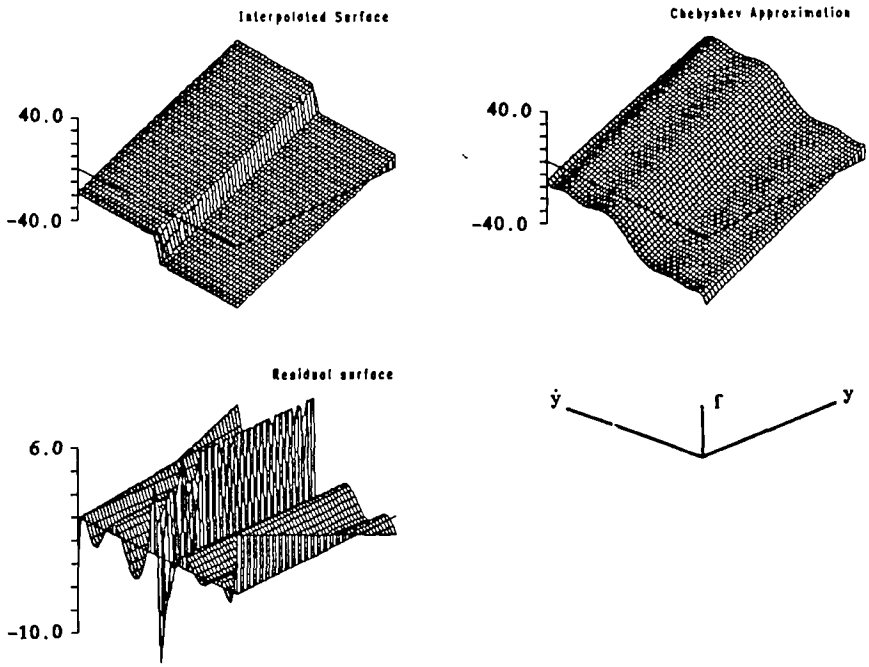

Figure 2.49. Comparison of the (1,9) Chebyshev model surface with the interpolated surface for the Coulomb friction system.

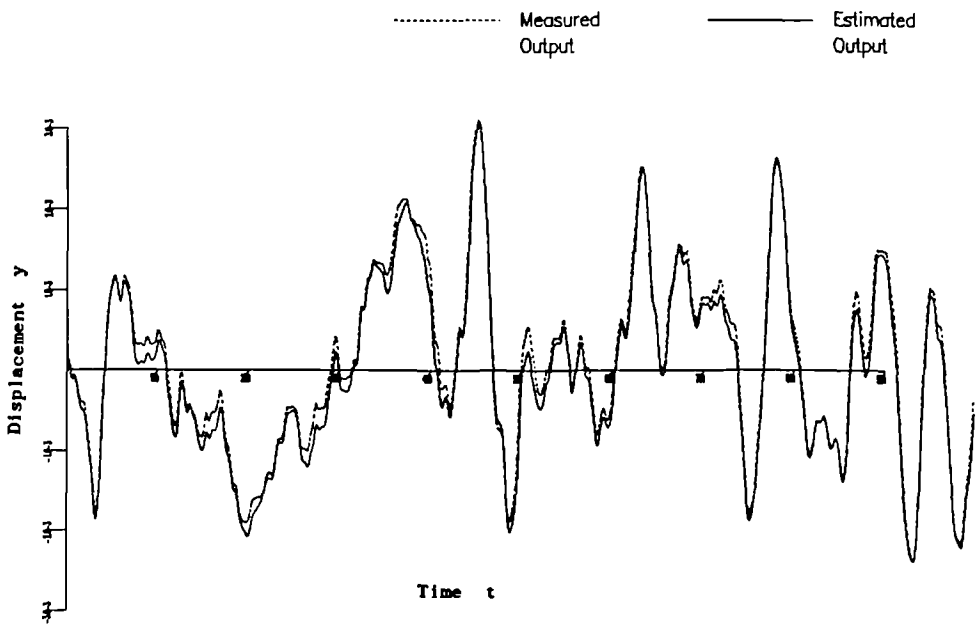

Normalised MSE : 6.87 Compared on 10000. points

Figure 2.50. Comparison of the model displacement data with the true displacement data for the Coulomb friction system.

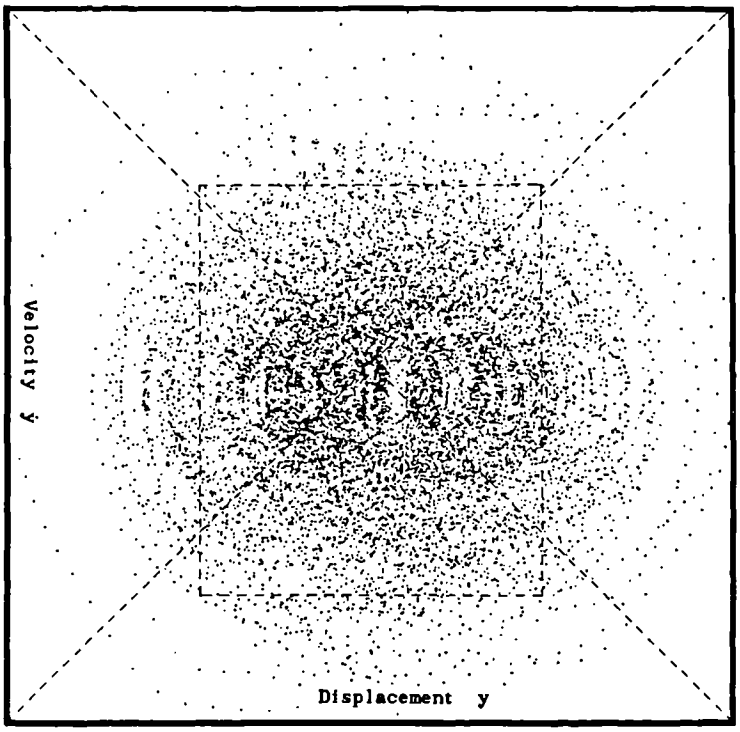

Figure 2.51. Distribution in the phase plane of 10000 data points for the simulated hysteretic system described in the text.

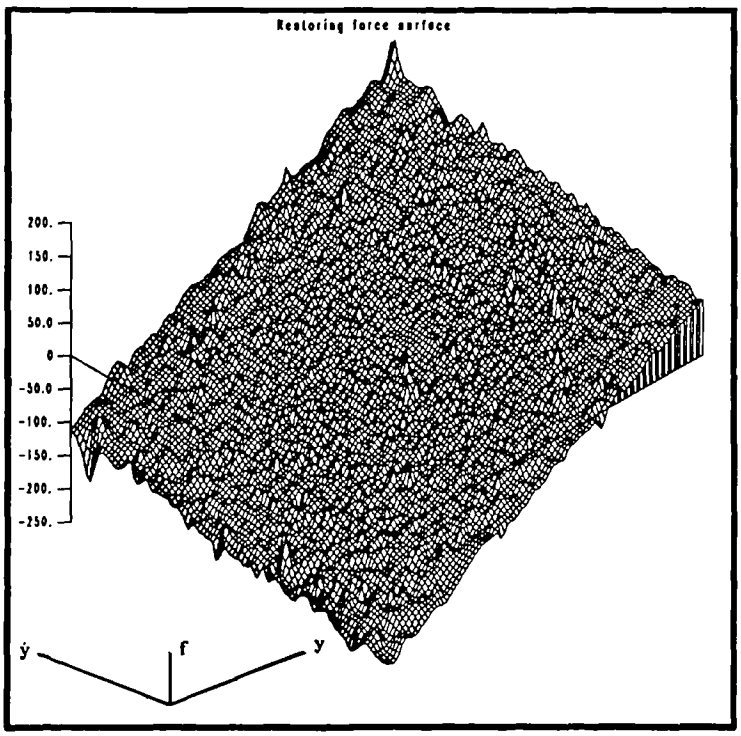

Figure 2.52. C^1 interpolated force surface for the hysteretic system.

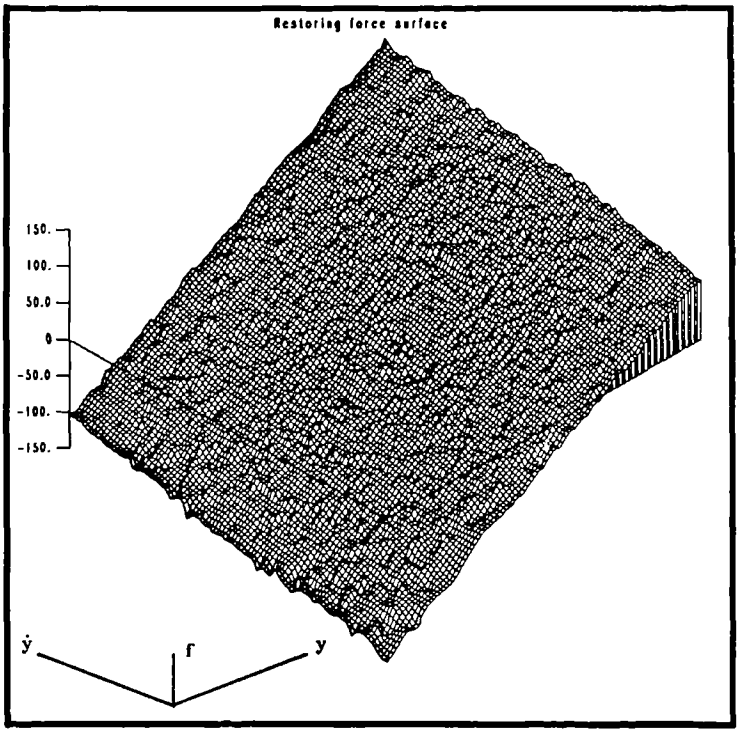

Figure 2.53. C^0 interpolated force surface for the hysteretic system.

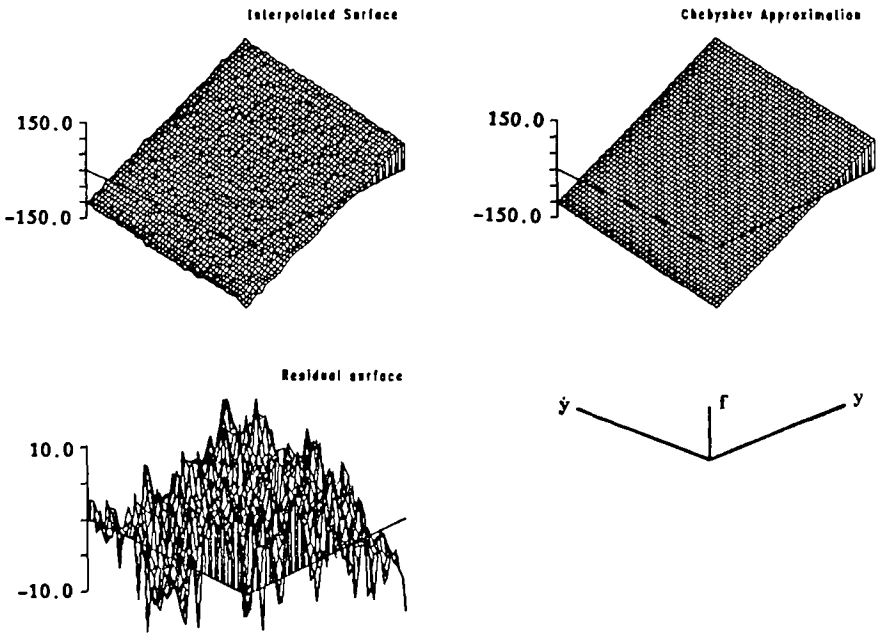

Figure 2.54. Comparison of the (1,1) Chebyshev model surface with the interpolated surface for the hysteretic system.

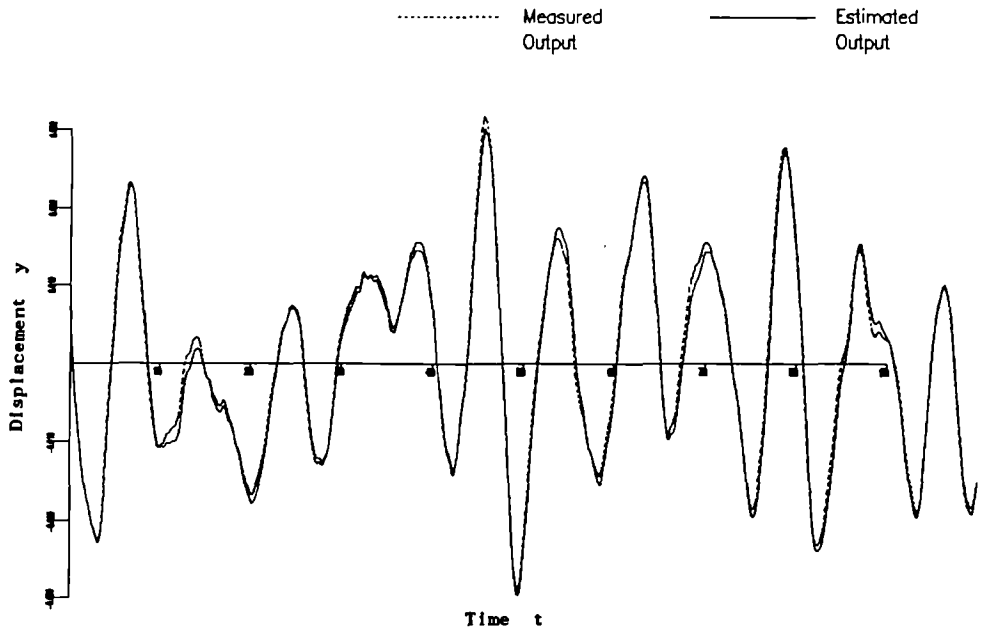

Figure 2.55. Comparison of the model displacement data with the true data for the hysteretic system.

Chebyshev coefficients for restoring force

	0	1	2	3
0				
1				
2				
3				

I terms

J terms

Table 2.1. Coefficients for the Chebyshev models for the linear system

MSE for various Chebyshev model orders.

	0	1	2	3
0	0.10000e+03	0.12113e+02	0.12309e+02	0.12309e+02
1	0.87978e+02	0.87758e-01	0.26570e+00	0.26395e+00
2	0.88018e+02	0.11108e+00	0.32274e+00	0.31998e+00
3	0.88018e+02	0.11488e+00	0.32654e+00	0.32038e+00

J order (max model order - x)

I order (x - model order)

Table 2.2. Mean-Square Errors (MSE) for the Chebyshev models given in Table 2.1.

Chebyshev coefficients for restoring force

	0	1	2	3
0	-.557738+00	.869888+01	-.387258+00	.109126-01
1	.722005+02	-.185974+01	-.104309-01	-.143308+01
2	-.231344+01	.330888-01	-.100564-02	.457335-01
3	.118214+02	-.310028+00	-.331716-01	-.308884+00
4	-.279828+01	.482418-01	.343888-03	.548825-01
5	-.316736-02	-.185388+00	-.276379-01	.137008-01

J terms

I terms

Table 2.3. Coefficients for the Chebyshev models for the cubic stiffness system.

MSE for various Chebyshev model orders.

	0	1	2	3	4	5					
0	0.110000E+03	0.883311E+02	0.883311E+02	0.883311E+02	0.883311E+02	0.883311E+02					
1	0.872944E+01	0.852413E+01	0.806535E+01	0.806535E+01	0.806535E+01	0.806535E+01					
2	0.380543E+01	0.317728E+01	0.318864E+01	0.318864E+01	0.318864E+01	0.318864E+01					
3	0.188713E+01	0.169833E+01	0.212216E+01	0.211284E+01	0.211284E+01	0.211284E+01					
4	0.120883E+01	0.120883E+01	0.307704E+01	0.604744E+00	0.604744E+00	0.604744E+00					
5	0.120883E+01	0.120883E+01	0.307704E+01	0.307704E+01	0.604744E+00	0.604744E+00					

J order (xtd - model order)

I order (x - model order)

Table 2.4. MSE table for the Chebyshev models given in Table 2.3.

Chebyshev coefficients for restoring force

	0	1	2	3	4	5	6	7	8
0	-.47419e+01	0.38888e+02	-.19435e+01	0.33333e-01					
1	0.39189e+02	-.19435e+01	0.16049e-01	0.14028e-02					
2	-.19672e+01	0.33333e-01	0.14028e-02	0.18025e-01	-.97324e-02	0.19744e-01	-.48815e-02	0.17125e-01	-.17758e-03

I terms

J terms

Table 2.5. Coefficients for the Chebyshev models for the system with quadratic damping.

MSE for various Chebyshev model orders.

	0	1	2	3	4	5	6	7	8		
0	0.100036+03	0.729586+02	0.730036+02	0.732736+02	0.731086+02	0.730886+02	0.730886+02	0.730886+02	0.721226+02		
1	0.381386+02	0.109186+01	0.111306+01	0.179186+00	0.214286+00	0.322386+00	0.212576+00	0.227076+00	0.253436+00		
2	0.383176+02	0.123976+01	0.133576+01	0.570816+00	0.697686+00	0.596386+00	0.606086+00	0.418446+00	0.441136+00		

I order (x - model order)

J order (max power - model order)

Table 2.6. MSE table for the Chebyshev models given in Table 2.6.

Chebyshev coefficients for restoring force.

	0	1	2	3	4
0	0.43268e+00	0.34174e+01	-1.1828e+00	-8.8817e-02	-7.7008e-01
1	0.31827e+01	0.19478e+00	-8.9400e-01	-8.8004e-01	-3.5668e-01
2	0.16943e+00	0.41987e+01	-1.4803e+00	-7.8227e-02	-8.5104e-01
3	-3.1945e-01	-3.2883e+00	-1.1919e-02	-3.3874e-02	0.4043?e-02
4	-7.2831e-01	-3.9988e-01	-4.4802e-02	-3.3539e-02	0.12271e-02

I terms

J terms

Table 2.7. Coefficients for the Chebyshev models of the Van der Pol oscillator system.

MSE for various Chebyshev model orders.

	0	1	2	3	4
0	0.10016e+03	0.84707e+02	0.84686e+02	0.84627e+02	0.84943e+02
1	0.59111e+02	0.30087e+02	0.30273e+02	0.30321e+02	0.30339e+02
2	0.55782e+02	0.11825e+00	0.22011e+00	0.22906e+00	0.24188e+00
3	0.55797e+02	0.31468e+00	0.41988e+00	0.43878e+00	0.45128e+00
4	0.55818e+02	0.33268e+00	0.44828e+00	0.46805e+00	0.48133e+00

I order (x - model order)

J order (XX - model order)

Table 2.8. MSE table for the Chebyshev models given in Table 2.7.

Chebyshev coefficients for restoring force.

	0	1	2
0	−.89170e+01	0.10382e+02	−.34827e+00
1	0.10284e+03	−.2256e+01	0.30798e-02
2	−.8928e+01	0.15453e+03	−.10185e-01
3	0.28273e+02	−.79801e+00	0.12886e-01
4	−.34117e+01	0.88877e-01	−.13023e-01
5	−.59178e+01	−.9088e-01	0.84988e-02
6	−.38823e+01	0.16857e-01	0.21718e-01
7	−.14508e+01	−.17688e+00	0.26348e-02
8	−.30798e+01	0.74727e-01	−.8258e-02
9	0.29943e+01	−.2624e+00	0.12082e-01

I terms

J terms

Table 2.9. Coefficients for the Chebyshev models for the piecewise-linear system.

MSE for various Chebyshev model orders.

	0	1	2
0	0.19[illegible]E+02	0.18[illegible]E+02	0.18[illegible]E+02
1	0.15[illegible]E+02	0.13[illegible]E+02	0.13[illegible]E+02
2	0.14[illegible]E+02	0.13[illegible]E+02	0.13[illegible]E+02
3	0.21[illegible]E+01	0.10[illegible]E+01	0.10[illegible]E+01
4	0.24[illegible]E+01	0.12[illegible]E+01	0.12[illegible]E+01
5	0.19[illegible]E+01	0.78[illegible]E+00	0.77[illegible]E+00
6	0.19[illegible]E+01	0.81[illegible]E+00	0.82[illegible]E+00
7	0.15[illegible]E+01	0.75[illegible]E+00	0.78[illegible]E+00
8	0.19[illegible]E+01	0.77[illegible]E+00	0.78[illegible]E+00
9	0.19[illegible]E+01	0.81[illegible]E+00	0.87[illegible]E+00

I order (x - model order)

J order (xtd - model order)

Table 2.10. MSE table for the Chebyshev models given in Table 2.9.

Chebyshev coefficients for restoring force.

	0	1	2	3	4	5	6	7	8	9
0	-.38691e+01	0.25412e+02	0.18010e+02	-.41118e+01	0.24887e+00	0.23994e-01	-.87105e+00	-.18353e+01	0.34883e+00	0.13712e+01
1	1	-.94823e+00	-.14370e-01	-.80568e+00	0.29297e-01	-.83571e+00	-.19433e-01	-.30598e+00	0.32997e-01	-.91229e+00

I terms

J terms

MSE for various Chebyshev model orders.

	0	1	2	3	4	5	6	7	8	9
0	0.10004e+03	0.34656e+02	0.74008e+02	0.88538e+02	0.88558e+02	0.87587e+02	0.87883e+02	0.87191e+02	0.87204e+02	0.88880e+02
1	0.70858e+02	0.54901e+01	0.39451e+01	0.31735e+01	0.31915e+01	0.22343e+01	0.23310e+01	0.18000e+01	0.18835e+01	0.15740e+01

I order (x - model order)

J order (xxx - model order)

Table 2.12. MSE table for the Chebyshev models given in Table 2.11.

Chebyshev coefficients for restoring force.

	0	1	2	3							
0	−1.1002e+02	0.36357e+02	−1.0800e+01	0.88832e+00							
1	0.13943e+03	−4.6019e+01	−5.3803e+01	−2.8206e+01							
2	−3.2261e+01	0.19982e+01	−5.7973e−01	0.21189e+00							
3	−1.9872e−01	−1.3483e+01	−3.3370e+00	−4.0259e+00							

I terms

J terms

Table 2.13. Coefficients for the Chebyshev models for the hysteretic system.

MSE for various Chebyshev model orders.

	0	1	2	3
0	0.100000e+03	0.929054e+02	0.925786e+02	0.925573e+02
1	0.723969e+01	0.188028e+00	0.197701e+00	0.200338e+00
2	0.749810e+01	0.396028e+00	0.417228e+00	0.422391e+00
3	0.749808e+01	0.583931e+00	0.414728e+00	0.416878e+00

J order (xdd - model order)

I order (x - model order)

Table 2.14. MSE table for the Chebyshev models given in Table 2.13.

CHAPTER 3

THE MASRI/CAUGHEY PROCEDURE - MDOF SYSTEMS

The work of the previous chapter indicated that for simulated SDOF systems Masri and Caughey's restoring force approach provides a useful technique for the identification of nonlinear systems. This would be of limited value if it was only applicable to SDOF systems. In fact, Masri,Caughey and Sassi have shown that the method allows a fairly straightforward extension to MDOF structural systems (10). This chapter is concerned with this extension.

3.1. Basic Theory.

The most natural language for the description of multi-degree-of-freedom (MDOF) systems is that of matrices and vectors. In the discussion which follows square brackets [ ] shall denote matrices and curved brackets { } column vectors. In addition the convention adopted is that the kernel letter of a generic matrix will be a capital and the diagonalised form of the matrix will be denoted by the small character of the same type. Thus [M] is the mass matrix and [m] is the diagonalised mass matrix. Transposition is indicated by a superscript T.

As before, one begins with Newton's second law

$$[M]\{\ddot{y}\} + \{f(y,\dot{y})\} = \{x(t)\} \qquad (1)$$

for a MDOF system. The assumption is that the mass of the system is concentrated at N points. The external forces on the system are then assumed to be applied at these points, the i^{th} entry of the vector {x} being the force at mass i. The i^{th} entry of the vector $\{\ddot{y}\}$ is the acceleration of mass i. The i^{th} component of {f} is the

internal or restoring force which attempts to return mass m_i to equilibrium when it is disturbed. This is already a rather restricted model. In general a structural system will have a continuous distribution of mass and hence an unlimited number of degrees-of-freedom. The model above has only N. This is reflected in the fact that the system in (1) has precisely N natural frequencies or resonances, the simplest continuous system will have an infinite set. For fairly obvious reasons, systems of the type above are sometimes called lumped-parameter systems. Under normal conditions one would use a band-limited input to excite a system i.e. one with a limited frequency range. This means that only a finite number of the system modes would contribute to the dynamics, one would excite up to say, the N^{th} natural frequency. Under these conditions one should be able to model the behaviour of the system accurately with an N degree-of-freedom system. Equation (1) is therefore adequate for most purposes.

The simplest situation possible is where the restoring force is linear i.e.

$$\{f\} = \{f_1\} = [C]\{\dot{y}\} + [K]\{y\} \qquad (2)$$

[C] is the damping matrix and [K] is the stiffness matrix for the system. If the forces are nonlinear, there may still be a regime where (2) is a good approximation e.g. if {f} is a polynomial and a small excitation is used. For such a system, one could determine the modal matrix $[\psi]$. Arguably the most common method of estimating the modal matrix is by curve-fitting to the system FRFs, a comprehensive reference on this technique is (7). Having obtained $[\psi]$ one can then change to the *normal coordinate* system specified by

$$\{u\} = [\psi]^T\{y\}$$

In this coordinate system (7), the equations of motion (1) become

$$[m]\{\ddot{u}\} + [c]\{\dot{u}\} + [k]\{u\} = [\psi]^T\{x\} = \{q\}$$

where $[m] = [\psi]^T[M][\psi]$ is diagonal, as are [c] and [k] with similar definitions. In order that [c] be diagonal proportional damping is assumed for the moment. The equations are now decoupled into N SDOF equations of motion.

$$m_i\ddot{u}_i + c_i\dot{u}_i + k_i u_i = q_i$$

where m_i, c_i and k_i are the diagonal entries of [m], [c] and [k] respectively. If the system is nonlinear this decoupling does not occur, one cannot find an appropriate linear transformation. However, since the underlying linear system can be decoupled, one can perhaps expect some simplification on changing to normal coordinates. Equation (1) becomes

$$[m]\{\ddot{u}\} + \{h(\{u\},\{\dot{u}\})\} = \{q(t)\} \qquad (3)$$

where $\{h\} = [\psi]^T\{f\}$. As before, the method requires estimates of $\{y\}$, $\{\dot{y}\}$ and $\{\ddot{y}\}$ for each sampling instant. However, one also needs estimates of the mass matrix and the modal matrix. Finding these quantities accurately is a non-trivial problem. The mass matrix in particular is rather awkward to determine (38). The technique of modal anlysis (7) allows one to estimate $[\psi]$. For the moment assume that estimates are available, the restoring force vector can then be calculated from (3)

$$\{h\} = \{q\} - [m]\{\ddot{u}\} = [\psi]^T.(\{x\} - [M]\{\ddot{y}\})$$

and the i^{th} component is given by

$$h_i = q_i - m_i\ddot{u}_i$$

These equations hold at each sampling instant. As an aid to clarity, the sampling instant labels are suppressed. Unfortunately h_i is not simply a function of u_i and $\dot{u}_i$. In general the nonlinearity of the system can cause a dependency on all the u's and $\dot{u}$'s. However, as a first approximation one assumes that the main contribution to h_i

is a function of u_i and $\dot{u}_i$. Just as for the SDOF systems one can interpolate the h_i data into a surface above the $(u_i,\dot{u}_i)$ plane and then fit a model of the form

$$h_i^{(1)}(u_i,\dot{u}_i) = \sum_m \sum_n C1(i)_{mn}\, T_m(u_i)\, T_n(\dot{u}_i) \qquad (4)$$

For the sake of clarity, the maps which carry the data onto the square $[-1,1]x[-1,1]$ have been omitted. However, one should bear in mind that they are neccessary for the evaluation of the coefficients above; consequently, the coefficients are sample-dependent. The expression (4) will hopefully capture all terms of the form $(u_i)^{\alpha}(\dot{u}_i)^{\beta}$. To include effects caused by the coupling of normal coordinates by the nonlinearity one would need terms of the form $(u_i)^{\alpha}(u_j)^{\beta}$ where $i \neq j$. Consideration of the Van der Pol oscillator suggests that one should add further terms of the form $(u_i)^{\alpha}(\dot{u}_j)^{\beta}$. Masri and Caughey et al. omit to mention that if the nonlinearity is in the damping forces one also needs terms of the form $(\dot{u}_i)^{\alpha}(\dot{u}_j)^{\beta}$. Hopefully one has then accounted for all the terms in h_i. In order to carry out this procedure, one uses (4) to form the first residual term $r_i^{(1)}$,

$$r_i^{(1)}(\{u\},\{\dot{u}\}) = h_i(\{u\},\{\dot{u}\}) - h_i^{(1)}(u_i,\dot{u}_i) \qquad (5)$$

Then by successively interpolating over the (u_i,u_j) planes and expanding, one forms the expression

$$h_i^{(2)}(\{u\}) = \sum_j \sum_m \sum_n C2(i)(j)_{mn}\, T_m(u_i)\, T_n(u_j)$$

$$\simeq r_i^{(1)}(\{u\},\{\dot{u}\})$$

including only those modes which interact with the i^{th} mode. Of course this might be all of them. Displacement/velocity coupling is accounted for in the same manner. One forms

$$r_i^{(2)}(\{u\},\{\dot{u}\}) = r_i^{(1)}(\{u\},\{\dot{u}\}) - h_i^{(2)}(\{u\})$$

and

$$h_i^{(3)}(\{u\},\{\dot{u}\}) = \sum_j \sum_m \sum_n C3(i)(j)_{mn}\, T_m(u_i)\, T_n(\dot{u}_j)$$

$$\simeq r_i^{(2)}(\{u\},\{\dot{u}\})$$

Finally one accounts for the velocity/velocity coupling using

$$r_i^{(3)}(\{u\},\{\dot{u}\}) = r_i^{(2)}(\{u\},\{\dot{u}\}) - h_i^{(3)}(\{u\},\{\dot{u}\})$$

and

$$h_i^{(4)}(\{\dot{u}\}) = \sum_j \sum_m \sum_n C4(i)(j)_{mn}\, T_m(\dot{u}_i)\, T_n(\dot{u}_j)$$

$$\simeq r_i^{(3)}(\{u\},\{\dot{u}\})$$

So the final restoring force model has the form

$$h_i(\{u\},\{\dot{u}\}) = h_i^{(1)}(u_i,\dot{u}_i) + h_i^{(2)}(\{u\}) + h_i^{(3)}(\{u\},\{\dot{u}\}) + h_i^{(4)}(\{\dot{u}\})$$

Because one has now accounted for the presence of (hopefully) all possible terms in h_i, one can remove the proportionality condition on the damping. It is clear that many expansions may be required in order to obtain an accurate model.

Before proceeding it is neccessary to specify how one forms the residual term in (5). One begins the procedure with a time series $h_i(t_k)$ for each component of the restoring force, t_k being the k^{th} sampling instant. In order to find the $u_i,\dot{u}_i$ dependence of the force, one forms the triplets $(u_i(t_k),\dot{u}_i(t_k),h_i(t_k))$, one for each sampling instant. A h_i surface is then interpolated over the $(u_i,\dot{u}_i)$ plane. Unfortunately, ordering the data with respect to u_i and $\dot{u}_i$ removes the ordering with respect to time and one has only a probabilistic relationship to specify the $(u_2,\dot{u}_2)$ dependent part of h_i at each point in the plane. The $(u_2,\dot{u}_2)$ values for each sample point are randomly distributed over the $(u_1,\dot{u}_1)$ plane. This means that one cannot

simply subtract the expansion (4) from the surface and then expand the remainder in terms of say (u_1,u_2). One has to subtract the $(u_1,\dot{u}_1)$ dependence (4) from the original *time-series* h_i and then interpolate a new surface over the (u_1,u_2) plane. Thus, the residual is formed as a time-series

$$r_i^{(1)}(\{u\},\{\dot{u}\})(t_k) = h_i(t_k) - h_i^{(1)}(u_i(t_k),\dot{u}_i(t_k)) \tag{6}$$

and the whole sequence, form triplets - interpolate - fit surface, must be repeated for each expansion term. The procedure is therefore extremely time-consuming if there are more than a small number of degrees-of-freedom. The probabilistic relationship between the variables alluded to above will be discussed in more detail shortly.

3.2. The Effect of Incorrectly Estimating the Mass Matrix.

As indicated, it is not a simple matter to produce an accurate estimate of the mass matrix for a structure. This section is concerned with identifying the effects of errors in the estimated masses. To simplify matters a SDOF system is considered first.

Assuming that m and $\ddot{y}$ have been accurately measured, the true restoring force is obtained from

$$f(y,\dot{y}) = x - m\ddot{y}$$

If the mass estimate $\hat{m}$ is in error, the calculated force

$$\hat{f}(y,\dot{y}) = x - \hat{m}\ddot{y}$$

is also in error. If $\hat{m} - m = \Delta m$, one can easily show that

$$\hat{f} = f - \Delta m\ddot{y} \qquad (7a)$$

or

$$\hat{f} = (\hat{m}/m)f - (\Delta m/m)x \qquad (7b)$$

Equation (7) shows clearly that f will be inaccurate for two reasons; (i) it will be scaled by a factor ($\hat{m}$/m) and (ii) it will be distorted by a 'noise' term, (Δm/m)x.

Consider the following example. The SDOF nonlinear system

$$\ddot{y} + 20\dot{y} + 10^4 y + 5\times10^9 y^3 = x(t)$$

was simulated with x a gaussian noise sequence with RMS value 150.0. In order to show the effects of a mass error a technique is anticipated from the next chapter. Briefly, one takes the $\dot{y}$ = 0, section from the restoring force surface and plots it, one can then fit least–squares linear and cubic terms to the resulting 'static stiffness' curve. The exact result is clearly $f_s(y) = 10^4 y + 5\times10^9 y^3$. However, if the incorrect mass value $\hat{m}$ is used to form the surface, one expects errors in the coefficients for the reasons given above. The estimated coefficients for various values of $\hat{m}$ are given in Table 3.1. Figure 3.1 shows the 'exact' stiffness curve for $\hat{m}$ = m = 1.0. Figures 3.2 and 3.3 show the curves obtained for $\hat{m}$ = 0.1 and $\hat{m}$ = 10.0 respectively.

It is clear from Table 3.1 that $\hat{f}$ scales roughly according to the rule

$$\frac{\hat{f}}{f} = \frac{\hat{m}}{m} \qquad (8)$$

as far as the stiffness curve is concerned. The damping coefficient estimates taken from the damping section (y = 0) of the force surface are also shown in Table 3.1. The scaling behaviour of the damping estimate is not so simple, the reason for this is not clear, but may be due to the fact that the damping term is small compared to the – (Δm/m)x term in (7b).

The apparent presence of a high degree of noise in Figures 3.2 and 3.3, can be easily explained in terms of equation (7a). This explanation is specific to the case of random excitation. However, it extends simply to other forms of forcing. In this equation the time dependence has effectively been removed

$$\Delta f(y,\dot{y}) = -\Delta m\ddot{y} \qquad (9)$$

So the error in the surface at a point $(y,\dot{y})$ is proportional to the acceleration, and the displacement and acceleration are highly correlated as follows. If one neglects the time dependence as in equation (9), the most one can say about $\ddot{y}$, given y, is that considered as random variables they have a joint probabilty distribution $P(y,\ddot{y})$ i.e. $P(y,\ddot{y})dyd\ddot{y}$ is the probability that y, is in the range (y, y + dy) and at the same time $\ddot{y}$ is in the interval ($\ddot{y}$, $\ddot{y}$ + $d\ddot{y}$). At a given point $q = (y_q,\dot{y}_q)$ the probability distribution for the acceleration is simply $P_q(\ddot{y}) = \alpha P(y_q,\ddot{y})$ where α is a normalisation factor fixed by the condition

$$\int d\ddot{y}\ \alpha P(y_q,\ddot{y}) = 1 \qquad (10)$$

This means that the error in the force surface at the point q is given by

$$\Delta f(y_q,\dot{y}_q) = -\Delta m.X_q$$

where X_q is a random variable with probability distribution $P_q(\ddot{y})$. If y and $\ddot{y}$ were not correlated with each other Δf would simply be a noise term independent of position. Figures 3.4 and 3.5 show an estimate of the joint probability function $P(y,\ddot{y})$. This was obtained simply by dividing the $(y,\ddot{y})$ plane into small squares and counting the number of sample points from the simulation in each square. The figures clearly show that y and $\ddot{y}$ are in fact anti-correlated, when y is large and positive $\ddot{y}$ is likely to be large and negative. This is not surprising, for a linear system under sine excitation the two signals will be proportional to each other. The correlation means

that Δf is position dependent and the coefficient estimates will be overestimated. Systematic over- or under-estimation of this sort is termed *bias*. This agrees with the scaling behaviour shown in (8).

This analysis can be extended directly to MDOF systems where the analogues of (7a) and (7b) are

$$\{\hat{f}\} = \{f\} - [\Delta m]\{\ddot{y}\}$$

$$\{\hat{f}\} = [\hat{m}][m]^{-1}\{f\} + [\Delta m][m]^{-1}\{x\}$$

3.3. The Effect of Incorrectly Estimating the Modal Matrix.

The best way of illustrating the problem here is by example. The two degree-of-freedom system

$$\begin{bmatrix} \ddot{y}_1 \\ \ddot{y}_2 \end{bmatrix} + 20\begin{bmatrix} \dot{y}_1 \\ \dot{y}_2 \end{bmatrix} + 10^4\begin{bmatrix} 2 & -1 \\ -1 & 2 \end{bmatrix}\begin{bmatrix} y_1 \\ y_2 \end{bmatrix} = \begin{bmatrix} x \\ 0 \end{bmatrix}$$

was simulated with x a Gaussian noise sequence band-limited from 0 to 200 Hz. The Masri/Caughey procedure was carried out using the modeshape estimate

$$[\psi] = \frac{1}{\sqrt{2}}\begin{bmatrix} 1 & 1 \\ \alpha & -1 \end{bmatrix}$$

Figures 6(a) to 6(d) show the effect on the force surface $h^{(1)}_1(u_1,\dot{u}_1)$ when α is 1.0, 0.9, 0.6 and 0.3 respectively. The correct value for α is 1. There is an apparent increase in noise on the surfaces as the error in $[\psi]$ becomes more serious. There is a simple explanation for this effect. Consider the system above with α = 0.5. In normal coordinates $\{u\} = [\psi]^T\{y\}$ the equations of motion become

$$\ddot{u}_1 + 20\dot{u}_1 + 12.6\dot{u}_2 + 13416u_1 + 37800u_2 = q = x/\sqrt{2}$$

$$\ddot{u}_2 + 12.6\dot{u}_1 + 20\dot{u}_1 + 37800u_1 + 30000u_2 = q = x/\sqrt{2}$$

The equations are not decoupled because of the error in the modal matrix. The restoring forces are now

$$h_1 = 20\dot{u}_1 + 12.6\dot{u}_2 + 13416u_1 + 37800u_2$$

$$h_2 = 12.6\dot{u}_1 + 20\dot{u}_2 + 37800u_1 + 30000u_2$$

As discussed in the previous section, when the surface $h_1^{(1)}(u_1,\dot{u}_1)$ is formed, all information about time is discarded when one assembles the data over the $(u_1,\dot{u}_1)$ plane. This means that the most one can say about the variation of the $(u_2,\dot{u}_2)$ variables which also contribute to $h_1^{(1)}$ is that they have well-defined joint probability distributions with, say, u_1 i.e. $P_1(u_1,u_2)$ and $P_2(u_1,\dot{u}_2)$. At a fixed point $q = (u_{1q},\dot{u}_{1q})$ the probability distribution for u_2 is $P_{1q}(u_2) = \alpha P_1(u_{1q},u_2)$ and that for $\dot{u}_2$ is $P_{2q} = \beta P_2(u_{1q},\dot{u}_2)$. The constants α and β are fixed by conditions like (10). It is now clear that over the point q the restoring force h_1 value will be

$$h_1 = 20u_1 + 12.6X_1 + 13416u_1 + 37800X_2$$

where X_1 is a random variable with probability distribution function $P_{1q}(\dot{u}_2)$ and X_2 is a random variable with p.d.f $P_{2q}(u_2)$. The interpolation procedure therefore sees a deterministic u_1 and $\dot{u}_1$ dependent part to h_1 with a stochastic part superimposed. If u_1, $\dot{u}_1$, u_2 and $\dot{u}_2$ are uncorrelated in pairs, the stochastic part will be a noise term independent of position. In general the variables will be correlated and the coefficients estimated from the surfaces will be biased. If a residual surface is now obtained it will be much smoother i.e.

$$r_1^{(1)}(u_2,\dot{u}_2) = 12.6\dot{u}_2 + 37800u_2$$

only if the coefficients have been correctly identified in the first step. If the estimates

are wrong one will not remove all the u_1 and $\dot{u}_1$ dependence and the residual surface will be noisy also.

There is another serious problem associated with errors in $[\psi]$. In using the transformation matrix $[\psi]^T$ to normal coordinates one will identify the wrong system. Consider the linear system

$$[M]\{\ddot{y}\} + [C]\{\dot{y}\} + [K]\{y\} = \{x\} \qquad (11)$$

The Masri Caughey procedure actually identifies the system

$$[\psi]^T[M][\psi].[\psi]^T\{\ddot{y}\} + [\psi]^T[C][\psi].[\psi]^T\{\dot{y}\} +$$

$$[\psi]^T[K][\psi].[\psi]^T\{y\} = [\psi]^T\{x\} \qquad (12)$$

In general, if $[\psi]$ is not estimated accurately it will not be orthonormal i.e. $[\psi]^T[\psi] \neq 1$. In this case the system specified by equation (12) is not physically equivalent to that specified by (11). They are not related by a linear transformation of coordinates. The remedy is almost trivial. If $[\psi]^{-1}$ is used throughout rather than $[\psi]^T$ the systems are equivalent, the change of coordinates is now $\{u\} = [\psi]^{-1}\{y\}$. There is nothing to be lost by adopting this modification, inversion of a matrix is a little more expensive than transposition but the inversion need only be carried out once. If the modal matrix is accurate then of course $[\psi]^{-1} = [\psi]^T$. If the estimate is bad the attempt to decouple the equations using the inverse $[\psi]^{-1}$ will be no worse than using the transverse $[\psi]^T$. The results of modifying the procedure in this way are illustrated in the next example.

The same system as in the previous example was simulated. Using the incorrect modal matrix

$$[\psi] = \begin{bmatrix} 1 & 1 \\ 0.5 & 0.5 \end{bmatrix}$$

The identification procedure was carried out on the data, first using the $[\psi]^T$ version of the procedure and then using the $[\psi]^{-1}$ version. Using each of the models found in turn the results of comparing the predicted displacements with the actual displacements are shown in Figures 3.7 and 3.8. The slightly modified procedure gives significantly better results.

3.4. Application of the Procedure to Simulated Systems.

The two degree-of-freedom nonlinear system

$$\begin{bmatrix} \ddot{y}_1 \\ \ddot{y}_2 \end{bmatrix} + 20\begin{bmatrix} \dot{y}_1 \\ \dot{y}_2 \end{bmatrix} + 10^4\begin{bmatrix} 2 & -1 \\ -1 & 2 \end{bmatrix}\begin{bmatrix} y_1 \\ y_2 \end{bmatrix}$$

$$+ 5\times10^9\begin{bmatrix} y_1^3 \\ 0 \end{bmatrix} = \begin{bmatrix} x \\ 0 \end{bmatrix}$$

was simulated with x(t) a noise sequence with RMS 150.0. The modal matrix for the underlying linear system is

$$[\psi] = \frac{1}{\sqrt{2}}\begin{bmatrix} 1 & 1 \\ 1 & -1 \end{bmatrix}$$

So the equations of motion in normal coordinates are

$$\ddot{u}_1 + c\dot{u}_1 + ku_1 + \tfrac{1}{4}k_3(u_1 + u_2)^3 = x/\sqrt{2}$$

$$\ddot{u}_2 + c\dot{u}_2 + 3ku_2 + \tfrac{1}{4}k_3(u_2 + u_1)^3 = x/\sqrt{2}$$

where $c = 20.0$, $k = 10^4$ and $k_3 = 5\times10^9$. The nonlinear restoring forces are,

$$h_1 = c\dot{u}_1 + ku_1 + \tfrac{1}{4}k_3u_1^3$$

$$+ \tfrac{1}{4}k_3(3u_1^2u_2 + 3u_1u_2^2 + u_2^3) \qquad (13a)$$

$$h_2 = c\dot{u}_2 + 3ku_2 + \tfrac{1}{4}k_3u_2^3 + \tfrac{1}{4}k_3(3u_2^2u_1 + 3u_2u_1^2 + u_1^3) \qquad (13b)$$

The results of applying the identification procedure are illustrated in Figures 3.9 to 3.10. The identification proceeds as follows

(i) Assemble the data for the $h_1^{(1)}(u_1,\dot{u}_1)$ expansion. The arrangement of data is shown in Figure 3.9. The reduced data set is shown within the dashed rectangle. The tesselation and triangulation are formed exactly as for the SDOF systems (Figure 3.10). The TILE package is used to form a C^0 surface, which is shown in Figure 3.11. Once again, the interpolation appears to be very noisy. The explanation is the same as before. h_1 is actually dependent on all four dynamical variables u_1, $\dot{u}_1$, u_2 and $\dot{u}_2$ however only u_1 and $\dot{u}_1$ are ordered for the interpolation. So considering equation (13b) this means the procedure sees above a given point $q = (u_{1q},\dot{u}_{1q})$ a deterministic term

$$h_d = c\dot{u}_1 + ku_1 + \tfrac{1}{4}k_3u_1^3$$

and a stochastic term

$$h_s = \tfrac{1}{4}k_3(3u_1^2X_q + 3u_1X_q^2 + X_q^3)$$

where X_q is a random variable with probability density function $P_q(u_2) = \alpha P(u_{1q},u_2)$. The joint probability density P is defined as before.

(ii) Fit a Chebyshev series to the interpolated surface (Figure 3.12). In this case a model of order (3,1) was chosen. Then subtract the model from the time data to form the first residual time–series $r_1^{(1)}$.

(iii) Assemble the residual force data over the (u_1,u_2) plane for the $h_1^{(2)}$ expansion. The distribution of data in this plane is shown in Figure 3.13. It is obvious from this

figure that the u_1 and u_2 data are quite strongly correlated. This means that the estimated coefficients in step (i) will be biased. However, at this stage one can correct for errors in the u_1 dependence. One then forms the interpolated surface (Figure 3.14) and fits a Chebyshev model. In this case the model order is (3,3) and the model surface is shown in Figure 3.15.

(iv) Carry out steps (i) to (iii) for h_2. (Figures 3.16 to 3.20.)

If one is concerned about the parameter bias one should iterate the above procedure until one has modelled the data correctly. For example, if one only makes one pass through the data as above, step (i) will introduce a $u_1{}^3\dot{u}_1$ term which is not corrected for at any subsequent stage. A spurious term of this sort can ruin any attemp to compare model predictions with actual data. There are two problems here. (a) Because of the large stochastic term in stage (i) the interpolation will introduce errors which will propogate through the procedure in the residual term and cannot be removed, iteration will not help here. (b) The procedure is already time-consuming enough. To identify a MDOF system by the methods above can take hours, iteration could multiply this into days, even if problem (a) does not occur and iteration is possible.

The final result is a Chebyshev series model of the nonlinear restoring forces {h}. To check the accuracy of the model the predicted displacements were compared with the actual displacements. The results are shown in Figures 3.21 and 3.22. Figure 3.21 shows the results if a linear model is used. Figure 3.22 gives the comparison for the full nonlinear model. The results are significantly better in the latter case as one would expect.

The analysis was then carried out on a system with a discontinuous nonlinearity; a three degree of freedom nonlinear system described by the equations of motion,

$$\begin{bmatrix} \ddot{y}_1 \\ \ddot{y}_2 \\ \ddot{y}_3 \end{bmatrix} + 20\begin{bmatrix} \dot{y}_1 \\ \dot{y}_2 \\ \dot{y}_3 \end{bmatrix} + 10^4\begin{bmatrix} 2 & -1 & 0 \\ -1 & 2 & -1 \\ 0 & -1 & 2 \end{bmatrix}\begin{bmatrix} y_1 \\ y_2 \\ y_3 \end{bmatrix}$$

$$+ \begin{bmatrix} 0 \\ f_{nl} \\ 0 \end{bmatrix} = \begin{bmatrix} 0 \\ x \\ 0 \end{bmatrix}$$

The response of the system was simulated with the same input as the previous example. The nonlinear force f_{nl} was a piecewise linear function with clearance 0.001. The system is illustrated in Figure 3.23.

The identification procedure was carried out exactly as in the previous example and the formation of the resulting expansions for h_1 and h_2 are illustrated in Figures 3.24 to 3.32. The restoring force surface for the second normal coordinate is flat because the modal matrix for the underlying linear system is

$$[\psi] = \frac{1}{2}\begin{bmatrix} 1 & \sqrt{2} & 1 \\ \sqrt{2} & 0 & -\sqrt{2} \\ 1 & -\sqrt{2} & 1 \end{bmatrix}$$

Thus the nonlinear force does not appear in the second normal mode. This illustrates nicely a drawback of the procedure, the change to normal coordinates shuffles the physical coordinates so one cannot tell from the h_i's where the nonlinearity might be. The derivation of the model for h_3 is not shown as it simply mirrors that for h_1.

The coefficents are not given above because unless the models can be translated into a polynomial model, they are meaningless. In the case of MDOF systems, the algebra involved in carrying out the exercise would be horrendous. If one is interested in easily obtaining physical parameters this procedure is not really suitable.

Because of the noise in a surface caused by interaction with other modes, one can no longer use the option of forming a C^1 surface using TILE. This is because two arbitrarily close points in say, the $(u_1,\dot{u}_1)$ plane can have quite large differences in the force values above them because of the random contibutions from other modes.

This means that the gradients will be overestimated and the interpolated surface will contain spurious peaks. This effect is shown in Figures 3.33 and 3.34. This is not just a problem with TILE. It is difficult to imagine how one could form a C^1 interpolation without estimating gradients. How would one find a second order Taylor approximation to a function without estimating the second derivatives?

3.5. How Useful is the Masri/Caughey Procedure.

The preceeding results indicate that it is possible to implement a reasonably direct version of the Masri/Caughey procedure practically. The systems studied are computer simulated, admittedly. However, almost all work on restoring force methods is restricted in the same way. It is useful to examine the claims made for the procedure in references **(10)** and **(11)**. The first claim is that the model is nonparametric. This is open to discussion. If ordinary polynomials were used rather than Chebyshev polynomials the method would almost certainly be called parametric. One would suppose that say, a piecewise linear function could be identified by a truly nonparametric procedure. At best, one would obtain a polynomial approximation using this method. Al-Hadid and Wright **(18)** consider the method to have found a nonparametric model if the system is polynomial and all terms have been identified, and a parametric model if a polynomial approximation only is obtained. This seems sensible, a nonparametric identification would pick a function from a function space. If the function is polynomial one can specify it exactly with a few parameters. The function space for cubics for example is four-dimensional. In this case nonparametric identification and parameter estimation coincide. Perhaps such argument is simply pedantry.

Secondly, it is claimed that the procedure is applicable to a broad class of systems with 'practically arbitrary nonlinearities (including hysteretic types)'. Certainly the method can identify a large number of nonlinearities. However, systems with memory are not included. The procedure simply cannot identify multi-valued force surfaces.

The best one can hope for is to replace the hysteresis loop with an equivalent viscous damper. One can not obtain information about the shape of the loop for example, by fitting polynomials in this way.

It is claimed that there is practically no restriction on the type of excitation used. This is certainly true and constitutes a statement about restoring force methods in general. The question of input design will be considered in some detail in Chapter 7. One should be aware that if the restoring force is not polynomial the model obtained will be sample-dependent. There is an implicit criticism here of the Volterra/Wiener functional series approach. It is true that if the functional kernels are obtained by time-domain correlation the input should theoretically be a Gaussian white noise sequence. However, the work of Gifford (8) indicates that the procedures will tolerate inputs which depart quite a lot from Gaussian. There has also been a good deal of work recently on obtaining the Volterra kernels from sine-testing and from impulse testing. A bibliography can be found in (8).

It is claimed that computer execution time and storage requirements are 'minimal'. This is true to an extent, the comparitive slowness of the present work is due to the use of an accurate interpolation procedure. One could certainly sacrifice a certain amount of accuracy and gain a good deal of speed. A very quick surface generating procedure is described in the next chapter which could be used to produce an interpolation which is at best C^0. The procedure is said to give a simple visualisation of the nonlinearity. This is true certainly. However, the better the interpolation, the better the surface. As before, comparison is made with the functional series approach. Since Masri and Caughey's original papers a great deal of work has been done. The higher order kernels can now be obtained very quickly by using nonlinear time-series methods (9,39). However, storage requirements for higher dimensional kernels are unavoidably large. The Masri/Caughey procedure requires one to store at any given time, a surface for each degree of freedom. As they remark, storage requirements are modest.

One concludes that the Masri/Caughey procedure has a number of useful features. It has also a number of drawbacks. The parameters obtained can be biased. The procedure does not provide confidence limits for the parameters. It is still time-consuming, as the coefficients are obtained from a double integration. Accuracy is only ensured by taking a fine enough grid, and this means the integrations take time.

The next chapters attempt to develop an identification procedure which has all the useful properties of the Masri/Caughey approach and as few as possible of the drawbacks.

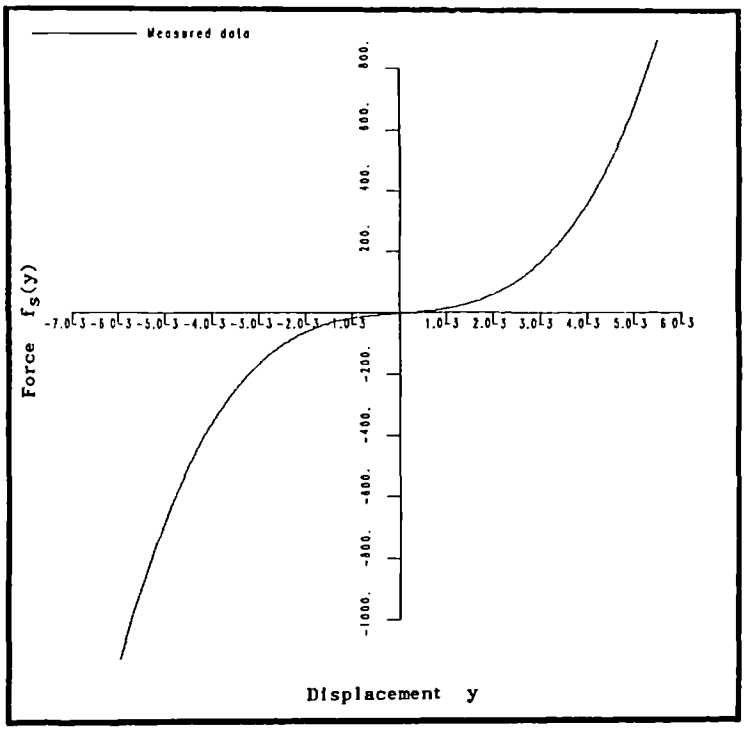

Figure 3.1. Stiffness section for the Duffing oscillator in the example in the text. Estimated mass $\hat{m}$ = 1.0, True mass m = 1.0.

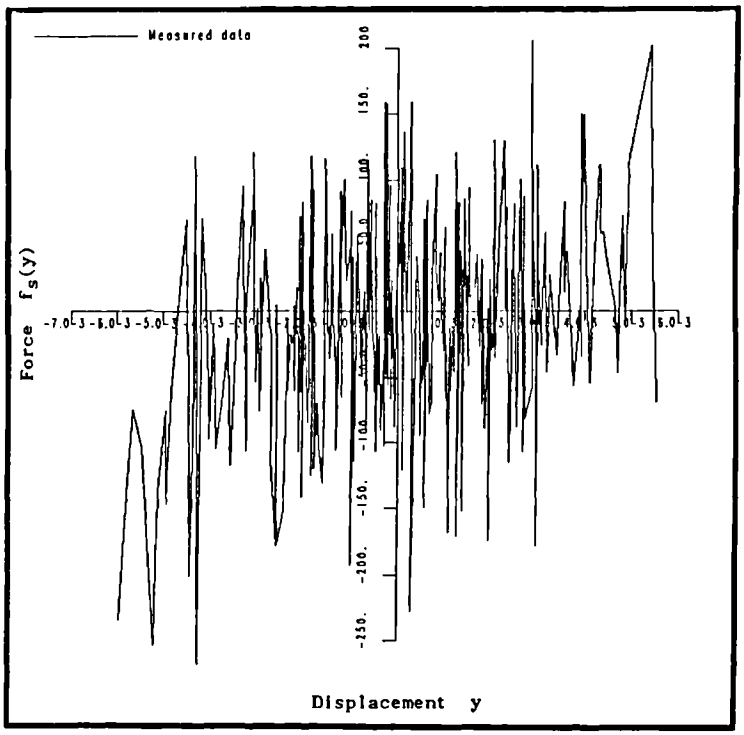

Figure 3.2. Stiffness section for the Duffing oscillator, $\hat{m}$ = 0.1, m = 1.0.

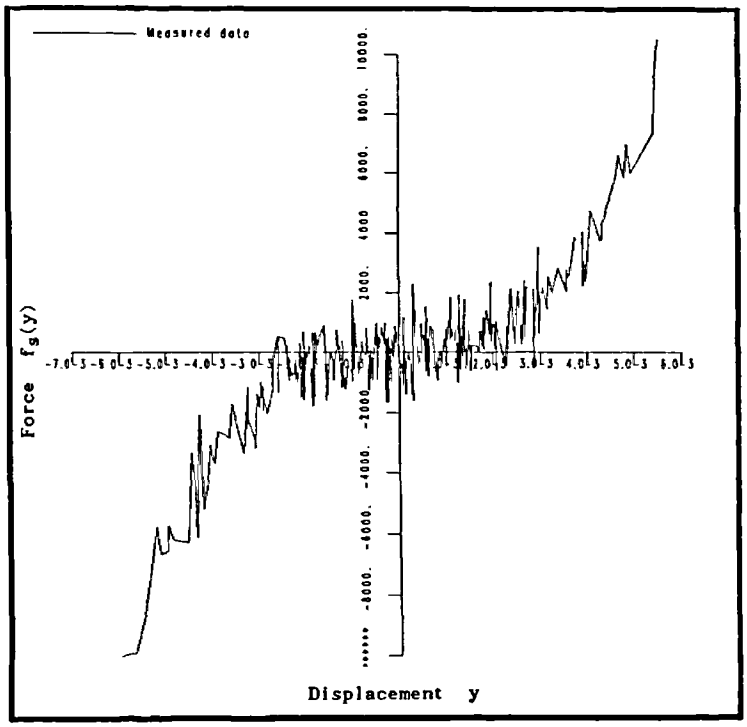

Figure 3.3. Stiffness section for the Duffing oscillator, $\hat{m} = 10.0$, $m = 1.0$.

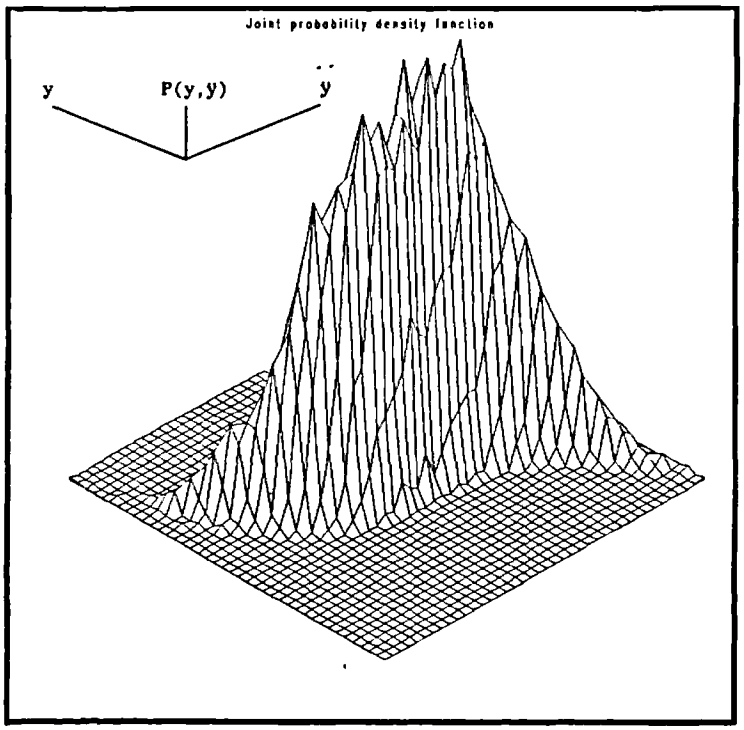

Figure 3.4. Joint probability distribution of displacement and acceleration for the Duffing oscillator system.

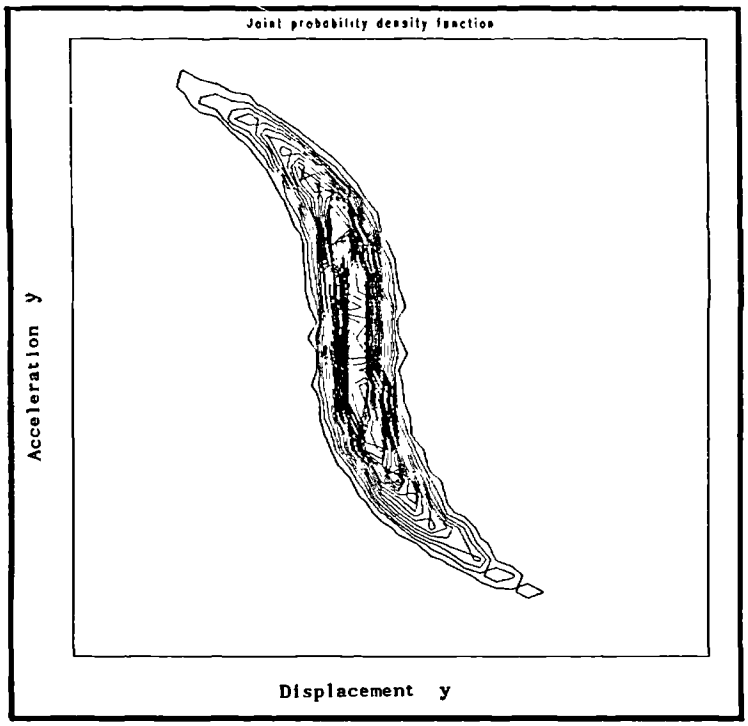

Figure 3.5. Contour map of the joint probabilty distribution in the previous figure.

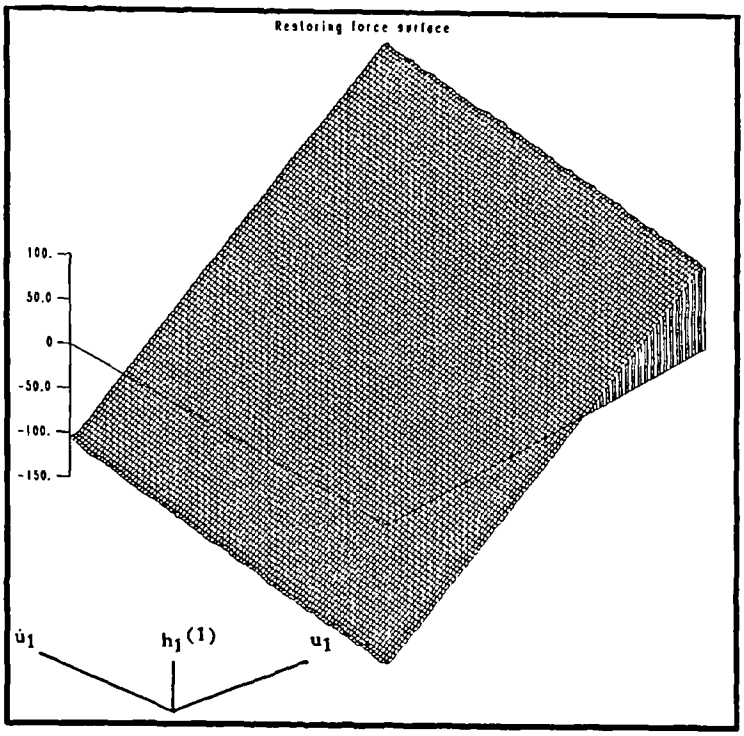

(a) α = 1.0

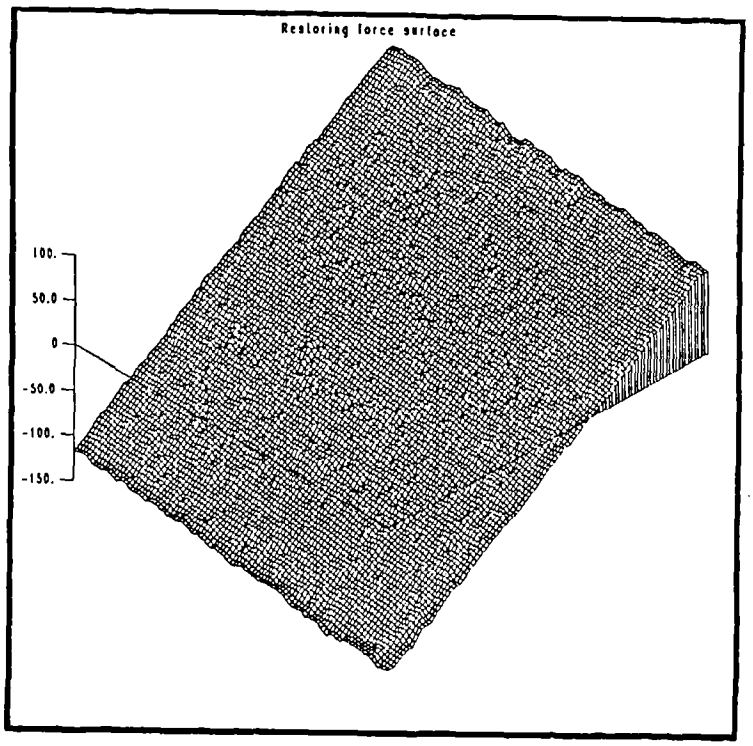

(b) α = 0.9

Figure 3.6. The effect of using the incorrect modeshape estimate on a force surface. The example shown is that from section 3.3.

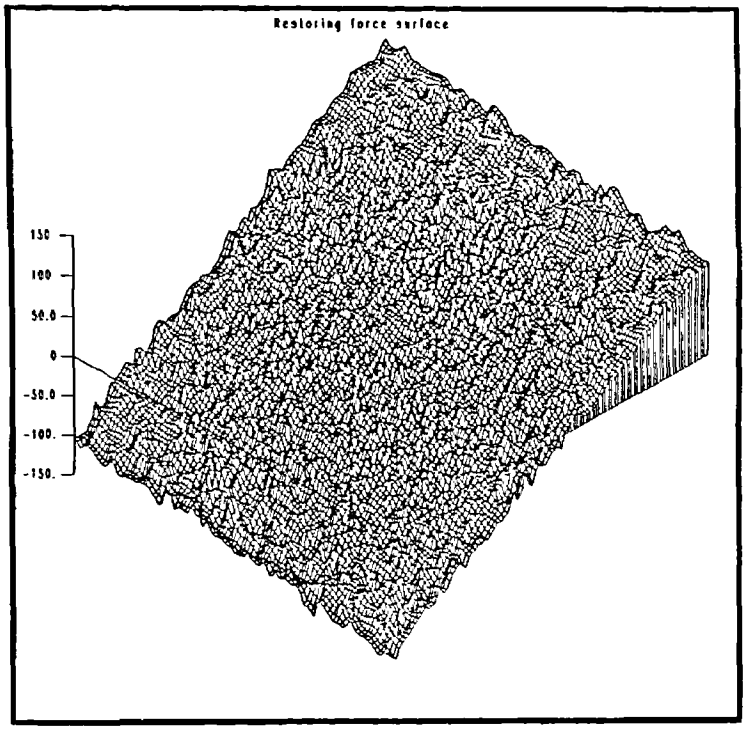

(c) α = 0.6

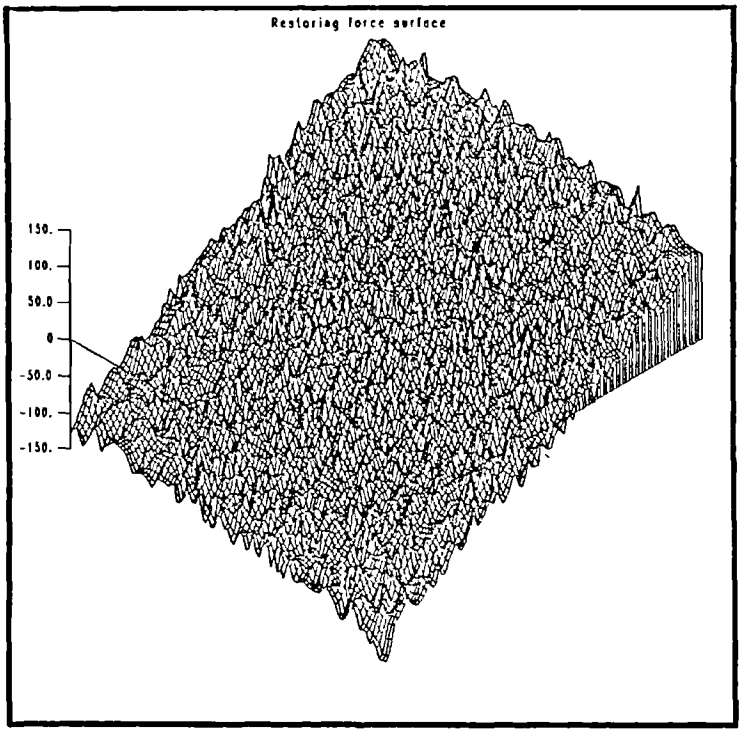

(d) α = 0.3

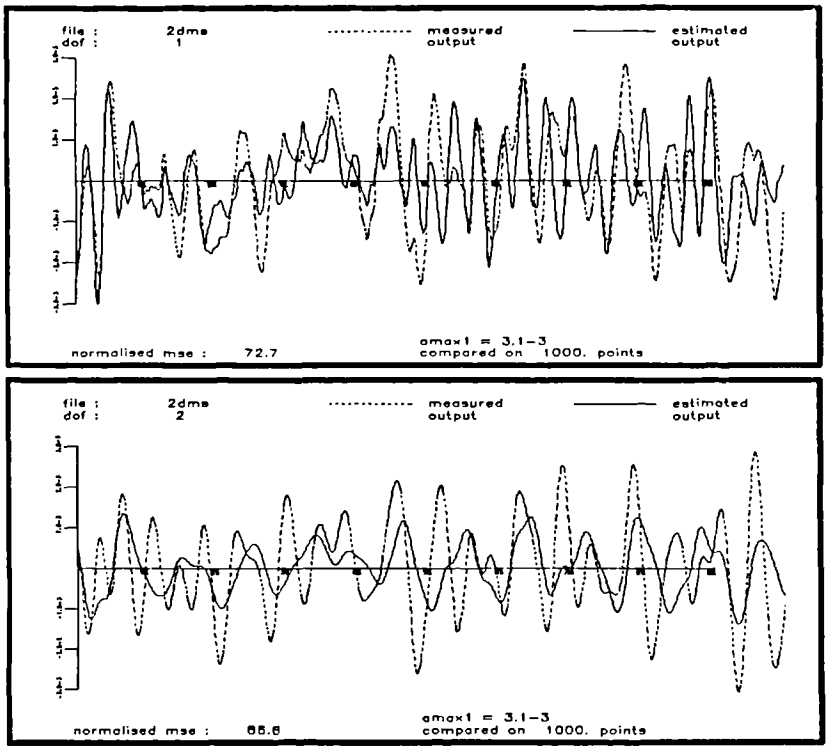

Figure 3.7. Comparison of predicted and measured time data for the two degree-of-freedom example in section 3.3. The $[\psi]^T$ procedure was used here.

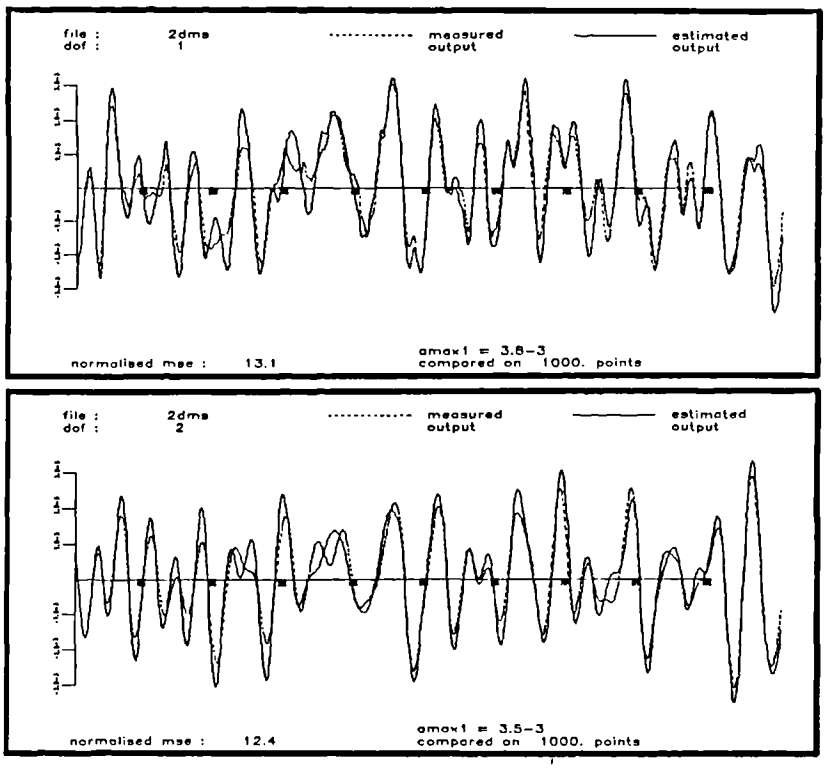

Figure 3.8. Comparison of predicted and measured time data for the two degree-of-freedom example in section 3.3. the $[\psi]^{-1}$ procedure was used here.

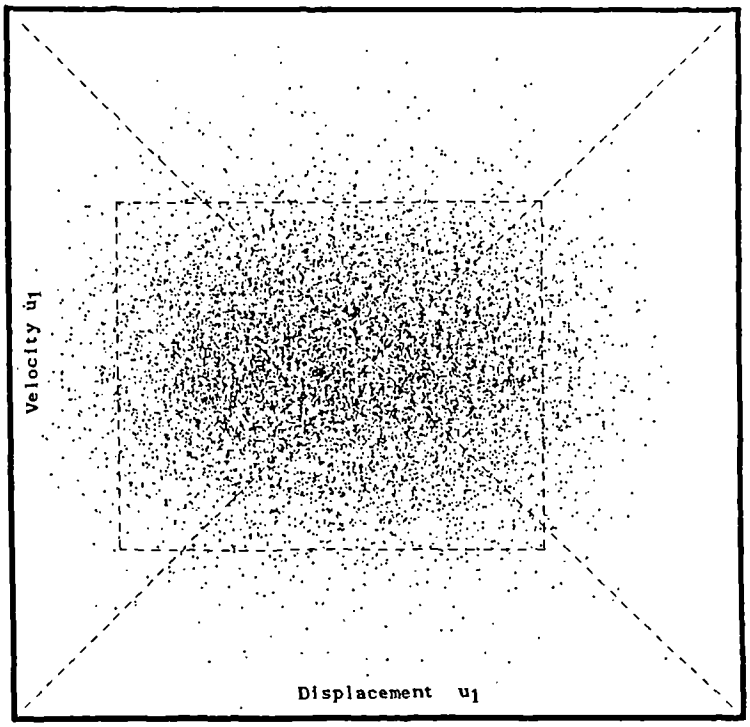

Figure 3.9. Data selected from the $(u_1,\dot{u}_1)$ plane for the interpolation of the surface $h_1^{(1)}(u_1,\dot{u}_1)$.

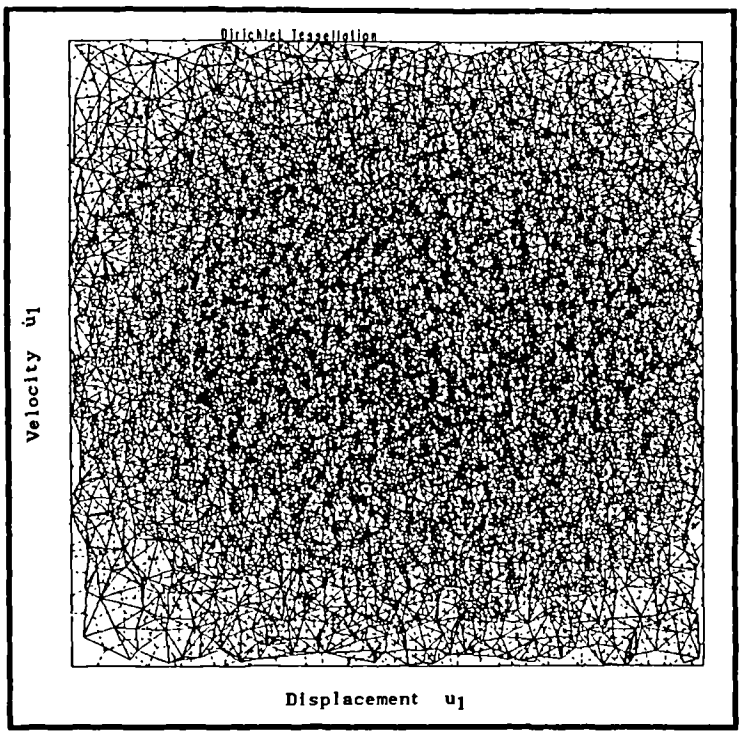

Figure 3.10. Tesselation and triangulation for the reduced data set shown in the previous example.

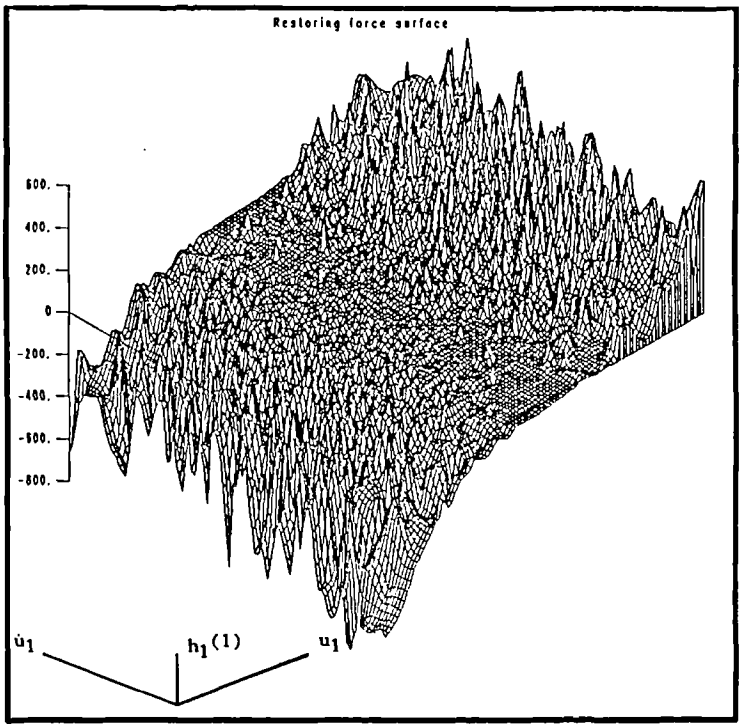

Figure 3.11. TILE4 interpolated surface $h_1^{(1)}(u_1,\dot{u}_1)$ for the cubic system of section 3.4.

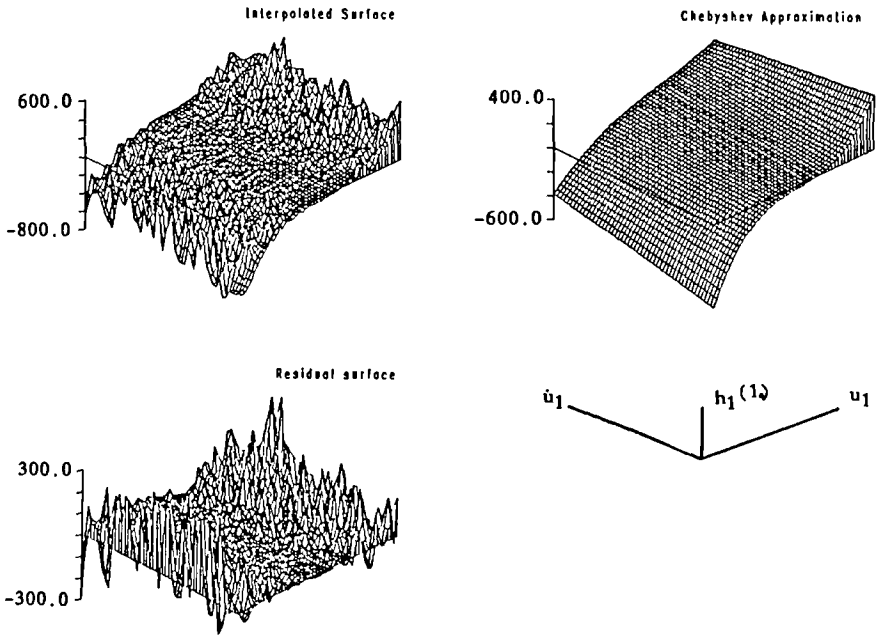

Figure 3.12. Chebyshev model fit of order (3,1) for the surface in Figure 3.11.

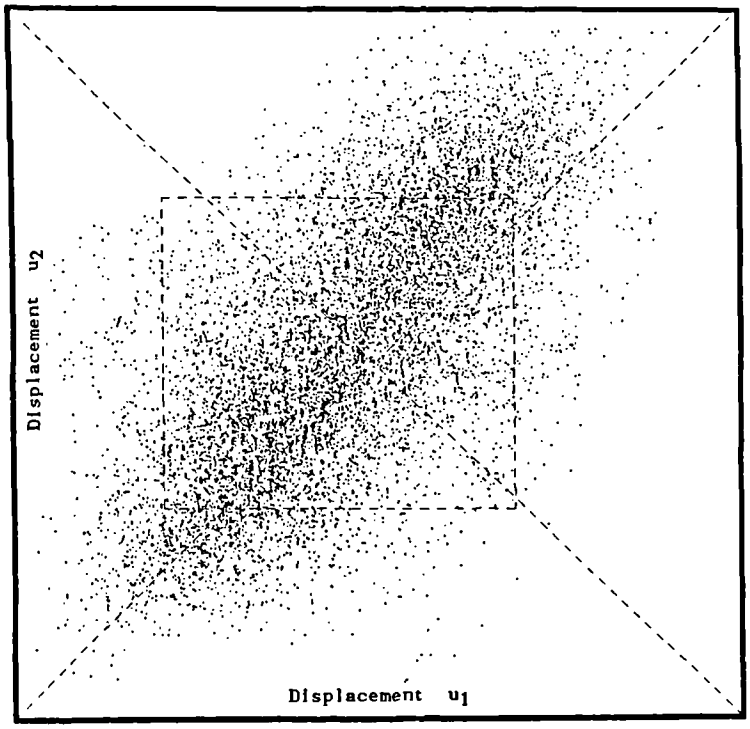

Figure 3.13. Data selected from the (u_1,u_2) plane for the interpolation of the surface $h_1^{(2)}(u_1,u_2)$.

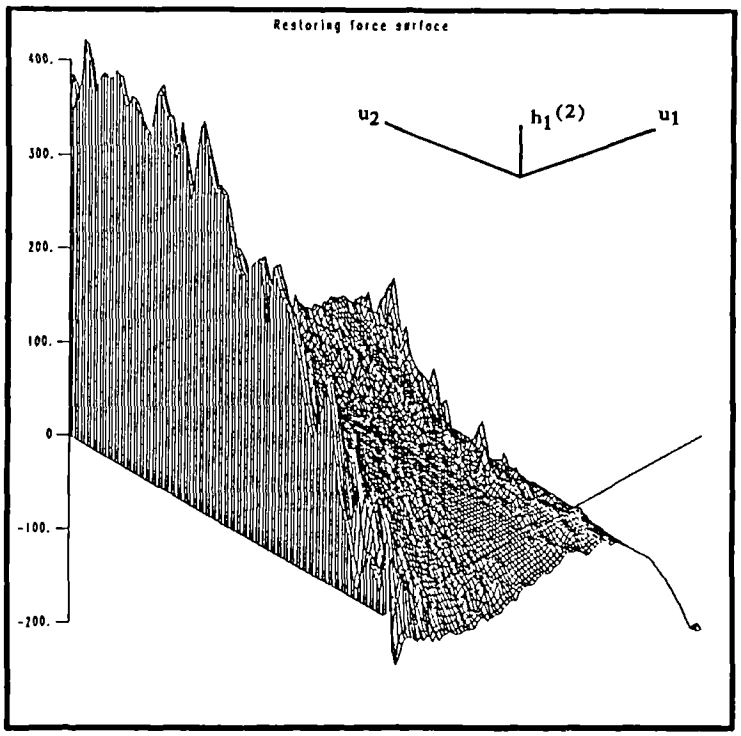

Figure 3.14. Interpolated surface - $h_1^{(2)}(u_1,u_2)$.

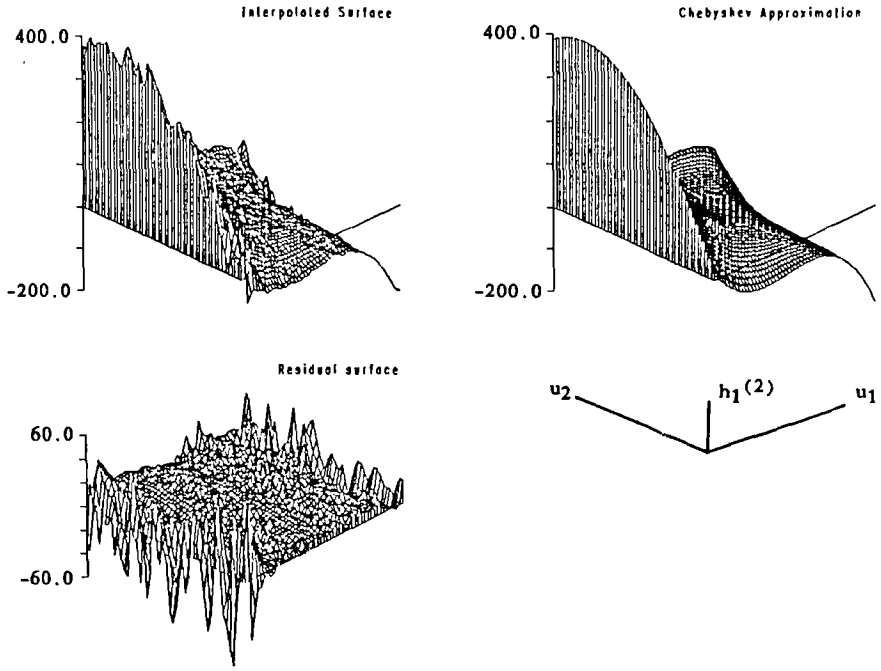

Figure 3.15. Chebyshev fit of order (3,3) to the surface in Figure 3.14.

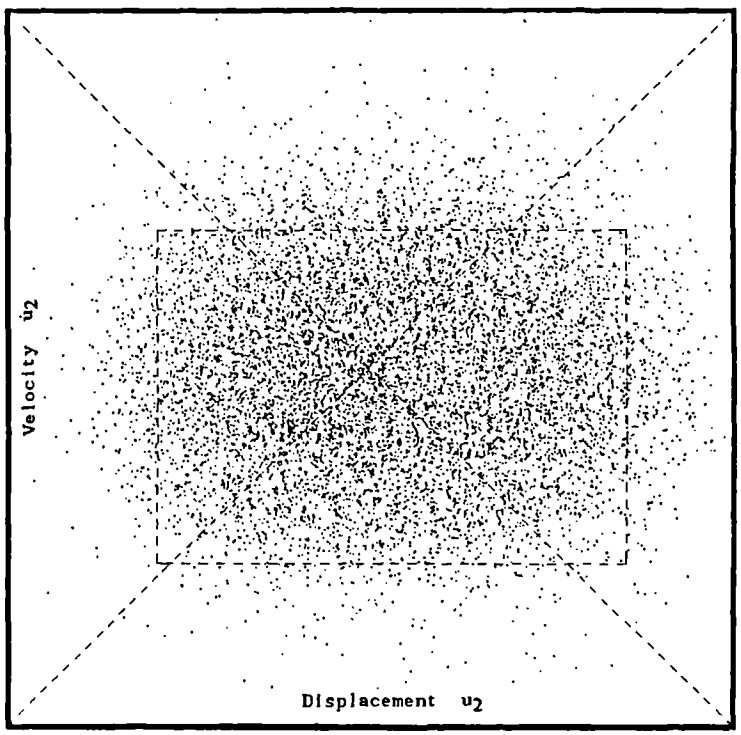

Figure 3.16. Data selected from the $(u_2,\dot{u}_2)$ plane for interpolation of the surface $h_2^{(1)}(u_2,\dot{u}_2)$.

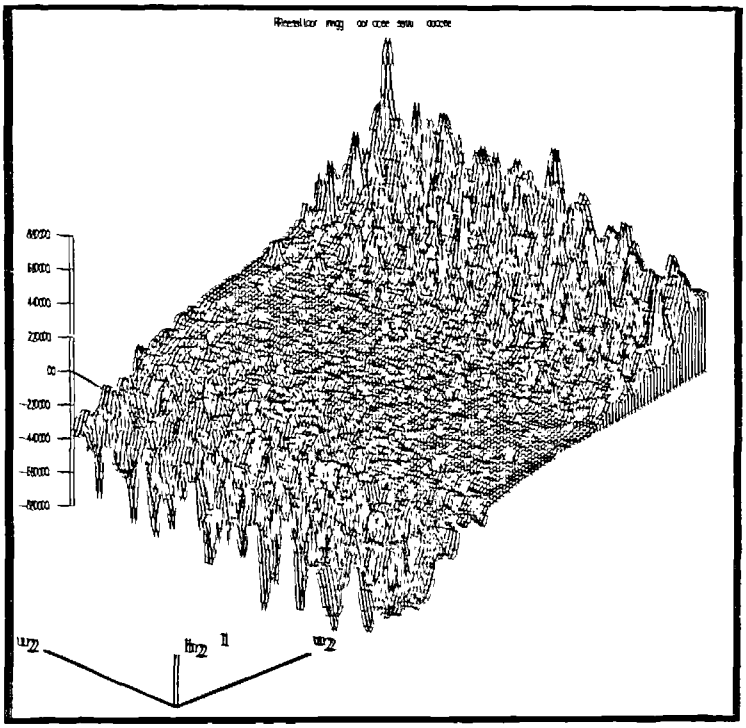

F gure 3 17. Interpolated surface - $h_2^{\,1}$ w_2 w_2)-

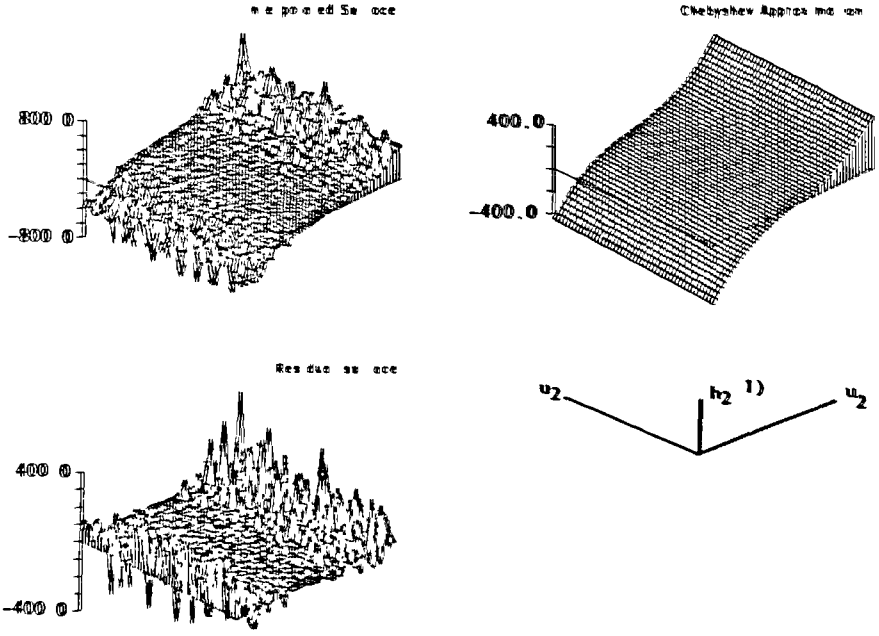

Figure 3 18 Chebyshev fit of order (3,1) to the surface in Figure 3 17.

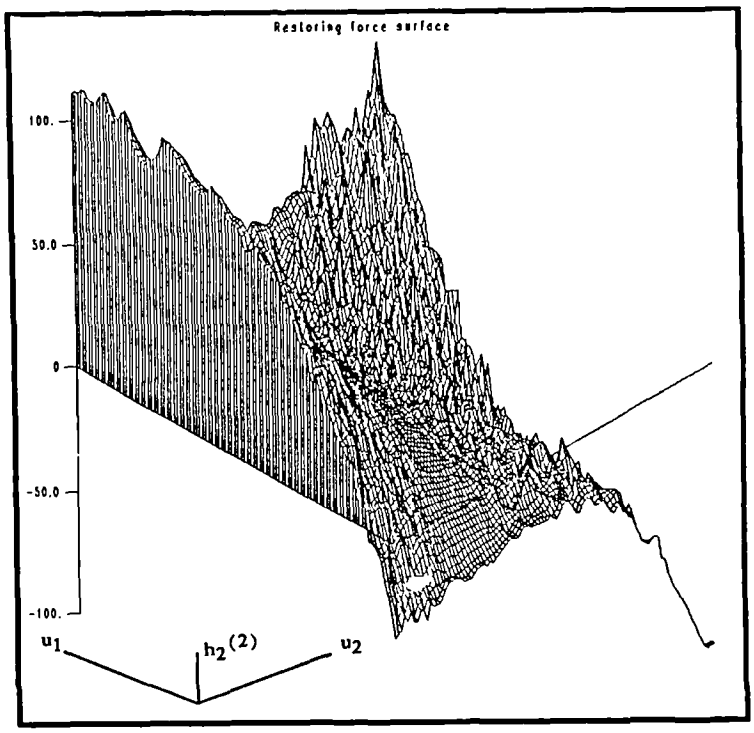

Figure 3.19. Interpolated surface - $h_2^{(2)}(u_2,u_1)$.

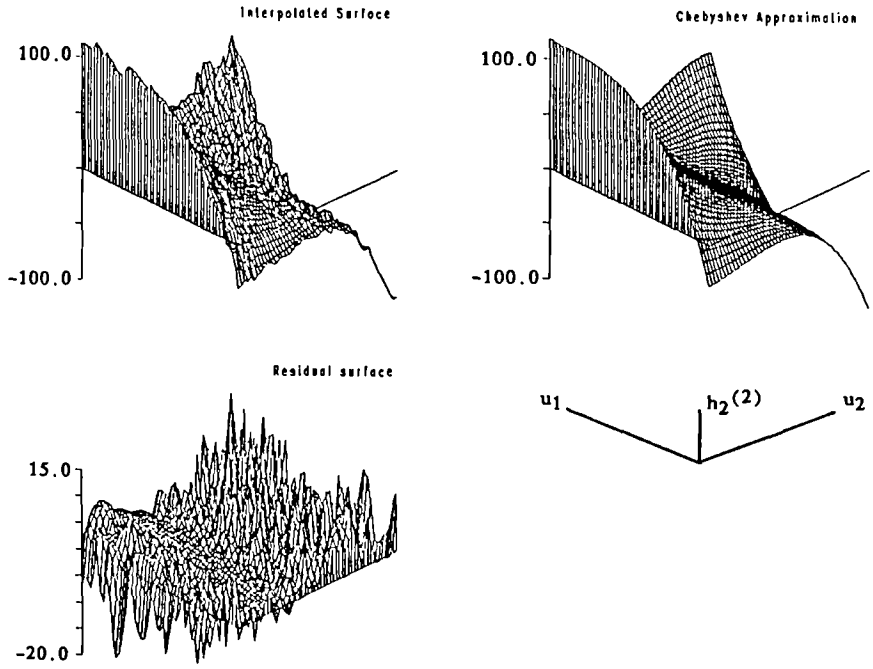

Figure 3.20. Chebyshev fit of order (3,3) to the surface in Figure 3.19.

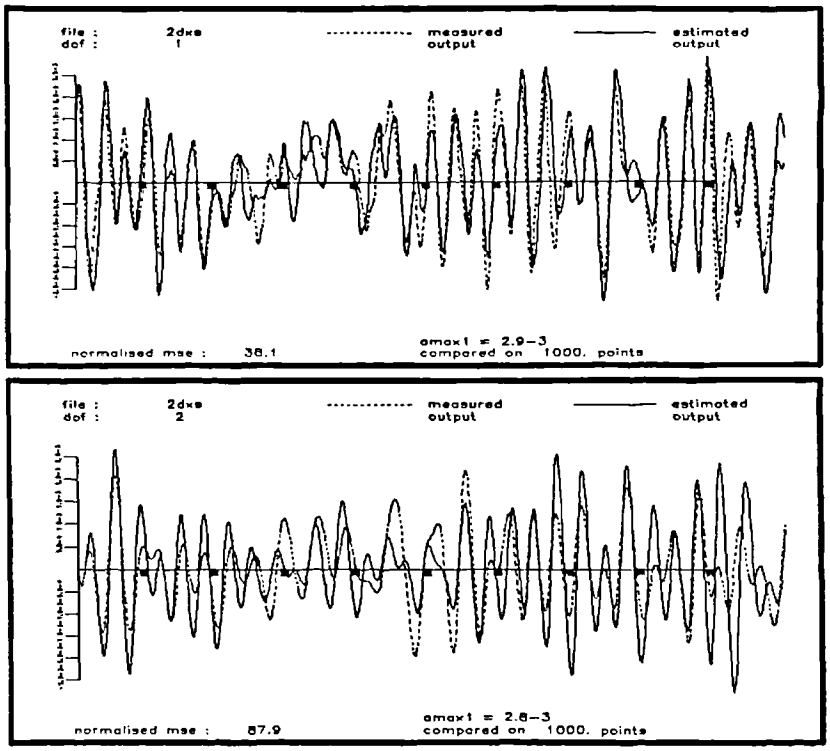

Figure 3.21. Comparison of predicted and measured time data - linear model ($h_1^{(1)}$ and $h_2^{(2)}$ used).

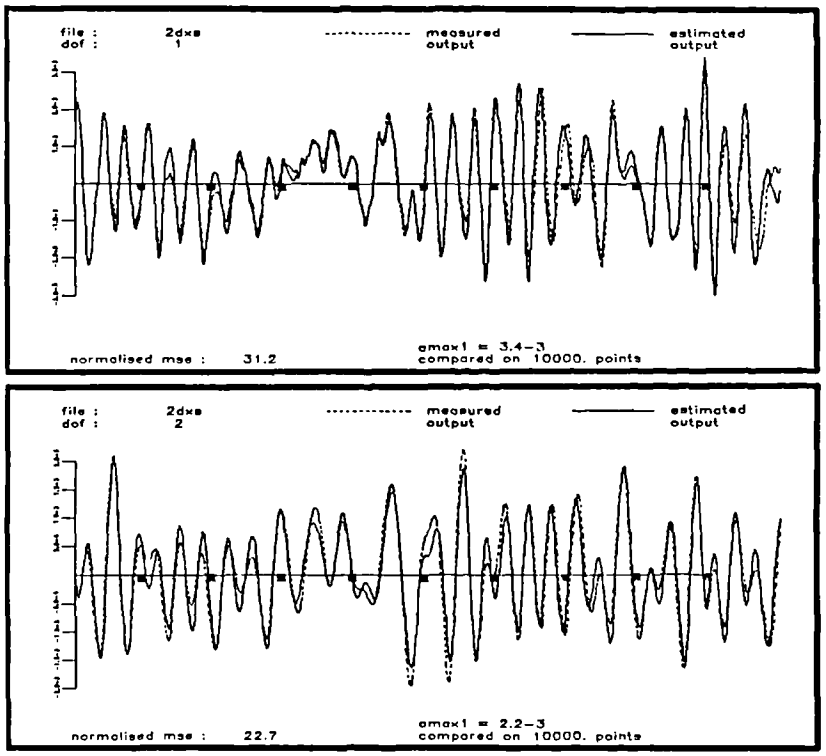

Figure 3.22. Comparison of predicted and measured time data - nonlinear model ($h_1^{(1)}$, $h_1^{(2)}$, $h_2^{(1)}$ and $h_2^{(2)}$ used).

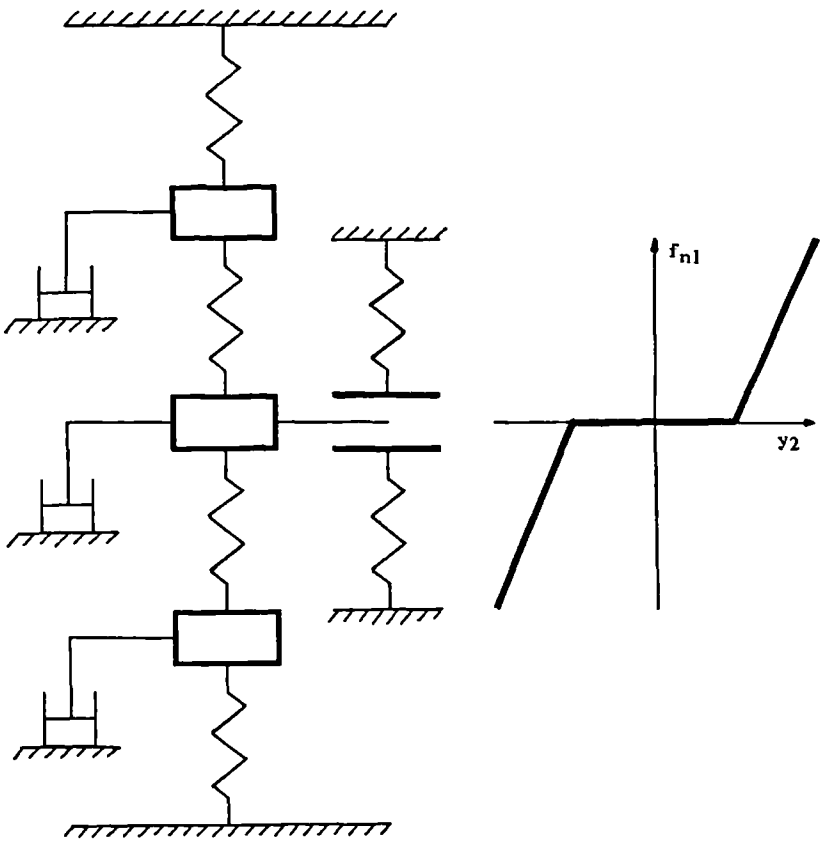

Figure 3.23. Three degree-of-freedom piecewise-linear system described in section 3.4.

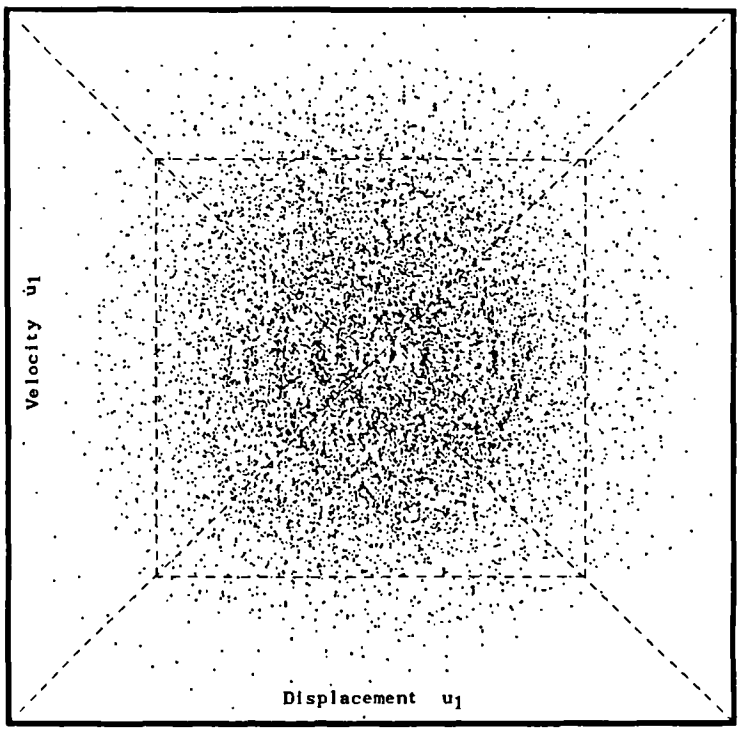

Figure 3.24. Data selected from $(u_1,\dot{u}_1)$ plane for interpolation of the surface $h_1^{(1)}(u_1,\dot{u}_1)$ for the MDOF piecewise-linear system.

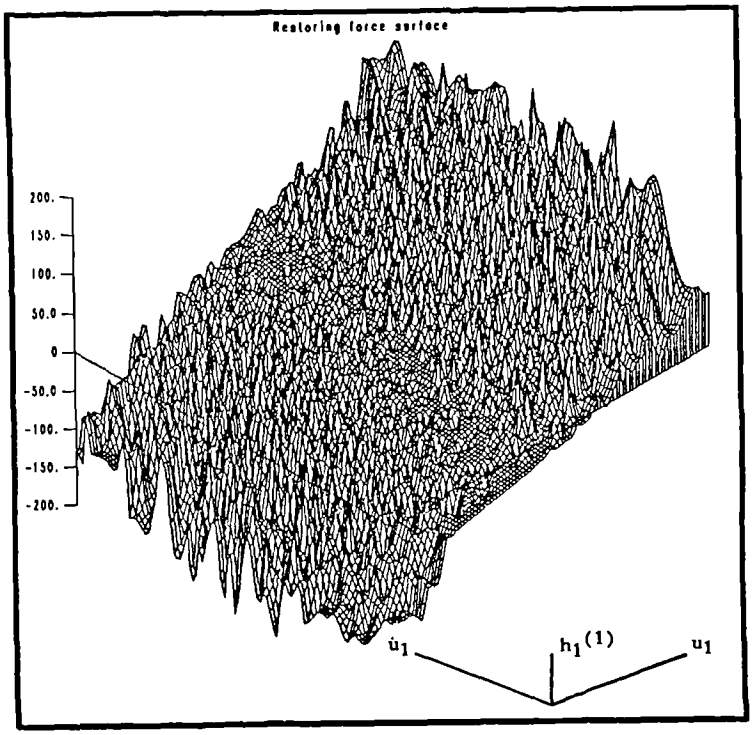

Figure 3.25. Interpolated surface - $h_1^{(1)}(u_1,\dot{u}_1)$.

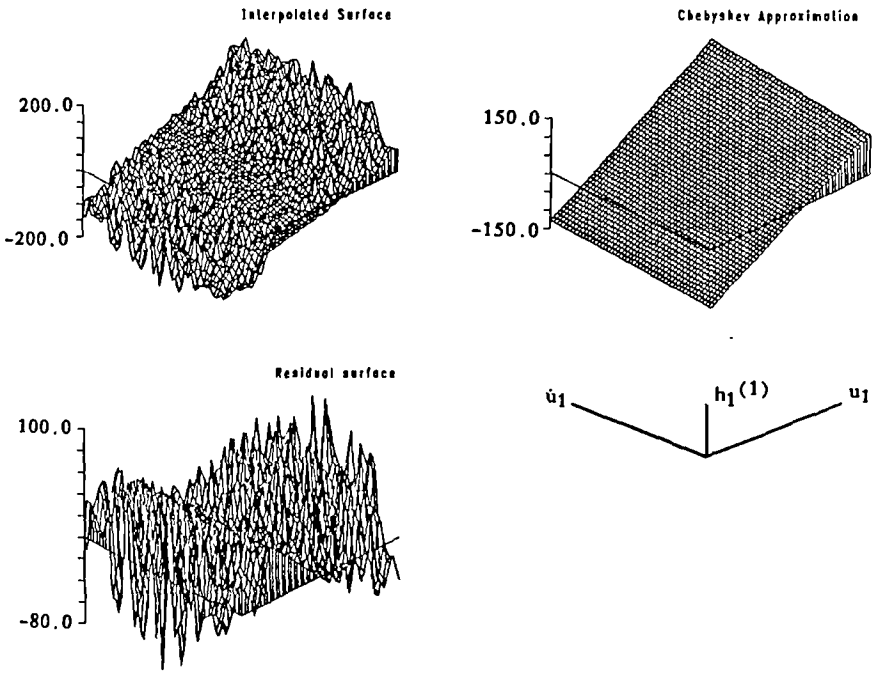

Figure 3.26. Chebyshev fit of order (1,1) to the interpolated surface in Figure 3.25.

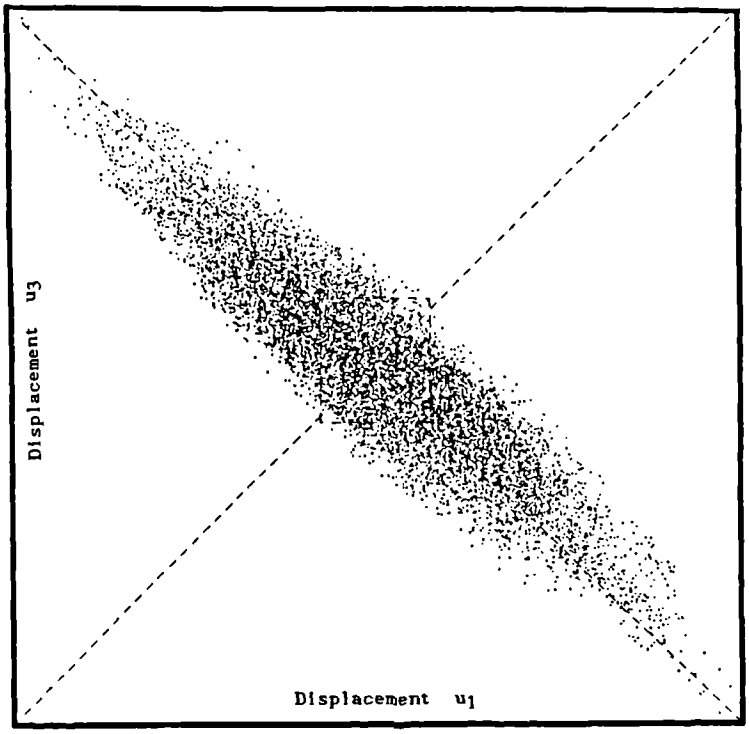

Figure 3.27. Data selected fom (u_1,u_3) plane for interpolation of the surface $h_1^{(2)}(u_1,u_3)$.

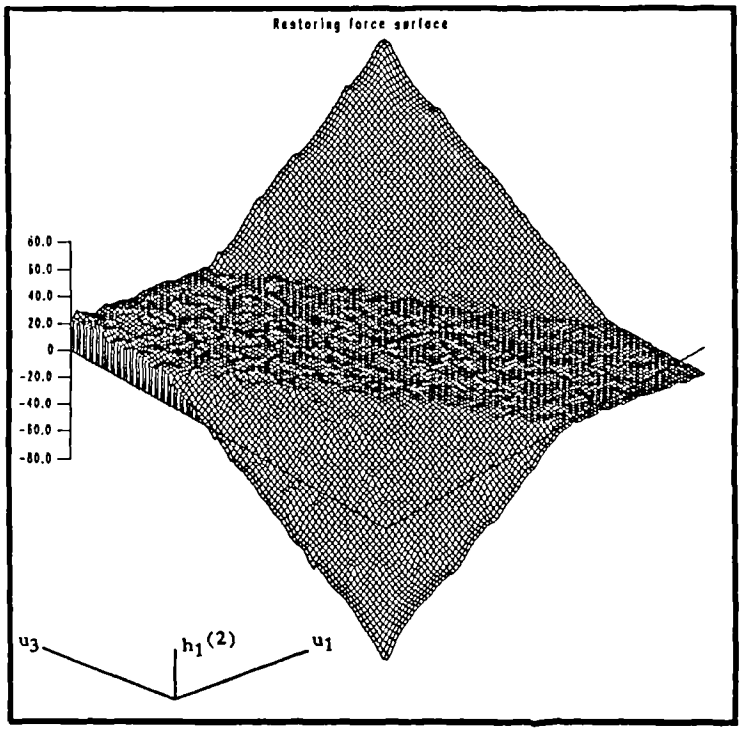

Figure 3.28. Interpolated surface - $h_1^{(2)}(u_1,u_3)$.

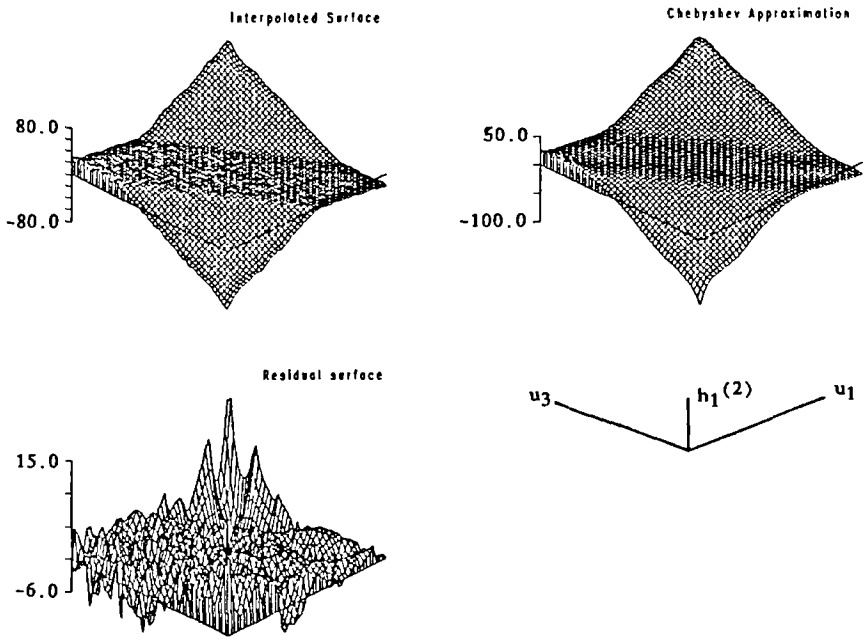

Figure 3.29. Chebyshev fit of order (8,7) to the interpolated surface in Figure 3.28.

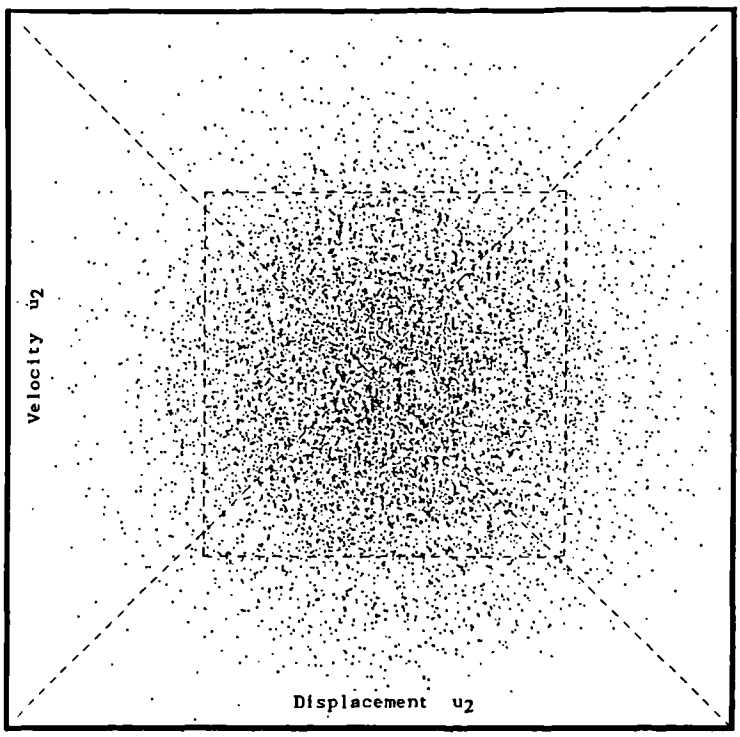

Figure 3.30. Data selected from $(u_2, \dot{u}_2)$ plane for interpolation of the surface $h_2^{(1)}(u_2, \dot{u}_2)$.

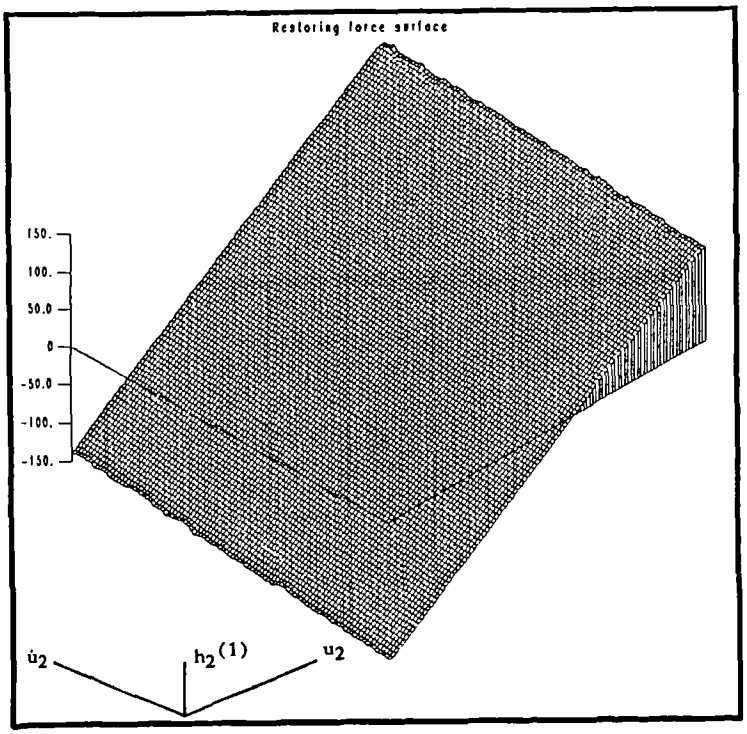

Figure 3.31. Interpolated surface - $h_2^{(1)}(u_2,\dot{u}_2)$.

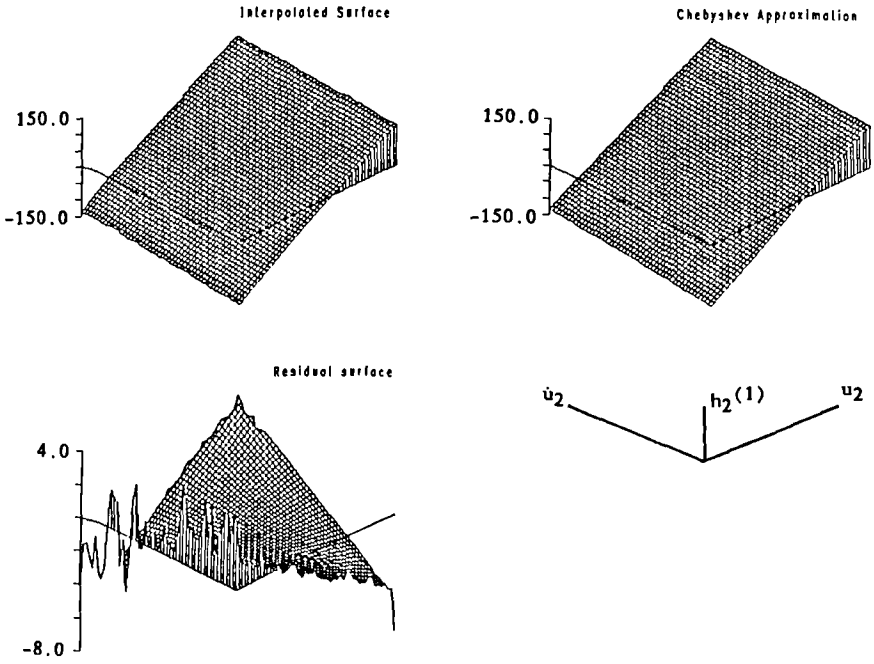

Figure 3.32. Chebyshev fit of order (1,1) to the interpolated surface in Figure 3.31.

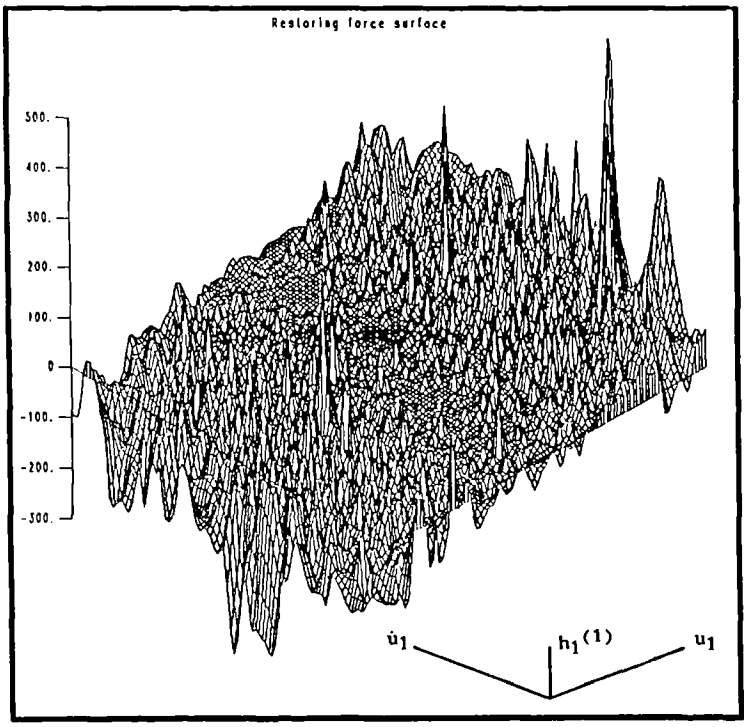

Figure 3.33. The surface $h_1^{(1)}(u_1,\dot{u}_1)$ - C^1 interpolation.

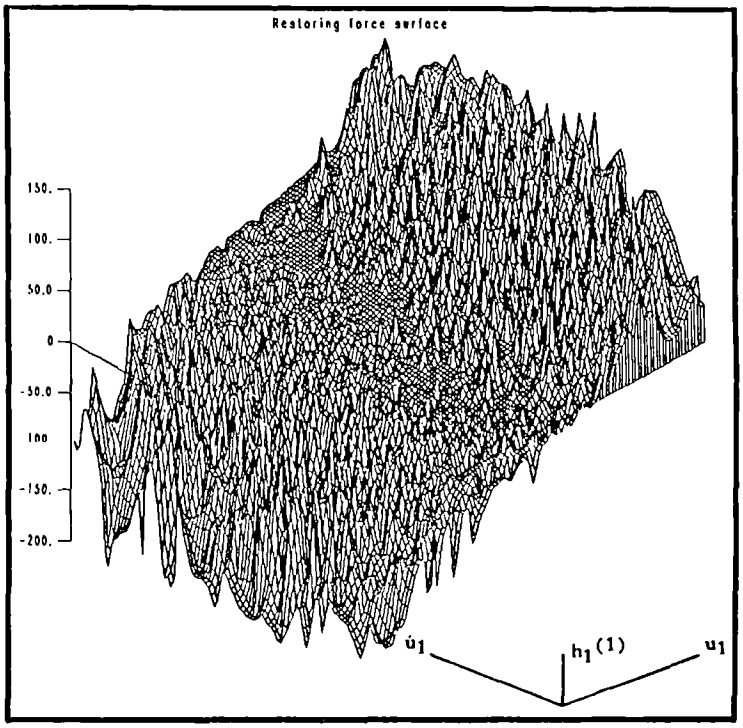

Figure 3.34. The surface $h_1^{(1)}(u_1,\dot{u}_1)$ - C^0 interpolation.

Exact Results : k3 = 5.000 e9
k1 = 1.000 e4
c = 2.000 e1

$\hat{m}$	0.10	0.40	0.70	1.00	1.30	1.60	10.0	
$\hat{k}3$	0.61	2.08	3.50	5.00	6.46	7.92	48.8	e9
$\hat{k}1$	0.20	0.47	0.73	1.00	1.27	1.53	9.00	e4
$\hat{c}$	1.79	1.87	1.94	2.00	2.08	2.15	4.14	e2
MSE($\hat{k}$)	84.9	20.6	2.24	0.00	0.69	1.83	10.0	%
MSE($\hat{c}$)	98.1	94.8	83.2	0.10	81.1	94.1	99.9	%

$\hat{k}3/k3$	0.12	0.42	0.70	1.00	1.29	1.58	9.76
$\hat{k}1/k1$	0.20	0.47	0.73	1.00	1.27	1.53	9.00
$\hat{c}/c$	0.90	0.94	0.97	1.00	1.04	1.08	2.08

Table 3.1. Dependence of the restoring force coefficients on the mass estimate for the SDOF Duffing oscillator considered in the text.

CHAPTER 4

LEAST-SQUARES PARAMETER ESTIMATION - SDOF SYSTEMS

There are a number of problems associated with the Masri/Caughey procedure. (i) It is time-consuming, (ii) there are many routes by which errors can enter the procedure, (iii) the restoring forces are expanded in terms of Chebyshev polynomials which rather obscures the physical meaning of the parameters, and (iv) one cannot obtain confidence limits for the parameters obtained. Direct least-squares parameter estimation can be used to overcome all of these problems. Parameter estimation has been applied successfully in the study of difference equations for a number of years now, both in the linear case (40) and the nonlinear case (41). However, it appears to have seen little use in the study of continuous systems; this is perhaps surprising as it is equally useful for this purpose as the arguments of this chapter will show.

4.1. The Normal Equations and Some Simple Estimation Theory.

As the objective of this work is to find the optimal procedure for identifying parameters for systems, having decided to use direct least-squares it is important to examine carefully the different algorithms which can be used. This section and those which follow consider the four least-squares methods which are arguably the most commonly used.

As an example, consider a SDOF system which is known to have the form

$$m\ddot{y} + ky^3 = x(t)$$

In order to identify the system fully one needs to estimate the values of the coefficients m and k. If the force x, displacement y and acceleration $\ddot{y}$ are sampled

at N instants t_i, one obtains N equations

$$m\ddot{y}_i + ky_i^3 = x_i = x(t_i)$$

where i = 1,...,N. This set of equations can be written in matrix form as

$$\begin{bmatrix} \ddot{y}_1 & y_1^3 \\ \ddot{y}_2 & y_2^3 \\ & \\ \ddot{y}_N & y_N^3 \end{bmatrix} \begin{bmatrix} m \\ k \end{bmatrix} = \begin{bmatrix} x_1 \\ x_2 \\ \\ x_N \end{bmatrix}$$

The matrix on the LHS containing the functions of the output data is called the design matrix and is denoted by [A]. $(m,k)^T$ is the parameter vector $\{\beta\}$. $(x_1,...,x_N)^T$ is $\{x\}$ the input vector. With this notation the equation directly above is

$$[A]\{\beta\} = \{x\} \qquad (1)$$

In general, the measured quantities will be corrupted by noise. If one assumes that all noise terms can be transferred to the input, equation (1) becomes

$$[A]\{\beta\} + \{\xi\} = \{x\} \qquad (2)$$

where $\{\xi\}$ is the vector of *residuals*, ξ_i is the difference between LHS and RHS in the i^{th} equation of motion, due to measurement errors. The assumption that noise can be transferred to the input can be justified in the case of linear systems (in the case of difference equations it is usually transferred to the output); it cannot be justified for nonlinear systems. However, correctly modelling the noise process is a complicated business and for high signal to noise ratios, equation (2) should hold quite well. For this reason the form (2) is adopted. Because the system of equations is overdetermined and [A] is not square, equation (2) cannot be inverted directly to give the parameters $\{\beta\}$. If one uses a set of estimated parameters $\{\hat{\beta}\}$ to predict the input $\{\hat{x}\}$ from a given set of output data, one obtains

$$[A]\{\hat{\beta}\} = \{\hat{x}\}$$

A measure of the accuracy of the estimate $\{\hat{\beta}\}$ is given by the function

$$I(\{\hat{\beta}\}) = (\{x\} - \{\hat{x}\})^T(\{x\} - \{\hat{x}\})$$

which is simply the sum of the squared error in x_i summed over the sampling instants. Expanding this equation gives

$$I(\{\hat{\beta}\}) = (\{x\} - [A]\{\hat{\beta}\})^T(\{x\} - [A]\{\hat{\beta}\})$$

$$= \{x\}^T\{x\} - \{\hat{\beta}\}^T[A]^T\{x\} - \{x\}[A]\{\hat{\beta}\} + \{\hat{\beta}\}^T[A]^T[A]\{\hat{\beta}\}$$

It is a reasonable assumption that, even in the presence of noise, this expression will be minimised if the estimated parameters are equal to the true parameters $\{\beta\}$. Taking the derivative of the equation above with respect to the estimate $\{\hat{\beta}\}$ gives

$$\frac{\partial I[\{\hat{\beta}\}]}{\partial\{\hat{\beta}\}^T} = -[A]^T\{x\} + [A]^T[A]\{\hat{\beta}\}$$

For the purposes of calculus $\{\hat{\beta}\}$ and $\{\hat{\beta}\}^T$ can be considered as independent variables in much the same way that a complex variable z and it's conjugate z^* can be considered independent. If I is a minimum the expession above vanishes, giving

$$[A]^T[A]\{\hat{\beta}\} = [A]^T\{x\} \qquad (3)$$

These equations are called the *normal equations*. The matrix $[A]^T[A]$ is now square and can be inverted (if the inverse exists) to give the *least-squared-error* or simply *least-squares* parameter estimate

$$\{\hat{\beta}\} = ([A]^T[A])^{-1}[A]^T\{x\} \qquad (4)$$

The method is completely general; consider the SDOF system

$$\sum_{i=1}^{P} \beta_i \, \theta_i(y,\dot{y},\ddot{y}) + \zeta = x \qquad (5)$$

where the *basis function* $\theta_i(y,\dot{y},\ddot{y})$ belongs to the parameter β_i. In the example above, $\theta_1(y,\dot{y},\ddot{y}) = \dot{y}$ and $\theta_2(y,\dot{y},\ddot{y}) = y^3$. One can form the design matrix as before, if one has P parameters

$$[A] = \begin{bmatrix} \theta_1(1) & \dots & \theta_p(1) \\ \theta_1(2) & \dots & \theta_p(2) \\ \\ \theta_1(N) & \dots & \theta_p(N) \end{bmatrix}$$

And $A_{ij} = \theta_j(i) = \theta_j(y_i,\dot{y}_i,\ddot{y}_i)$. The design equations are obtained as before

$$[A]\{\beta\} + \{\zeta\} = \{x\}$$

except now the general matrix [A] is N x P, $\{\beta\}$ is P x 1 and {x} is N x 1.

An important question at this point is whether the parameter estimate is accurate. The reality of the situation is that if one had used a different set of sampled data one would have probably obtained a slightly different estimate. This means that the estimate $\{\hat{\beta}\}$ is actually a random sample from a population of possible estimates. In this case, the strongest condition one could hope for is that the expected value of the estimates $E(\{\hat{\beta}\})$ should be equal to the true parameters. The *bias* of an estimator is defined as

$$b(\{\hat{\beta}\}) = E(\{\hat{\beta}\}) - \{\beta\}$$

and the expectation is taken over all possible sets of sampled data. Clearly $b(\{\hat{\beta}\}) = 0$ for an accurate or unbiased estimator. The basic elements of estimation theory

outlined here are presented essentially as they are in (42). For the least–squares estimator above, a sufficient condition for obtaining an unbiased estimate is that the residual sequence ζ_i should be a zero–mean white gaussian noise sequence uncorrelated with the input x_i.

Given that the estimates $\{\hat{\beta}\}$ are distributed randomly about the true parameters (if the estimator is unbiased), one can try to obtain the variance of the distribution. This gives one information about the possible spread in values of the estimates. The covariance matrix is defined as

$$C(\{\hat{\beta}\}) = E[\ (\{\hat{\beta}\} - \{\beta\})(\{\hat{\beta}\} - \{\beta\})^T\ ] \qquad (6)$$

As $E(\{\hat{\beta}\}) = \{\beta\}$ for an unbiased estimator, the diagonal entries of C are the variances of the parameters. Now,

$$\{\hat{\beta}\} = (\ [A]^T[A]\ )^{-1}[A]^T\{x\}$$

substituting

$$\{x\} = [A]\{\beta\} + \{\zeta\}$$

from (2) gives

$$\{\hat{\beta}\} = (\ [A]^T[A]\ )^{-1}[A]^T\ (\ [A]\{\beta\} + \{\zeta\}\ )$$

$$= \{\beta\} + (\ [A]^T[A]\ )^{-1}[A]^T\{\zeta\}$$

or

$$\{\hat{\beta}\} - \{\beta\} = (\ [A]^T[A]\ )^{-1}[A]^T\{\zeta\}$$

substituting this expression into equation (6) gives

$$C(\{\hat{\beta}\}) = E[\ ([A]^T[A])^{-1}[A]^T\{\zeta\}\{\zeta\}^T[A]([A]^T[A])^{-1}\ ]$$

The residuals are the only stochastic variables in this expression, therefore

$$C(\{\hat{\beta}\}) = ([A]^T[A])^{-1}[A]^T.E[\ \{\zeta\}\{\zeta\}^T\ ].[A]([A]^T[A])^{-1}$$

If one assumes that the residuals at different sampling instants are uncorrelated with each other i.e. $E(\zeta_i\zeta_j) = 0$ if $i \neq j$, and also that the residual signal is weakly stationary in that it's variance σ_ζ^2 is independent of the sampling instant, then

$$E[\ \{\zeta\}\{\zeta\}^T\ ] = \sigma_\zeta^2[1_N]$$

where $[1_N]$ is the N x N unit matrix. Substituting this into the previous equation gives the final result

$$C(\{\hat{\beta}\}) = \sigma_\zeta^2\ ([A]^T[A]\ )^{-1} \qquad (7)$$

In particular, the standard deviation for the estimate of the i^{th} parameter $\hat{\beta}_i$ is

$$\sigma_i := \sigma_\zeta.[\ ([A]^T[A])^{-1}_{ii}\ ]^{\frac{1}{2}} \qquad (8)$$

If the parameter estimates are distributed with a Gaussian distribution, standard probability theory gives a 95% probability that the true parameters are in the range

$$\{\hat{\beta}\} \pm 1.96\{\sigma\}$$

A practical problem associated with this method is that the different columns in [A] may vary greatly in size. If one returns to the original (y,y^3) example, one can see that if the y data has variance 10.0, the y^3 data will have variance 1000.0 and the resulting [A] matrix is, up to orders of magnitude

$$\begin{bmatrix} 10^2 & 10^4 \\ 10^4 & 10^6 \end{bmatrix}$$

and A_{11}/A_{22} is 10^{-4}. Matrices which have elements greatly varying in size in this manner are difficult to invert, they tend to be ill-conditioned. The solution to this problem is to scale the data before one enters it into the design matrix. All the elements of each column are divided by the standard deviation of the column. This gives a design matrix with all elements the same order of magnitude. After the parameter estimation step one can recover the physical parameters by simply rescaling.

Unfortunately, even after scaling, the normal equations approach can still fail if the matrix $[A]^T[A]$ is singular. This situation occurs if for example, the columns of [A] are linearly dependent. However, there are other approaches to least-squares estimation which can diagnose such problems and deal with them. Two such methods are described in the following sections.

4.2. The Orthogonal Estimator.

The othogonal solution of least-squares problems has been around for some time now (43). The particular approach described here is that of Billings and his associates who have used it with great success in the study of nonlinear difference equation models of systems (41)(44)(45). As this particular approach is arguably less familiar than other least-squares schemes, it is described in detail here. As before one starts with the basic design equations

$$[A]\{\beta\} = \{x\} \qquad (2)$$

neglecting noise for the moment. It is useful to rewrite this in the form

$$\{\theta_1\}\beta_1 + \{\theta_2\}\beta_2 + \ldots + \{\theta_p\}\beta_p = \{x\} \qquad (9)$$

where the vector $\{\theta_i\}$ is the i^{th} column of [A]. This vector is formed from the basis function θ_i values at each sampling instant. Clearly [A] is ($\{\theta_1\},\ldots,\{\theta_p\}$) (one can regard a matrix as a vector of vectors). So {x} is a linear superposition of the column vectors of [A]. These vectors lie in a N dimensional vector space V_N where N is the number of samples. However, there are only P of them so at most they span a P–dimensional subspace of V_N. This subspace is called the *range* of [A]. Clearly, the vector {x} need not lie in this subspace; only if it does will the equations (2) have a solution. If {x} does not lie in the range of [A] the equations have no solution. However, one can find the parameters $\{\hat{\beta}\}$ which are mapped to the closest point in the range from {x}; these parameters are the least–squares estimates. If the columns of [A] are linearly dependent the dimension of the range will be less than P and the solution if it exists will not be unique. This is the geometrical background to the problem, the utility of the definitions given here will be demonstrated in the remainder of this section and in that which follows.

Suppose that there exists a P x P matrix [T] such that $[T]^{-1}[T] = 1$ and that

$$[W] = [A][T]^{-1} \tag{10}$$

is column orthogonal i.e. if [W] = ($\{W_1\},\ldots,\{W_p\}$) then

$$\langle W_i, W_j \rangle = \delta_{ij} . \|W_i\| \tag{11}$$

where $\langle u,v \rangle$ is the scalar product of the vectors {u} and {v}, defined by

$$\langle u,v \rangle = \langle v,u \rangle = \sum_{i=1}^{N} u_i v_i$$

and $\|u\|$ is the length of the vector {u}, $\|u\| = \langle u,u \rangle^{\frac{1}{2}}$. δij is the Kronecker delta. For two non–zero vectors, this product is zero if and only if the vectors are orthogonal; one can easily show that

$$\langle u,v\rangle = \|u\|\,\|v\| \cos\theta$$

where θ is the angle between the vectors.

If one defines the *auxilary* parameters $\{g\}$ by

$$\{g\} = [T]\{\beta\} \tag{12}$$

then one has,

$$[A]\{\beta\} = [A][T]^{-1}[T]\{\beta\} = [W]\{g\} = \{x\} \tag{13}$$

or, in terms of the columns of [W]

$$\{W_1\}g_1 + \ldots + \{W_i\}g_i + \ldots + \{W_p\}g_p = \{x\}$$

Taking the scalar product of this equation with $\{W_j\}$ gives

$$\langle W_1,W_j\rangle g_1 + \ldots + \langle W_i,W_j\rangle g_i + \ldots + \langle W_p,W_j\rangle g_p = \langle x,W_j\rangle$$

and using the orthogonality relation (11) gives

$$g_j = \frac{\langle W_j,x\rangle}{\langle W_j,W_j\rangle} = \frac{\langle W_j,x\rangle}{\|W_j\|} \tag{14}$$

and one can obtain the auxilary parameters one at a time, unlike the situation using the normal equations where the parameters are obtained *en bloc*.

The question one is faced with now is how to construct [T]. The first step is to obtain the orthogonal basis $\{W_1\},\ldots,\{W_p\}$ from $\{\theta_1\},\ldots\{\theta_p\}$. This can be done using the following simple procedure.

First, define $\{W_1\} = \{\theta_1\}$. The rest of the basis is obtained sequentially. To form $\{W_2\}$ one takes $\{\theta_2\}$ and subtracts from it the component parallel to $\{W_1\}$ i.e.

$$\{W_2\} = \{\theta_2\} - \frac{\langle W_1, \theta_2 \rangle}{\langle W_1, W_1 \rangle} \cdot \{W_1\}$$

Taking the scalar product of this expression with $\{W_1\}$ gives

$$\langle W_1, W_2 \rangle = \langle W_1, \theta_2 \rangle - \frac{\langle W_1, \theta_2 \rangle}{\langle W_1, W_1 \rangle} . \langle W_1, W_1 \rangle$$

which is zero as required. Next, one forms $\{W_3\}$ by subtracting from $\{\theta_3\}$ components parallel to $\{W_2\}$ and $\{W_1\}$ etc. The result is an orthogonal set. One can write the procedure in matrix form

$$\begin{bmatrix} W_1(1) & \dots & W_p(1) \\ W_1(2) & \dots & W_p(2) \\ & & \\ W_1(N) & \dots & W_p(N) \end{bmatrix} = \begin{bmatrix} \theta_1(1) & \dots & \theta_p(1) \\ \theta_1(2) & \dots & \theta_p(2) \\ & & \\ \theta_1(N) & \dots & \theta_p(N) \end{bmatrix}$$

$$- \begin{bmatrix} W_1(1) & \dots & W_p(1) \\ W_1(2) & \dots & W_p(2) \\ & & \\ W_1(N) & \dots & W_p(N) \end{bmatrix} \begin{bmatrix} 0 & \alpha_{12} & \alpha_{13} & \dots & \alpha_{1p} \\ 0 & 0 & \alpha_{23} & \dots & \alpha_{2p} \\ & & & & \\ 0 & 0 & 0 & \dots & 0 \end{bmatrix}$$

where $\alpha_{ij} = \langle W_i, \theta_j \rangle / \langle W_i, W_i \rangle$. If the matrix with entries α_{ij} above the diagonal and zeroes elsewhere is denoted by $[\alpha]$, the equation above can be written in matrix form.

$$[W] = [A] - [W][\alpha]$$

or

$$[W] . ([1_p] + [\alpha]) = [A]$$

which finally gives us the [T] matrix by comparing the last equation with (10) i.e. $[T] = [1_p] + [\alpha]$ or

$$[T] = \begin{bmatrix} 1 & \alpha_{12} & \alpha_{13} & \cdots & \alpha_{1p} \\ 0 & 1 & \alpha_{23} & \cdots & \alpha_{2p} \\ & & & & \\ 0 & 0 & 0 & \cdots & 1 \end{bmatrix}$$

Computing the inverse of [T] is straightforward as the matrix is already upper-triangular. One simply carries out the backsubstitution part of the Gaussian elimination algorithm **(33)**. If the elements of $[T]^{-1}$ are labelled t_{ij} then one calulates the j^{th} column from the equations

$$\begin{bmatrix} 1 & \alpha_{12} & \alpha_{13} & \cdots & \alpha_{1p} \\ 0 & 1 & \alpha_{23} & \cdots & \alpha_{2p} \\ \vdots & & & & \vdots \\ 0 & 0 & 0 & \cdots & 1 \end{bmatrix} \begin{bmatrix} t_{1j} \\ t_{2j} \\ \vdots \\ t_{pj} \end{bmatrix} - \begin{bmatrix} 0 \\ \cdot \\ 1 \\ \cdot \\ 0 \end{bmatrix}$$

where the 1 on the RHS is in the j^{th} position. Backsubstitution gives

$$t_{ij} = 0 \quad \text{if} \quad i > j$$

$$t_{ij} = 1 \quad \text{if} \quad i = j$$

$$t_{ij} = -\sum_{k=i+1}^{j} \alpha_{jk}\, t_{kj} \quad \text{if} \quad i < j$$

Having constructed the inverse of [T], one can now recover the physical parameters from the auxilary parameters, using

$$\{\hat{\beta}\} = [T]^{-1}\{g\} \qquad (15)$$

This is all rather complicated and begs the question; what is wrong with the normal equations? Consider again equation (9). The dimension of the range of [A] is called the *rank* r. If the column vectors are linearly dependent, the rank of A is clearly less than P, $r = P - n$ for some integer n. n is called the *nullity* of [A]. Now, a basic theorem of linear algebra states that the rank of $[A]^T[A]$ is the same as that of [A]. A further theorem states that if the rank of a P x P matrix is less than P, the matrix is singular **(46)**. In this case, one cannot solve the normal equations.

Unfortunately things are seldom as clear cut as this. The vectors $\{\theta_i\}$ may be *close* to linear dependence in which case $[A]^T[A]$ will be close to singular. Under these circumstances roundoff errors can become very important. In this case the normal equations are soluble and one will obtain a set of parameters $\{\hat{\beta}\}$; however, they will typically have very large magnitudes so that the model depends on very delicate cancellations between them in order to reproduce the measured data $\{x\}$. This is clearly not very encouraging if one wishes to use the model for forecasting.

A very simple argument serves to justify these statements. Suppose one considers the normal equations where the RHS has a small error $\{\delta x\}$, perhaps due to roundoff

$$[A]^T[A]\{\hat{\beta}\} = [A]^T (\{x\} + \{\delta x\})$$

The error in the estimated parameters is then $([A]^T[A])^{-1}\{\delta x\}$ which can be arbitrarily large if $[A]^T[A]$ is close to singularity.

The orthogonal estimator allows one to overcome this problem. If the $\{\theta_i\}$ are linearly dependent, the procedure informs one in the following way. Suppose $\{\theta_j\}$ depends on $\{\theta_{j-1}\},\ldots,\{\theta_1\}$ which are linearly independent. As the subspace spanned by $\{W_{j-1}\},\ldots,\{W_1\}$ is the same as that spanned by $\{\theta_{j-1}\},\ldots,\{\theta_1\}$, $\{\theta_j\}$ is linearly dependent on the $\{W\}$ vectors so subtracting off components parallel to them will eventually produce the zero-vector, i.e. $\{W_j\} = \{0\}$ and $\|W_j\| = 0$. So if one finds a $\{W_j\}$ with length zero at some stage, the data vectors are linearly dependent and one should remove $\{\theta_j\}$ and the corresponding parameter from the calculation. If the procedure is allowed to continue unchecked there will be a division by zero at the next stage. So orthogonal estimation allows one to diagnose linear dependence.

It still remains to show why (14) is a least-squares estimator. Consider again the equations

$$\{x\} = [A]\{\beta\} + \{\xi\}$$

If one has found the correct structural form for the equations of motion, then $\{x\}$ will lie inside the range of [A]. If one has missed out some terms, or the measurements are noisy, the residual vector $\{\zeta\}$ will effectively push $\{x\}$ outside the range (Figure 4.1). If one thinks of the vectors as position vectors, the vectors can be identified with points in the space V_N. In this case the distance between the point specified by the model and that specified by the data $\{x\}$ is the length of the residual vector $\{\zeta\}$ which is $\|\zeta\|$.

Now, the smallest distance between the point $\{x\}$ and the hyperplane spanned by the $\{W_i\}$ which is the range, is the perpendicular distance. So the least–squares condition, which is that $\|\zeta\|$ is a minimum, is satisfied if the vector $\{\zeta\}$ is perpendicular to the range. It is sufficient for this that $\{\zeta\}$ be perpendicular to all the $\{W_i\}$. i.e.

$$\langle \zeta, W_i \rangle = 0 \qquad \forall\ i$$

i.e. (putting in the {}'s for once for clarity)

$$\langle \{x\} - \sum_j g_j \{W_j\} , \{Wi\} \rangle = 0$$

$$\langle x, W_i \rangle - \sum_j g_j \langle W_i, W_j \rangle = 0$$

and orthogonality (11) gives

$$g_j = \frac{\langle x, W_j \rangle}{\langle W_j, W_j \rangle}$$

which is equation (9) as required.

This approach applies just as well if the design matrix [A] is used rather than the auxilary [W]. In this case, the least–squares condition is

$$\langle \zeta, \theta_i \rangle = 0 \qquad \forall\ i$$

i.e

$$< \{x\} - \sum_{j=1}^{P} \beta_j \{\theta_j\} , \{\theta_i\} > = 0$$

$$<x, \theta_i> = \sum_{j=1}^{P} \beta_j <\theta_i, \theta_j>$$

writing the θ terms as components of [A] and expanding the scalar products gives

$$\sum_{k=1}^{N} x_k A_{ki} = \sum_{j=1}^{P} \beta_j \left(\sum_{k=1}^{N} A_{ik} A_{ij} \right)$$

or in matrix form,

$$[A]^T\{x\} = [A]^T[A]\{\beta\}$$

and the normal equations are recovered as one might expect.

The final task is the evaluation of the covariance matrix. Clearly one could use equation (7); however, this requires a matrix inversion. One can obtain it directly from the auxilary model. As [W] is column orthogonal, $[W]^T[W]$ is diagonal. A moments thought shows that the i^{th} diagonal element is $\|W_i\|^2$. These lengths have already been calculated during the construction of the orthogonal basis. This means that $([W]^T[W])^{-1}$ is also diagonal with i^{th} element $\|W_i\|^{-2}$. So, for practically no extra effort one has the covariance matrix for the auxilary parameters

$$[C]_g = \sigma_\zeta^2 \left([W]^T[W] \right)^{-1}$$

As $\{g\}$ and $\{\beta\}$ are related by the linear transformation $\{g\} = [T]\{\beta\}$, the covariance matrix is (8)

$$[C] = [T]^{-1}[C]_g[T]$$

The orthogonal estimator has a number of advantages. The auxilary parameters can be obtained one at a time. As Billings and Tsang (45) remark, the estimator allows a P-dimensional estimation problem to be reduced to P one-dimensional ones. This means that if one needs to add more terms to the model, one need not re-estimate those parameters already obtained, only the transformation from {g} to {β} needs to be re-done. If one is dealing properly with noise the deterministic terms and the noise terms can be uncoupled by this procedure, this gives a very clear indication that the parameter estimates will be unbiased. The algorithm allows one to pinpoint exactly where linear dependence is causing problems. A considerably more detailed discussion of the relevant theory can be found in (44).

4.3. Singular Value Decomposition.

The discussion in this section relies fairly heavily on (33) and chapter 9 of (47).

A fairly deep theorem of linear algebra states that if one has a M x N matrix [A] and M $\geq$ N, then [A] can be decomposed as follows

$$[A] = [U][\sum][V]^T \qquad (16)$$

where [U] is a M x N column orthonormal matrix such that $[U]^T[U] = 1$, $[\sum]$ = $diag(s_1,\ldots,s_p)$ is a N x N diagonal matrix and [V] is a N x N column orthonormal matrix i.e $[V]^T[V] = 1$. As [V] is square it is also row orthonormal $[V][V]^T = 1$.

Consider the case when [A] is square. [U] is now square and consequently row orthonormal. The inverse of [A] is easily seen to be

$$[A]^{-1} = [V][\sum]^{-1}[U]^T \qquad (17)$$

and $[\sum]^{-1}$ is $diag(s_1^{-1},\ldots,s_p^{-1})$. It is therefore obvious that [A] can only be singular

if one of the s_i is equal to zero. The s_i are called the *singular values* of [A]. The number of non-zero singular values is equal to the rank of [A]. Problems can also occur if one of the singular values is very small, in this case it's value may be composed mainly of roundoff errors. This would indicate that the columns are close to linear dependence. In order to diagnose this problem one can define the *condition number* for the matrix [A] which is the largest singular value divided by the smallest. If the condition number is infinite, the matrix is singular, if it is large the matrix is close to singular. The condition number tells one if linear dependence is a problem or not.

Consider the situation where [A] is nonsingular and {x} is in the range of [A] (this is guaranteed if [A] is square). In this case the solution of the design equations is simply

$$\{\hat{\beta}\} = [A]^{-1}\{x\} = [V][\sum]^{-1}[U]^T\{x\}$$

$$= [V].diag(s_1^{-1},\ldots,s_p^{-1}).[U]^T \qquad (18)$$

The next situation of interest is when [A] is singular but {x} is still in the range of [A]. The solution still exists, however $[A]^{-1}$ does not. The solution in this case is not unique. To obtain *one* solution one simply replaces each s_i^{-1} in $[\sum]^{-1}$ corresponding to a zero singular value by zero and evaluates expression (18). If $[\sum_d]^{-1}$ denotes the matrix with appropriate deletions, then

$$\{\hat{\beta}\} = [V][\sum_d]^{-1}[U]^T \qquad (19)$$

Some explanation is neccessary. If [A] is singular there will exist vectors {y} such that

$$[A]\{y\} = \{0\}$$

these vectors form a subspace of the parameter space called the *nullspace*. The dimension of the nullspace is the nullity mentioned previously. It is because of these vectors that the solution is not unique. Consider the solution of (19) above, one can add any vector {y} from the nullspace to $\{\hat{\beta}\}$ and still have a solution i.e.

$$[A](\{\hat{\beta}\} + \{y\}) = [A]\{\hat{\beta}\} + [A]\{y\} = \{x\} + \{0\}$$

It is shown in (33) that the solution $\{\hat{\beta}\}$ given by (19) is the unique solution of minimum length i.e. $\|\hat{\beta}\|$ is smallest for this estimate.

Singular value decomposition works in this way because the $\{V_i\}$ column vectors corresponding to zero singular values form an orthonormal basis for the nullspace. Similarly the $\{U_i\}$ vectors corresponding to non-zero singular values form an orthogonal basis for the range. The estimate for $\{\hat{\beta}\}$ given by (19) removes the contribution from the nullspace vectors $\{V_i\}$, because their contribution is proportional to s_i^{-1} which has been zeroed. The orthogonal estimator suffers from the same problem; in that case one is told which are the linearly dependent vectors and one has to remove them until [A] has full rank i.e. no nullspace. SVD not only diagnoses the problem it simply ignores the nullspace.

Finally one has the situation which is of most interest; {y} is not in the range of [A] whether it is singular or not. In this case, the remarkable equation (19) gives the least-squares solution. Again, the proof is given in (33).

If one wishes to know the covariance matrix, the derivation proceeds exactly as for equation (7) and the result is given by

$$[C] = \sigma_\zeta^2 \, [V][\sum_d]^{-2}[V]^T$$

In practice, problems are caused if some of the singular values are very small. One then defines a tolerance ϵ so that if any singular values are less than ϵ they are

deleted as if they were zero. The *effective nullity* n_ϵ is the number of singular values $< \epsilon$. The *effective rank* is then $P - n_\epsilon$. The important point about SVD is that one must delete small singular values, then SVD is foolproof. If one does not delete small values then SVD is as badly behaved as the normal equations.

4.4. Recursive Least-squares (RLS).

The solution of the least-squares problem by any of the methods above requires that all the data should be present. They cannot be used in real-time. Such procedures are called *off-line*. It is sometimes useful to carry out procedures *on-line* and have the parameter estimates updated each time a new data sample becomes available. Estimators which work in this way are call *recursive*. It is a fairly simple matter to make the least-squares procedure recursive. The arguments are based on the normal equations. The details of the derivation are given in **(42)** or **(50)**, the results are as follows

Suppose $\{\hat{\beta}\}_i$ is the parameter estimate at the i^{th} sampling instant and $[P]_i = ([A]^T[A])_i^{-1}$ is the estimate of the covariance matrix at sampling instant i (this is really the covariance matrix divided by the variance of the residuals ζ_i). At sampling instant i+1 one measures the present x_i and y_i, $\dot{y}_i$ and $\ddot{y}_i$, so one can calculate values for all the basis fuctions $\{\Theta\}_{i+1}^T = \{ \theta_1(i+1),\ldots,\theta_p(i+1) \}$. The parameter estimates are updated as follows

$$\{\hat{\beta}\}_{i+1} = \{\hat{\beta}\}_i + \{K\}_{i+1} \cdot (x_{i+1} - \{\Theta\}_{i+1}^T \cdot \{\hat{\beta}\}_i)$$

$$[P]_{i+1} = [P]_i - \{K\}_{i+1} \cdot \{\Theta\}_{i+1}^T \cdot [P]_i$$

where

$$(K)_{i+1} = \frac{[P]_i (\Theta)_{i+1}}{1 + (\Theta)_{i+1}^T . [P]_i . (\Theta)_{i+1}}$$

One starts the recurrence with $\{\hat{\beta}\}_0 = \{0\}$. One sets $[P] = \alpha[1_p]$ initially with $\alpha = 10^4$ or some other large number. The reason for this is that the diagonal elements of [P] are proportional to the standard deviations of the parameters, so one starts off with large values to express the fact that one has little confidence in the initial estimate.

Recursive Least-Squares can be shown to be a convergent procedure. If the conditions on the noise mentioned in section 1 are satisfied, RLS always converges to the true parameters, if they are not RLS may converge to biased parameters.

The method essentially solves the normal equations without inverting a matrix. Another useful property is, one can choose an accuracy for the parameters, then check to see if each step is changing the parameters by less than this accuracy, if so one can stop the recurrence. In situations where convergence is fast, this method can be quite useful. Fast RLS schemes are also possible where one only updates the diagonal elements of [P], this can speed things up considerably without changing the fact that one converges to the true parameters **(48)**.

4.5. Comparison of the Methods.

The operation counts below refer only to multiplications, the assumption being that additions are relatively negligible.

(i) The Normal Equations.

As the inverse covariance matrix $[A]^T[A]$ is symmetric, the number of multiplications required for it's formation is $\frac{1}{2}$ P(P+1)N $\approx \frac{1}{2} P^2N$. The matrix inversion is carried out using an LU decomposition as described in **(33)** for which the operation count is ≈

P^3 (If the covariance matrix is not required one can use the LU decomposition to solve the normal equations without inversion, in which case the operation count is $P^3/3$). Back substitution generates another $PN + P^2$ operations. This gives a operation count of $P^3 + \frac{1}{2} P^2N$ to leading order.

Considering speed separately, the normal equations have the advantage of simplicity. To implement the procedure, the most difficult operations one needs to understand are matrix multiplication and inversion. Problems occur if the matrix $[A]^T[A]$ is singular, the method cannot find a solution. More serious is the case when the matrix is nearly singular, the method will propose a solution but does not indicate that the parameters can not neccessarily be trusted. One could of course obtain the determinant of $[A]^T[A]$ and check to see that it is not too small. If one is using a pivoting procedure to obtain the inverse, the determinant is obtained as a bonus being simply the product of the pivots. More simply the presence of a very small pivot is a good indicator that the matrix is nearly singular. However, even if one suspects something is wrong one cannot find out what one should do the data to improve the conditioning ot the problem i.e which columns of [A] one should remove.

(ii) The Orthogonal Estimator.

Computing the [T] matrix requires $\frac{1}{2} P(P-1)N \approx \frac{1}{2} P^2N$ operations as it is upper triangular. Generating the auxilary data also requires $\frac{1}{2} P(P-1)N \approx \frac{1}{2} P^2N$ multiplications. Generating the auxilary parameters costs 2PN. After a little elementary algebra one can see that inverting the [T] matrix requires

$$\frac{1}{12} P(P+1)(2P+1) - \frac{1}{4} P(P+1) \approx \frac{1}{6} P^3$$

Finally generating the true parameters requires $\frac{1}{2} P(P-1)$. This gives an overall count of $P^3/6 + P^2N$ to leading order. This count is only smaller than that for the normal equations if $N < 5P/3$ which is rather unlikely, consequently, using the orthogonal estimator is generally slightly slower than using the normal equations.

The orthogonal estimator has a number of advantages over the normal equations. The most important being that one can use it to find where linear dependence is causing problems in the data set. One then has to remove the offending data. By this method one makes the estimation problem one of full rank. The parameters are estimated one at a time so if the model needs to be enlarged, one need not re-estimate previously obtained parameters.

(iii) Recursive Least-Squares.

Calulating the {K} vector at each step costs $2P^2 + P$ multiplications. The [P] matrix and $\{\hat{\beta}\}$ vector require $2P^2$ and 2P respectively. This gives an overall operation count of $(4P^2+3P)N$. As the available N is usually a good deal larger than P this method is much slower than the the two previous methods. One can speed things up by stopping the recursion when the parameters have converged to values with an appropriate accuracy. Using a Fast RLS scheme **(48)** reduces the order of the leading term from $\approx P^2N$ to $\approx PN$ – a considerable saving.

From the point of view of conditioning RLS is no better than the normal equations. It provides no more and no less information. It is useful if one wishes to estimate parameters in real-time. This method can also be used to track slowly varying parameters; in fact, it will be put to this use in Chapter 10.

(iv) Singular Value Decomposition.

The routine for SVD used in this work is a 'black-box' routine lifted from **(33)**. This makes an operation count a little complicated. However, the routine is divided into two steps. First, a Householder reduction to bidiagonal form is used. Secondly the QR algorithm is used. Both of these procedures are iterative in that they repeat until some convergence criterion is satisfied. According to **(33)** the Householder stage has an operation count of between $2P^3/3$ and $4P^3/3$. The QR step has an operation count of aprroximately $3P^3$. This gives an overall operation count of approximately $4P^3$.

This suggests that SVD is one of the slower of the algorithms considered.

The great advantage that SVD has over the other methods is that if one deletes singular values as discussed above, the method is foolproof. It not only indicates the order of singularity of [A] i.e. the nullity, it then ignores the problems and goes on to find a least-squares estimate in the *effective* range of [A]. Computationally the method is rather more difficult to use than the others, witness the use of the routine from (33) as a 'black-box'. However, it is arguably the most reliable. If one wishes to use a routine without a reasonably deep understanding of the underlying theory, this is the one.

In order to test the various implementations of these procedures, data for a Duffing oscillator system described by the equation of motion

$$\ddot{y} + 20\dot{y} + 10^4 y + 5x10^9 = x(t)$$

was simulated. The methods were then used to fit parametric models of the form

$$m\ddot{y} + \sum_{i=0}^{L} \sum_{j=0}^{M} a_{ij}\, y^i \dot{y}^j = x(t)$$

of varying order P = (L+1)(M+1) + 1, with N equal to 1000. The result is a graph of time taken against number of parameters and is shown in Figure 4.2. The results agree well with the analysis above. In all cases the methods gave parameter estimates of the same degree of accuracy. One should bear in mind that the problem in this case is quite well-conditioned.

4.6. Displaying the Force Data Without Interpolating.

The direct least-squares methods described above do not produce restoring force

surfaces naturally in the course of their use as the Masri/Caughey procedure does. However, the force surfaces provide a direct visual means of identifying the nonlinearity e.g. the presence of a piecewise-linear force would be obvious from the force surface; one could not tell this from the coefficients of a polynomial approximation. Clearly some means of generating the surfaces within the framework of the direct least-squares approach is desirable. One is faced with the problem of obtaining the force data on a regular array so that one can plot it. Two methods are used in the work which follows.

(a) Sections.

The idea used here is a modified version of the procedure used by Masri and Caughey to overcome the extrapolation problem. The stiffness curve or section is obtained by choosing a narrow band of width δ through the origin parallel to the y axis, one then records all pairs of values $(y_i, f(y_i,\dot{y}_i))$ such that $-\frac{1}{2}\delta \leq \dot{y}_i \leq \frac{1}{2}\delta$. The y_i values saved are then placed in increasing order and one can plot the $y_i \rightarrow f_i$ graph. This procedure gives one a slice through the force surface at $\dot{y} = 0$. It is essentially the static stiffness curve. The procedure is illustrated in Figure 4.3. The same procedure can be used to give the damping curve at $y = 0$. If the restoring force separates i.e.

$$f(y,\dot{y}) = f_d(\dot{y}) + f_s(y)$$

then identification of the damping and stiffness sections is sufficient to identify the system.

(b) Crawley/O'Donnell Surfaces.

This method of constructing the force surface was introduced by Crawley and O'Donnell (55). One begins with the triplets obtained from the integration procedure $(y_i,\dot{y}_i,f_i)$. One then divides the rectangle in the phase-plane $[y_{min},y_{max}]x[\dot{y}_{min},\dot{y}_{max}]$

into small grid squares. If a grid square contains sample points $(y_i,\dot{y}_i)$, the force values above those points is averaged to give a force value above the centre of the square. This gives a scattering of force values on the regular grid defined by the centres of the squares. One then checks all empty squares; if an empty square has three neighbours each with a force value defined, the values are averaged to give the value over the new square. One repeats this step until no new points over the grid are produced. Because the values are defined over a regular grid, the surface (perhaps with holes) is easy to plot. The procedure is illustrated in Figure 4.4. Almost all the surfaces obtained from now on are constructed by this method.

Unfortunately, if one insists on using three neighbours, the process invariably stops before the data region is covered. Alternatively one can define an iterative procedure such that a force value is defined on an empty square if it has two neighbours with data. Although one can construct configurations where even this is insufficient to propogate values over the entire grid, they are extremely unlikely to occur in practice. Clearly, before one tries the two-neighbour steps, one exhausts the possibilities using three neighbours. One can also carry out an initial step using four neighbours, this does not usually generate many new points.The surfaces obtained can be classified as follows :

(i) The three neighbour extended surface is exact for a linear function in one direction and a constant function in the other. It is not C^1 as this requires the surface to be exact for a bilinear function.

(ii) The two neighbour extended surface is exact only for a constant surface. Because of this it will tend to level out away from the data. For this region it should only be used on a reduced data set where the area of phase-plane is evenly covered.

The surfaces obtained are therefore inferior to those obtained form the TILE4 package described in Chapter 2. However, they more than make up for the lack of accuracy by their speed of construction. A timed example is given in the next section.

If the Crawley/O'Donnell surface does cover the data region, one can take values from the centres of the squares and use them in the Masri/Caughey procedure i.e. one can estimate Chebyshev coefficients by integration.

4.7. Simulated SDOF Systems.

In order to compare the more direct methods described above, with the Masri/Caughey procedure described in the previous two chapters, the same systems considered in Chapter 2 are identified here using the least-squares techniques. The plots are obtained using the simple ideas described in the previous section. For each system considered the details of the simulation and the inputs used in each case can be found in section 4 of Chapter 2 together with the plots which show the distribution of the data in the phase plane.

In all cases below, the first 1000 points of data from the simulation are used for the parameter estimation. All 10000 points are used to form the force surface. A multinomial model of the form

$$\Delta m.\ddot{y} + \sum_{i=0}^{m}\sum_{j=0}^{n} a_{ij}\, y^i \dot{y}^j = x(t) - m_e\ddot{y} \qquad (20)$$

is fitted. The quantities on the RHS are known, m_e is an initial estimate for the mass. The correction to the mass Δm, and the polynomial coefficients a_{ij} are the parameters to be estimated. If the intial mass is set to zero, Δm provides a mass estimate. The reason for splitting the mass coefficient in this way is that the $m\ddot{y}$ term would usually be much larger than any of the polynomial terms. One says that the $m\ddot{y}$ term contributes most to the variance of the RHS. Because of this, the estimator may not obtain polynomial coefficients very accurately if the term is small and consequently swamped by the mass-acceleration. Removing as much of the mass term as possible increases the percentage contribution of the polynomial terms to the RHS.

Because of this they will be obtained more accurately. Clearly one could obtain the initial estimate by fitting parameters with $m_e = 0$. Similarly, one could use initial estimates for all parameters, and this is the approach used in (49) where more traditional frequency-domain methods are used to correct parameter estimates for linear systems, the initial estimate coming from finite element analysis. However, it was found that in this case the accuracy of the procedure was only really sensitive to the mass estimate.

There are $P = (m+1)(n+1) + 1$ parameters to estimate and the basis functions are $\dot{y}$ and the $y^i\dot{y}^j$'s. In order to construct the design matrix the rectangular array of basis functions is mapped into a one-dimensional array as follows.

$$\theta_k(y,\dot{y},\ddot{y}) = y^i\dot{y}^j$$

where $k = jn + i + 1 < P$. Finally

$$\theta_p(y,\dot{y},\ddot{y}) = \ddot{y}$$

As Al-Hadid and Wright (18) have pointed out, one can include basis functions for well-known nonlinearities if one wishes. For example, the Coulomb friction function and the quadratic damping function

$$\theta_f(y,\dot{y},\ddot{y}) = \mathrm{sgn}(\dot{y}) = \dot{y}/|\dot{y}|$$

$$\theta_d(y,\dot{y},\ddot{y}) = \dot{y}|\dot{y}|$$

Having obtained estimates of the parameters, one can use the model to form the predicted RHS for the equation (20). One can then plot the comparison and find the MSE for the model fit. One can also make an estimate of the significance of each of the model terms as follows. Each model term, say $a_{12}y\dot{y}^2$, is estimated at each sampling instant and the variance of the resulting time-series is obtained. This variance is then expressed as a percentage of the total variance of the RHS. This

quantity shall be called the *significance factor*, it is essentially the Error Reduction Ratio of Korenburg et.al.**(44)**. One then sets a threshold contribution. If any term contributes less than the threshold it is discarded as insignificant. One of the properties of the orthogonal approach is that the significance test can be carried out for the auxilary model. In the simulations which follow the threshold is set at 0.01%.

Alternatively the stiffness and damping models can be identified by estimating least-squares coefficients for a model of the form

$$\sum a_i y^i \quad or \quad \sum a_i \dot{y}^i$$

i.e. the basis functions for the fit are simply $\theta_i(y,\dot{y},\dot{y}) = y^i$ or $\dot{y}^i$. The data used for fitting the model is simply that obtained for the purpose of plotting the sections. Usually all model orders up to 10^{th} are obtained and their MSE values are calculated. A good indicator of the correct model order n is that the MSE drops sharply in moving from an $(n-1)^{th}$ order model to one of order n. It is clear that this method does not allow one to identify systems with cross-term nonlinearities.

The examples are considered in the same order as in Chapter 2. The first is the linear system described by the equation,

$$\ddot{y} + 40\dot{y} + 10^4 y = x(t)$$

This was simulated exactly as before (see section 2.4). The coefficents for a multinomial model of the form (20) were estimated using the orthogonal estimator. (In all cases which follow the initial mass estimate is taken to be 1.0. It was found that a first estimation always obtained the correct mass value to five or six significant figures.) The results were

	Exact	Estimated	% error
Δm	0.0	0.00000006	-
a_{01}	40.00	40.000031	7.8×10^{-5}
a_{10}	10000.0	9999.9951	4.9×10^{-5}

The estimated standard deviations for the two parameters above were 6.1×10^{-6} and 5.9×10^{-4} giving 95% confidence limits of $\pm$ 1.2×10^{-5} and $\pm$ 1.2×10^{-3} respectively. These clearly agree with the accuracies obtained above. As the exact values are known, there is little point in giving the standard deviations, from now on the percentage error only will be quoted for simulations. Comparison of the true data and that predicted by the model is shown in Figure 4.5. The MSE for the comparison is 8.7×10^{-12} which is obviously insignificant. The % errors for the coefficients and the model MSE using the Masri/Caughey procedure were of the order 0.1 - 0.01 (Section 2.4). The restoring force surface obtained by Crawley and O'Donnell's procedure is shown in Figure 4.6. One of the characteristics of the three-neighbour version of the surface shown here is that there is no surface over regions with no data. The surface shown is just as informative as that produced by TILE and took a fraction of the time to create.

The stiffness section is shown in Figure 4.7 and the damping section in Figure 4.8. In each case a linear curve-fit to the data is shown also. The damping curve appears to be noisy, there is a simple explanation for this. The 'noise' occurs because the data for the section is taken from a band of finite width. This means that the contribution from the stiffness force is not zero but varies between $-\frac{1}{2}.k\delta$ and $+\frac{1}{2}.k\delta$ where k is the linear stiffness and δ is the width of the band. Because the sample points are distributed randomly in the plane and y appears to be uncorrelated with $\dot{y}$, the deviations at each $\dot{y}$ are independent and so appear to be noise. Similary the error at a point on the stiffness curve is given by $\pm$ $\frac{1}{2}.c\delta$. If the bands for each section have the same size then one has (neglecting the fact that the y and $\dot{y}$ axes have different scales)

$$\frac{\text{maximum deviation from the } \dot{y} \text{ curve}}{\text{maximum deviation from the } y \text{ curve}} = \frac{k}{c}$$

which is 250 in this case. Clearly the damping curve will appear noisier than the stiffness. This ratio is actually an upper bound as the scaling has not been considered. Curve fitting to the stiffness section gave values for the coefficients a_{01} and a_{10} of 40.075 and 9995.9 respectively. The difference in accuracy is purely attributable to the 'noise' in the sections.

The next system considered was the Duffing oscillator system with equation of motion,

$$\ddot{y} + 20\dot{y} + 10^4 y + 5\text{x}10^9 y^3 = x(t)$$

(see section 2.4.). The orthogonal estimator was used to obtain the parameters and 1000 points of data were used. The significant least–squares coefficients were

	Exact	Estimated	% error
a_{01}	20.00	20.000023	$1.2\text{x}10^{-4}$
a_{10}	10000.0	10000.087	$8.7\text{x}10^{-4}$
a_{30}	$5.0\text{x}10^9$	$4.99998\text{x}10^9$	$4.9\text{x}10^{-4}$

The computer output for this example is shown in Table 4.1. The comparison of the true data and the predicted data is shown in Figure 4.9. The model MSE of $4.33\text{x}10^{-10}$ is negligible again. The force surface is shown in Figure 4.10, the cubic nature of the nonlinearity is very clearly indicated. The stiffness and damping sections are shown in Figures 4.11 and 4.12 respectively. The best model fits are also shown in each case. Linear for the damping and cubic for the stiffness. Using the least–squares estimator on the data taken for the section plots, one obtains linear parameters of 20.03 and 9984.6 and a cubic term of $5.003\text{x}10^9$.

The next example was the system with nonlinear damping. The equation of motion was,

$$\ddot{y} + 20\dot{y} + 100\dot{y}|\dot{y}| + 10^4 y = x(t)$$

As indicated previously, this example is a little more interesting as the nonlinear function does not have a polynomial representation. One can only approximate. A model of order (1,3) was used initially, i.e. terms up to $y.\dot{y}^3$ were included. The resulting approximation was

$$f(y,\dot{y}) = 37.37\dot{y} + 126.44\dot{y}^3 + 9953.9y$$

all other terms being discarded as insignificant. A comparison of predicted and measured data gave an MSE of 0.016. The comparison is shown in Figure 4.13. Fitting a model of order (1,7) gave the result

$$f(y,\dot{y}) = 29.41\dot{y} + 274.56\dot{y}^3 - 609.85\dot{y}^5 + 651.42\dot{y}^7 + 9986.0y$$

It is encouraging that all even powers of the velocity have been rejected as insignificant. In this this case the comparison gave an MSE of 0.001. This example provides one with a warning about the careless use of 'special' basis functions as suggested in (18). The data is so well described by the 7^{th} order polynomial that if one had also included a basis function of the form $\dot{y}|\dot{y}|$, one would almost certainly have introduced near linear dependence into the estimation. The comparison is shown in Figure 4.14. The restoring force surface obtained from the data is shown in Figure 4.15. The variation in the damping direction is small but visible. The stiffness section is shown in Figure 4.16, the linearity is evident. Estimating the stiffness from the section gave a value of 10001.1. The damping section is shown in Figure 4.17 together with the seventh order curve-fit. The fitting procedure gave the following 7^{th} order model

$$f(y,\dot{y}) = 29.59\dot{y} + 268.48\dot{y}^3 - 568.21\dot{y}^5 + 578.83\dot{y}^7 + 10001.1y$$

One notices that the higher order terms are slightly different from those obtained from the multinomial model. This is because the higher order terms are less significant (in the sense that they contribute less to the variance of the model) and are estimated less accurately. One can see this immediately from the standard deviations shown in Table 4.2. Because their contributions are small over the range considered, the innaccurate parameters do little damage to the model comparison. However, if one were to predict responses outside this range one might find that the results were very innacurate. At the risk of being repetetive, this is why parameter estimation is input dependent.

The next system studied was the Van der Pol oscillator described by the equation

$$\ddot{y} - 0.2(1 - y^2)\dot{y} + y = x(t)$$

The multinomial model estimator gave parameters for a (2,1) model

	Exact	Estimated	% error
a_{01}	-0.2	-0.19996555	0.0173
a_{10}	1.0	0.99994242	0.0058
a_{21}	0.2	0.19999556	0.0023

all other coefficients were rejected as insignificant. The comparison between predicted and measured data is shown in Figure 4.18. The MSE for the comparison was $1.57\text{x}10^{-7}$. The three–neighbour version of the restoring force surface is shown in Figure 4.19. There are large areas where the sample points are very sparse, this produces a correspondingly small area of force surface, which also contains holes. If one transfers attention to the reduced data set shown in Figure 2.30 one can form

the two-neighbour version of the surface, this is shown in Figure 4.20. In this case the surface covers all the area. However, the surface is visibly less smooth in regions with less data. It is worth comparing this surface with the C^1 surface from the TILE package (Figure 2.33).

The stiffness and damping sections are shown in Figures 4.21 and 4.22 respectively. In each case the section is linear. This clearly shows that the sections are inadequate for the identification of nonlinear cross terms. Fitting linear models to the sections gave a linear stiffness of 1.0043 and a linear damping coefficient of −0.1992. The linear terms are therefore accurately estimated.

The next example is the piecewise linear system described by the equation,

$$\ddot{y} + 20\dot{y} + 10^4 y = x(t)$$

in the range $-0.001 \leq y \leq 0.001$. Outside this range the stiffness is a factor of 11 times greater. Again, this system can only be approximated by a polynomial model. A model of order (5,1) was estimated. The result was

$$f(y,\dot{y}) = 20.26\dot{y} - 1.363\times10^3 y + 2.248\times10^{11} y^3 + 1.387\times10^{12} y^4 - 1.809\times10^{16} y^5$$

In this case, the estimator has kept the y^4 term. The significance factor for the term was 0.162%. Another interesting point is that the linear term in the expansion has the wrong sign, this is neccessary for a good fit to the full nonlinear forces. One learns from this that the linearised equations of motion for a system cannot neccessarily be obtained from the nonlinear model by truncating the model above the $y\dot{y}$ term. This is a simple consequence of the fact that the terms $y^i\dot{y}^j$ do not form an orthonormal set. The comparison between predicted and actual data is shown in Figure 4.23. The MSE for the comparison was 1.26. The restoring force surface is shown in Figure 4.24. The piecewise linear nature of the surface is very clearly

shown. The stiffness section is shown in Figure 4.25 together with a 9^{th} order curve fit. The damping section is shown in Figure 4.26. The 9^{th} order model obtained from these sections is

$$\begin{aligned} f(y,\dot{y}) &= 19.99\dot{y} - 3.973\times10^{3}y + 2.870\times10^{4}y^{3} \\ &+ 2.529\times10^{10}y^{3} + 1.198\times10^{11}y^{4} - 2.50\times10^{15}y^{5} \\ &- 3.112\times10^{16}y^{6} + 2.771\times10^{19}y^{7} + 2.12\times10^{21}y^{8} \\ &+ 4.975\times10^{24}y^{9} \end{aligned}$$

All the stiffness coefficients are different from those of the multinomial model as the model order is different. The significance factors are not calculated for the section models. If they were, one would expect the even terms above to be deleted.

The penultimate example is the Coulomb friction system with equation of motion,

$$\ddot{y} + 20\dot{y} + 10\,\mathrm{sgn}(\dot{y}) + 10^{4}y = x(t)$$

This is the most difficult system to model with a polynomial as it is discontinous. A model of order (1,9) was fitted. The estimator retained thirteen terms. The coefficients are shown in table 4.3. Some of the significant terms are cross terms, this may be due to the fact that there is a vanishing probability that sample points should fall on the line of discontinuity in the phase plane. As no points are on the boundary, it's shape is not known. The estimator is free to reduce the squared errors by a small amount by fitting a function with an irregular boundary between the upper region and the lower region of the force surface. The comparison between predicted and measured data is shown in figure 4.27. The MSE for the comparison is 2.36, this shows the difficulty of approximating the system by a multinomial. The restoring force surface is shown in Figure 4.28, one can see that the boundary between the upper and lower surfaces is irregular.

The stiffness section is shown in Figure 4.29. The curve clearly jumps intermittently

between two levels. The explanation is simple. No matter how narrow a band is taken for the section points, because the centre of the band runs along the discontinuity,some points will be above the discontinuity and some will be below. The arrangement of upper and lower points will be random, giving the stiffness section observed. Figure 30 shows the damping section, the discontinuity appears very clearly in this graph also. The 9^{th} order polynomial curve fit is also shown. As expected, the fit is not very good.

The subject of the final example is the Bouc–Wen Hysteresis model represented by the equations,

$$\ddot{y} + 15.08\dot{y} + 5684.89y + z = x(t)$$

$$\dot{z} = 1000\dot{y} - 1.5|\dot{y}|.z.|z| + 1.5\dot{y}|z|^2$$

A linear model was fitted to the $(y,\dot{y},\ddot{y})$ data. The resulting model was

$$f(y,\dot{y}) = 17.63\dot{y} + 6727.3y$$

As with the Masri/Caughey procedure described in Chapter 2, the model includes an additional viscous damping term with coefficient (17.63 − 15.08) = 2.55. This allows the model linear system to dissipate energy at the same rate as the hysteretic system. Also, the stiffness coefficent includes the coefficient of the $\dot{y}$ term in the second equation. The effective linear stifness should be approximately 5684.89 + 1000.0 = 6684.89. The comparison between predicted and measured data is shown in Figure 4.31. The MSE for the comparison is 0.074, indicating an excellent fit. The force surface for this system is actually multi–valued. However, the size of the hysteresis loop is not very large so one obtains a nearly flat surface using Crawley and O'Donnell's method (Figure 4.32). The stiffness and damping sections also appear to be straight lines with a little noise superimposed (Figures 4.33 and 4.34). The linear damping and stiffness coefficients obtained from the sections were 17.34 and 6839.7 respectively.

The comparisons between measured and predicted data used in this section are between the measured RHS of (20) and the predicted RHS. A more stringent test is the one used in chapter 2, where the coefficient estimates were used to predict the displacement by integrating the estimated equations of motion. The estimated and measured displacements were then compared. In the examples above, the coefficients are obtained with five- to seven-figure accuracy, there is little point in carrying out such a comparison. The only situation where such small errors in the coefficients could cause large errors in the predicted output is if the system were chaotic. In this case, the output is unpredictable no matter how accurate the coefficients are.

4.8. Comparison with the Masri/Caughey Procedure.

It has been stated in Chapter 2 that the Chebyshev polynomial expansion is almost a minimax polynomial expansion i.e. the polynomial approximation which minimises the difference between a function and it's approximation over the approximating range. This sounds rather like the least-squares criterion. In fact the Masri/Caughey procedure is a least-squares estimator. This result is proved in Appendix B.

So the Masri/Caughey procedure and the least-squares method are seen to be equivalent in theory. In practice, it is obvious from a comparison between the results of the previous section and those of chapter 2 that the direct least-squares procedure is considerably more accurate. It remains to compare the time taken by the two methods. The system chosen for the comparison was the Van der Pol oscillator of the examples in section 7 above. The timings for the various routines given below do not include the time taken to read or write data, as whether one uses one large program to carry out the procedure or a number of smaller programs can simply be considered a matter of personal taste. The timings do not include inessential plotting times. The timings for the identifications were as follows

(i) Least-Squares.

The time taken to fit the least-squares coefficients to a (2,1) model in example (4) was 4.2 seconds. For a (4,2) model, the time was 16.1 seconds. This included the time for scaling the design matrix but not for carrying out the significance test. The orthogonal estimator was used.

(ii) Masri/Caughey.

In order to choose the reduced data set it was neccessary to plot all 10000 points of data, this took 142.4 seconds.

The next stage is the interpolation stage. The reduced data set contained 7913 points. The construction of the TILE C^1 surface (Figure 2.33) took 578.9 seconds. The construction of a TILE C^0 surface took 450.5 seconds. Finally, the construction of the Crawley/O'Donnell (CD) surface (Figure 4.20) took 3.0 seconds. These constructions are in decreasing order of accuracy.

The final stage is the calculation of the Chebyshev coefficients, each coefficient requiring a double integration over a 100x100 grid. The timings here were 43.8 seconds for a (2,1) model and 57.6 for a (4,2) model. The results are summarised in the following table.

Method	Time - (2,1)	Time - (4,2)
Least-squares	4.2	16.1
Masri/Caughey (C^1)	765.1	778.9
Masri/Caughey (C^0)	636.7	650.5
Masri/Caughey (CD)	189.2	203.0

This shows that the direct least-squares method is considerably faster than the

Masri/Caughey procedure. The only possible advantage remaining with the Masri/Caughey procedure is that the use of orthogonal polynomials means that one can truncate a given model and have the best model at that lower order without re-estimating coefficients. In fact, one has this option using the least-squares procedure also. Instead of using the multinomial basis functions shown in (20), one simply uses basis functions of the form

$$\theta_k(y,\dot{y},\ddot{y}) = T_i[\,\zeta(y)\,].T_j[\,\dot{\zeta}(\dot{y})\,]$$

where $k = nj + i + 1 < p$. As in Chapter 2, ζ and $\dot{\zeta}$ are the maps which carry data onto the region $[-1,1]x[-1,1]$. A least-squares estimation of a (2,1) model for the Van der Pol oscillator data using the Chebyshev basis above, gave the results

	Exact	Estimated	% error
a_{00}	0.28523213	0.28523210	$1.05x10^{-5}$
a_{01}	54.649864	54.649738	$2.31x10^{-4}$
a_{10}	7.3983140	7.3983040	$1.35x10^{-4}$
a_{11}	8.4603481	8.4603291	$2.24x10^{-4}$
a_{20}	0.089150546	0.089160604	$1.02x10^{-2}$
a_{21}	56.559067	56.558922	$2.56x10^{-4}$

The output form the program is shown in Table 4.4. The a_{20} term has a significance factor of only $6.34x10^{-5}$ so it is discarded. This means that the MSE for the comparison between predicted and measured data jumps from $3.4x10^{-10}$ to $6.34x10^{-5}$. The comparison is shown in Figure 4.35. The time for the identification of a (4,2) model was 18.6 seconds, this is higher than the time of 16.1 seconds for an ordinary model because the Chebyshev polynomials have to be evaluated to form the design matrix. This means that by direct least-squares methods one can carry out the Masri/Caughey expansions in a small fraction of the time required by an interpolation based method.

One concludes that direct least–squares methods are faster, more accurate and require less storage than the Masri/Caughey procedure. In addition, they allow one to determine the standard deviations for the parameters which in turn allow one to construct confidence limits.

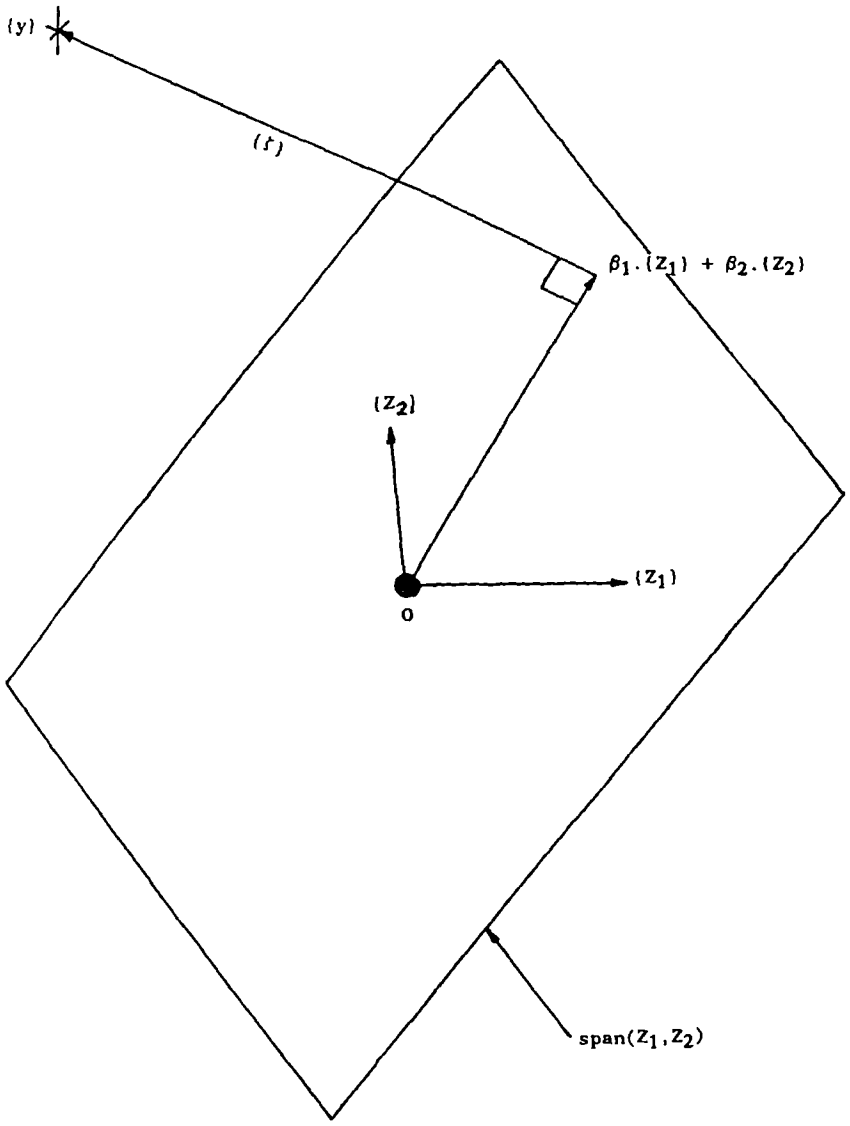

$$(y) = \beta_1.(Z_1) + \beta_2.(Z_2) + (\varepsilon)$$

Figure 4.1. The geometrical interpretation of least-squares estimation.

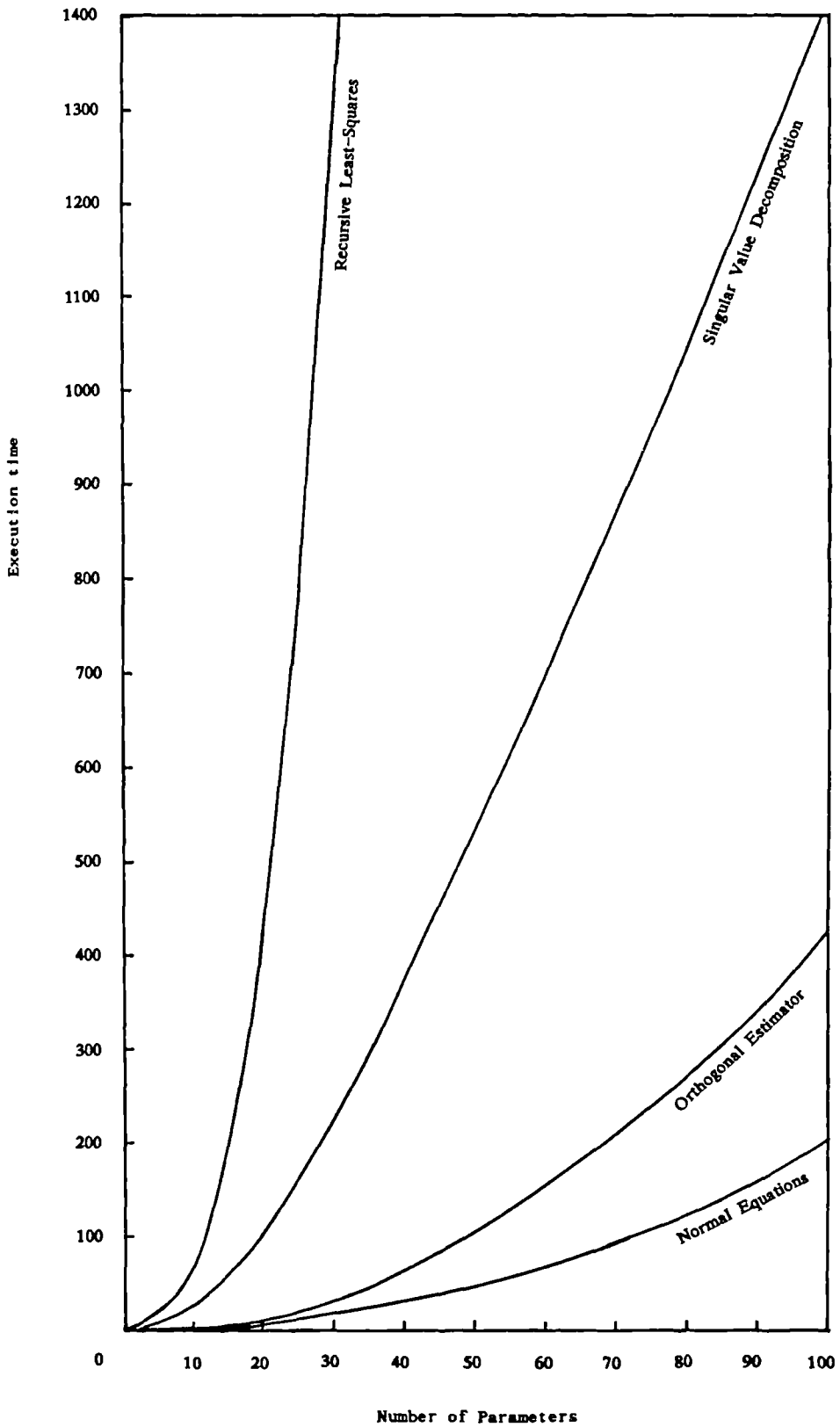

Figure 4.2. Comparison of the least-squares methods described in the text.

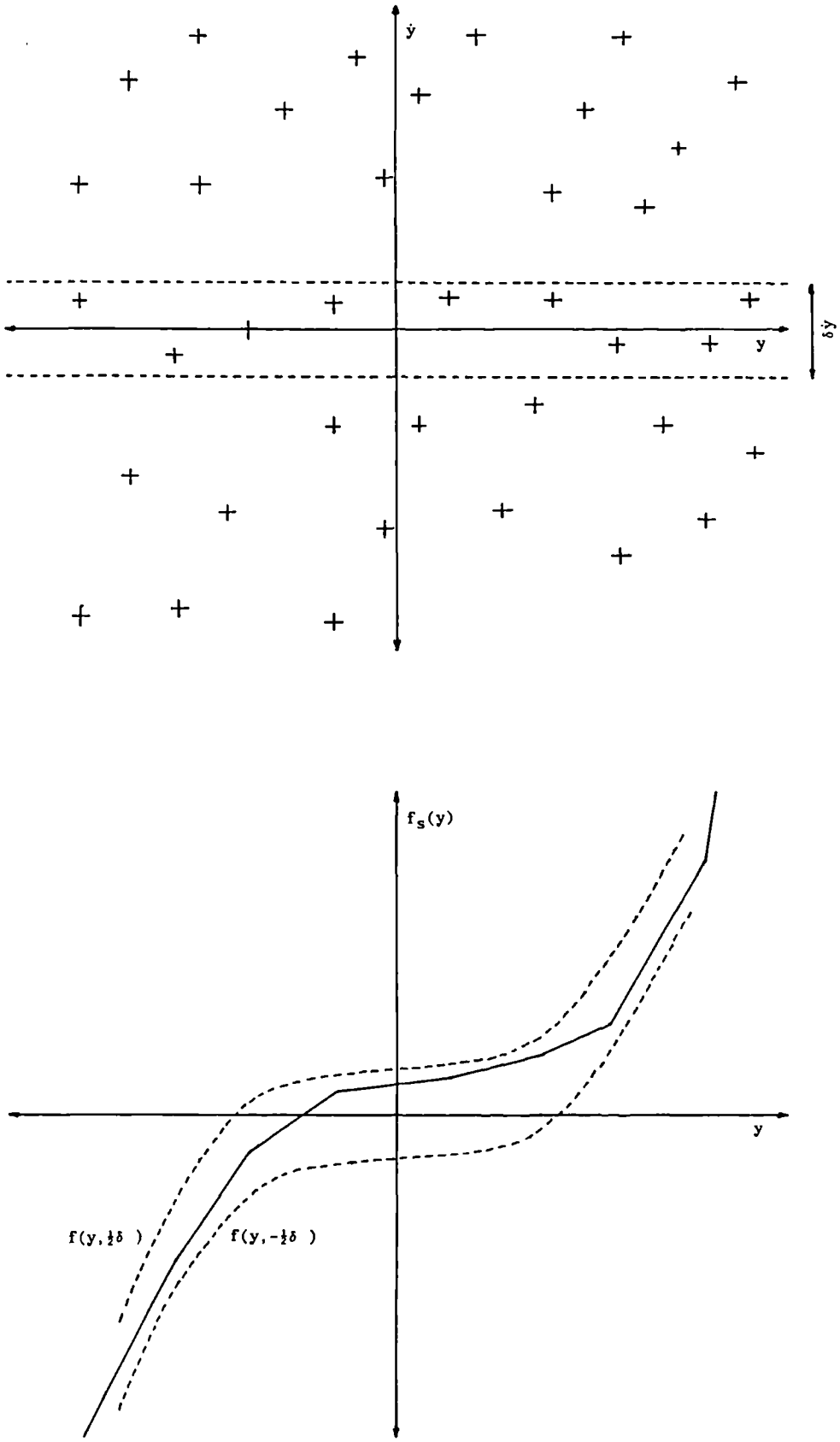

Figure 4.3. Formation of the stiffness section.

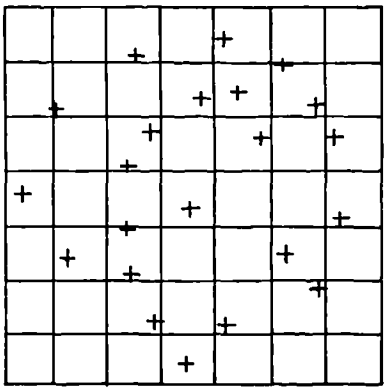

Initial data

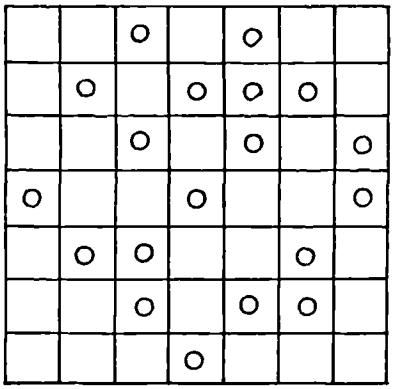

(1)

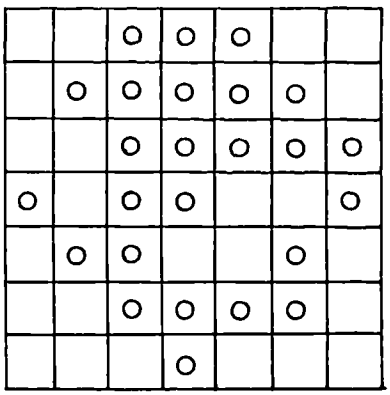

(2)

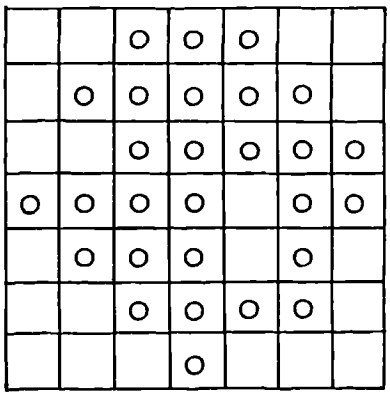

(3)

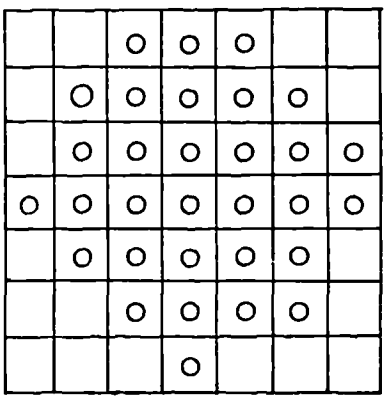

(4)

+ Initial data point

O Averaged data point

Figure 4.4. Formation of the Crawley/O'Donnell surface.

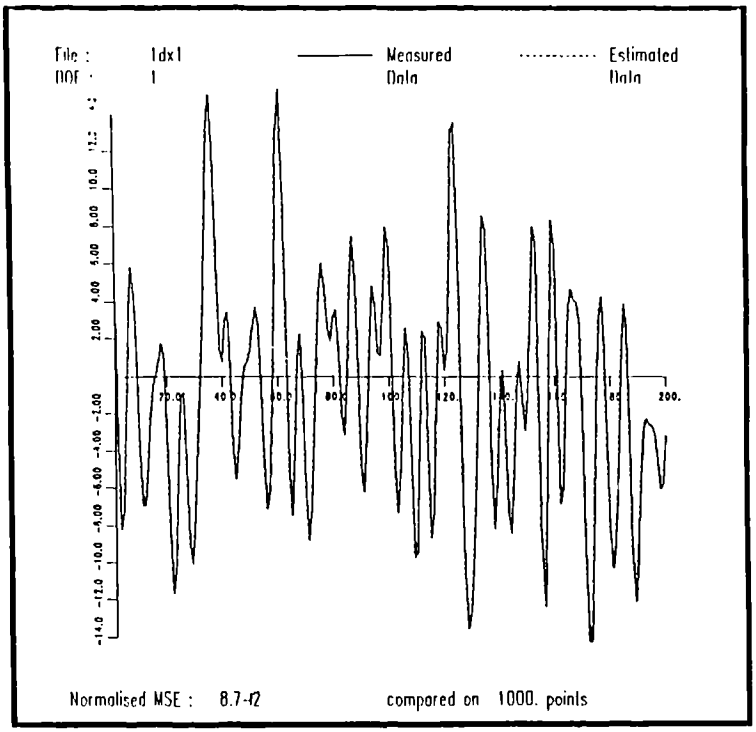

Figure 4.5. Comparison of the true time data and that predicted by the least-squares model for the linear system described in the text.

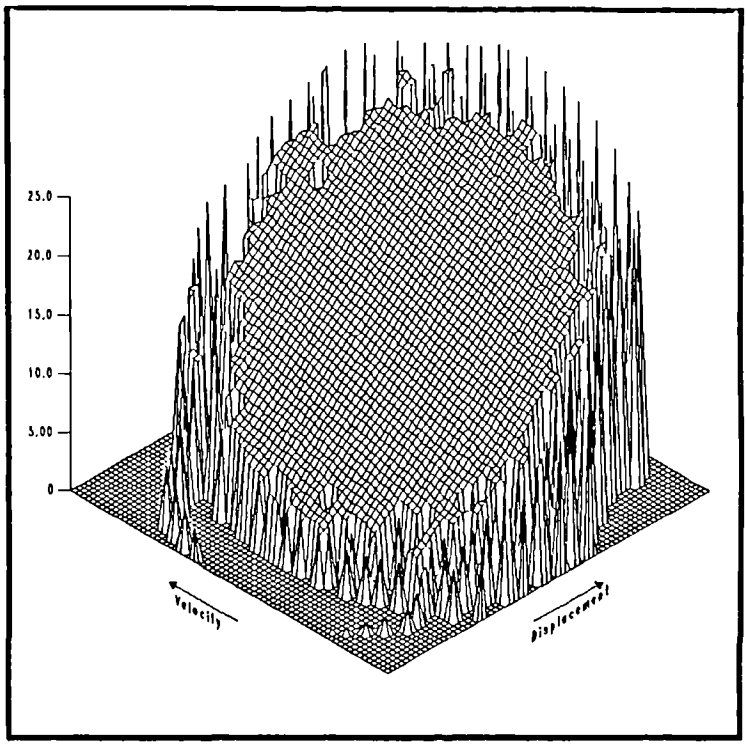

Figure 4.6. Restoring force surface (Crawley/O'Donnell type) for the linear system.

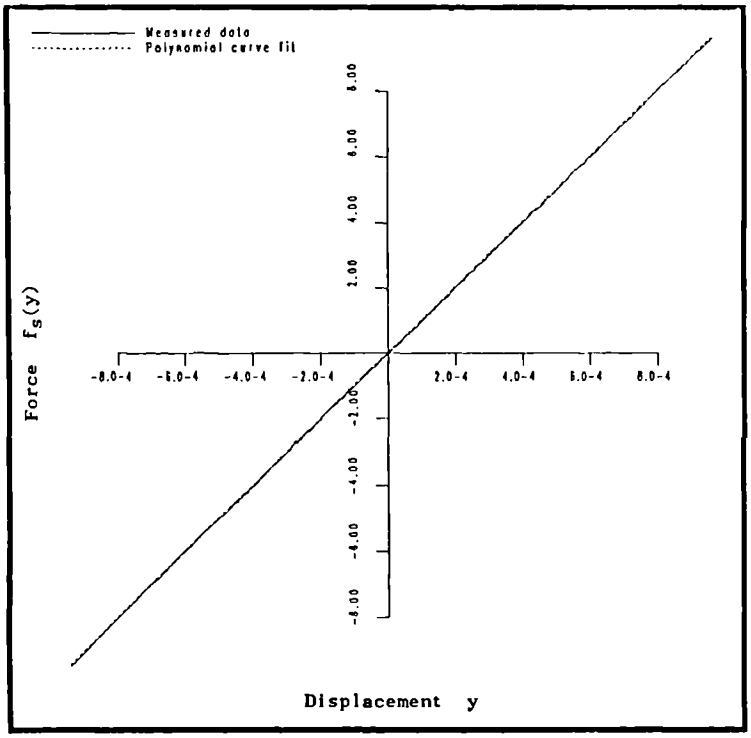

Figure 4.7. Stiffness section for the linear system.

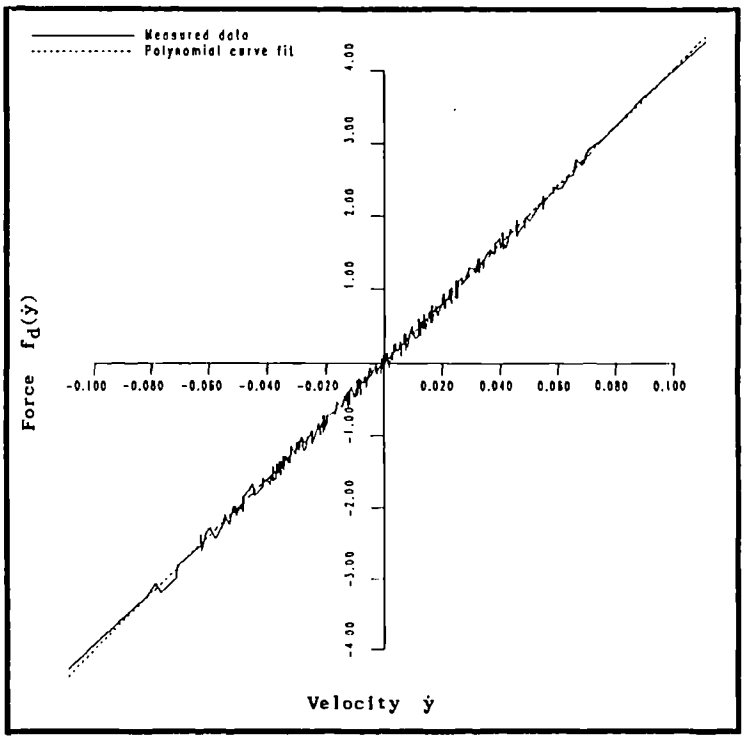

Figure 4.8. Damping section for the linear system.

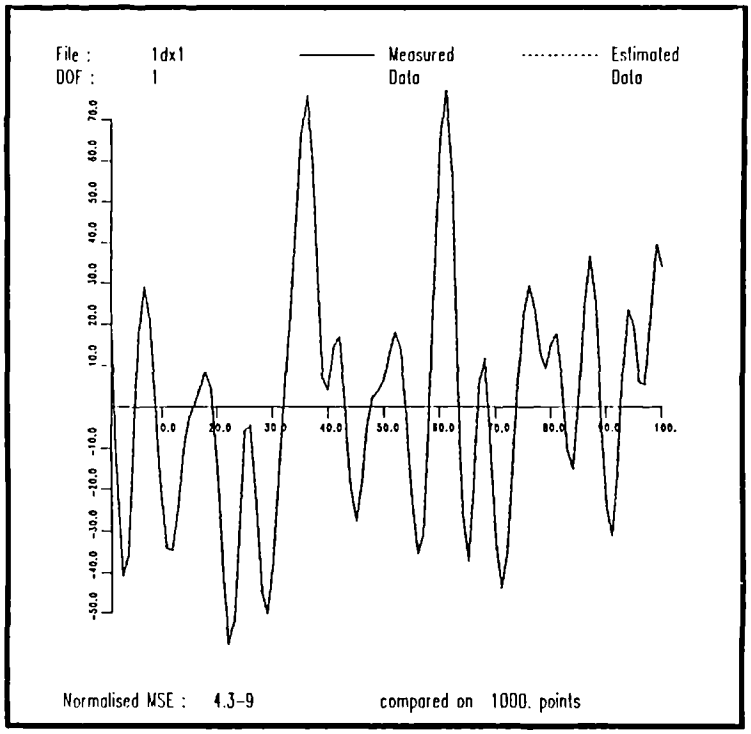

Figure 4.9. Comparison of the true and predicted data for the cubic stiffness system.

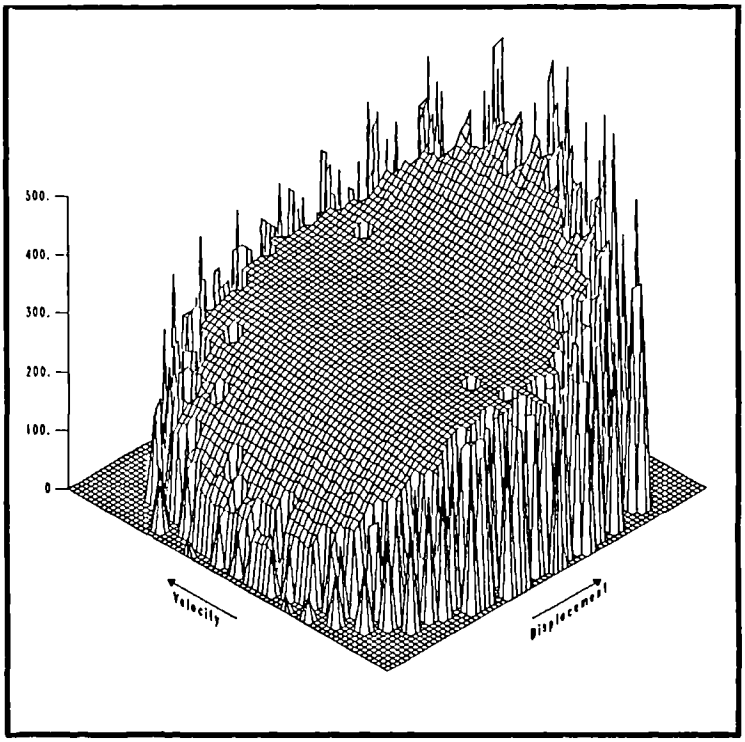

Figure 4.10. Restoring force surface for the cubic stiffness system.

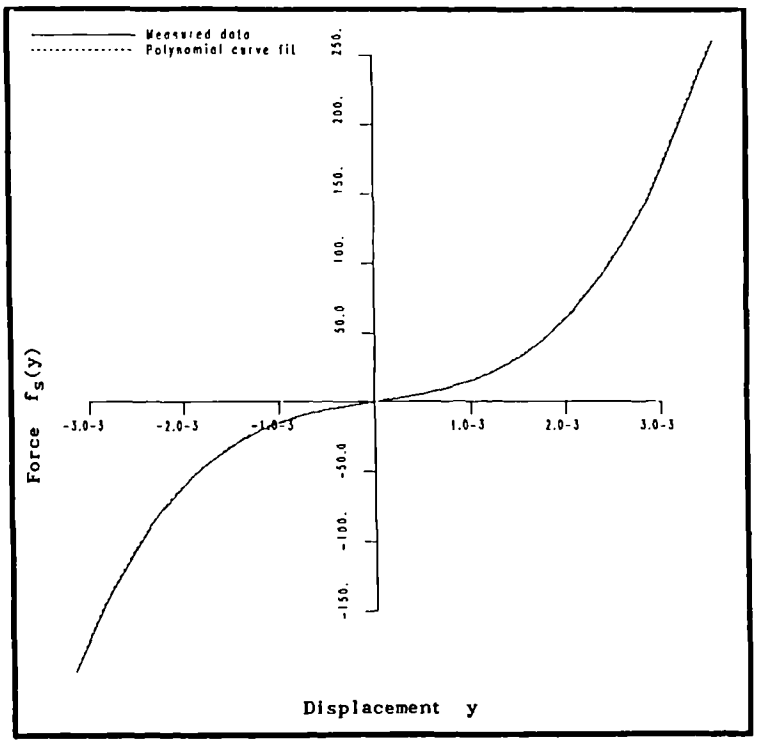

Figure 4.11. Stiffness section for the cubic stiffness system.

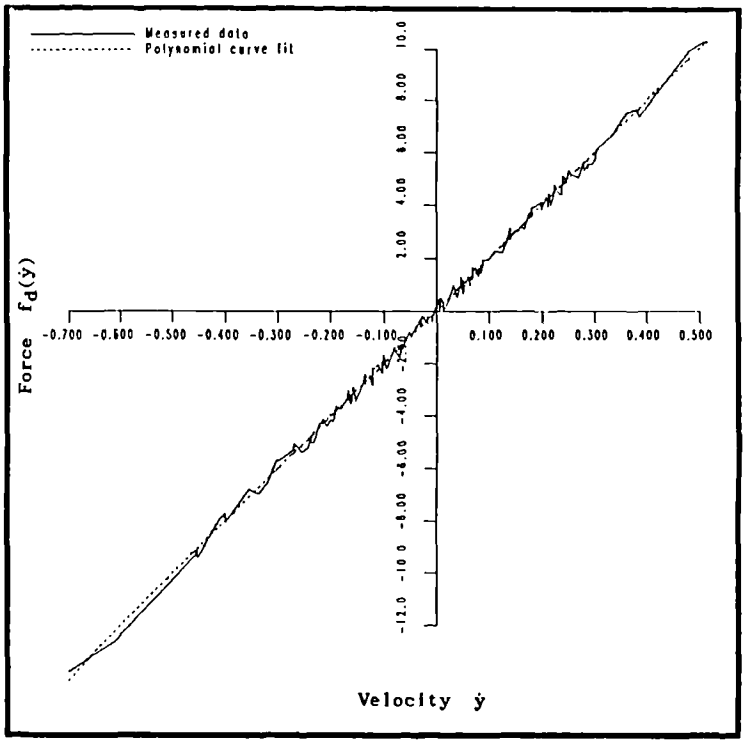

Figure 4.12. Damping section for the cubic stiffness system.

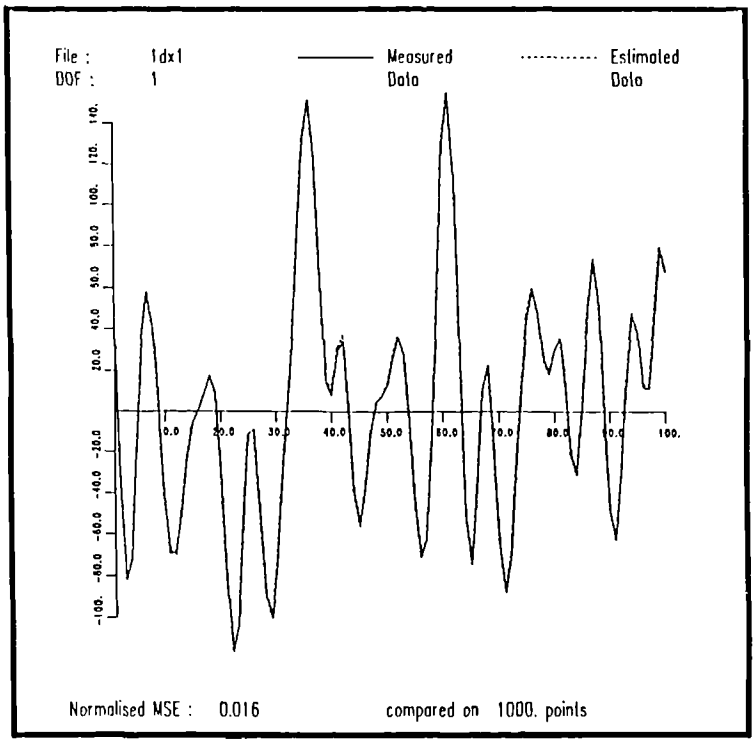

Figure 4.13. Comparison of the true data and that predicted by a (1,3) polynomial model for the system with quadratic damping described in the text.

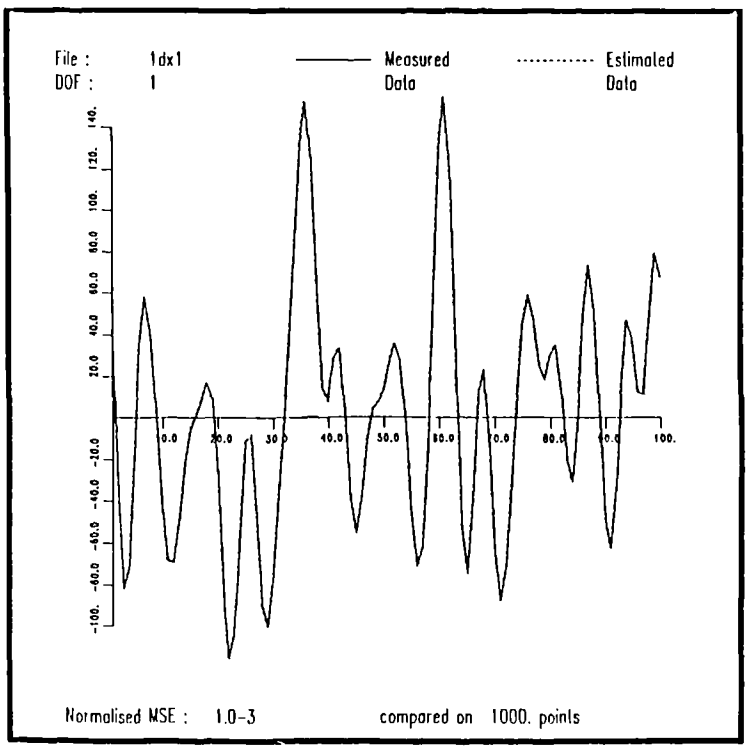

Figure 4.14. Comparison of the true data and that predicted by a (1,7) polynomial model for the quadratic damping system.

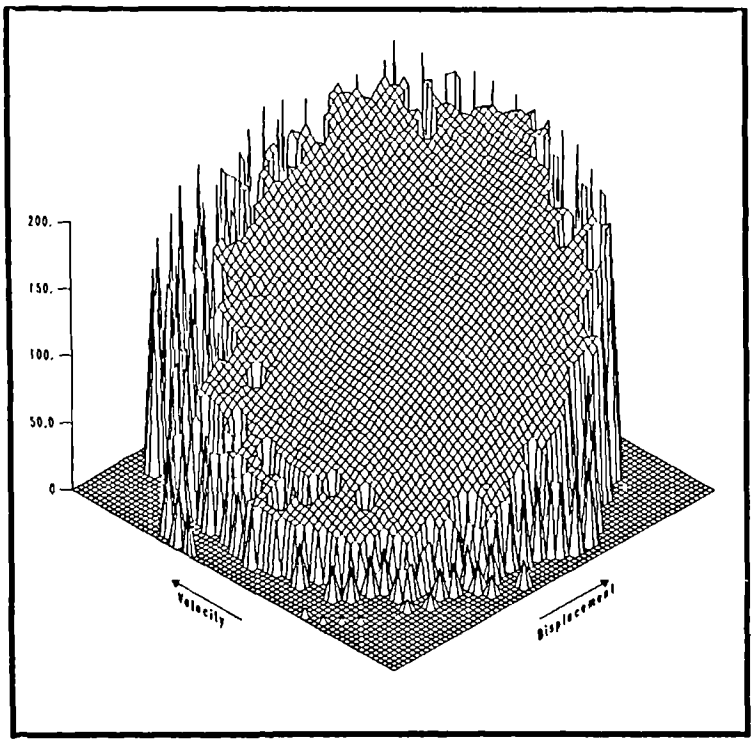

Figure 4.15. Restoring force surface for the quadratic damping system.

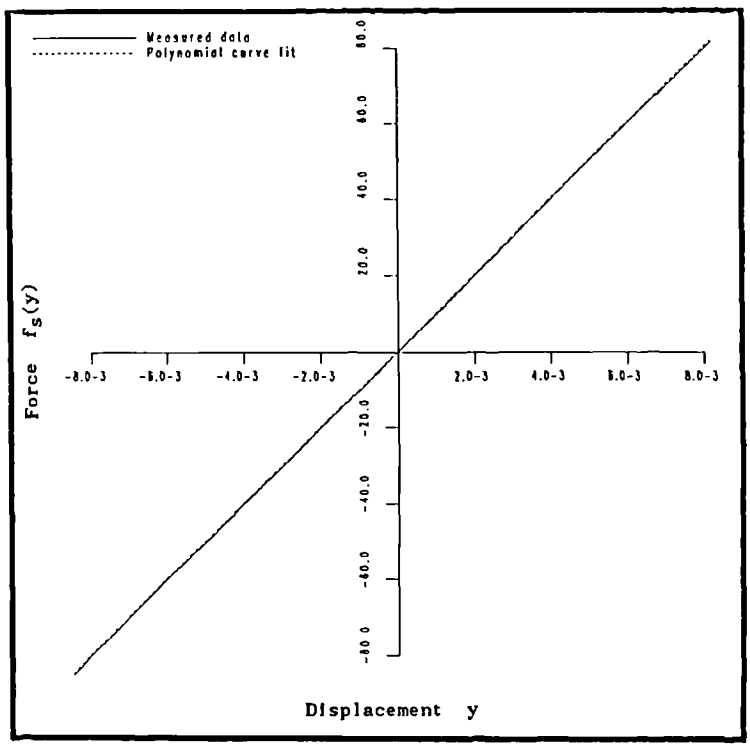

Figure 4.16. Stiffness section for the quadratic damping system.

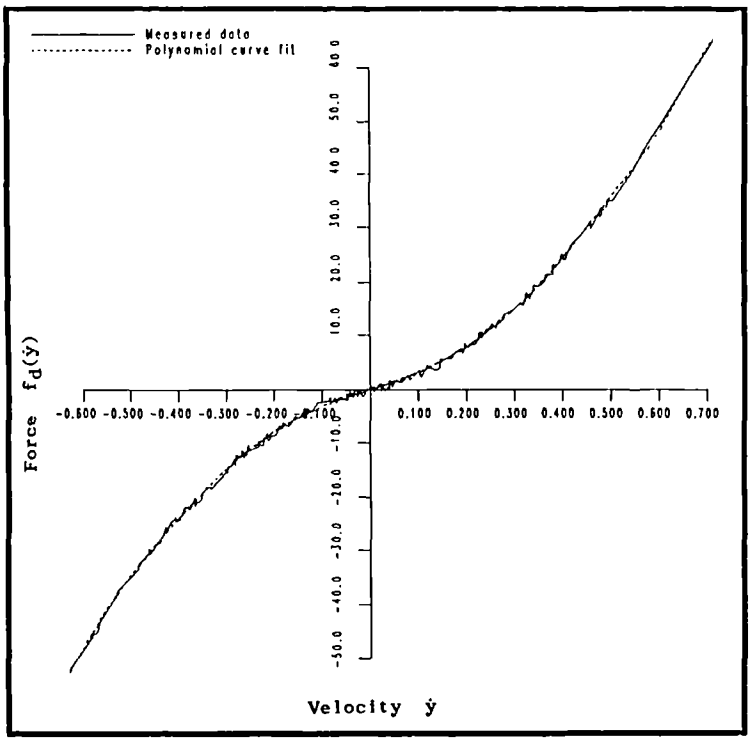

Figure 4.17. Damping section for the quadratic damping system.

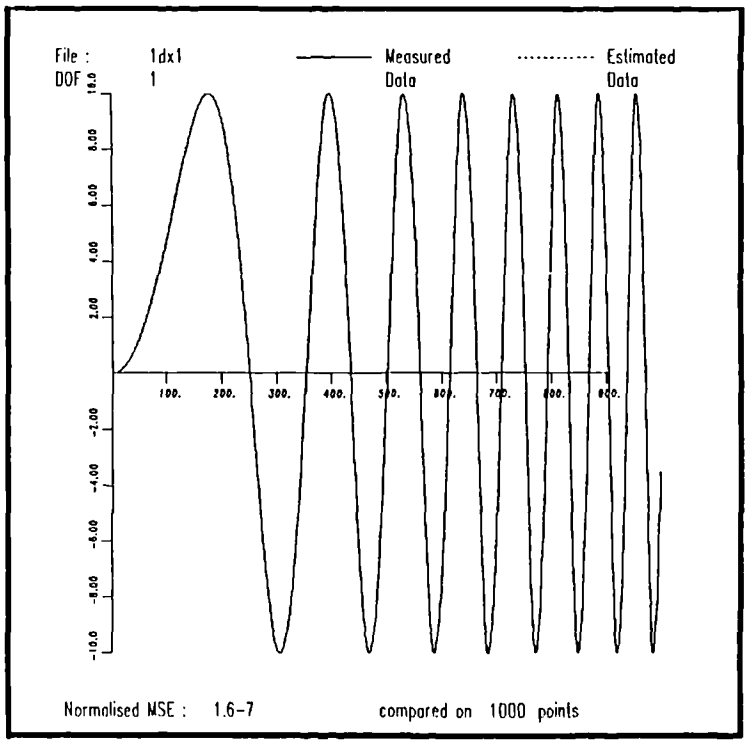

Figure 4.18. Comparison of the true and predicted data for the Van der Pol oscillator system described in the text.

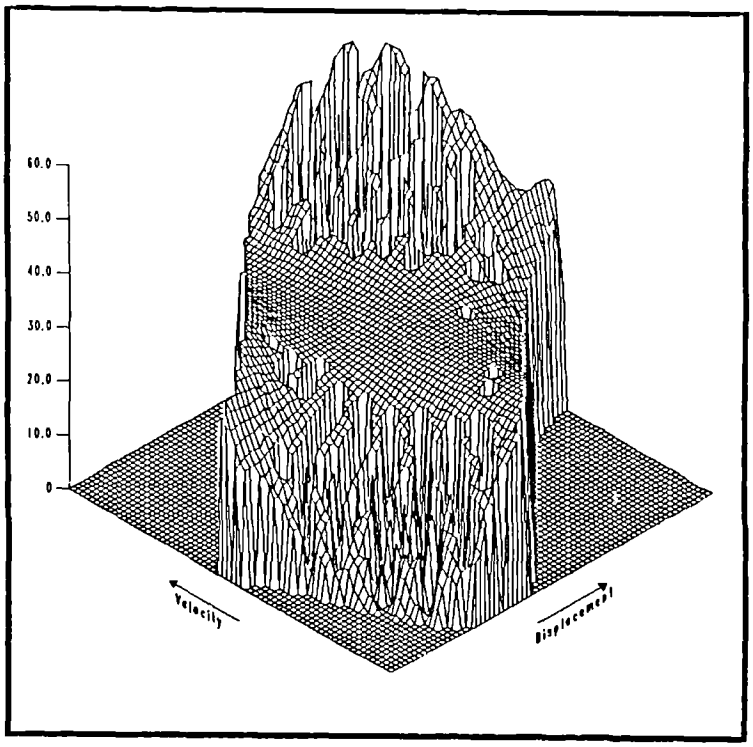

Figure 4.19. Restoring force surface for the Van der Pol oscillator system - obtained using three-neighbour averaging.

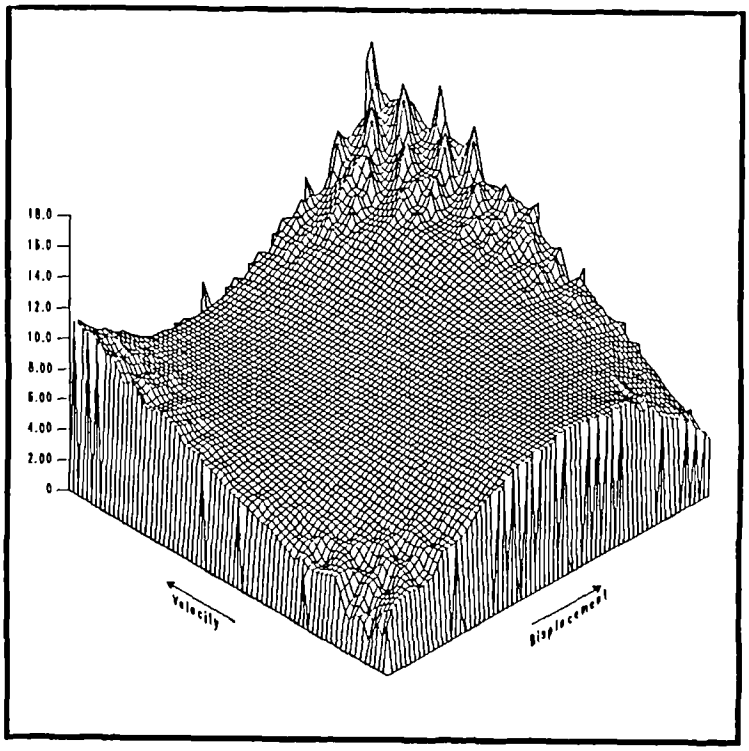

Figure 4.20. Restoring force surface for the Van der Pol oscillator system - obtained using two-neighbour averaging.

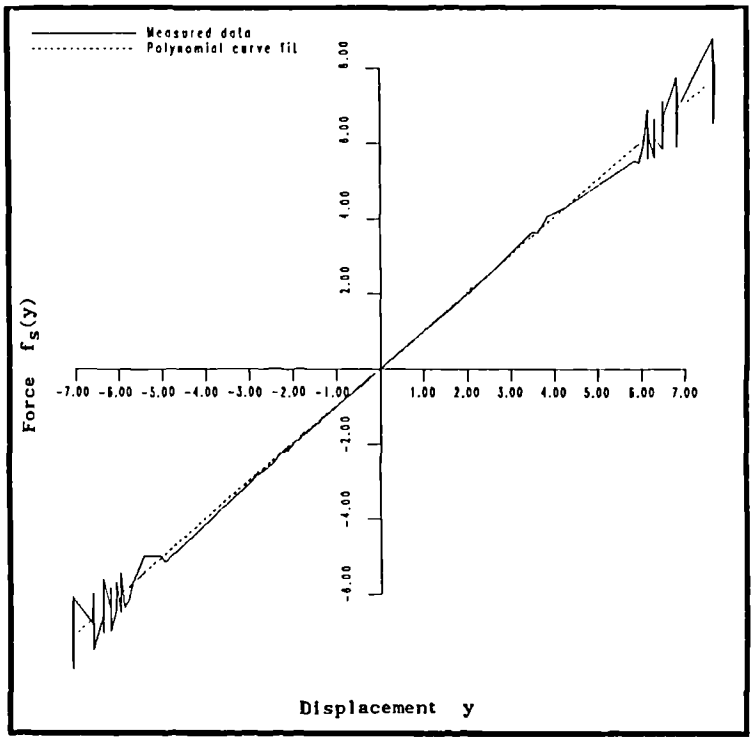

Figure 4.21. Stiffness section for the Van der Pol oscillator.

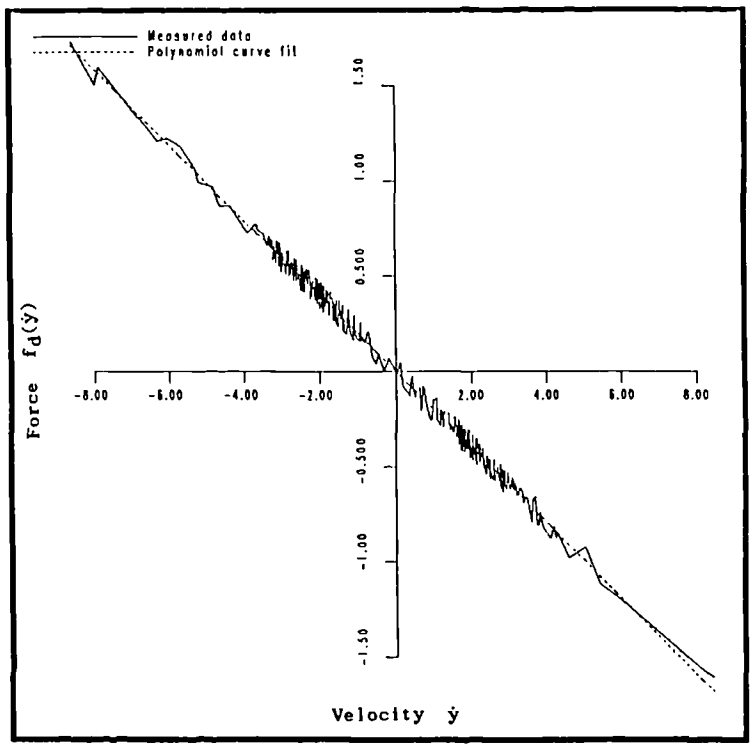

Figure 4.22. Damping section for the Van der Pol oscillator.

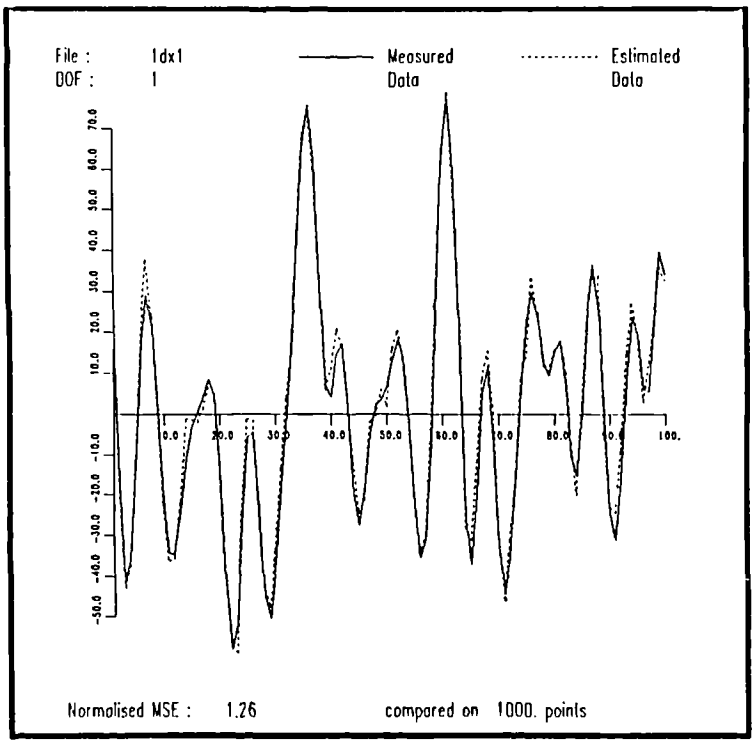

Figure 4.23. Comparison of the true and predicted data for the piecewise-linear system described in the text.

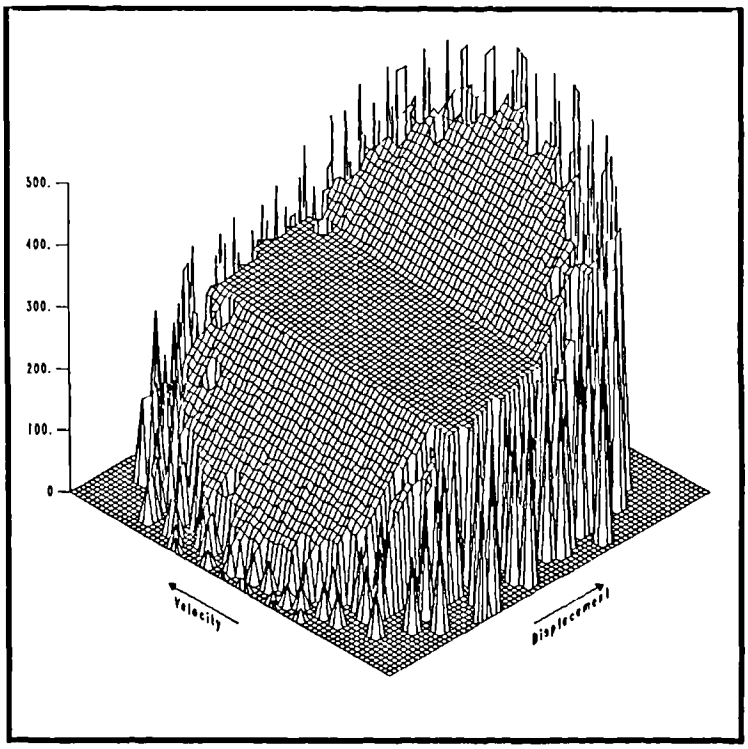

Figure 4.24. Restoring force surface for the piecewise-linear system.

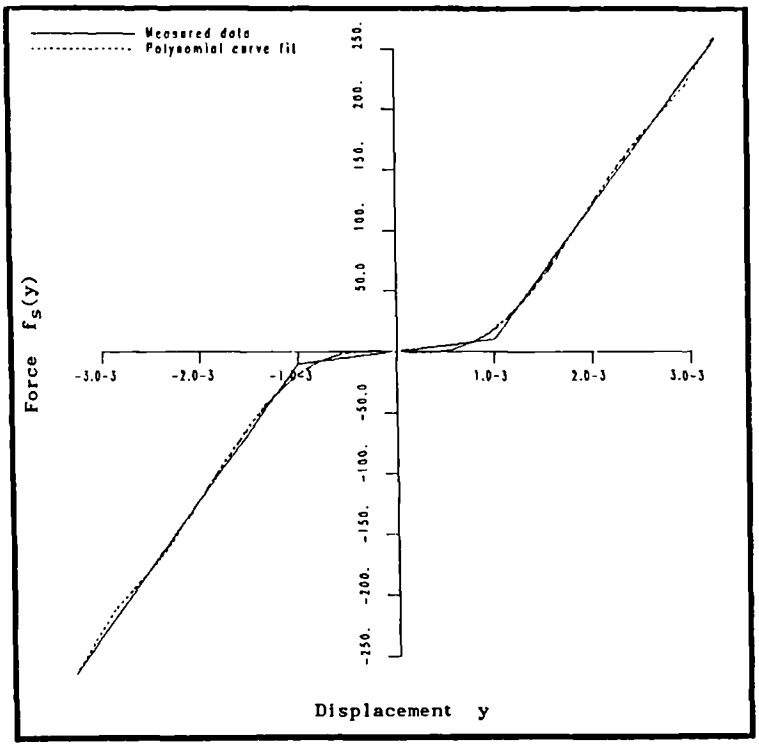

Figure 4.25. Stiffness section for the piecewise-linear system.

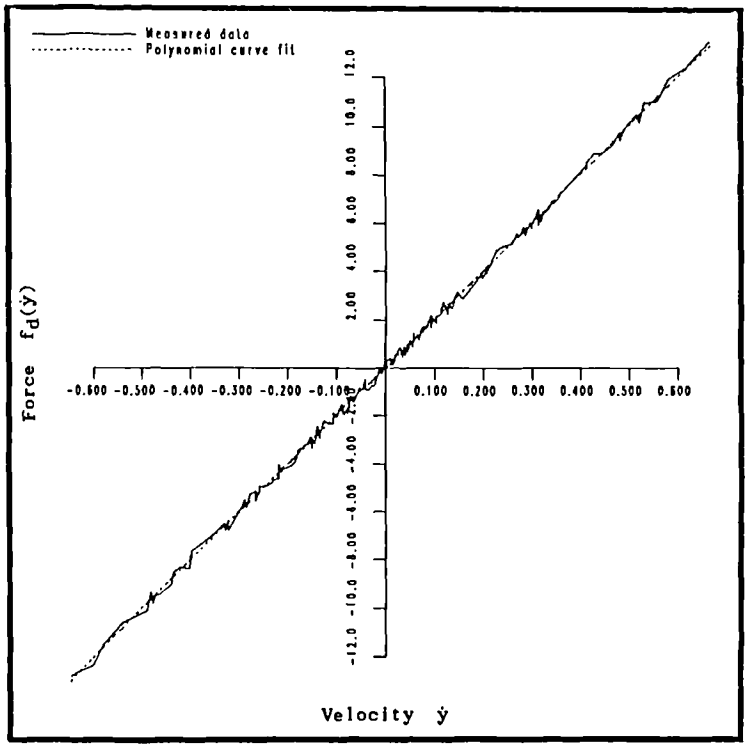

Figure 4.26. Damping section for the piecewise-linear system.

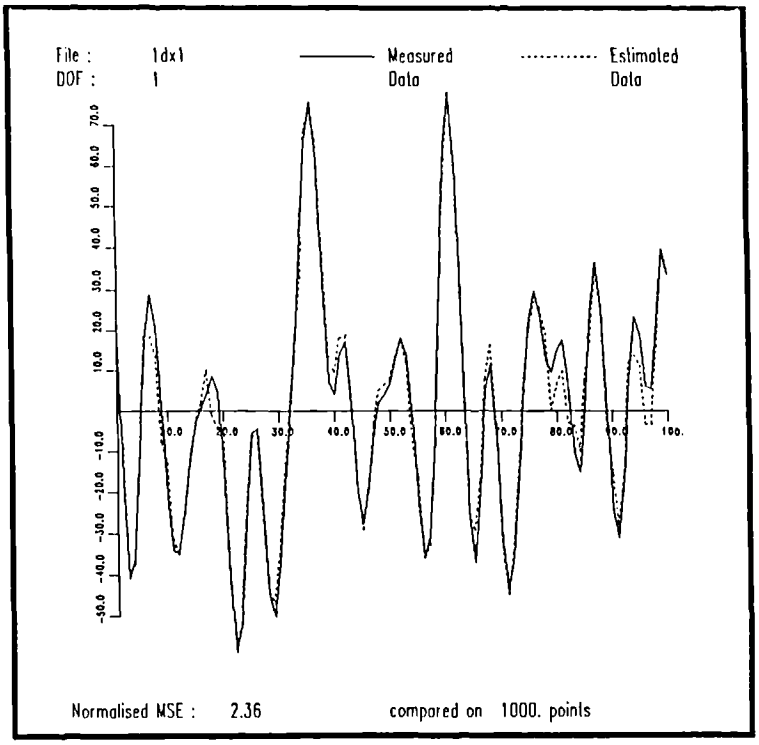

Figure 4.27. Comparison of the true and predicted data for the model of the Coulomb friction system described in the text.

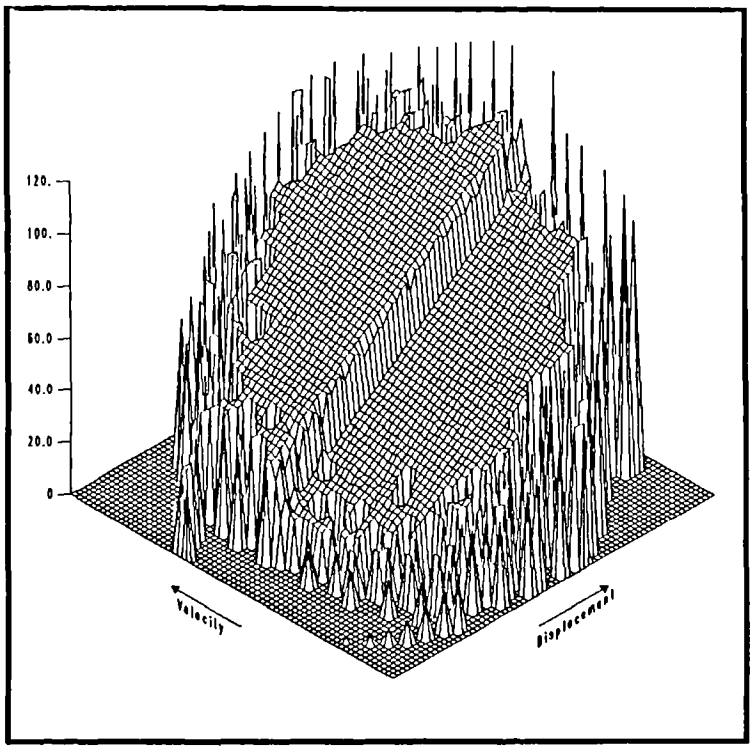

Figure 4.28. Restoring force surface for the Coulomb friction system.

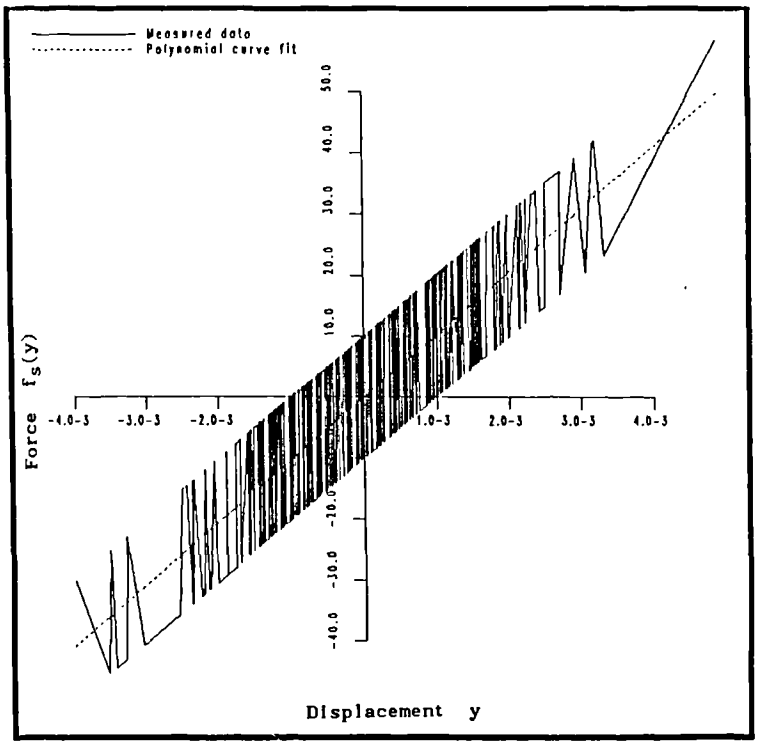

Figure 4.29. Stiffness section for the Coulomb friction system.

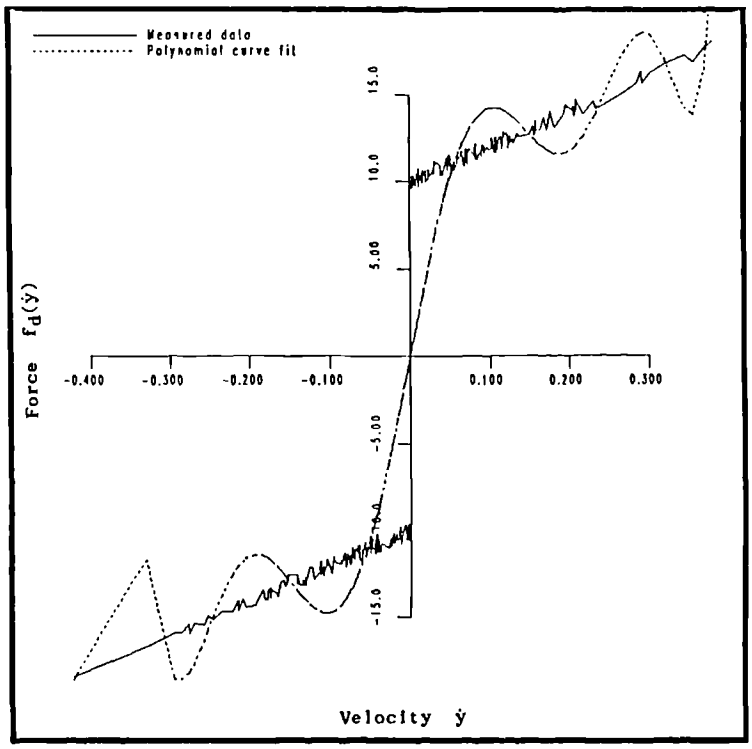

Figure 4.30. Damping section for the Coulomb friction system.

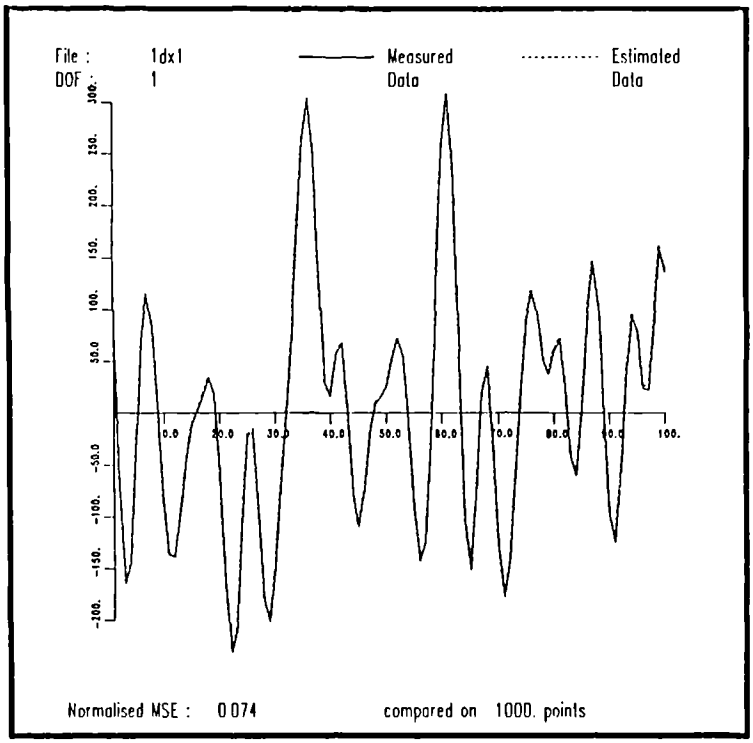

Figure 4.31. Comparison between true and predicted data for the hysteretic system described in the text.

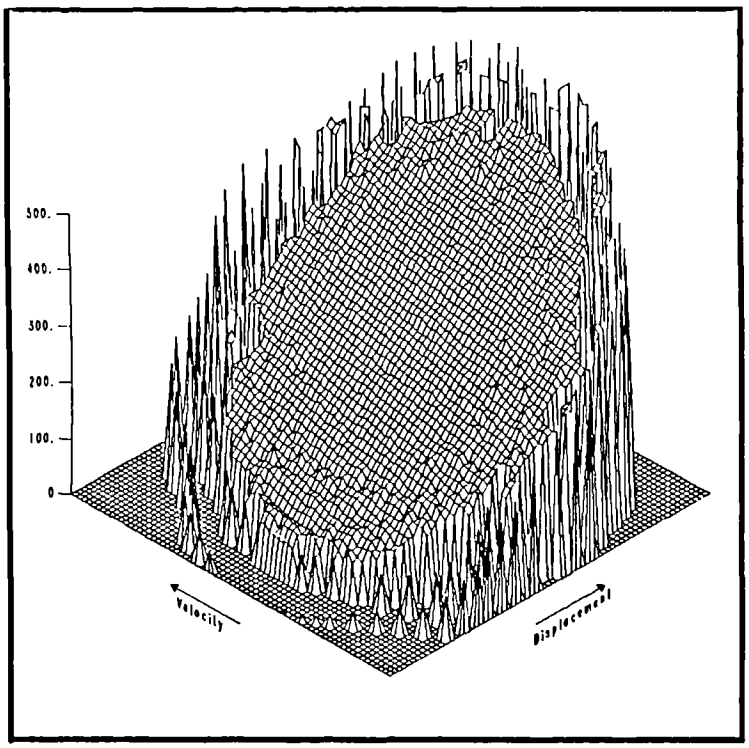

Figure 4.32. Restoring force surface for the hysteretic system.

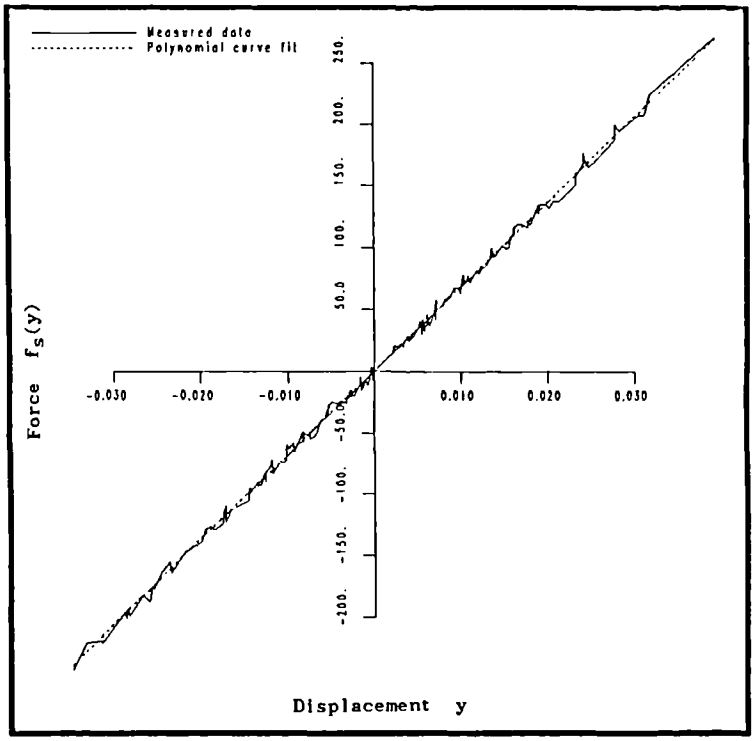

Figure 4.33. Stiffness section for the hysteretic system.

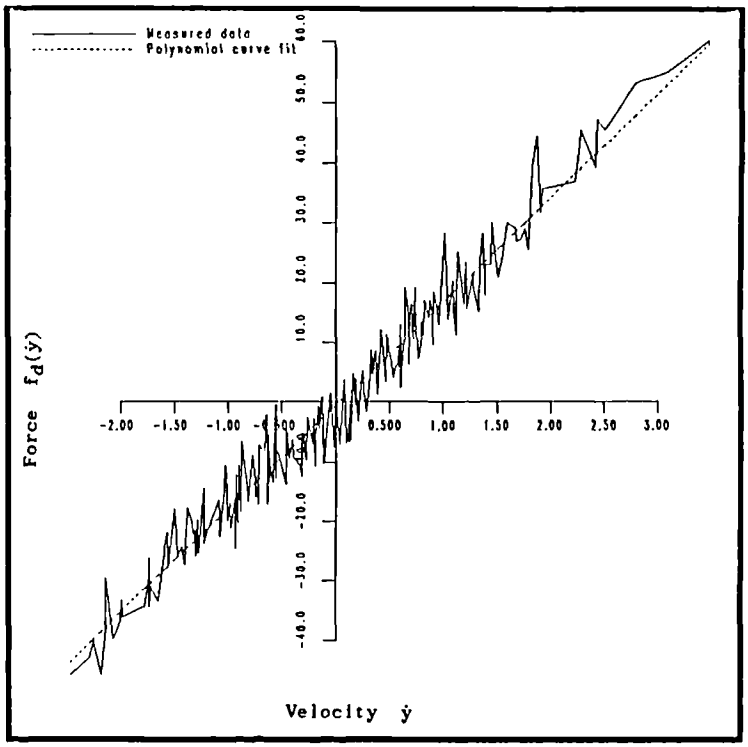

Figure 4.34. Damping section for the hysteretic system.

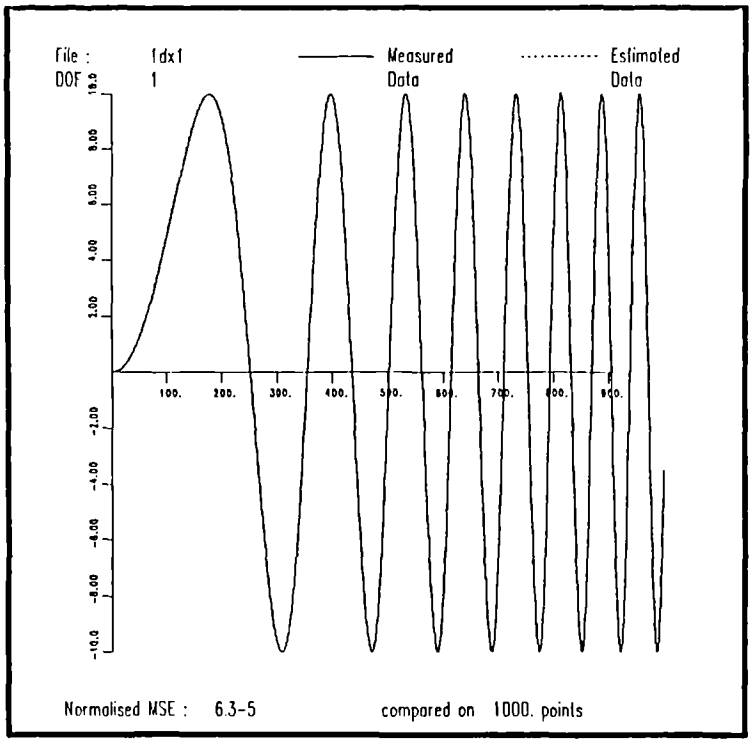

Figure 4.35. Comparison between true data and that predicted by a (2,1) Chebyshev model for the Van der Pol oscillator.

```
* Coefficients for system : 1dx1

* Mass corrected to :  0.99999970e+00

  a( 0: 0)  0.43617779e-05   s( 0: 0)  0.21968820e-11
  a( 0: 1)  0.20000023e+02   s( 0: 1)  0.18655244e+01
  a( 1: 0)  0.10000087e+05   s( 1: 0)  0.17571732e+02
  a( 1: 1)  0.92633357e-02   s( 1: 1)  0.57367706e-12
  a( 2: 0)  0.36072439e+00   s( 2: 0)  0.79792726e-13
  a( 2: 1) -0.56263989e+00   s( 2: 1)  0.67925164e-14
  a( 3: 0)  0.49999754e+10   s( 3: 0)  0.72433151e+02
  a( 3: 1) -0.40317437e+04   s( 3: 1)  0.14980104e-11

* MSE estimate :  0.43272896e-09

* Significant coefficients

  a( 0: 1)  0.20000023e+02   std( 0: 1)  0.35255912e-03
  a( 1: 0)  0.10000087e+05   std( 1: 0)  0.57437547e-01
  a( 3: 0)  0.49999754e+10   std( 3: 0)  0.27717064e+05

* MSE estimate :  0.43342663e-09
```

Table 4.1. Estimated coefficients for a (3,1) polynomial model of the cubic stiffness system described in the text.

```
* Coefficients for system : 1dx1

* Mass corrected to :  0.99991637e+00

  a( 0: 0)  0.24037039e-01   s( 0: 0)  0.16679791e-04
  a( 0: 1)  0.29412050e+02   s( 0: 1)  0.17427596e+01
  a( 0: 2) -0.12774162e+01   s( 0: 2)  0.55800012e-03
  a( 0: 3)  0.27455914e+03   s( 0: 3)  0.62679195e+01
  a( 0: 4)  0.10854147e+02   s( 0: 4)  0.28706761e-02
  a( 0: 5) -0.60985010e+03   s( 0: 5)  0.29701328e+01
  a( 0: 6) -0.19111641e+02   s( 0: 6)  0.10307526e-02
  a( 0: 7)  0.65142474e+03   s( 0: 7)  0.44714123e+00
  a( 1: 0)  0.99860488e+04   s( 1: 0)  0.23137569e+02
  a( 1: 1) -0.11353043e+03   s( 1: 1)  0.19622619e-03
  a( 1: 2)  0.70319342e+03   s( 1: 2)  0.12500623e-02
  a( 1: 3)  0.29199675e+04   s( 1: 3)  0.51421141e-02
  a( 1: 4) -0.63556406e+04   s( 1: 4)  0.69075800e-02
  a( 1: 5) -0.18138193e+05   s( 1: 5)  0.17629625e-01
  a( 1: 6)  0.13825540e+05   s( 1: 6)  0.34382432e-02
  a( 1: 7)  0.30354666e+05   s( 1: 7)  0.58674603e-02

* MSE estimate :  0.79055439e-03

* Significant coefficients

  a( 0: 1)  0.29412050e+02   std( 0: 1)  0.73777968e+00
  a( 0: 3)  0.27455914e+03   std( 0: 3)  0.68447094e+01
  a( 0: 5) -0.60985010e+03   std( 0: 5)  0.57249924e+02
  a( 0: 7)  0.65142474e+03   std( 0: 7)  0.45474176e+03
  a( 1: 0)  0.99860488e+04   std( 1: 0)  0.69543221e+02

* MSE estimate :  0.10429000e-02
```

Table 4.2. Estimated Coefficients for a (1,7) model of the quadratic damping system.

```
* Coefficients for system : 1dx1

* Mass corrected to :  0.98047501e+00

  a( 0: 0) -0.65301888e-01   s( 0: 0)  0.50295412e-03
  a( 0: 1)  0.28116757e+03   s( 0: 1)  0.96496445e+02
  a( 0: 2)  0.75559364e+02   s( 0: 2)  0.24832259e+00
  a( 0: 3) -0.20762311e+05   s( 0: 3)  0.10027693e+04
  a( 0: 4) -0.64575498e+04   s( 0: 4)  0.62161818e+01
  a( 0: 5)  0.71290763e+06   s( 0: 5)  0.53352134e+04
  a( 0: 6)  0.15397697e+06   s( 0: 6)  0.18538443e+02
  a( 0: 7) -0.10004910e+08   s( 0: 7)  0.60512568e+04
  a( 0: 8) -0.10601463e+07   s( 0: 8)  0.53967700e+01
  a( 0: 9)  0.48427836e+08   s( 0: 9)  0.91339111e+03
  a( 1: 0)  0.95422061e+04   s( 1: 0)  0.13305131e+02
  a( 1: 1)  0.43732571e+03   s( 1: 1)  0.28821416e-03
  a( 1: 2)  0.33637652e+05   s( 1: 2)  0.57677846e-01
  a( 1: 3) -0.82371805e+05   s( 1: 3)  0.17033761e-01
  a( 1: 4) -0.83454031e+06   s( 1: 4)  0.10359116e+00
  a( 1: 5)  0.45943735e+07   s( 1: 5)  0.20644416e+00
  a( 1: 6) -0.25091713e+07   s( 1: 6)  0.43137949e-02
  a( 1: 7) -0.89147256e+08   s( 1: 7)  0.39755771e+00
  a( 1: 8)  0.14510166e+09   s( 1: 8)  0.79146318e-01
  a( 1: 9)  0.51725258e+09   s( 1: 9)  0.77216752e-01

* MSE estimate :  0.20930667e+01

* Significant coefficients

  a( 0: 1)  0.28116757e+03   std( 0: 1)  0.22552971e+02
  a( 0: 2)  0.75559364e+02   std( 0: 2)  0.14467059e+03
  a( 0: 3) -0.20762311e+05   std( 0: 3)  0.95478790e+03
  a( 0: 4) -0.64575498e+04   std( 0: 4)  0.60802617e+04
  a( 0: 5)  0.71290763e+06   std( 0: 5)  0.39359293e+05
  a( 0: 6)  0.15397697e+06   std( 0: 6)  0.24977689e+06
  a( 0: 7) -0.10004910e+08   std( 0: 7)  0.16422676e+07
  a( 0: 8) -0.10601463e+07   std( 0: 8)  0.10415498e+08
  a( 0: 9)  0.48427836e+08   std( 0: 9)  0.69202528e+08
  a( 1: 0)  0.95422061e+04   std( 1: 0)  0.20747168e+04
  a( 1: 4) -0.83454031e+06   std( 1: 4)  0.72095570e+07
  a( 1: 5)  0.45943735e+07   std( 1: 5)  0.50818284e+08
  a( 1: 7) -0.89147256e+08   std( 1: 7)  0.23363046e+10

* MSE estimate :  0.23589919e+01
```

Table 4.3. Estimated coefficients for a (9,1) polynomial model of the piecewise-linear system.

```
* Coefficients for system : 1dx1

* Estimation type : Orthogonal

* Expansion type : Chebyshev Polynomial

* Mass corrected to :  0.99999714e+00

  a( 0: 0)  0.28523210e+00   s( 0: 0)  0.17547554e+00
  a( 0: 1)  0.54649738e+02   s( 0: 1)  0.65526538e+03
  a( 1: 0)  0.73983040e+01   s( 1: 0)  0.57717682e+02
  a( 1: 1)  0.84603291e+01   s( 1: 1)  0.23627956e+01
  a( 2: 0)  0.89160604e-02   s( 2: 0)  0.63406005e-04
  a( 2: 1)  0.56558922e+02   s( 2: 1)  0.41422495e+03

* MSE estimate :  0.33951142e-09

* Significant coefficients

  a( 0: 0)  0.28523210e+00   std( 0: 0)  0.64307824e-03
  a( 0: 1)  0.54649738e+02   std( 0: 1)  0.20166186e-02
  a( 1: 0)  0.73983040e+01   std( 1: 0)  0.92672562e-03
  a( 1: 1)  0.84603291e+01   std( 1: 1)  0.52307085e-02
  a( 2: 1)  0.56558922e+02   std( 2: 1)  0.64338590e-02

* MSE estimate :  0.63409760e-04
```

Table 4.4 Estimated coefficients for a (2, 1) Chebyshev model for the Van der Pol oscillator system.

CHAPTER 5

LEAST-SQUARES PARAMETER ESTIMATION - MDOF SYSTEMS

5.1. Transmissibility.

Before proceeding to the study of MDOF systems proper, it is useful to describe the relative acceleration or transmissibility approach to identification. Under certain circumstances one can reduce a MDOF problem to an SDOF-like problem by adopting this approach. Consider a mass m attached to a system by a single elastic link as in Figure 5.1. The acceleration of the mass m is $\ddot{y}_m$ and the acceleration of the point of attachment to the system is $\ddot{y}_b$. If one forms the relative acceleration $\ddot{\delta}$ = $\ddot{y}_m$ - $\ddot{y}_b$, one can write the equation of motion for the mass m in the following forms.

$$m\ddot{y}_m + c(\dot{y}_m - \dot{y}_b) + k(y_m - y_b) = 0 \qquad (1a)$$

$$m\ddot{y}_m + c\dot{\delta} + k\delta = 0 \qquad (1b)$$

$$m\ddot{\delta} + c\dot{\delta} + k\delta = -m\ddot{y}_b \qquad (1c)$$

where δ is the relative displacement etc. It is equation (1b) which is of greatest interest here. If $\ddot{y}_m$ and $\ddot{y}_b$ are measured, one can form $\ddot{\delta}$ and integrate twice to form $\dot{\delta}$ and δ. One can then fit a parametric model of the form (1b) to the data. One should note that if (m,c,k) is a set of parameters which minimise the squared error, then so is (αm,αc,αk) where α is an arbtirary number. This means that one can only identify parameters up to an overall scale. One fixes the scale by setting m = 1. This means that one actually estimates c' = c/m and k' = k/m from

$$c'\dot{\delta} + k'\delta = -\ddot{y}_m \qquad (2)$$

Clearly, one is not restricted to fitting a linear model to the restoring force in the link. One can fit the more general model

$$f'(\delta,\dot{\delta}) = \sum_{i=0}^{m}\sum_{j=0}^{n} a'_{ij}\,\delta^{i}\,\dot{\delta}^{j} = -\ddot{y}_m \qquad (3)$$

where $f'(\delta,\dot{\delta}) = f(\delta,\dot{\delta})/m$ and $f(\delta,\dot{\delta})$ is the restoring force function for the link. As in the linear case all coefficients are determined up to an overall scale, $a'_{ij} = a_{ij}/m$.

Example 1. The two degree–of–freedom system shown in Figure 5.2 was simulated and a parametric model of the form (3) with m = 3 and n = 1 was fitted to the data using a least–squares parameter estimator. The resulting coefficient estimates were

$$\hat{c}' = 20.000015$$
$$\hat{k}' = 9999.9961$$
$$\hat{k}'_3 = 5.0000005\times10^{9}$$

A comparison of the measured acceleration $\ddot{y}_m$ and that predicted by the model gave an MSE of 2.6×10^{-12}. For transmissibility data the restoring force surface is very simple to construct. One does not need an *a priori* estimate of the mass. One simply takes the triplets of sampled and integrated data $(\delta,\dot{\delta},-\ddot{y}_m)$ and constructs the *scaled* force surface using Crawley and O'Donnell's technique (55). The surface obtained from the example above is shown in Figure 5.3.

To sum up, using transmissibility data one can identify all parameters for a system up to a constant scale without measuring or estimating the mass. If the mass is known, the scale factor is known. This is only possible because equation (1b) has a zero on the right–hand side.

5.2. MDOF Lumped Parameter Systems.

The object of this section is to demonstrate a means of identifying an N degree-of-freedom lumped parameter system when the system is excited by an arbitrary number of inputs. The mass of the system is assumed to be concentrated at N measurement points, m_i being the mass at point i. Each point is then assumed to be connected to each other point by a link, point i is connected to point j by the link l_{ij}. Each point i is connected to ground by the link l_{ii}. The situation is illustrated in Figure 5.4 for a three degree-of-freedom system.

If the masses are displaced and released, they are restored to equilibrium by the internal forces in the links. The forces are assumed to depend only on the relative velocities and relative displacements of the ends of the links. If $\delta_{ij} = y_i - y_j$ is the displacement of measurement point i relative to point j and $\dot{\delta}_{ij} = \dot{y}_i - \dot{y}_j$ is the corresponding relative velocity, one has

$$\text{Force in link } l_{ij} \;:=\; f_{ij}(\delta_{ij}, \dot{\delta}_{ij})$$

As l_{ii} is the link with ground $\delta_{ii} = y_i$ and $\dot{\delta}_{ii} = \dot{y}_i$. Clearly, as links l_{ij} and l_{ji} are the same

$$f_{ji}(\delta_{ji}, \dot{\delta}_{ji}) \;=\; -f_{ij}(\delta_{ij}, \dot{\delta}_{ij}) \;=\; -f_{ij}(-\delta_{ji}, -\dot{\delta}_{ji}) \qquad (4)$$

If an external force $x_i(t)$ is now applied at each point i, one can readily see that the equations of motion of the system are

$$m_i\ddot{y}_i + \sum_{j=1}^{N} f_{ij}(\delta_{ij}, \dot{\delta}_{ij}) \;=\; x_i(t) \qquad i = 1,..,N \qquad (5)$$

As mentioned before, this type of system if linear, has N natural frequencies or modes. This means that one would hope to be able to model a real system with N effective

natural frequencies (i.e. a system with only N modes excited) by a set of equations like (5). If one measures the N accelerations and input forces at each point, one can find the relative accelerations and integrate to find the values of the variables δ_{ij} and $\dot{\delta}_{ij}$ at each sampling instant. One can then estimate parameters for a least-squares model of the form

$$\Delta m_i . \ddot{y}_i + \sum_{j=1}^{N} f_{ij}(\delta_{ij}, \dot{\delta}_{ij}) = \Delta m_i . \ddot{y}_i +$$

$$\sum_{j=1}^{N} \sum_{k=0}^{m} \sum_{l=0}^{p} a_{(ij)kl} \, (\delta_{ij})^k (\dot{\delta}_{ij})^l = x_i - m_{ei} . \ddot{y}_i \qquad (6)$$

where m_{ei} is an initial estimate for m_i as used in the last chapter. Using arguments suggested by the transmissibility approach, one can see that if there is no excitation at point i, one can still find all the coefficients up to an overall scale by fitting a model of the form.

$$\sum_{j=1}^{N} f'_{ij}(\delta_{ij}, \dot{\delta}_{ij}) = \sum_{j=1}^{N} \sum_{k=0}^{m} \sum_{l=0}^{p} a'_{(ij)kl} \, (\delta_{ij}, \dot{\delta}_{ij})$$

$$= -\ddot{y}_i \qquad (7)$$

where $a'_{(ij)kl} = a_{(ij)kl}/m_i$. Models of the form (6) shall be referred to as *inhomogeneous* while those of the form (7) shall be called *homogeneous* in keeping with the terminology of the theory of differential equations.

In terms of the expansion coefficients, the symmetry relation (4) becomes

$$a_{(ij)kl} = (-1)^{k+l+1} . a_{(ji)kl} \qquad (8)$$

or

$$m_i . a'_{(ij)kl} = (-1)^{k+l+1} . m_j . a'_{(ji)kl} \qquad (9)$$

This model allows one to determine the type and location of nonlinearities within the

system. If a term of the form $(\delta_{23})^3$ appears in the expansions, then one deduces that there is a cubic stiffness nonlinearity between points 2 and 3. Al-Hadid and Wright (18) proposed the inclusion of difference terms in least-squares models with the location of nonlinearities in mind. The type of model above has also been proposed independently by Yang and Ibrahim (16).

Suppose now that all the inputs x_i are zero except one, without loss of generality this can be chosen to be x_1. This type of system shall henceforth be referred to as a SIMO (Single-Input Multi-Output) system. The equations of motion become

$$m_1.\ddot{y}_1 + \sum_{j=1}^{N} f_{1j}(\delta_{1j},\dot{\delta}_{1j}) = x_1 \qquad (10a)$$

$$\ddot{y}_i + \sum_{j=1}^{N} f'_{ij}(\delta_{ij},\dot{\delta}_{ij}) = 0 \qquad i = 2,..,N \qquad (10b)$$

Now, one can identify all terms in the $\ddot{y}_2$ equation up to an overall scale - the unknown m_2. Similarly one identifies all terms in the $\ddot{y}_3$ equation up to the scale factor m_3. If there is a link l_{23} between the masses m_2 and m_3, then the $\ddot{y}_2$ and $\ddot{y}_3$ equations will contain terms f'_{23} and f'_{32} respectively. Now, as

$$m_2.f'_{23} = m_3.f'_{32}$$

One can transfer the scale factor m_2 from the $\ddot{y}_2$ equation to the $\ddot{y}_3$ equation. One simply multiplies the coefficients for the $\ddot{y}_3$ equation by m_3/m_2. This ratio is fixed by choosing any pair of coefficients from terms common to the expansions of f'_{23} and f'_{32}. For example one could choose the linear stiffness coefficients, in which case according to equation (9)

$$\frac{m_2}{m_3} = \frac{a_{(23)10}}{a_{(32)10}}$$

Now all the coeffcients in the $\ddot{y}_2$ and $\ddot{y}_3$ are estimated up to one overall scale factor

- m_2. One can now transfer this factor to the $\ddot{y}_4$ coefficients by the same method if there is a link l_{24} or l_{34}. In fact, one can propagate the scale factor through all the equations because every measurement point is connected to every other point by a sequence of links. This is an almost trivial observation, based on the following argument. If a point i is not connected to a point j by movement along a sequence of links, then the system must consist of two disjoint pieces, one of which contains point i, the other containing point j. If the two pieces are disjoint, they cannot affect each others dynamics in any way. In this case one should be studying the two pieces as two separate dynamical systems. In fact, the subsystem which does not contain the excitation point 1 will remain at rest. One is therefore justified in considering only connected systems. The preceding arguments serve to show that without measuring the input, just the accelerations $\ddot{y}_1$ to $\ddot{y}_N$, one can identify almost all parameters in a SIMO system up to one overall scale factor, this scale factor being one of the masses arbitrarily chosen. The only parameters one cannot obtain are those for the link l_{11}. This is because f_{11} only appears in the first equation. This assumes that one is not exciting the system at a nodal point

If the input x_1 is measured, one fits an inhomogeneous model to the $\ddot{y}_1$ equation. The coefficients in this equation are absolute so the estimates can be used to obtain absolute values for all other coefficients by the method above. Summarising, one can identify all parameters in an MDOF system by exciting at one measurement point only.

Yang and Ibrahim (16) observe the unforced equations of motion, and fit homogeneous models as above to all the equations. The overall scale required is then fixed by knowledge of the total mass of the system. Effectively, this means that one can identify all parameters without using any inputs at all!

If one now restricts attention to linear systems, one can simplify the notation a great deal. One writes

$$a_{(ij)01} = \gamma_{ij}$$

$$a_{(ij)10} = \mu_{ij}$$

and the equations of motion are

$$m_1 . \ddot{y}_1 + \sum_{j=1}^{N} \gamma_{1j} . \dot{\delta}_{1j} + \sum_{j=1}^{N} \mu_{1j} . \delta_{1j} = x_1 \qquad (11)$$

$$\ddot{y}_i + \sum_{j=1}^{N} \gamma'_{ij} . \dot{\delta}_{ij} + \sum_{j=1}^{N} \mu'_{ij} . \delta_{ij} = 0 \qquad i \neq 1$$

where $\gamma'_{ij} = \gamma_{ij}/m_i$ and $\mu'_{ij} = \mu_{ij}/m_i$. One can carry out the procedure described above and obtain estimates for the m_i, γ_{ij} and μ_{ij}. The usual damping and stiffness matrices [C] and [K] are then obtained from the simple realtions

$$c_{ij} = -\gamma_{ij} \qquad k_{ij} = -\mu_{ij} \qquad i \neq j \qquad (12a,b)$$

$$c_{ii} = \sum_{j=1}^{N} \gamma_{ij} \qquad k_{ii} = \sum_{j=1}^{N} \mu_{ij} \qquad (12c,d)$$

The symmetry conditions (8) become

$$\gamma_{ij} = \gamma_{ji}$$

$$\mu_{ij} = \mu_{ji}$$

which become in turn, through the equations (12a) to (12d)

$$c_{ij} = c_{ji} \qquad (13a)$$

$$k_{ij} = k_{ji} \qquad (13b)$$

One concludes that the model adopted forces symmetry conditions on the damping and stiffness matrices.

The method described above is now tested on a number of simulated systems.

Example 2. The linear system described by the following equations,

$$\begin{bmatrix} 1 & 0 & 0 \\ 0 & 2 & 0 \\ 0 & 0 & 3 \end{bmatrix}\begin{bmatrix} \ddot{y}_1 \\ \ddot{y}_2 \\ \ddot{y}_3 \end{bmatrix} + 20.\begin{bmatrix} 2 & -1 & 0 \\ -1 & 2 & -1 \\ 0 & -1 & 2 \end{bmatrix}\begin{bmatrix} \dot{y}_1 \\ \dot{y}_2 \\ \dot{y}_3 \end{bmatrix}$$

$$+ 10^4.\begin{bmatrix} 2 & -1 & 0 \\ -1 & 2 & -1 \\ 0 & -1 & 2 \end{bmatrix}\begin{bmatrix} y_1 \\ y_2 \\ y_3 \end{bmatrix} = \begin{bmatrix} x_1 \\ 0 \\ 0 \end{bmatrix}$$

was simulated with x_1 a Gaussian noise sequence with variance 10.0. The signal was band-limited into the interval (0,200)Hz. A timestep of 1 ms was used. The accelerations, velocities and displacements were all taken from the simulation.

An inhomogeneous (2,2) model with an initial mass estimate of $m_{el} = 1.0$ was fitted to give the $\ddot{y}_1$ equation of motion. As before, an (m,p) model is one which includes powers of δ up to δ^m and powers of $\dot{\delta}$ up to $\dot{\delta}^p$. The results of the identification are shown in Table 1. Homogeneous (2,2) and (1,1) models were fitted to give the $\ddot{y}_2$ and $\ddot{y}_3$ equations of motion respectively. The results are shown in Tables 2 and 3. The link classification is given in each table. This is obtained simply by checking which terms appear to be significant in the expansions. The coefficient estimates are collected together below

$$a_{(11)01} = \gamma_{11} = 20.000341$$
$$a_{(11)10} = \mu_{11} = 1.0000034 \times 10^4$$
$$a_{(12)01} = \gamma_{12} = 20.000147$$
$$a_{(12)10} = \mu_{12} = 1.0000023 \times 10^4$$

$$a'_{(21)01} = \gamma'_{21} = 9.9999971$$
$$a'_{(21)10} = \mu'_{21} = 5.0000020\times10^{3}$$
$$a'_{(23)01} = \gamma'_{23} = 9.9999828$$
$$a'_{(23)10} = \mu'_{23} = 5.0000029\times10^{3}$$

$$a'_{(32)01} = \gamma'_{32} = 6.6666503$$
$$a'_{(32)10} = \mu'_{32} = 3.3333335\times10^{3}$$
$$a'_{(33)01} = \gamma'_{33} = 6.6666884$$
$$a'_{(33)10} = \mu'_{33} = 3.3333342\times10^{3}$$

(dropping the carets which are usually used to indicate estimates). The scale factor for the $\ddot{y}_2$ equation of motion is obtained from the relation $m_2 = a_{(12)01}/a'_{(21)01}) = 2.00004$, the factor for $\ddot{y}_3$ is then obtained from $m_3 = m_2.a'_{(23)01}/a'_{(32)01} = 3.000007$. These factors allow one to form the $[\gamma]$ and $[\mu]$ matrices. The damping and stiffness matrices [C] and [K] then follow from equations (12a) to (12d). The estimates are

$$[C] = 10.\begin{bmatrix} 4.000043 & -2.000009 & 0.000000 \\ -2.000009 & 4.000009 & -2.000000 \\ 0.000000 & -2.000000 & 4.000011 \end{bmatrix}$$

$$[K] = 10^{4}.\begin{bmatrix} 2.000006 & -1.000002 & 0.000000 \\ -1.000002 & 2.000005 & -1.000003 \\ 0.000000 & -1.000003 & 2.000005 \end{bmatrix}$$

Beacause it is possible that say, $c_{12}.\dot{y}_2$ might be a significant term in the $\ddot{y}_1$ equation while the $c_{21}.\dot{y}_1$ term is deleted from the $\ddot{y}_2$ equation, the [C] and [K] matrices above are 'symmetrised' i.e. if both $\hat{c}_{12}$ and $\hat{c}_{21}$ are considered significant they are both replaced by the average $\frac{1}{2}(\hat{c}_{12} + \hat{c}_{21})$. If only $\hat{c}_{12}$ is significant, $\hat{c}_{21}$ is defined equal to $\hat{c}_{12}$. The coefficients above are quoted to seven significant figures in order to demonstrate how accurate the procedure is when the data is free from noise. It is clearly unrealistic to expect accuracy of this sort when one is using experimental data. In the examples which follow the coefficients are only quoted to four figures even

though they are usually as accurate as those above.

The MSE's for comparisons between measured and predicted right-hand sides for each equation were

$$\begin{aligned} MSE(1) &= 2.4\text{x}10^{-9} \\ MSE(2) &= 3.0\text{x}10^{-11} \\ MSE(3) &= 8.5\text{x}10^{-12} \end{aligned}$$

A useful feature of the link model approach is that restoring force surfaces arise naturally for each link. For each link l_{ij} the force f_{ij} or f'_{ij} can be plotted over the $(\delta_{ij},\dot{\delta}_{ij})$ plane. However, in the MDOF case one cannot partition the data in each equation into parts depending on each set of link variables until after the model has been fitted. One can only plot the model surfaces. This is straightforward, for l_{ij} one determines the maximum and minimum values of δ_{ij} and $\dot{\delta}_{ij}$ and evaluates the model expansion for the link on a regular grid over the region $[\delta_{ij(min)},\delta_{ij(max)}]\text{x}[\dot{\delta}_{ij(min)},\dot{\delta}_{ij(max)}]$. This provides the data for the surface plot. This technique is used in the following examples.

Example 3. This is the same system as in Chapter 3, Example 4. The system described by the equations of motion,

$$\begin{bmatrix} \ddot{y}_1 \\ \ddot{y}_2 \end{bmatrix} + 20.\begin{bmatrix} \dot{y}_1 \\ \dot{y}_2 \end{bmatrix} + 10^4.\begin{bmatrix} 2 & -1 \\ -1 & 2 \end{bmatrix}\begin{bmatrix} y_1 \\ y_2 \end{bmatrix}$$

$$+ 5.0\text{x}10^9.\begin{bmatrix} y_1{}^3 \\ 0 \end{bmatrix} = \begin{bmatrix} x_1 \\ 0 \end{bmatrix}$$

was simulated with x_1 a Gaussian noise sequence with RMS 150.0, band-limited as before. The sampling is 1 kHz. The accelerations, velocities and displacements were obtained from the simulation.

An inhomogeneous (4,2) model was fitted for the $\ddot{y}_1$ equation. The fitted equation is

$$\ddot{y}_1 + 20.00.\dot{y}_1 + 1.000x10^4.y_1 + 5.000x10^9.y_1^3$$
$$+ 0.9999x10^4.(y_1 - y_2) = x_1$$

The MSE for the comparison of predicted with measured output was $1.0x10^8$. The comparison is shown in Figure 5.5. The link surfaces or force surfaces for links l_{11} and l_{12} are shown in Figures 5.6 and 5.7 respectively.

A homogeneous (2,2) model was fitted for the $\ddot{y}_2$ equation. The results obtained were

$$\ddot{y}_2 + 20.00.\dot{y}_2 + 1.000x10^4.y_2$$
$$+ 1.000x10^4.(y_2 - y_1) = 0$$

The link surfaces for this equation are simply planes above phase space. There is no need to transfer any scale factors in this case as the true mass matrix is the 2x2 unit. The overall equations of motion obtained are

$$\begin{bmatrix} \ddot{y}_1 \\ \ddot{y}_2 \end{bmatrix} + \begin{bmatrix} 20.00 & 0.0 \\ 0.0 & 20.00 \end{bmatrix} \begin{bmatrix} \dot{y}_1 \\ \dot{y}_2 \end{bmatrix} +$$

$$10^4. \begin{bmatrix} 2.000 & -1.000 \\ -1.000 & 2.000 \end{bmatrix} \begin{bmatrix} y_1 \\ y_2 \end{bmatrix} +$$

$$\begin{bmatrix} 5.000x10^9 \\ 0.0 \end{bmatrix} \begin{bmatrix} y_1^3 \\ 0 \end{bmatrix} = \begin{bmatrix} x_1 \\ 0 \end{bmatrix}$$

The results are perfect. If one were using experimental data one would not obtain this sort of accuracy. In that case, to improve the estimates one re-estimates parameters using a (3,1) model for the first equation and a (1,1) model for the second as the best parameters will usually be for the model with the correct order.

Example 4. is the three degree-of-freedom piecewise linear system considered earlier

in Chapter 3. The equations are repeated here for convenience

$$\begin{bmatrix} \ddot{y}_1 \\ \ddot{y}_2 \\ \ddot{y}_3 \end{bmatrix} + 20. \begin{bmatrix} \dot{y}_1 \\ \dot{y}_2 \\ \dot{y}_3 \end{bmatrix}$$

$$+ 10^4. \begin{bmatrix} 2 & -1 & 0 \\ -1 & 2 & -1 \\ 0 & -1 & 2 \end{bmatrix} \begin{bmatrix} y_1 \\ y_2 \\ y_3 \end{bmatrix} + \begin{bmatrix} 0 \\ f_{nl} \\ 0 \end{bmatrix} = \begin{bmatrix} 0 \\ x_1 \\ 0 \end{bmatrix}$$

The piecewise linear force f_{nl} is shown in Figure 3.26. The excitation $x_1(t)$ is the same as in the previous example.

A homogeneous (2,2) model was fitted for the $\dot{y}_1$ equation. After deleting insignificant coefficients the equation was estimated as

$$\ddot{y}_1 + 20.00.\dot{y}_1 + 1.000\text{x}10^4.y_1 + 1.000\text{x}10^4.(y_1 - y_2) = 0$$

The MSE for comparing the model data with measured data was $8.2\text{x}10^{-9}$. The link classification correctly indicated that all links to mass m_1 were linear.

An inhomogeneous (5,1) model was fitted for the $\dot{y}_2$ equation. The identification data is given in Table 4. After deleting insignificant coefficients, the estimated equation was

$$\ddot{y}_2 + 18.96.\dot{y}_2 - 1.089\text{x}10^4.y_2 + 0.984\text{x}10^4.(y_2 - y_1) + 1.024\text{x}10^4.(y_2 - y_3) + 2.157\text{x}10^{12}.y_2^3 - 1.575\text{x}10^{17}.y_2^5 = x$$

The MSE for the data comparison was 0.652 and the results are shown in Figure 5.8. The link surfaces for l_{21}, l_{22} and l_{23} are shown in Figures 5.9, 5.10 and 5.11 respectively. The l_{22} surface resembles a piecewise linear surface. However, a higher order approximation than fifth-order is needed. The stiffness section for the l_{22}

surface is shown in Figure 5.12

A homogeneous (2,2) model was fitted for the $\ddot{y}_3$ equation. The significant terms in the equation gave the model

$$\ddot{y}_3 + 20.00.\dot{y}_3 + 1.000x10^4.y_3 + 1.000x10^4.(y_3 - y_2) = 0$$

The data comparison gave an MSE of $6.5x10^{-12}$.

The overall fitted model was therefore

$$\begin{bmatrix} \ddot{y}_1 \\ \ddot{y}_2 \\ \ddot{y}_3 \end{bmatrix} + \begin{bmatrix} 20.00\cdot\dot{y}_1 \\ 18.96.\dot{y}_2 \\ 20.00.\dot{y}_3 \end{bmatrix}$$

$$+ 10^4.\begin{bmatrix} 2.000 & -1.000 & 0.0 \\ -0.984 & 0.919 & -1.024 \\ 0.0 & -1.000 & 2.000 \end{bmatrix}\begin{bmatrix} y_1 \\ y_2 \\ y_3 \end{bmatrix}$$

$$+ \begin{bmatrix} 0.0 \\ 2.157x10^{12}.y_2^3 - 1.575x10^{17}.y_2^5 \\ 0.0 \end{bmatrix} = \begin{bmatrix} 0 \\ x \\ 0 \end{bmatrix}$$

As one might expect, the linear term k_{22} is estimated badly as part of it appears in the polynomial expansion for the piecewise linear function.

These results indicate that for simulated systems, one can accurately identify the equations of motion using only one input. The location of the nonlinear terms within the linked structure is easy to determine. One would hope that if a real nonlinear structure was well described by a lumped parameter model of the type above, the location of the nonlinear elements within the model would correspond to the location within the real system.

5.3. Use of Reciprocity Relations.

The reason why the link-model approach of the last section works for SIMO systems can be traced back to the symmetry conditions (4). For linear systems in particular, one obtains the symmetry relations for the damping and stiffness matrices (13). These relations can actually be obtained from a much more general argument.

In order to obtain the equations of motion of an N degree-of-freedom system, one can define or construct a Lagrangian function $L(\{y\},\{\dot{y}\},\ldots)$ which depends on all the displacements y_i and all the velocities $\dot{y}_i$ etc. (51). One way of determining the function L is through the equation $L = T - V$ where $T(\{y\},\{\dot{y}\},\ldots)$ is the kinetic energy of the system and $V(\{y\},\{\dot{y}\},\ldots)$ is the potential energy. The unforced equations of motion of the system are then obtained from the Euler-Lagrange equations

$$\frac{\partial L}{\partial y_i} - \frac{d}{dt}\left[\frac{\partial L}{\partial \dot{y}_i}\right] = 0 \qquad i = 1,\ldots,N \qquad (14)$$

One can now ask for the most general Lagrangian which defines a linear system. Because the Euler-Lagrange equations contain a time-derivative operator, one should only include $\{y\}$ and $\{\dot{y}\}$ terms in the Lagrangian. If L were to contain a $\ddot{y}$ term, the equations of motion would contain a $\dddot{y}$ term. It is known that equations containing third derivatives or higher have causality problems, an example being the Abraham-Lorenz-Dirac equation for a particle in an electric field; in this case the particle can accelerate *before* radiation hits it (52). In requiring causal equations one restricts the form of the Lagrangian. Also, if one requires linear equations of motion, the Lagrangian has to be a homogeneous quadratic in it's dependent variables. This means that the most general Lagrangian which one can write down is

$$L(\{y\},\{\dot{y}\}) = \sum_{i=1}^{N}\sum_{j=1}^{N}\left(y_i A_{ij} y_j + y_i B_{ij}\dot{y}_j + \dot{y}_i D_{ij}\dot{y}_j \right) \qquad (15)$$

Now, consider the term $\sum \sum y_i A_{ij} y_j$. The matrix [A] can be split into symmetric parts and anti–symmetric parts as follows

$$[A] = [A^s] + [A^a]$$

$$A_{ij} = \tfrac{1}{2}(A_{ij} + A_{ji}) + \tfrac{1}{2}(A_{ij} - A_{ji}) = A^s{}_{ij} + A^a{}_{ij}$$

It is a simple matter to show that

$$\sum_{i=1}^{N} \sum_{j=1}^{N} y_i \, A^a{}_{ij} \, y_j = 0$$

So, without loss of generality one can define [A] to be symmetric. Exactly the same argument applies to [D].

Substituting the Lagrangian (15) into the Euler–Lagrange equations (14) gives the equations of motion

$$\sum_{j=1}^{N} 2D_{ij}.\ddot{y}_j + \sum_{j=1}^{N} (Bji - Bij).\dot{y}_j - \sum_{j=1}^{N} 2A_{ij}.y_j = 0$$

Clearly, one can now make the identifications [D] = $\frac{1}{2}$[M], [A] = $-\frac{1}{2}$[K] and [C] = $[B]^T - [B] = 2[B^a]$.

By a quite general argument, one has therefore arrived at a symmetric mass matrix and a symmetric stiffness matrix. The symmetry condition on [K] produces the phenomenon known as *reciprocity*. Whereby, if one applies a unit force at measurement point i in a system and measures the resulting displacement at point j, one would measure the same displacement at point i if the force is applied at point j.

Unfortunately, this argument produces an antisymmetric damping matrix. As

antisymmetry of the damping matrix does not correspond to a recognisable physical phenomenon as symmetry of the stiffness matrix does, one usually defines the damping matrix in another form. If one chooses the damping matrix symmetric, one obtains agreement with the lumped parameter model of the previous section. One can go one step further as Modal Analysts do **(7)**, and assume that the damping is *proportional* i.e.

$$[C] = \alpha[M] + \beta[K]$$

where α and β are arbitrary constants. The advantage of this condition is that it assures that [M], [C] and [K] are simultaneously diagonalisable.

The assumption that [K] and possibly [C] is symmetric is the basis for Mohammad's method **(26)** of identifying SIMO systems. By assuming reciprocity at the outset, the identification proceeds with rather less effort than for the link-model approach. Another factor which motivated this approach was the requirement that all results should be compatible with finite element analysis. The method shall be demonstrated on the two degree-of-freedom linear system

$$m_{11}\cdot\ddot{y}_1 + c_{11}\cdot\dot{y}_1 + c_{12}\cdot\dot{y}_2 + k_{11}\cdot y_1 + k_{12}\cdot y_2 = x$$

$$m_{22}\cdot\ddot{y}_2 + c_{21}\cdot\dot{y}_1 + c_{22}\cdot\dot{y}_2 + k_{21}\cdot y_1 + k_{22}\cdot y_2 = 0$$

The first of these equations is identified using an inhomogeneous (1,1) model. Estimates of the parameters $\hat{m}_{11}$, $\hat{c}_{11}$, $\hat{c}_{12}$, $\hat{k}_{11}$ and $\hat{k}_{12}$ are obtained. Now, assumimg that reciprocity holds, one rewrites the second equation in the form

$$m_{22}\cdot\ddot{y}_2 + c_{22}\cdot\dot{y}_2 + k_{22}\cdot y_2 = - c_{12}\cdot\dot{y}_1 - k_{12}\cdot y_1$$

and the RHS is known from the measured data and the previous estimates. This allows one to estimate $\hat{m}_{22}$, $\hat{c}_{22}$ and $\hat{k}_{22}$. There is no scale ambiguity here as the second equation has now become inhomogeneous. The method extends directly to

MDOF nonlinear systems (26). Referring back to the earlier argument, if one is unsure about the symmetry of [C] one need only feed back the k estimates from the earlier equations into later equations.

If the method is applied to the three degree-of-freedom system of example 2, one obtains the parameter estimates given in Table 5. Because one does not need to explicitly transfer scales between equations or map the $[\gamma]$ matrix to the [C] matrix etc. this method is easier to code and faster to run than using the link approach. One can also see that the number of parameters required in successive estimations decreases, this also contributes to the speed of the approach. The advantages of the link approach are that one can more easily use *a priori* knowledge of the system as one deals with one equation at a time. It may also be more accurate than Mohammad's method as one can sometimes feed back badly estimated parameters using the latter approach; one can see that the errors in the estimated parameters will then be magnified in each successive step through the equations. Using the link approach one can easily choose only those parameters which are significant and/or have small standard deviations for calculating the scale factors.

5.4. Linear Dependence and the Mass Matrix.

It will have been noticed by now that the mass matrix is assumed diagonal throughout this chapter. The reason for this is that one can only identify a SIMO system by the methods of this chapter if this condition is satisfied. One might ask how one might observe a system with a full mass matrix anyway. One possible way is through the reduction of a system of N equations to a system with $M < N$. Suppose one is studying a system specified by three translational states x,y,z and three rotational states θ,ψ,ζ. One might wish to obtain the set of three equations which model the system behaviour best and yet only contain the translational variables. Methods for obtaining these approximate equations exist, Guyan reduction (53) is an example. A feature of these methods is that the reduced system equations will usually contain a

full mass matrix. Now, suppose that one is experimentally studying data from a real system of the type described above and only measuring the translational variables (which is usually the case). If one fits the best least–squares three DOF model i.e. that which descibes the data best, one might reasonably expect it to resemble the reduced model described above. This rather loose argument motivates the following discussion.

Consider the two degree–of–freedom system

$$m_{11}\cdot\ddot{y}_1 + m_{12}\cdot\ddot{y}_2 + c_{11}\cdot\dot{y}_1 + c_{12}\cdot\dot{y}_2 + k_{11}\cdot y_1 + k_{12}\cdot y_2 = x$$

$$m_{21}\cdot\ddot{y}_1 + m_{22}\cdot\ddot{y}_2 + c_{21}\cdot\dot{y}_1 + c_{22}\cdot\dot{y}_2 + k_{21}\cdot y_1 + k_{22}\cdot y_2 = 0$$

One might expect to obtain the parameters for the first equation by fitting a least–squares model, one cannot. The reason being that one can add an arbitrary multiple α of the second equation to the first to obtain

$$(m_{11} + \alpha m_{21})\ddot{y}_1 + (m_{12} + \alpha m_{22})\ddot{y}_2 + (c_{11} + \alpha c_{21})\dot{y}_1 +$$
$$(c_{12} + \alpha c_{22})\dot{y}_2 + (k_{11} + \alpha k_{21})y_1 + (k_{12} + \alpha k_{22})y_1 = x$$

Now, the design matrix for this equation is identical to that for the first equation of the pair above. So is the RHS vector {x} for the least–squares problem. This means that an entire family of parameter estimates labelled by an arbitrary real (or complex for that matter!) number α minimises the squared error. Only one of this family (α = 0) is correct. In general the estimates corresponding to a random, unknown α will be obtained and there is no way of recovering the true values. One obtains

$$\hat{m}_{11} = m_{11} + \alpha m_{21} \qquad \hat{m}_{12} = m_{12} + \alpha m_{22}$$
$$\hat{c}_{11} = c_{11} + \alpha c_{21} \qquad \hat{c}_{12} = c_{12} + \alpha c_{22}$$
$$\hat{k}_{11} = k_{11} + \alpha k_{21} \qquad \hat{k}_{12} = k_{12} + \alpha k_{22}$$

Another way of looking at this is to observe that while one is trying to fit to the first equation, the second equation can be regarded simply as a statement of the linear dependence of the fitting variables. The reason why these problems do not occur for SIMO systems is obvious, in that case, each equation contains a variable $\dot{y}_i$ which does not appear in any other.

Suppose one were to try and fit a model with no off-diagonal mass terms. This amounts to fixing one condition $\hat{m}_{12} = 0$. Unfortunately though, this condition is actually satisfied for one of the family of estimates described above, namely that with $\alpha = -m_{12}/m_{22}$. However, it is not satisfied for the true estimate. The estimates which minimise the squared error in this case are

$$\begin{aligned} \hat{m}_{11} &= m_{11} - m_{12}m_{21}/m_{22} & \hat{m}_{12} &= 0 \\ \hat{c}_{11} &= c_{11} - m_{12}c_{21}/m_{22} & \hat{c}_{12} &= c_{12} - m_{12}c_{22}/m_{22} \\ \hat{k}_{11} &= k_{11} - m_{12}k_{21}/m_{22} & \hat{k}_{12} &= k_{12} - m_{12}k_{22}/m_{22} \end{aligned} \qquad (17)$$

One can demostrate this effect using the following example

Example 5. The system

$$\begin{bmatrix} 1 & 0.5 \\ 0.5 & 1 \end{bmatrix}\begin{bmatrix} \ddot{y}_1 \\ \ddot{y}_2 \end{bmatrix} + 20.\begin{bmatrix} \dot{y}_1 \\ \dot{y}_2 \end{bmatrix} +$$

$$10^4.\begin{bmatrix} 2 & -1 \\ -1 & 2 \end{bmatrix}\begin{bmatrix} y_1 \\ y_2 \end{bmatrix} = \begin{bmatrix} x \\ 0 \end{bmatrix}$$

was simulated with x a Gaussian noise sequence filtered into the range (0,200)Hz. If an inhomogeneous (1,1) model were fitted to the first equation with the off-diagonal mass term zeroed. One would expect the following results from equations (17): $\hat{m}_{11} = 0.75$, $\hat{c}_{11} = 20.0$, $\hat{c}_{12} = -10.0$, $\hat{k}_{11} = 2.5\text{x}10^4$ and $\hat{k}_{12} = -2.0\text{x}10^4$. Mohammad's method was used to estimate parameters from the data and the results shown in Table 6 agree almost perfectly with the theoretical predictions.

Exactly the same effect occurs for MDOF systems of higher order. If there are N degrees-of-freedom, one can add a multiple α_i i = 2,,,N of the i^{th} equation to the first equation without changing the design matrix etc. for estimating the first equations parameters. In this case one has a N-1 parameter set of possible estimates all of which minimise the squared error. Zeroing the N-1 off-diagonal mass terms fixes N-1 conditions on the variables α_i. The resulting constraint equations will have a unique solution which will certainly not correspond to the true estimates unless the solution is the trivial one.

One concludes that one cannot identify parameters for a SIMO system if the mass matrix has off-diagonal terms. One must excite such a system at *all* measurement points.

5.5. Comparison with the Masri/Caughey Procedure.

The last chapter showed how one could fit Masri/Caughey type models to SDOF systems using direct least-squares methods; there being no need for interpolation or integration. One can fit the same sort of models for MDOF systems in exactly the same manner. One simply estimates coefficients for models of the form

$$\Delta m_i . \ddot{y}_i + \sum_{j=1}^{N} \sum_{k=0}^{m} \sum_{l=0}^{p} C_{(ij)kl} . T_k[\zeta_{ij}(\delta_{ij})] . T_l[\dot{\zeta}_{ij}(\dot{\delta}_{ij})] = x_i - m_{ei} . \ddot{y}_i \qquad (18)$$

or

$$\sum_{j=1}^{N} \sum_{k=0}^{m} \sum_{l=0}^{p} C'_{(ij)kl} . T_k[\zeta_{ij}(\delta_{ij})] . T_l[\dot{\zeta}_{ij}(\dot{\delta}_{ij})] = -\ddot{y}_i \qquad (19)$$

This approach has all the advantages previously mentioned over the Masri/Caughey procedure. In addition one can estimate all the coefficients in an equation in one go by this method. The Masri/Caughey procedure can only handle two expansion variables

at a time as one has to order the two variables then plot the surface over the appropriate region of the phase space. By estimating all coefficients at once, one also avoids the biasing which plagues the Masri/Caughey approach. Overall there is an enormous increase in speed over the procedure based on interpolation/integration.

Example 6. Models of the form above were used to identify the data from example 2. A (4,2) model of the form (18) was fitted to give the first equation of motion. The results are given in Table 5.7. The coefficients were estimated as follows.

Coefficient	Estimate	Exact	% error
$c_{(11)00} + c_{(12)00}$	1.852	-0.968	291.0
$c_{(11)01}$	36.223	36.230	0.02
$c_{(11)10}$	624.21	624.09	0.02
$c_{(11)20}$	0.418	0.427	2.1
$c_{(11)30}$	190.27	190.23	0.02
$c_{(12)10}$	70.9	70.9	0.0

In this case the constants calculated for the ζ maps were only recorded to four significant figures, this is why the exact and estimated coefficients differ slightly, it is the exact coefficients which are slightly in error. The MSE for the comparison between measured and predicted data for the RHS of (18) was 2.8×10^{-3}. This relatively high error for a simulation is due to the fact that the (0,0) and (2,0) terms were deleted as a result of setting the significance threshold too high. One can see from Table 5.7 that if these terms had been retained, the model MSE would have been 5.7×10^{-9}. The comparison is shown in Figure 5.13. The link surfaces for links l_{11} and l_{12} are shown in Figures 5.14 and 5.15 respectively. As one might expect they are identical to those in Figures 5.6 and 5.7.

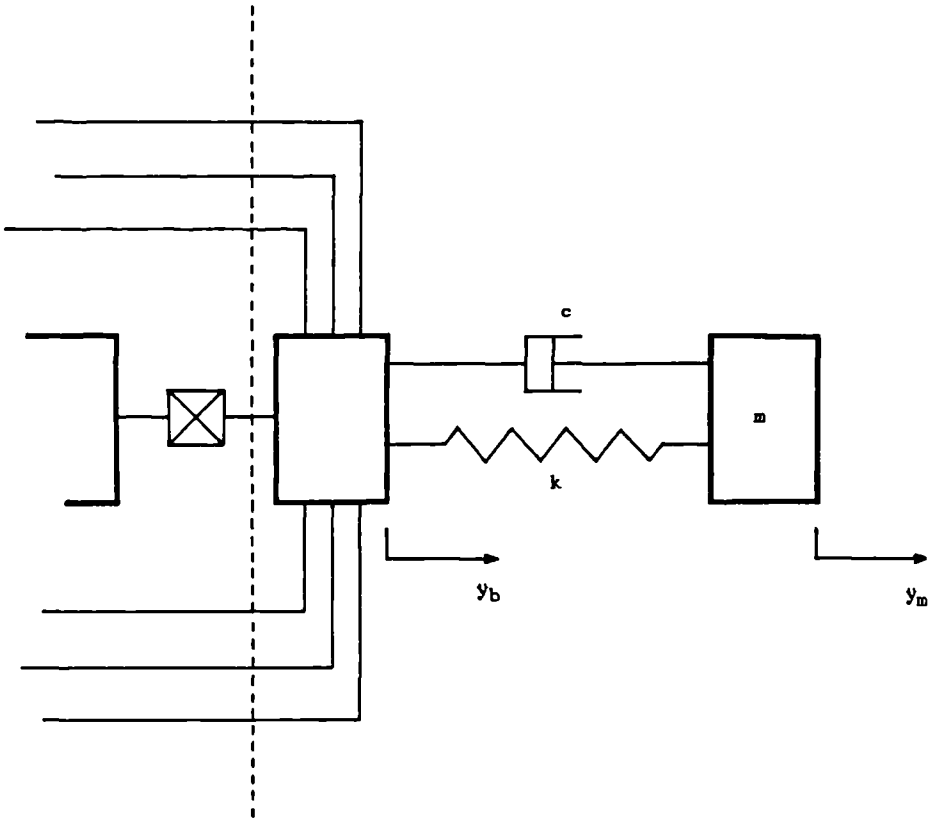

Figure 5.1. MDOF system showing the SDOF-like transmissibility sub-system.

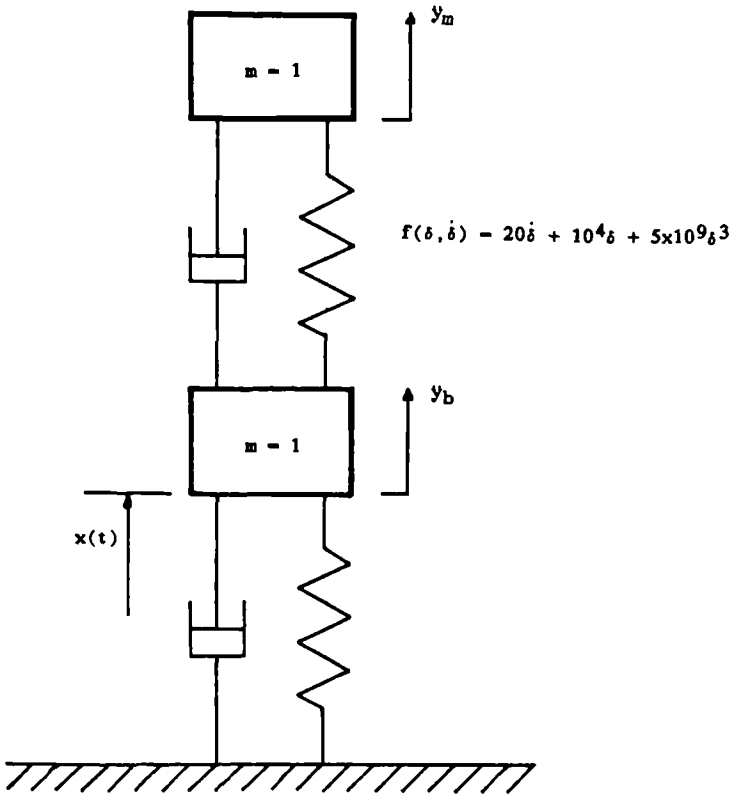

Figure 5.2. Two degree-of-freedom system with a cubic stiffness term.

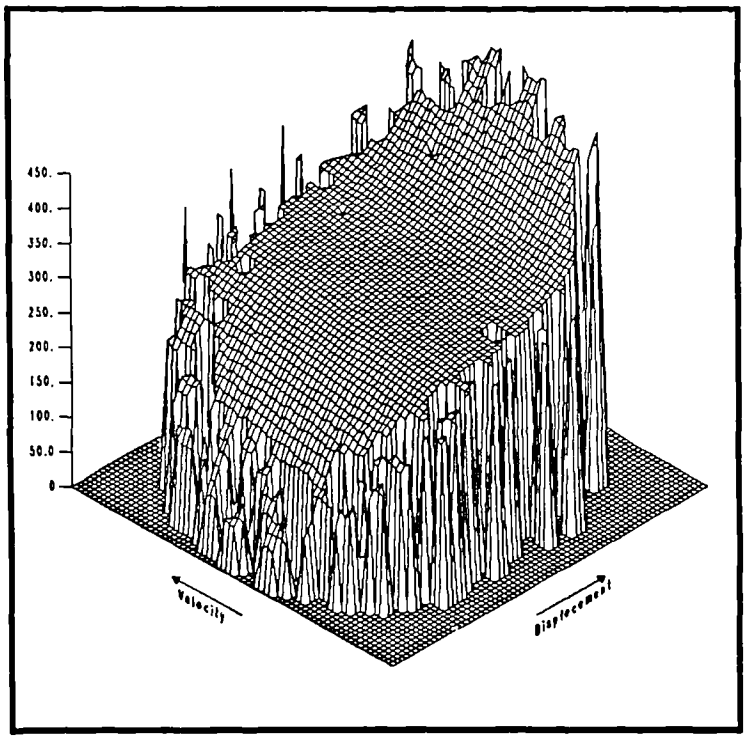

Figure 5.3. Restoring force surface obtained by transmissibility analysis of the system in the previous figure.

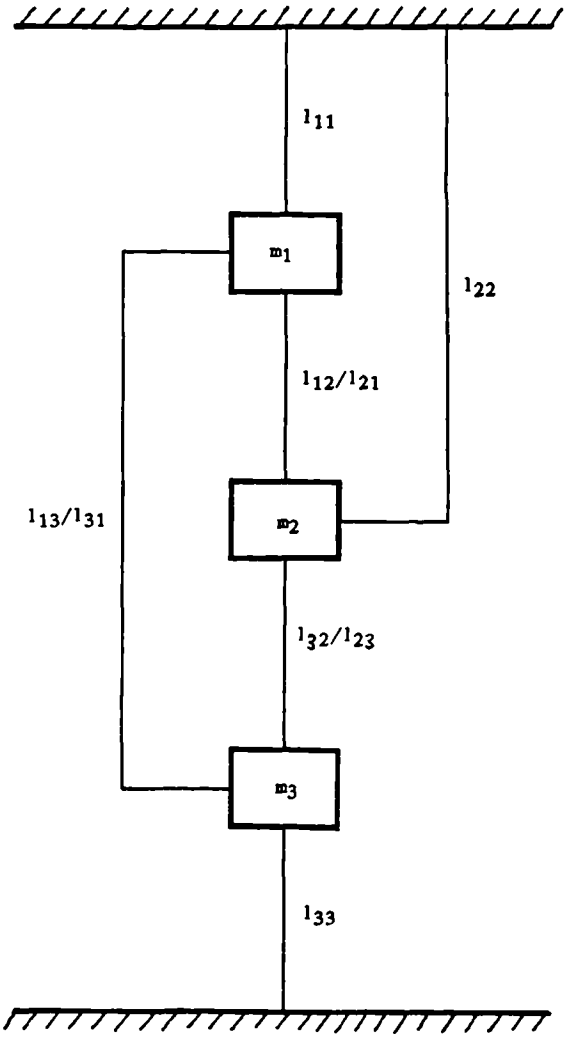

Figure 5.4. Link model of a three degree-of-freedom system.

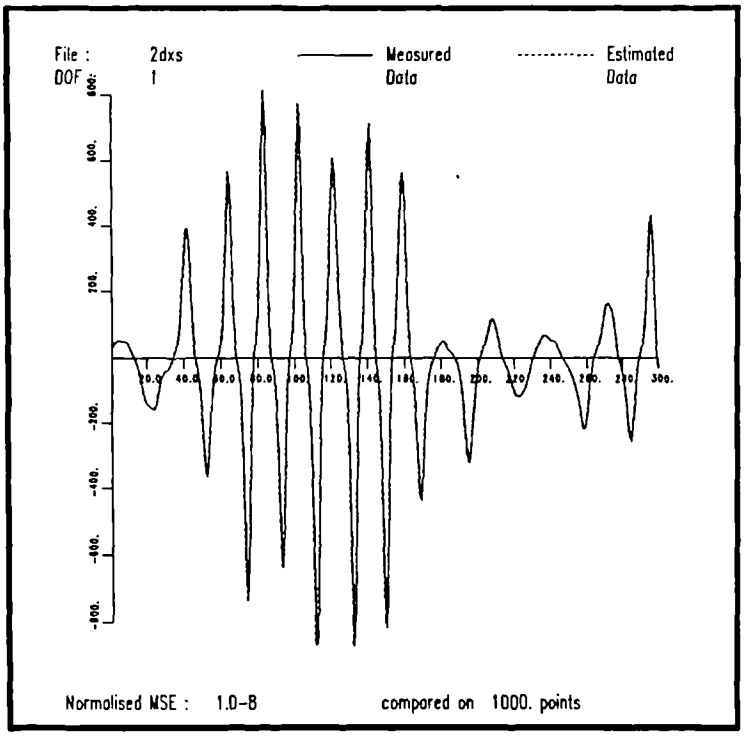

Figure 5.5. Comparison of the measured data and that predicted by the model for the two degree-of-freedom nonlinear system described in the text.

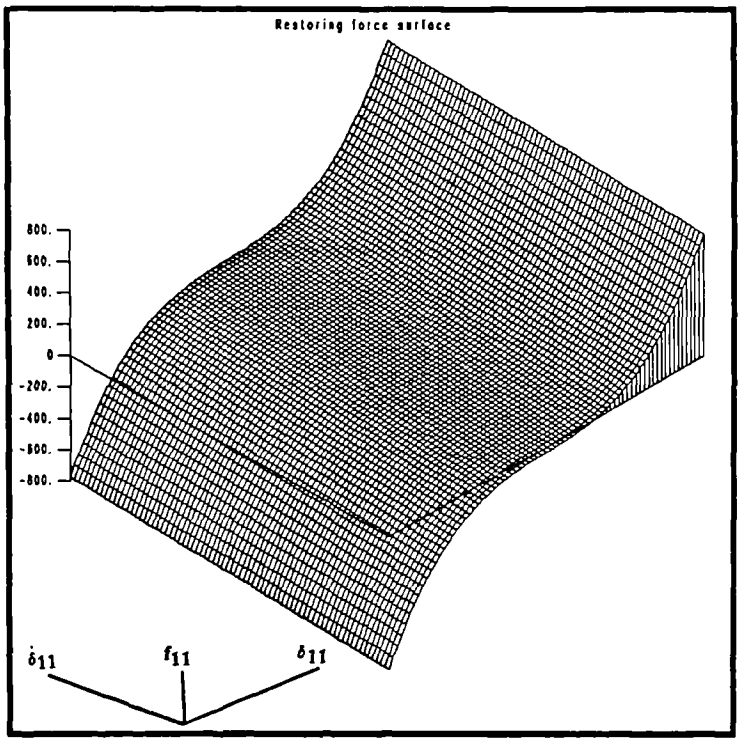

Figure 5.6. Restoring force surface for link l_{11} of the two degree-of-freedom nonlinear system.

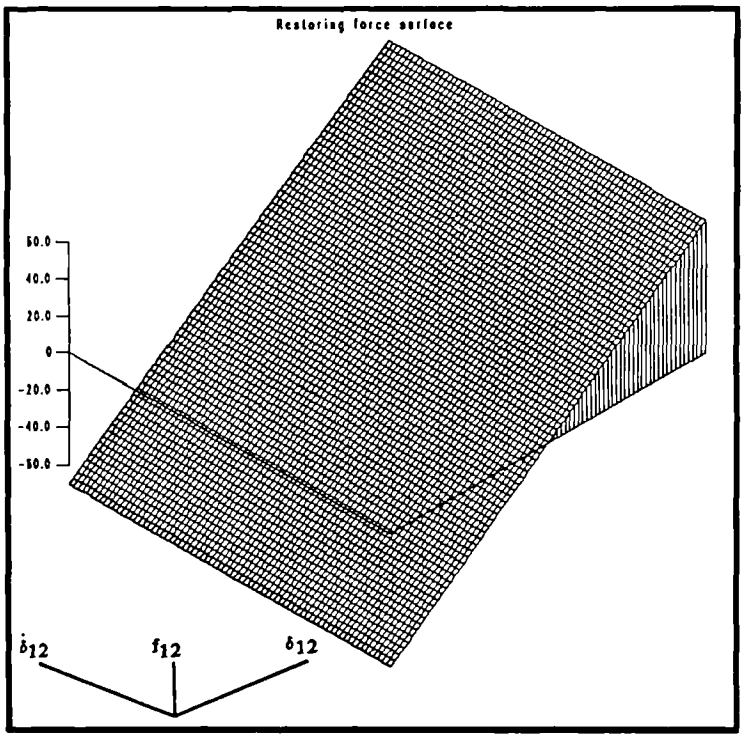

Figure 5.7. Restoring force surface for link l_{12} of the two degree-of-freedom nonlinear system.

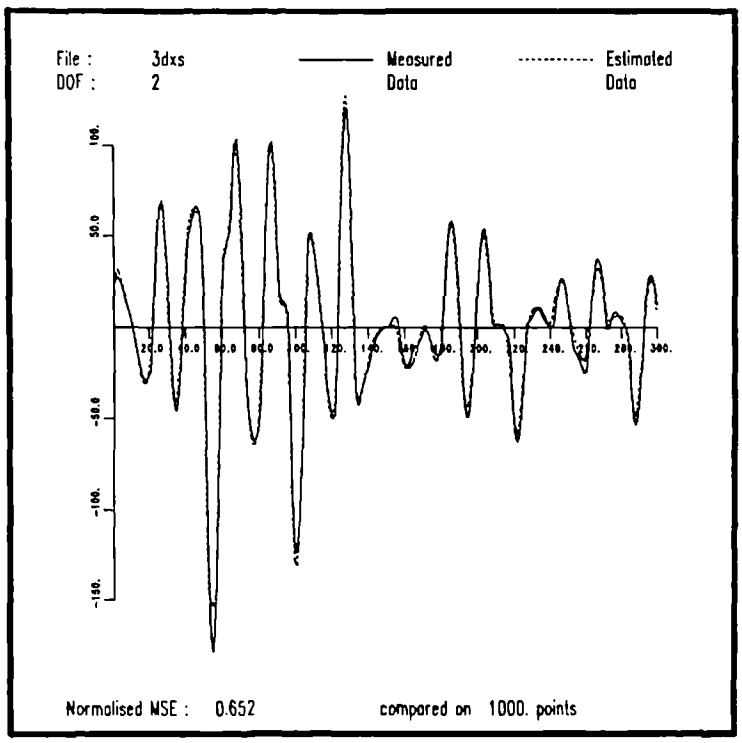

Figure 5.8. Comparison of the measured and predicted data for the three degree-of-freedom piecewise-linear system described in the text.

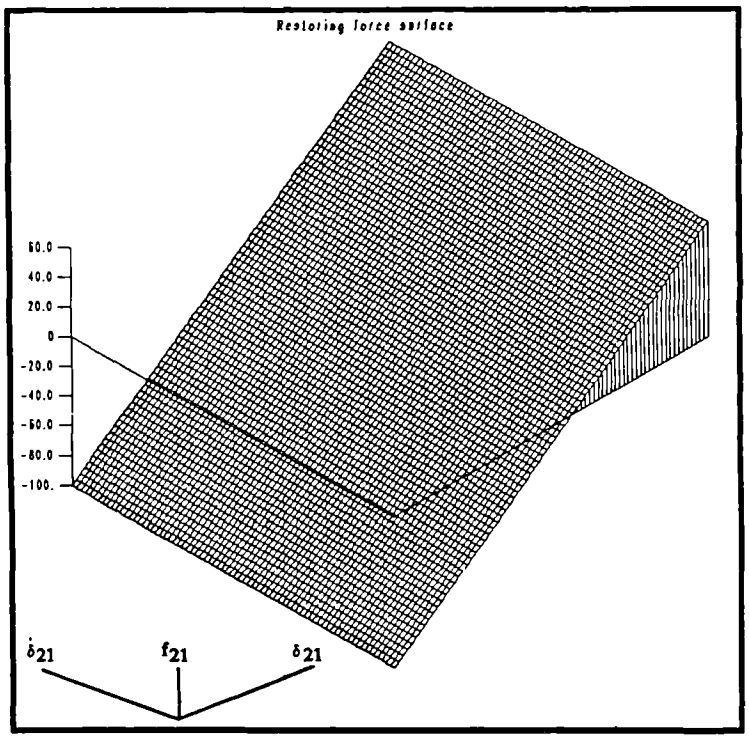

Figure 5.9. Restoring force surface for link l_{21} of the three degree-of-freedom piecewise-linear system.

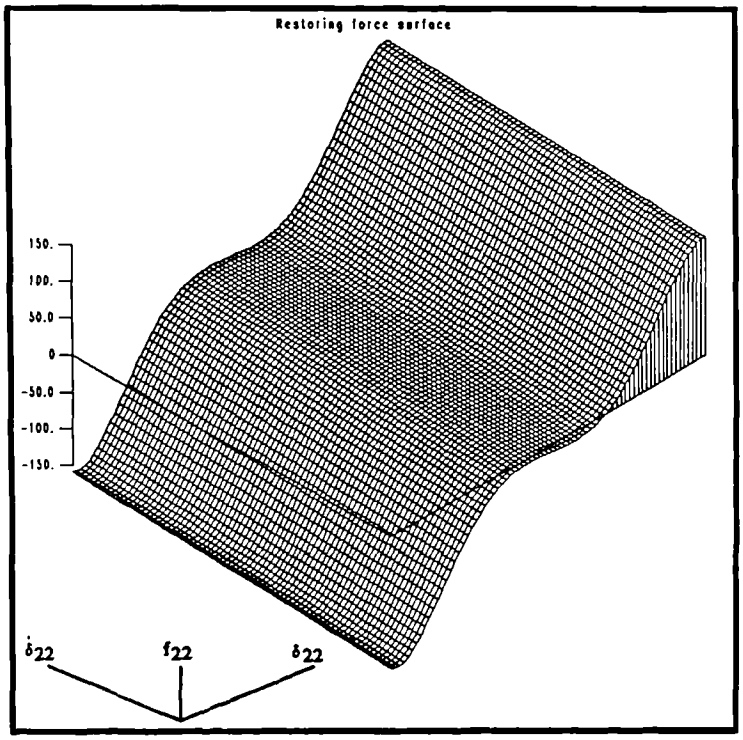

Figure 5.10. Restoring force surface for link l_{22} of the three degree-of-freedom piecewise-linear system.

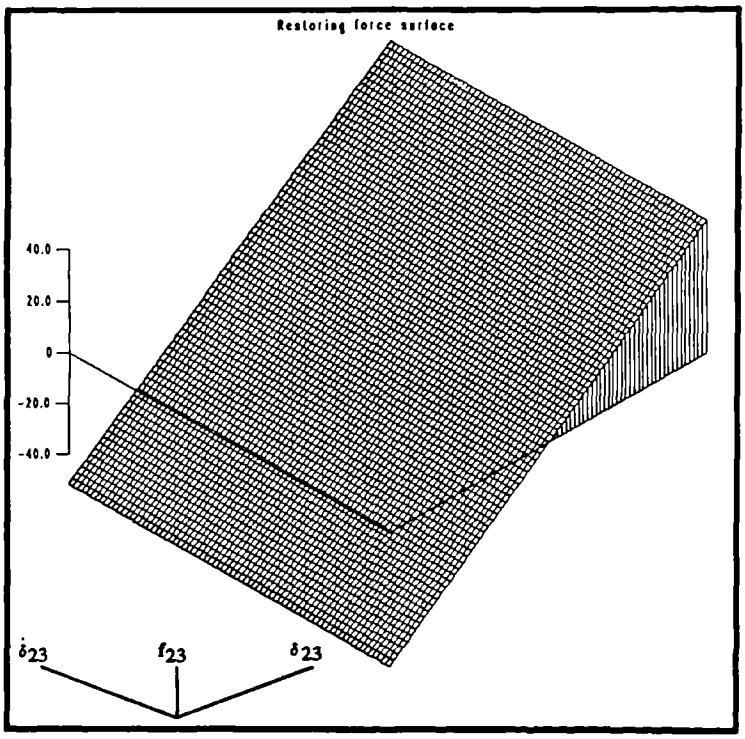

Figure 5.11. Restoring force surface for link l_{23} of the three degree-of-freedom piecewise-linear system.

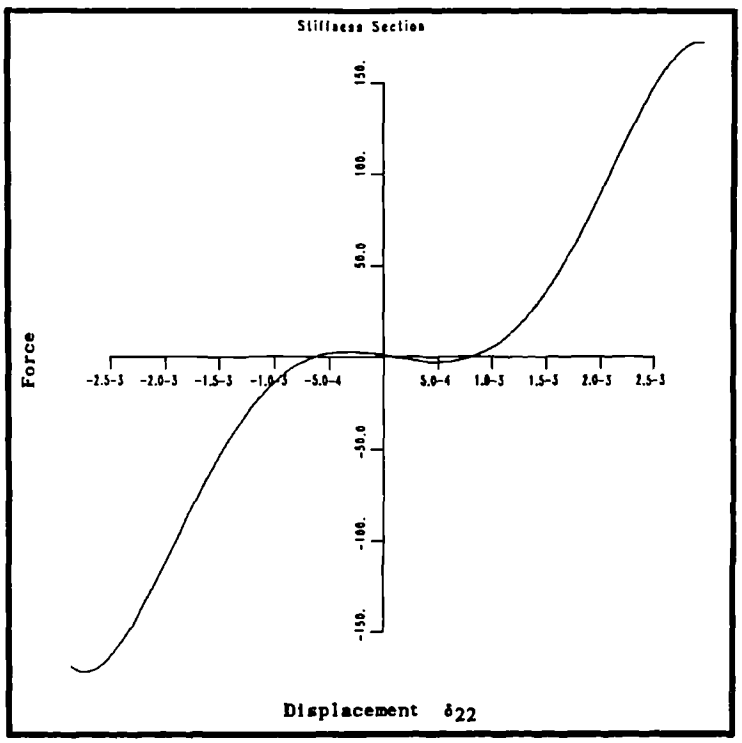

Figure 5.12. Stiffness section for link l_{22} of the three degree-of freedom piecewise-linear system.

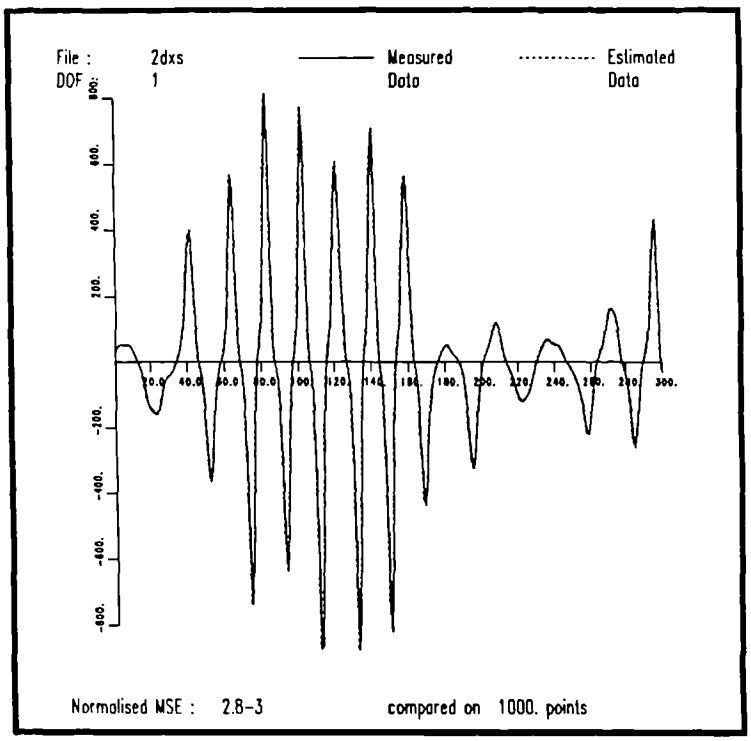

Figure 5.13. Comparison of the measured data and that predicted by the *Chebyshev model for the two degree-of-freedom* nonlinear system described in the text.

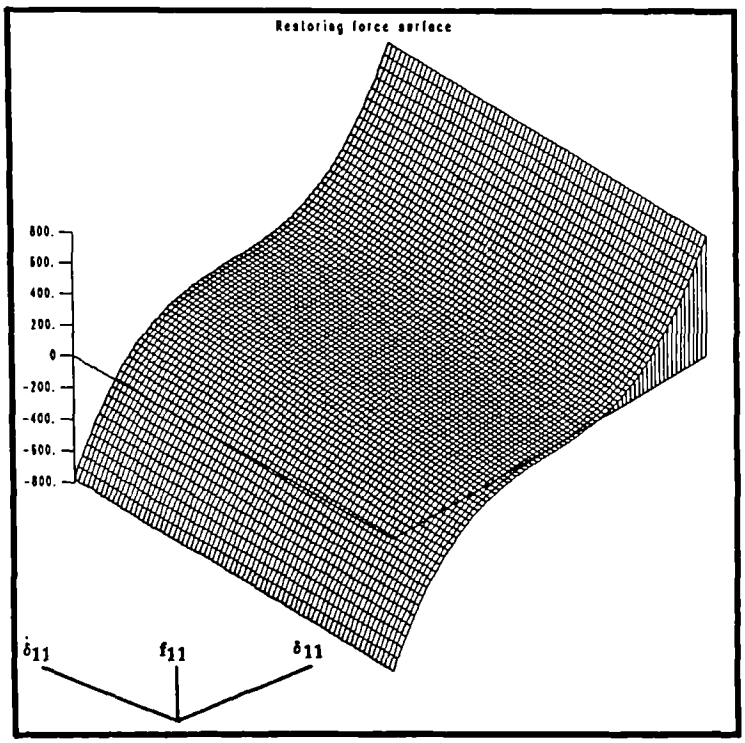

Figure 5.14. Restoring force surface for link l_{11} of the two degree-of-freedom nonlinear system.

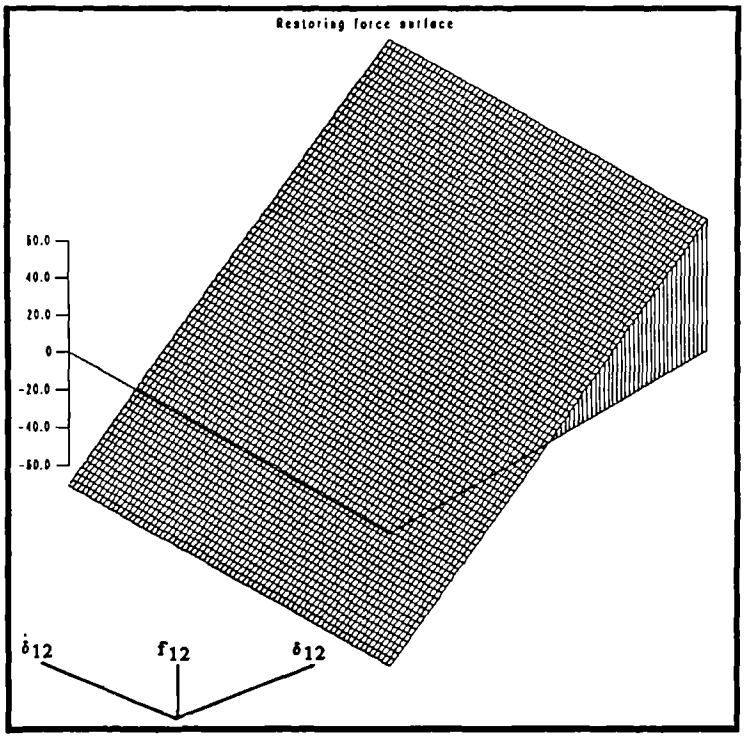

Figure 5.15. Restoring force surface for link l_{12} of the two degree-of-freedom nonlinear system.

```
Coefficients for system : 3dgn

Corrected mass value :  0.10000000e+01

* Coefficients for links to node  1

  a( 1: 0: 0) -0.27015250e-06   s( 1: 0: 0)  0.53124822e-12
  a( 1: 0: 1)  0.20000341e+02   s( 1: 0: 1)  0.16480259e+01
  a( 1: 0: 2)  0.26861641e-02   s( 1: 0: 2)  0.44208921e-10
  a( 1: 1: 0)  0.10000034e+05   s( 1: 1: 0)  0.29682320e+02
  a( 1: 1: 1)  0.33385888e+00   s( 1: 1: 1)  0.13964462e-10
  a( 1: 1: 2) -0.10858138e+02   s( 1: 1: 2)  0.16170400e-10
  a( 1: 2: 0)  0.36508930e+02   s( 1: 2: 0)  0.39551692e-10
  a( 1: 2: 1) -0.11950016e+04   s( 1: 2: 1)  0.13490104e-10
  a( 1: 2: 2) -0.46904848e+05   s( 1: 2: 2)  0.17651131e-10

  a( 2: 0: 0)  0.00000000e+00   s( 2: 0: 0)  0.00000000e+00
  a( 2: 0: 1)  0.20000147e+02   s( 2: 0: 1)  0.23590772e+01
  a( 2: 0: 2) -0.22302293e-03   s( 2: 0: 2)  0.61093925e-12
  a( 2: 1: 0)  0.10000023e+05   s( 2: 1: 0)  0.27643862e+02
  a( 2: 1: 1)  0.10646132e+00   s( 2: 1: 1)  0.19950211e-11
  a( 2: 1: 2)  0.59412336e+01   s( 2: 1: 2)  0.10862791e-10
  a( 2: 2: 0)  0.25976746e+02   s( 2: 2: 0)  0.18421197e-10
  a( 2: 2: 1) -0.30048757e+04   s( 2: 2: 1)  0.13477504e-09
  a( 2: 2: 2) -0.45049990e+04   s( 2: 2: 2)  0.43657805e-12

  a( 3: 0: 0)  0.00000000e+00   s( 3: 0: 0)  0.00000000e+00
  a( 3: 0: 1) -0.46000932e-03   s( 3: 0: 1)  0.10569973e-08
  a( 3: 0: 2) -0.18796795e-02   s( 3: 0: 2)  0.33824214e-10
  a( 3: 1: 0) -0.62280431e-01   s( 3: 1: 0)  0.13133679e-08
  a( 3: 1: 1) -0.17510749e+00   s( 3: 1: 1)  0.61872209e-11
  a( 3: 1: 2)  0.26819061e+02   s( 3: 1: 2)  0.23976496e-09
  a( 3: 2: 0) -0.41100540e+02   s( 3: 2: 0)  0.77515896e-10
  a( 3: 2: 1)  0.18889279e+04   s( 3: 2: 1)  0.82161791e-10
  a( 3: 2: 2)  0.11959226e+05   s( 3: 2: 2)  0.47902606e-11

* MSE estimate :  0.41215276e-09

* Coefficients for links to node  1

  a( 1: 0: 1)  0.20000341e+02   std( 1: 0: 1)  0.71176721e-04
  a( 1: 1: 0)  0.10000034e+05   std( 1: 1: 0)  0.83949631e-02

  a( 2: 0: 1)  0.20000147e+02   std( 2: 0: 1)  0.98503740e-04
  a( 2: 1: 0)  0.10000023e+05   std( 2: 1: 0)  0.83066123e-02


* MSE estimate :  0.23891757e-08

* Linear/Nonlinear link classification

( Node1  ) to ( Ground )

Linear stiffness
Linear damping


( Node1  ) to ( Node2  )

Linear stiffness
Linear damping


( Node1  ) to ( Node3  )

No direct stiffness term
No direct damping term
```

Table 5.1. Coefficients for a (2,2) model for the restoring force in the first equation of motion for the three degree-of-freedom linear system described in the text.

```
* Coefficients for system : 3dgn

* Degree of freedom :  2

* Mass normalised to :  1

* Coefficients for links to node  2

  a( 1: 0: 0)  0.10430813e-06   s( 1: 0: 0)  0.00000000e+00
  a( 1: 0: 1)  0.99999971e+01   s( 1: 0: 1)  0.42133803e+01
  a( 1: 0: 2) -0.27772916e-04   s( 1: 0: 2)  0.41360605e-13
  a( 1: 1: 0)  0.50000020e+04   s( 1: 1: 0)  0.49358498e+02
  a( 1: 1: 1) -0.52834094e-01   s( 1: 1: 1)  0.35107585e-11
  a( 1: 1: 2) -0.13604659e+01   s( 1: 1: 2)  0.40556694e-11
  a( 1: 2: 0)  0.45638328e+01   s( 1: 2: 0)  0.25004066e-11
  a( 1: 2: 1) -0.11591269e+03   s( 1: 2: 1)  0.14329562e-11
  a( 1: 2: 2)  0.12617638e+05   s( 1: 2: 2)  0.19628793e-10

  a( 2: 0: 0)  0.00000000e+00   s( 2: 0: 0)  0.00000000e+00
  a( 2: 0: 1)  0.29099136e-04   s( 2: 0: 1)  0.64883975e-11
  a( 2: 0: 2) -0.52818246e-04   s( 2: 0: 2)  0.51004360e-14
  a( 2: 1: 0) -0.16868679e-02   s( 2: 1: 0)  0.44532707e-11
  a( 2: 1: 1)  0.90017155e-01   s( 2: 1: 1)  0.21740235e-11
  a( 2: 1: 2)  0.78195316e+00   s( 2: 1: 2)  0.72112692e-13
  a( 2: 2: 0) -0.19539708e+01   s( 2: 2: 0)  0.35033703e-12
  a( 2: 2: 1) -0.50522065e+01   s( 2: 2: 1)  0.65214681e-15
  a( 2: 2: 2) -0.25536506e+05   s( 2: 2: 2)  0.67606307e-11

  a( 3: 0: 0)  0.00000000e+00   s( 3: 0: 0)  0.00000000e+00
  a( 3: 0: 1)  0.99999828e+01   s( 3: 0: 1)  0.11914002e+01
  a( 3: 0: 2)  0.28971603e-03   s( 3: 0: 2)  0.41942052e-12
  a( 3: 1: 0)  0.50000029e+04   s( 3: 1: 0)  0.27035810e+02
  a( 3: 1: 1)  0.16240120e+00   s( 3: 1: 1)  0.61468452e-11
  a( 3: 1: 2)  0.28669672e+01   s( 3: 1: 2)  0.11737759e-11
  a( 3: 2: 0) -0.32610195e+01   s( 3: 2: 0)  0.41172624e-12
  a( 3: 2: 1)  0.35777969e+03   s( 3: 2: 1)  0.16480470e-11
  a( 3: 2: 2)  0.17435625e+05   s( 3: 2: 2)  0.18928195e-11

* MSE estimate :  0.75774713e-10
```

```
* Coefficients for system : 3dgn

* Degree of freedom :  2

* Mass normalised to :  1

* Coefficients for links to node  2

  a( 1: 0: 1)  0.99999971e+01   std( 1: 0: 1)  0.24658699e+01
  a( 1: 1: 0)  0.50000020e+04   std( 1: 1: 0)  0.40651462e+03

  a( 3: 0: 1)  0.99999828e+01   std( 3: 0: 1)  0.65258298e+01
  a( 3: 1: 0)  0.50000029e+04   std( 3: 1: 0)  0.55061536e+03

* MSE estimate :  0.30231793e-10

* Linear/Nonlinear link classification

  ( Node2  ) to ( Node1  )

  Linear stiffness
  Linear damping

  ( Node2  ) to ( Ground )

  No direct stiffness term
  No direct damping term

  ( Node2  ) to ( Node3  )

  Linear stiffness
  Linear damping
```

Table 5.2. Coefficients for a (2,2) model for the restoring force in the second equation of motion for the three degree-of-freedom linear system described in the text.

```
* Coefficients for system : 3dgn

* Degree of freedom :  3

* Mass normalised to :  1


* Coefficients for links to node  3

  a( 1: 0: 0)  0.29802322e-07   a( 1: 0: 0)  0.00000000e+00
  a( 1: 0: 1) -0.72665630e-05   a( 1: 0: 1)  0.62229536e-11
  a( 1: 1: 0)  0.83409500e-03   a( 1: 1: 0)  0.55571216e-11
  a( 1: 1: 1)  0.94259717e-02   a( 1: 1: 1)  0.42303343e-12

  a( 2: 0: 0)  0.00000000e+00   a( 2: 0: 0)  0.00000000e+00
  a( 2: 0: 1)  0.66666503e+01   a( 2: 0: 1)  0.17486160e+01
  a( 2: 1: 0)  0.33333335e+04   a( 2: 1: 0)  0.39680428e+02
  a( 2: 1: 1) -0.15067588e+00   a( 2: 1: 1)  0.17473550e-10

  a( 3: 0: 0)  0.00000000e+00   a( 3: 0: 0)  0.00000000e+00
  a( 3: 0: 1)  0.66666884e+01   a( 3: 0: 1)  0.64820707e+00
  a( 3: 1: 0)  0.33333342e+04   a( 3: 1: 0)  0.37209972e+02
  a( 3: 1: 1)  0.13366137e+00   a( 3: 1: 1)  0.47059552e-11

* MSE estimate :  0.37391396e-10
```

```
* Linear/Nonlinear link classification

  ( Node3  ) to ( Node1  )

  No direct stiffness term
  No direct damping term

  ( Node3  ) to ( Node2  )

  Linear stiffness
  Linear damping

  ( Node3  ) to ( Ground )

  Linear stiffness
  Linear damping
```

```
* Coefficients for system : 3dgn

* Degree of freedom :  3

* Mass normalised to :  1


* Coefficients for links to node  3

  a( 2: 0: 1)  0.66666503e+01 · std( 2: 0: 1)  0.31552546e+01
  a( 2: 1: 0)  0.33333335e+04   std( 2: 1: 0)  0.24146648e+03

  a( 3: 0: 1)  0.66666884e+01   std( 3: 0: 1)  0.42166753e+01
  a( 3: 1: 0)  0.33333342e+04   std( 3: 1: 0)  0.22208449e+03

* MSE estimate :  0.85419441e-11
```

Table 5.3. Coefficients for a (1,1) model for the restoring force in the third equation of motion for the three degree-of-freedom linear system described in the text.

```
* Coefficients for system : 3dxs

* Degree of freedom :  2

* Mass normalised to :  1

* Coefficients for links to node  2

  a( 1: 0: 0)  0.46875000e+00   s( 1: 0: 0)  0.00000000e+00
  a( 1: 0: 1) -0.79775929e+00   s( 1: 0: 1)  0.56869248e-02
  a( 1: 1: 0)  0.98404717e+04   s( 1: 1: 0)  0.41040012e+02
  a( 1: 1: 1) -0.31077484e+03   s( 1: 1: 1)  0.91483267e-02
  a( 1: 2: 0)  0.14878655e+05   s( 1: 2: 0)  0.18364912e-02
  a( 1: 2: 1)  0.60797320e+05   s( 1: 2: 1)  0.10307074e-01
  a( 1: 3: 0) -0.27214025e+05   s( 1: 3: 0)  0.46341879e-06
  a( 1: 3: 1)  0.13726579e+08   s( 1: 3: 1)  0.24307223e-01
  a( 1: 4: 0) -0.32680982e+09   s( 1: 4: 0)  0.37655998e-02
  a( 1: 4: 1) -0.10671901e+10   s( 1: 4: 1)  0.88438960e-02
  a( 1: 5: 0)  0.51883495e+11   s( 1: 5: 0)  0.81053088e-02
  a( 1: 5: 1) -0.36810928e+11   s( 1: 5: 1)  0.74169907e-03

  a( 2: 0: 0)  0.00000000e+00   s( 2: 0: 0)  0.00000000e+00
  a( 2: 0: 1)  0.18967934e+02   s( 2: 0: 1)  0.59915763e+00
  a( 2: 1: 0) -0.10891846e+05   s( 2: 1: 0)  0.73256378e+01
  a( 2: 1: 1)  0.31143822e+02   s( 2: 1: 1)  0.25816371e-05
  a( 2: 2: 0) -0.79514194e+06   s( 2: 2: 0)  0.67692816e-01
  a( 2: 2: 1)  0.17363463e+06   s( 2: 2: 1)  0.25943998e-03
  a( 2: 3: 0)  0.21569210e+11   s( 2: 3: 0)  0.44685974e+03
  a( 2: 3: 1)  0.15855643e+09   s( 2: 3: 1)  0.92506240e-03
  a( 2: 4: 0)  0.15137048e+12   s( 2: 4: 0)  0.96410140e-01
  a( 2: 4: 1)  0.21795781e+10   s( 2: 4: 1)  0.87967197e-06
  a( 2: 5: 0) -0.15749357e+16   s( 2: 5: 0)  0.82025551e+02
  a( 2: 5: 1) -0.35739039e+14   s( 2: 5: 1)  0.13247784e-02

  a( 3: 0: 0)  0.00000000e+00   s( 3: 0: 0)  0.00000000e+00
  a( 3: 0: 1)  0.42104995e+00   s( 3: 0: 1)  0.65863825e-03
  a( 3: 1: 0)  0.10239522e+05   s( 3: 1: 0)  0.14496451e+02
  a( 3: 1: 1) -0.14881815e+04   s( 3: 1: 1)  0.28775388e-01
  a( 3: 2: 0) -0.65482078e+05   s( 3: 2: 0)  0.34021973e-02
  a( 3: 2: 1) -0.28882272e+06   s( 3: 2: 1)  0.93791541e-02
  a( 3: 3: 0) -0.43512320e+08   s( 3: 3: 0)  0.32804970e-01
  a( 3: 3: 1)  0.24512290e+09   s( 3: 3: 1)  0.83601765e-01
  a( 3: 4: 0)  0.53234135e+10   s( 3: 4: 0)  0.67991163e-02
  a( 3: 4: 1)  0.17008454e+11   s( 3: 4: 1)  0.60762619e-02
  a( 3: 5: 0)  0.17532288e+13   s( 3: 5: 0)  0.16272387e-01
  a( 3: 5: 1) -0.74630504e+13   s( 3: 5: 1)  0.19984940e-01

* MSE estimate :  0.62136430e+00
```

```
* Coefficients for system : 3dxs

* Degree of freedom :  2

* Mass normalised to :  1

* Coefficients for links to node  2

  a( 1: 1: 0)  0.98404717e+04   std( 1: 1: 0)  0.14770295e+04

  a( 2: 0: 1)  0.18967934e+02   std( 2: 0: 1)  0.17072847e+02
  a( 2: 1: 0) -0.10891846e+05   std( 2: 1: 0)  0.43369180e+04
  a( 2: 3: 0)  0.21569210e+11   std( 2: 3: 0)  0.24345833e+10
  a( 2: 5: 0) -0.15749357e+16   std( 2: 5: 0)  0.29756899e+15

  a( 3: 1: 0)  0.10239522e+05   std( 3: 1: 0)  0.25475056e+04

* MSE estimate :  0.65195405e+00

* Linear/Nonlinear link classification

  ( Node2  ) to ( Node1  )

  Linear stiffness
  No direct damping term

  ( Node2  ) to ( Ground )

  Nonlinear stiffness : order  5
  Linear damping

  ( Node2  ) to ( Node3  )

  Linear stiffness
  No direct damping term
```

Table 5.4. Coefficients for a (5,1) model for the restoring force in the second equation of motion for the three degree-of-freedom piecewise-linear system described in the text.

```
 * Parameter Estimates (RLS)

 * System : 3dgn

 * Mass matrix :

 0.99999839e+00 0.00000000e+00 0.00000000e+00
 0.00000000e+00 0.19999906e+01 0.00000000e+00
 0.00000000e+00 0.00000000e+00 0.29999747e+01

 * Damping matrix :

 0.40000031e+02-0.19999849e+02-0.36170371e-04
-0.19999849e+02 0.40000050e+02-0.19999994e+02
-0.36170371e-04-0.19999994e+02 0.39999783e+02

 * Stiffness matrix :

 0.19999957e+05-0.99999854e+04-0.21662798e-02
-0.99999854e+04 0.19999932e+05-0.99999482e+04
-0.21662798e-02-0.99999482e+04 0.19999857e+05

 * MSE (1) :  0.25008928e-09
 * MSE (2) :  0.53652155e-09
 * MSE (3) :  0.84677570e-09

 * Significant coefficients

 * Mass matrix :

 0.99999839e+00 0.00000000e+00 0.00000000e+00
 0.00000000e+00 0.19999906e+01 0.00000000e+00
 0.00000000e+00 0.00000000e+00 0.29999747e+01

 * Damping matrix :

 0.40000031e+02-0.19999849e+02 0.00000000e+00
-0.19999849e+02 0.40000050e+02-0.19999994e+02
 0.00000000e+00-0.19999994e+02 0.39999783e+02

 * Stiffness matrix :

 0.19999957e+05-0.99999854e+04 0.00000000e+00
-0.99999854e+04 0.19999932e+05-0.99999482e+04
 0.00000000e+00-0.99999482e+04 0.19999857e+05

 * MSE (1) :  0.24832336e-09
 * MSE (2) :  0.53652155e-09
 * MSE (3) :  0.84677570e-09
```

Table 5.5. *Estimates for the mass, damping and stiffness matrices for the three degree-of-freedom linear system. The estimates were obtained using Mohammad's method.*

```
 * Parameter Estimates (RLS)

 * System : 2dxs

 * Mass matrix :

 0.74999833e+00 0.00000000e+00
 0.00000000e+00 0.20207560e+00

 * Damping matrix :

 0.20000023e+02-0.99999847e+01
 0.49932465e+02 0.39964729e+02

 * Stiffness matrix :

 0.24999930e+05-0.19999951e+05
-0.19999951e+05 0.25436526e+04

 * MSE (1) :  0.45953530e-09
 * MSE (2) :  0.87909889e+02

 * Significant coefficients

 * Mass matrix :

 0.74999833e+00 0.00000000e+00
 0.00000000e+00 0.20207560e+00

 * Damping matrix :

 0.20000023e+02-0.99999847e+01
 0.49932465e+02 0.39964729e+02

 * Stiffness matrix :

 0.24999930e+05-0.19999951e+05
-0.19999951e+05 0.25436526e+04

 * MSE (1) :  0.45953530e-09
 * MSE (2) :  0.87909889e+02
```

Table 5.6. Estimates of the parameter matrices for the two degree-of-freedom system with full mass matrix described in the text.

```
Coefficients for system : 2dxs

Corrected mass value :  0.10000000e+01

* Coefficients for links to node  1

  a( 1: 0: 0)  0.18520263e+01   s( 1: 0: 0)  0.62783058e-02
  a( 1: 0: 1)  0.36223049e+02   s( 1: 0: 1)  0.39605850e+00
  a( 1: 0: 2)  0.12941776e-02   s( 1: 0: 2)  0.18616448e-08
  a( 1: 1: 0)  0.62420959e+03   s( 1: 1: 0)  0.15486536e+03
  a( 1: 1: 1) -0.10509141e-02   s( 1: 1: 1)  0.63281248e-10
  a( 1: 1: 2) -0.59868689e-02   s( 1: 1: 2)  0.89234407e-08
  a( 1: 2: 0)  0.41793460e+00   s( 1: 2: 0)  0.16855686e-03
  a( 1: 2: 1) -0.53960116e-05   s( 1: 2: 1)  0.48265339e-14
  a( 1: 2: 2)  0.30285801e-03   s( 1: 2: 2)  0.53514162e-10
  a( 1: 3: 0)  0.19026918e+03   s( 1: 3: 0)  0.35333511e+02
  a( 1: 3: 1) -0.11979634e-02   s( 1: 3: 1)  0.22348071e-09
  a( 1: 3: 2) -0.54068589e-02   s( 1: 3: 2)  0.17681291e-07
  a( 1: 4: 0)  0.25696785e-03   s( 1: 4: 0)  0.56315379e-10
  a( 1: 4: 1) -0.17608661e-03   s( 1: 4: 1)  0.46051544e-11
  a( 1: 4: 2) -0.12522335e-03   s( 1: 4: 2)  0.78322401e-11

  a( 2: 0: 0)  0.00000000e+00   s( 2: 0: 0)  0.00000000e+00
  a( 2: 0: 1)  0.12020324e-02   s( 2: 0: 1)  0.52328170e-09
  a( 2: 0: 2) -0.18195603e-02   s( 2: 0: 2)  0.34348095e-08
  a( 2: 1: 0)  0.70899879e+02   s( 2: 1: 0)  0.16297904e+01
  a( 2: 1: 1)  0.12953313e-02   s( 2: 1: 1)  0.88816773e-10
  a( 2: 1: 2)  0.18344108e-01   s( 2: 1: 2)  0.65627908e-07
  a( 2: 2: 0) -0.17923253e-02   s( 2: 2: 0)  0.32923229e-08
  a( 2: 2: 1)  0.46465470e-03   s( 2: 2: 1)  0.47630590e-10
  a( 2: 2: 2) -0.14145105e-02   s( 2: 2: 2)  0.11296368e-08
  a( 2: 3: 0)  0.70565101e-02   s( 2: 3: 0)  0.48804360e-07
  a( 2: 3: 1)  0.11076084e-02   s( 2: 3: 1)  0.22483768e-09
  a( 2: 3: 2)  0.10501681e-01   s( 2: 3: 2)  0.62521650e-07
  a( 2: 4: 0) -0.66733838e-03   s( 2: 4: 0)  0.39058207e-09
  a( 2: 4: 1)  0.22744841e-03   s( 2: 4: 1)  0.90791723e-11
  a( 2: 4: 2) -0.48009027e-03   s( 2: 4: 2)  0.11422117e-09

* MSE estimate :  0.57634701e-08

* Coefficients for links to node  1

  a( 1: 0: 1)  0.36223049e+02   std( 1: 0: 1)  0.39852451e+02
  a( 1: 1: 0)  0.62420959e+03   std( 1: 1: 0)  0.34696133e+02
  a( 1: 3: 0)  0.19026918e+03   std( 1: 3: 0)  0.34092312e+02

  a( 2: 1: 0)  0.70899879e+02   std( 2: 1: 0)  0.11539881e+03

* MSE estimate :  0.27749063e-02

* Link maxima and minima

 Link no.      dmin          dmax          vmin          vmax

       1    -.5337e-020.5341e-02-.1770e+010.1853e+01
       2    -.7030e-020.7147e-02-.1870e+010.1947e+01

* Linear/Nonlinear link classification

  ( Node1  ) to ( Ground )

  Nonlinear stiffness : order  3
  Linear damping

  ( Node1  ) to ( Node2  )

  Linear stiffness
  No direct damping term
```

Table 5.7. Coefficients for a (4,2) Chebyshev model for the restoring force in the first equation of motion for the two degree-of-freedom nonlinear system described in the text.

CHAPTER 6

INTEGRATION AND DIFFERENTIATION OF MEASURED TIME DATA

The arguments of the previous chapters indicate that as the restoring force methods can accurately identify the equations of motion for simulated dynamical systems, they show a great deal of promise as a means of identifying real structures. The main problem with the methods is that the displacement, velocity and acceleration must be obtained simultaneously at each sampling instant. This would require a great deal of equipment, particularly for MDOF systems. For each degree-of-freedom one would require four transducers and four charge amplifiers. Instrumentation is also required to sample the data and carry out the analogue to digital conversion. A truly pragmatic approach to the procedure demands that only one signal should be measured and the other two should be estimated from it. This chapter is concerned with determining which signal should be measured and which numerical integration and/or differentiation procedures should be used to determine the other two. As the work progressed, a similar study by Stephens and Yao **(54)** was brought to the attention of the author. Their paper describes various methods of data processing for earthquake acceleration records. The present study is rather more comprehensive and attempts to describe the results in a more analytical fashion. The other main difference between the present study and **(54)** is that when one is dealing with earthquake data, one has no control over the input excitation and consequently the output acceleration. When one is testing a mechanical structure in the laboratory (and often in practice), one has a considerable amount of flexibility in choosing the form of the input force. The next chapter attempts to determine how one can make use of this flexibility. This chapter is concerned with the data processing problems. If one is only going to measure one type of output signal per degree-of-freedom, one is essentially faced with two choices.

a) One can measure $\ddot{y}(t)$ and numerically integrate the signal to produce $\dot{y}(t)$ and $y(t)$.

b) One can measure $y(t)$ and numerically differentiate to obtain $\dot{y}(t)$ and $\ddot{y}(t)$.

There are of course other strategies, Crawley and O'Donnell (55) measure displacement and acceleration and then form the velocity using an optimisation scheme. However, the present work is concerned with reporting results obtained in trying to implement procedures a) and b) on a digital computer. (Analogue integration has been used with a certain amount of success (25), however it does suffer from most of the problems which arise in the numerical or digital integration.)

The methods of integration considered fall into two categories. (1) Time domain methods i.e. the trapezium rule, Simpson's rule and Tick's rule. (2) Frequency domain methods, i.e Fourier transform methods. It is assumed throughout that the data is sampled correctly i.e. the sampling frequency is high enough to eliminate aliasing problems. Shannon's theorem demands that one should sample at a frequency at least twice the highest frequency of interest in the data. Some of the methods applied in this chapter require the time signal to vary smoothly from sample point to sample point, for this reason the data is usually sampled at over ten times the highest frequency of interest.

6.1. Time Domain Integration.

There are two main problems associated with the integration, the introduction of spurious low frequency components into the integrated signal and the introduction of high frequency components. By using the techniques developed later in section 6.1.3 one can show that the trapezium rule only suffers from the first of these problems. For this reason the trapezium rule is used in the following discussion.

6.1.1. Low Frequency Problems.

In this chapter the data is usually obtained from a computer simulation of the system described by the equation of motion,

$$\ddot{y} + 40\dot{y} + 10^4 y = x(t)$$

where x(t) is a Gaussian white noise sequence $\bar{x} = 0$, $\sigma_x = 1.0$. The system was simulated using a fourth-order Runge-Kutta procedure. The time-step or sampling interval was 0.001 seconds, giving a sampling frequency of 1 kHz. As usual, a low-pass Butterworth filter was used on the input to produce a signal in the range 0 - 200 Hz. The undamped natural frequency of the system above is 100 rad/s or 15.92 Hz. This means that the sampling is carried out at approximately thirty times the highest frequency of interest. Clearly aliasing is not a problem.

As y, $\dot{y}$ and $\ddot{y}$ are all available from the simulation one can compare the result of the integration procedures with the 'exact' results. When a least-squares model of the form

$$m\ddot{y} + c\dot{y} + ky + \alpha = x$$

was fitted to the data, the results were

$$\hat{m} = 1.0000000$$

$$\hat{c} = 40.000000$$

$$\hat{k} = 1.0000001 \times 10^4$$

$$\bar{\alpha} = 0.0$$

and the model MSE was zero. Because of this result one can be confident that in future, any errors in the parameters reflect the accuracy of the integration procedure and not that of the parameter estimation algorithm. The force surface obtained from

this simulation is shown in Figure 6.1. The flatness of the surface clearly reflects the fact that the system is linear.

A number of attempts were made to obtain force surfaces by integrating the simulated $\ddot{y}(t)$ data.

Example 1. The trapezium rule

$$y_i' = y_{i-1}' + \frac{\Delta t}{2} (y_i + y_{i-1}) \qquad (1)$$

(where ' indicates the integrated signal) was used to integrate the data $\ddot{y}(t_k)$. Each step introduced a constant of integration

$$\dot{y}(t) = \int dt\ \ddot{y}(t) + A$$

$$y(t) = \int dt\ \dot{y}(t) + At + B$$

One can clearly see the spurious mean level A in $\dot{y}$ and the linear drift component At + B in y in Figures 6.2 and 6.3. Alternatively if one looked at the Fourier transforms or spectra for $\dot{y}(t)$ and y(t) one would see an unwanted peak in the low frequencies (Figures 6.4 and 6.5). The $\omega = 0$ or d.c. line is most severely affected. A least-squares parameter fit to the estimated data produced the model

Coefficient	% error
$\hat{m} = 0.773$	2.27
$\hat{c} = 42.9$	7.25
$\hat{k} = 0.968 \times 10^4$	3.2
$\hat{\alpha} = -0.11$	∞

and the model MSE i.e. MSE(f) is 69.8%. The parameter fit isn't too bad considering how corrupt the data is. However, plotting the force surface produces the

result shown in Figure 6.6. It is impossible to infer linearity of the system from this surface.

Usually when one integrates a function the constant of integration is fixed by say, initial data $\dot{y}(0) = A$. Unfortunately when one is dealing with a stream of time data one does not have such a condition. However, under certain conditions (x(t) is a zero-mean sequence, $f(y,\dot{y})$ is an odd function of it's arguments) one can assume that $\dot{y}(t)$ and y(t) are zero-mean signals. This means that one can set A and B equal to the appropriate values by removing the mean level from $\dot{y}(t)$ and removing a least-squares linear trend from y(t).

Example 2. Again the signal $\ddot{y}(t)$ was integrated twice using the trapezium rule. The mean of the resulting signal $\dot{y}(t)$ was estimated and removed numerically. Similarly, a least-squares straight line was fitted to the y(t) data and removed. The comparison between the exact and estimated signals is shown in Figures 6.7 and 6.8. The estimate is much better, $MSE(\dot{y}) = 0.718$ and $MSE(y) = 12.4$. It is clear that the mean removal is sufficient to fix the velocity estimate to a high order of accuracy, however, higher order polynomial trends remain in the displacement and these must be removed by other methods. The parameter estimates for this data are

Coefficient	% error
$\hat{m} = 0.997$	0.3
$\hat{c} = 40.02$	0.05
$\hat{k} = 0.939 \times 10^4$	6.1
$\hat{a} = 0.068$	∞

and the MSE for the model is 7.18%. The force surface obtained is shown in Figure 6.9. The force surface and model coefficients are much better now, but the surface still does not compare favourably with the 'exact' one. One can improve the results by removing higher order trends from the displacement. Before discussing this, another effect is worth mentioning. When one measures x(t) and $\ddot{y}(t)$ it is possible that a

d.c./mean level can be introduced by the instrumentation. Before constructing the force surface this must be removed. It seems reasonable to do this before the integration step. However, this may cause problems. Although $\ddot{y}(t)$ may be a zero-mean signal any *finite* sample of $\ddot{y}$ will have a non-zero mean value $\ddot{y}_s$, so subtracting this produces a signal $\ddot{y} - \ddot{y}_s$ which is not zero-mean. Integrating this signal, one obtains

$$\dot{y}(t) = \int dt\ \ddot{y}(t) - \ddot{y}_s t + A$$

$$y(t) = \int dt\ \dot{y}(t) - \frac{\ddot{y}_s}{2}.t^2 + At + B$$

and it is now necessary to remove a linear trend from $\dot{y}(t)$ and a quadratic trend from y(t). The rather dramatic result of removing the $\ddot{y}$ mean initially on the integrated displacement is shown in Figure 6.10.

It is obvious from the examples above that one is not removing all the low-frequecy contamination from the displacement signal. There are essentially two ways of removing low-frequency trends, namely least-squares polynomial trend removal and high-pass filtering.

First, polynomial trend removal is considered. A model of the form

$$y(t) = \sum_{n=1}^{nmax} a_n t^n$$

is fitted and the identified trend is removed from the data. The results of fitting and removing polynomials of various orders are displayed in Table 6.1. It is clear from the table that there is little point in removing trends of order higher than n = 6. In fact, if one removes trends of too high an order, one is also removing low frequency data which should be there. This means that the MSE begins to increase with polynomial order after passing through a (rather shallow) minimum.

The alternative to this is high-pass filtering. Again, a balancing act is required. If the

chosen cut-off is too low the data remains corrupted. If the cut-off is too high one removes data which should be there. It is unfortunate, but there appears to be no simple method of distinguishing between the actual data and the low-frequency noise introduced by the integration procedure. Table 6.2. shows the integration error as a function of cut-off frequency.

Example 3. The data was integrated as before. The velocity and displacement data were high-pass filtered using a digital Butterworth filter with cut-off at 1.0 Hz. The resulting data gave MSE($\dot{y}$) = 0.709 and MSE(y) = 4.61. A least-squares fit produced the results

Coefficients	% error
$\hat{m} = 0.974$	2.6
$\hat{c} = 40.6$	1.5
$\hat{k} = 0.899 \times 10^4$	10.1
$\hat{\alpha} = 0.0$	0.0

with a model MSE of 11.2%. It is worth mentioning that as the force surface is linear, if the input force and acceleration had been filtered in the same way as the velocity and displacement data a perfect force surface would have been obtained. This is not the case for a nonlinear system as one is essentially assuming that the principle of superposition applies when one makes the above assertion.

It is a fairly simple matter to show that polynomial trend removal is equivalent to high-pass filtering. Suppose one is given a record of time data of length T seconds sampled at Δt second intervals. If one fits a polynomial of order n to the data, one can account for n zero-crossings in the record. As there are two zero-crossings per cycle, this accounts for n/2 cycles. n/2 cycles in T seconds indicates a signal of frequency $n/(2T)$ or $n/(2N\Delta t)$ where N is the number of points in the record. This means that removing a polynomial trend of order n is equivalent to high-pass filtering with cut-off $n/(2N\Delta t)$.

Filtering can be rather time consuming as the data must be passed through the filter both forwards and backwards in order to zero the phase lag introduced by a generic filter. The phase lag can manifest itself as a time delay which destroys the simultaneity of the input and output. This can produce serious distortions in the force surface.

6.1.2 High Frequency Problems.

The other two time domain methods considered here, Simpson's rule and Tick's rule both suffer from the same low-frequency problems as the trapezium rule. Unfortunately they are also unstable at high frequencies. This means that the integrated signals must be band-pass filtered rather than simply high-pass filtered.

Simpson's rule is given by

$$y'_{n+1} = y'_{n-1} + \frac{\Delta t}{3}.(y_{n+1} + 4y_n + y_{n-1}) \qquad (2)$$

where the signal y' is the integral of y as before. Tick's rule is given by the slightly more complicated formula

$$y'_{n+1} = y'_{n-1} + \Delta t.(0.3854y_{n+1} + 1.2832y_n + 0.3854y_{n-1})$$

Although the latter algorithm is slightly better over the low frequencies than Simpson's rule, it is more badly behaved i.e. more unstable at high frequencies.

Example 4. The same system as before was simulated with x(t) a Gaussian white-noise sequence band-limited to 5-40 Hz i.e. the acceleration contained no high frequency part. The data was then integrated using Tick's rule. An enormous high-frequency component was introduced into the signal as shown in Figure 6.11.

Simpson's rule is intermediate between the trapezium rule and Tick's rule i.e. it has similar low frequency behaviour and intermediate high frequency behaviour. It was

found throughout that for the examples considered, the extra accuracy offered by Simpson's rule was unimportant if the data was sampled at an appropriately high rate.

Example 5. The same signal as in example 4 above was integrated using the trapezium rule. The mean was removed from the estimated velocity and a linear drift component was removed from the estimated displacement. The resulting errors were MSE($\dot{y}$) = 0.159 and MSE(y) = 0.197. The comparisons are shown in Figures 6.12 and 6.13. An LS parameter estimation yielded the results

Coefficients	% error
$\hat{m} = 1.02$	2.0
$\hat{c} = 40.6$	1.5
$\hat{k} = 1.03 \times 10^4$	3.0
$\hat{\alpha} = 0.00$	0.0

and a model MSE of 0.08%. The force surface obtained is shown in Figure 6.14. The results are excellent. This example clearly suggests that, rather than using more complicated data processing, one should choose the excitation for the system in such a way as to minimize processing problems. After filtering the input, there appears to be so little energy in the output at low frequencies that the integration procedure does not magnify it to the extent that it becomes a problem. These ideas will be considered in more detail in the following chapter.

Integration of a signal can be thought of as the solution of the simplest type of differential equation. This means that numerical routines for the integration of ordinary differential equations could be used. Best and Stricklin (57) compare six methods, namely, the centred difference method, Runge-Kutta, Houbolt's method, Newmark's method, the Wilson theta method and the harmonic acceleration method. They test the methods on a number of second order systems. All these algorithms except the centred difference method are more complex and time consuming than those considered in this paper.

6.1.3. Frequency Characteristics of Integration Formulae.

It is now time to justify some of the remarks which have been made. Using ideas from Hammings book **(56)**, one can obtain the frequncy behaviour of the integration formulae considered above. The simplest case is the trapezium rule. In this section, a time scale is used such that $\Delta t = 1$. This means that the sampling frequency is also 1, so the Nyquist frequency is 0.5, the angular Nyquist frequency is π. Using these conventions the trapezium rule (1) becomes

$$y_i = y_{i-1} + \tfrac{1}{2}(x_i + x_{i-1})$$

where x_i is the sampled input to the algorithm, and y_i is the integral. Using the backward difference operator $Z^{-1} = \exp(-d/dt)$, one can write the formula in the form

$$(1 - Z^{-1})y_i = \tfrac{1}{2}(1 + Z^{-1})x_i$$

so

$$y_i = \tfrac{1}{2}.\frac{(1 + Z^{-1})}{(1 - Z^{-1})} x_i$$

so the pulse transfer function **(59)** for the integrator is

$$G(Z) = \tfrac{1}{2}.\frac{(1 + Z^{-1})}{(1 - Z^{-1})}$$

The more usual transfer function is obtained by simply substituting $Z = e^{i\omega}$. In this case

$$H(\omega) = \frac{(1 + e^{i\omega})}{2(1 - e^{i\omega})}$$

$$= \frac{\cos(\omega/2)}{2i.\sin(\omega/2)}$$

Now, following Hamming, one can introduce a transfer function $Ha(\omega)$, which is a useful measure of the accuracy of the formula. It is defined as

$$Ha(\omega) = \frac{F(\text{estimated result})}{F(\text{true result})}$$

Now, if $x = e^{i\omega t}$ the true integral is $e^{i\omega t}/i\omega$, and the estimated result is

$$\frac{\cos(\omega/2)}{2i.\sin(\omega/2)} . e^{i\omega t}$$

so $Ha(\omega)$ for the trapezium rule is given by

$$Ha(\omega) = \cos(\omega/2) . \left[\frac{\omega/2}{\sin(\omega/2)} \right]$$

This is equal to unity at $\omega = 0$, and monotonically decreases to zero at $\omega = \pi$. This means that the trapezium rule only integrates constant signals without error. It underestimates the integral at all other frequencies.

Now, if one considers Simpson's rule (2) in the units of this section

$$y_{i+1} = y_{i-1} + (1/3)(x_{i+1} + 4x_i + x_{i-1})$$

or

$$(Z - Z^{-1})y_i = (1/3)(Z + 4 + Z^{-1})x_i$$

and the pulse transfer function is

$$C(Z) = \frac{Z + 4 + Z^{-1}}{3(Z - Z^{-1})}$$

Giving

$$H(\omega) = \frac{2 + \cos(\omega)}{3.\sin(\omega)}$$

Probing with the signal $x = e^{i\omega t}$ yields the final result.

$$Ha(\omega) = \frac{2 + \cos(\omega)}{3(\sin(\omega)/\omega)}$$

and one can see easily that Ha(ω) tends to unity as ω tends to zero. This is the same behaviour as the trapezium rule. However, unlike the trapezium rule, Ha(ω) for Simpson's rule tends to infinity as ω approaches the Nyquist frequency, indicating instability at high frequencies. In Figure 6.15, Ha(ω) is shown for the three integration rules condidered above. It shows clearly that Simpson's rule and Tick's rule become unreliable at high frequencies. There are in fact a whole family of Tick's rules, each is designed to make Ha(ω) flat over some region of the Nyquist interval. The one considered above is flat over the first half of the interval i.e. up to f = 0.25. The penalty one pays for the flat response is that Ha(ω) tends to infinity faster beyond some frequency.

It still remains to show why these methods are unstable at low frequencies. The reason is if one considers Ha(ω) for the trapezium rule it is only the whole story if x is known to an infinite precision. If the x_i have a measurement error or simply a truncation error associated with them ζ_i, then the estimated integral is given by

$$\begin{aligned} \hat{y}_i &= G(Z).(x_i + \zeta_i) \\ &= y_i + G(Z).\zeta_i \end{aligned}$$

using the linearity of the procedure. So the error in the integral is given simply by

$$\epsilon_i = \hat{y}_i - y_i = G(Z).\zeta_i$$

So the transfer function *F*(output noise)/*F*(input noise) is given by cot(ω/2)/2i as above. This tends to infinity as ω tends to 0. This means that the trapezium rule greatly magnifies errors at low frequencies. It also shows that the integration is unstable under small perturbations. As the other two methods have the same Ha(ω) at low frequencies, they must suffer from the same problem.

In the examples considered above, the highest frequency of interest is 50Hz when the band-limited input is used. The Nyquist frequncy is 500Hz. This gives a normalised value of 0.05 for the highest frequency of interest. One can see from Figure 6.15

that up to this frequency the procedures are almost indistinguishable as regards accuracy. One is therefore justified in using the simplest rule to integrate. The trapezium rule offers a considerable saving in time if it can be used as one does not need to low-pass filter the output.

If frequencies are present in the signal up to say, one quarter of the Nyquist limit, one would probably need to use Tick's rule. At this upper limit, one can see from the diagram that $Ha(\omega)$ for the trapezium rule is less than 0.8, if one integrated twice one would only obtain 60% of the data at this frequency. If Simpson's rule were used, $Ha(\omega)$ is about 1.1 so integrating twice would give an overestimate by about 20%. One can see that Tick's rule gives a gain of unity right up to 0.25 just as it was designed to do. Figure 6.15 is of considerable use in choosing the appropriate integrator for a problem.

6.2 Frequency Domain Integration.

The theoretical basis of the Fourier transform method of integration is simple if

$$Y_a(\omega) = \int_{-\infty}^{+\infty} dt\ e^{-i\omega t}\ \ddot{y}(t) = F\{\ddot{y}(t)\}$$

is the Fourier transform (FT) of the acceleration $\ddot{y}(t)$, then $Y_a(\omega)/i\omega = Y_v(\omega)$ is the FT of the velocity and $Y_a(\omega)/(-\omega^2) = Y_d(\omega)$ is the FT of the displacement. This means that in the frequency domain, division by $i\omega$ is equivalent to integration in the time domain. The mean removal can be carried out by simply setting the $\omega = 0$ line (one uses the digital FFT) to zero. Of course, one cannot divide by i0 anyway.

At first sight this seems like a very attractive way of looking at the problem, however it turns out to be beset by the same problems as the time domain methods and also to have a few of it's own.

The first problem to arise concerns the nature of the acceleration signal. This need

not be periodic and consequently the Fourier transform will have leakage problems (58). One effect of leakage can be the introduction of low frequency trends into the acceleration signal which will be magnified by the integration. Figure 6.16 shows the Fourier transform of (a) a sine wave which was periodic over the number of points taken and (b) of a sine wave which was not. One can see that energy has 'leaked' out to higher and lower frequencies. It is the low frequencies that cause problems for integration. To avoid this one multiplies the N points of data to be transformed, by a window. The window used in this study is the Hanning window (58). The Hanning window is only close to unity in the centre so only velocity and displacement data obtained from the centre of the window are reliable. To process the whole acceleration record one steps through the data using a series of overlapping Fourier transforms. The loss factor is the percentage of data discarded from each FT. The effect of multiplying by the windows is the introduction of an amplitude modulation into the signal, this can be made negligible by taking a high enough loss factor. Unfortunately one may need many Fourier transforms. It is possible that other windows may be more efficient.

Example 6. First, the system was excited with a sine-wave periodic over each 32 sample points. The acceleration obtained was then integrated twice by the method above using a 1024 point Fourier transform with no windowing. There were no leakage effects and the integration was very accurate, The MSE for the comparison with the exact data was 0.562 and the comparison is shown in Figure 6.17. Next, the same data was integrated using a Hanning window and a loss factor of 80%. The comparison with the exact data is shown in Figure 6.18. The MSE of 0.854 is still excellent. The only difference between the two procedures is that the second produced a small amplitude modulation. The acceleration was then obtained for a sine excitation periodic over 31 sample points. When the integration was carried out as before without windowing, the results were as shown in Figure 6.19. A large low frequency component has been introduced, the very high MSE of 344.0 for the comparison reflects this. The integration was then carried out using the window and the same loss factor as before. The results are now considerably improved. The comparison MSE is

0.909. The comparison is shown in Figure 6.20. The results are indistinguisable from those in Figure 6.18. This example shows that the leakage problem is reduced by windowing.

The next and most serious problem is the magnification of low frequency trends in the data by the integration procedure.

Data was simulated for the system as in example 1. The acceleration data was then integrated using a 1024 point FFT. A Hanning window and a loss factor of 80% were used. The $\omega = 0$ line was deleted. The resulting errors for the velocity and displacement data were MSE($\dot{y}$) = 1.01 and MSE(y) = 3.51. A parameter estimation yielded

Coefficients	% error
$\hat{m} = 1.002$	0.2
$\hat{c} = 42.4$	6.0
$\hat{k} = 1.012 \times 10^4$	1.2
$\hat{\alpha} = 0.0$	0.0

with a model MSE of 3.85%. The results compare favourably with the time domain methods, however, the FT method is considerably more time consuming.

Table 6.3. shows the displacement and velocity error if one uses various different loss factors and numbers of lines for the FFT.

The low frequency component appears to arise because in integrating the data twice one had to divide by $-\omega^2$. This means that any noise in the data at low frequencies will be magnified by a factor ω^{-2}. Thus errors at $\omega = 0$ could be infinite. There will almost always be some noise at low frequencies as aliasing will fold back energy from high frequency noise into this region to add to any noise already present. This is of course the frequency-domain analogue of the time-domain noise magnification

mechanism discussed earlier.

The way around this problem, used successfully by Al-hadid and Wright (18) is to choose a cut-off ω_c by integrating the data and looking at the *averaged* transform of the displacement, one chooses the cut-off above any spurious low frequency peaks. The integration is then repeated except this time the value of $Y(\omega)$ for each $\omega < \omega_c$ is replaced in each FT by the value on a line segment joining Y(0) to $\bar{Y}(\omega_c)$ the averaged value of Y at ω_c.

A much simpler way of dealing with this problem is to stop it arising in the first place.

Data was simulated as in the previous example except that x(t) was filtered to give a band-limited input 5-30 Hz. Again a 1024 point FFT was used with an 80% loss factor. The velocity and displacement errors were respectively 0.44 and 0.52. Parameter estimation gave the model

Coefficients	% error
$\hat{m} = 1.005$	0.05
$\hat{c} = 40.9$	2.25
$\hat{k} = 1.06 \times 10^4$	6.00
$\hat{\alpha} = 0.00$	0.00

with a model MSE of 0.34%. The force surface obtained is shown in Figure 6.21. The linearity of the system is evident. Note that the division by ω^2 means that the FT method does not suffer from high frequency problems.

6.3. Initial Conditions.

It is important to mention a point concerning initial conditions and integration

constants. It is not always appropriate to fix constants of integration by removing the mean level. If one considers a system with a symmetric (i.e. even) nonlinearity, then even if the input is zero-mean the system will generate a mean level as an essential part of the output. The way around this problem is to modify ones experimental procedure. At the same time as one records the acceleration data one can take a sample of displacement data in order to estimate the mean level, the integrated data can then be adjusted to have this mean level. A much simpler procedure is to start recording data with the system at rest before the input force is applied. This fixes the initial conditions as $y(0) = 0$, $\dot{y}(0) = 0$. After the integration the null data can be deleted.

6.4. Differentiation of Measured Time Data.

Because differentiation is defined as a limiting process it is difficult to carry out numerically. The approximation

$$\frac{dy}{dt} = \lim_{\delta t \to 0} \frac{\delta y}{\delta t} \simeq \frac{\Delta y}{\Delta t} \qquad (\Delta y, \Delta t \text{ finite})$$

will clearly become better as one takes smaller and smaller Δt. Unfortunately this is the sort of operation which will produce significant errors from round-off when one tries to perform the calculation on a computer (unless one has accuracy to an arbitrary number of decimal places as in ADA (60), even so the equipment used for the data capture will have limited accuracy). Thus numerical differentation requires one to walk a tightrope between approximation errors and round-off errors. For this reason it is not recommended that one should measure $y(t)$ and numerically differentiate to form $\dot{y}(t)$ and $\ddot{y}(t)$ for the force surface problem. Unfortunately there are some situations where one has no choice. For example if one applied the method to a rotor system in order to estimate bearing coefficients, one would not easily be able to measure the vertical and horizontal accelerations of the rotor, one usually uses a non-contact displacement transducer in rotor dynamic problems. For this reason

some methods of numerical differentiation are considered.

6.5. Time Domain Differentiation.

6.5.1. Centred Difference Formulae.

These formulae implement the differentiation as a digital filter or recursion relation, the 3,5, and 7 point centred difference formulae are given by

$$\dot{y}_i = (y_{i+1} - y_{i-1})/2\Delta t \qquad (4)$$

$$\dot{y}_i = [-y_{i+2} + y_{i-2} + 8(y_{i+1} - y_{i-1})]/(12\Delta t) \qquad (5)$$

$$\dot{y}_i = [2(y_{i+3} - y_{i-3}) - 13(y_{i+2} - y_{i-2}) + 50(y_{i+1} - y_{i-1})]/(60\Delta t) \qquad (6)$$

It is important to monitor the remainder terms when using these formulae. A careful analysis including them indicates one is not guaranteed greater accuracy if one uses a higher order formulae.

For the final example, the system used in the previous examples was simulated with input x(t) a Gaussian sequence band-limited in the range 0-200 Hz. The resulting displacement data was then differentiated twice using a five-point centred difference. The resulting velocity and acceleration errors were 0.015 and 7.84 respectively. Again the velocity estimate is almost perfect. A least-squares parameter estimation gave

Coefficients	% errors
$\hat{m} = 0.961$	3.90
$\hat{c} = 55.2$	38.0
$\hat{k} = 0.98 \times 10^4$	2.0
$\hat{\alpha} = 0.0$	0.0

with a model MSE of 19.5%. The force surface obtained is shown in Figure 6.22. The reason why the model is so much in error even though the parameters are quite good is because the error in $\dot{y}(t)$ appears as a time-shift (Figure 6.23) and this decorrelates $x(t)$ and $\dot{y}(t)$. This is reflected in the parameter estimate, innaccuracies in the damping generate phase errors or time-lags in the output. The reason for this shift is not obvious. One might suggest that the algorithm, considered as a digital filter is not zero-phase and one could solve the problem by taking the derivatives in both the forward and backward directions and then averaging the result. However, this does not help, in the case of this example anyway.

The results of using the various centred difference formulae on the data of example 9 are shown in Table 6.4.

As with the integration formulae one can obtain the frequency characteristics of each of the formulae above by using the techniques of section 6.1.3.

6.5.2. Differentiating Fitted Polynomials.

This method is very simple in principle. One fits a polynomial to N data points (N odd) such that the point at which the derivative is required is at the centre. One then takes the analytic derivative of the fitted polynomial. This is rather time consuming and for low orders of polynomial simply reproduces the results of using centred differences (slight deviations arise due to the way the algorithms are programmed). The results of differentiating the data of example 9 using various polynomial orders are shown in Table 6.5.

If one were to use this method, one would have to be sure that the data is sampled correctly. If it is undersampled the situation shown in Figure 6.24 might arise.

6.6. Frequency Domain Differentiation.

The basis of this method is exactly the same as for integration except that to differentiate one multiplies the Fourier transform by $i\omega$ instead of dividing, i.e. $Y_V(\omega) = i\omega Y_d(\omega)$. It is obvious from the frequency-domain argument that differentiation greatly magnifies high frequency noise.

The leakage problem is exactly the same as for integration and is dealt with in exactly the same way. Table 6.6. shows the errors in the differentiated signals as a function of loss factor (Hanning window used) and number of FFT lines.

If one differentiates the data of the previous example using this method one still observes the phase drift in the acceleration data obtained. The method in terms of the continous Fourier transform is zero-phase. In fact $Ha(\omega)$ is 1. (This is true if one disregards the effects of windowing etc. If one takes account of these effects correctly one would arrive at a more complicated form for $Ha(\omega)$.)

In conclusion then, numerical differentiation of time data clearly has problems. For this reason it is suggested that one should always measure acceleration and integrate to obtain velocity and displacement.

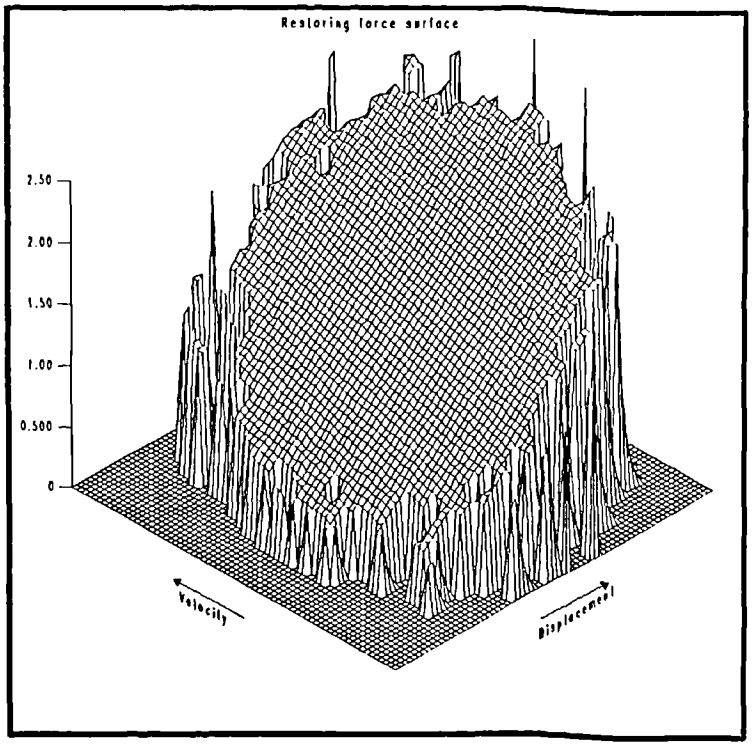

Figure 6.1. Exact restoring force surface for the simulated linear system used in the examples in the text.

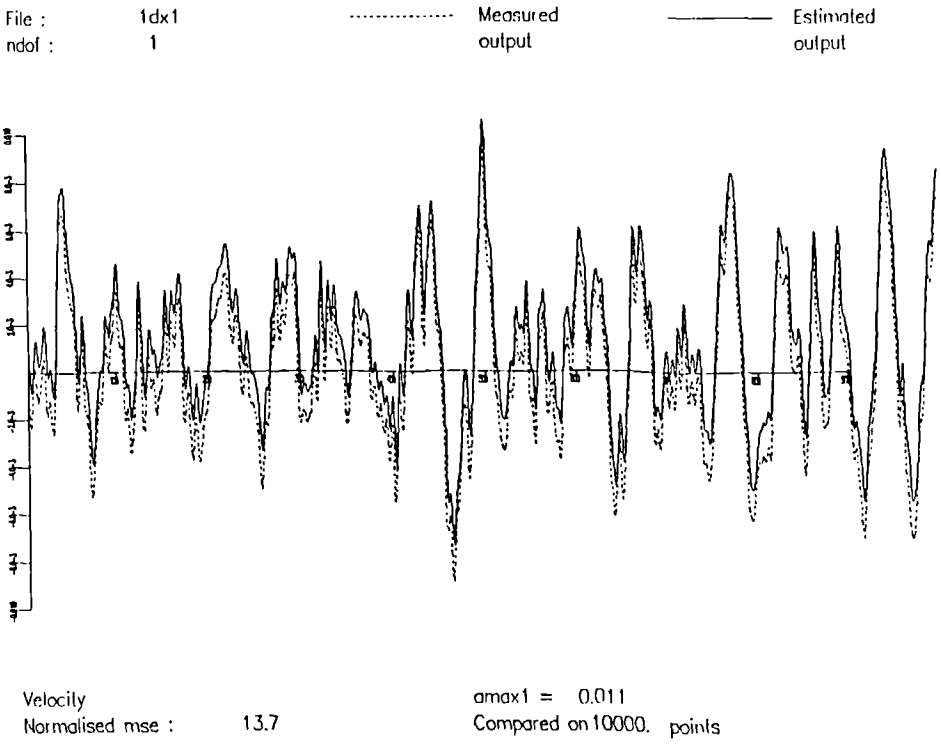

Figure 6.2. Comparison of the exact and estimated velocity data for example 1 in the text.

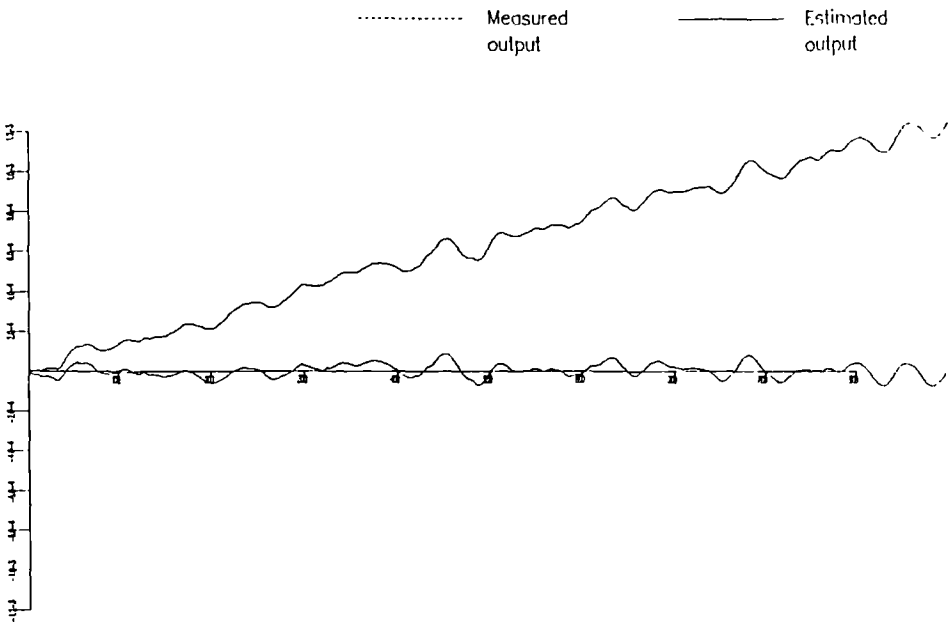

Figure 6.3. Comparison of the exact and estimated displacement data for example 1.

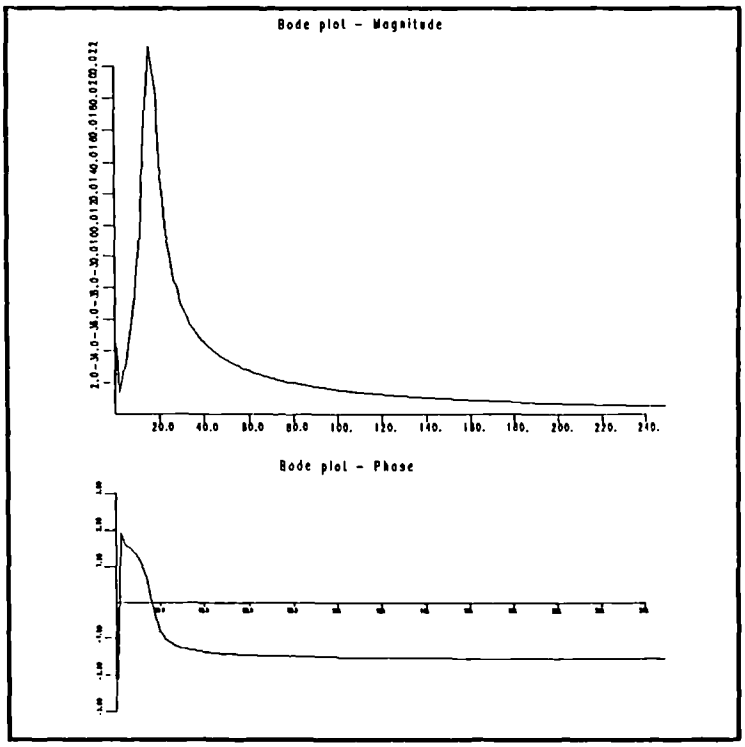

Figure 6.4. Mobility transfer function obtained using the estimated velocity data in Example 1.

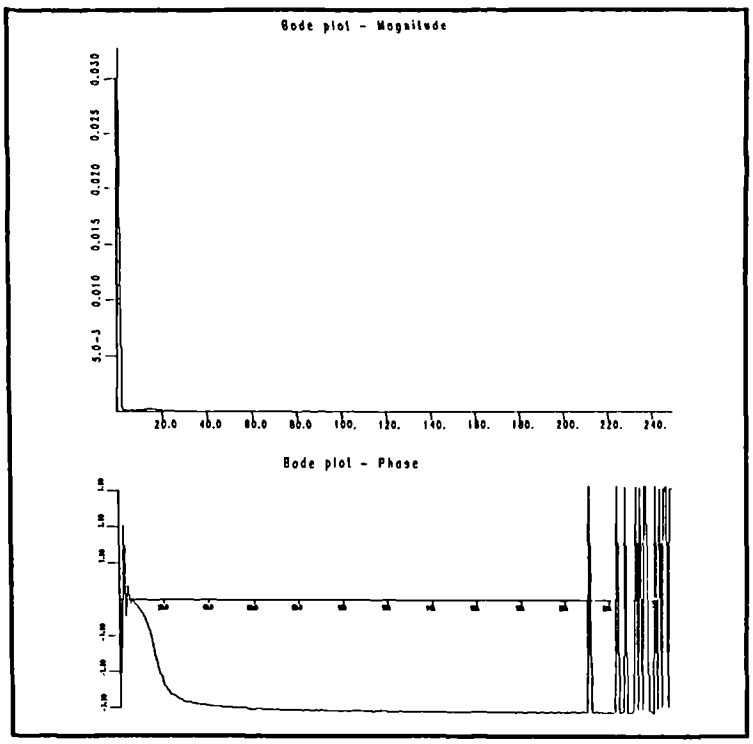

Figure 6.5. Receptance transfer function obtained using the estimated displacement data in Example 1. The Transfer function blows up at low frequencies.

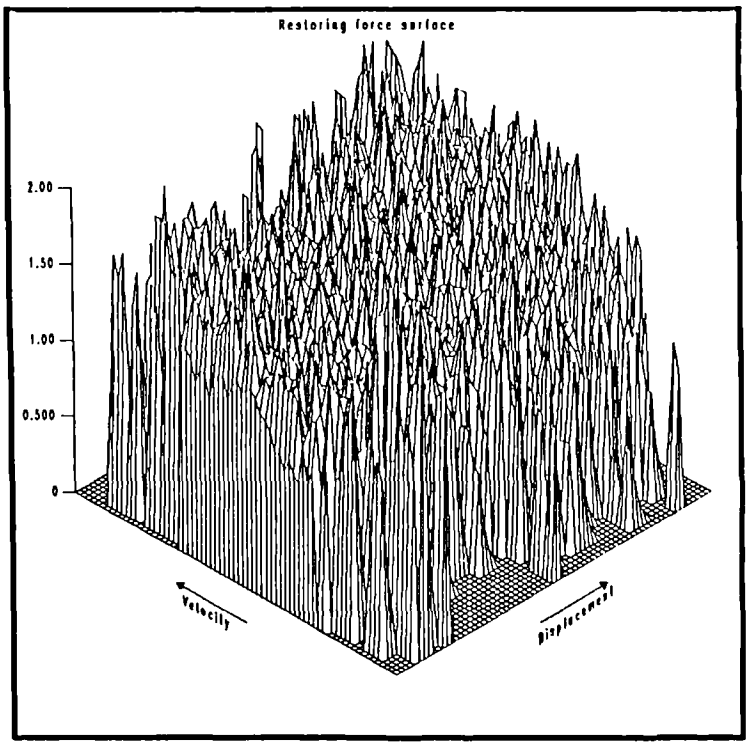

Figure 6.6. Restoring force surface constructed using the estimated velocity and displacement data obtained in example 1.

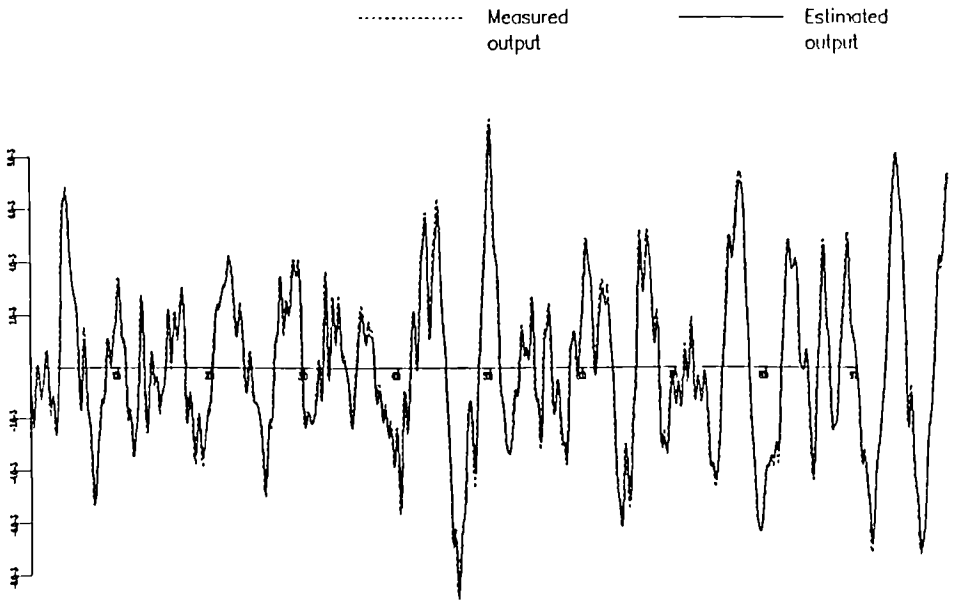

Figure 6.7. **Comparison of the exact and estimated velocity data for example 2. In this case the mean has been removed from the estimated data.**

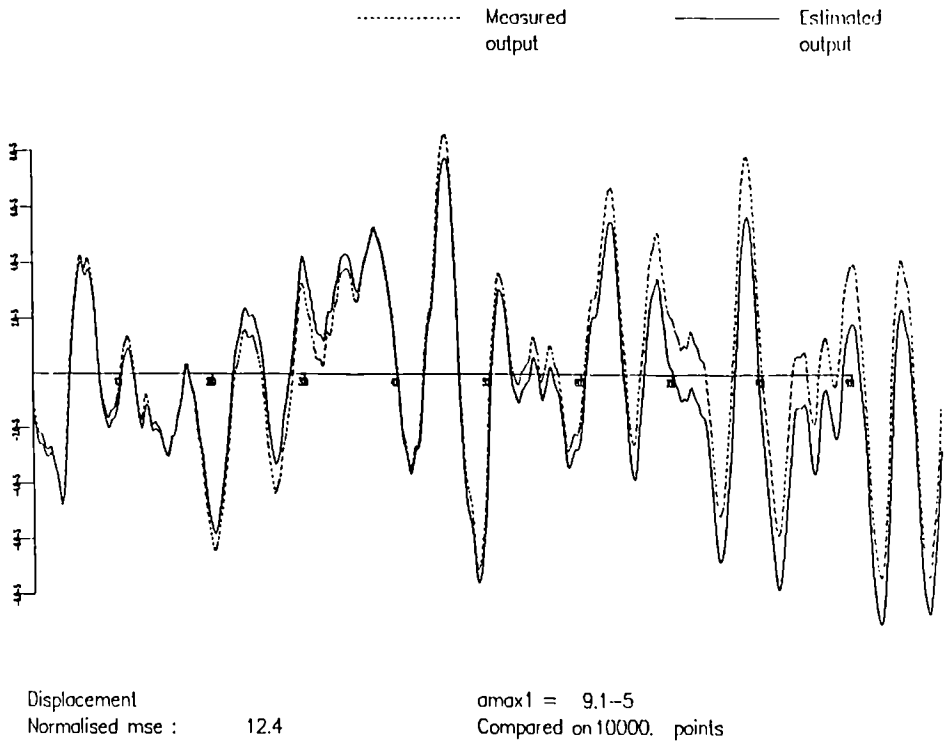

Figure 6.8. **Comparison of the exact and estimated displacement data from example 2. In this case a linear drift component has been removed from the estimated data.**

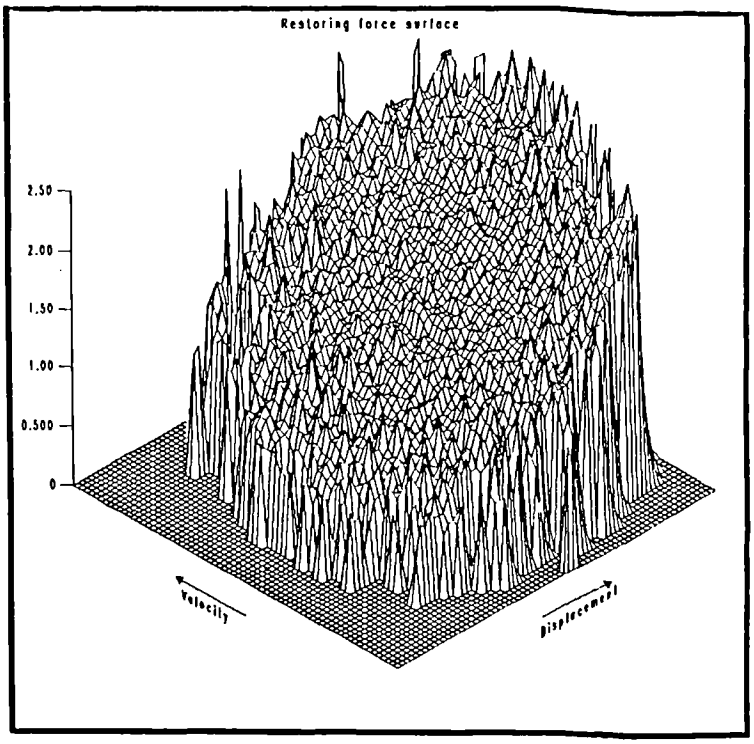

Figure 6.9. Force surface obtained using the estimated velocity and displacement data from example 2.

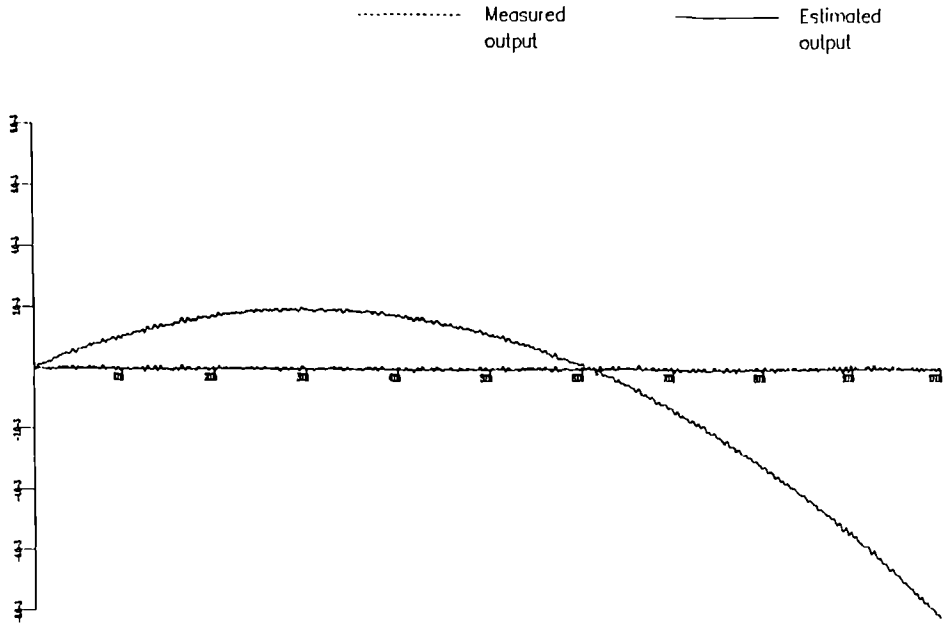

Figure 6.10. Comparison of the exact displacement data from example 2. with that estimated by integration *after* the acceleration mean-level was removed. The introduction of a quadratic trend is clearly shown.

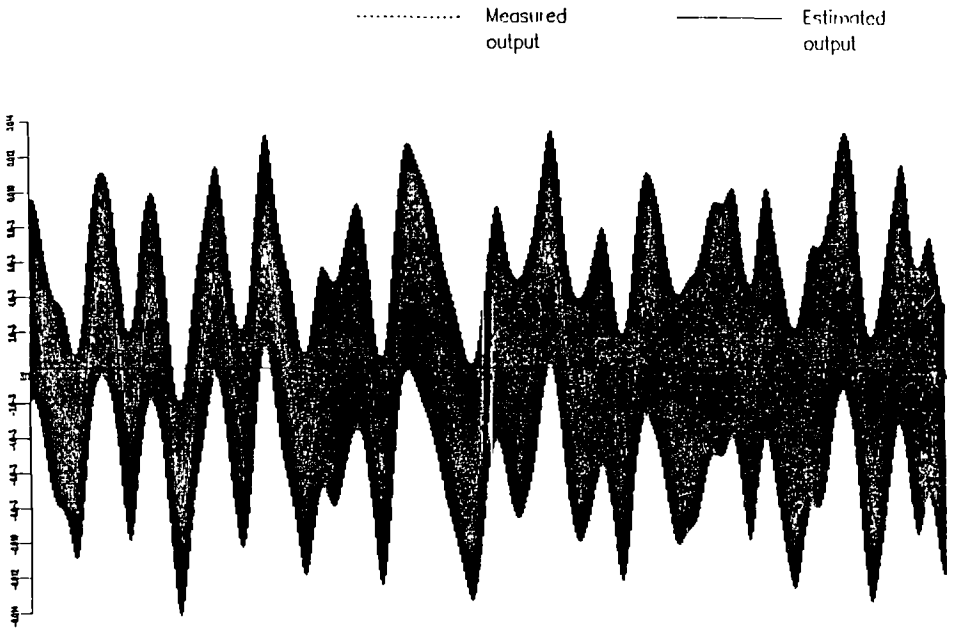

Figure 6.11. Comparison of exact and estimated displacement data showing the large high-frequency component introduced into the estimate if Tick's rule is used.

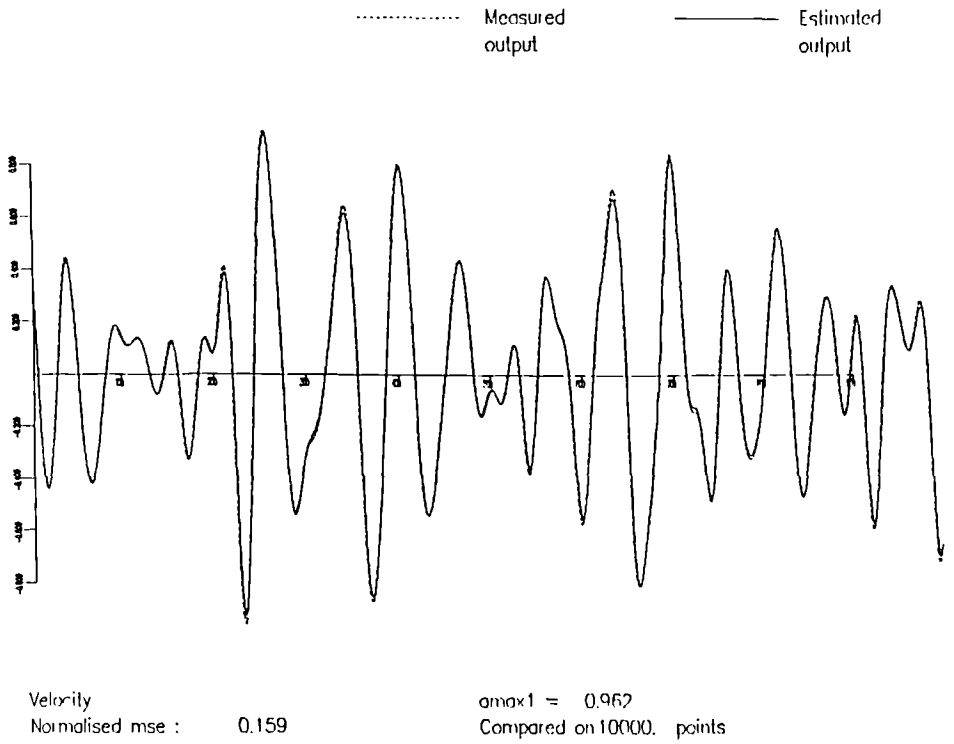

Figure 6.12. Comparison of exact and estimated velocity data if the system is excited by a band-limited input and the trapezium rule is used for integration. (Example 5 in the text.)

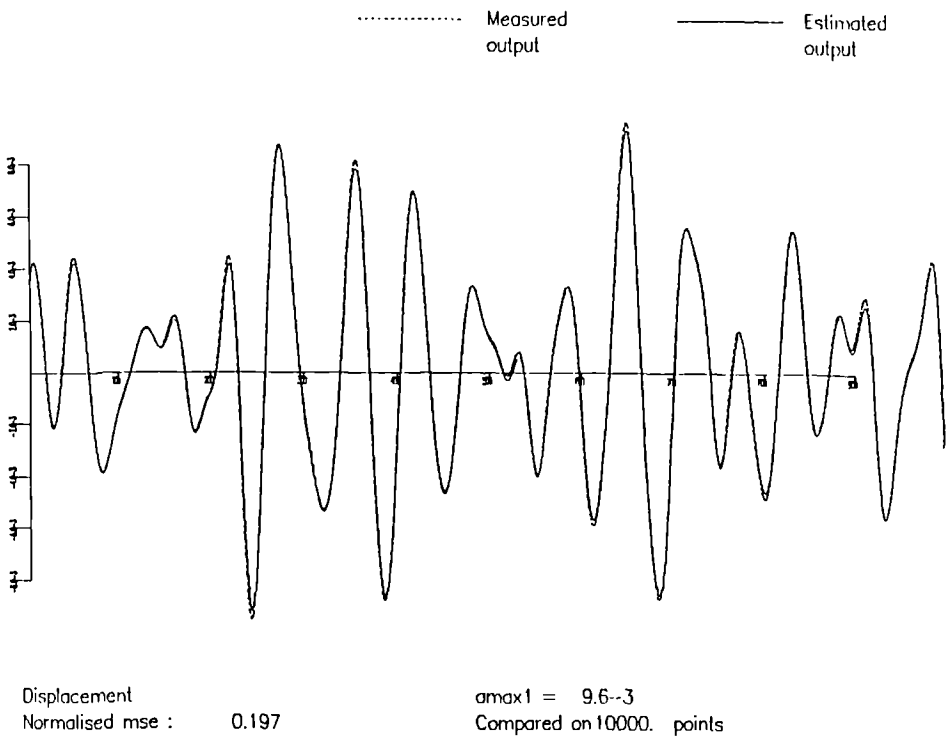

Figure 6.13. Comparison of exact and estimated displacement data if the system is excited by a band-limited input and the trapezium rule is used.

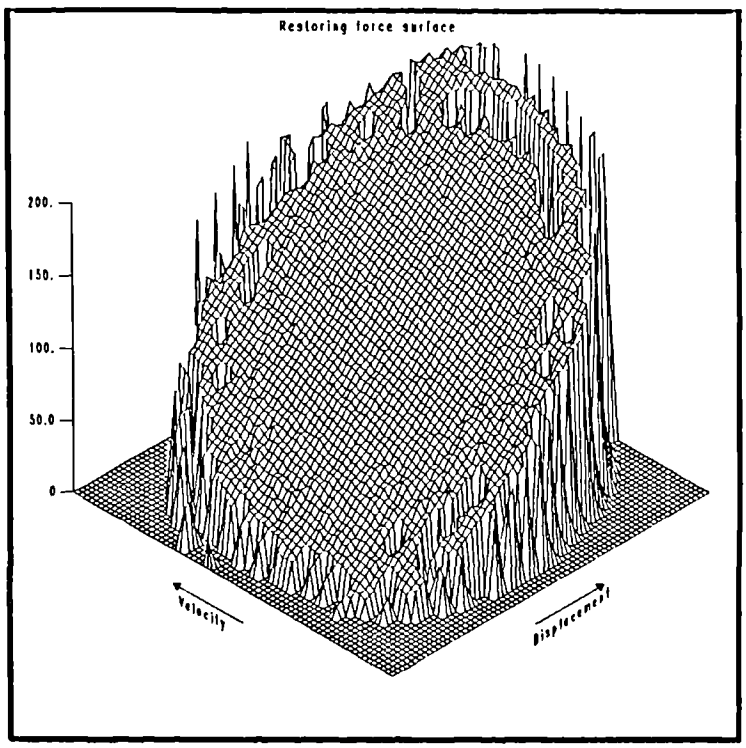

Figure 6.14. Force surface obtained using the estimated velocity and displacement data from the previous two figures.

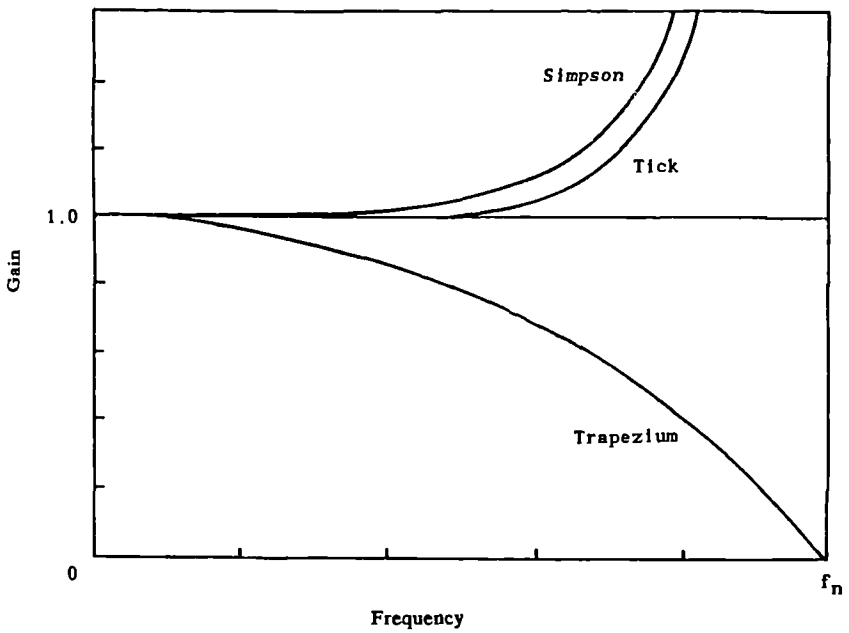

Figure 6.15. Frequency Response Functions for various time-domain integration procedures.

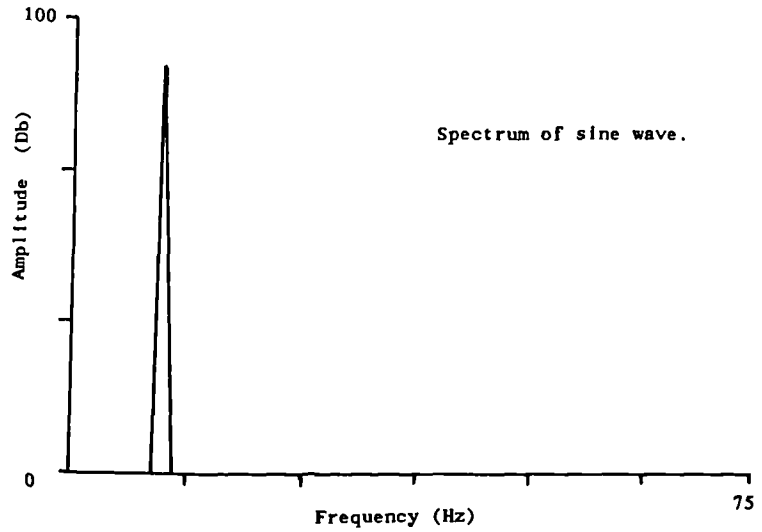

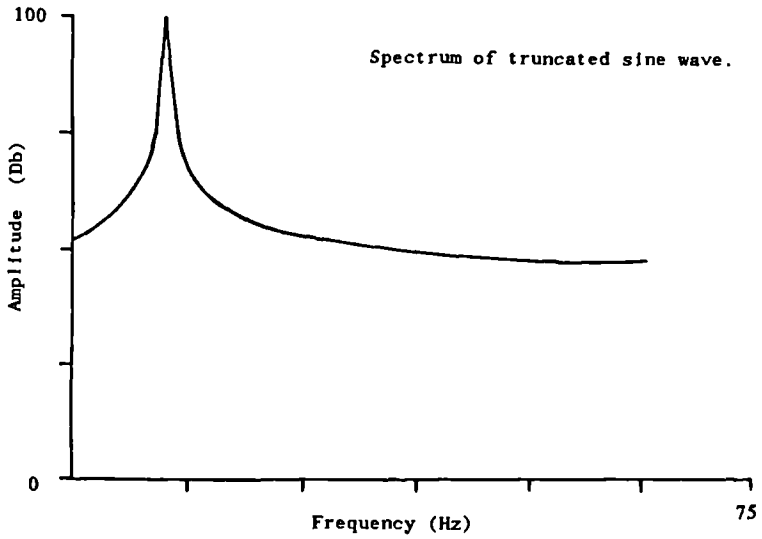

Figure 6.16. The effect of leakage on the spectrum of a sine wave.

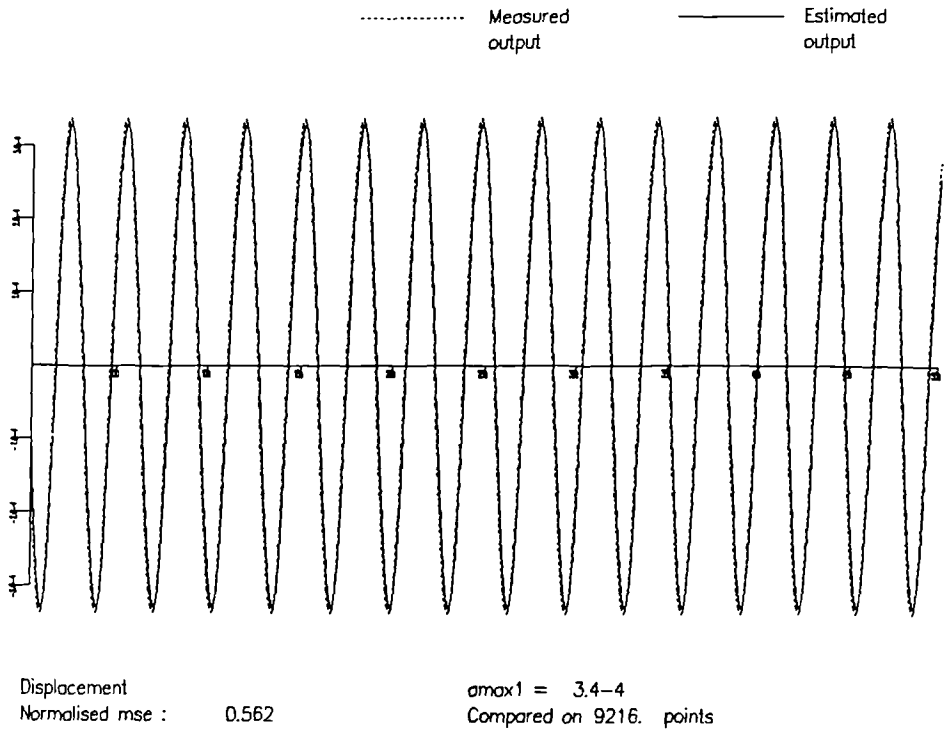

Figure 6.17. *Comparison of the exact and estimated displacement* **data when the system is excited by a sine wave which is periodic over the FFT rectangular window.**

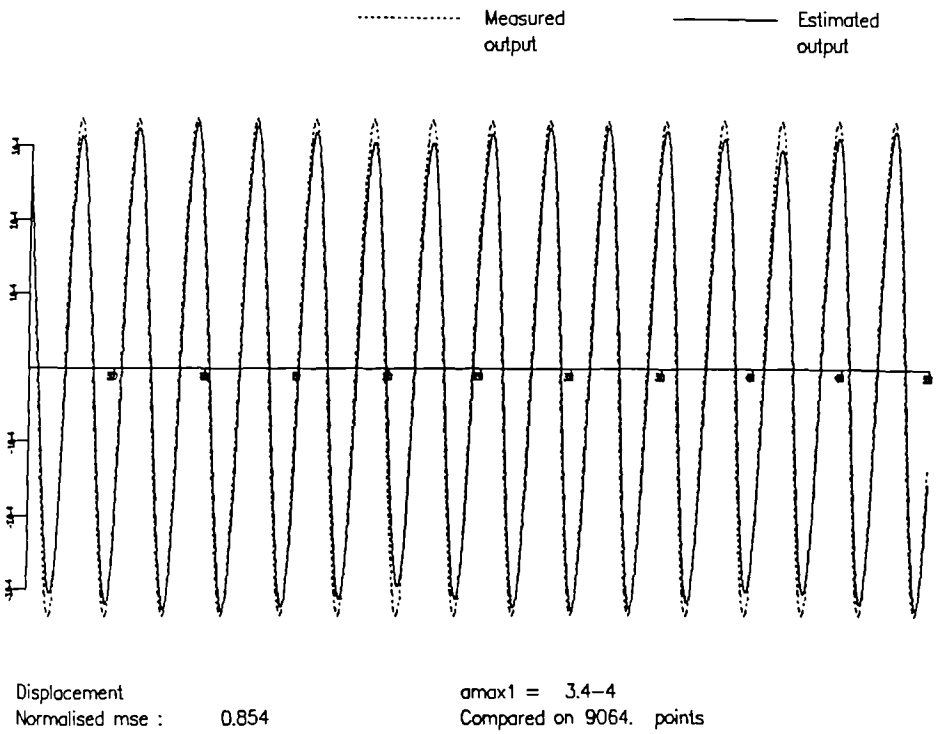

Figure 6.18. **Comparison of the exact and estimated displacement data when the excitation is a sine wave which is periodic over the FFT. Hanning window used.**

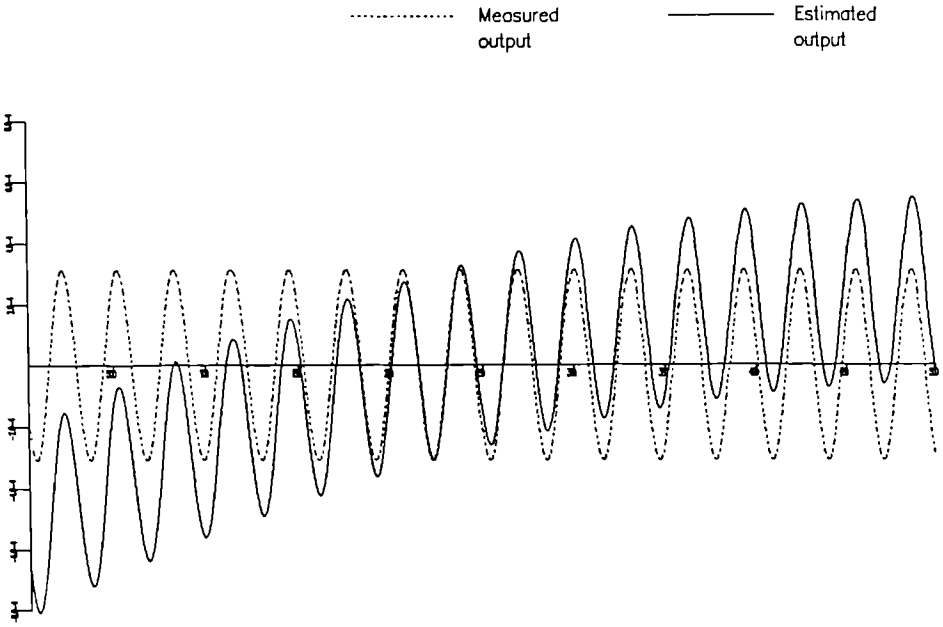

Displacement amax1 = 8.1-4
Normalised mse : 344. Compared on 9216. points

Figure 6.19. **Comparison of the exact and estimated displacement data when the excitation is a sine wave not periodic over the FFT window. Rectangular window used.**

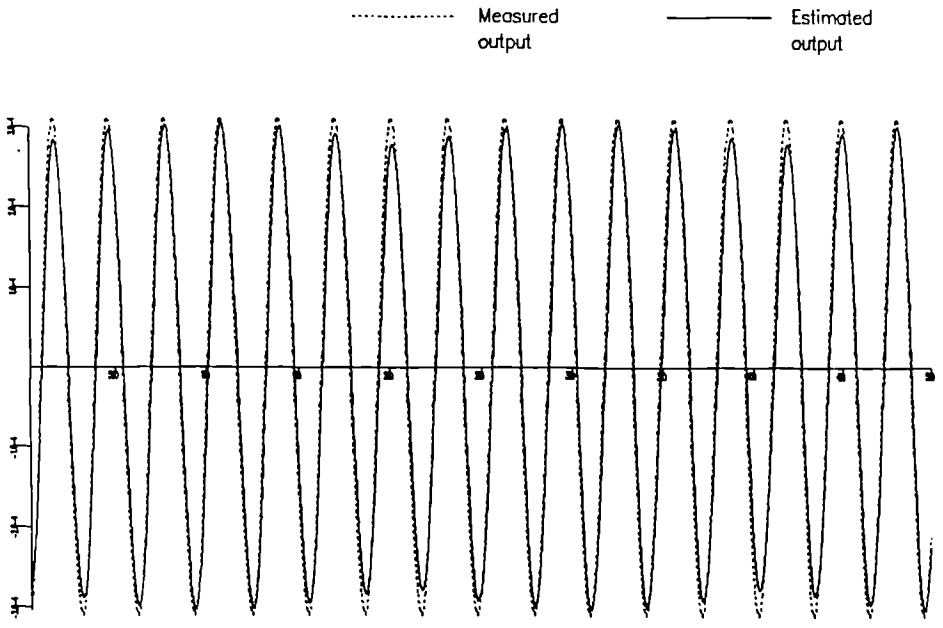

Displacement amax1 = 3.1-4
Normalised mse : 0.909 Compared on 9064. points

Figure 6.20. **Comparison of the exact and estimated displacement data when the excitation is a sine wave not periodic over the FFT window. Hanning window used.**

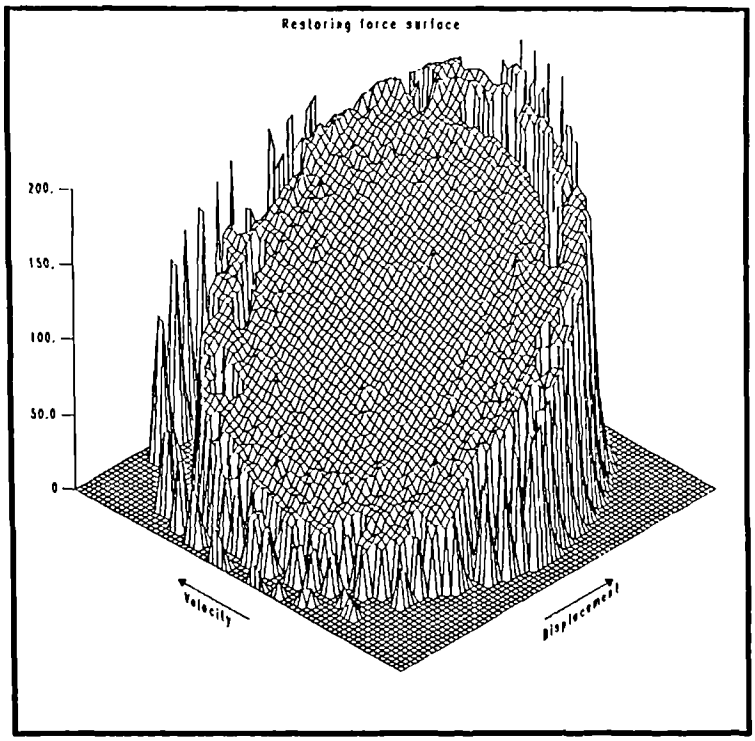

Figure 6.21. Force surface obtained using velocity and displacement data from frequency domain integration of acceleration data. The system is excited with a band-limited signal.

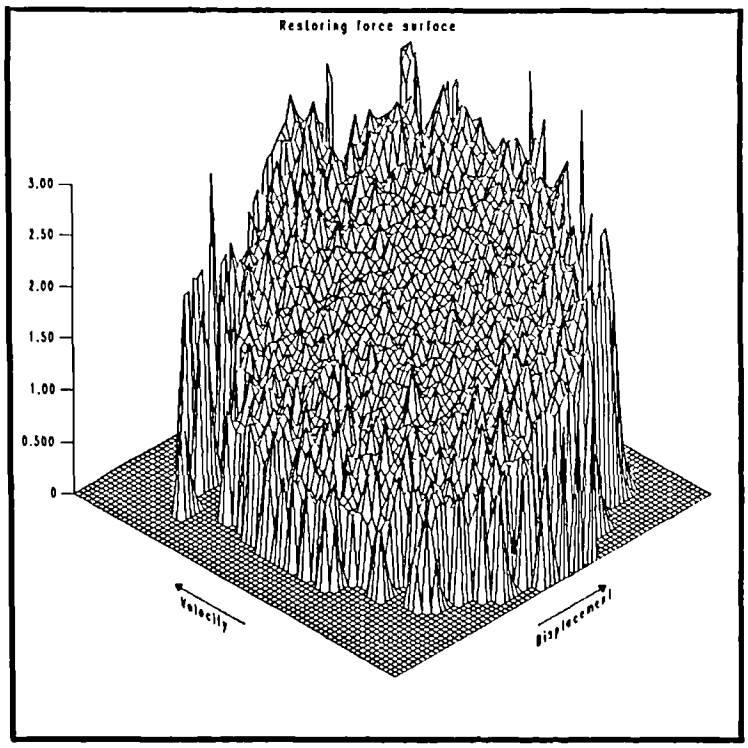

Figure 6.22. Force surface obtained using velocity and acceleration data from a five point centred difference formula.

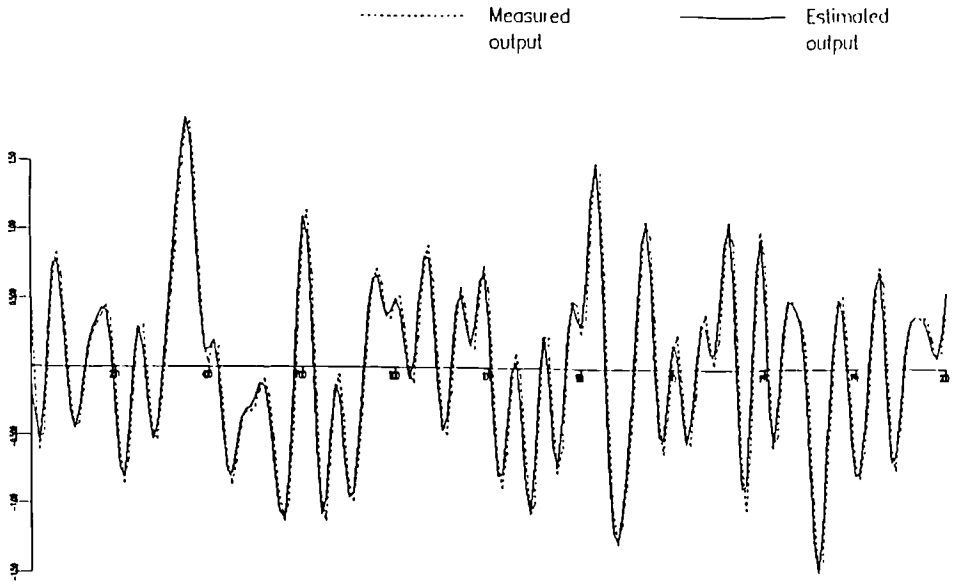

Figure 6.23. Comparison of exact and estimated acceleration data obtained by using the five point centred difference formula twice on displacement data.

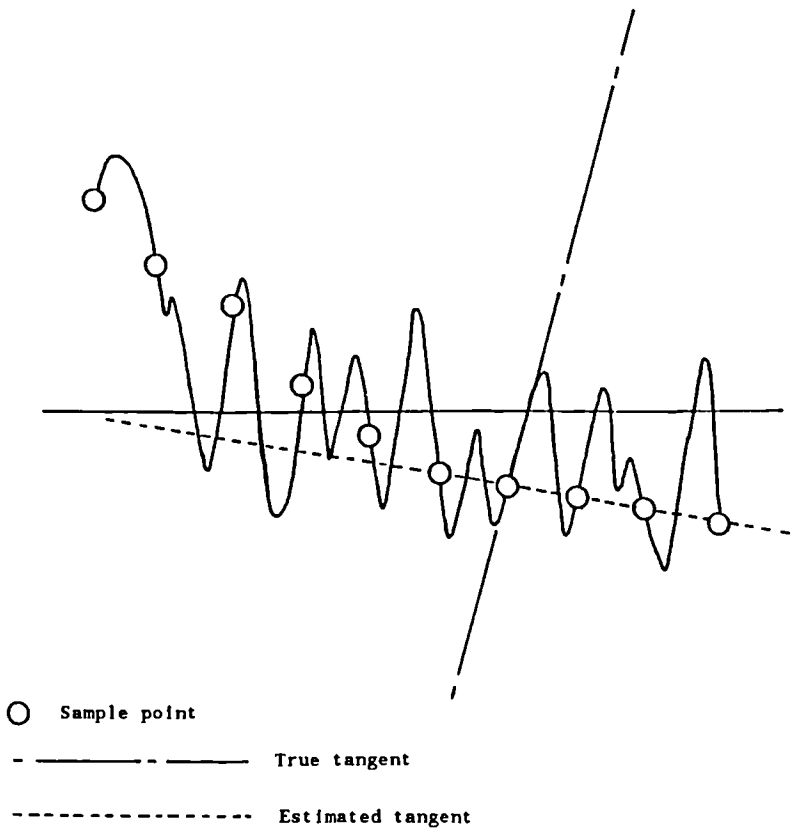

Figure 6.24. The affect of undersampling on the estimation of derivatives.

Order	MSE($\dot{y}$)	MSE(y)
1	0.718	12.353
2	0.718	7.604
3	0.718	5.208
4	0.719	4.969
5	0.719	5.119
6	0.718	4.085
7	0.719	4.080
8	0.718	4.061
9	0.718	4.037
10	0.718	5.653

Table 6.1. Normalised Mean-Square Errors (MSEs) in the estimated velocity and displacement if polynomial trends of various orders are removed.

Cut-off (Hz)	MSE($\dot{y}$)	MSE(y)
0.5	0.700	8.029
1.0	0.709	4.609
2.0	0.715	4.318
3.0	0.811	6.172

Table 6.2. MSEs for the integrated velocity and displacement data after high-pass filtering to remove the low frequency component introduced by the integration.

Number of Lines \ Loss Factor (%)	50	60	70	80	90	95	99
128	43.783 10.276	34.065 6.278	31.602 3.909	29.792 2.708	28.472 2.465	28.276 2.395	28.171 2.376
256	17.307 7.316	13.832 4.040	12.512 2.129	11.840 1.119	10.337 0.861	10.226 0.821	10.191 0.816
512	10.335 6.543	8.108 3.605	5.825 1.888	4.750 1.009	4.645 0.732	4.559 0.702	4.544 0.694
1024	9.577 6.648	6.818 3.648	4.539 1.738	3.513 1.006	3.639 0.721	3.552 0.687	3.563 0.685

Table 6.3. MSEs for the integrated velocity and displacement. The FT method of integration was used with various different window loss factors and numbers of lines in the FFT. The upper number in each pair is MSE(y) and the lower number is MSE(ẏ).

	MSE(ẏ)	MSE(y)
3 Point	0.017	8.600
5 Point	0.016	7.836
7 Point	0.007	8.213

Table 6.4. MSEs for the differentiated time data. Centred difference formulae of various orders were used.

Order	MSE($\dot{y}$)	MSE($\ddot{y}$)
2	0.138	9.080
4	0.015	9.836
6	0.012	8.093
8	0.014	8.185

Table 6.5. MSEs for the estimated derivatives. Polynomial curve-fitting was used.

Loss Factor (%)

Number of lines	50	60	70	80	90	95	99
128	9.771 16.177	5.884 13.124	3.306 11.237	1.660 10.048	0.691 9.392	0.508 9.469	0.471 9.410
256	6.903 14.040	4.134 11.737	2.316 10.409	1.162 9.411	0.812 9.492	0.730 9.356	0.714 9.394
512	6.357 13.645	3.769 11.328	4.223 11.500	2.402 10.291	2.537 10.722	3.088 10.964	2.550 10.760
1024	10.187 17.449	8.890 16.511	5.045 12.743	4.940 13.594	4.648 13.229	4.695 13.412	4.702 13.361

Table 6.6. MSEs for the velocity and acceleration estimates. The FT method of differentiation was used with various different window loss factors and numbers of lines for the FFT. The upper number in each pair is the velocity error, the lower number is the acceleration error.

CHAPTER 7

INPUT DESIGN FOR THE IDENTIFICATION PROCEDURE

The results obtained in the previous chapter using a band-limited input suggest that one can significantly reduce the data processing required in obtaining a force surface by choosing an appropriate excitation. There are two main criteria involved in deciding if an input is useful. (a) It should allow as simple an integration procedure ($\ddot{y} \rightarrow \dot{y} \rightarrow y$) as possible without sacrificing accuracy, and (b) it should generate a phase trajectory $(y(t),\dot{y}(t))$ which covers as much of the phase plane as possible thus allowing one to construct a connected and continuous force surface.

This chapter is composed of a series of simple case studies, one for each type of input. In each case both a linear and a nonlinear system are excited with the particular input and the results are examined. The linear system is

$$\ddot{y} + 40\dot{y} + 10^4 y = x(t)$$

and the nonlinear system (a Duffing oscillator) is

$$\ddot{y} + 20\dot{y} + 10^4 y + 5\times10^9 y^3 = x(t)$$

In each case the simplest integration procedure which produces acceptably accurate results is determined. The force surfaces displayed are constructed by the Crawley/O'Donnell method. In addition, the stiffness and damping sections are obtained.

7.1. Broadband Noise.

True white noise is impossible to produce as it would contain an infinite amount of energy, also the input must be low-pass filtered to avoid the instability problems of the Runge-Kutta procedure. In this case the term broadband means a Gaussian white noise sequence x(t) with $\bar{x} = 0$ and $\sigma_x = 100.0$ filtered to produce a signal in the range 0-200 Hz. The timestep for the simulation is 0.001 seconds. The first 4000 points (4 seconds) of data generated were discarded so that the signal would be free of transients. As far as the restoring force methods are concerned the transients cause no problem as the system equations of motion are still satisfied. However, it is convenient to consider the case of an impulse excitation separately.

7.1.1. Linear System.

The integration was performed using the trapezium rule. The estimated velocity data simply needed a drift removal. Because the input contained a low frequency component it was necessary to high-pass filter the displacement data. Trial and error showed that the best results were obtained with a filter cut-off at 1.5 Hz. The errors for the estimated velocity and displacement were respectively 0.714 and 3.85. The estimated phase trajectory is shown in Figure 7.1. It clearly covers a wide area of the phase plane. A least-squares parameter estimate gave the results

Coefficients	% error
$\hat{m} = 1.013$	1.3
$\hat{c} = 41.33$	3.3
$\hat{k} = 1.02 \times 10^4$	2.0

with a model MSE of 0.553%. There is little point in giving the standard deviations of these parameters as the true results are known. The force surface obtained from the data is shown in Figure 7.2. The linearity of the system is clearly shown

7.1.2. Nonlinear System.

The same input as for the linear system was used except that it was scaled by a factor of 0.1 so that $\sigma_x = 10.0$. Exactly the same integration procedure was used. Again the optimum cut–off was found to be 1.5Hz. The estimated velocity and displacement had comparison errors of 0.36 and 1.72 respectively. The phase trajectory looks essentially the same as in the linear case. In fact, in almost all cases which follow the phase trajectories for the linear and nonlinear systems are qualitatively the same. The only exception being the chaotic system of section 8. It is therefore only neccessary to plot one of them for each type of input. A least–squares estimate using the model

$$m\ddot{y} + c\dot{y} + ky + k_3 y^3 = x(t)$$

gave the parameters

Coefficients	% error
$\hat{m} = 0.992$	0.8
$\hat{c} = 20.5$	1.25
$\hat{k} = 0.983 \times 10^4$	1.7
$\hat{k}_3 = 5.32 \times 10^9$	6.4

with a model MSE of 1.264%. The stiffness section calculated from the data is shown in figure 7.3. It is clear that one is dealing with a hardening cubic nonlinearity. Regarding the parameter estimation, it is important to get the level of the excitation right. If the input level is too low the nonlinearity is not excited sufficiently and the nonlinear parameters cannot be estimated accurately. If the input level is too high the highest order nonlinear term will dominate and it will be difficult to estimate the lower order terms accurately, including of course, the linear terms. It is because of this that, in the cases which follow, the input applied to the linear system may differ *quantitatively* from that applied to the nonlinear system, in that amplitudes and

frequencies may differ slightly.

7.1.3. Comments.

The broadband signal is clearly very useful for covering a wide area of the phase plane, this means that one can obtain a reasonable expanse of force surface. Unfortunately the integration is complicated by the need to use a high-pass filter. An important factor in obtaining a smooth force surface is the mass estimate. In this case the mass is determined to within one or two per cent of the true value. The force surface obtained indicates that this level of accuracy is acceptable.

7.2. Band-Limited Noise.

In this case the input force is a zero-mean Gaussian white noise sequence filtered using a Butterworth digital filter to give a signal in the range 5-40 Hz. For the linear system σ_x = 100.0, for the nonlinear system σ_x = 10.0. Again, the simulation was allowed to run until the transient died out before the data was recorded.

7.2.1. Linear System.

The data was integrated using the trapezium rule. The mean was removed from the velocity and a least-squares linear drift was removed from the displacement. In this case MSE($\dot{y}$) = 0.159 and MSE(y) = 0.197. Clearly the agreement between the exact and the estimated data is excellent. The parameter estimation produced the results,

Coefficients	% error
$\hat{m}$ = 1.02	2.0
$\hat{c}$ = 40.6	1.5
$\hat{k}$ = 1.04 x 10^4	4.0

with a model MSE of 0.082%.

7.2.2. Nonlinear System.

The same integration procedure was used i.e. trapezium rule/drift removal. The procedure gave the results MSE($\dot{y}$) = 0.083 and MSE(y) = 0.128. Once again the agreement between actual and estimated data is excellent. 1000 points (1 second) of the estimated phase trajectory are shown in Figure 7.4. Parameter estimation gave

Coefficients	% error
$\hat{m} = 1.0007$	0.07
$\hat{c} = 20.2$	1.00
$\hat{k} = 1.008 \times 10^4$	0.80
$\hat{k}_3 = 5.23 \times 10^9$	4.6

with a model MSE of 0.086%. The stiffness section constructed from the estimated data is shown in Figure 7.5. The cubic nature of the nonlinearity is very clearly shown.

7.2.3. Comments.

The band-limited input is a very useful one. A large area of phase space is covered and the absence of a low frequency part from the input means that a very simple integration procedure can be used. The parameter estimation is very good, only k_3 is not obtained very accurately in the nonlinear system. This is probably because with the comparitively low level of input used, not much curvature is generated in the force surface i.e. the contribution of the nonlinear part of the restoring force is relatively small. In this case the small amount of noise introduced by the integration procedure would be sufficient to blur the estimation of k_3 slightly.

One can expect a whole class of input types to produce similar results to the above

e.g. pseudorandom sequences, multisines (i.e. Schroeder waveforms (61)), and possibly pseudorandom binary sequences.

7.3. Harmonic Input.

7.3.1. Linear System.

The system excitation is given by x(t) = 100.0sin(80t) i.e. is at 80 rad/s. As before the simulation was allowed to continue until the transient had died out.

The integration procedure is again very simple, trapezium rule followed by linear drift removal. The resulting estimation errors for the velocity and displacement respectively were 0.173 and 0.175. The estimated phase trajectory was the ellipse which is characteristic of harmonically excited linear systems. The parameter estimation results were

Coefficients	% error
$\hat{m} = -0.126$	112.6
$\hat{c} = 35.3$	11.75
$\hat{k} = 0.524 \times 10^4$	47.6

and are appallingly inaccurate, yet the model MSE is 0.19%. Fortunately there is a simple explanation for this. Given a harmonic input of the form $x(t) = X\sin(\omega t)$ for a linear system one must have a harmonic output of the form $y(t) = Y\sin(\omega t+\varphi)$. (For simplicity the phase φ can be transferred to the input.) This means that the equation of motion

$$m\ddot{y} + c\dot{y} + ky = x(t)$$

becomes

$$-m\omega^2 Y.\sin(\omega t) + c\omega Y.\cos(\omega t) + kY.\sin(\omega t) = X.\sin(\omega t-\varphi)$$

$$\therefore \quad (-m\omega^2 Y + \alpha Y).\sin(\omega t) + c\omega Y.\cos(\omega t) + (kY - \alpha Y).\sin(\omega t) = X.\sin(\omega t-\varphi)$$

is identically satisfied, and so therefore is

$$\left\{ m - \frac{\alpha}{\omega^2} \right\} \ddot{y} + c\dot{y} + (k - \alpha)y = X.\sin(\omega t-\varphi)$$

so the parameter estimation could generate the parameters corresponding to an arbitrary value of α, (m_α, k_α). If one knows, say, the correct mass then one can recover the correct value of k, because

$$(m - m_\alpha)\omega^2 = \alpha$$

and therefore

$$k = k_\alpha + (m - m_\alpha)\omega^2$$

If the values $m_\alpha = -0.126$, $k_\alpha = 5.24 \times 10^3$, m = 1.0 and ω = 80.0 are substituted into the equation above, one obtains $k = 1.24 \times 10^4$ example above, giving an error of 24%. It is now clear that one cannot use a harmonic input if one is interested in estimating the parameters of a linear system. One cannot obtain all the coefficients unless one initially knows some of them.

The force surface for this particular input is useless because the phase trajectory is a closed curve. The stiffness section will be correct, but only by accident – two points are sufficient to define a straight line.

7.3.2. Nonlinear System.

The excitation used this time was x(t) = 100.sin(70t). Again, the transients were allowed to die out. A great deal of harmonic distortion was present in the acceleration signal.

The trapezium rule followed by a drift removal was used to integrate the data. The errors in the estimated signals were MSE($\ddot{y}$) = 0.298 and MSE(y) = 0.303. The estimated phase trajectory is shown in Figure 7.6. One observes the characteristic limit cycle of the Duffing oscillator. Parameter estimation yielded the results

Coefficients	% error
$\hat{m} = 0.93$	7.0
$\hat{c} = 12.00$	40.0
$\hat{k} = 1.02 \times 10^4$	2.0
$\hat{k}_3 = 4.80 \times 10^9$	4.0

with a model MSE of 0.01%. So, for the nonlinear system the parameter estimate is much better. The reason for this is that the output contains harmonics. For the Duffing oscillator the displacement will have the form

$$y(t) = a_1 \sin(\omega t) + a_3 \sin(3\omega t) + \ldots$$

if one ignores the phases, which have no affect on the argument. The acceleration is

$$\ddot{y}(t) = -a_1\omega^2 \sin(\omega t) + -9a_3\omega^2 \sin(3\omega t) + \ldots$$

Clearly, the harmonics break the linear dependence between displacement and acceleration. This would be obvious from looking at the data as the harmonics are weighted differently in the two signals. If the level of excitation is low the parameter estimator will still have difficulty in finding the physical values of m and k. For this

case one cannot plot the stiffness section. However, the projection of $f(y,\dot{y})$ onto the $\dot{y} = 0$ plane indicates the nature of the nonlinearity very clearly (Figure 7.7).

7.3.3. Comments.

The harmonic input is very simple to generate and allows a very simple integration procedure. Unfortunately it is useless for the purposes of constructing a force surface. In addition, it should not be used if one desires an accurate parameter estimation unless the system is nonlinear and the level of excitation is high enough to break the linear dependence between displacement and acceleration. If the transient had been included an accurate parameter estimation might have been possible, this effect is considered in the next section.

7.4. Two Harmonic Inputs - 'Beating'.

If two harmonic inputs are superposed i.e. $x(t) = A\sin(\omega_1 t) + B\sin(\omega_2 t)$, the result is a 'beat' signal i.e. an amplitude modulated signal with carrier frequency $\omega_c = \omega_1 - \omega_2$.

7.4.1. Linear System.

The input signal used had the form $x(t) = 10\sin(100t) + 10\sin(101t)$. The beat frequency is therefore 1 rad/s. Steady-state data was used as before.

The data was integrated using the trapezium rule with drift removal. The velocity and displacement errors were 0.044 and 0.047 respectively. 5500 points of the estimated phase trajectory are shown in Figure 7.8. The integration is clearly very accurate and one can see that the trajectory covers the phase plane very effectively. The parameter estimates are

Coefficients	% error
$\hat{m} = 0.961$	3.9
$\hat{c} = 40.9$	2.29
$\hat{k} = 0.983 \times 10^4$	1.7

with a model MSE of 0.000128. Given the remarkable accuracy of the model one might expect the parameter estimates to be better. The explanation is again probably linear dependence. if y(t) = 10[sin(100t) + sin(101t)] then $\dot{y}(t)$ = −10[10000sin(100t) + 10100sin(101t)] and $\dot{y}(t) \approx -10000y(t)$ to within 1%. As one would expect from the model MSE the force surface is nearly perfect (Figure 7.9).

7.4.2. Nonlinear system.

The input used was x(t) = 10(sin(80t) + sin(81t)). Again, giving a beat frequency of 1 rad/s. One would expect this input to be better for nonlinear systems because the harmonics in the output will help to break the linear dependence. However the same harmonics may possibly reduce the accuracy of the integration.

The data was integrated using the trapezium rule followed by a drift removal. The resulting velocity and displacement estimates had errors of 0.503 and 0.525 respectively. Parameter estimation produced the results

Coefficients	% error
$\hat{m} = 1.006$	0.6
$\hat{c} = 10.7$	46.5
$\hat{k} = 1.02 \times 10^4$	2.0
$\hat{k}_3 = 5.10 \times 10^9$	2.2

with a model MSE of 0.005%. This data produces an excellent restoring force surface and stiffness section as shown in Figures 7.10 and 7.11. The damping section shown in Figure 7.12 is a different matter. An interesting effect occurs here, the damping

appears to be very nonlinear. If one considers the estimated velocity (Figure 7.13) one can see an amplitude dependent error in the estimate, an underestimation in fact. This means that the force values f_i are associated with the wrong points in the phase plane $(\hat{y}_i,\hat{\dot{y}}_i)$. If the error in $\hat{\dot{y}}$ depends on how large $\dot{y}$ is, then the force surface will have a nonlinear $\hat{\dot{y}}$ dependence. The 'nonlinearity' of the damping section is of a softening type, this is the explanation for the fact that the parameter estimator drastically underestimated the damping coefficient c. This effect is unfortunate, one must be careful that one is actually identifying a nonlinearity and not simply a systematic error in the integration procedure.

7.4.3. Comments.

This appears to be a very useful type of input. It is fairly simple to generate. The simplest integration procedure can be used with accuracy. Coverage of the phase plane depends on the closeness of the two frequecies chosen, in this case the frequencies are close enough to give excellent results. Figure 7.14. shows the estimated phase trajectory for $\omega_1 = 100$, $\omega_2 = 110$ for the linear system. In this case the coverage is not very good, however the errors in the velocity and displacement estimates and the model error were close to those obtained for the input considered in section 4.1 above. Once more, if the system is linear the parameter estimates may be unreliable as a result of linear dependence.

7.5. Harmonic Input with Time Dependent Amplitude.

7.5.1 Linear System.

The system was excited by x(t) = 10t.sin(100t), i.e. at constant frequency 100 rad/s with a linearly growing amplitude. Data was recorded after the transient had died out.

As before the trapezium rule/drift removal procedure proved acceptable for the

integration of the data. The errors were MSE($\dot{y}$) = 0.044 and MSE(y) = 0.049. Parameter estimation produced the results

Coefficients	% error
$\hat{m}$ = 0.299	70.1
$\hat{c}$ = 41.1	2.75
$\hat{k}$ = 0.301 x 10^4	69.9

with a model MSE of 0.029. The disappointing parameter estimation is again due to linear dependence. The amplitude used is slowly varying, so over short time scales the input is harmonic. As one would expect from the model MSE the force surface and stiffness section obtained from this data are excellent.

7.5.2 Nonlinear System.

The system was excited with the signal x(t) = 10t.sin(80t). The acceleration data was integrated exactly as in the previous section. The errors in the estimated velocity and displacement were 1.16 and 3.34 respectively. The displacement estimate is good initially but begins to deviate from the true data as the amplitude increases and harmonic distortion effects become large. The estimated phase trajectory is shown in Figure 7.15. Parameter estimation produced the following coefficients

Coefficients	% error
$\hat{m}$ = 1.005	0.5
$\hat{c}$ = 14.5	27.5
$\hat{k}$ = 1.02 x 10^4	2.0
$\hat{k}_3$ = 5.11 x 10^9	2.2

with a model MSE of 0.0066%. This estimate was made on 1000 points near the start of the recored where the harmonic distortion was not too high, surprisingly perhaps, a second estimate based on points where distortion was considerable produced

results which were almost as good. The force surface obtained from this data is shown in Figure 7.16. The cubic nature of the nonlinearity is evident. The level of excitation here is fairly high, correspondingly the amount of curvature in the force surface is high. This is probably the reason why the damping coefficient is innacurately estimated even though the estimated velocity is good. The effect of the damping term is small compared to that of the cubic stiffness.

7.5.3. Comments.

This is an extremely simple input to use experimentally. The simplest integration procedure can be used. Coverage of the phase plane depends on how fast the amplitude is increased, The slower the rate of increase, the higher the density of points in the phase plane. However, if one increases the amplitude quickly, more area is covered. The results of this section indicate that for parameter estimation purposes this type of input it is only suitable for reasonably well excited nonlinear systems. By using faster variation of the amplitude or different time-dependencies it may be suitable for linear systems. This type of input was used by Crawley and O'Donnell (55). They allowed the amplitude to rise to a maximum and then fall linearly to zero.

7.6. Harmonic Input with Time Dependent Frequency - 'Chirp'.

7.6.1. Linear System.

The input $x(t) = 20\sin(20t + 18t^2)$ was used. The frequency changes linearly from ω = 20 rad/s at t = 0, to ω = 380 rad/s at t = 10 seconds. Clearly it is a simple matter to ensure that no low frequency component is included. In this case the transient is included, however, it is small.

The data was integrated by the trapezium rule/drift removal method. The errors in

the estimated velocity and displacement are given by MSE($\dot{y}$) = 0.25 and MSE(y) = 0.34. Parameter estimation gave

Coefficients	% error
$\hat{m}$ = 0.716	28.4
$\hat{c}$ = 15.7	60.8
$\hat{k}$ = 0.967 x 10^4	3.3

with a model MSE of 0.54%. As the model error is small the poor parameter estimation can probably be attributed to linear dependence again.

7.6.2. Nonlinear System.

The input x(t) = 10.sin(20t + $18t^2$) was used. Again the transient is included. A very clear jump phenomenon was displayed as the excitation frequency passed through the region of the resonance.

The data was integrated as in the last section. The velocity and displacement estimates were a little innacurate towards the beginning of the record but settled down. The overall errors were MSE($\dot{y}$) = 0.048 and MSE(y) = 0.237. The estimated phase trajectory is shown in Figure 7.17. The jump is shown clearly. Parameter estimation on the 1000 points centred around the jump region (where the nonlinearity is most evident), gave the results

Coefficients	% error
$\hat{m}$ = 1.008	0.8
$\hat{c}$ = 20.5	2.5
$\hat{k}$ = 1.03 x 10^4	3.0
$\hat{k}_3$ = 5.34 x 10^9	6.8

with a model MSE of 0.008%. This data allows the construction of the force surface

shown in Figure 7.18. The surface is excellent; the cubic nature of the nonlinearity is clearly shown.

7.6.3. Comments.

This particular input gave qualitatively the same results as the rest of the class studied which included swept–sines and stepped–sines. All these signals can be produced fairly simply. All can be produced with no low frequency part so the simplest integration procedure can be used. Coverage of the phase plane is good, so large expanses of force surface can be obtained. If one is concerned with parameter estimation, there are no problems with nonlinear systems, but one must take care to sweep the frequency fast enough to eliminate linear dependence in the case of linear systems.

One point common to the last two types of input studied is that they both produced velocity and displacement data which was more accurate in some parts than others. If one is concerned about accuracy in the parameter estimation it is a good idea to fit models to different sections of the data and choose the parameters which minimise the model error or perhaps have smallest standard deviations. Of course, one must make sure that the excitation levels are high enough in each section for the nonlinear parameters to show up clearly.

7.7. Impulse Excitation.

In this case the impulse was simulated by starting the Runge–Kutta procedure with zero displacement but a finite value for the velocity. This situation is equivalent to exciting the system with a true Dirac impulse which would give the system infinite acceleration at $t = 0$. In this section the two systems have the same coefficients as before except that c, the damping coefficient is 2.0. This change is made so that one can capture a reasonable amount of data before the damping brings the system to a standstill. As an alternative the sampling frequency could have been increased. The

small damping was chosen to demonstrate that the integration procedure does not require the system to be highly damped. c = 20.0 corresponds to 10% of critical damping, c = 40.0 to 20% while c = 2.0 represents only 1%.

Another point which needs to be mentioned concerns the parameter estimation procedure. During the recording of the data the equation of motion is

$$m\ddot{y} + f(y,\dot{y}) = 0$$

Consequently, one can only obtain the coefficients up to an overall scale. As in the transmissibility case (Section 5.1), in order to plot the force surface this scale is fixed by setting m = 1. Because the mass can be fixed at an arbitrary value it is not neccessary to carry out a parameter estimation before plotting the surface. Another important consequence of fixing the mass is that linear dependence is no longer a problem.

7.7.1 Linear System.

The initial velocity was taken to be 100.0. Trapezium rule integration followed by drift removal proved sufficient to estimate the velocity and displacement. The errors were MSE($\dot{y}$) = 0.0001 and MSE(y) = 0.016. The integrated phase trajectory is shown in Figure 7.19. The force surface obtained by setting m = 1 is shown in Figure 7.20 in this figure the 'stray' points have been removed i.e. those grid squares which contain isolated points have had their force values zeroed.

7.7.2. Nonlinear System.

The initial velocity was taken as 10.0. The same integration procedure as the previous section was used. The estimated velocity and displacement had errors of 0.308 and 0.346 respectively. The force surface and stiffness section obtained from this data after setting m = 1 were excellent (Figures 7.21 and 7.22).

7.7.3. Comments.

The class of impulsive inputs – including step functions – are potentially the most simple of all. They are excellent for obtaining force surfaces provided the sampling interval is taken small enough for a large number of oscillations to be recorded. If one strikes the system then observes the unforced motion, one can only obtain the parameters for the system up to an overall scale. If a finite duration impulse is used (any other type is not physically realisable anyway), as long as one records a non-zero x(t) at some instant, one should be able to carry out a parameter estimation.

A further important point about impulse responses is that they are not zero-mean signals. Taking this to extremes, if the system is critically damped or overdamped the signal y(t) will be positive (or negative) for all time. At lower levels of damping the system will oscillate but the mean of the output will be non-zero. This means that one must start recording the data before the system is struck. This fixes the initial data as that corresponding to the equilibrium condition of the system.

7.8. A Chaotic System.

This system is included mainly for interest. Ueda's Duffing oscillator system (1)

$$\ddot{y} + 0.05y + y^3 = 7.5.\cos(t)$$

was simulated. The initial conditions y(0) = 3.0 and $\dot{y}(0)$ = 4 were chosen in order to ensure that no transient was present. Although the input force is harmonic the output of the system contains energy associated with a continuous range of frequencies. Althougth the output contains low frequencies a trapezium rule/drift removal integration was found sufficiently accurate. The errors for the estimated velocity and displacement data were 0.17 and 1.07 respectively. 2000 points of the estimated phase

trajectory is shown in Figure 7.23. The coverage of the phase plane is excellent as in the case of the random input. Parameter estimation yielded the results

Coefficients	% errors
$\hat{m} = 0.999$	0.1
$\hat{k} = 0.0489$	2.2
$\hat{k}_3 = 1.005$	0.5

with a model MSE of 0.08%. The force surface is shown in figure 7.24.

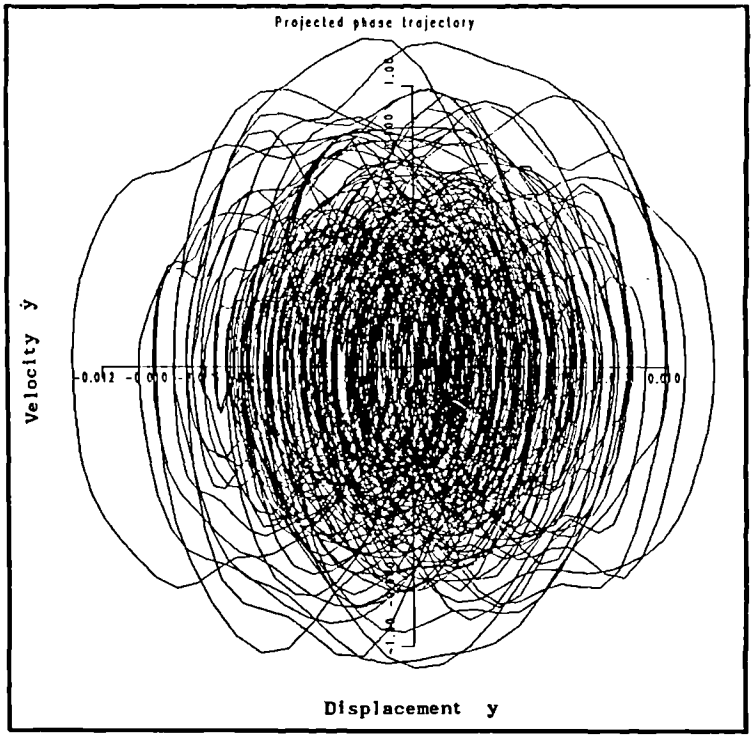

Figure 7.1. Phase trajectory based on estimated velocity and displacement data for a linear system subjected to a broadband excitation.

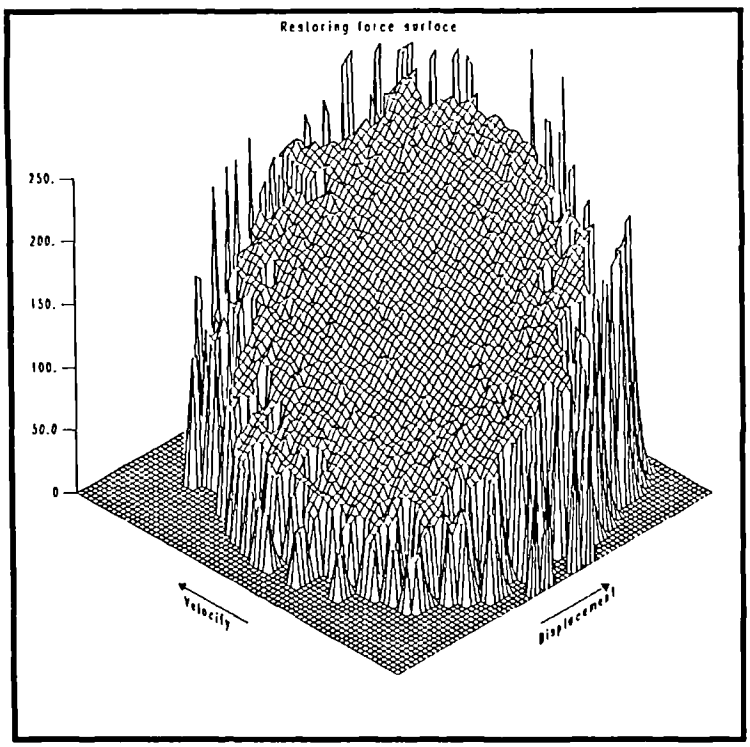

Figure 7.2. Estimated restoring force surface for a linear system subjected to a broadband excitation.

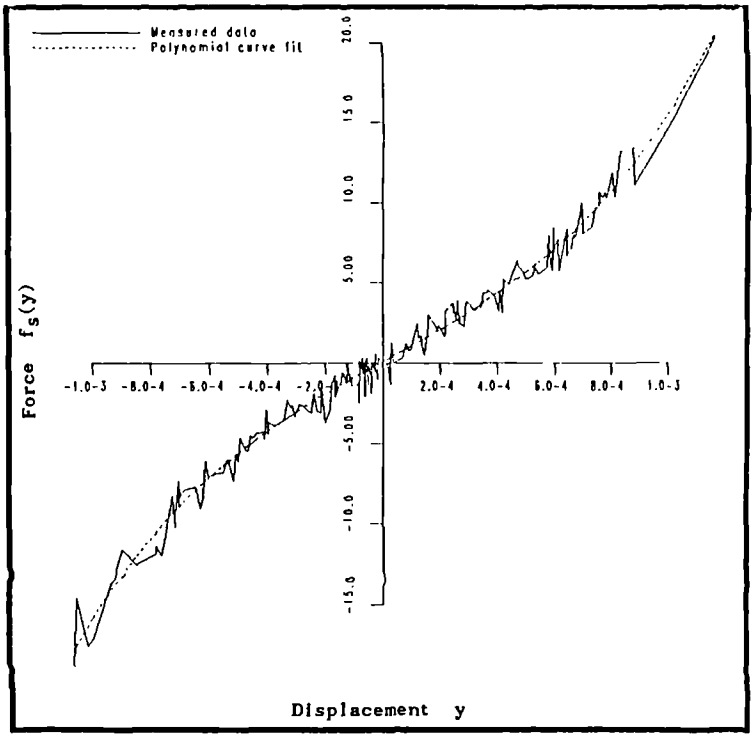

Figure 7.3. Estimated stiffness section for a nonlinear system with cubic stiffness subjected to broadband excitation.

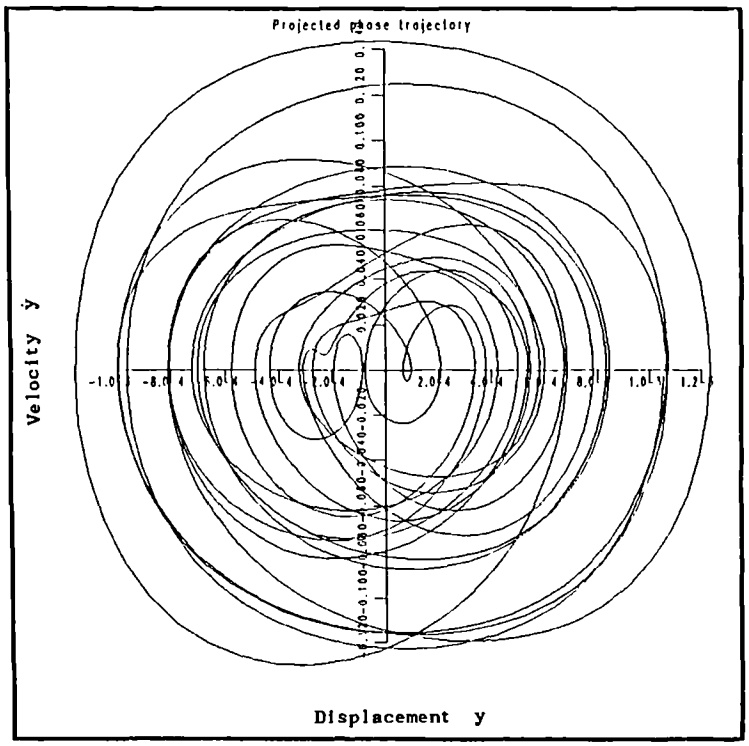

Figure 7.4. Estimated phase trajectory for a system with cubic stiffness subjected to a band-limited random excitation.

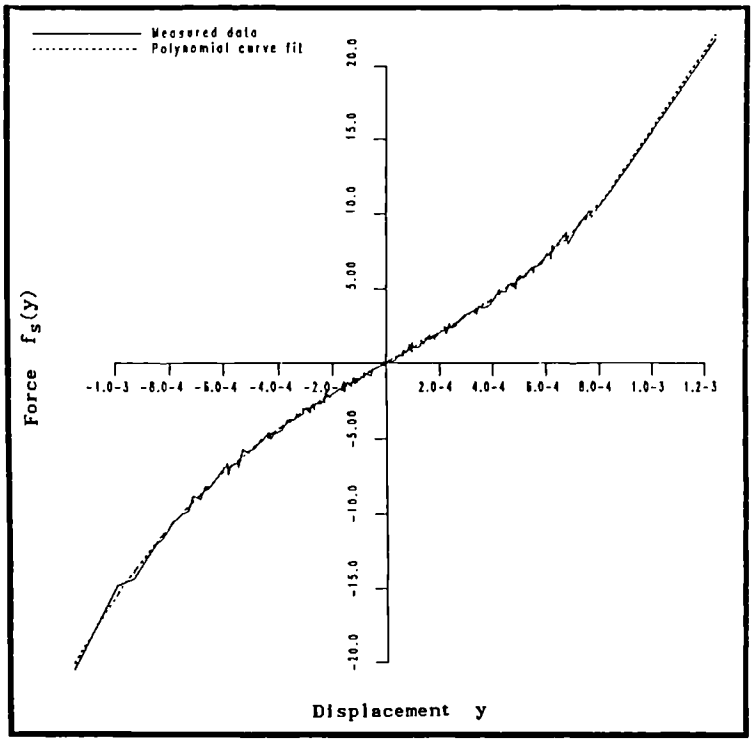

Figure 7.5. Estimated stiffness section for a system with cubic stiffness subjected to a band-limited random excitation.

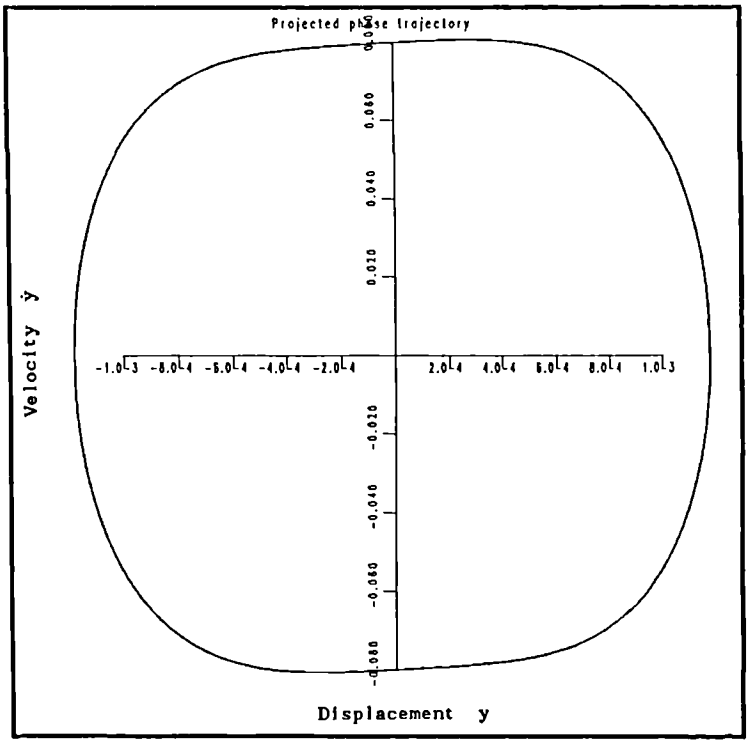

Figure 7.6. Estimated phase trajectory for a Duffing oscillator system subjected to a harmonic input.

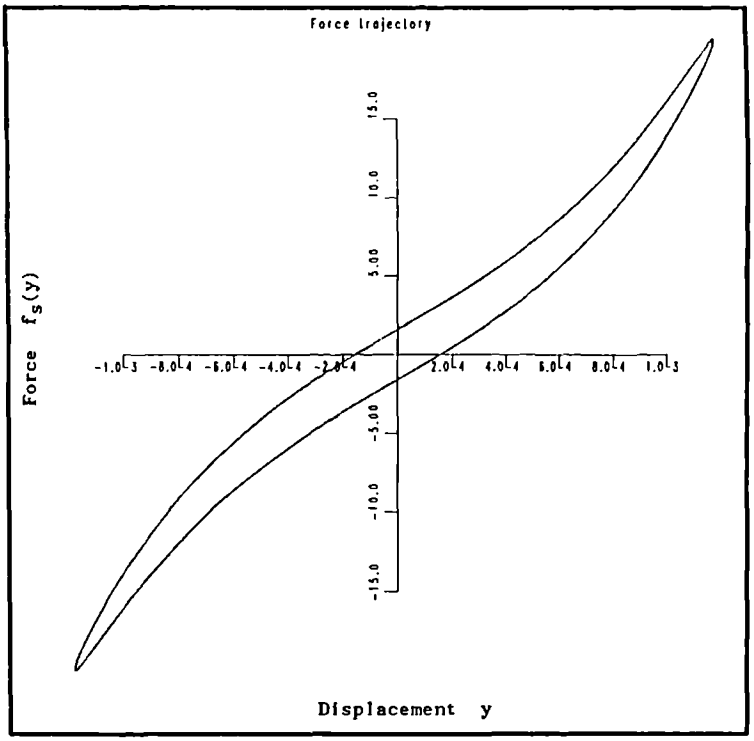

Figure 7.7. Projection onto the plane $\dot{y} = 0$ of the estimated force surface for the harmonically excited Duffing oscillator.

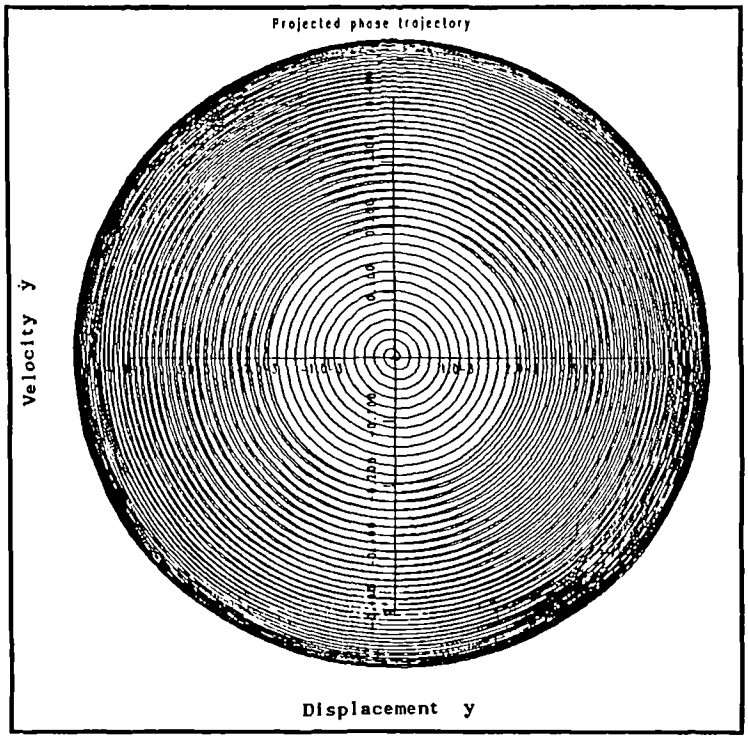

Figure 7.8. Estimated phase trajectory for a linear system excited by two sinusoidal forces of differing frequencies.

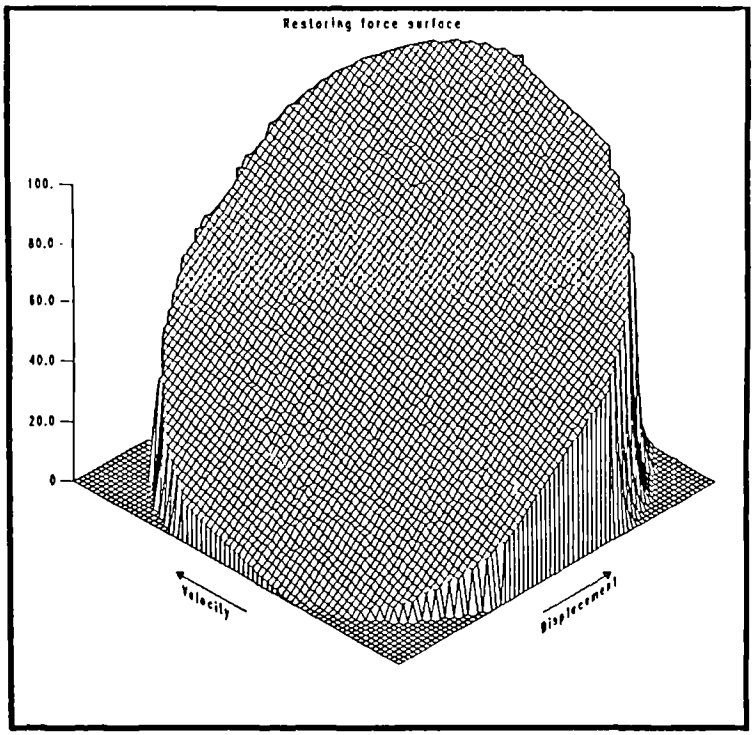

Figure 7.9. Estimated restoring force surface for a linear system excited by two sinusoidal forces of differing frequencies.

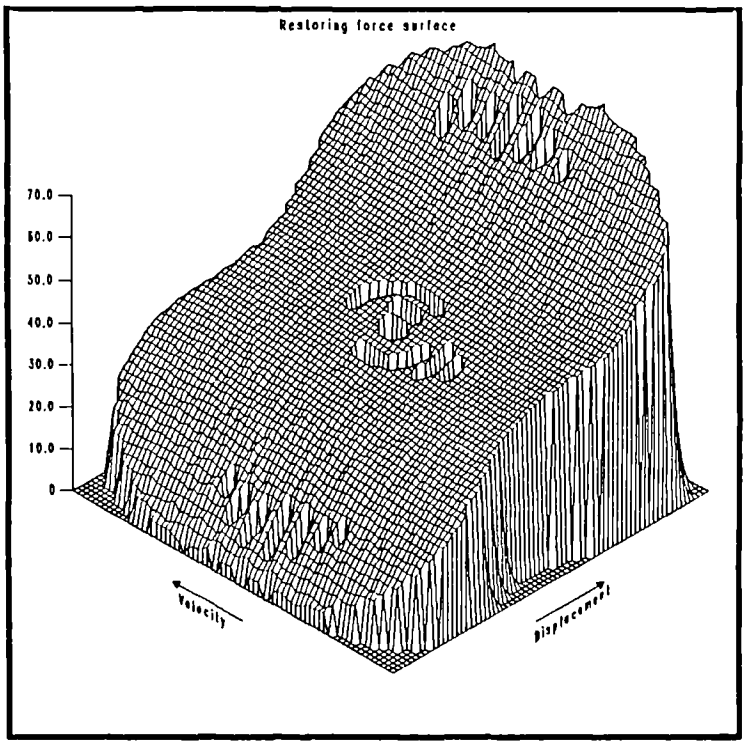

Figure 7.10. Estimated restoring force surface for a Duffing oscillator system excited by two distinct sinusoidal forces.

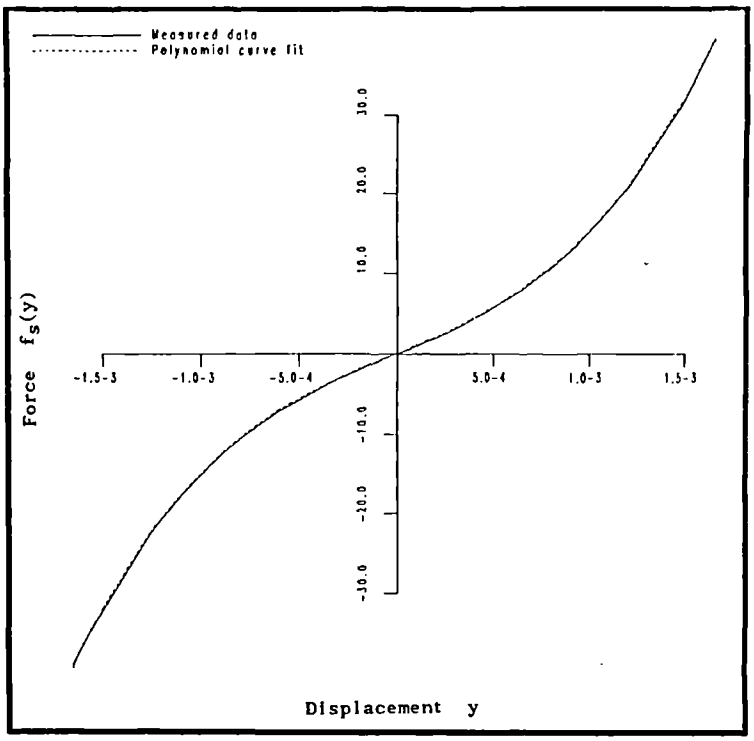

Figure 7.11. Estimated stiffness section for a Duffing oscillator system excited by two distinct sinusoidal forces.

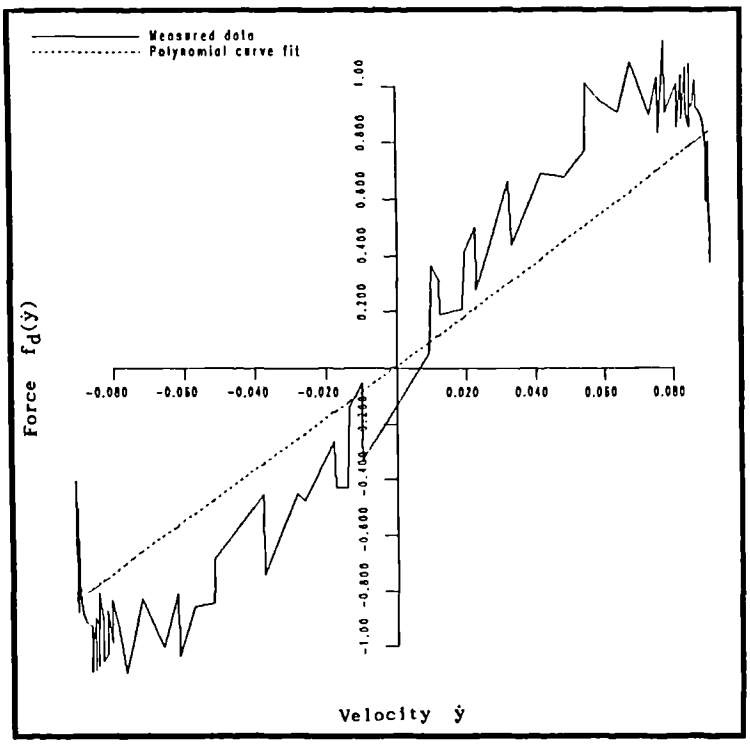

Figure 7.12. Estimated damping section for a Duffing oscillator system excited by two distinct sinusoidal forces.

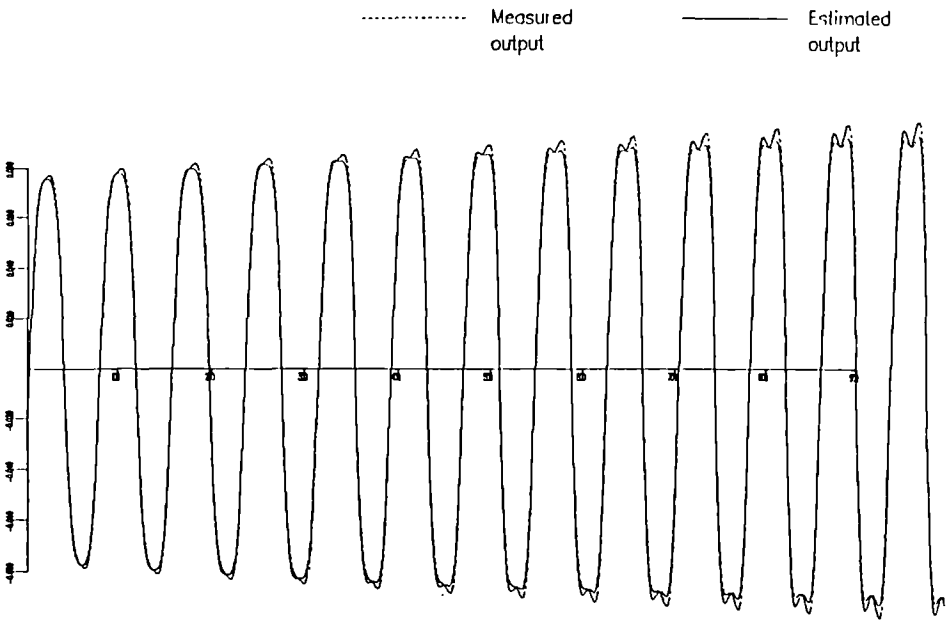

Figure 7.13. Comparison of the exact and estimated velocity data for a Duffing oscillator excited by two distinct sinusoidal forces.

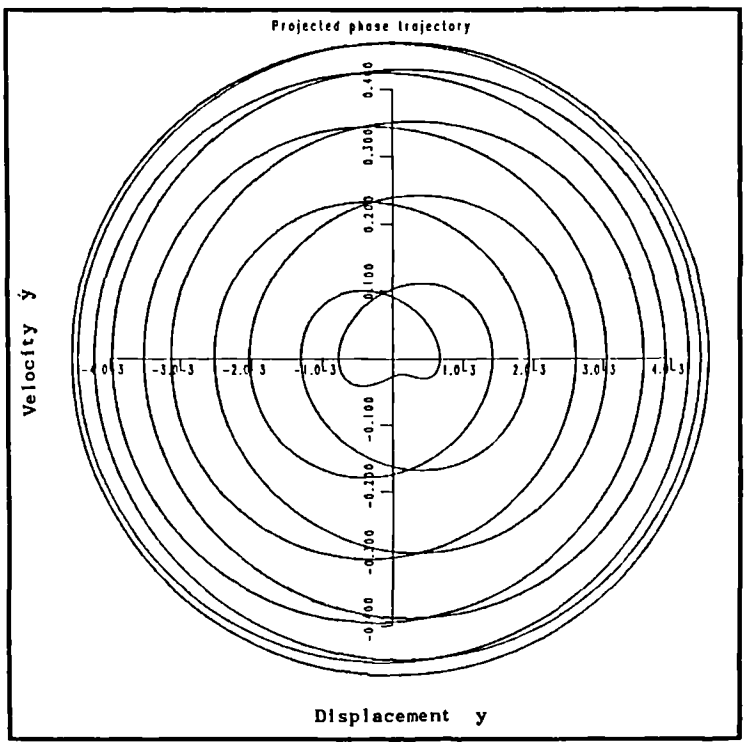

Figure 7.14. Estimated phase trajectory for a linear system excited by two sinusoidal forces.

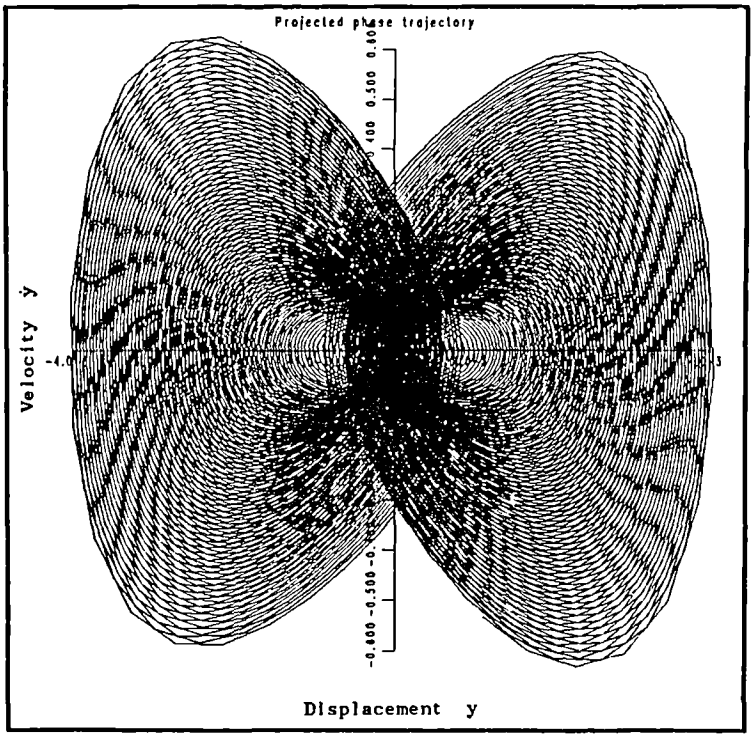

Figure 7.15. Estimated phase trajectory for a Duffing oscillator system excited by a harmonic force with time-dependent amplitude.

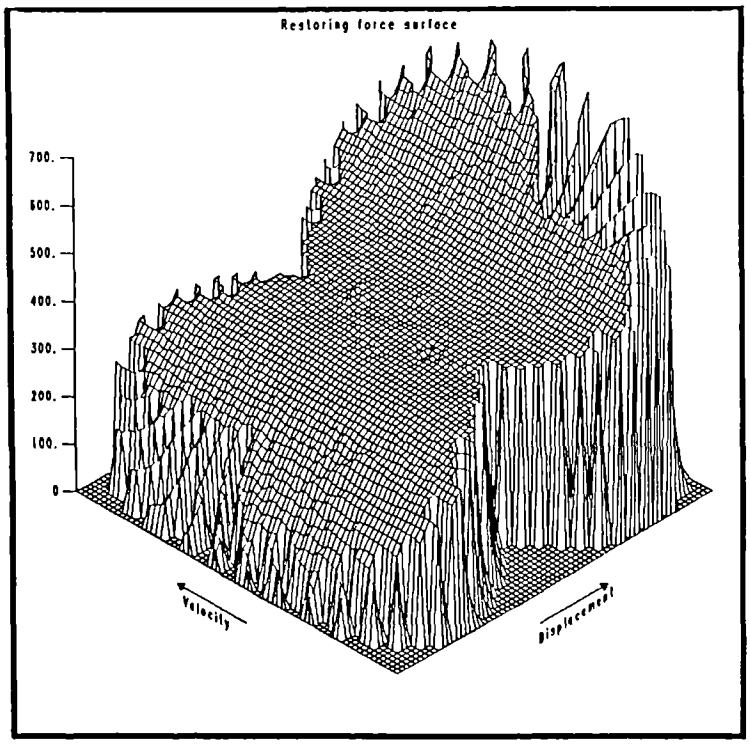

Figure 7.16. Estimated restoring force surface for a Duffing oscillator system excited by a harmonic force with time-dependent amplitude.

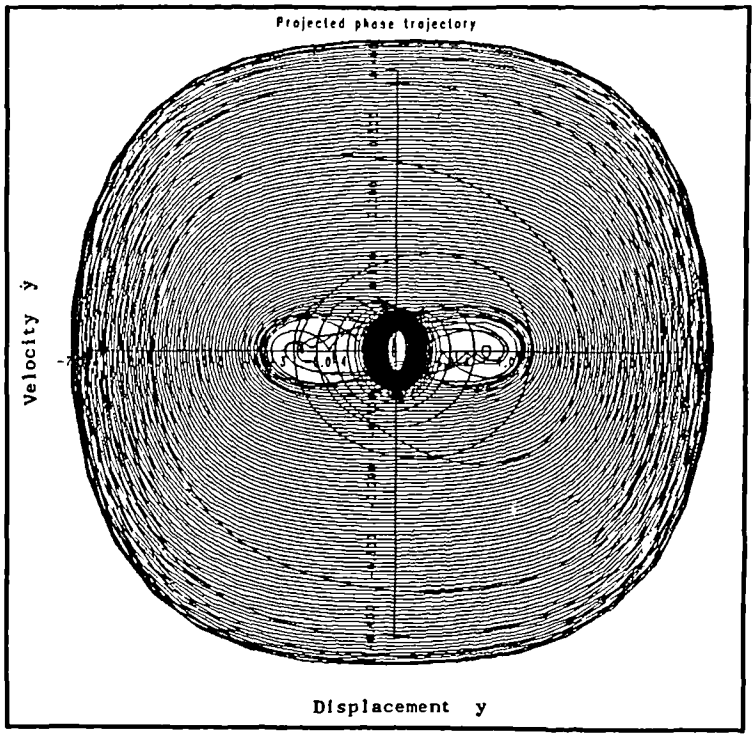

Figure 7.17. Estimated phase trajectory for a Duffing oscillator system excited by a 'chirp' signal.

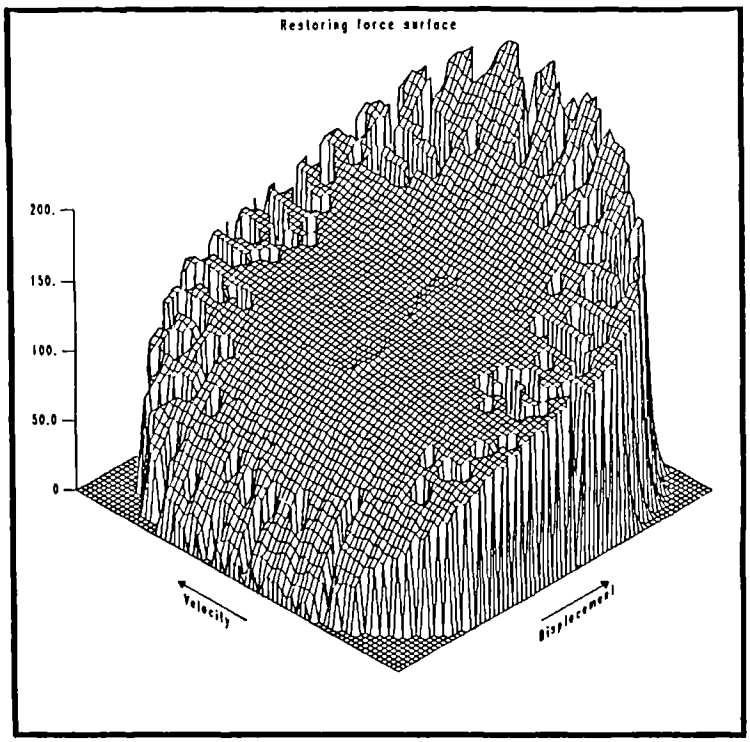

Figure 7.18. Estimated restoring force surface for a Duffing oscillator system excited by a 'chirp' signal.

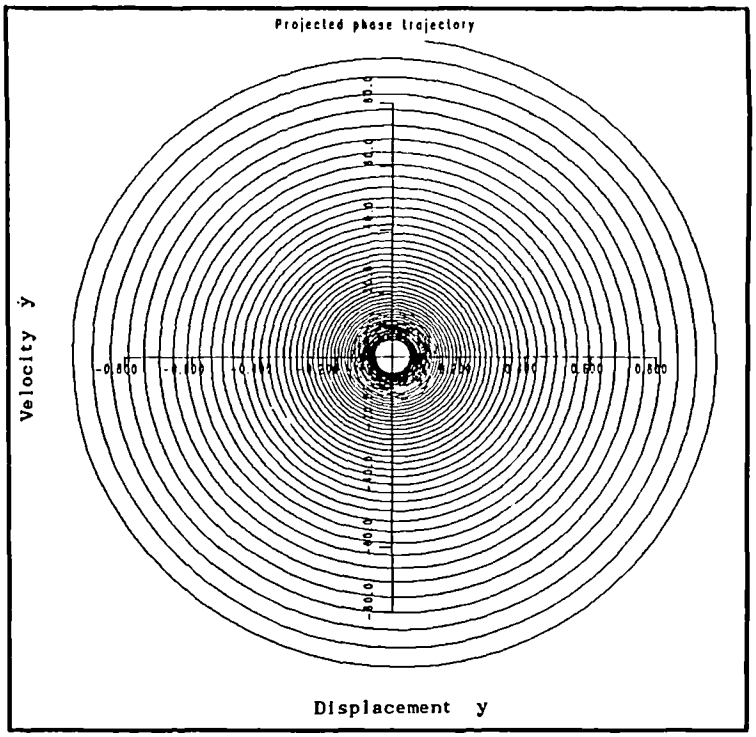

Figure 7.19. Estimated phase trajectory for a linear system excited by a Dirac impulse.

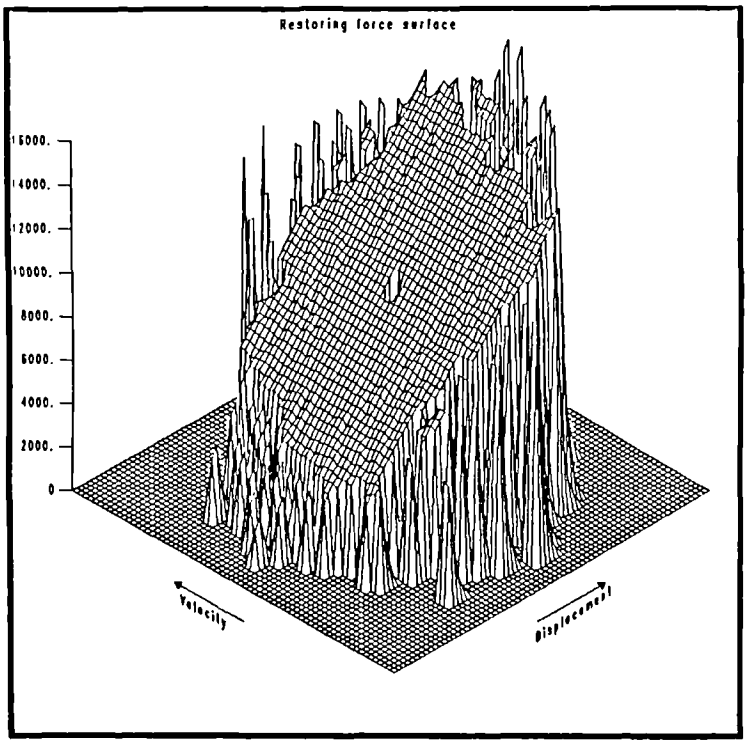

Figure 7.20. Estimated restoring force surface for a linear system excited by a Dirac impulse.

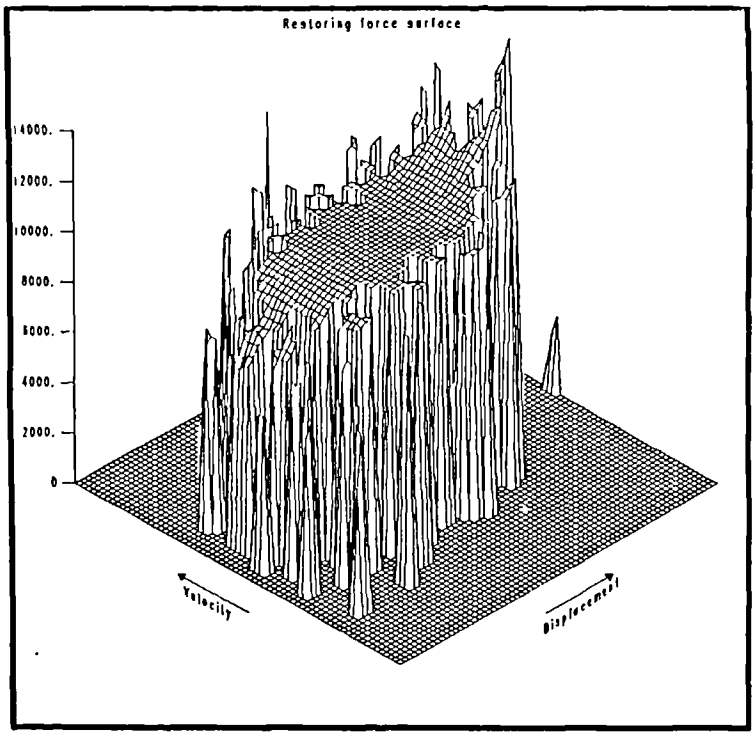

Figure 7.21. Estimated restoring force surface for a Duffing oscillator system excited by a Dirac impulse.

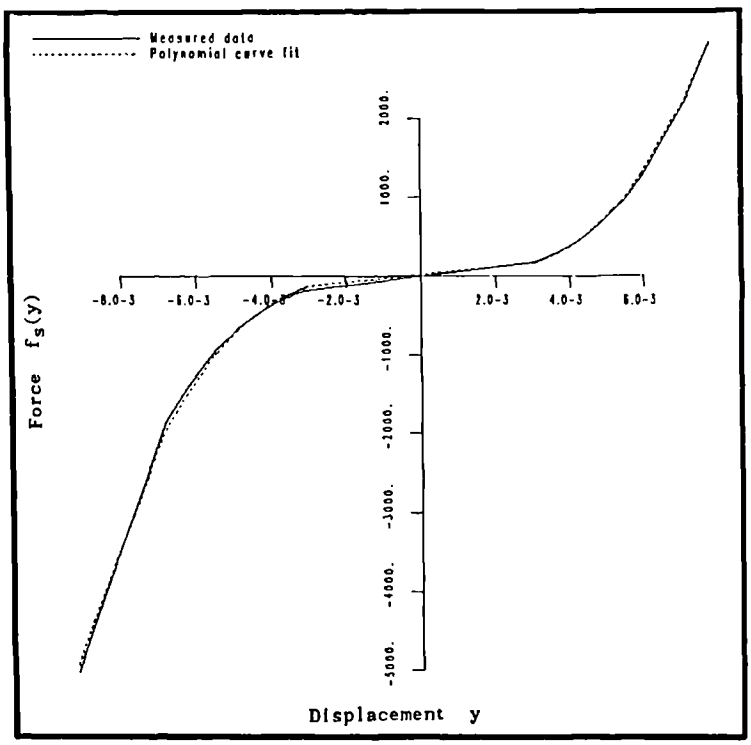

Figure 7.22. Estimated stiffness section for a Duffing oscillator system excited by a Dirac impulse.

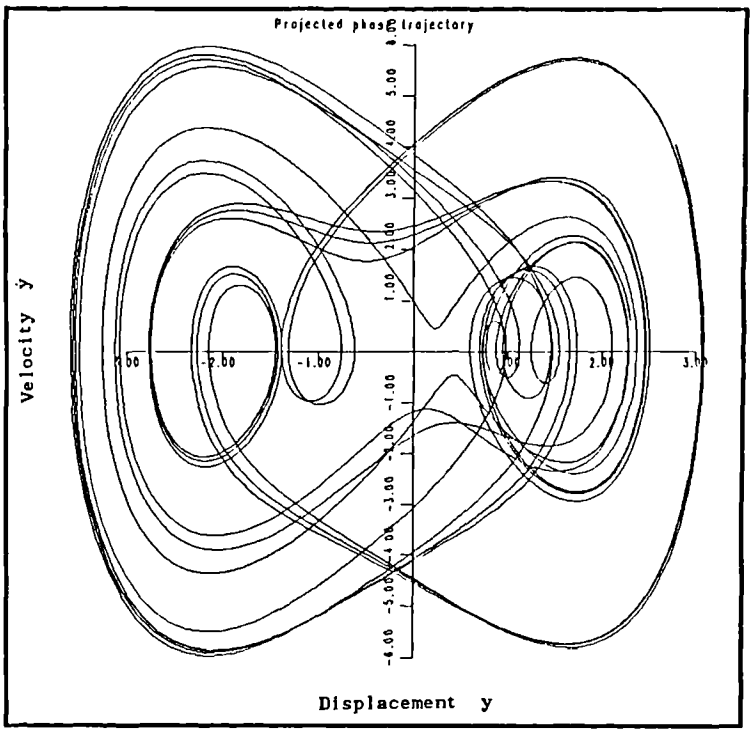

Figure 7.23. Estimated phase trajectory for a chaotic system subjected to harmonic excitation.

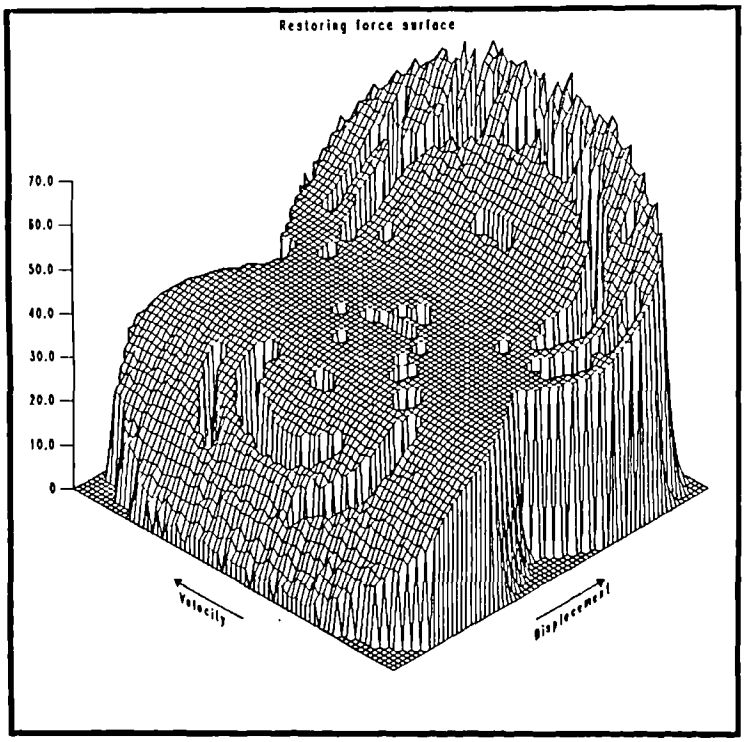

Figure 7.24. Estimated restoring force surface for a chaotic system subjected to harmonic excitation.

CHAPTER 8

EXPERIMENTS ON SDOF SYSTEMS

It has been established in the previous chapters that the force surface method can accurately identify simulated systems. The real test of a procedure's utility is if it can adequately deal with real systems. This chapter describes an attempt to determine how well the method works in a series of experiments. This chapter is restricted to SDOF systems.

8.1. Sampling and Interpolation.

The problem one is faced with in an experiment is that the input force and acceleration response must be sampled simultaneously at each sampling instant. The instrument for sampling used for this study is the CED 1401 intelligent interface (62). This can sample on up to sixteen channels. However, the channels are multiplexed. If sampling is carried out on n channels with a sampling interval Δt, the channels are sampled in order $\Delta t/n$ apart. For example, if x(t) is sampled on channel 0 and $\ddot{y}(t)$ on channel 1, the signals are recorded as follows

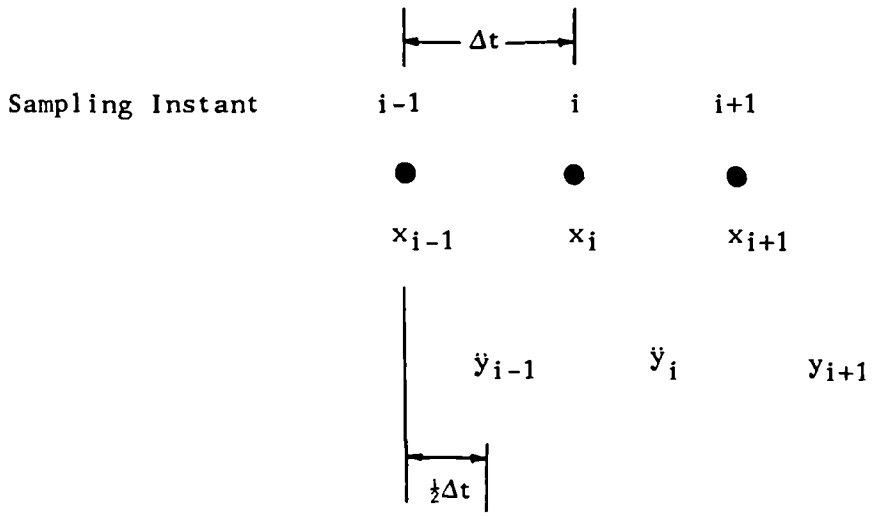

Consider Figure 8.1a, the points marked B are the sampled values from the CED 1401. The points marked A are the values of the $\dot{y}(t)$ signal when the associated x(t) was sampled. One clearly needs a method of calculating the A values from the B's. Fortunately, this is quite straightforward. One can use polynomial interpolation (33). A polynomial is fitted to the B values, the fitted polynomial is then evaluated at the times when the x(t) was sampled. This procedure is illustrated in Figure 8.1b where $\hat{A}_3$ is obtained. The effect of this is to shift the $\dot{y}(t)$ data forward in time by a distance $\Delta t/2$.

If one is using this approach it is important that the sampling frequency be high enough. If the data is undersampled, the polynomial through the B points will not lie close to the data and it will be impossible to accurately shift the data forward. This situation is shown in Figure 8.2. A_3 is the value required, $\hat{A}_3$ is the value obtained from the interpolation. A cubic polynomial is shown fitted to the points B_1 to B_4. It is also important to keep the polynomial order as small as possible as high order polynomials may differ wildly from the actual data over the fitting range while still passing through the sample points.

In order to test the procedure, $\dot{y}(t)$ data was simulated for the linear system

$$\ddot{y} + 20\dot{y} + 10^4 y = x(t)$$

with x(t) a noise sequence with variance 1.0 band-limited into the range (5,30)Hz. The sampling frequency used was 1 kHz. Two hundred points of the original data are shown in Figure 8.3a. The data is then shifted forward by one sampling interval using a sixth order polynomial, the results are shown in Figure 8.3b. Finally, the data is shifted back by the same amount. Figure 8.3c shows that the twice-shifted data overlays the original data almost perfectly. This example is sufficient to give one confidence in the method.

It is a useful exercise to determine the effect on the estimated coefficients if the

time-lag from the sampling device is not corrected for. Suppose one is studying the linear system

$$m\ddot{y} + c\dot{y} + ky = x(t) \qquad (1)$$

The sampled signals are $x(t)$ and $\ddot{y}(t + \lambda\Delta t)$ where $\lambda\Delta t << 1$. Now if $\ddot{y}(t + \lambda\Delta t)$ is denoted by $\ddot{z}(t)$, one has

$$\ddot{z}(t) = \ddot{y}(t + \lambda\Delta t) = \ddot{y}(t) + \lambda\Delta t.\dddot{y}(t) + O(\lambda^2\Delta t^2)$$

$$\dot{z}(t) = \dot{y}(t + \lambda\Delta t) = \dot{y}(t) + \lambda\Delta t.\ddot{y}(t) + O(\lambda^2\Delta t^2)$$

$$z(t) = y(t + \lambda\Delta t) = y(t) + \lambda\Delta t.\dot{y}(t) + O(\lambda^2\Delta t^2)$$

and consequently

$$\ddot{y}(t) = \ddot{z}(t) - \lambda\Delta t.\dddot{z}(t) + O(\lambda^2\Delta t^2)$$

$$\dot{y}(t) = \dot{z}(t) - \lambda\Delta t.\ddot{z}(t) + O(\lambda^2\Delta t^2)$$

$$y(t) = z(t) - \lambda\Delta t.\dot{z}(t) + O(\lambda^2\Delta t^2)$$

Substituting these expressions into equation (1) gives the equation of motion for $\dot{z}(t)$ up to order $\lambda\Delta t$.

$$- m\lambda\Delta t.\dddot{z}(t) + (m - c\lambda\Delta t).\ddot{z}(t) + (c - k\lambda\Delta t).\dot{z}(t) + k.z(t) = x(t) + O(\lambda^2\Delta t^2) \qquad (2)$$

This means that if one estimates coefficients for the $x(t)$, $\ddot{y}(t)$ system without shifting the data, one should expect to obtain the following estimates.

$$\hat{m} = m - c\lambda\Delta t + O(\lambda^2\Delta t^2)$$

$$\hat{c} = c - k\lambda\Delta t$$

$$\hat{k} = k$$

A 'noise' term $\zeta(t) = -m\lambda\Delta t.\dddot{z}(t)$ is also induced. As y(t) and $\ddot{y}(t)$ are anticorrelated, one would also expect $\dot{y}(t)$ and y(t) to be and hence $\dot{z}(t)$ and z(t). This means that the 'noise' term above will bias the estimate of the damping coefficient, this effect being added to the shift above. In fact, the noise term would cause an overestimate of the damping. As an example consider the system used in the simulation earlier, m = 1, c = 20, k = 10^4 and $\Delta t = 10^{-3}$. If one assumes a λ value of 0.5 as one would expect from the CED for a two channel system, one obtains

$$\zeta(t) = 0.0005.\dddot{z}(t)$$

$$\hat{m} = 0.99$$

$$\hat{c} = 15.0$$

$$\hat{k} = 1.0\times10^4$$

and the damping term is changed by 25% while the mass term is only changed by 1%. The stiffness is unchanged. The $\zeta(t)$ may well affect the estimations in practice. One concludes from this analysis that time/phase lags in the data will affect the damping estimates most severely. In fact if

$$k > \frac{c}{\lambda\Delta t} \qquad (3)$$

the damping estimate could be negative.

This analysis can be extended straightforwardly to MDOF systems. Suppose one studies a SIMO system with a diagonal mass matrix [m] and damping and stiffness matrices [C] and [K] respectively, and further that the input channel is used as the reference channel. In the general case, the acceleration measured at node j will be shifted in time by an amount $\lambda_j\Delta t$. So if $y^{(n)}$ denotes $d^n y/dt^n$

$$y_j^{(n)}(t) = z_j^{(n)}(t) - \lambda_j\Delta t.z_j^{(n+1)}(t) + O(\lambda^2\Delta t^2)$$

The i^{th} equation of motion for the x,y system is

$$m_{ii}\ddot{y}_i + \sum_{j=1}^{N} c_{ij}.\dot{y}_j + \sum_{j=1}^{N} k_{ij}.y_j = \delta_{1i}.x(t) \qquad (4)$$

so the i^{th} equation of motion for the x,z system is

$$m_{ii}.(\ddot{z}_i - \lambda_i\Delta t.\dddot{z}_i) + \sum_{j=1}^{N} c_{ij}.(\dot{z}_j - \lambda_j\Delta t.\ddot{z}_j)$$

$$+ \sum_{j=1}^{N} k_{ij}.(z_j - \lambda_j\Delta t.\dot{z}_j) = \delta_{1i}.x(t) + O(\lambda^2\Delta t^2)$$

i.e.

$$- m_{ii}\lambda_i\Delta t.\dddot{z}_i + \sum_{j=1}^{N} \left\{ \delta_{ij}m_{jj} - c_{ij}\lambda_j\Delta t \right\}.\ddot{z}_j +$$

$$\sum_{j=1}^{N} \left\{ c_{ij} - k_{ij}\lambda_j\Delta t \right\}.\dot{z}_j + \sum_{j=1}^{N} k_{ij}.z_j =$$

$$\delta_{1i}.x(t) + O(\lambda^2\Delta t^2) \qquad (5)$$

and the situation is almost exactly the same as for the SDOF system. The coefficient estimates for [m] and [C] are shifted as follows

$$\hat{m}_{ij} = \delta_{ij}m_{jj} - c_{ij}\lambda_j\Delta t + O(\lambda^2\Delta t^2)$$

$$\hat{c}_{ij} = c_{ij} - k_{ij}\lambda_j\Delta t$$

while the stiffness matrix remains unchanged. In addition, all the coefficient estimates will be affected by the noise term

$$\zeta_i = - m_{ii}\lambda_i\Delta t.\dddot{z}_i$$

A point worth observing is that the z(t) equations of motion (5) have a full mass matrix. The system is still a SIMO system, so one might expect problems with linear dependence as discussed in Chapter 5. This would perhaps be the case if the z terms are small; if they are large they might be expected to break the linear dependence.

They would of course severely affect the coefficient estimates in this case.

8.2. Noise.

As this chapter is concerned with experimental data for the first time, it is the appropriate place to discuss the effects of noise on the measured data. The integration procedures described in Chapter 6 introduced errors into the velocity and displacement data and it was evident that the parameter estimation was fairly insensitive to those errors. However, it is important to determine the effect of errors in the measured data on the integration itself, and the subsequent parameter estimates. As usual, the study is based on a number of simulations.

Example 1. The system

$$\ddot{y} + 40\dot{y} + 10^4 y = x(t)$$

was simulated, with x(t) a Gaussian noise sequence with RMS 10.0 and zero mean, band-limited into the range (0,200)Hz. To each of the signals x, y, $\dot{y}$ and $\ddot{y}$, A white Gaussian noise term was added. In each case the RMS value of the noise was a fixed percentage α % of the RMS value of the signal. For each α used, a linear least-squares model was fitted to the noisy data. The results are tabulated below together with the MSE for the model (predicted data compared with measured data).

α	$\hat{m}$	$\hat{c}$	$\hat{k}$	MSE
1.0	0.9997	39.98	1.0000×10^4	0.021
2.0	0.9990	39.96	0.9995×10^4	0.084
5.0	0.9951	39.90	0.9951×10^4	0.524
10.0	0.9826	39.79	0.9787×10^4	2.053

The comparison between predicted and measured data for α = 5.0 is shown in Figure

8.4. The force surface for this case is shown in Figure 8.5. The values of the parameter estimates above indicate that the estimation procedure is quite insensitive to measurement noise. The force surface is still discernably linear.

Example 2. The same system as above was simulated with x(t) a Gaussian noise sequence of RMS 10.0 band-limited into the range (5,40)Hz. A percentage α = 1.0% of white Gaussian noise was added to the signals x(t) and $\ddot{y}$(t). The signal $\ddot{y}$(t) was then integrated twice using the trapezium rule followed by a linear drift removal from $\ddot{y}$(t) and y(t). The resulting velocity and displacement data are shown in Figure 8.6. The small amount of noise introduced at low frequencies is sufficient to introduce significant low-frequency trends into the estimated displacement.

The integration was then repeated using the trapezium rule followed by a band-pass filter with lower and upper cut-offs 5 Hz and 40 Hz respectively. The resulting data are shown in Figure 8.7. The low frequency problems are absent. Using the noisy input and acceleration data and the estimated velocity and displacement data in the least-squares procedure gives a linear model with coefficients $\hat{m}$ = 1.015, $\hat{c}$ = 41.02 and $\hat{k}$ = 1.033×10^4. The MSE for comparing the predicted data with the measured data was 0.08%. The force surface is shown in Figure 8.8.

The same procedure was repeated for a simulation where α = 5.0%. The comparison between estimated and 'exact' velocity is shown in Figure 8.9, The MSE for the comparison is 0.689. One can see that the estimate is very good. The same comparison for the displacement data is shown in Figure 8.10 with MSE 1.66. This indicates that the integration procedure is insensitive to measurement noise provided one removes the low frequency component. Because of aliasing, this also entails removing the noise component above the Nyquist frequency. These results indicate that for experimental data, one is usually going to be faced with filtering the integrated data even if a band-limited input is used. A parameter estimation using the data above gave coefficients $\hat{m}$ = 0.98, $\hat{c}$ = 41.32 and $\hat{k}$ = 0.964×10^4. The comparison between measured and predicted data is shown in Figure 8.11, the MSE being 0.41.

The force surface is shown in Figure 8.12. These results are encouraging; both the least-squares estimator and the integration procedure appear to be reliable in the presence of measurement noise. Having reassured oneself about this, one can proceed to the study of experimental systems.

8.4. A Nonlinear Cantilever Beam.

The system studied in this section is a beam made of mild steel, mounted vertically with an encastré end and a free end as shown in Figure 8.13. If the amplitude of transverse motion of the beam exceeds a fixed limit, projections fixed on either side of the beam make contact with a steel bush fixed in a steel cylinder surrounding the lower portion of the beam. By changing the bush one can vary the clearance gap on either side of the beam. In the experiments below a clearance of 0.5 mm was used. Clearly when the beam is in contact with the bush, the effective length of the beam is lowered, this gives an effective increase in stiffness. Overall, for transverse deflections, the beam has a piecewise-linear stiffness. Initial tests on the beam indicated that is was very lightly damped indeed. To increase the possibility of identifying the damping coefficient for the system, the damping was increased by placing constrained layer damping material on both sides. Separate tests were carried out on the beam at low and high levels of excitation.

8.3.1. Low Excitation Tests.

The purpose of carrying out experiments with small levels of forcing is to study the behaviour of the beam as a linear system. Beacause of linearity at low levels the beam is amenable to a theoretical study. The dimensions and material contants etc. for the beam are listed below

Length L : 0.7 m

Width w : 2.525×10^{-2} m

Thickness t	:	1.25×10^{-2} m
Density ρ	:	7800 Kgm^{-3}
Young's modulus E	:	2.01×10^{11} Nm^{-2}
Second moment of area I	:	4.1097×10^{-9} m^4
Mass per unit length M	:	2.462 Kgm^{-2}
EI	:	826.05 Nm^2

According to Blevins **(63)**, The first two natural frequencies of a cantilever (fixed-free) beam are given by

$$f_i = \frac{1}{2\pi} (\lambda_i/L)^2 (EI/m)^{\frac{1}{2}} \quad Hz$$

where λ_1 is 1.8751 and λ_2 is 4.6941. This gives theoretical natural frequencies of 16.05 Hz and 100.62 Hz.

In order to test these predictions, an impulse test was carried out on the beam. The beam was struck at the level of the shaker link (Figure 8.13) with a PCB instrumented hammer and the response was obtained using an Endevco 213E accelerometer placed at the end of the beam. The Frequency Response Function (FRF) was displayed on a Scientific Atlanta SD380 spectrum analyser. The FRF is shown in Figure 8.14. This indicates that the first two natural frequencies are at 15.0 Hz and 97.0 Hz. These are overestimates because the accelerometer at the top increases the effective mass of the beam. This in turn will reduce the natural frequencies. The test was repeated with the accelerometer also placed at the level of the shaker link. The natural frequencies obtained in this case were 15.5 Hz and 98.5 Hz. This is acceptably close to the theoretical results, closer agreement could have been reached by removing the cylindrical cover and placing the acceleromater at the base of the beam. This test gives one confidence that the system is behaving as a fixed-free beam.

One can now proceed to estimate the theoretical stiffness of the beam. If a unit force is applied at a distance 'a' metres from the free end of the beam (i.e. at the point where the shaker is attached, a = 0.495 m), Simple beam theory (64) shows that the displacement y at a distance d metres from the free end is given by

$$y(d) = \frac{1}{6EI}\left[[d-a]^3 - 3(L-a)^2 d + 3(L-a)^2 L - (L-a)^3 \right] \qquad (6)$$

where [...] is a Macauley bracket which vanishes if the argument is negative. This shows that the stiffness constant

$$k(d) = \frac{\text{force applied at a}}{\text{displacement measured at d}}$$

is given by

$$k(d) = \frac{6EI}{[d-a]^2 - 3(L-a)^2 d + 3(L-a)^2 L - (L-a)^3}$$

When the displacement is measured at the same point as the force is applied i.e. at d = a, the stiffness is referred to below as the *direct stiffness* k_d and the theoretical value is $k_d = 9.654 \times 10^4$ Nm^{-1}. When the displacement is measured at the free end of the beam, the stiffness is referred to as the *cross stiffness* k_c and has theoretical value $k_c = 2.769 \times 10^4$ Nm^{-1}.

The first and second natural frequencies are seen to be well separated. This means that one could hopefully band-limit the input around the first frequency so that only the first mode is excited. If this is the case, as the first mode is the bending mode (which resembles the static deflection curve), one might reasonably expect the system to behave as an SDOF system with stiffness k(d) when the response $\ddot{y}_d(t)$ is measured at the point d metres form the free end. With these assumptions, the equations of motion are seen to be

$$m(d).\ddot{y}_d(t) + c(d).\dot{y}_d(t) + k(d).y_d(t) = x(t)$$

The mass m(d) is fixed by the requirement that the natural frequency f_1 of the system is given by

$$2\pi f_1 = (k(d)/m(d))^{\frac{1}{2}}$$

Two experiments were carried out. In both cases the excitation signal was a zero-mean white Gaussian noise sequence band-pass filtered into the range (10,20)Hz. The input signal was produced using a Korman noise generator and filter modules. This was then passed through a KEMO VBF/4 filter in order to sharpen the cut-offs. The signal was then amplified using a Gearing and Watson SS30 amplifier and passed on to a Gearing and Watson V20B electrodynamic shaker. The shaker was attached to the beam by a rigid link. The arrangement is shown in Figure 10.15. The input force was measured using a Kistler 9311A force transducer in series with a Bruel and Kaer 2635 charge amplifier. The response was measured using an Endevco 213E accelerometer also with a B & K 2635 charge amplifier. Finally, the data was sampled using the CED 1401 intelligent interface as described in section 8.1.

In the first of the tests at low level, the accelerometer was placed near the free end of the beam at the cross stiffness point. 5000 points of data were obtained from the CED 1401 with a sampling frequency of 500 Hz. The data was transferred from the 1401 to a HP 310 computer. Finally the data was transferred to the Sun 3/50 workstation where the following analysis was carried out. The acceleration data was shifted forward in time by half a sampling interval. One hundred points of the sampled signal together with the shifted signal are shown in Figure 8.16. The shifted data was then integrated twice to give $\dot{y}(t)$ and y(t). A Trapezium rule integration was used followed by the application of a filter with pass-band (10,20)Hz. Five hundred points of data were deleted from each end of the data records in order to eliminate any filter transients. The phase trajectory for the data obtained is shown in Figure 8.17.

A linear least–squares model was fitted to 1000 points of the data. Using an initial estimate for the mass of m_i = 0.0, the following results were obtained

$$\hat{m}_c \quad (Kg) \qquad = \quad 3.113$$
$$\hat{c}_c \quad (Nm^{-1}s) \quad = \quad 0.872$$
$$\hat{k}_c \quad (Nm^{-1}) \qquad = \quad 2.771x10^4 \pm 80.90$$

as shown in Table 8.1. The damping coefficient was deleted as insignificant. The stiffness value shows excellent agreement with the theoretical estimate of $2.769x10^4$. The natural frequency of the model above is 15.01 Hz, again ahowing excellent agreement with the measured value of 15.0 Hz. Comparing the measured and predicted inputs (RHS's) gave a MSE of 0.08 as shown in Figure 8.18. The estimated restoring force surface is shown in Figure 8.19, it is almost perfectly flat as required.

A more stringent test of the model was now applied. As with the SDOF simulations in Chapter 2, the model equations of motion were stepped forward in time using the measured input x(t) as the forcing term, the model displacements obtained were then compared with the displacements from the integration procedure. Two comparisons were made, one using all the coefficients above and one with the damping coefficient set to zero. The first comparison gave a MSE of 8.88, the second gave a MSE of 7.45. This simply reaffirms how little confidence one has in the damping estimate, the damping is too small to estimate with any accuracy. Five hundred points of the second comparison are shown in Figure 8.20.

The procedure used above to step the equations of motion forward in time was an adaptive fifth–order Runge–Kutta procedure which used linear interpolation to estimate the value of x(t) in between sampling instants. Although this is considerably more complicated than the fourth–order scheme used previously, it was deemed neccessary to use some procedure which did not hold the forcing term constant over a sampling interval.

In the second low-level test, the response was measured at the direct point. In all other respects the experimental procedure and data processing were identical to the test above. In this case a linear least-squares fit produced the coefficients

$$\hat{m}_d \quad (Kg) \qquad = \quad 10.03$$
$$\hat{c}_d \quad (Nm^{-1}s) \quad = \quad 1.389$$
$$\hat{k}_d \quad (Nm^{-1}) \qquad = \quad 9.69x10^4 \pm 0.28x10^4$$

Again, the damping coefficient was deleted. As before, the estimated stiffness agrees very well with the theoretical value of $9.65x10^4$ Nm^{-1}. The natural frequency of the model is 15.66 Hz in almost direct agreement with the value of 15.5 Hz obtained from the SD380 spectrum analyser. Comparing measured and predicted inputs gave an MSE of 2.43 in this case and the comparison is shown in Figure 8.21. The restoring force surface is shown in Figure 8.22. Comparing the predicted and 'measured' displacements using the fifth-order Runge-Kutta procedure gave an MSE of 3.28; the comparison is shown in Figure 8.23.

8.3.2. High Excitation Test.

This test was carried out with the accelerometer at the cross point. The level of excitation was increased until the projections on the side of the beam began to make contact with the bush. As before, the input signal was band-limited into the range (10,20)Hz. Figure 8.24 shows the input and output spectra, one can see that the output contains a significant component at higher frequencies. Because of this, the data was recorded using a sampling frequency of 2.5 kHz. Two hundred points of input and response data are shown in Figure 8.25. One can see that the high frequency content of the acceleration signal will make accurate shifting difficult. Because of this, the data was processed in two ways.

In the first case, the data was integrated without shifting. The trapezium rule was used followed by filtering into the interval (10,200)Hz. In order to estimate the mass for the surface plot a linear least-squares model was fitted which gave $\hat{m}$ = 2.24 Kg.

The restoring force surface is shown in Figure 8.26. The stiffness section is shown in Figure 8.27 together with a fifth-order curve-fit. The section clearly shows a piecewise-linear characteristic with singularities at around ± 0.6 mm. This is close to the design clearances of ± 0.5 mm. The damping section is shown in Figure 8.28. The fact that the damping appears to be negative is explicable in terms of the inequality (3). If the values of c and k for the linear tests above are used together with $\lambda = 0.5$ and $\Delta t = 1/2500$, one can see that negative damping estimates are expected for both the direct and cross points.

In the second case the data was shifted forward in time by half a sampling instant using a fourth-order interpolating polynomial. The results of the shift are shown in Figure 8.29, they are clearly not very accurate. However, the stiffness section (Figure 8.30) shows a clear piecewise-linear characteristic with singularities at ± 0.6 mm.

8.4. The ETH Box.

The box in question is a collection of three analogue circuits, each of which behaves as a nonlinear SDOF system. The box was provided by Dr. A. Fracheboug of ETH-Zentrum in Zurich. The idea was for a number of research groups with interests in system identification to attempt to determine the 'equations of motion' of each circuit or to simply determine the form of the nonlinearity. The Heriot-Watt Univeristy group used Wiener/Volterra series, Hilbert transform and restoring force surface approaches, while S.Billings and K.M.Tsang at Sheffield University used NARMAX modelling and Higher order transfer functions. The results obtained were found to be consistent.

The equation for each circuit has the form

$$m\ddot{y} + c\dot{y} + ky + g(y,\dot{y}) = x(t)$$

One supplies a voltage signal x(t) to input terminal of the box and records the output voltage y(t). Each circuit has an overload indicator which signals that the output has saturated because a certain input level has been reached. Unfortunately, for the restoring force method it is unsatisfactory to measure y(t) and numerically differentiate. To overcome this problem, the box was opened and the output signal was taken from the circuit before the final two integrators, this gave an acceleration signal (possibly with a scale factor). To confirm that the signal obtained was actually acceleration, the Frequency Response Function was obtained using the SD380 spectrum analyser. The Nyquist plot showed the FRF to be of inertance type (7), confirming the nature of the signal. This action is justified by the fact that one usually has control over what type of signal one measures, it is usually acceleration which is measured in structural vibration tests.

The input signal chosen for circuit 1 was a swept-sine generated in the SD380 analyser. For circuits 2 and 3, a random input was used which was obtained from a Korman noise generator with filter modules in series with a KEMO VBF/4 filter. In all cases the signal was then passed to a Gearing and Watson SS30 amplifier. As the input and output signals were voltages, transducers and charge amplifiers were not needed. The signals were sampled directly using the analyser in the case of circuit 1, and the CED 1401 for circuits 2 and 3.

8.4.1. Circuit 1.

Tests at low levels indicated that the system had a linear natural frequency of 150 Hz. At higher levels the resonant frequency was observed to shift downward, indicating a softening stiffness nonlinearity i.e a polynomial stiffness with negative leading coefficient. This was confirmed by a Hilbert transform analysis carried out by other members of the dynamics group, the results of which are shown in Figure 8.31. In the Nyquist plane, the transform is rotated anti-clockwise. This indicates the presence of a softening stiffness
nonlinearity as described in chapter 1.

The input used for the restoring force identification was a swept–sine, the frequency increasing from 80 Hz to 280 Hz over the 12000 points of data sampled. The amplitude of the input used was 3.5 V, any increase in this excitation level caused the circuit to overload. A sampling frequency of 1280 Hz was used, the sampling was carried out using the SD380 analyser. After sampling the data was stored in the analyser's time buffer. The data was then transferred to a HP 300 computer, and then to a Sun 3/50 workstation where the the analysis was carried out. The 12000 points of input and response data are shown in Figure 8.32. The acceleration data was integrated twice using the trapezium rule followed by filtering into the interval (30,400)Hz. As in the previous section, 500 points of data were removed from each end of the data records to eliminate any filter transients.

Having prepared the data least–squares models of the form

$$\Delta m.\ddot{y} + \sum_{i=0}^{m} \sum_{j=0}^{n} y^i \dot{y}^j = x(t) - m_i.\ddot{y} \qquad (7)$$

were fitted to data points 2000 to 3000. The initial mass estimate used was m_i = 3.10, a value obtained from a previous test at low levels. Two models were fitted, a linear model and a nonlinear model of order (3,2). The resulting coefficients in each case are shown in Table 8.2. When a comparison was made between predicted and measured data, the MSE values were 9.40 for the linear model and 0.066 for the (3,2) model. The nonlinear model obtained is

$$\begin{aligned} f(y,\dot{y}) = {} & -0.1307 + 331.5\dot{y} - 5.557\times10^{4}\dot{y}^2 \\ & + 3.214\times10^{6}y + 5.381\times10^{10}y^2 - 3.3\times10^{15}y^3 \\ & - 6.56\times10^{6}y\dot{y} \end{aligned}$$

However, the constant and cross terms have small significance factors, 0.23% and 0.17% respectively, if they were discarded the MSE would rise to about 0.466, this is still much better than the linear model.

Three hundred points of the comparison for the nonlinear model are shown in Figure 8.33. Using the mass of 3.175 from the (3,2) estimate, the force surface for the system was obtained and is displayed in Figure 8.34. The surface appears to be almost linear. However, if one looks at the stiffness section with a cubic curve-fit superimposed (Figure 8.35), one can see that the stiffness actually has a nonlinear characteristic. The actual improvement in the fit that one obtains if one moves from a quadratic to the cubic approximation shown is small, this indicates that the quadratic term dominates. The damping section is shown in Figure 8.36 with a quadratic curve-fit. The (3,2) model appears to be valid for all the data as the sections are obtained from all 12000 points. Curve-fitting to the sections gives a model

$$f(y,\dot{y}) = -0.065 + 327.0\dot{y} - 5.477\times10^{4}\dot{y}^{2} + 3.168\times10^{6}y + 5.308\times10^{10}y^{2} - 2.99\times10^{15}y^{3}$$

which agrees quite well with the one above.

The conclusion reached is that circuit 1 is a SDOF system with quadratic stiffness and softening cubic stiffness terms and a quadratic damping term. Quadratic stiffness terms always produce a softening characteristic independently of the sign of the coefficient (65). Hence, this identification is consistent with the Hilbert transform results.

8.4.2. Circuit 2.

Tests at low levels indicated that this system also had a linear resonance at 150 Hz. At higher levels of excitation the resonant frequency shifted upwards. This fact, together with the Hilbert transforms (Figure 8.37) indicate that the system has a hardening stiffness nonlinearity.

In this case, a band-limited random input in the range (100,200)Hz was used for the restoring force surface identification. The level of excitation was increased until the resonant frequency shifted up to 154 Hz. Beyond this level, the circuit overloaded.

The input and response signals were recorded on the CED 1401 using a sampling frequency of 1 kHz. As above, the data was passed to Sun computer for analysis. The acceleration data was shifted forward in time by half a sampling instant. The shifted data was then integrated using the trapezium rule followed by high-pass filtering with cut-off 100 Hz. . Least-squares models of order (1,1), (3,1) and (5,1) were fitted and the results are shown in Table 3. When a comparison of predicted and measured data was made for each model, the results were

Model Order	MSE	Mass
(1,1)	0.0556	3.28
(3,1)	0.0181	3.33
(5,1)	0.0185	3.33

One hundred points of the comparison for the (3,1) model are shown in Figure 8.38, there is almost perfect agreement. As the MSE for the (5,1) model is slightly greater than that for the (3,1) model one concludes that the system has a cubic stiffness. This is confirmed by the fact that the only terms considered significant in the (5,1) are those from the (3,1) model, and also by the fact that the two sets of coefficients agree (Table 8.3). The restoring force surface is shown in Figure 8.39. Even more than for the first circuit, the surface appears to be linear. However, one can see the cubic nature of the nonlinearity clearly if one considers the stiffness section with linear and cubic curve fits superimposed (Figures 8.40 and 8.41). The cubic curve-fit overlays the data almost perfectly. The damping section is shown in Figure 8.42, the linear curve-fit is clearly adequate to describe the damping.

The conclusion reached is that circuit 2 is a SDOF system with a hardening cubic stiffness nonlinearity. The equation of motion can be read off from Table 8.3b.

8.4.3. Circuit 3.

The main problem associated with the identification of the first two circuits was that

the box tended to overload before the nonlinear dynamics could be sufficiently excited. No such problem existed with circuit 3. Low level tests indicated that the linear resonance was at 477.5 Hz. At higher levels of excitation the resonance shifted downwards by a great amount. It was possible to move the resonance to 200 Hz without overloading the circuit. This fact, together with the Hilbert transforms (Figure 8.43), indicate that the system possesses a very strong softening stiffness nonlinearity.

The excitation signal used in this case was a random signal band-limited into the range (200,300)Hz. The level of excitation was increased until the resonance had shifted down to approximately 300 Hz. Eight thousand points of the input and response data were sampled on the CED 1401 using a sampling frequency of 2500 kHz. The data was then passed to the Sun computer. The acceleration was integrated twice using the trapezium rule followed by filtering into the range (100,500)Hz. After cutting out data to remove the filter transients, 7000 points remained.

Initially, it proved rather difficult to fit a model of the form (7). Because of this, a mass estimate was not available to form the force surface. The mass was estimated by repeatedly curve-fitting a ninth-order polynomial to the stiffness section and adjusting the mass estimate each time until the MSE for the curve fit was a minimum. The mass estimate obtained from this procedure was 3.60 giving an MSE of 0.291. The corresponding stiffness section is shown in Figure 8.44, It shows a very clear softening piecewise linear characteristic. The damping section is shown in Figure 8.45, the damping appears to be linear. Using the mass value above, the restoring force surface was obtained (Figure 8.46). This surface is rather interesting. At low velocities, the stiffness characteristics are piecewise linear as indicated by the section at $\dot{y} = 0$. However, at higher velocities the stiffness characteristics are linear. This can be seen more clearly in a contour plot of the surface (Figure 8.47). This indicates that significant cross-terms are present in the restoring force. Armed with this knowledge, a (9,3) model was fitted. The coefficients are shown in Table 8.4. The MSE for the comparison between predicted and measured output is 0.765, 240 points of the comparison are shown in Figure 8.48. If one looks again at the damping section, one

can see that the scatter in the data is higher at low velocities, corresponding to the fact that the stiffness is greater there.

The conclusion here is that circuit 3 was perhaps intended to be a softening piecewise linear system. In fact, this is only the case for low velocities. At high velocities cross-terms become significant.

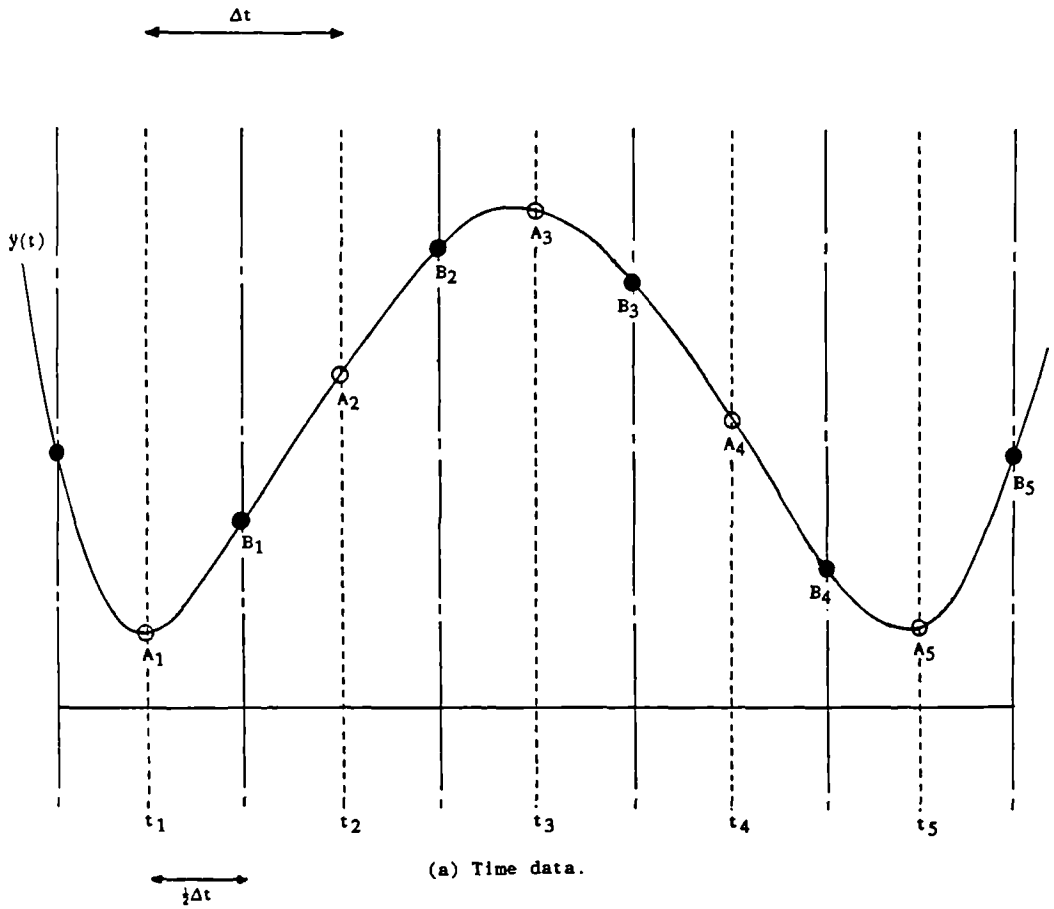

(a) Time data.

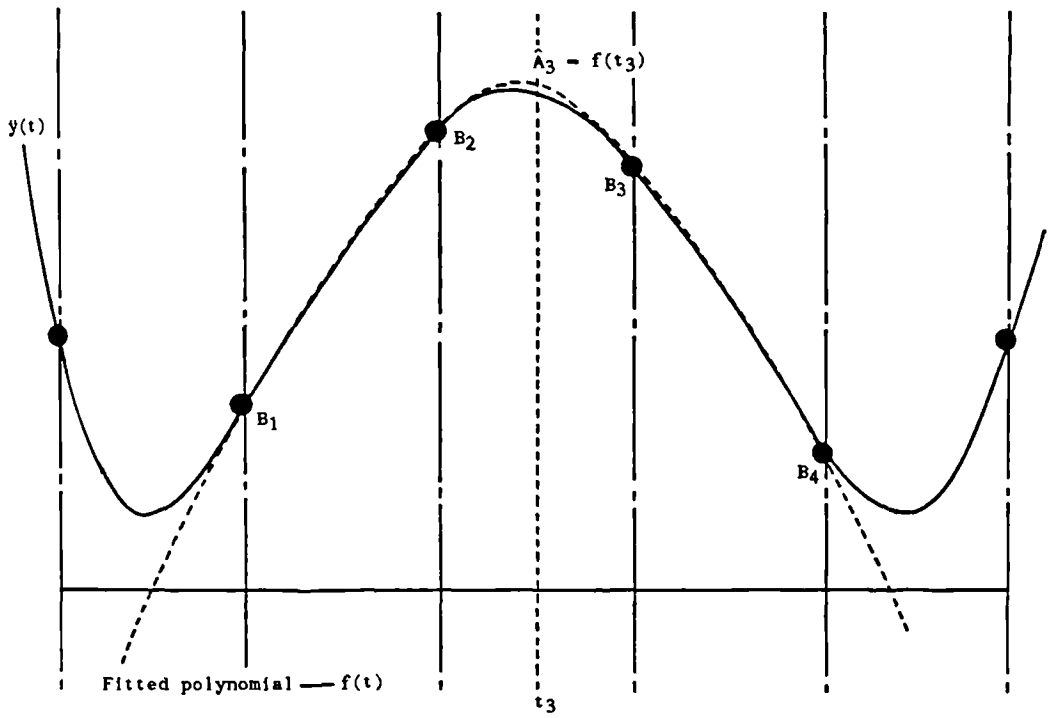

(b) Time data with curve-fit.

Figure 8.1. The shifting procedure for the time data.

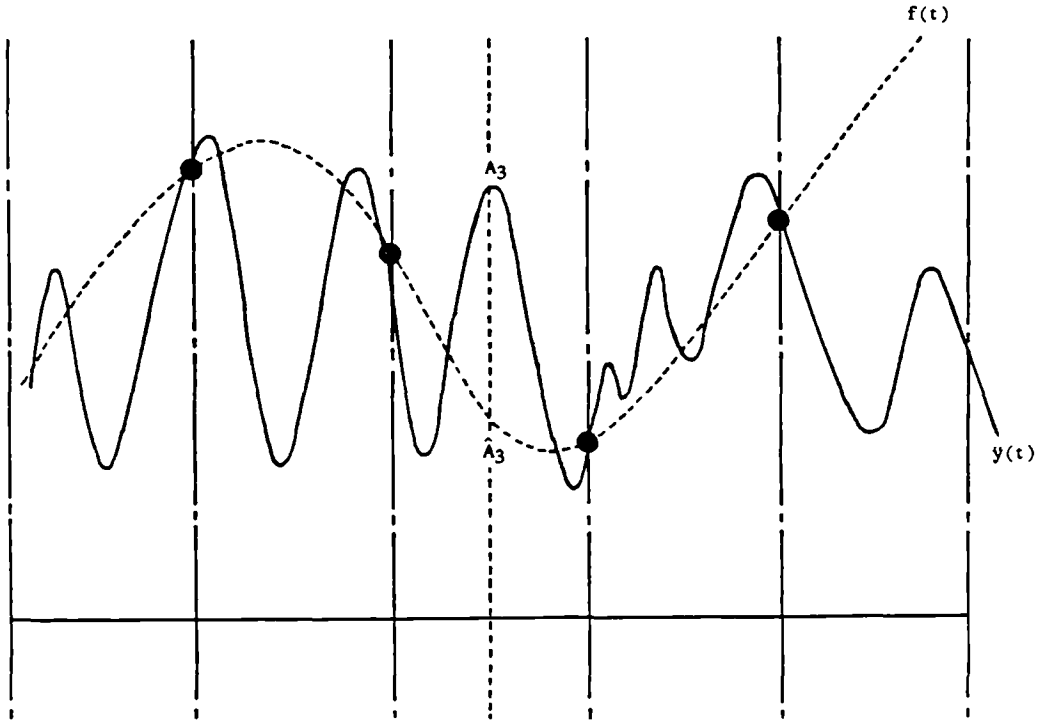

Figure 8.2. The effect of undersampling on the fitting procedure

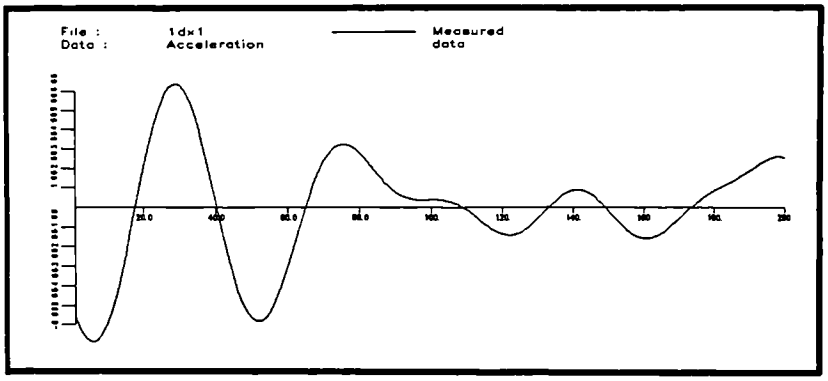

(a) Sampled data.

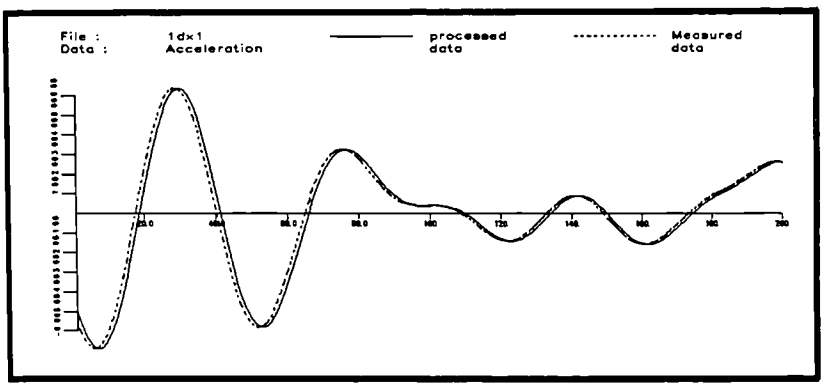

(b) Sampled data with shifted data.

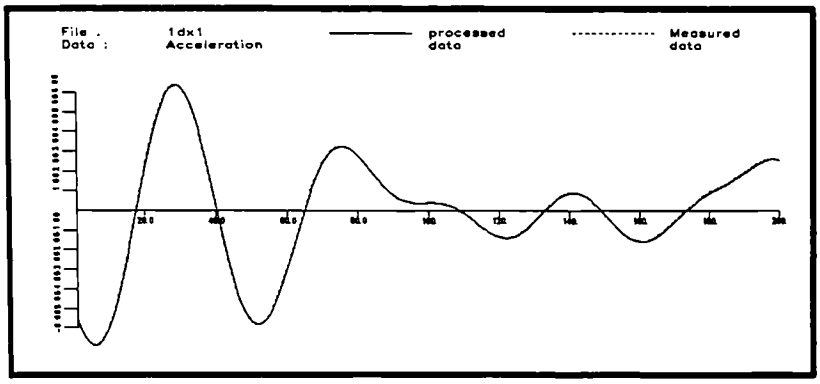

(c) Sampled data with twice shifted data.

Figure 8.3. Verification that the shifting procedure works.

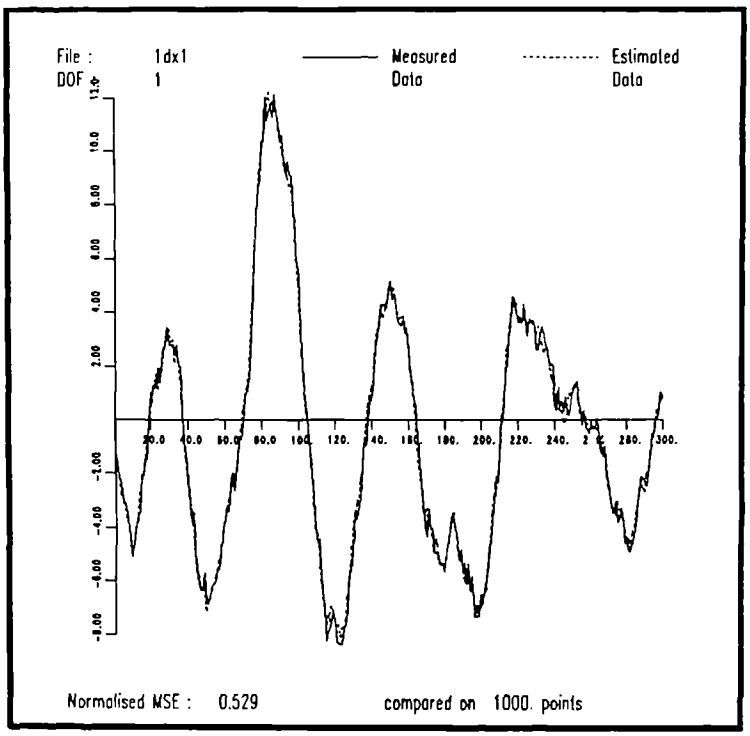

Figure 8.4. Comparison of true time data and that predicted by a model for a simulated linear system with 5% noise added to the time data.

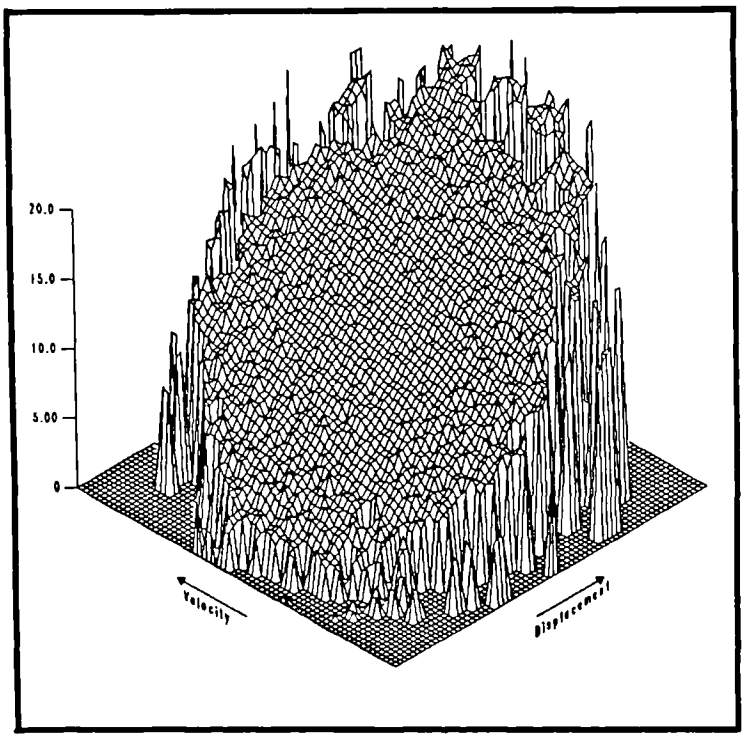

Figure 8.5. Estimated restoring force surface for a linear system with 5% noise added to the time data.

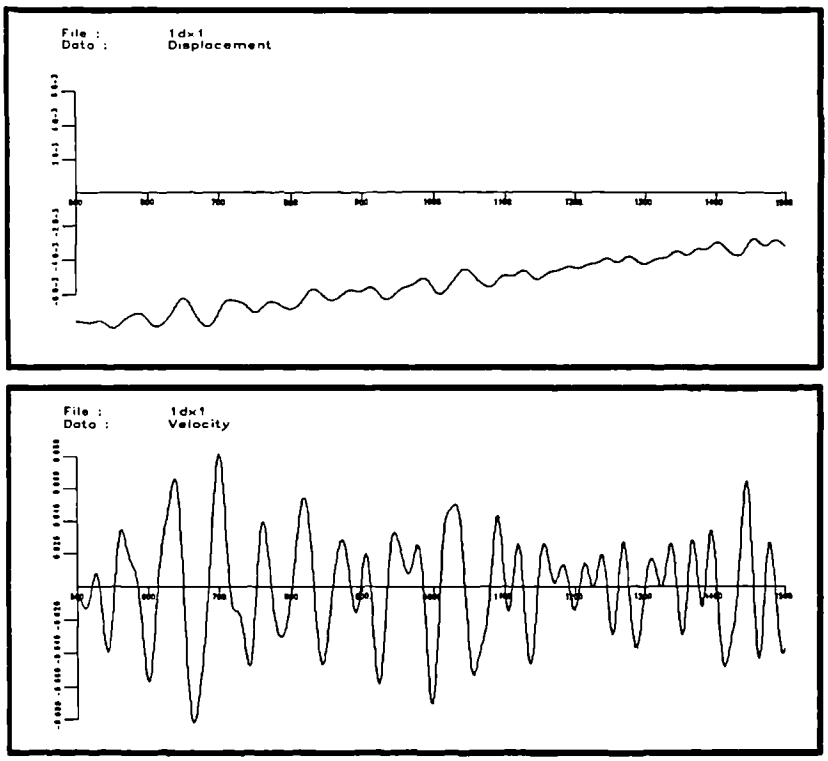

Figure 8.6. Estimated displacement and velocity data for a linear system with 1% noise added to the time data. Trapezium rule used for integration.

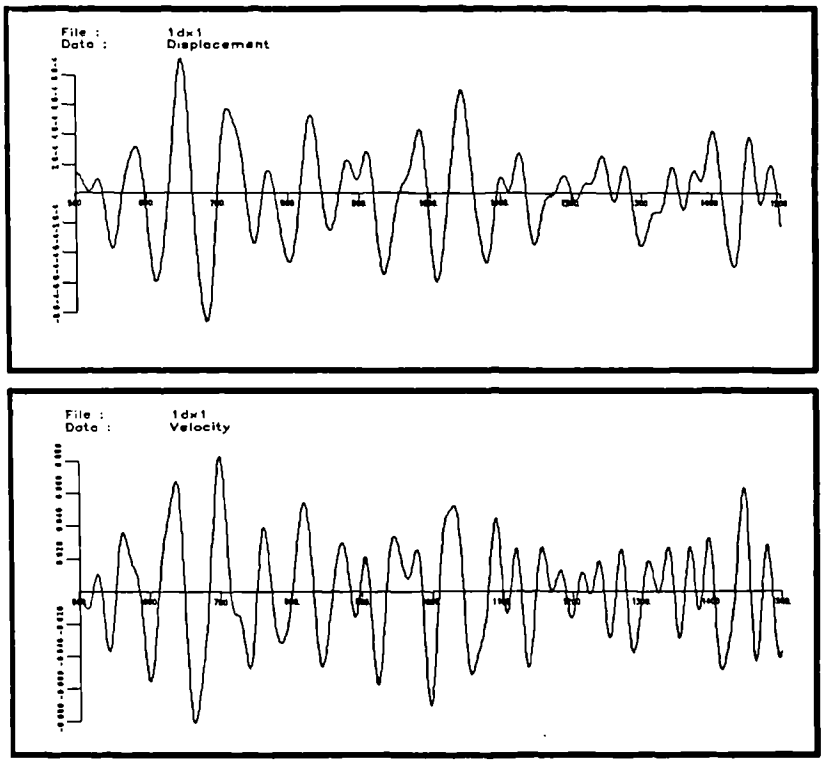

Figure 8.7. Estimated displacement and velocity data for a linear system with 1% noise added. Trapezium rule/band-pass filter used for integration.

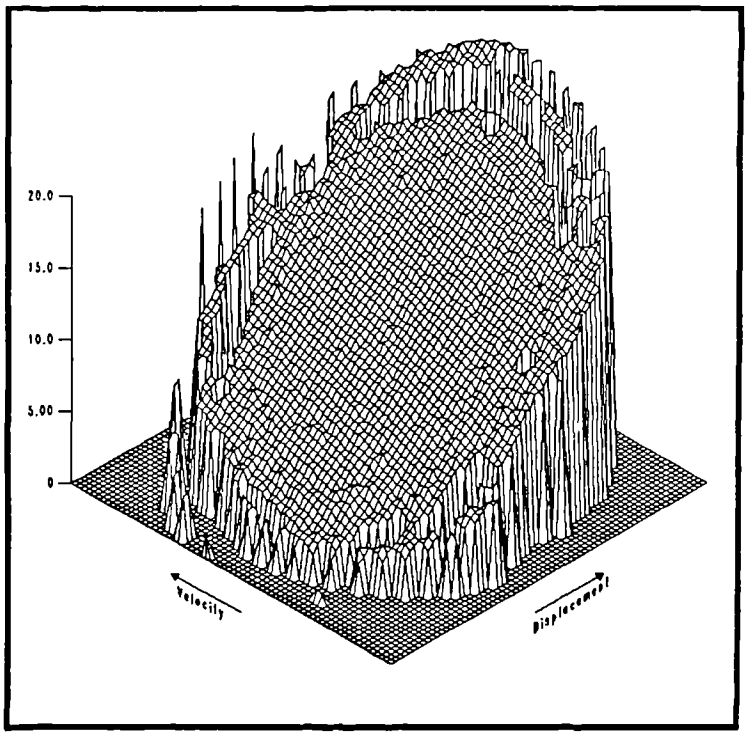

Figure 8.8. Estimated restoring force surface obtained using the data in the previous figure.

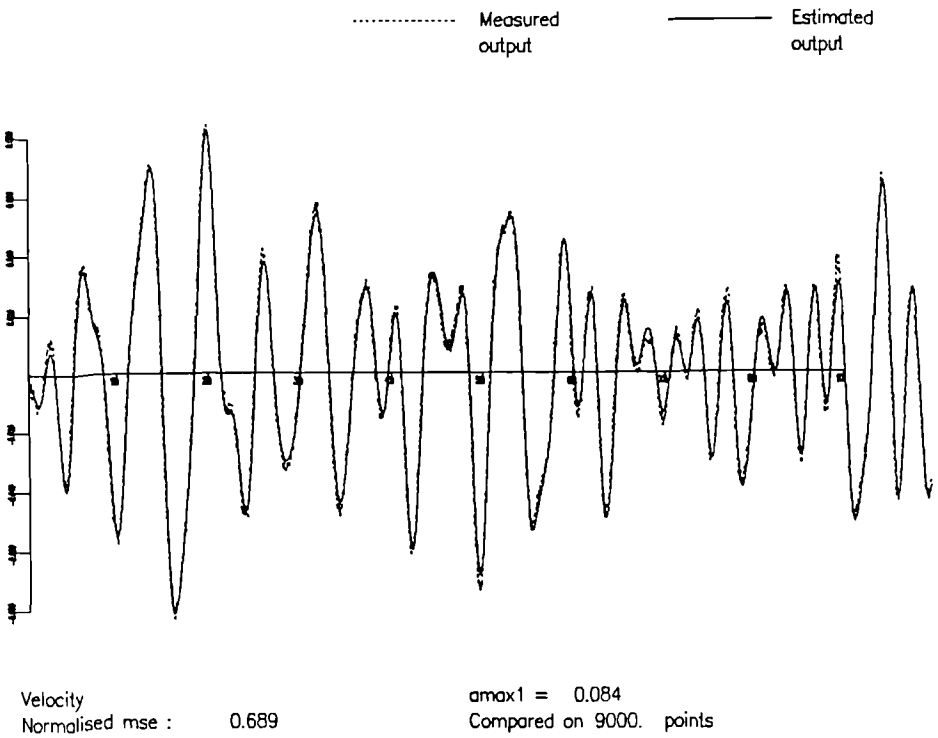

Figure 8.9. Comparison of the true velocity data with that estimated by integration, for the linear system with 5% noise added to the time data.

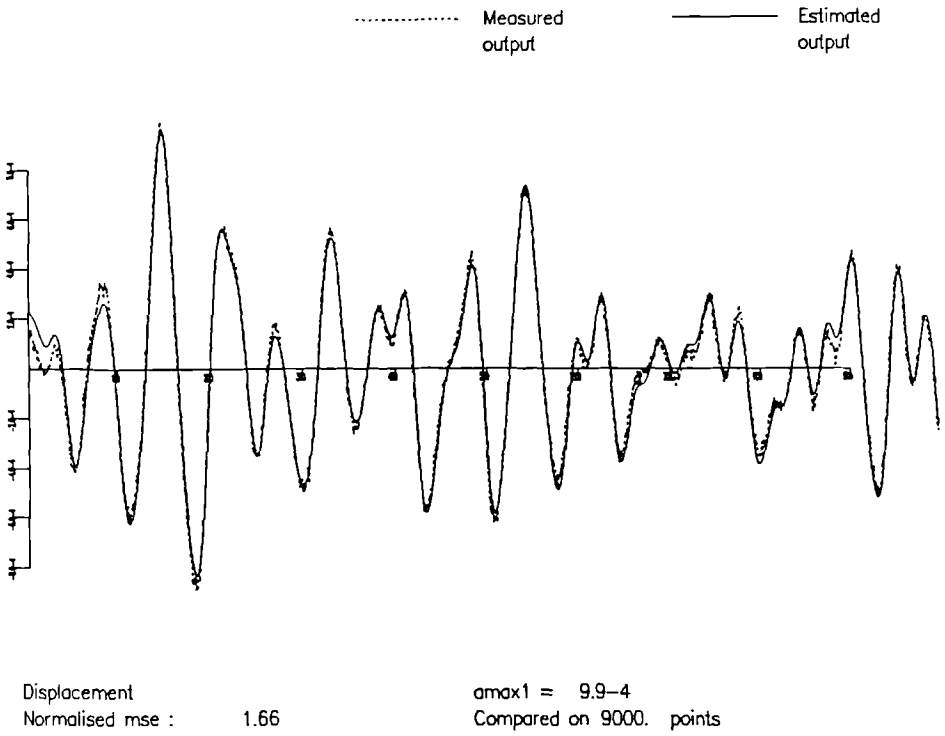

Figure 8.10. Comparison of the true displacement data with that estimated by integration. Linear system with 5% noise added.

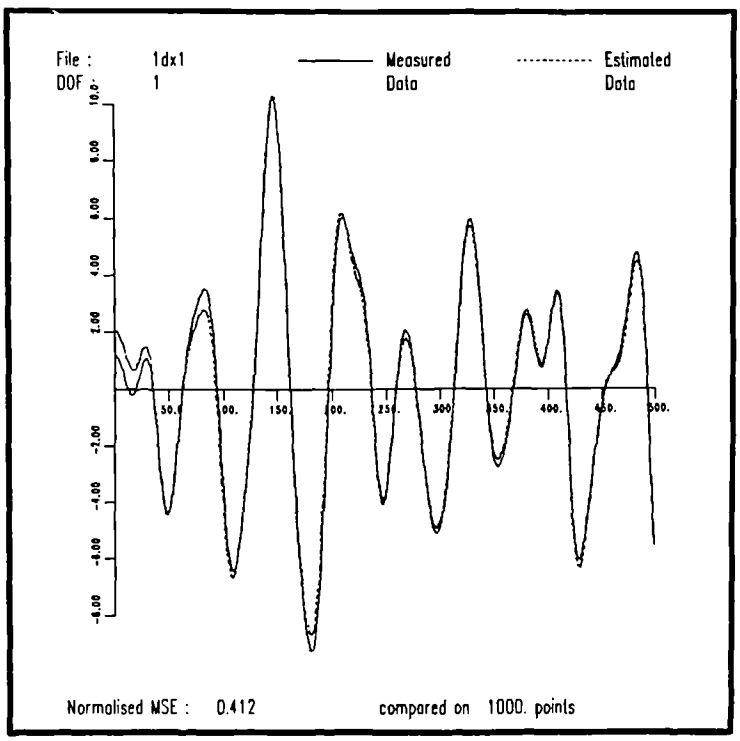

Figure 8.11. Comparison of measured system data with that predicted by a model. Linear system with 5% noise added.

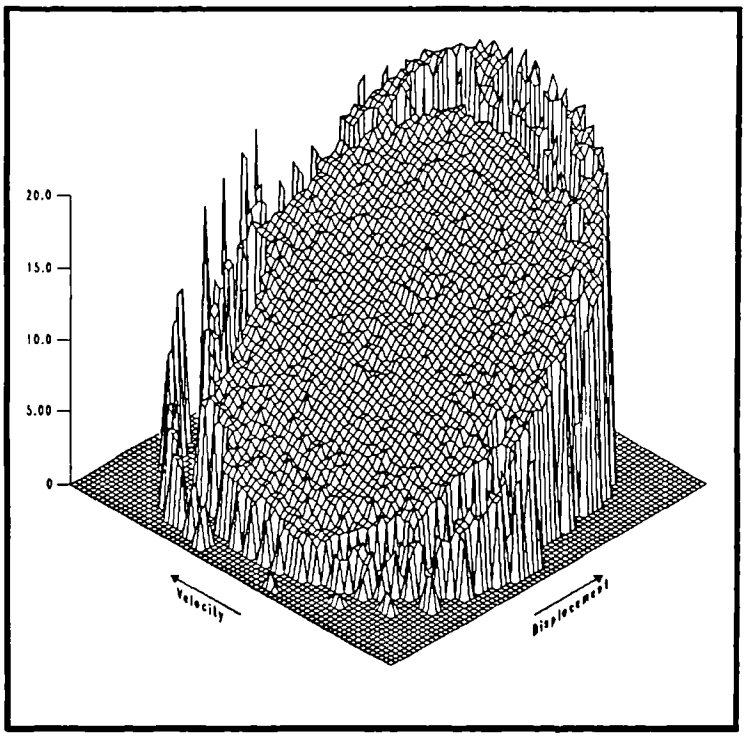

Figure 8.12. Estimated restoring force surface for the simulated linear system with 5% noise added.

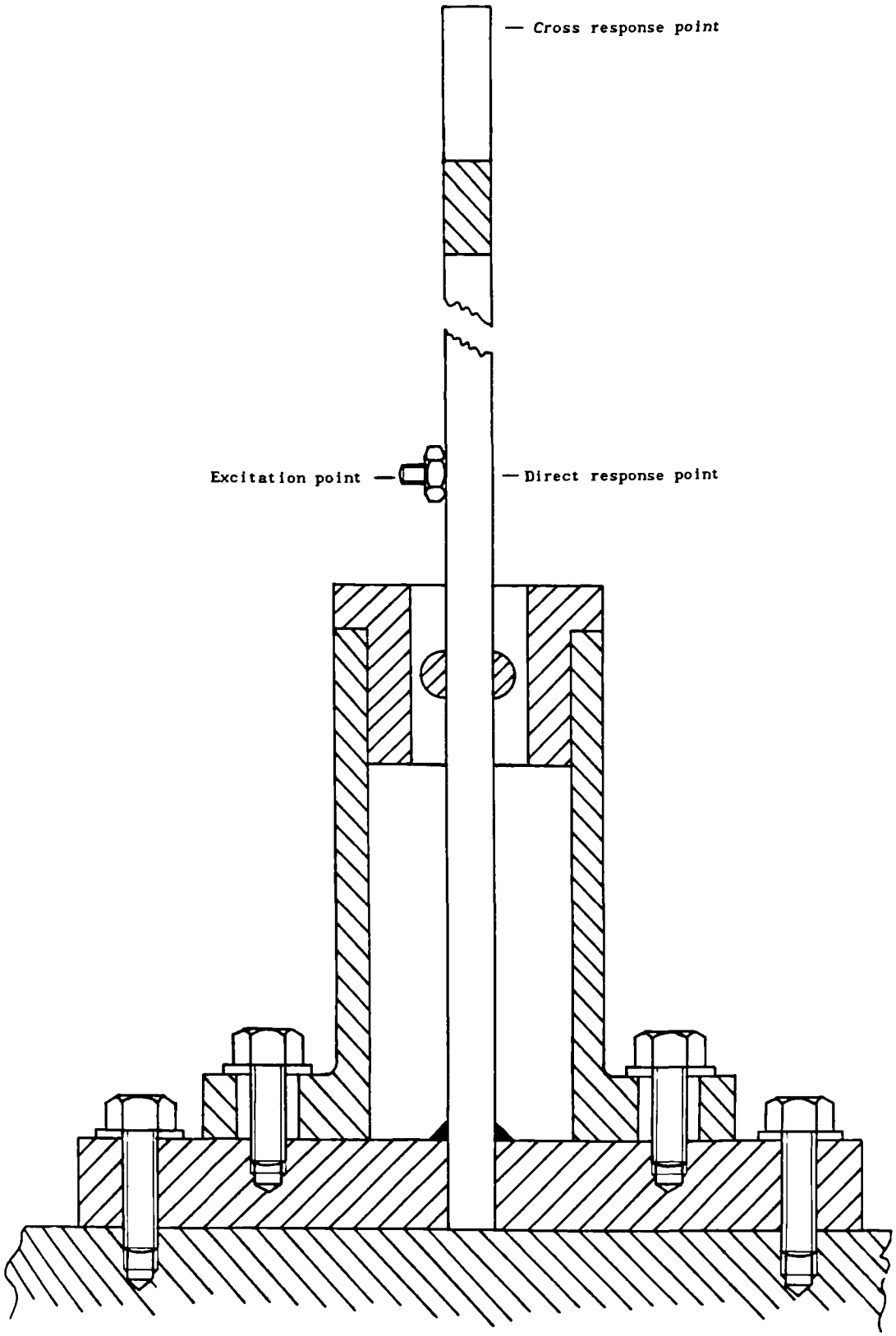

Figure 8.13. Nonlinear cantilever rig.

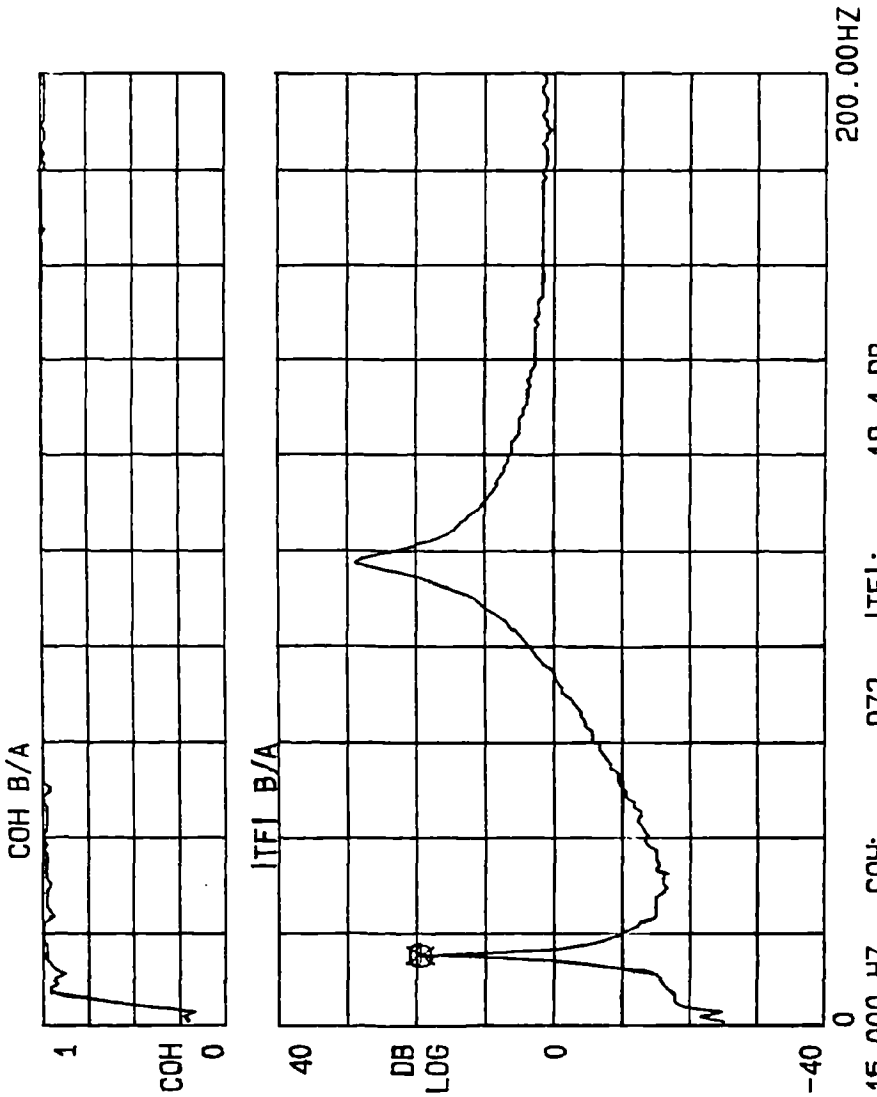

Figure 8.14. Frequency response function for the cantilever at low level of excitation.

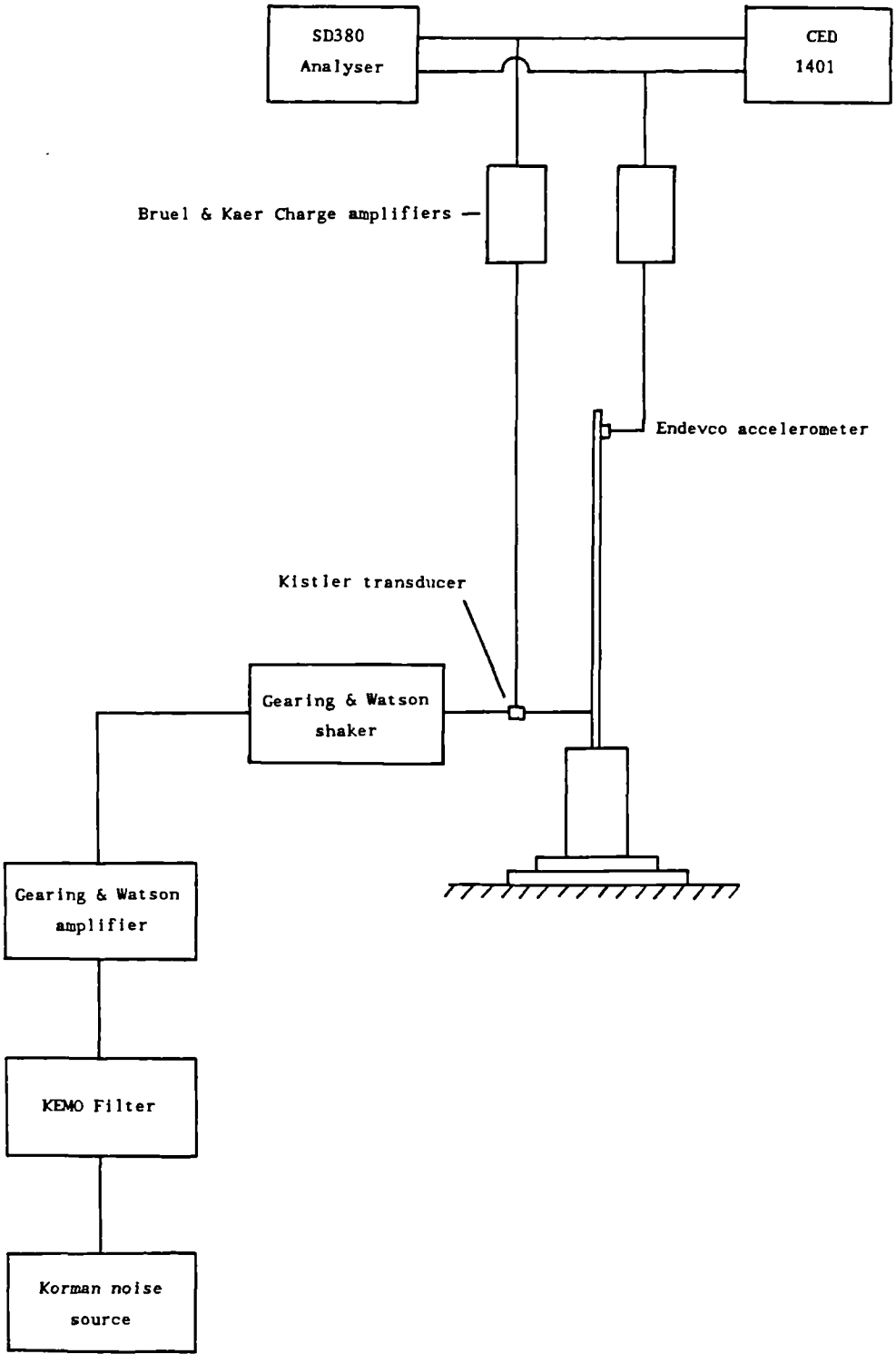

Figure 8.15. Instrumentation for cantilever experiments.

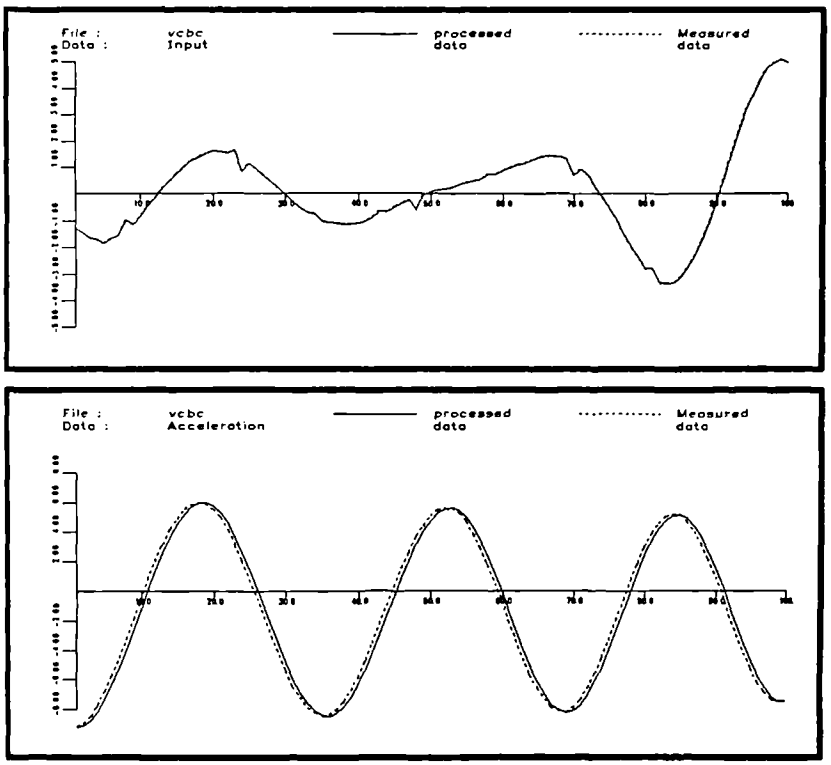

Figure 8.16. Sample of measured input and response data showing the shifted response.

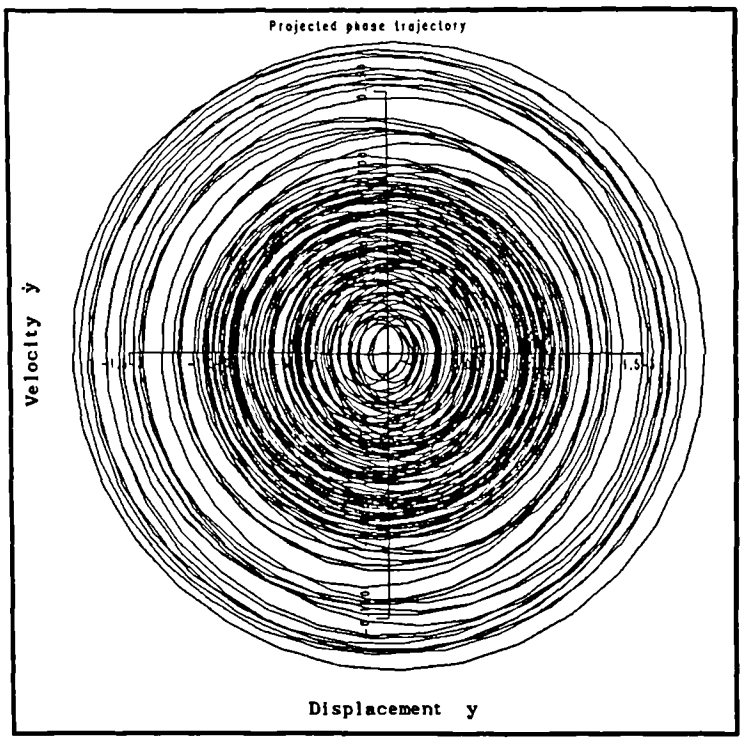

Figure 8.17. Estimated phase trajectory for the cantilever at low level of excitation. Response taken at the cross point.

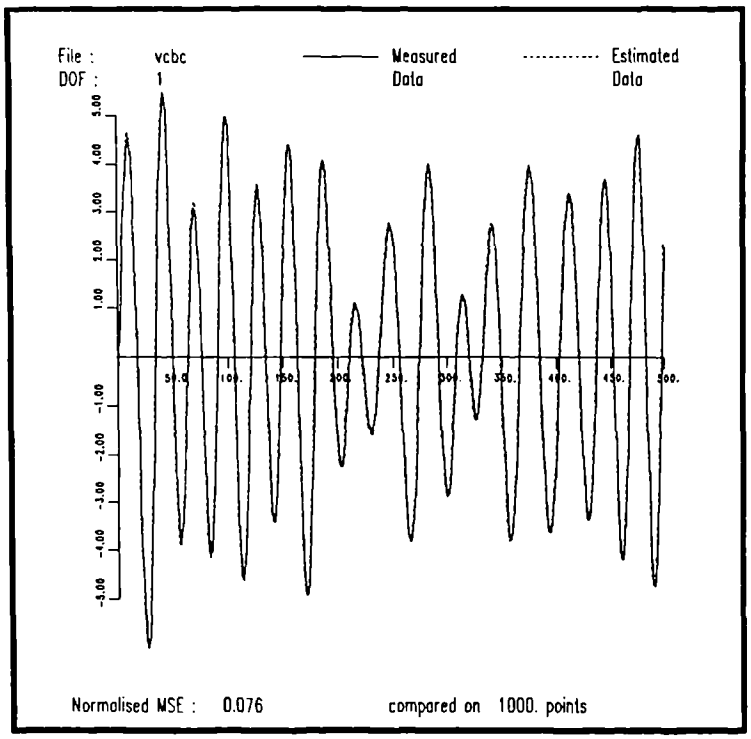

Figure 8.18. Comparison of measured data and that predicted from a linear model for the cantilever. Data taken from the cross point.

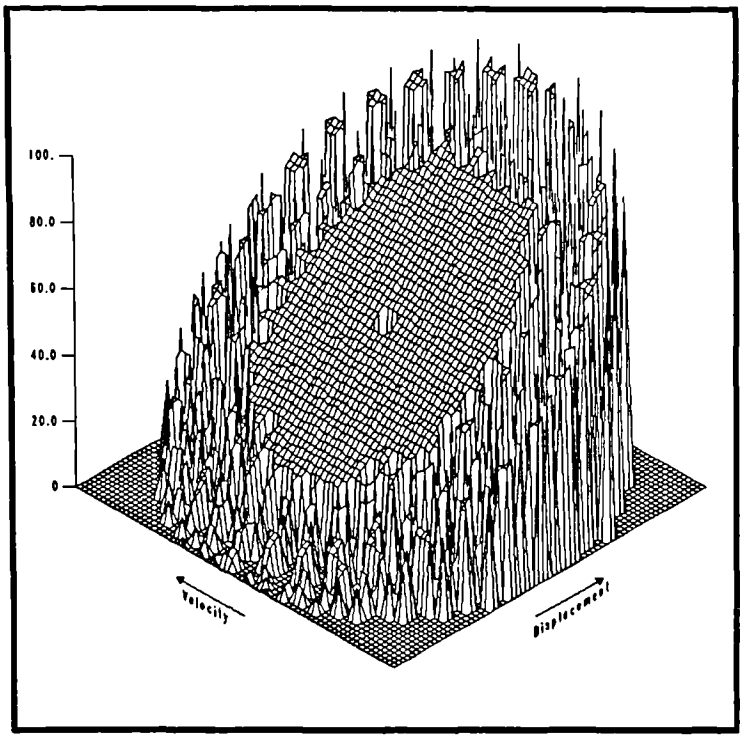

Figure 8.19. Estimated restoring force surface for the cantilever at low level of excitation. Data taken from the cross point.

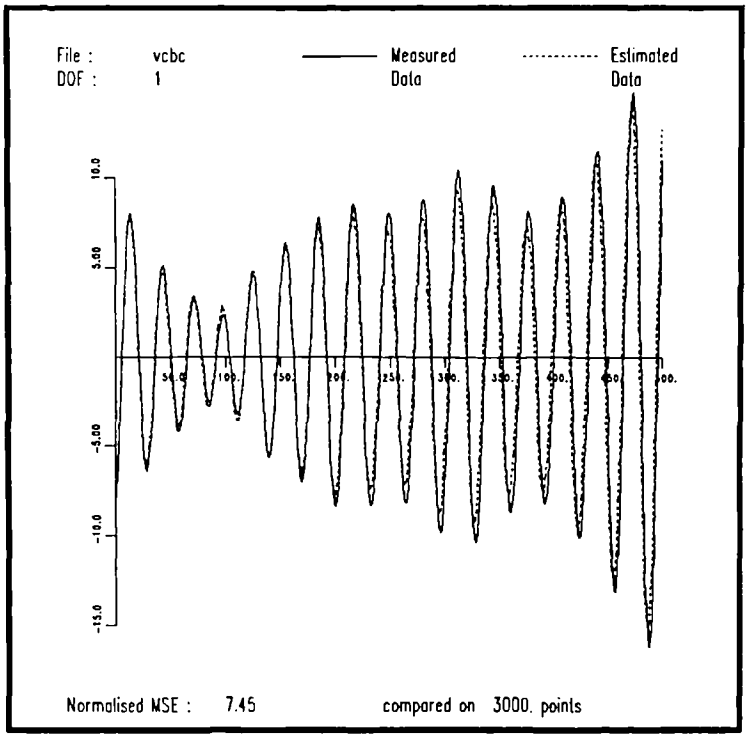

Figure 8.20. Comparison of the displacement data obtained by integration with that predicted by the model when the measured input was applied. Data taken from the cross point.

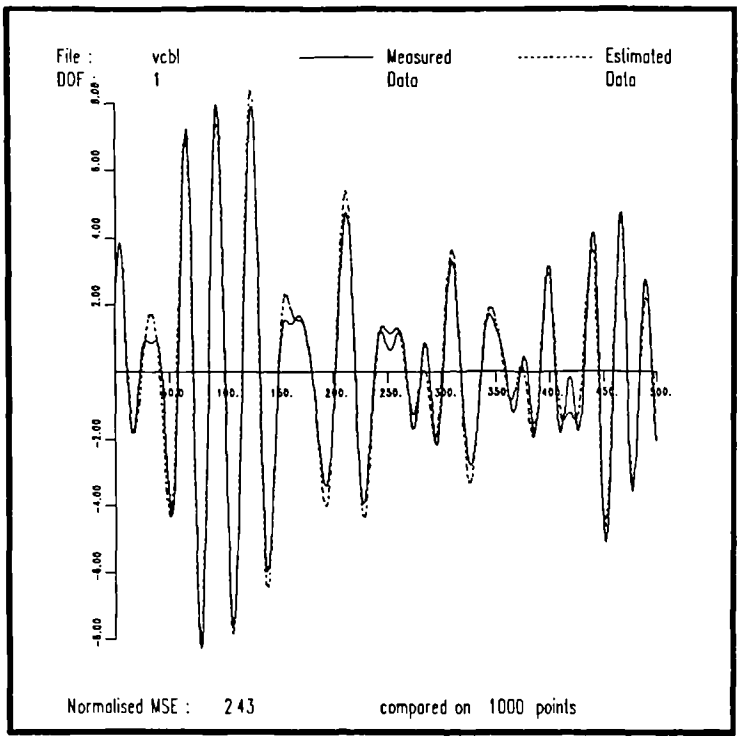

Figure 8.21. Comparison of measured data and that predicted from a linear model for the cantilever. Data taken from the direct point.

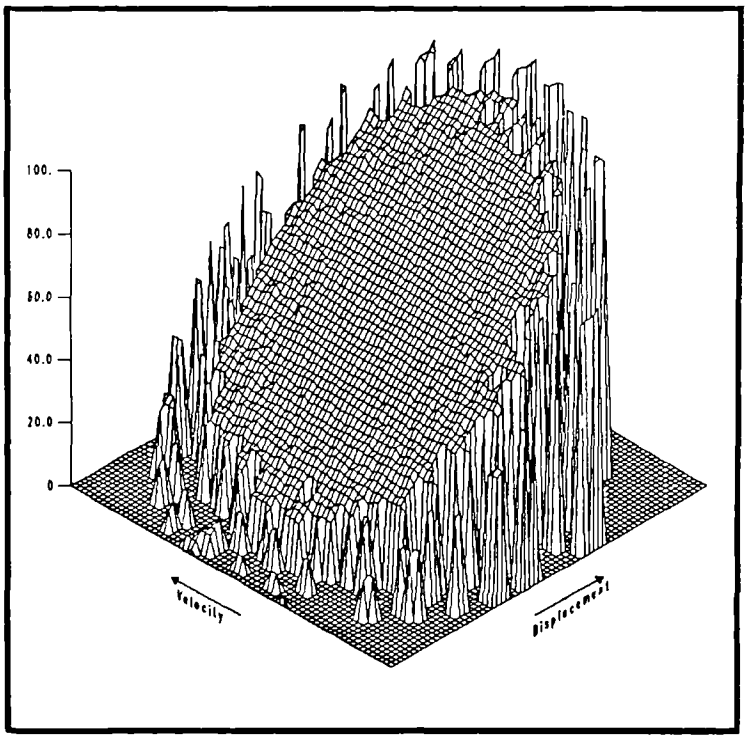

Figure 8.22. Estimated restoring force surface for the cantilever at low level of excitation. Data taken from the direct point.

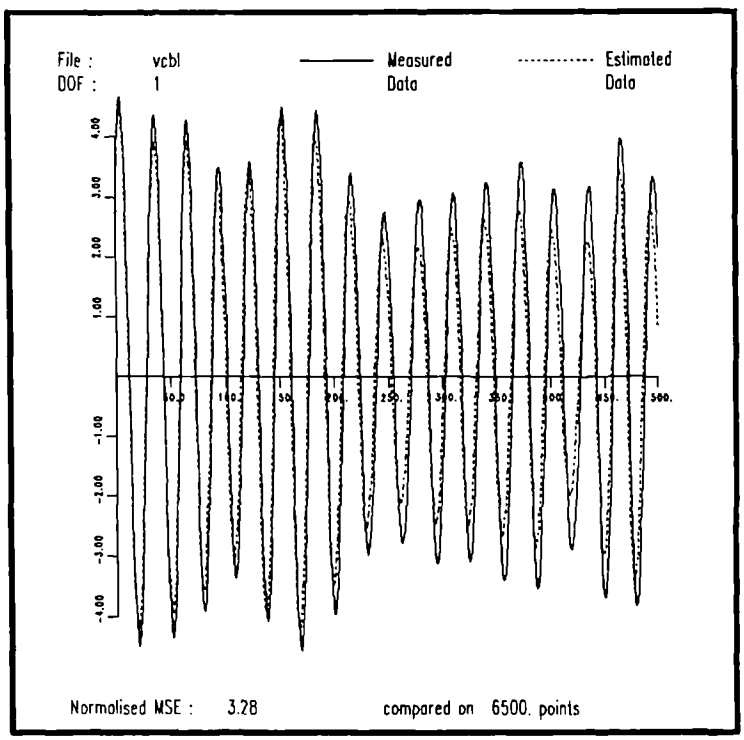

Figure 8.23. Comparison of the displacement data obtained by integration with that predicted by the model when the measured input was applied. Data taken from the direct point.

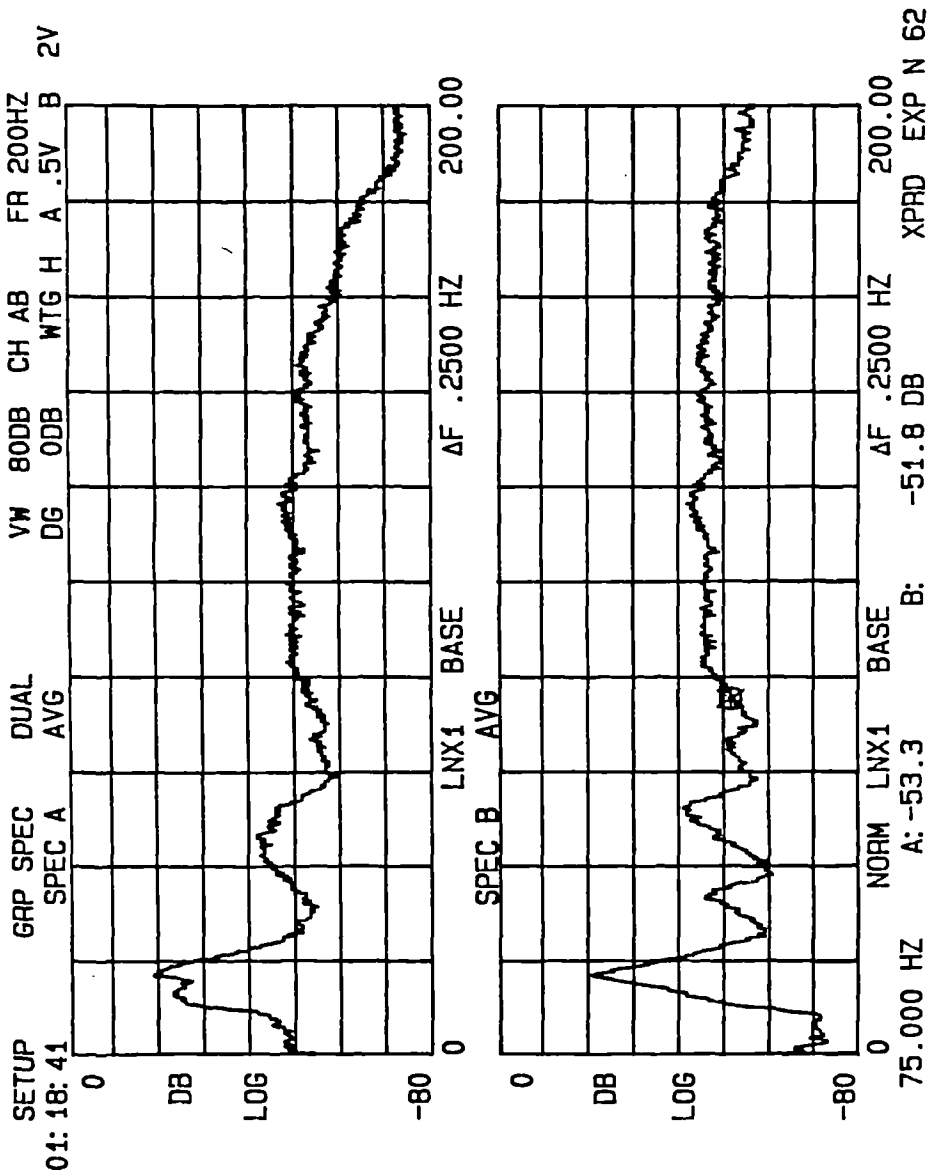

Figure 8.24. Input and response spectra for the cantilever test at high level of excitation.

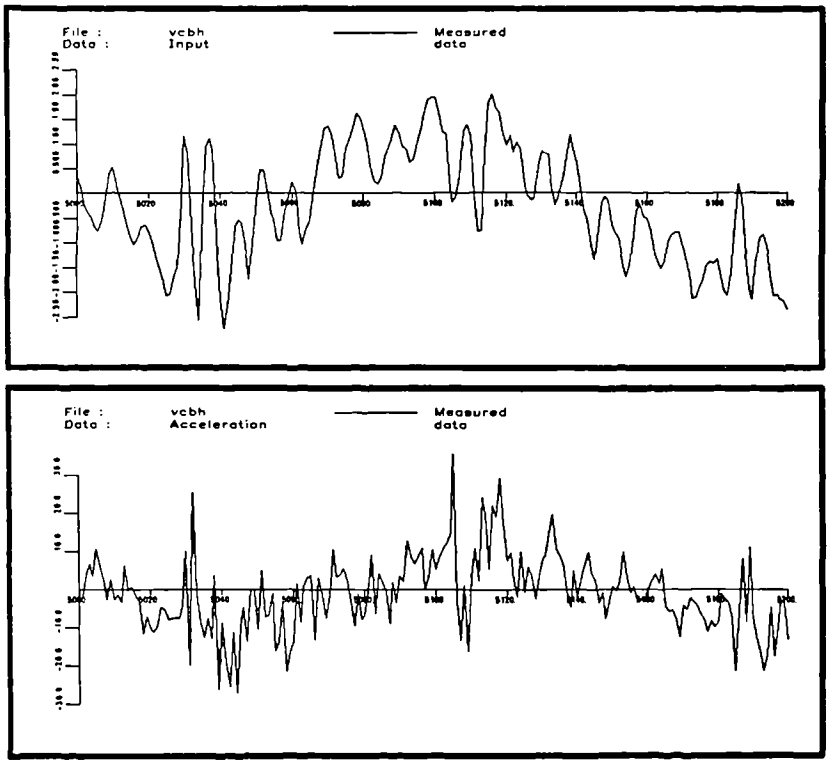

Figure 8.25. Input and response data for the cantilever experiment at high level of excitation.

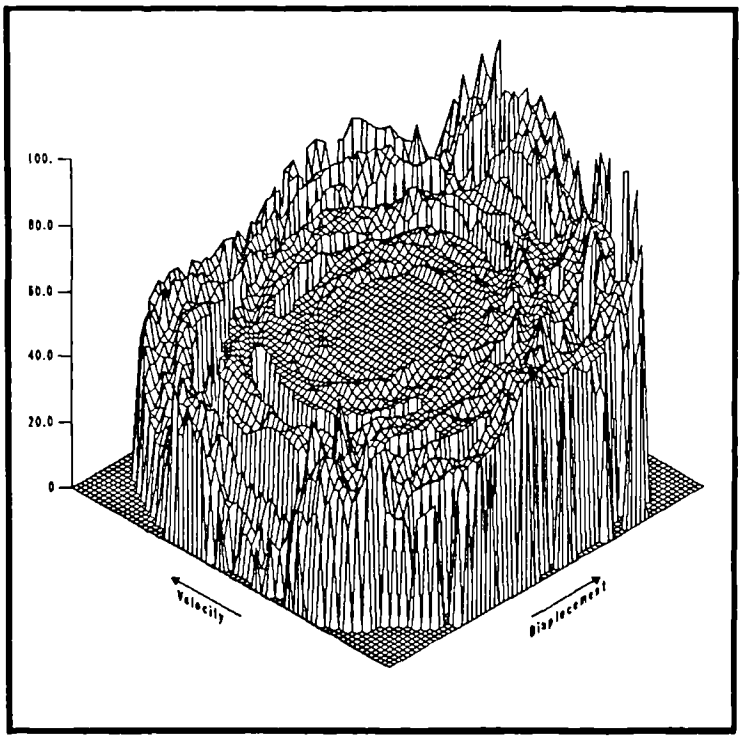

Figure 8.26. Estimated restoring force surface for the cantilever at high excitation. The response data was not shifted.

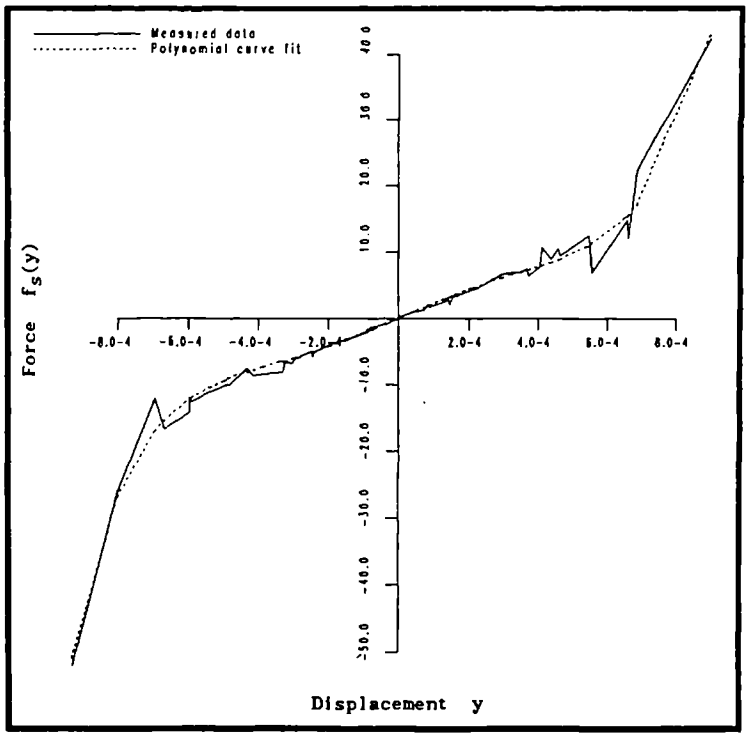

Figure 8.27. Estimated stiffness section for the cantilever subject to a high level of excitation. The response data was not shifted.

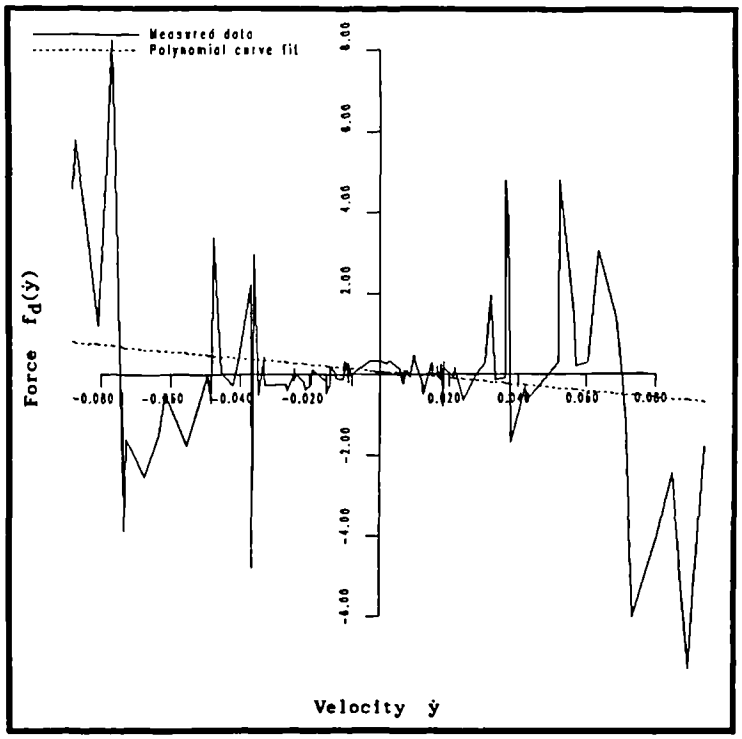

Figure 8.28. Estimated damping section for the cantilever at a high level of excitation. The response data was not shifted.

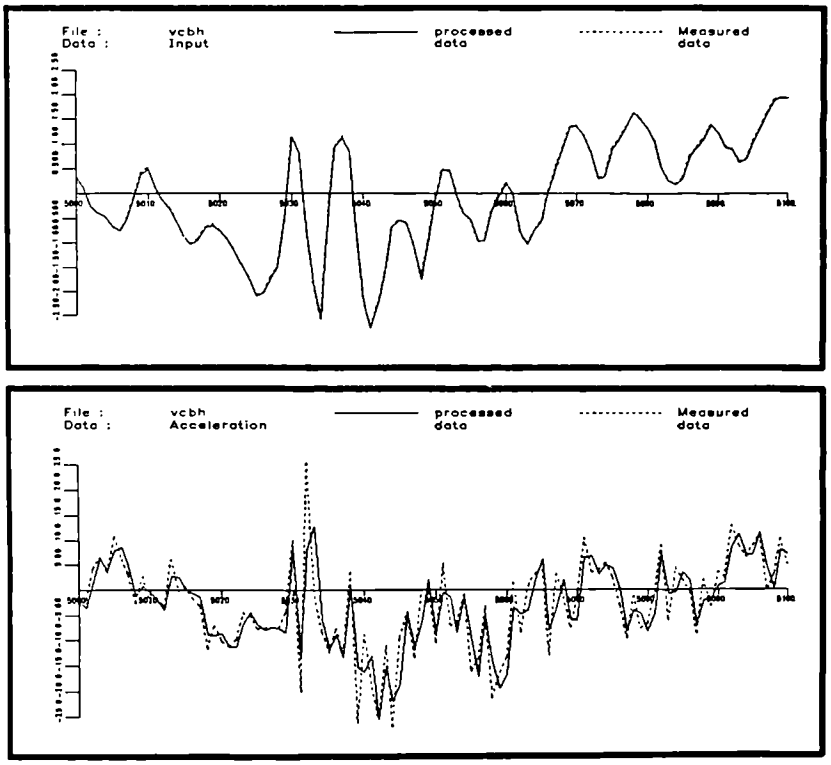

Figure 8.29. Input and response data together with the shifted response data for the cantilever at a high level of excitation.

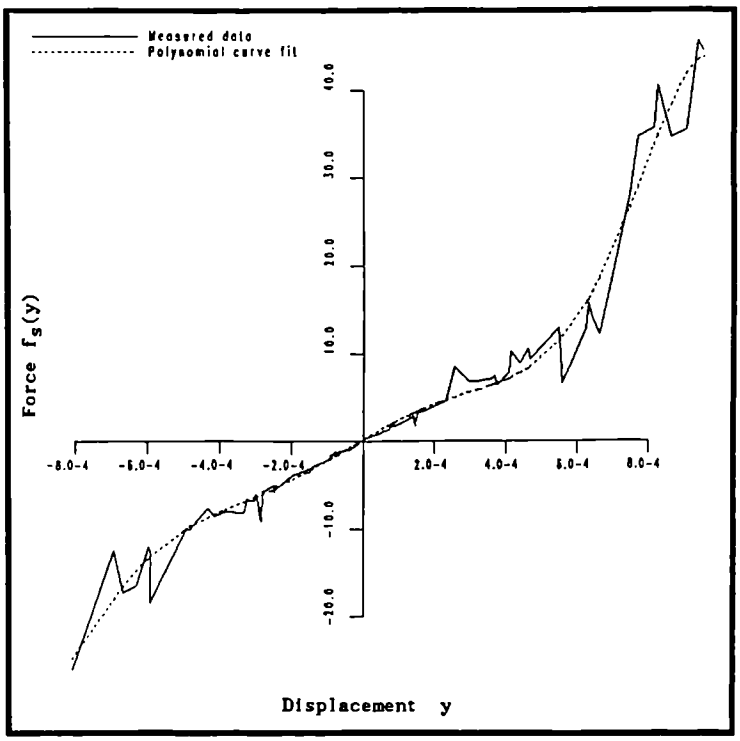

Figure 8.30. Estimated stiffness section for the cantilever at a high level of excitation. The response data was shifted.

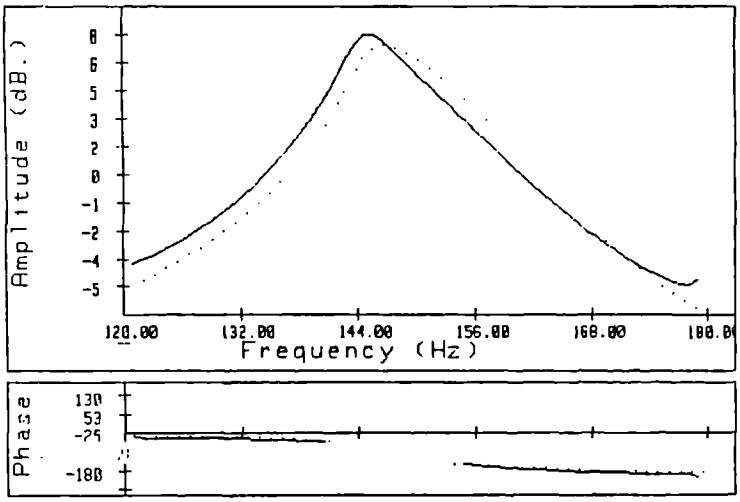

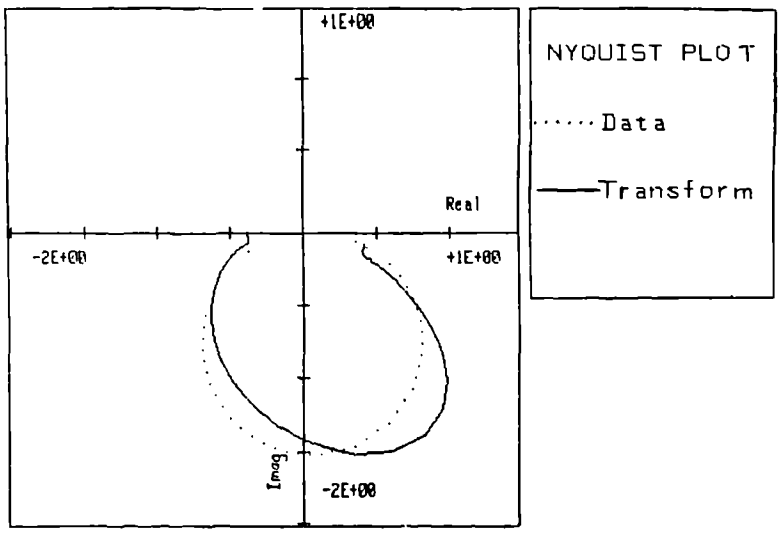

Figure 8.31. Frequency response function and Hilbert transform for ETH-1 at a high level of excitation.

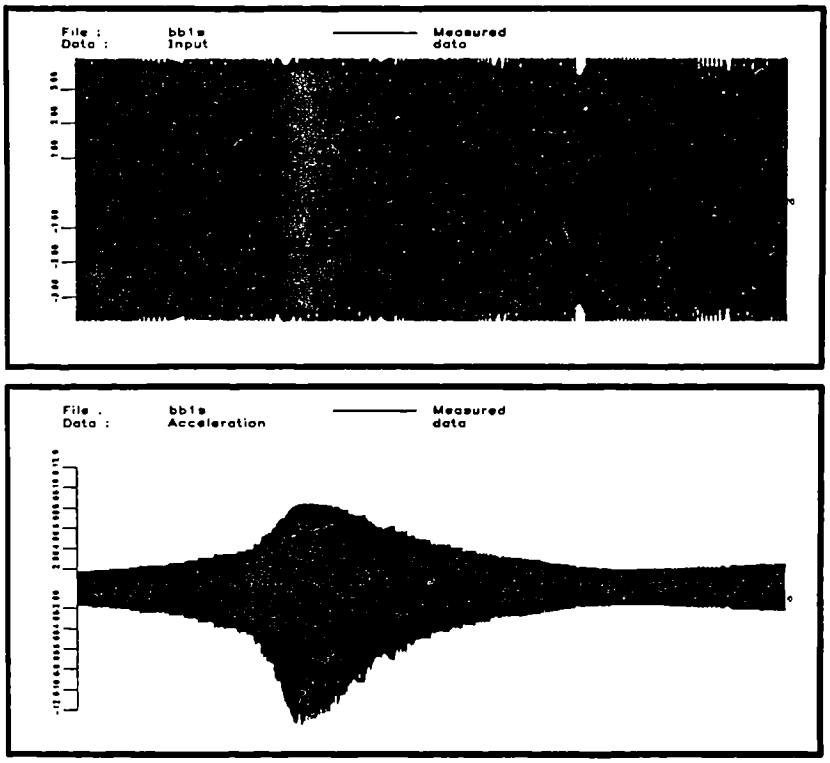

Figure 8.32. Swept-sine input and response data for the test of ETH-1.

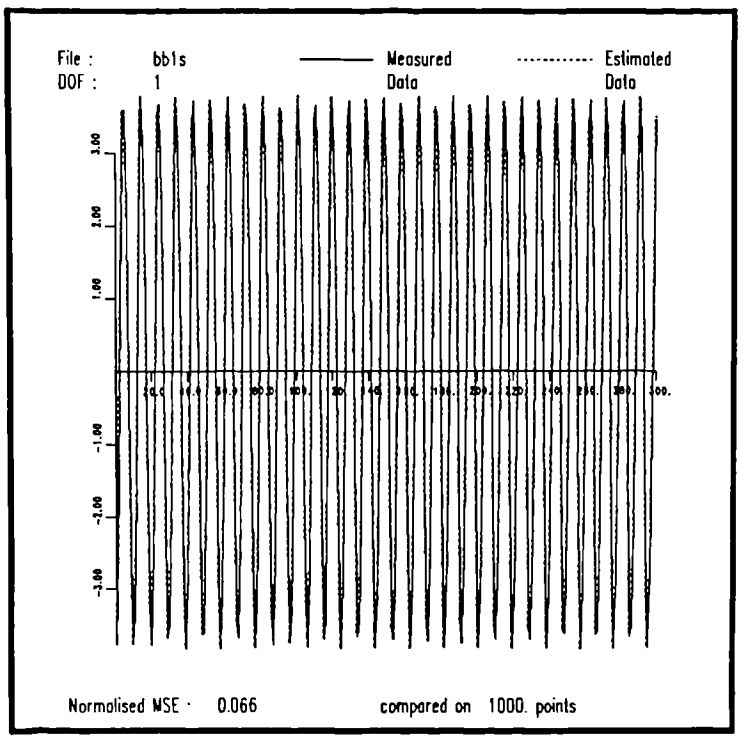

Figure 8.33. Comparison of measured data and that predicted using the (3,2) model for ETH-1.

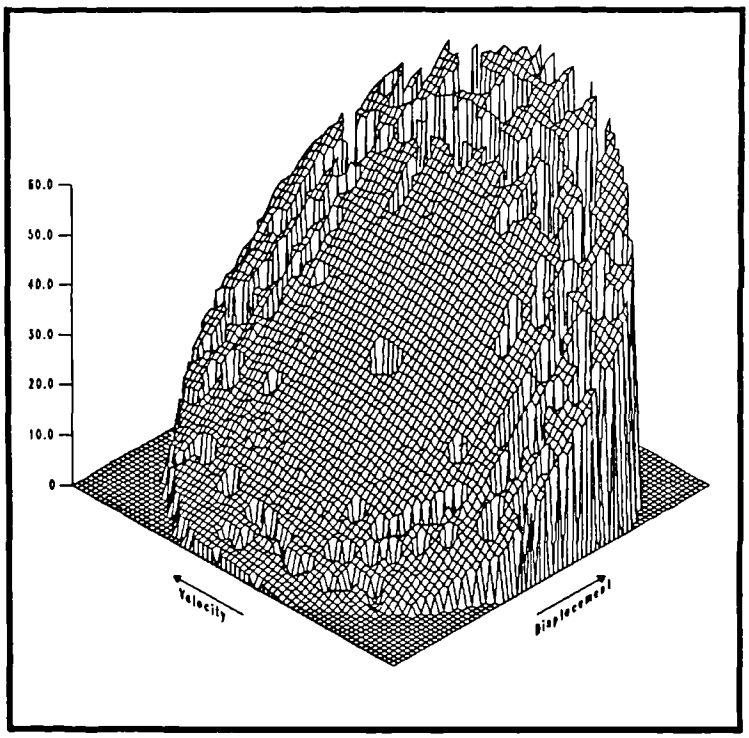

Figure 8.34. Estimated restoring force surface for ETH-1.

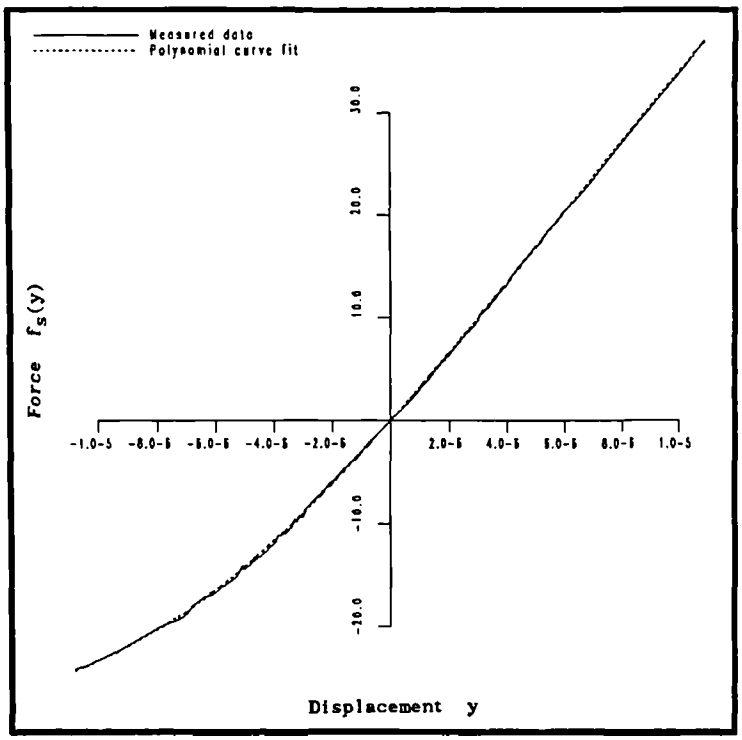

Figure 8.35. Estimated stiffness section and cubic curve-fit for ETH-1.

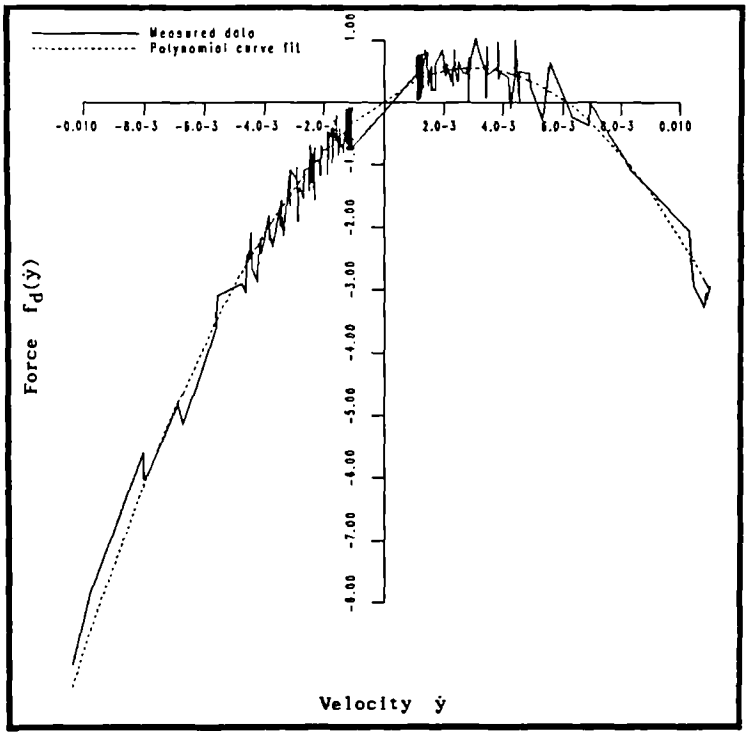

Figure 8.36. Estimated damping section and quadratic curve-fit for ETH-1.

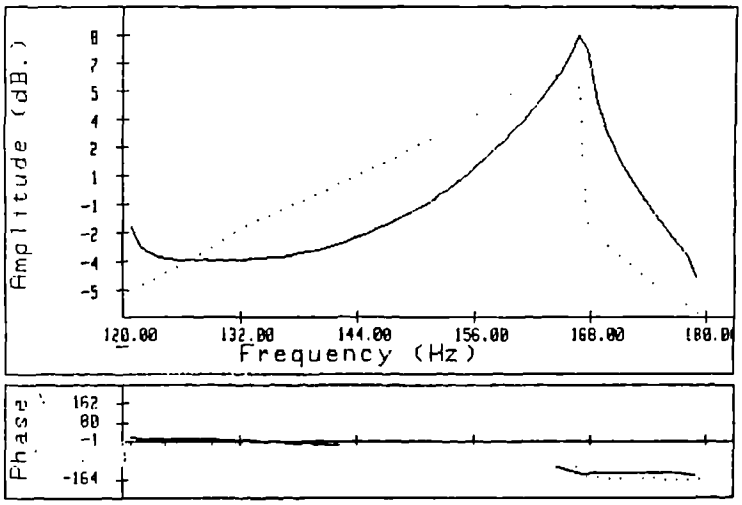

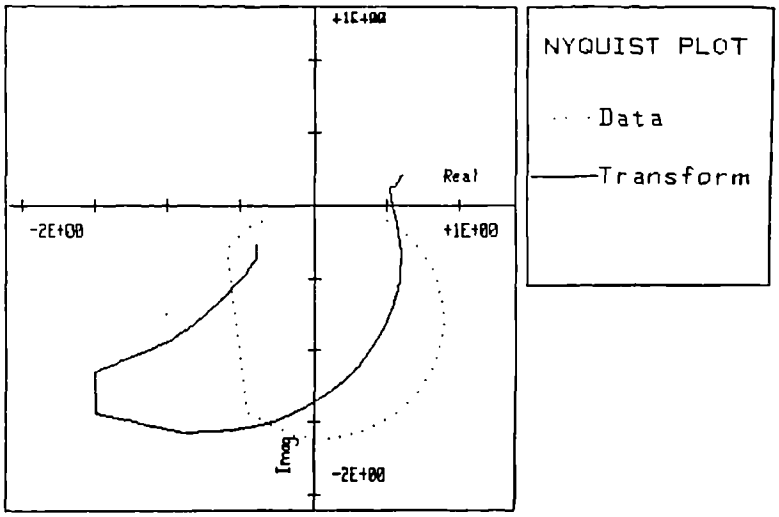

Figure 8.37. Frequency response function and Hilbert transform for ETH-2 at a high level of excitation.

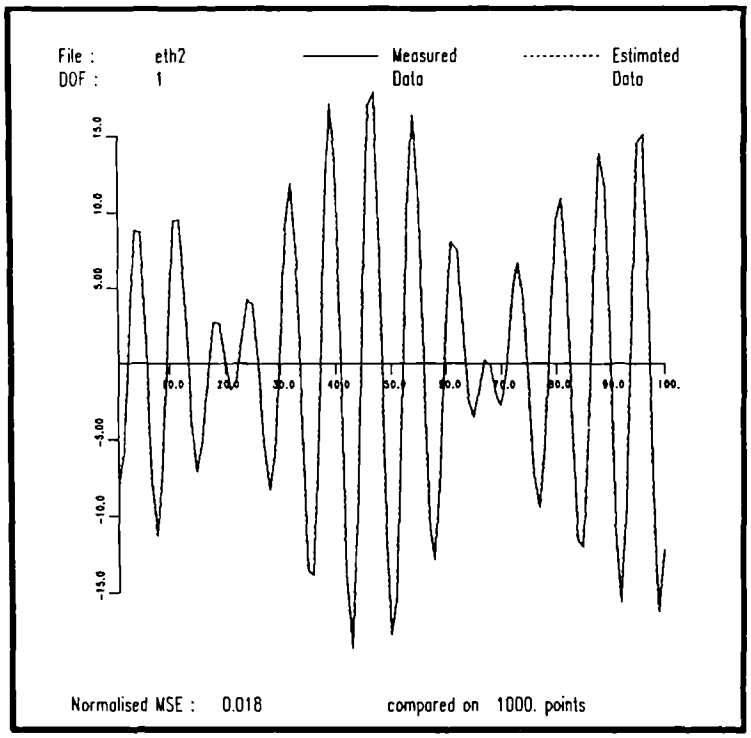

Figure 8.38. *Comparison of measured data and that predicted by the (3,1) model of ETH-2.*

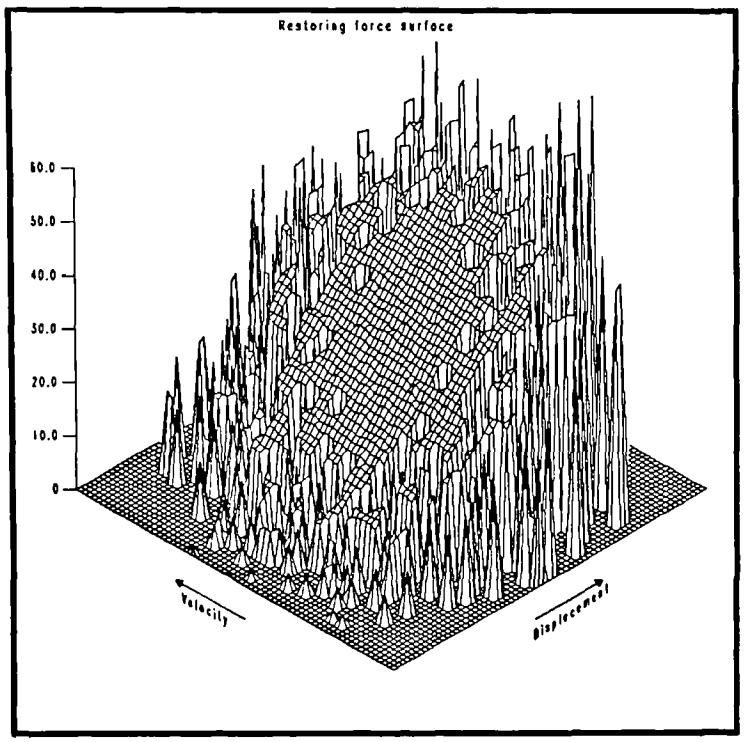

Figure 8.39. Estimated restoring force surface for ETH-2.

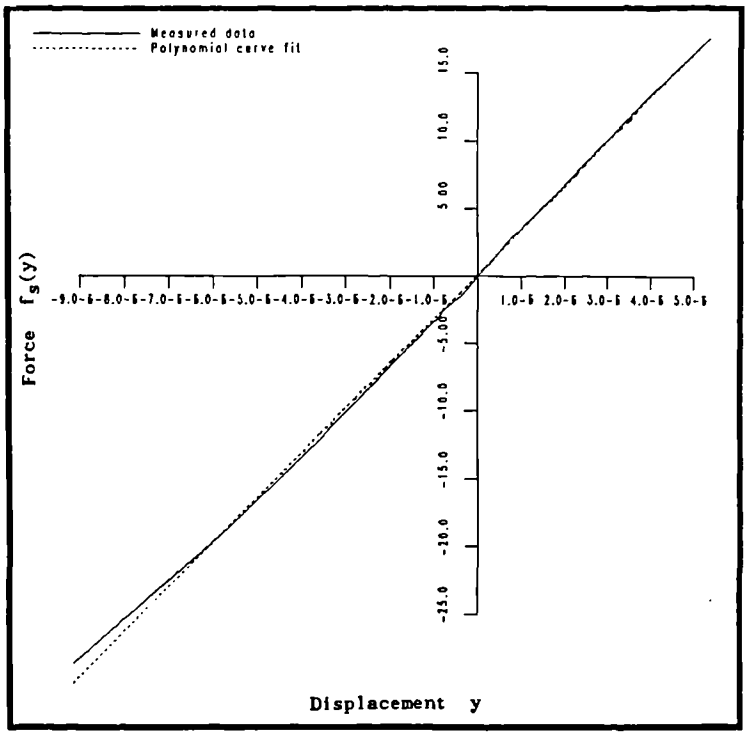

Figure 8.40. Estimated stiffness section and linear curve-fit for ETH-2.

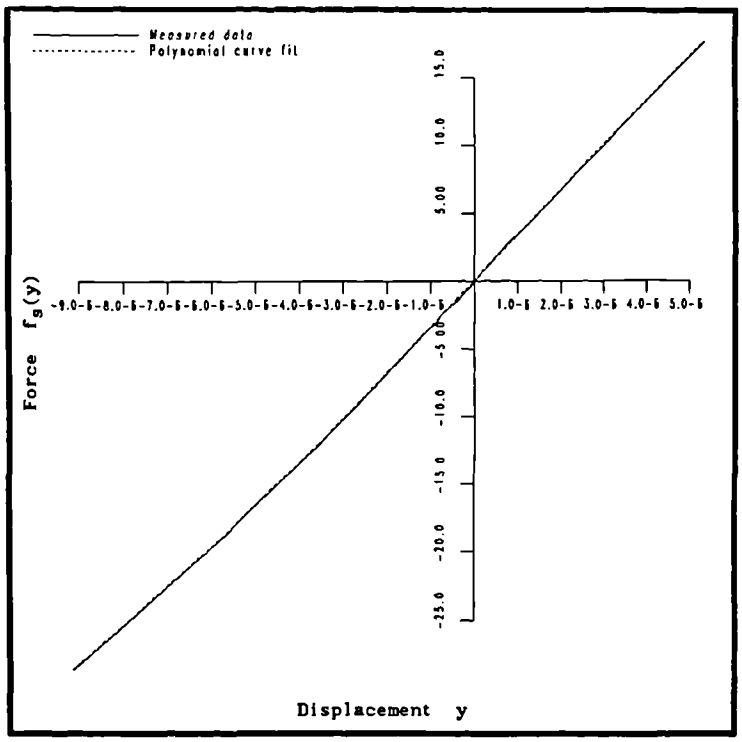

Figure 8.41. Estimated stiffness section and cubic curve-fit for ETH-2.

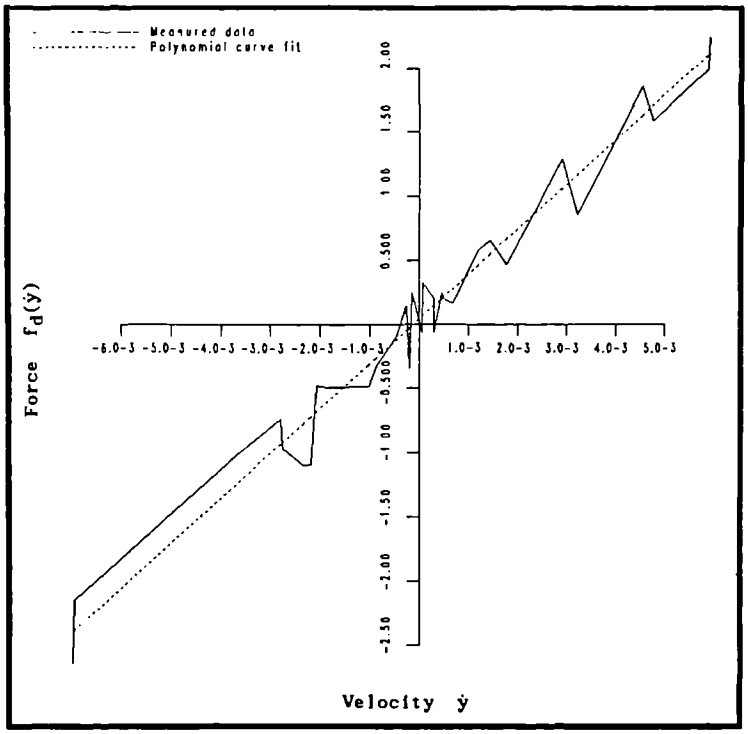

Figure 8.42. Estimated damping section and linear curve-fit for ETH-2.

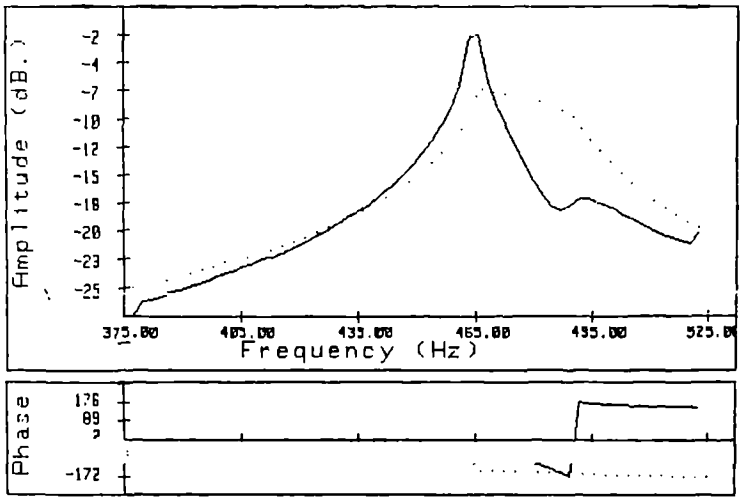

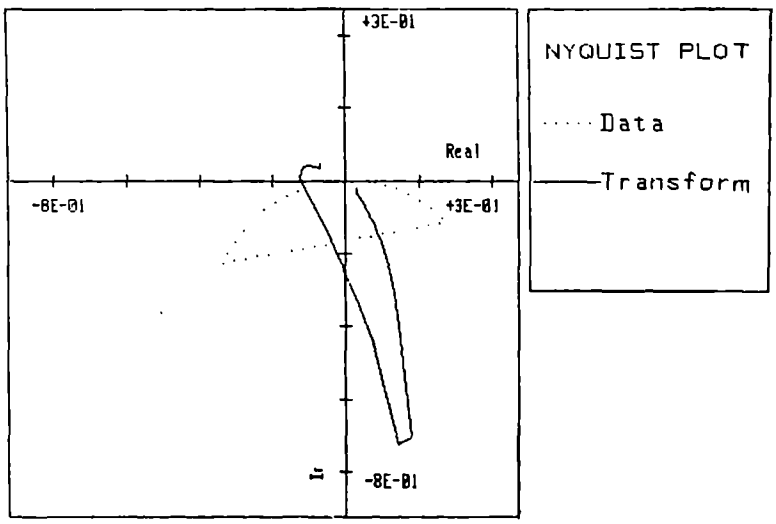

Figure 8.43. Frequency response function and Hilbert transform for ETH-3 at high level of excitation.

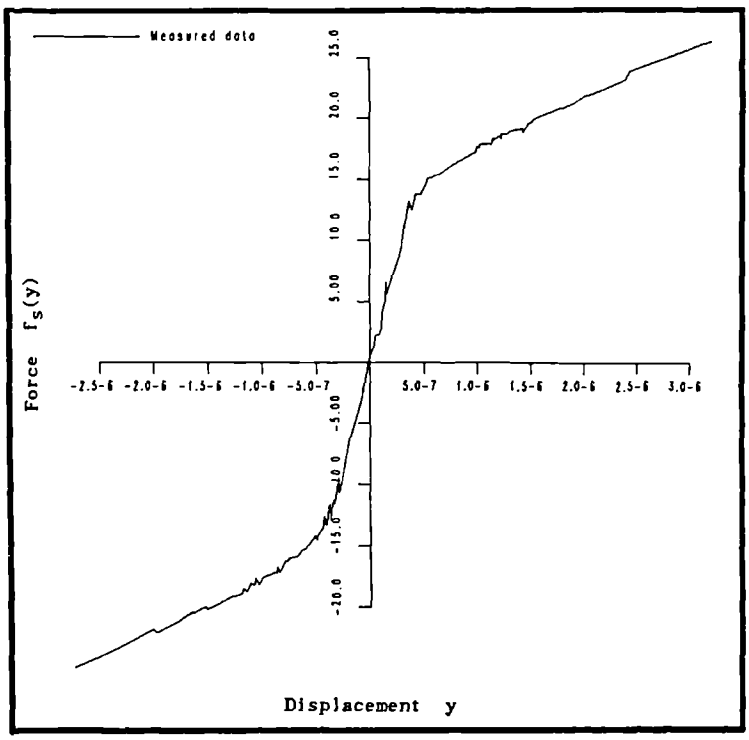

Figure 8.44. Estimated stiffness section for ETH-3.

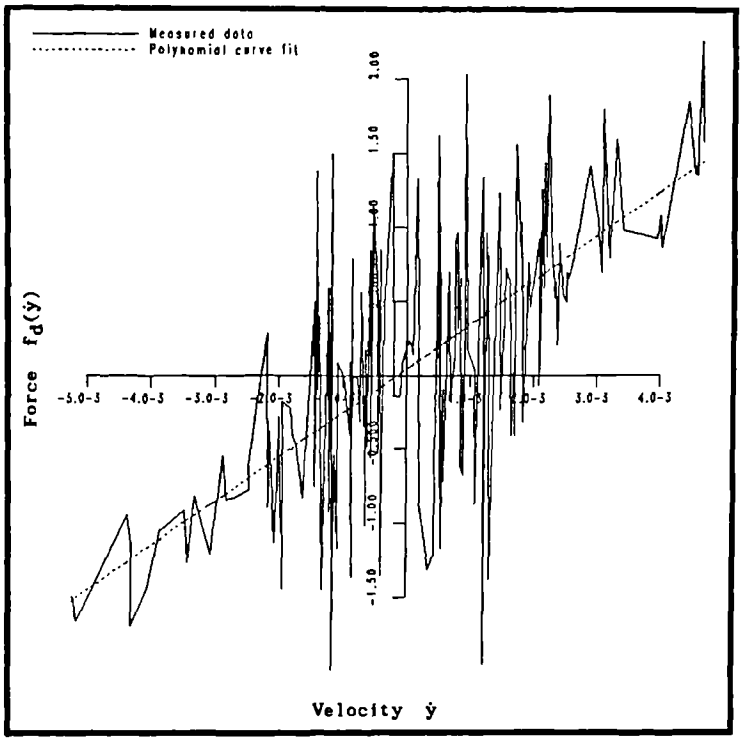

Figure 8.45. Estimated damping section and linear curve-fit for ETH-3.

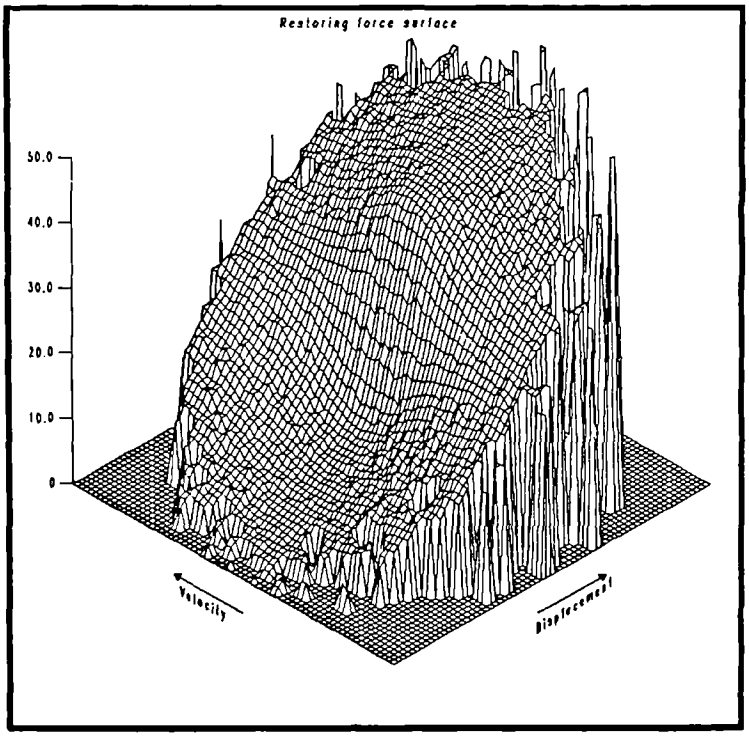

Figure 8.46. Estimated restoring force surface for ETH-3.

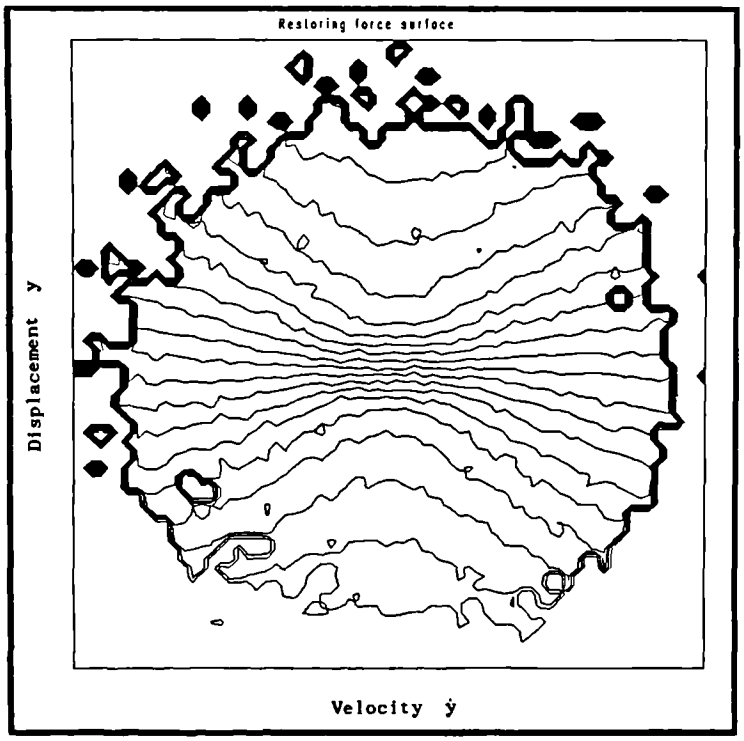

Figure 8.47. Contour map of the estimated force surface for ETH-3.

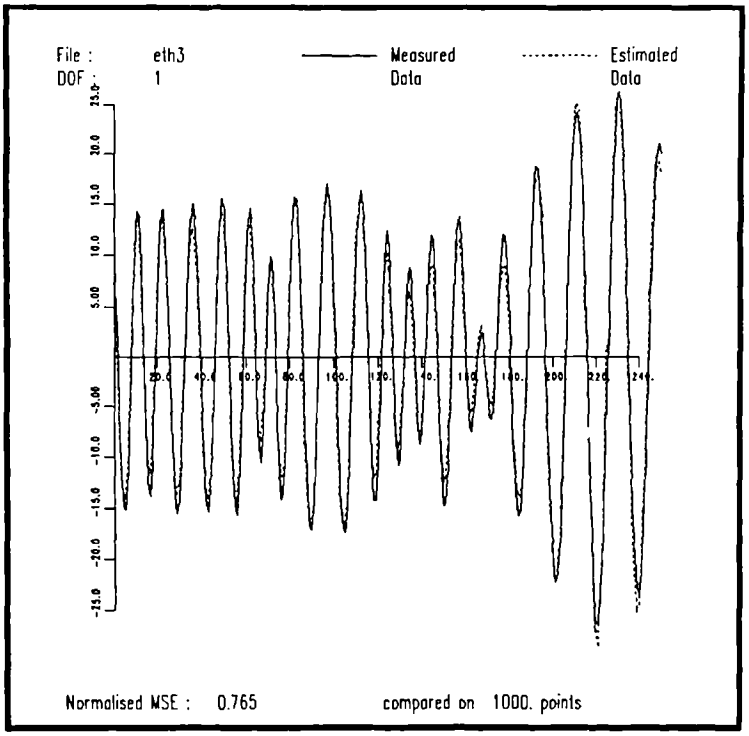

Figure 8.48. Comparison of the measured data with that predicted by the (9,3) model for ETH-3.

```
 * Coefficients for system : vcbc

 * Estimation type : Orthogonal

 * Expansion type : Polynomial

 * Mass corrected to :  0.31133380e+01

   a( 0: 0) -0.16639438e-03   s( 0: 0)  0.24384852e-06
   a( 0: 1)  0.87239575e+00   s( 0: 1)  0.37119884e-01
   a( 1: 0)  0.27718961e+05   s( 1: 0)  0.38027429e+04
   a( 1: 1) -0.12959176e+02   s( 1: 1)  0.39803244e-05

 * MSE estimate :  0.38624682e-01

 * Significant coefficients

   a( 1: 0)  0.27718961e+05   std( 1: 0)  0.41276905e+02

 * MSE estimate :  0.75733989e-01
```

Table 8.1. Estimated coefficients for a linear model of the cantilever at low levels of excitation. Data taken from the cross point.

```
* Estimation type : Orthogonal

* Expansion type : Polynomial

* Mass corrected to :  0.46988106e+00

  a( 0: 0)  0.19647665e-02   s( 0: 0)  0.59056183e-04
  a( 0: 1)  0.34194412e+03   s( 0: 1)  0.34194778e+02
  a( 1: 0)  0.81748531e+06   s( 1: 0)  0.23530894e+03
  a( 1: 1) -0.71238540e+07   s( 1: 1)  0.22498158e+00

* MSE estimate :  0.94039049e+01

* Significant coefficients

  a( 0: 1)  0.34194412e+03   std( 0: 1)  0.65363716e+02
  a( 1: 0)  0.81748531e+06   std( 1: 0)  0.59569430e+05
  a( 1: 1) -0.71238540e+07   std( 1: 1)  0.16909300e+08

* MSE estimate :  0.94039593e+01
```

(a) (1,1) Model.

```
* Estimation type : Orthogonal

* Expansion type : Polynomial

* Mass corrected to :  0.31754453e+01

  a( 0: 0) -0.13074569e+00   s( 0: 0)  0.23694375e+00
  a( 0: 1)  0.33145114e+03   s( 0: 1)  0.29109579e+02
  a( 0: 2) -0.55565996e+05   s( 0: 2)  0.31875908e+02
  a( 1: 0)  0.32143860e+07   s( 1: 0)  0.32962654e+04
  a( 1: 1) -0.65600750e+07   s( 1: 1)  0.17285502e+00
  a( 1: 2) -0.56987968e+09   s( 1: 2)  0.42137861e-01
  a( 2: 0)  0.53806957e+11   s( 2: 0)  0.41116726e+02
  a( 2: 1)  0.22143354e+12   s( 2: 1)  0.72984244e-02
  a( 2: 2) -0.44049562e+14   s( 2: 2)  0.81160935e-02
  a( 3: 0) -0.32995829e+16   s( 3: 0)  0.93649483e+01
  a( 3: 1) -0.11719096e+17   s( 3: 1)  0.10727526e-02
  a( 3: 2)  0.22018443e+19   s( 3: 2)  0.93840359e-03

* MSE estimate :  0.80339741e-02

* Significant coefficients

  a( 0: 0) -0.13074569e+00   std( 0: 0)  0.24076128e-01
  a( 0: 1)  0.33145114e+03   std( 0: 1)  0.55066071e+01
  a( 0: 2) -0.55565996e+05   std( 0: 2)  0.12361018e+04
  a( 1: 0)  0.32143860e+07   std( 1: 0)  0.50431011e+04
  a( 1: 1) -0.65600750e+07   std( 1: 1)  0.14245353e+07
  a( 2: 0)  0.53806957e+11   std( 2: 0)  0.11727013e+10
  a( 3: 0) -0.32995829e+16   std( 3: 0)  0.19773813e+15

* MSE estimate :  0.66206329e-01
```

(b) (3,2) Model.

Table 8.2. Estimated coefficients for polynomial models of ETH-1.

Input mass : 3.330089

Mass error : 0.52449849e-01

New mass estimate : 0.32776387e+01

p(0: 0) = 0.33845409e-03	s(0: 0) = 0.10585832e-06
p(0: 1) = 0.34867441e+03	s(0: 1) = 0.10850862e+01
p(1: 0) = 0.32182248e+07	s(1: 0) = 0.95793808e+02
p(1: 1) = 0.24577680e+05	s(1: 1) = 0.53720331e-07

MSE for model : 0.055562

"Significant coefficients" :

p(0: 1) = 0.34867441e+03	s(0: 1) = 0.10850862e+01
p(1: 0) = 0.32182248e+07	s(1: 0) = 0.95793808e+02

MSE for model : 0.055562

(a) (1,1) Model.

Input mass : 3.330089

Mass error : 0.18229561e-04

New mass estimate : 0.33300705e+01

p(0: 0) = -0.10138735e-04	s(0: 0) = 0.94992660e-10
p(0: 1) = 0.34834955e+03	s(0: 1) = 0.10830654e+01
p(1: 0) = 0.33561600e+07	s(1: 0) = 0.10418134e+03
p(1: 1) = 0.25206881e+06	s(1: 1) = 0.56506083e-05
p(2: 0) = 0.38817628e+08	s(2: 0) = 0.42470384e-06
p(2: 1) = 0.15687697e+11	s(2: 1) = 0.60930688e-06
p(3: 0) = -0.28613537e+16	s(3: 0) = 0.10860196e+00
p(3: 1) = -0.89951991e+16	s(3: 1) = 0.86816090e-05

MSE for model : 0.018127

"Significant coefficients" :

p(0: 1) = 0.34834955e+03	s(0: 1) = 0.10830654e+01
p(1: 0) = 0.33561600e+07	s(1: 0) = 0.10418134e+03
p(3: 0) = -0.28613537e+16	s(3: 0) = 0.10860196e+00

MSE for model : 0.018131

(b) (3,1) Model.

Input mass : 3.330089

Mass error : -0.81316277e-03

New mass estimate : 0.33309019e+01

p(0: 0) = -0.13058231e-02	s(0: 0) = 0.15757493e-05
p(0: 1) = 0.34199725e+03	s(0: 1) = 0.10439249e+01
p(1: 0) = 0.33570023e+07	s(1: 0) = 0.10423363e+03
p(1: 1) = 0.27827059e+06	s(1: 1) = 0.68863860e-05
p(2: 0) = 0.31625968e+09	s(2: 0) = 0.28191360e-04
p(2: 1) = 0.13980201e+13	s(2: 1) = 0.48388778e-02
p(3: 0) = -0.27896309e+16	s(3: 0) = 0.10322578e+00
p(3: 1) = -0.38653057e+16	s(3: 1) = 0.16030475e-05
p(4: 0) = -0.53641637e+19	s(4: 0) = 0.22248127e-04
p(4: 1) = -0.26756782e+23	s(4: 1) = 0.42039533e-02
p(5: 0) = -0.15461313e+25	s(5: 0) = 0.12175536e-03
p(5; 1) = -0.10553603e+27	s(5: 1) = 0.40781670e-05

MSE for model : 0.017522

"Significant coefficients" :

p(0: 1) = 0.34199725e+03	s(0: 1) = 0.10439249e+01
p(1: 0) = 0.33570023e+07	s(1: 0) = 0.10423363e+03
p(3: 0) = -0.27896309e+16	s(3: 0) = 0.10322578e+00

MSE for model : 0.018580

(c) (5,1) Model.

Table 8.3. Estimated coefficients for polynomial models of ETH-2.

```
Timedata filename : c01eth3

Input mass :     3.600000

Mass error :  0.53036493e+00

New mass estimate :  0.30696349e+01

p( 0: 0) = -0.23626830e+00      s( 0: 0) =  0.29564882e-01
p( 0: 1) =  0.32546014e+03      s( 0: 1) =  0.25160563e+00
p( 0: 2) =  0.25606955e+05      s( 0: 2) =  0.16656676e-01
p( 0: 3) = -0.43581828e+06      s( 0: 3) =  0.71295566e-04
p( 1: 0) =  0.23042330e+08      s( 1: 0) =  0.39249219e+03
p( 1: 1) = -0.91376712e+08      s( 1: 1) =  0.24395691e-01
p( 1: 2) = -0.10861275e+13      s( 1: 2) =  0.32208279e+02
p( 1: 3) =  0.28851787e+14      s( 1: 3) =  0.29263410e+00
p( 2: 0) =  0.71270302e+12      s( 2: 0) =  0.15857300e+01
p( 2: 1) = -0.21904226e+14      s( 2: 1) =  0.48399037e-02
p( 2: 2) = -0.52425780e+17      s( 2: 2) =  0.21881112e+00
p( 2: 3) = -0.70201522e+18      s( 2: 3) =  0.43605024e-03
p( 3: 0) = -0.10878223e+20      s( 3: 0) =  0.22363337e+04
p( 3: 1) =  0.25102345e+21      s( 3: 1) =  0.31763947e+01
p( 3: 2) =  0.82021970e+24      s( 3: 2) =  0.22824791e+03
p( 3: 3) = -0.65612477e+26      s( 3: 3) =  0.14148501e+02
p( 4: 0) = -0.50167805e+24      s( 4: 0) =  0.33978649e+02
p( 4: 1) =  0.13489168e+26      s( 4: 1) =  0.55390999e-01
p( 4: 2) =  0.40373872e+29      s( 4: 2) =  0.28960919e+01
p( 4: 3) =  0.22723415e+31      s( 4: 3) =  0.78479469e-01
p( 5: 0) =  0.30323178e+31      s( 5: 0) =  0.97272539e+04
p( 5: 1) = -0.14410672e+33      s( 5: 1) =  0.42797661e+02
p( 5: 2) = -0.23542789e+36      s( 5: 2) =  0.58733081e+03
p( 5: 3) =  0.34098914e+38      s( 5: 3) =  0.94238670e+02
p( 6: 0) =  0.10137888e+36      s( 6: 0) =  0.90329521e+02
p( 6: 1) = -0.21045613e+37      s( 6: 1) =  0.66698007e-01
p( 6: 2) = -Inf                 s( 6: 2) =  0.45312877e+01
p( 6: 3) = -Inf                 s( 6: 3) =  0.43232346e+00
p( 7: 0) = -Inf                 s( 7: 0) =  0.97633984e+04
p( 7: 1) =  Inf                 s( 7: 1) =  0.80741348e+02
p( 7: 2) =  Inf                 s( 7: 2) =  0.33673843e+03
p( 7: 3) = -Inf                 s( 7: 3) =  0.11078708e+03
p( 8: 0) = -Inf                 s( 8: 0) =  0.24343206e+02
p( 8: 1) =  Inf                 s( 8: 1) =  0.32182983e-02
p( 8: 2) =  Inf                 s( 8: 2) =  0.67903370e+00
p( 8: 3) =  Inf                 s( 8: 3) =  0.19945651e+00
p( 9: 0) =  Inf                 s( 9: 0) =  0.13489303e+04
p( 9: 1) = -Inf                 s( 9: 1) =  0.17200325e+02
p( 9: 2) = -Inf                 s( 9: 2) =  0.25393970e+02
p( 9: 3) =  Inf                 s( 9: 3) =  0.16635258e+02

MSE for model :  0.765297
```

Table 8.4. Estimated coefficients for a (9,3) polynomial model for ETH-3.

CHAPTER 9

EXPERIMENTS ON AN MDOF SYSTEM

The identification procedure described in the previous chapters has proved to be of use in the study of simulated systems and SDOF experiments. The final and most important test of the utility of the procedure is made by observing it's performance in the attempted identification of an experimental MDOF system. Both linear and nonlinear systems are considered.

9.1. The Linear System.

The system used for the linear experiment was a mild steel cantilever (fixed-free) beam mounted so that it's motion was confined to a horizontal plane. In order to make the system behave as far as possible like a system with a finite number of degrees-of-freedom, three lumped masses in the form of mild steel cylinders were attached to the beam at equally spaced points along it's length. The system was one of two developed by other researchers, the other system from the pair being a fixed-fixed beam which was studied using Volterra/Wiener series methods in (8). As in the case of the vertical cantilever described in Chapter 8, the damping in the system was very small. To increase the energy dissipation in the system, constrained layer damping material was fixed to both sides of the beam in between the cylinders. The arrangement of the system is shown in Figure 10.1. The various geometrical and material constants for the system are as follows

Beam

Length L : 0.762 m

Width w : 2.54×10^{-2} m

Thickness t : 6.35×10^{-3} m

Density ρ : 7800 Kgm^{-3}

Young's Modulus E : 2.01×10^{11} Nm^{-2}

Second moment of area I : 5.394×10^{-10} m^4

Mass per unit length m : 1.258 Kgm^{-1}

EI : 111.658 Nm^2

Lumped Masses

Mass m_m : 0.455 Kg

Spacing d : 0.254 m

In order to determine the theoretical natural frequencies of the system, one needs an estimate of the mass matrix [M] and stiffness matrix [K]. One assumes that the system can be treated as a three DOF lumped parameter system, the mass is assumed to be concentrated at the three cylinders which served as the measurement points. The labelling of the points is given in Figure 10.1. Using the masses of the cylinders alone one obtains

$$[M] = \begin{bmatrix} 0.455 & 0.000 & 0.000 \\ 0.000 & 0.455 & 0.000 \\ 0.000 & 0.000 & 0.455 \end{bmatrix} \quad (Kg)$$

Now, the mass of the beam is assigned to the measurement points as follows. The mass of beam within a distance d/2 of a point is assigned to that point. A length d of beam has a mass 1.258d Kg, so the final mass matrix is estimated as

$$[M] = \begin{bmatrix} 0.7745 & 0.0000 & 0.0000 \\ 0.0000 & 0.7745 & 0.0000 \\ 0.0000 & 0.0000 & 0.6148 \end{bmatrix} \quad (Kg)$$

The stiffness matrix is assumed to be determined by the properties of the beam alone and is estimated via the flexibility matrix [A] defined as follows (66); a_{ij} is the deflection at measurement point i due to a unit force at point j. Equation 8.6 immediately gives

$$a_{ij} = \{ [a_i - a_j]^3 - 3a_i(L - a_j)^2 + 3L(L - a_j)^2 - (L - a_j)^3 \}/(6EI) \qquad (1)$$

where a_j is the distance of point j from the free end of the beam. In terms of the spacing between the points, $a_1 = 2d$, $a_2 = d$ and $a_3 = 0$. A simple calculation showed that

$$[A] = \frac{d^3}{6EI} \begin{bmatrix} 2 & 5 & 8 \\ 5 & 16 & 28 \\ 8 & 28 & 54 \end{bmatrix} \quad (N^{-1}m)$$

The stiffness matrix is then obtained by inverting the flexibility matrix i.e.

$$[K] = [A]^{-1}$$

The result is

$$[K] = 10^5 \begin{bmatrix} 1.2579 & -0.7233 & 0.1887 \\ -0.7233 & 0.6919 & -0.2516 \\ 0.1887 & -0.2516 & 0.1101 \end{bmatrix} \quad (Nm^{-1})$$

Given the mass and stiffness matrices, one can solve the eigenvalue problem

$$-\omega_i^2[M]\{\psi_i\} = [K]\{\psi_i\}$$

for the natural frequncies $f_i = \omega_i/2\pi$, and the modeshapes $\{\psi_i\}$. In this case, the first three predicted natural frequencies were 4.76 Hz, 22.34 Hz and 77.11 Hz. Now, as the integration procedure for the force surface method requires a band-limited input to be used, it would have proved difficult to excite the first mode and still have no signal at lower frequencies. For this reason, a helical compression spring was placed between point 3 and ground as shown in Figure 9.2. A static test showed the spring to have a stiffness constant of 1.106×10^4 Nm^{-1}. The modification to the system stiffness matrix is minimal, k_{33} changes from 0.1101×10^5 to 0.2207×10^5. However, the first natural frequency changes dramatically. Solving, the new eigenvalue problem gives natural frequencies 17.20 Hz, 32.00 Hz and 77.23 Hz.

The arrangement of the experiment is shown in Figure 9.2. The input was produced by a Korman noise generator and filter modules. The signal was then passed through a KEMO VBF/4 Filter in order to sharpen the signal cut-offs. The signal was then amplified using a Gearing and Watson SS30 amplifier and passed on to a Gearing and Watson V20B electrodynamic shaker. The shaker was attached at masurement point 1 using a rigid link.

A Kistler 9311A force transducer was placed between the shaker and the mass m_1 in order to measure the input force x(t). Endevco 213E accelerometers were placed on each of the cylinders for measuring the output signals $y_1(t)$, $y_2(t)$ and $y_3(t)$. The signals from the transducers were then passed to Bruel and Kaer 2635 charge amplifiers. The signals were then sampled and digitised using the CED 1401 intelligent interface under the control of a HP 300 series computer. The sampled data was finally passed from the HP to a Sun 3/50 workstation where the analysis was carried out.

The first experiment carried out on the system was a modal analysis to accurately determine the natural frequencies of the system. The transfer functions $Y_1(\omega)/X(\omega)$, $Y_2(\omega)/X(\omega)$ and $Y_3(\omega)/X(\omega)$ were obtained on a Scientifica Atlanta SD380 analyser. The first of these transfer functions is shown in Figure 9.3. Curve-fitting to the transfer functions showed that the first three natural frequencies were 16.914 Hz, 31.781 Hz and 77.778 Hz. These values showed fairly good agreement with the theoretical estimates, and therefore gave a certain amount of confidence in the estimated mass and stiffness matrices. The output spectrum for the system when excited by a band-limited input in the range (10,100)Hz is shown in Figure 9.4. There is clearly no significant contribution from higher modes than the third. Because of this, one would expect the system to be well-modelled by a three degree-of-freedom model if the input is band-limited in this way.

An experiment was then carried out with the intention of fitting least-squares linear models of the type given in equation (5.11) to the data. The excitation used was a noise sequence band-limited into the range (10,100)Hz. The data x, y_1, y_2 and y_3 were captured on channels 0, 1, 2 and 3 of the CED system. The sampling frequency used was 1666.6 Hz. 3000 points per channel were taken.

After passing the data to the Sun computer it was shifted in time as described in Chapter 8 in order to restore simultaneity of the samples, x was taken as the reference channel so the y_1 data was shifted forward in time by a distance $\Delta t/4$, the

$\dot{y}_2$ data was shifted forward by $2\Delta t/4$ and the $\dot{y}_3$ data by $3\Delta t/4$, Δt being the sampling interval. The shift was accomplished very accurately. The acceleration signals were integrated using the trapezium rule followed by band-pass filtering into the range (10,100)Hz. 500 points were then deleted from the beginning and end of each channel in order to remove any filter transients. This left 2000 points per channel.

A inhomogeneous (1,1) model was fitted to the data points 500 to 1500 in order to estimate the $\dot{y}_1$ equation of motion. The identification data including the significance factors and standard deviations is given in Table 9.1. The estimated form of the equation is

$$0.8585\ddot{y}_1 - 4.33\dot{y}_1 + 7.87\times10^4 y_1 + 10.1(\dot{y}_1 - \dot{y}_2) + 8.33\times10^4(y_1 - y_2) - 2.23\times10^4(y_1 - y_3) = x$$

Comparing the predicted and measured data gave a MSE of 0.035, the comparison is shown in Figure 9.5. In all the models for this system the significance threshold was set at 0.1%.

A homogeneous (1,1) model was fitted for the $\dot{y}_2$ and $\dot{y}_3$ equations of motion, The identification data is shown in tables 9.2 and 9.3. The estimated equations were

$$\ddot{y}_2 + 9.11\times10^4(y_2 - y_1) - 3.55\times10^4 y_2 + 3.34\times10^4(y_2 - y_3) = 0$$

$$\ddot{y}_3 + 6.84(\dot{y}_3 - \dot{y}_1) - 7.13\dot{y}_3 - 3.85\times10^4(y_3 - y_1) + 4.63\times10^4(y_3 - y_2) + 3.00\times10^4 y_3 = 0$$

The comparisons between measured and predicted data were made and gave MSE values of 0.176 and 0.066, the data is shown in Figures 9.6 and 9.7.

The scale factors were transferred from the first equation of motion to the other two

as described in Chapter 5, giving the $[\gamma]$ and $[\mu]$ matrices, the symmetrised [C] and [K] matrices were then obtained. The final results were

$$[M] = \begin{bmatrix} 0.8595 & 0.0000 & 0.0000 \\ 0.0000 & 0.9152 & 0.0000 \\ 0.0000 & 0.0000 & 0.5800 \end{bmatrix} \text{(Kg)} \qquad (2a)$$

$$[C] = 10. \begin{bmatrix} 1.4060 & -1.0094 & -0.3966 \\ -1.0094 & 1.0094 & 0.0000 \\ -0.3966 & 0.0000 & -0.0171 \end{bmatrix} \text{(Nsm-1)} \qquad (2b)$$

$$[K] = 10^5. \begin{bmatrix} 1.3969 & -0.8334 & 0.2233 \\ -0.8334 & 0.7949 & -0.2869 \\ 0.2233 & -0.2869 & 0.2379 \end{bmatrix} \text{(Nm}^{-1}\text{)} \qquad (2c)$$

These compare favourably with the theoretical results. Using the estimated [M] and [K] matrices, the first three model natural frequencies were calculated. Again, agreement was good, the results being

Frequency	Experimental	Model	% error
f_1	16.914	17.044	0.77
f_2	31.781	32.247	1.47
f_3	77.529	77.614	0.11

As a final test, the fifth-order Runge-Kutta procedure described in the previous chapter was used to estimate the displacement time-histories from the model when forced by the signal x(t). The MSE values for the comparisons were 2.13, 4.01 and 9.82. These values were obtained by setting the damping matrix to zero, if the estimated damping matrix was used the MSE values increased. This shows how little confidence one has in the damping estimates. This is because the structure is very lightly damped, and the damping forces contribute very little to the restoring forces.

The results of the experiment are seen to be very good. However, one is entitled to

ask the question, do these parameters correspond to actual *physical* masses and stiffnesses? In an attempt to answer this, the following experiment was carried out. An additional 1 Kg mass was attached to measurement point 2 and the experimental procedure was repeated exactly as above using the same type of excitation. The Transfer function $Y_1(\omega)/X(\omega)$ was obtained and is shown in Figure 9.8. The experimental values for the natural frequencies were obtained from the analyser. This time Mohammad's method (26) as described in Chapter 5, was used to identify the system, the resulting matrices were

$$[M] = \begin{bmatrix} 0.8888 & 0.0000 & 0.0000 \\ 0.0000 & 1.9297 & 0.0000 \\ 0.0000 & 0.0000 & 0.7097 \end{bmatrix} \quad (Kg)$$

$$[C] = \begin{bmatrix} 9.5525 & 5.6652 & 0.0000 \\ 5.6652 & 0.0000 & 0.0000 \\ 0.0000 & 0.0000 & 0.0000 \end{bmatrix} \quad (Nsm^{-1})$$

$$[K] = 10^5 . \begin{bmatrix} 1.3709 & -0.8099 & 0.2245 \\ -0.8099 & 0.7841 & -0.3014 \\ 0.2245 & -0.3014 & 0.2646 \end{bmatrix} \quad (Nm^{-1})$$

The MSE values for comparing predicted and measured data for each equation were 0.940, 0.130 and 0.989, indicating an excellent fit again. The results have changed very little from those of the previous experiment, the only exception being that m_{22} has increased by 1.01 Kg. This result gives one confidence that the parameters obtained by the method are physical. The natural frequencies for the model were obtained, the results being

Frequency	Experimental	Model	% error
f_1 (Hz)	13.624	13.252	2.73
f_2	29.124	29.846	2.48
f_3	69.500	69.365	0.19

Again, showing good agreement.

9.2. The Nonlinear System.

The final experimental system considered was based on work in (8). The same experimental arrangement as in the previous section was used with a number of modifications. An additional accelerometer was placed at measurement point 2 (Bruel and Kaer 4934) the signal obtained was then passed to a B & K 2635 charge amplifier which was used to integrate the signal giving an output proportional to velocity $\dot{y}_2$. The velocity signal was then passed through a nonlinear electronic circuit which produced an output proportional to velocity cubed i.e. $\dot{y}_2^3$. The cubed signal was then amplified in a Gearing and Watson SS20 amplifier. Finally, the output from the amplifier was used to drive a Ling Dynamics V403 electrodynamic shaker which was attached via a rigid link to measurement point 2. The overall effect of this feedback loop is to introduce a restoring force at measurement point 2 proportional to the cube of the velocity at point 2. The layout of the feedback loop is shown in Figure 9.9. The electronic circuit was designed and constructed in the Department of Mechanical Engineering at Heriot-Watt University.

The experimental procedure was the same as in the linear case. The excitation used was a noise sequence in the range (10,100)Hz. Figure 9.10 shows the transfer function for the system with the feedback shaker attached, but no signal through the nonlinear circuit. The damping in the system is clearly increased by the presence of the shaker. The natural frequencies for the system with the shaker attached (but passive) are approximately 19 Hz, 32 Hz and 74.9 Hz. The level of excitation used was recorded by simply marking the position of the amplitude dial on the input amplifier. The cubic circuit was then switched in, the amplitude of the feedback amplifier signal was increased until a noticeable increase in damping and loss of coherence was obtained in the transfer function as shown in Figure 9.11. The coherence function (58) plotted in the upper section of the figure is a simple indicator of the presence of nonlinearity or noise. For clean signals produced by a linear system, the coherence is 1.0 over the frequency range of the excitation. The position of the dial on the feedback amplifier was then marked.

4000 sampled points of data were obtained for each channel x, $\dot{y}_1$, $\dot{y}_2$ and $\dot{y}_3$ using the CED box. After passing the data to the computer, each channel was shifted forward in time as described in the previous section. The measured and shifted data for the $\dot{y}_3$ channel is shown in Figure 9.11, the shifting has clearly been accomplished with a high degree of accuracy. The acceleration signals were then integrated using the trapezium rule followed by filtering. In this case the pass-band used was (10,300) Hz, the high cut-off was chosen so that any third harmonic content in the data would be retained. As before, 500 points were removed from the beginning and end of each record in order to eliminate transients.

The $\dot{y}_1$ equation of motion was obtained by fitting an inhomogeneous (1,1) model to 1000 points of the remaining data. The estimated equation was

$$0.872\ddot{y}_1 - 22.4\dot{y}_1 + 8.59\times10^4 y_1 + 20.7(\dot{y}_1 - \dot{y}_2) + 7.96\times10^4(y_1 - y_2) - 2.31\times10^4(y_1 - y_3) = x$$

The comparison between measured and predicted data gave an MSE of 0.056, and is shown in Figure 9.13. The very low MSE indicates that the equation is adequately described by a (1,1) model i.e. it has no nonlinear terms. As a check, a (3,3) model was fitted to the same data. All but the linear terms were discarded as insignificant, the mass and stiffness terms did not change but the damping values did slightly, this was further indication that the damping values are not to be trusted.

The second equation of motion was obtained by fiiting a homogeneous (1,3) model. An initial estimate using 1000 points of data indicated the presence of a term cubic in $\dot{y}_2$. However, the term only contributed 3% of the variance of $-\dot{y}_2$, i.e. it's significance factor was 3.0. In order to improve the chances of identifying this term accurately a (1,3) model was then fitted using 2500 points of data. The identification data is given in Table 9.4. The estimation gave

$$\ddot{y}_2 - 16.7(\dot{y}_2 - \dot{y}_1) + 154.3\dot{y}_2 + 8.45\times10^4(y_2 - y_1) -$$
$$2.93\times10^4 y_2 + 3.07\times10^4(y_2 - y_3) +$$
$$228.(\dot{y}_2 - \dot{y}_1)^3 - 183.\dot{y}_2^2 + 5.63\times10^3\dot{y}_2^3 = 0$$

The MSE for the comparison between predicted and measured data was 0.901, the comparison is shown in Figure 9.14. The MSE obtained when a (1,1) model was tried was 1.77, this increase indicates that the equation truly requires a nonlinear model. The force surfaces for links l_{21}, l_{22} and l_{23} are shown in Figures 9.15, 9.16 and 9.17 respectively. One can see from Figure 9.15 that the surface is almost flat even though a cubic term is present in the force model for the link. Also, the significance factor of the cubic term in f_{21} is only 0.17% indicating that it if one discards it the MSE for the model will only rise to approximately 1.06. A further indication that this term should be discarded is that if one calculates the 95% confidence interval, one finds that the estimated coefficient is 228 ± 482 so one cannot even assert which sign the term has. Finally, no nonlinear term appears in the f_{12} expansion obtained above. Similar remarks apply to the quadratic term in f_{22}, the estimate is −183 ± 503 and the significance factor is only 0.13%. This means that if both the terms discussed are removed, the MSE will rise to approximately 1.21 which is still significantly better than the nonlinear model. Finally, the cubic term in f_{22} must be retained as the estimate gives 5630 ± 4882 for the coefficient, the coefficient is larger than the error. Also, the significance factor for this term is 2.6. Finally, one can see from the force surface in Figure 9.16 that the cubic term is significant. One concludes that the procedure has identified a cubic velocity term in the link connecting measurement point 2 to ground.

The $\ddot{y}_3$ equation was obtained by fitting a homogeneous (1,1) model to 1000 points of data. The estimated equation was

$$\ddot{y}_3 + 8.37(\dot{y}_3 - \dot{y}_1) + 27.1(\dot{y}_2 - \dot{y}_1) - 36.4\dot{y}_3 -$$
$$3.98\times10^4(y_3 - y_1) + 4.47\times10^4(y_3 - y_2) +$$
$$3.35\times10^4 y_3 = 0$$

The comparison between predicted and measured data gave an MSE of 0.31 and is shown in Figure 9.18. Again, the low MSE indicates that a linear model is adequate. To check, a (3,3) model was fitted and all but the linear terms were discarded as insignificant.

After transferring the scales from the y_1 equation to the other two, the $[\gamma]$ and $[\mu]$ matrices were constructed as before, and from them the [M], [C] and [K] matrices of the underlying linear system were obtained, i.e. the system which one would obtain if all nonlinear terms were deleted. The results were

$$[M] = \begin{bmatrix} 0.8720 & 0.0000 & 0.0000 \\ 0.0000 & 0.9648 & 0.0000 \\ 0.0000 & 0.0000 & 0.5804 \end{bmatrix} \quad (Kg)$$

$$[C] = 10. \begin{bmatrix} 0.3107 & -2.0690 & -0.4858 \\ -2.0690 & 19.0250 & -1.2116 \\ -0.4858 & -1.2116 & -0.4129 \end{bmatrix} \quad (Nsm^{-1})$$

$$[K] = 10^5. \begin{bmatrix} 1.4240 & -0.7960 & 0.2310 \\ -0.7960 & 0.7950 & -0.2711 \\ 0.2310 & -0.2711 & 0.2345 \end{bmatrix} \quad (Nm^{-1})$$

These parameters show good agreement with those in (2a,b,c). The only difference being the significant increase in the damping c_{22}, this is of course due to the linear damping introduced by the shaker. Solving the eigenvalue problem using these matrices gives natural frequencies of 19.6 Hz, 32.1 Hz and 76.3 Hz for the linear system, giving good agreement with the frequencies shown in Figure 9.10.

All that remained to be done now was to determine the true cubic coefficient in the experiment. In order to do this a force transducer was placed between the feedback shaker and its connection to measurement point 2 as shown in Figure 9.19. The excitation level and the feedback amplifier level were then set as they were in the identification experiment. The characteristics of the nonlinear circuit were obtained by

exciting the circuit with a sinusoid and fitting a polymonial to the measured input and output voltages (8). The results were

$$V_2 = 1.34.V_1 + 1.25.V_1^2 + 0.713.V_1^3 \qquad (3)$$

where V_1 is the input voltage and V_2 is the output voltage (see Figure 9.19). The gain factor $V_1/\dot{y}_2$ is obtained from the relevant charge amplifier settings as

$$V_1 = 31.6\dot{y}_2 \qquad (4)$$

Substituting into equation (3) gives

$$V_2 = 42.34.\dot{y}_2 + 1248.2.\dot{y}_2^2 + 22498.\dot{y}_2^3 \qquad (5)$$

The gain factor V_F/F is again fixed by the approriate charge amplifier settings

$$V_F = 31.6F \qquad (6)$$

To find the missing gain factor F/V_2, the quadratic and cubic parts of the circuit were switched out leaving only the linear term. The signals $V_1(t)$ and $V_F(t)$ were passed to a spectrum analyser and the transfer function $V_1(\omega)/V_F(\omega)$ was obtained, this is shown in Figure 9.20. The transfer function magnitude is fairly constant at about 0.16, this gives the final gain factor as

$$V_F = -6.06V_1$$

which implies, using (4) and (6) that the overall gain is given by

$$F = -6.06\dot{y}_2$$

comparing this final equation with (5) shows that the force characteristics would be

$$F = -(6.06.\dot{y}_2 + 178.7.\dot{y}_2^2 + 3220.\dot{y}_2^3)$$

if all parts of the circuit were switched in. Finally one concludes that the nonlinear restoring force between measurement point 2 and ground when only the cubic term was used was

$$F = -3220.\dot{y}_2^3$$

The coefficient value estimated by the identification procedure was 5630 ± 4882. The percentage error is 75%. The estimation has the right order of magnitude and the error interval of the estimate encloses the true value.

These results are encouraging, although the coefficient for the nonlinear term could be better, the identification procedure has correctly identified the type and location of the nonlinearity.

In Summary, the results of this chapter indicate that the direct least–squares procedure can be used to identify real i.e. experimental MDOF systems, both linear and nonlinear with a fair degree of accuracy. The method actually gives a set of equations of motion for the system, which is a considerable gain over most other methods.

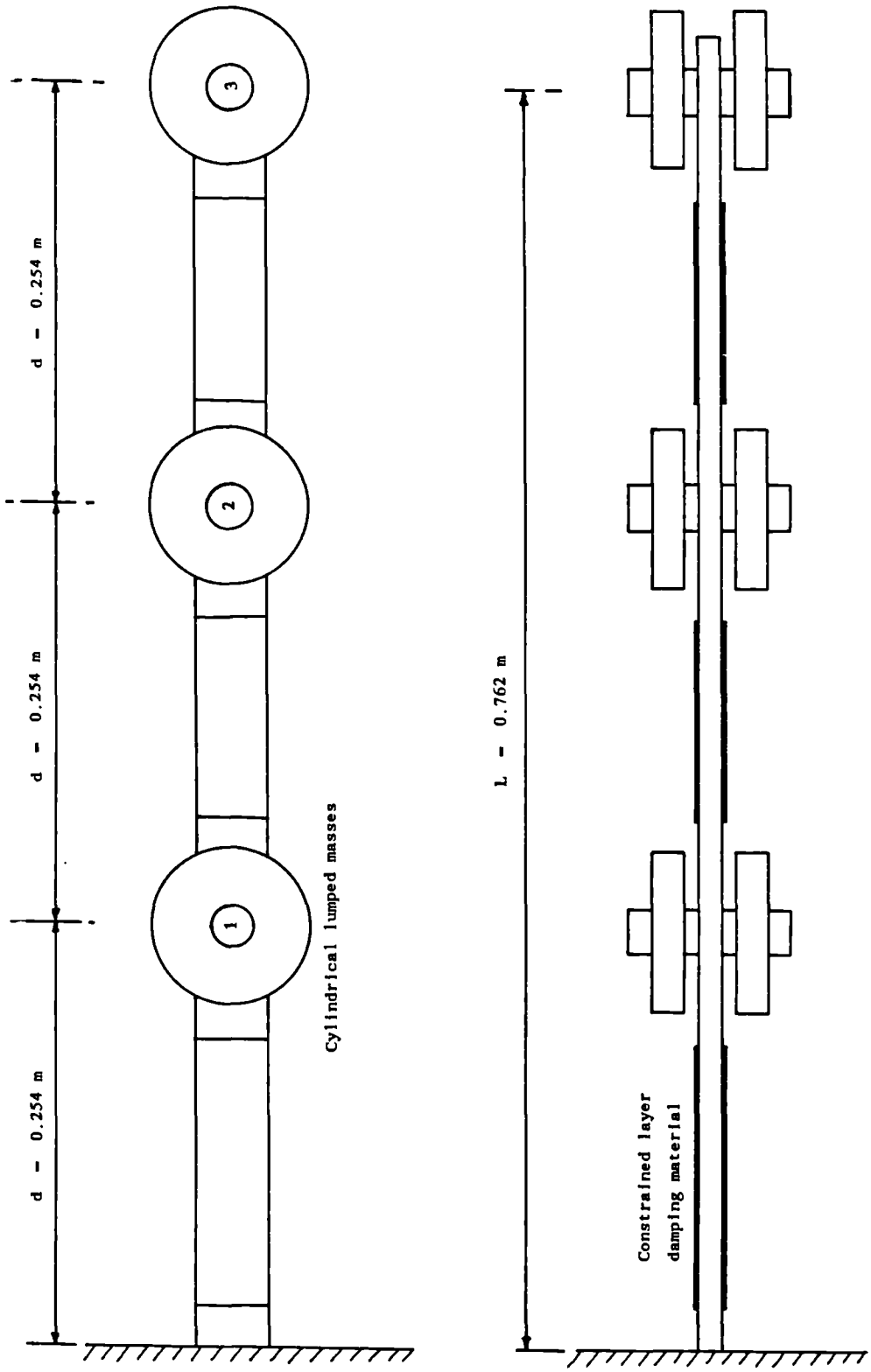

Figure 9.1. Linear 'three degree-of-freedom' experimental rig.

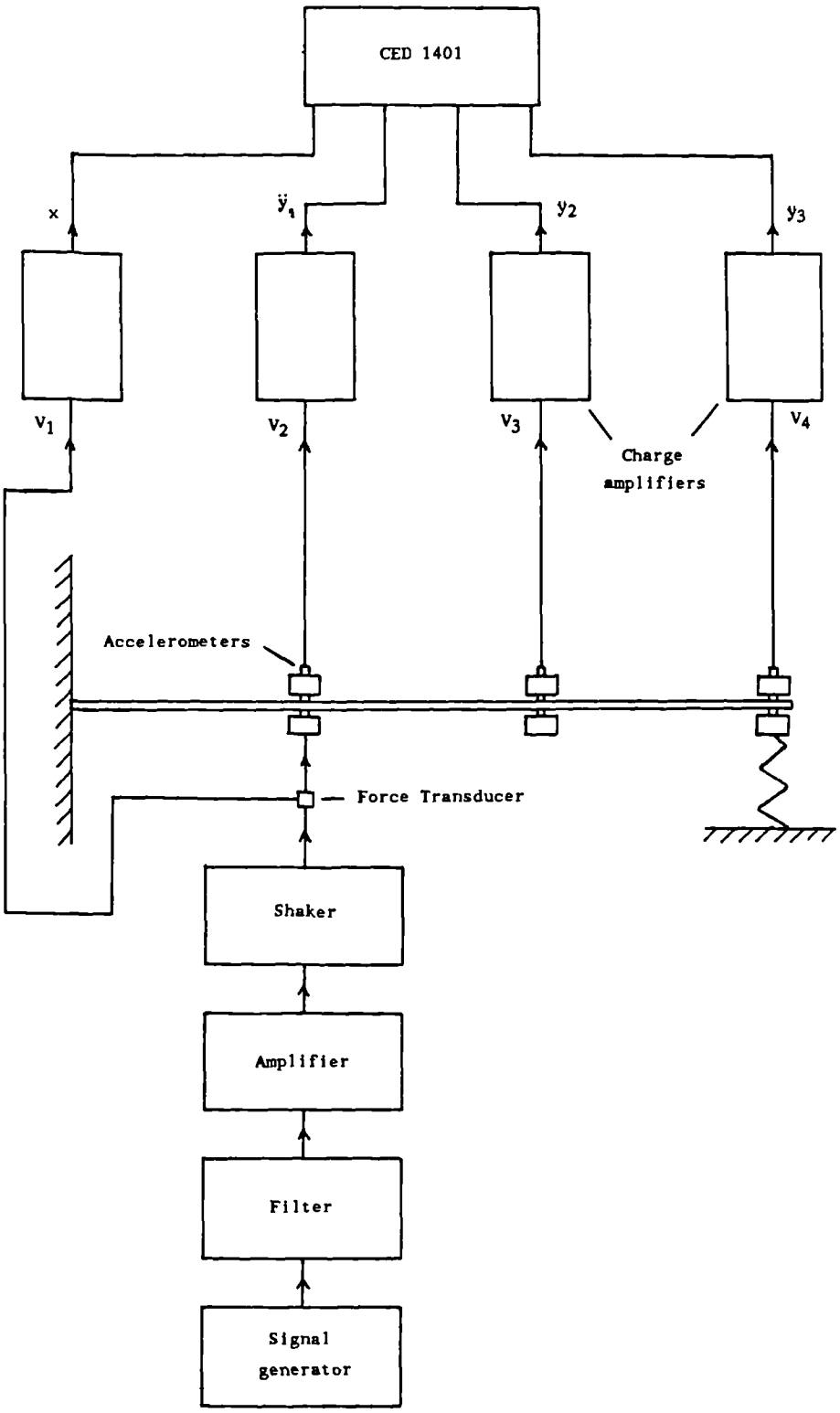

Figure 9.2. Instrumentation for the experiments on the three degree-of-freedom system.

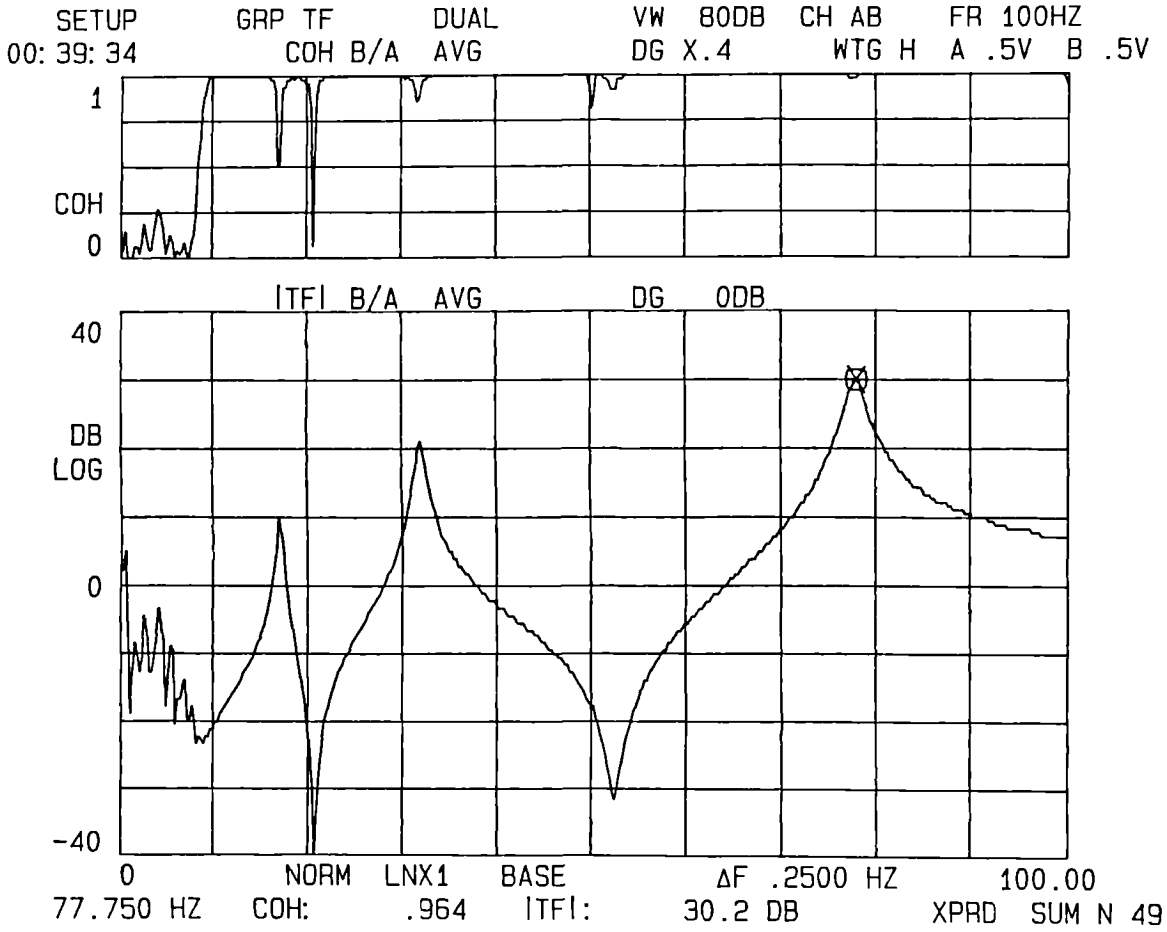

Figure 9.3. Y_1/X frequency response function for the linear three degree-of-freedom system.

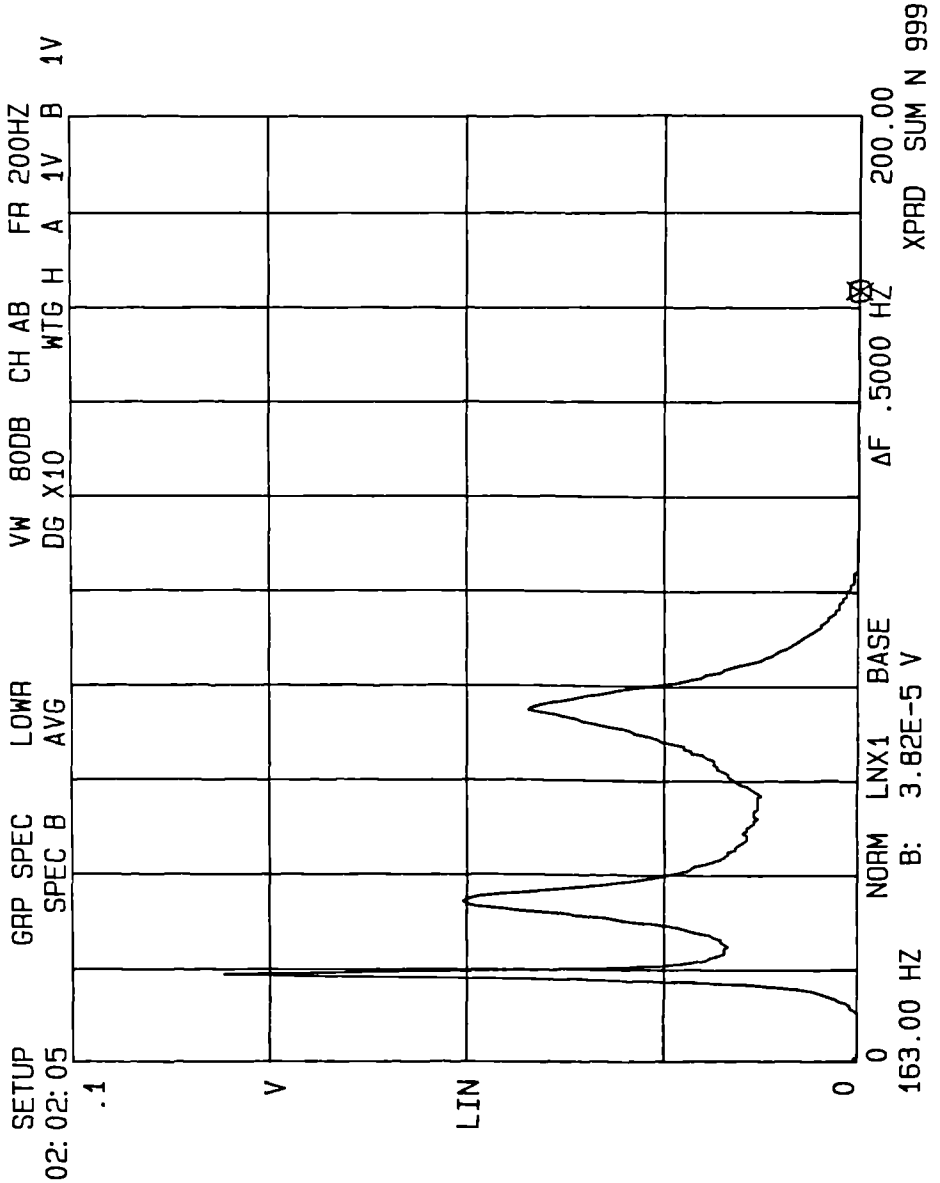

Figure 9.4. Output spectrum for the linear three degree-of-freedom system under excitation by random signal in the range 10 Hz to 100 Hz.

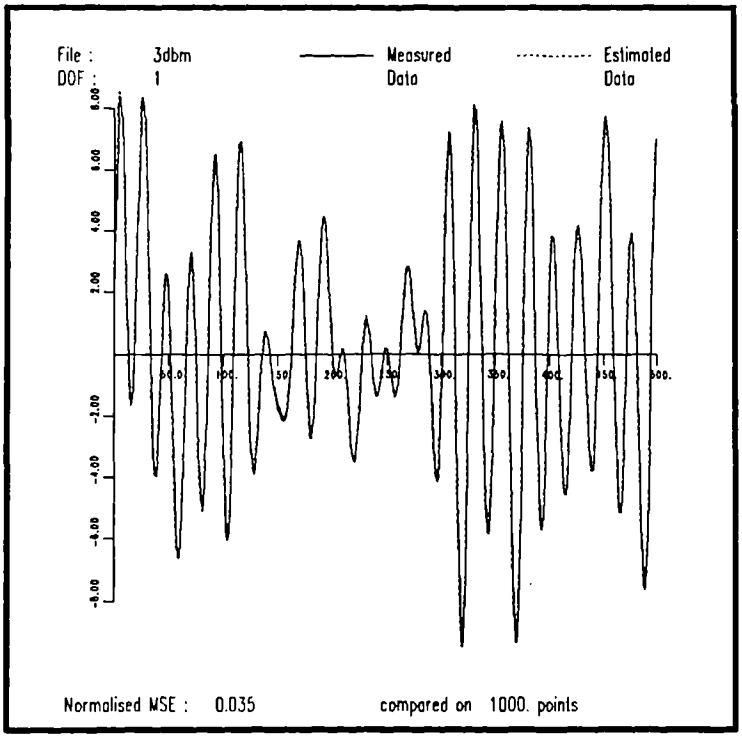

Figure 9.5. Comparison of measured data and that predicted by a linear model for the first equation of of motion for the linear 3DOF system.

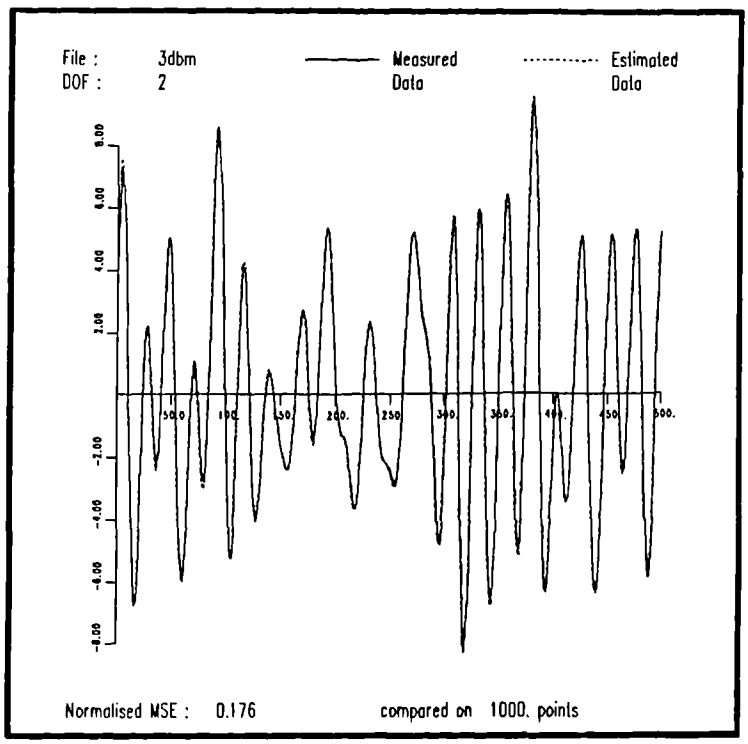

Figure 9.6. Comparison of measured data and that predicted by a linear model for the second equation of of motion for the linear 3DOF system.

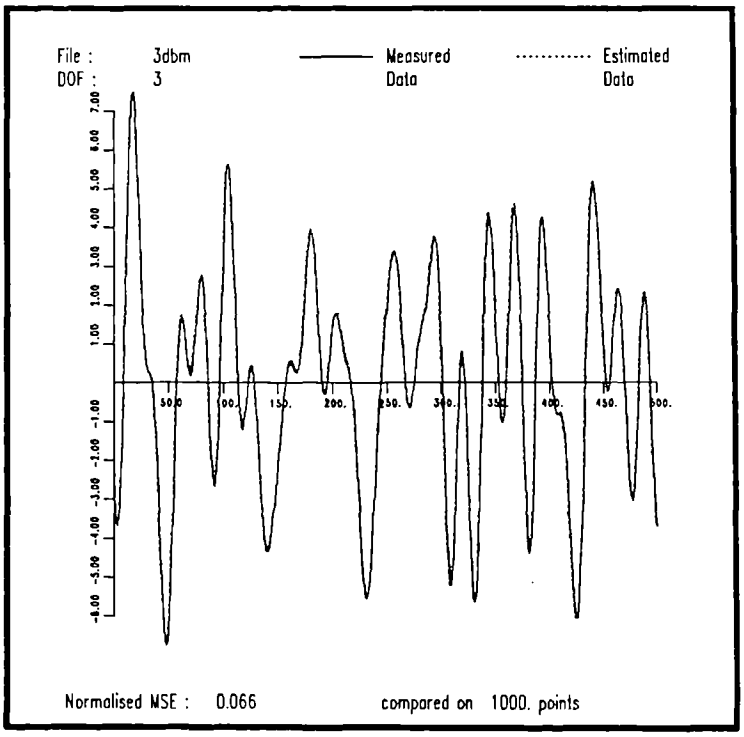

Figure 9.7. Comparison of measured data and that predicted by a linear model for the third equation of of motion for the linear 3DOF system.

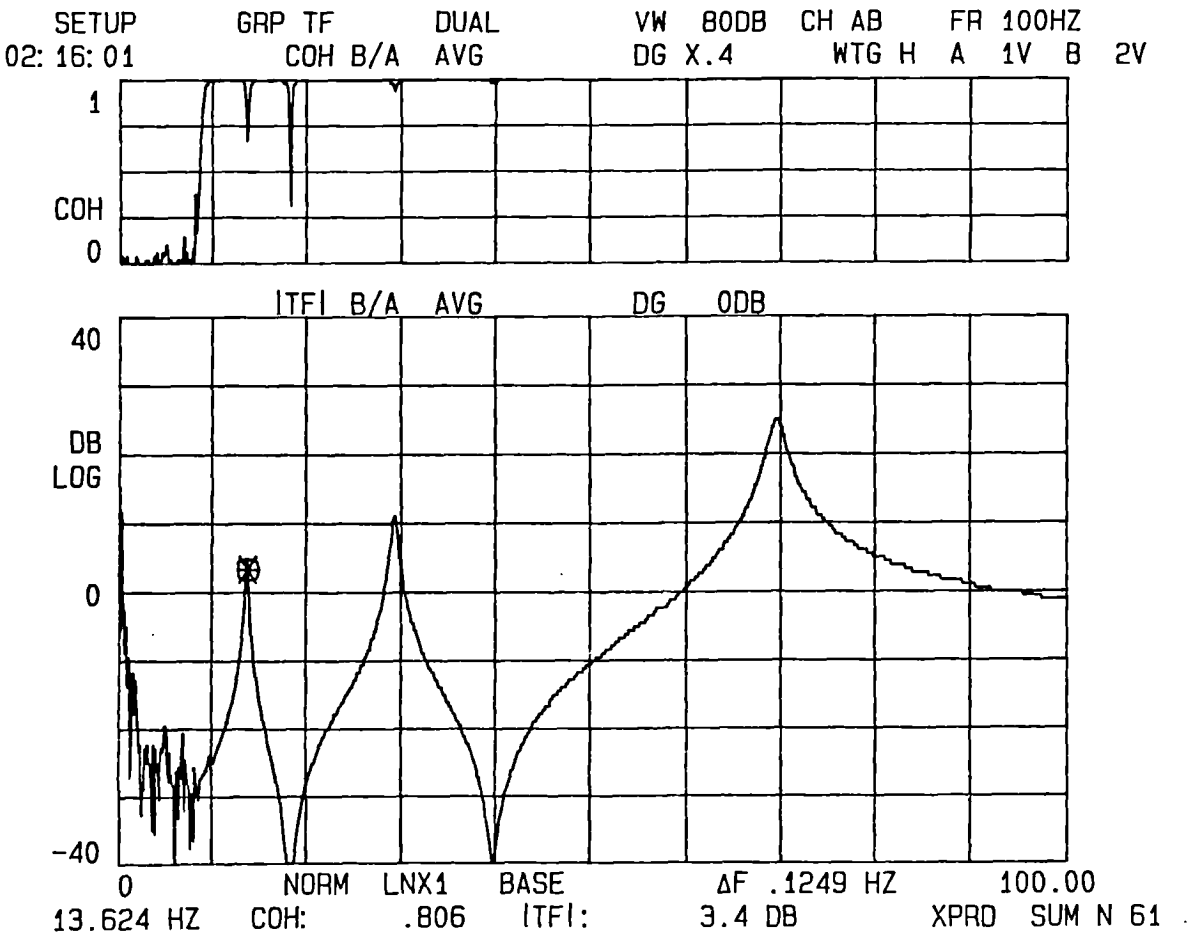

Figure 9.8. Y_1/X frequency response function for the linear 3DOF system with a 1 Kg mass added to the second measurement point.

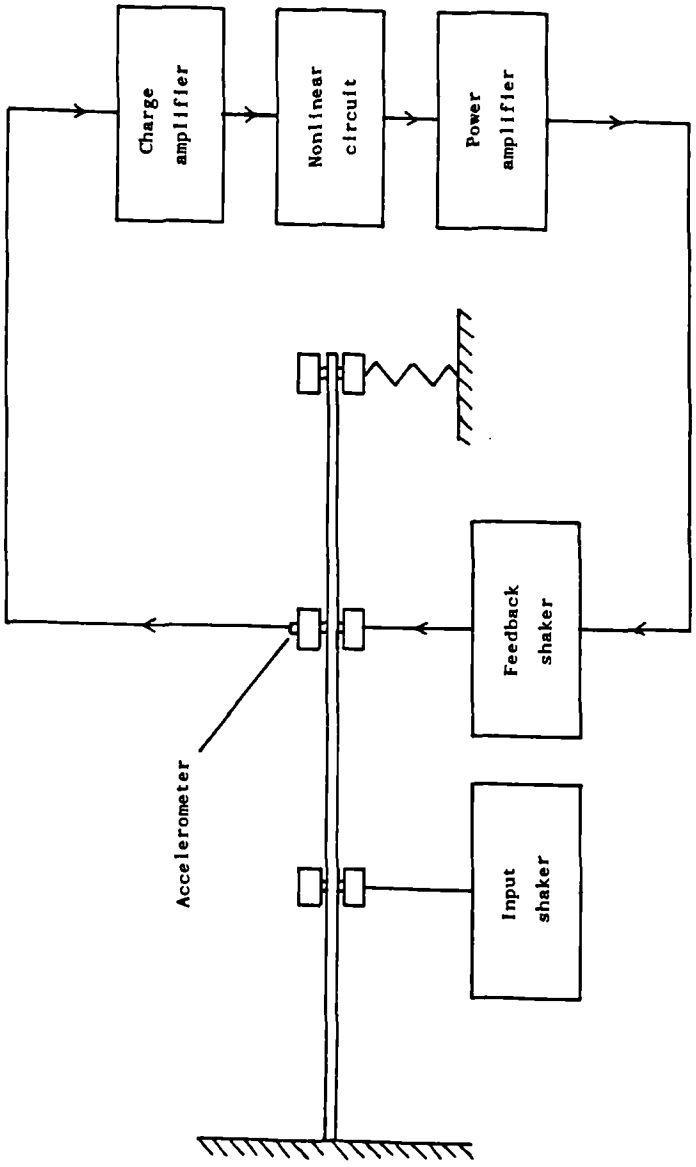

Figure 9.9. Feedback loop for the introduction of a nonlinear force into the linear 3DOF system.

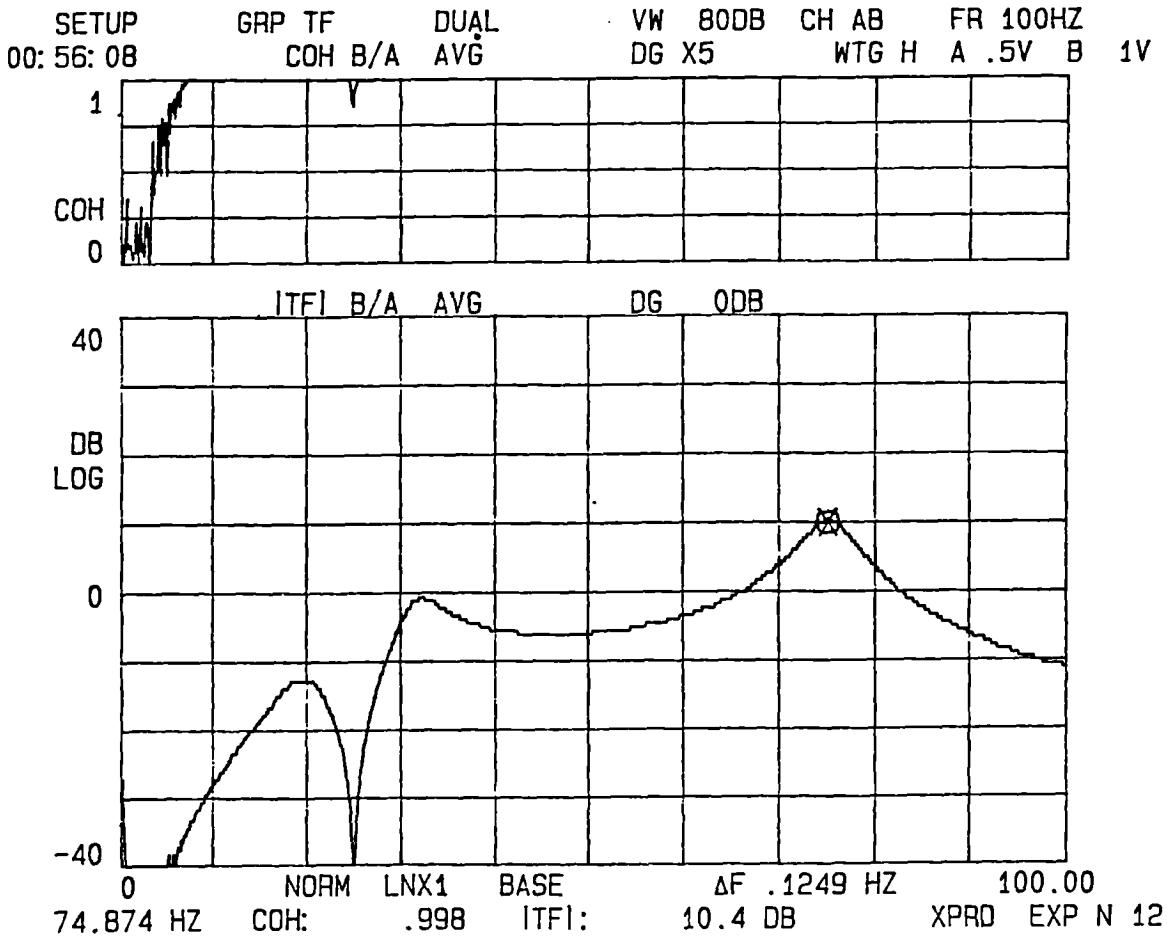

Figure 9.10. Y_1/X frequency response function for the linear 3DOF system with the feedback shaker attached but passive.

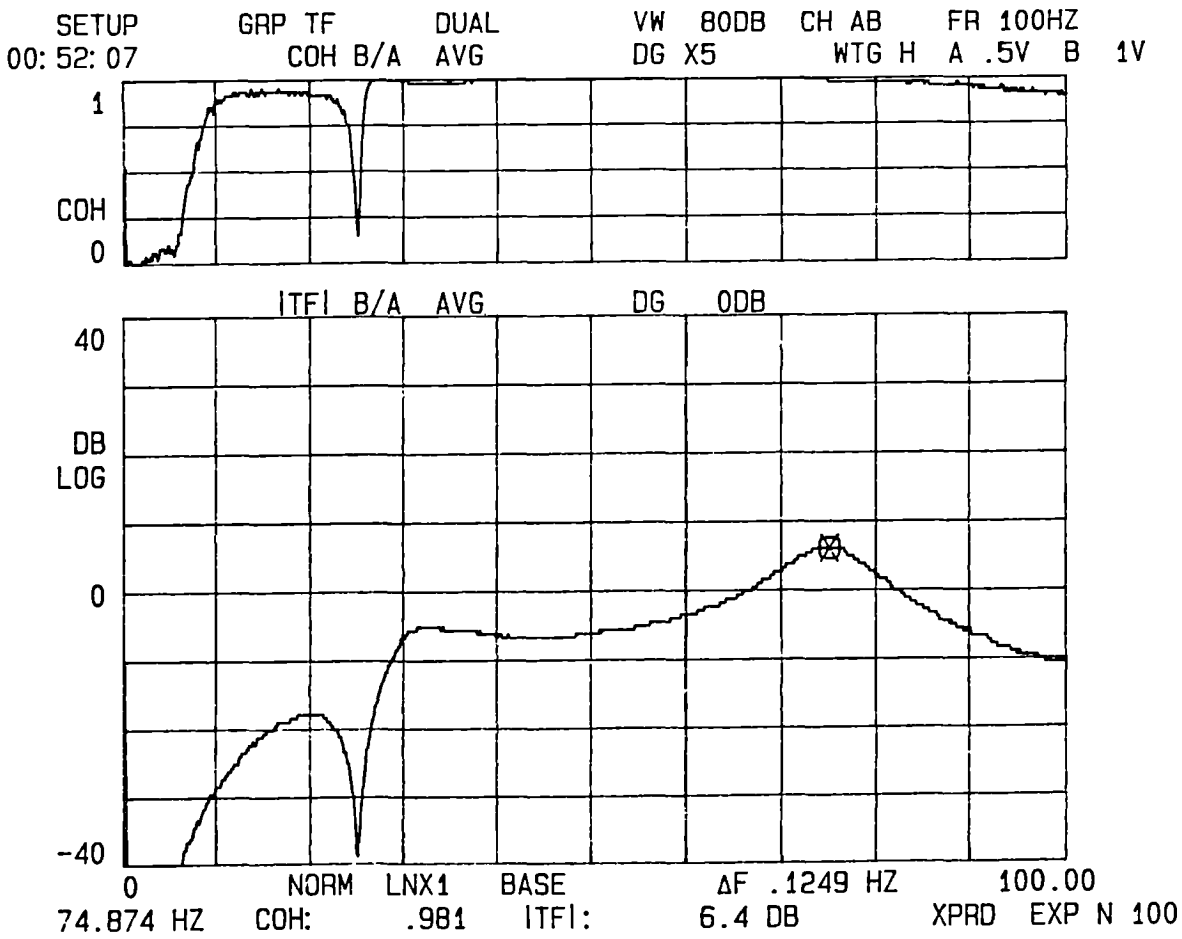

Figure 9.11. Y_1/X frequency response function for the linear 3DOF system with the feedback shaker producing a nonlinear restoring force.

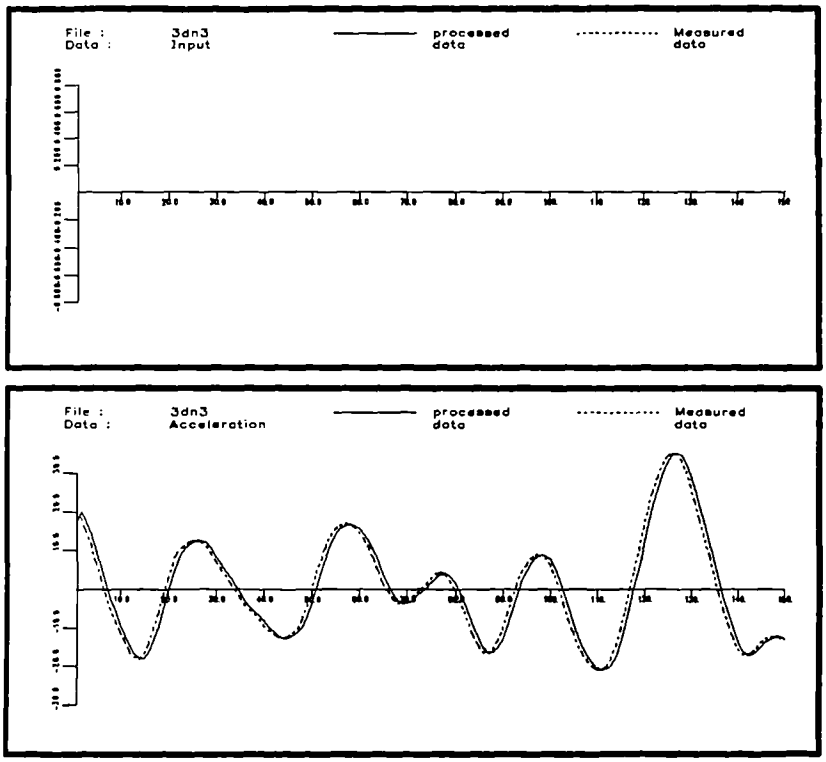

Figure 9.12. Measured Input and $\ddot{y}_3$ response data showing the shifted response data.

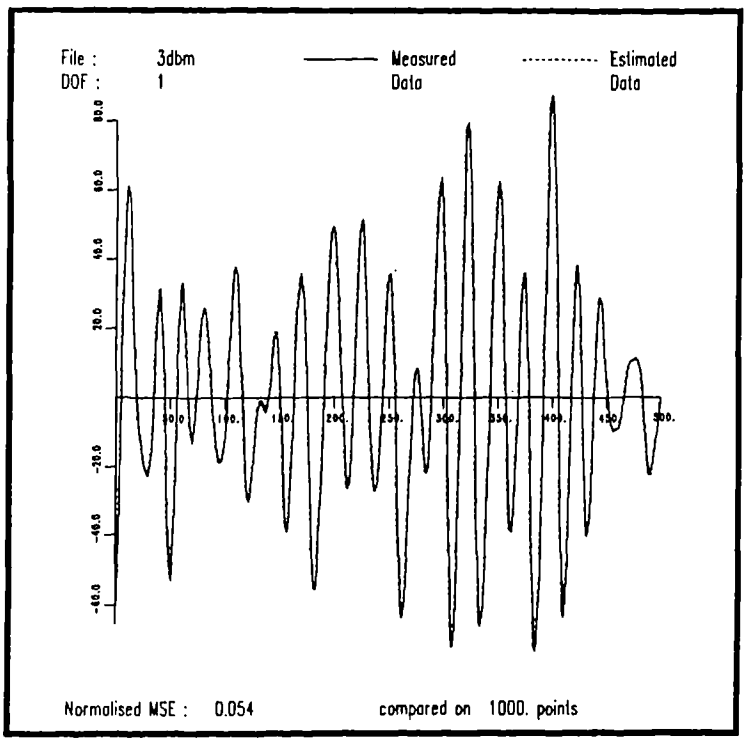

Figure 9.13. Comparison of measured data and that predicted by a linear model for the first equation of of motion for the nonlinear 3DOF system.

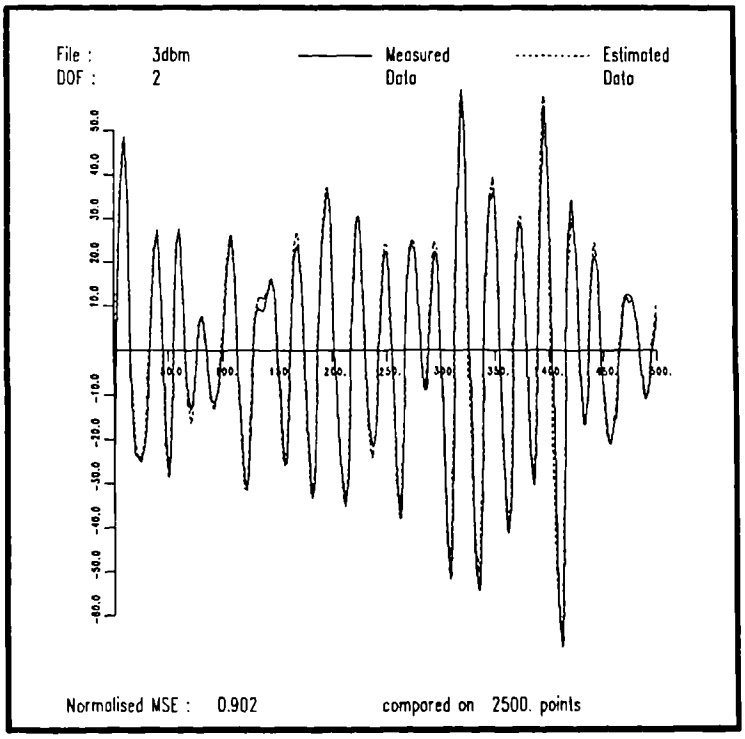

Figure 9.14. Comparison of measured data and that predicted by a nonlinear model for the second equation of of motion for the nonlinear 3DOF system.

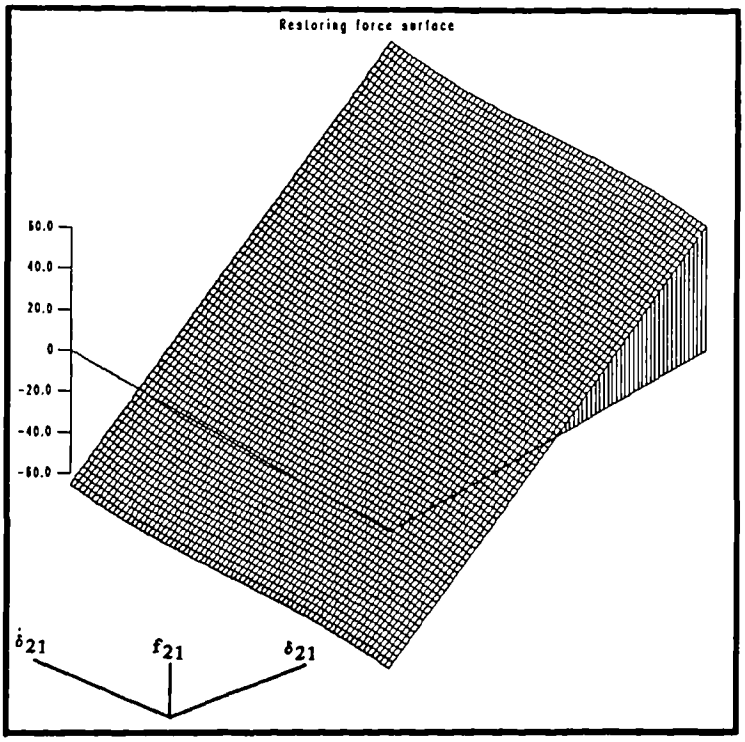

Figure 9.15. Restoring force surface for link l_{21} in the nonlinear 3DOF system.

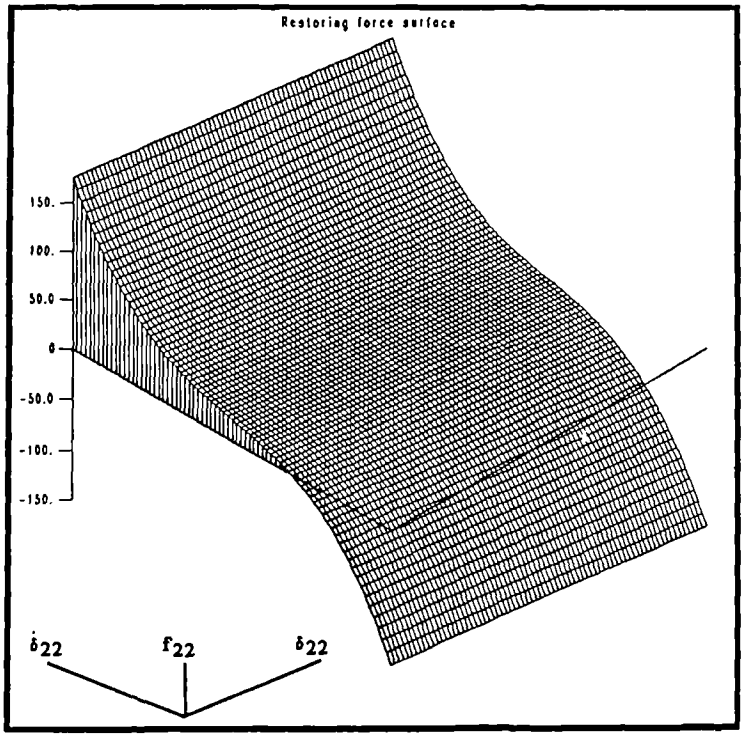

Figure 9.16. Restoring force surface for link l_{22} in the nonlinear 3DOF system.

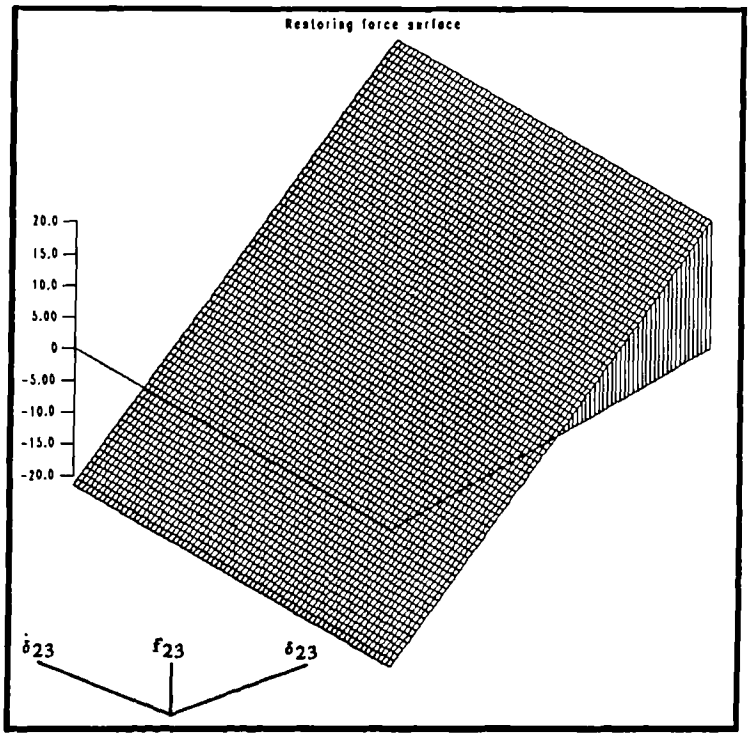

Figure 9.17. Restoring force surface for link l_{23} in the nonlinear 3DOF system.

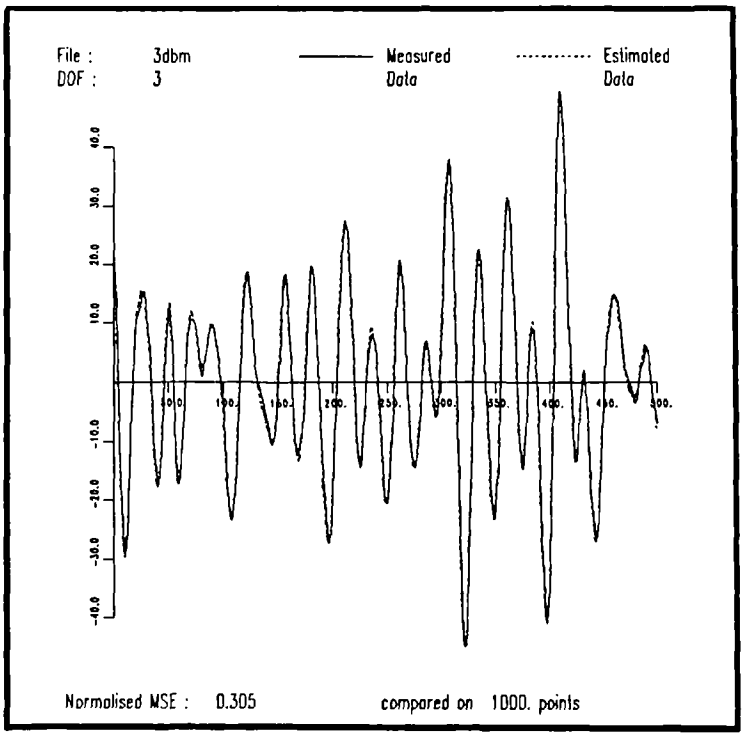

Figure 9.18. Comparison of measured data and that predicted by a linear model for the third equation of of motion for the nonlinear 3DOF system.

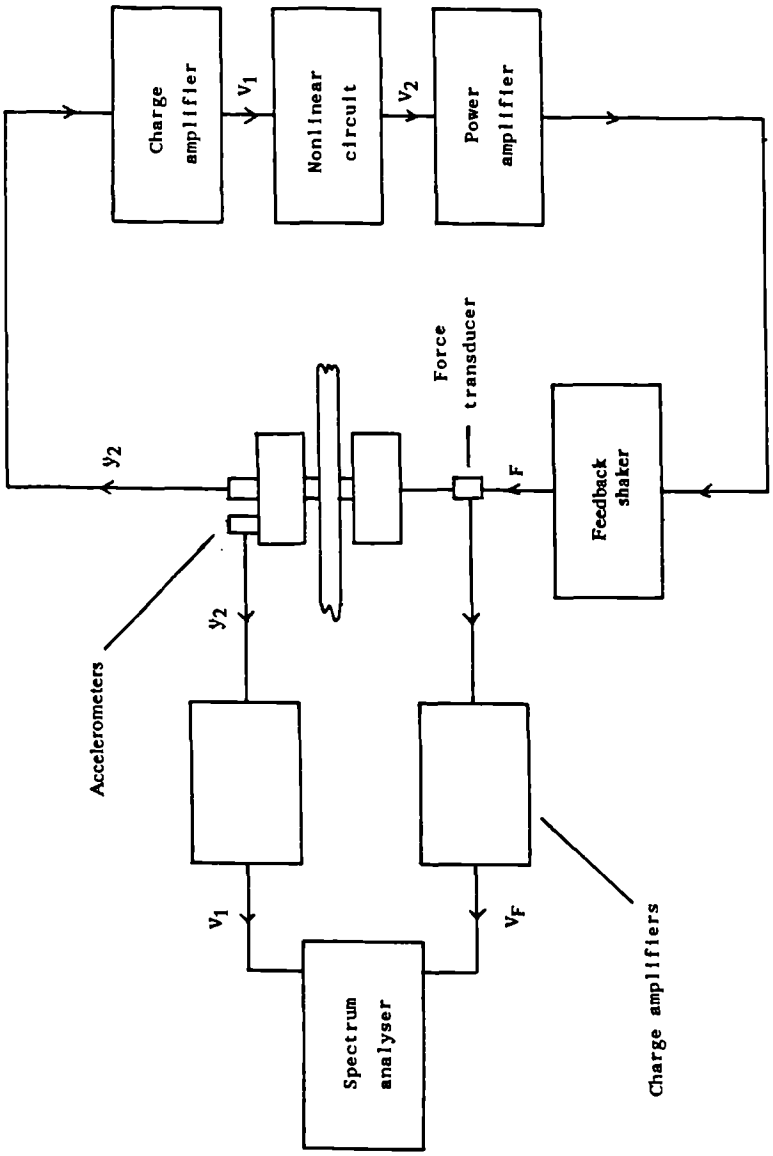

Figure 9.19. Calibration experiment for the nonlinear 3DOF system.

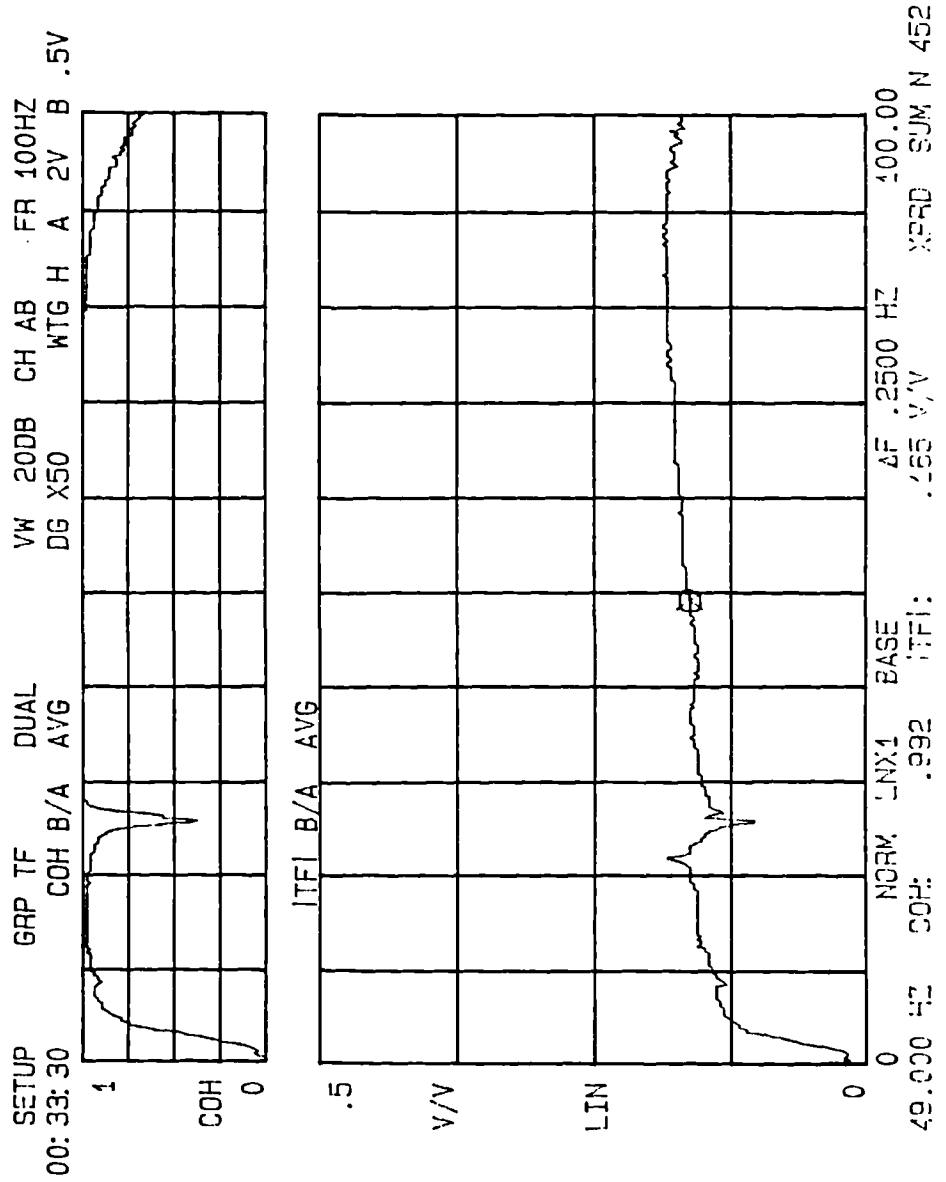

Figure 9.20. V_1/V_F transfer function measured in the calibration experiment.

```
Coefficients for system : 3dbm

Corrected mass value :  0.85949999e+00

* Coefficients for links to node  1

  a( 1: 0: 0)  0.40283203e-02   s( 1: 0: 0)  0.11240279e-03
  a( 1: 0: 1) -0.43298974e+01   s( 1: 0: 1)  0.10495524e-01
  a( 1: 1: 0)  0.78679336e+05   s( 1: 1: 0)  0.63332321e+02
  a( 1: 1: 1) -0.15646159e+03   s( 1: 1: 1)  0.17601408e-07

  a( 2: 0: 0)  0.00000000e+00   s( 2: 0: 0)  0.00000000e+00
  a( 2: 0: 1)  0.10093966e+02   s( 2: 0: 1)  0.14840727e+00
  a( 2: 1: 0)  0.83343516e+05   s( 2: 1: 0)  0.13483986e+03
  a( 2: 1: 1)  0.36901421e+04   s( 2: 1: 1)  0.51289957e-04

  a( 3: 0: 0)  0.00000000e+00   s( 3: 0: 0)  0.00000000e+00
  a( 3: 0: 1) -0.68396693e+00   s( 3: 0: 1)  0.87285251e-03
  a( 3: 1: 0) -0.22327586e+05   s( 3: 1: 0)  0.31858860e+02
  a( 3: 1: 1) -0.31311501e+04   s( 3: 1: 1)  0.15237379e-03

* MSE estimate :  0.34117058e-01

* Coefficients for links to node  1

  a( 1: 0: 1) -0.43298974e+01   std( 1: 0: 1)  0.15698470e+01
  a( 1: 1: 0)  0.78679336e+05   std( 1: 1: 0)  0.46140118e+03

  a( 2: 0: 1)  0.10093966e+02   std( 2: 0: 1)  0.68127739e+00
  a( 2: 1: 0)  0.83343516e+05   std( 2: 1: 0)  0.34370822e+03

  a( 3: 1: 0) -0.22327586e+05   std( 3: 1: 0)  0.13755908e+03

* MSE estimate :  0.35119697e-01

* Linear/Nonlinear link classification

  ( Node1  ) to ( Ground )

  Linear stiffness
  Linear damping

  ( Node1  ) to ( Node2  )

  Linear stiffness
  Linear damping

  ( Node1  ) to ( Node3  )

  Linear stiffness
  No direct damping term
```

Table 9.1. Estimated coefficients for a (1,1) polynomial model for the first equation of motion of the three degree-of-freedom linear system

```
 * Coefficients for system : 3dbm

 * Degree of freedom :  2

 * Mass normalised to :  1


 * Coefficients for links to node  2

   a( 1: 0: 0) -0.48828125e-02   s( 1: 0: 0)  0.00000000e+00
   a( 1: 0: 1) -0.17816147e+01   s( 1: 0: 1)  0.55020377e-02
   a( 1: 1: 0)  0.91058961e+05   s( 1: 1: 0)  0.19153053e+03
   a( 1: 1: 1)  0.10045221e+05   s( 1: 1: 1)  0.45231299e-03

   a( 2: 0: 0)  0.00000000e+00   s( 2: 0: 0)  0.00000000e+00
   a( 2: 0: 1)  0.81481304e+01   s( 2: 0: 1)  0.75985685e-01
   a( 2: 1: 0) -0.35547785e+05   s( 2: 1: 0)  0.52211178e+02
   a( 2: 1: 1) -0.95321309e+04   s( 2: 1: 1)  0.49578532e-03

   a( 3: 0: 0)  0.00000000e+00   s( 3: 0: 0)  0.00000000e+00
   a( 3: 0: 1)  0.31853068e+01   s( 3: 0: 1)  0.28017942e-01
   a( 3: 1: 0)  0.33384648e+05   s( 3: 1: 0)  0.54613537e+02
   a( 3: 1: 1)  0.34854004e+04   s( 3: 1: 1)  0.17973383e-03


 * MSE estimate :  0.47315024e-01
```

```
 * Linear/Nonlinear link classification

   ( Node2  ) to ( Node1  )

   Linear stiffness
   No direct damping term


   ( Node2  ) to ( Ground )

   Linear stiffness
   No direct damping term


   ( Node2  ) to ( Node3  )

   Linear stiffness
   No direct damping term
```

```
 * Coefficients for system : 3dbm

 * Degree of freedom :  2

 * Mass normalised to :  1


 * Coefficients for links to node  2

   a( 1: 1: 0)  0.91058961e+05   std( 1: 1: 0)  0.63332727e+03

   a( 2: 1: 0) -0.35547785e+05   std( 2: 1: 0)  0.47290417e+03

   a( 3: 1: 0)  0.33384648e+05   std( 3: 1: 0)  0.23399791e+03


 * MSE estimate :  0.17600454e+00
```

Table 9.2. Estimated coefficients for a (1,1) polynomial model for the second equation of motion of the three degree-of-freedom linear system

```
* Coefficients for system : 3dbm

* Degree of freedom :  3

* Mass normalised to :  1


* Coefficients for links to node  3

  a( 1: 0: 0)  0.19531250e-02   s( 1: 0: 0)  0.00000000e+00
  a( 1: 0: 1)  0.68381968e+01   s( 1: 0: 1)  0.17612873e+00
  a( 1: 1: 0) -0.38501766e+05   s( 1: 1: 0)  0.19125078e+03
  a( 1: 1: 1) -0.27414263e+04   s( 1: 1: 1)  0.23589864e-03

  a( 2: 0: 0)  0.00000000e+00   s( 2: 0: 0)  0.00000000e+00
  a( 2: 0: 1)  0.59192163e+00   s( 2: 0: 1)  0.16419583e-02
  a( 2: 1: 0)  0.46261414e+05   s( 2: 1: 0)  0.17796895e+03
  a( 2: 1: 1)  0.13839548e+04   s( 2: 1: 1)  0.48091511e-04

  a( 3: 0: 0)  0.00000000e+00   s( 3: 0: 0)  0.00000000e+00
  a( 3: 0: 1) -0.71340771e+01   s( 3: 0: 1)  0.13175473e+00
  a( 3: 1: 0)  0.30049697e+05   s( 3: 1: 0)  0.11621576e+03
  a( 3: 1: 1) -0.33735208e+04   s( 3: 1: 1)  0.22124090e-03

* MSE estimate :  0.64142011e-01
```

```
* Linear/Nonlinear link classification

  ( Node3  ) to ( Node1  )

    Linear stiffness
    Linear damping


  ( Node3  ) to ( Node2  )

    Linear stiffness
    No direct damping term


  ( Node3  ) to ( Ground )

    Linear stiffness
    Linear damping
```

```
* Coefficients for system : 3dbm

* Degree of freedom :  3

* Mass normalised to :  1


* Coefficients for links to node  3

  a( 1: 0: 1)  0.68381968e+01   std( 1: 0: 1)  0.71514571e+00
  a( 1: 1: 0) -0.38501766e+05   std( 1: 1: 0)  0.23937126e+03

  a( 2: 1: 0)  0.46261414e+05   std( 2: 1: 0)  0.15271228e+03

  a( 3: 0: 1) -0.71340771e+01   std( 3: 0: 1)  0.96666116e+00
  a( 3: 1: 0)  0.30049697e+05   std( 3: 1: 0)  0.17690149e+03

* MSE estimate :  0.66241875e-01
```

Table 9.3. Estimated coefficients for a (1,1) polynomial model for the third equation of motion of the three degree-of-freedom linear system

```
 * Coefficients for system : 3dbm

 * Degree of freedom :  2

 * Mass normalised to :  1

 * Coefficients for links to node  2

   a( 1: 0: 0)  0.69531250e+00   s( 1: 0: 0)  0.00000000e+00
   a( 1: 0: 1) -0.16771366e+02   s( 1: 0: 1)  0.67426652e+00
   a( 1: 0: 2) -0.18631772e+01   s( 1: 0: 2)  0.16172027e-03
   a( 1: 0: 3)  0.22869301e+03   s( 1: 0: 3)  0.16702117e+00
   a( 1: 1: 0)  0.84452586e+05   s( 1: 1: 0)  0.10857234e+03
   a( 1: 1: 1) -0.17575605e+05   s( 1: 1: 1)  0.47063664e-01
   a( 1: 1: 2)  0.75378062e+04   s( 1: 1: 2)  0.23311246e-03
   a( 1: 1: 3)  0.64347525e+06   s( 1: 1: 3)  0.65859981e-01

   a( 2: 0: 0)  0.00000000e+00   s( 2: 0: 0)  0.00000000e+00
   a( 2: 0: 1)  0.15427815e+03   s( 2: 0: 1)  0.17893520e+02
   a( 2: 0: 2) -0.18304352e+03   s( 2: 0: 2)  0.13098469e+00
   a( 2: 0: 3)  0.56297539e+04   s( 2: 0: 3)  0.26246119e+01
   a( 2: 1: 0) -0.29348428e+05   s( 2: 1: 0)  0.90539846e+01
   a( 2: 1: 1) -0.15652909e+05   s( 2: 1: 1)  0.70437146e-02
   a( 2: 1: 2)  0.25861909e+06   s( 2: 1: 2)  0.14041881e-01
   a( 2: 1: 3) -0.18025930e+06   s( 2: 1: 3)  0.77158795e-04

   a( 3: 0: 0)  0.00000000e+00   s( 3: 0: 0)  0.00000000e+00
   a( 3: 0: 1) -0.15205666e+01   s( 3: 0: 1)  0.56255874e-02
   a( 3: 0: 2) -0.19376213e+02   s( 3: 0: 2)  0.15325763e-01
   a( 3: 0: 3) -0.75451012e+02   s( 3: 0: 3)  0.17021768e-01
   a( 3: 1: 0)  0.30748771e+05   s( 3: 1: 0)  0.34462215e+02
   a( 3: 1: 1)  0.29437480e+04   s( 3: 1: 1)  0.29448934e-02
   a( 3: 1: 2)  0.38126682e+03   s( 3: 1: 2)  0.12598650e-05
   a( 3: 1: 3) -0.89329586e+05   s( 3: 1: 3)  0.28751923e-02

 * MSE estimate :  0.73786420e+00

 * Linear/Nonlinear link classification

   ( Node2  ) to ( Node1  )

   Linear stiffness
   Nonlinear damping : order  3

   ( Node2  ) to ( Ground )

   Linear stiffness
   Nonlinear damping : order  3

   ( Node2  ) to ( Node3  )

   Linear stiffness
   No direct damping term

 * Coefficients for system : 3dbm

 * Degree of freedom :  2

 * Mass normalised to :  1

 * Coefficients for links to node  2

   a( 1: 0: 1) -0.16771366e+02   std( 1: 0: 1)  0.11308486e+02
   a( 1: 0: 3)  0.22869301e+03   std( 1: 0: 3)  0.24621257e+03
   a( 1: 1: 0)  0.84452586e+05   std( 1: 1: 0)  0.34717124e+04

   a( 2: 0: 1)  0.15427815e+03   std( 2: 0: 1)  0.34635288e+02
   a( 2: 0: 2) -0.18304352e+03   std( 2: 0: 2)  0.25703009e+03
   a( 2: 0: 3)  0.56297539e+04   std( 2: 0: 3)  0.24906714e+04
   a( 2: 1: 0) -0.29348428e+05   std( 2: 1: 0)  0.43054966e+04

   a( 3: 1: 0)  0.30748771e+05   std( 3: 1: 0)  0.19817064e+04

 * MSE estimate :  0.90152758e+00
```

Table 9.4. Estimated coefficients for a (1,3) polynomial model for the second equation of motion of the three degree-of-freedon nonlinear system

CHAPTER 10

IDENTIFICATION OF TIME-DEPENDENT PARAMETERS

One of the first assumptions which was made in order that parameter estimation techniques could be applied was that the parameters have no explicit time-dependence, i.e. the restoring forces vary in time only because y(t) and $\dot{y}(t)$ vary. The purpose of this chapter is to indicate that it is possible to obtain useful information about the system even if this assumption is relaxed. The initial impetus for this work was provided by the arrival of some experimental data from the Los Alamos National Laboratories, New Mexico, U.S.A. The analysis of the data carried out by the Los Alamos group seemed to indicate that the stiffness of the structure had changed during the course of the experiment. Recorded here is an attempt to refine that analysis.

10.1. The Experimental Data - Analysis in Batches.

The data was provided on a cartridge tape. The experiment concerns the excitation of a scaled structure mounted on a slide table using a recorded earthquake excitation. The structure under test is depicted in Figure 10.0 (taken from (67)). Two channels of data were provided, the base acceleration $\ddot{y}_b$ and the response acceleration $\ddot{y}_m$. The data are shown in Figure 10.1. 4000 points were provided in each channel; however, only the points 1-2500 were considered for this work as the input signal appeared to be negligible outside this range. The sampling interval was 0.001 seconds. The data has also been high-pass filtered with cut-off 18 Hz.

The Los Alamos group integrated the relative acceleration $\ddot{\delta} = \ddot{y}_m - \ddot{y}_b$ to form the relative velocity $\dot{\delta}$ and the relative displacement δ. They then assumed a linear equation of motion for the system of the form

$$(k/m)\delta + (c/m)\dot{\delta} = -\ddot{y}_m \qquad (1)$$

and used a least-squares estimator to obtain parameter estimates for k' = k/m and c' = c/m. An overall fit using all data points 200-1800 gave values of c' = 49.12 and k' = 161280. They then divided the data into three disjoint sets and estimated parameters for each set, the results were

Points	k'	c'
100 - 600	170 460.	53.26
700 - 1000	150 560.	47.19
1000 - 1500	154 910.	41.71

The stiffness for the first batch is higher than that for the second, while the second and third batches agree quite well. The Los Alamos group concluded from this that the structural stiffness had changed somewhere in the first batch, possibly through failure of the structure. Using the model parameters to predict the data in each batch they then compared it with the measured data, and obtained reasonable agreement. This gives some confidence in the estimated parameters.

Initially the present study used the same approach as the Los Alamos group. The relative acceleration was integrated twice using the trapezium rule to obtain the relative velocity and displacement. Unfortunately, the integrations introduced spurious low-frequency trends into the relative displacement data as described in Chapter 6. These proved to be impossible to remove by subtracting low-order polynomial trends. Because the data had already been high-pass filtered with a cut-off at 18 Hz, the trends were removed by re-filtering all the data with the same cut-off. This also had the effect of fixing the initial conditions. The integrated data is shown in Figure 10.2. At the same time, the correlation test of Billings (68) was applied in order to test for nonlinearity. The results shown in Figure 10.3 indicate that the cross-correlation function is well within the 95% confidence interval for a null result. This indicates that the system is either linear or has a purely odd nonlinearity.

Because one cannot tell what the effect of a filter transient will be, the first analysis discarded the first 500 points of data. The sample points were renumbered so that point j in the following discussion corresponds to point j+500 in the original data. The original sample numbers will be given in brackets where appropriate. Points 0 - 1800 (500–2300) were divided into batches of 200 points and parameters were estimated for a model of the form (1). The standard recursive least–squares estimator described in Chapter 4 was used. The results were:

Points	k'	± error
0 - 200	159 116	56 195
200 - 400	156 993	32 783
400 - 600	163 279	45 540
600 - 800	162 096	34 513
800 - 1000	159 723	35 161
1000 - 1200	185 572	5 777
1200 - 1400	194 912	3 976
1400 - 1600	188 371	3 685
1600 - 1800	188 319	1 443

Points	c'	± error
0 - 200	55.83	112.6
200 - 400	46.03	62.23
400 - 600	48.44	85.75
600 - 800	39.98	64.95
800 - 1000	41.62	65.88
1000 - 1200	25.29	10.45
1200 - 1400	17.60	7.21
1400 - 1600	22.19	6.62
1600 - 1800	20.67	2.58

In order to check the accuracy of the estimations, the acceleration response was calculated using the model parameters for each batch and then a comparison was

made with the true data for each batch. The results are shown in Figures 10.4 to 10.12. In all cases one can see that the agreement is excellent. The MSE values for the batches were:

Points	MSE
0 - 200	0.63
200 - 400	0.43
400 - 600	1.12
600 - 800	0.51
800 - 1000	0.51
1000 - 1200	0.46
1200 - 1400	0.54
1400 - 1600	0.33
1600 - 1800	0.17

The small values of the MSE values indicate that the parameter estimates are good. This in turn indicates the the recursive least–squares algorithm used is converging to an acceptable result in 200 points or less.

The stiffness values and their 95% confidence intervals are plotted in Figure 10.13. These results appear to indicate that there is a change in stiffness from about 160 000 to about 190 000 at sample point 1000 (1500). This change in stiffness corresponds to a change in the amplitude of the signals, they are reduced by a factor of 10. No information is given about this sudden change in excitation level. The change in stiffness may or may not be significant. The damping coefficient appears to change also; it decreases steadily over the time interval considered. Having said this, one should be careful of making statements about the damping given that the error bounds on the damping coefficient are very large.

This study indicates that the change in stiffness which the Los Alamos group identified must occur between points 0 and 500 of the original data as it is not indicated above. The data was integrated once more, except this time only 100 points were

discarded in order to eliminate the filter transient. In the following discussion sample point j corresponds to sample point j+100 in the original data. A least–squares fit to points 1 to 500 (100–600) gave values k' = 177 880 and c' = 52.29 which agrees well with the results obtained from Los Alamos. Dividing the first 400 points into two batches of 200 points gave the results

Points	k'	± error
0 - 200	213 074	121 194
200 - 400	175 219	100 382

Points	c'	± error
0 - 200	47.59	236.03
200 - 400	50.52	186.14

The stiffnesses for the first 400 points are therefore considerably higher than those observed in the data following. The comparisons of predicted with measured data for each batch are shown in Figures 10.14 and 10.15. The MSE values being 1.53 and 0.63 for the first and second sets respectively. The good agreement indicates that the filter transient probably didn't cause too many problems. If one makes that assumption, the results obtained above are very consistent with those of the Los Alamos group. There appears to have been a marked decrease in stiffness over the first 0.4 seconds of data. There is also an increase in stiffness at about 1.5 seconds. The damping appears to decrease steadily over the interval considered. The stiffess is plotted against time in Figure 10.16, in this case the error bars are omitted.

10.2. Recursive Estimation with Forgetting Factors.

The analysis of the previous section depended on the rather arbitrary division of the data into batches. This section introduces a method which allows one to examine the

variation in the parameters from point to point.

Because the recursive least–squares (RLS) procedure is iterative, one would expect that one could display the parameters at each sampling instant and thus show the variation with time. However, the RLS estimator is completely equivalent to the normal equations, which are an off–line estimator. They produce the same results on a given set of data. This means that the parameters obtained are averaged over all the points considered. The reason for this is that the recursion above effectively remembers *all* past data so it tries to generate parameters which describe the data at long past instants as well as the data at present. In order to show the variation of a parameter with time one needs some way of making the algorithm forget past data values. One limits the least–squares criterion to points in the recent past. This is achieved by taking the squared error J at instant i+1 to be

$$J_{i+1} = \lambda J_i + ((\ddot{y}_m)_{i+1} - \{x\}_{i+1}^T \{\beta\}_i)^2$$

One can see that if the 'forgetting factor' λ is less than one, the effect of past data is exponentially weighted out. The effect of this modification on the normal RLS recursion relations is simple. One begins as before and iterates as follows **(42),(50)**

$$\{\beta\}_{i+1} = \{\beta\}_i + \{K\}_{i+1} . ((\ddot{y}_m)_{i+1} - \{x\}_{i+1}^T . \{\beta\}_i)$$

$$[P]_{i+1} = (1/\lambda)([1] - \{K\}_{i+1}\{x\}_{i+1}^T) . [P]_i$$

$$\{K\}_{i+1} = \frac{[P]_i \{x\}_{i+1}}{\lambda + \{x\}_{i+1}^T [P]_i \{x\}_{i+1}}$$

A possible problem with this modification is that convergence of the algorithm is only *guaranteed* mathematically if λ is 1.0. However, if one uses a λ in the range 0.9 to 0.99 one can obtain information about the time–dependence of the parameters if the procedure converges. The effect of using the modified algorithm is shown in the following examples

(1) The following SDOF system was simulated using a fourth order Runge–Kutta procedure to integrate the equations of motion.

$$\ddot{y} + 40\dot{y} + k(t)y = x(t)$$

The stiffness k(t) is 10000.0 for $t < 6$ and 5000.0 for $t > 6$. The excitation used was a zero–mean Gaussian noise sequence of variance 10.0 band–limited into the range 0–200 Hz. A time–step of 0.001 seconds was used corresponding to a sampling frequency of 1 kHz. 4000 points of data from $t = 4$ to $t = 8$ were saved.

A parametric model of the form

$$m\ddot{y} + c\dot{y} + ky = x(t)$$

was fitted. As the equation is non–homogeneous and the input has been measured one can obtain the absolute values of c and k. All 4000 points of data were processed each time. First, $\lambda = 1$ gave the results shown in Figures 10.17 and 10.18 for the stiffness and damping parameters as functions of time. The averaging effect on the stiffness parameter is clearly shown. The final values of m,c and k for this run are 0.969, 40.4 and 6660.0 respectively. The identification was then repeated with $\lambda = 0.95$. The final values in this case are 1.0000000, 40.000000 and 5000.0000, perfect. The parameters are shown as functions of time in Figures 10.19–10.21. The stiffness is shown in Figure 10.19. Figure 10.20 shows how quickly the stiffness parameter makes the transition between values. Finally, the damping is shown in Figure 10.21. There is a sharp notch in the damping graph corresponding to the stiffness transition point. Figures 10.22 to 10.25 show the results of using $\lambda = 0.97$ and $\lambda = 0.99$ on the stiffness graphs. The final parameters are almost as good. However, the transition time between stiffnesses increases with λ. In the figures above the transition should take place at sample point 2000. The results are summarised in the following table:

λ	Final Stiffness	Transition Time seconds (points)
1.00	6660.00488	2.0 (2000)
0.99	5000.00005	0.45 (450)
0.98	5000.00005	0.15 (150)
0.97	5000.00000	0.07 (70)
0.96	5000.00005	0.07 (70)
0.95	5000.00000	0.06 (60)

(2) The next example is of a SDOF system which has for it's equation of motion the forced damped Mathieu equation. This type of equation is of considerable interest in the study of randomly excited marine structures (69). The equation used was

$$\ddot{y} + 40\dot{y} + 10^4.(1 + \tfrac{1}{2}.\cos(2\pi t))y = x(t)$$

The same excitation and sampling interval was used as in the previous example. As a random excitation was used, there were none of the stability problems associated with harmonic forcing of a Mathieu oscillator. Again, 4000 points of data ($4.0 \leq t \leq 8.0$) were taken corresponding to four periods of the stiffness variation. The first parameter/time graphs were obtained using $\lambda = 1$. The results are shown in Figures 10.26 and 10.27. As before the stiffness curve tends towards an average value. The damping curve is little disturbed. The final values for m, c and k(t) are 0.9557, 40.503 and 8022.6 respectively. The correct values are 1.0, 40.0 and 15000.0. The identification was then repeated using $\lambda = 0.9$. The stiffness graph is shown in Figure 10.28; the harmonic variation is captured very well indeed. The damping graph (Figure 10.29) shows a little disturbance to the damping estimate. However, the final values for the parameters are estimated as 1.0002, 40.03 and 14988.9 showing excellent agreement with the true values. The stiffness graphs for intermediate values of λ (0.975, 0.95, 0.925) are shown in Figures 10.30–10.32. The results are summarised in the following table:

λ	Final Stiffness	Final Damping	Final Mass
1.00	8022.6333	40.503830	0.95570004
0.975	14386.319	41.470818	0.99861252
0.95	14958.351	40.109737	1.0004003
0.925	14982.580	40.049244	1.0002798
0.90	14988.971	40.037243	1.0002012

The results from these simulations indicate that the 'forgetful' recursive least-squares algorithm can be used to track the time-variation of structural parameters. The next task is to apply the method to the data provided by the Los Alamos group.

Points 100 to 2500 from the original data set were considered. To recap, the first 100 points were removed as one would expect them to be corrupted by a filter transient introduced during the integration procedure. The stiffness graph obtained with $\lambda = 1$ is shown in Figure 10.33. There is a fairly sharp drop in stiffness over the first 400 points after which the graph settles to an averaged value. The damping (Figure 10.34) rises to a maximum over the first 400 points then settles. Next the identification was repeated with $\lambda = 0.95$. In this case, the alogrithm clearly failed to converge. The procedure was repeated with $\lambda = 0.99$. In this case the results obtained are quite good. As shown in Figure 10.35, the stiffness falls over the first 400 points as before; however, now there is a small variation between points 400 and 1400 and finally a rise to a steady plateau between points 1400 and 2400. The final stiffness in this case is 182568 which agrees well with the value for the final batch obtained in section 1. The graph also agrees quite well with that obtained previously (Figure 10.16). The damping graph (Figure 10.36) shows the steady decline in damping indicated by the batch analysis. The results of using the 'forgetful' estimator are therefore consistent with the earlier analysis of the data in batches which are in turn consistent with the analysis by the Los Alamos group.

Thanks are due to Drs C.R.Farrar and E.Endebrock of the Los Alamos National Laboratories, U.S.A. for providing us with a chance to try out these methods on

some experimental data. Thanks are also due to the sponsors of the testing program, the United States Nuclear Regulatory Commission's Office of Nuclear Regulatory Research for the permission to include the results of the study in the thesis.

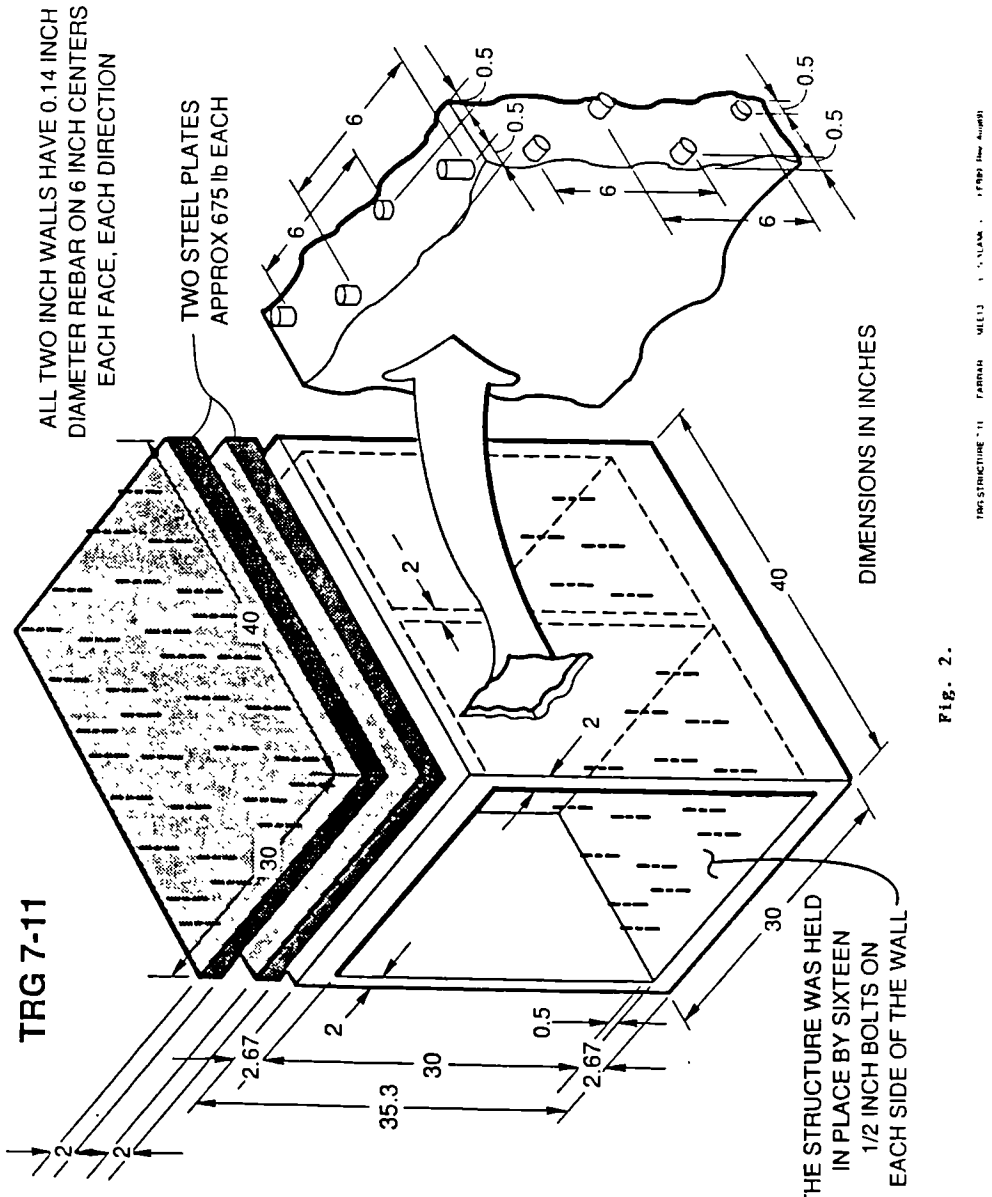

Figure 10.0. Geometry of the scaled structure under test in the Los Alamos Experiments.

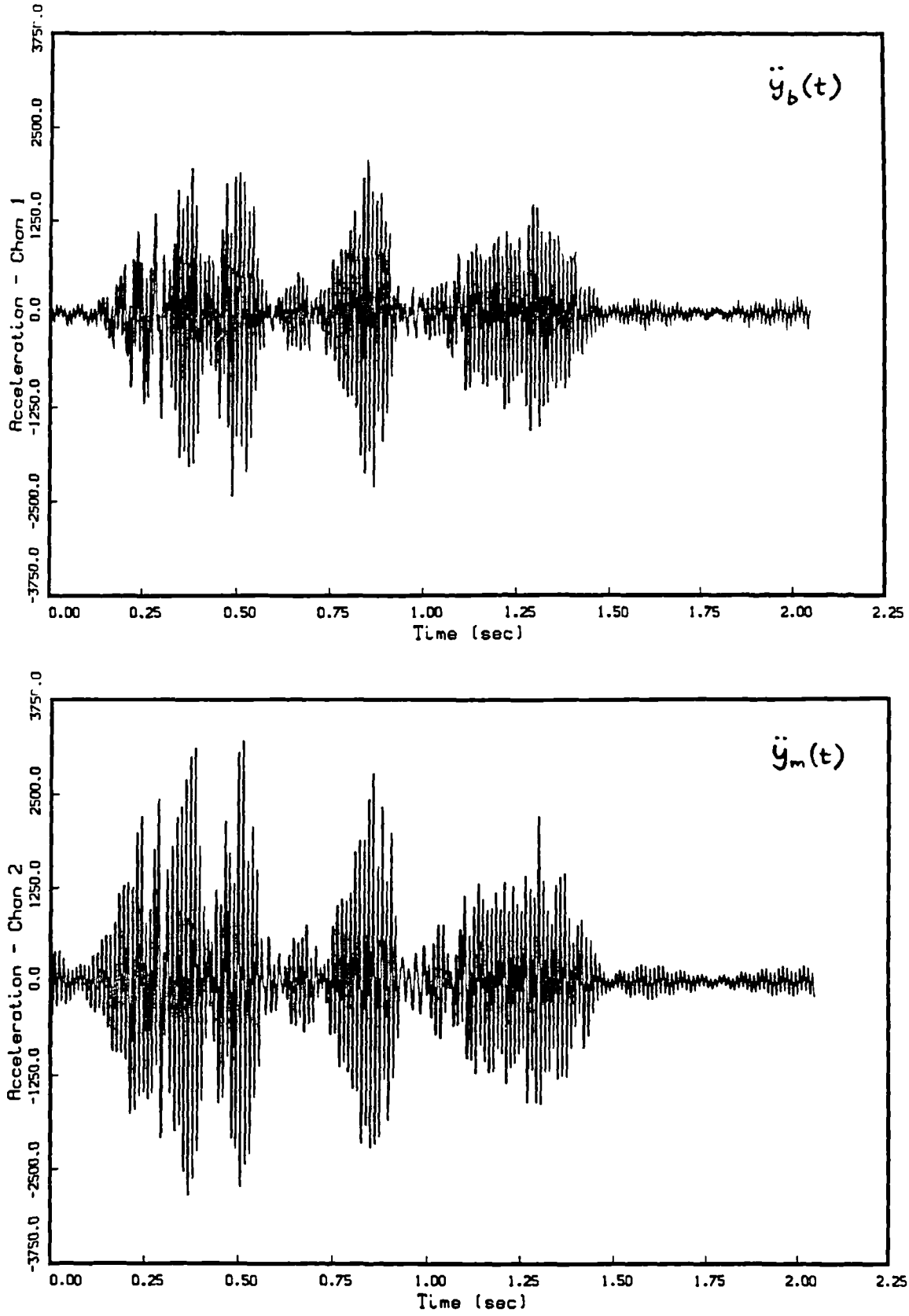

Figure 10.1 Base acceleration and response acceleration data provided by the Los Alamos group.

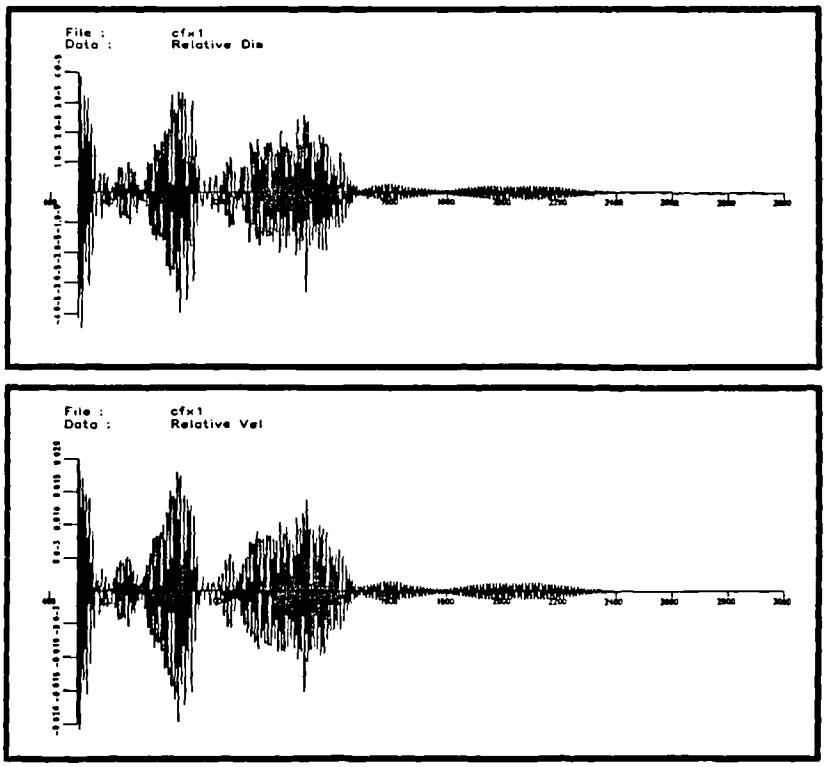

Figure 10.2 Relative displacement and velocity data obtained from trapezium rule integration and high-pass filter.

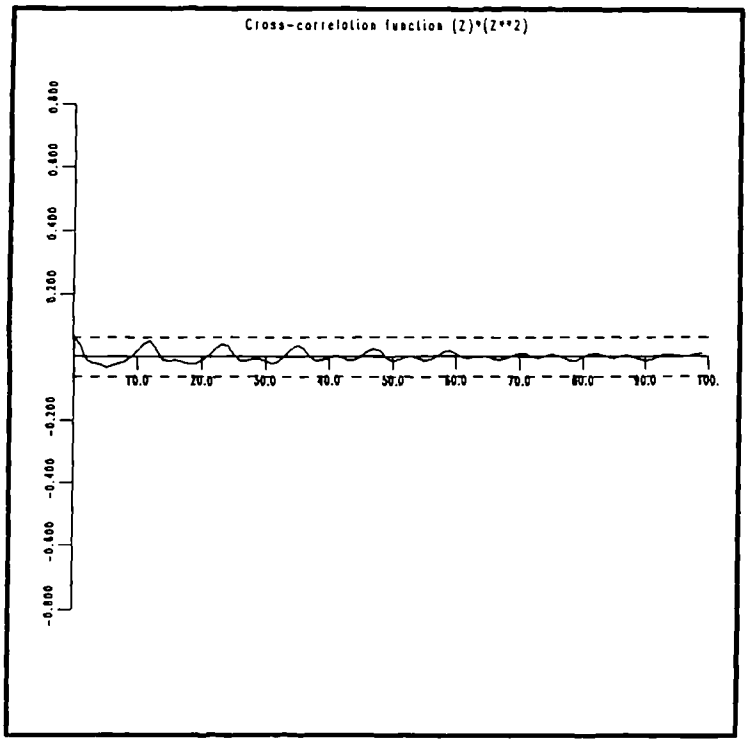

Figure 10.3 Cross-correlation function for the nonlinear structure detection test.

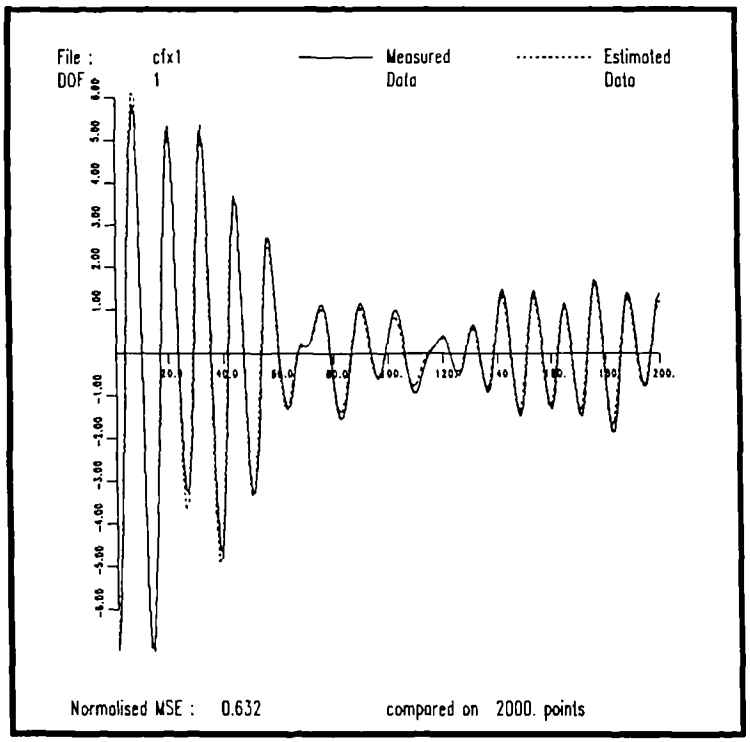

Figure 10.4 Comparison of measured data and predicted data for batch 1.

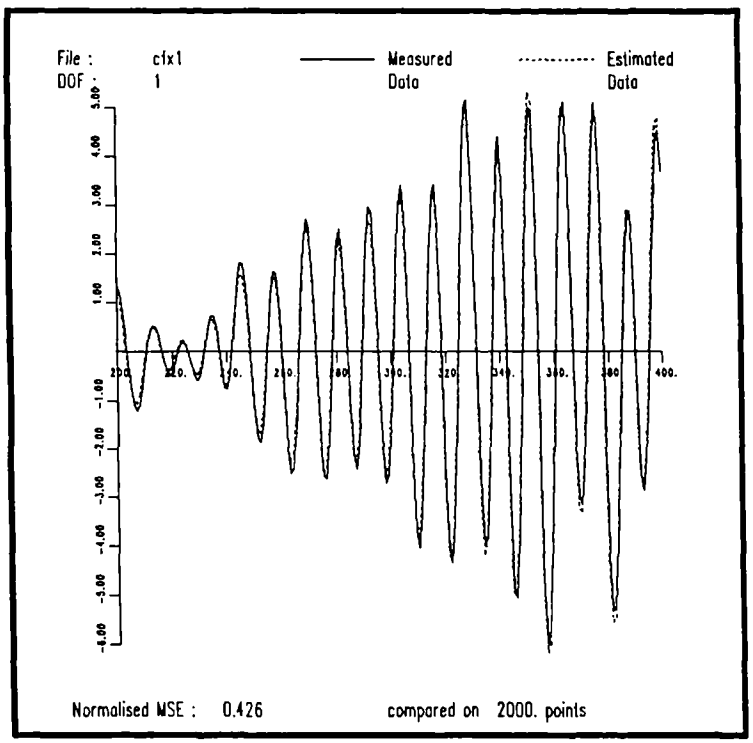

Figure 10.5 Comparison of measured data and predicted data for batch 2.

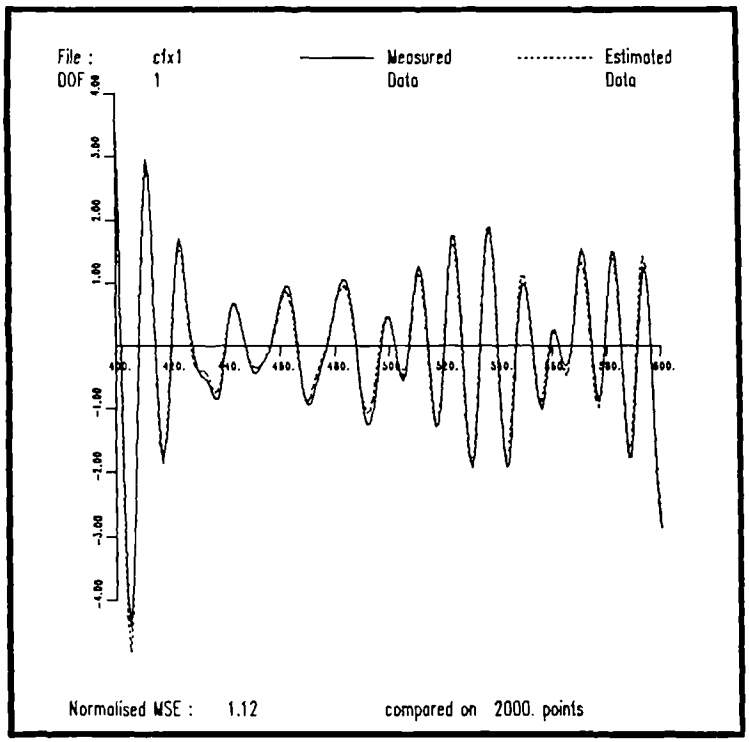

Figure 10.6 Comparison of measured data and predicted data for batch 3.

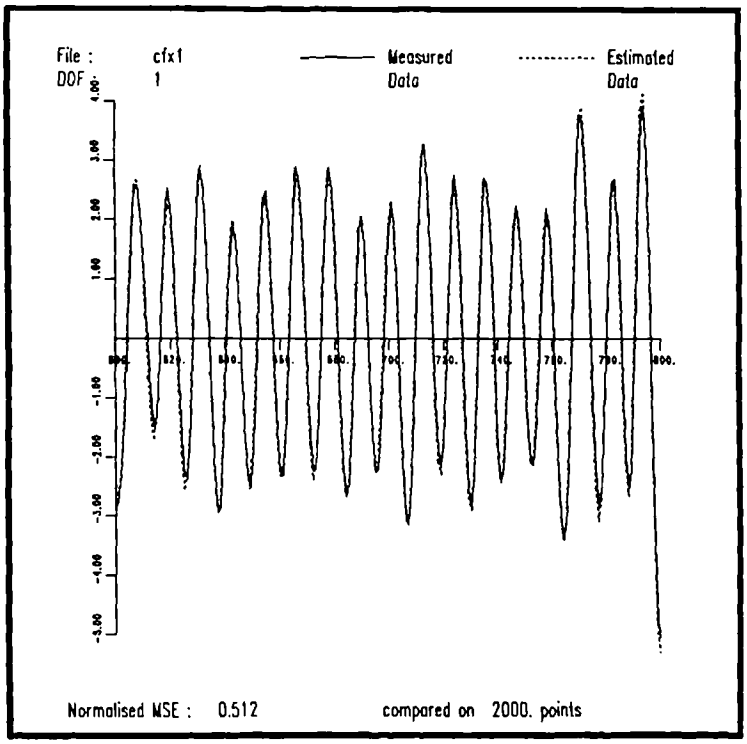

Figure 10.7 Comparison of measured data and predicted data for batch 4.

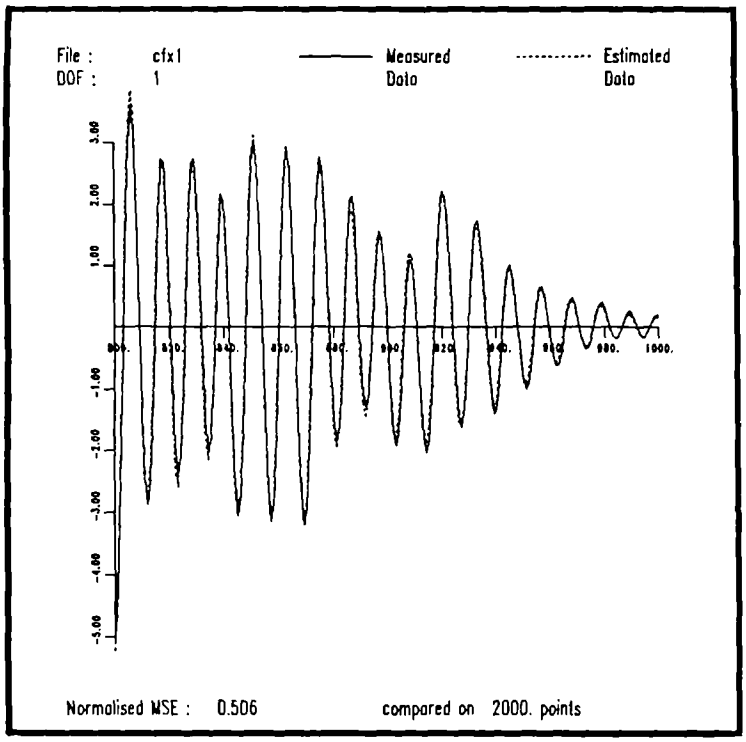

Figure 10.8 Comparison of measured data and predicted data for batch 5.

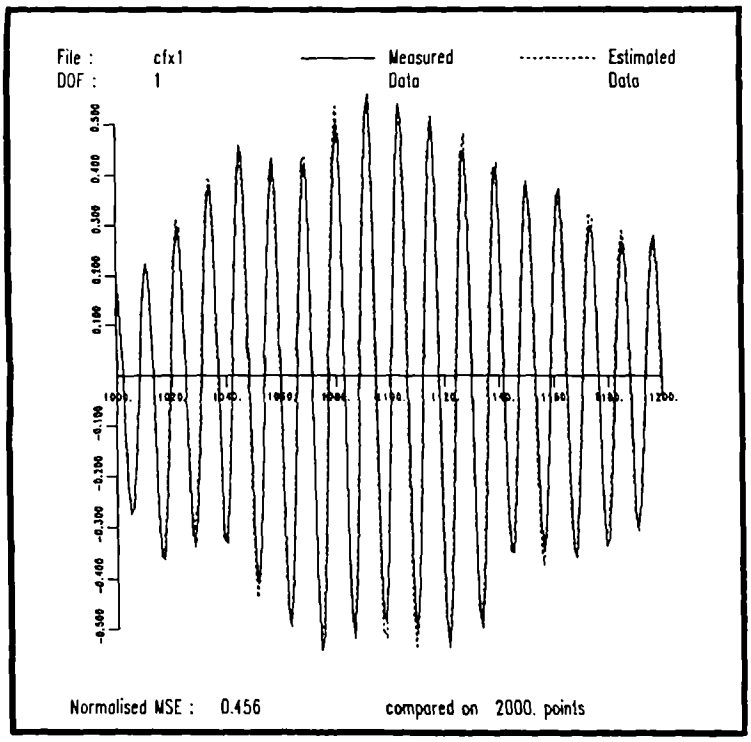

Figure 10.9 Comparison of measured data and predicted data for batch 6.

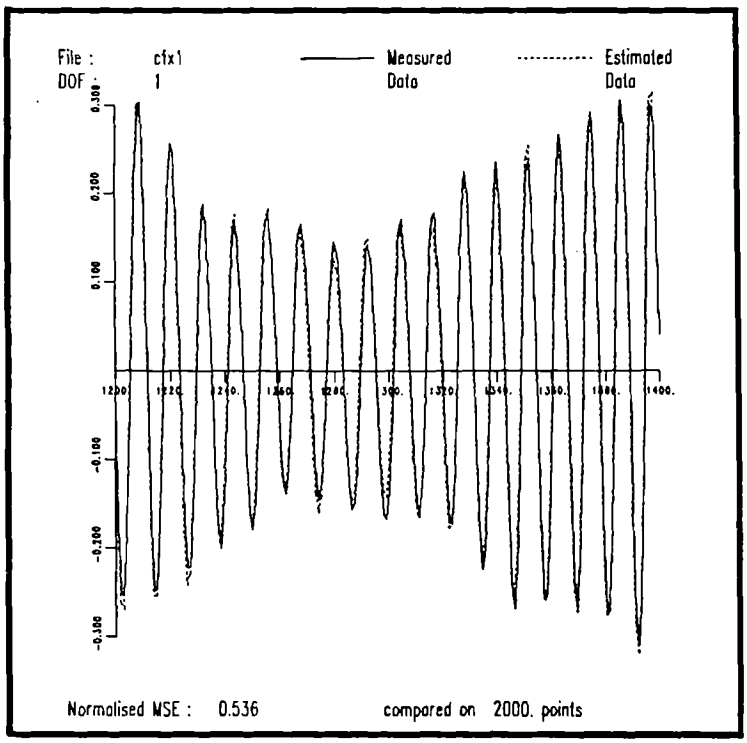

Figure 10.10 Comparison of measured data and predicted data for batch 7.

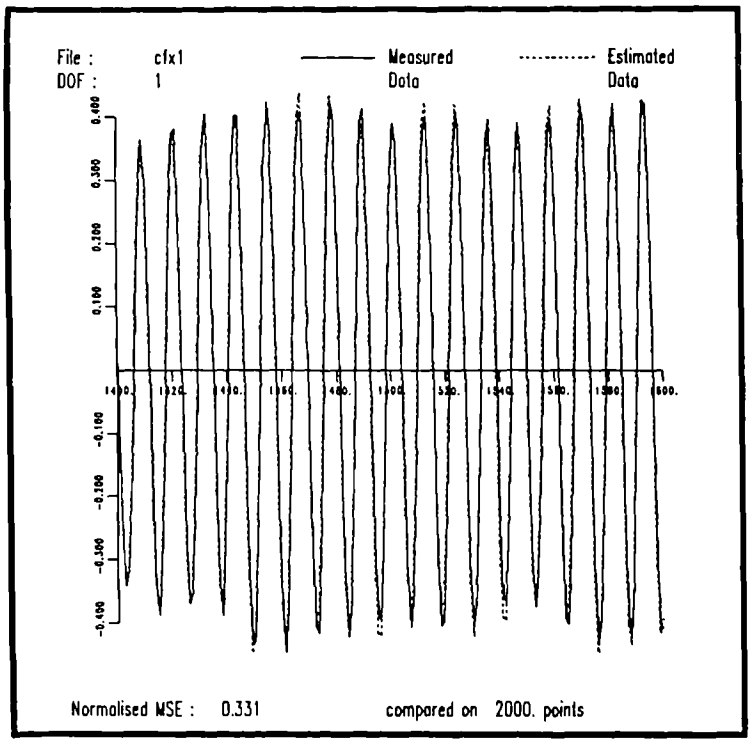

Figure 10.11 Comparison of measured data and predicted data for batch 8.

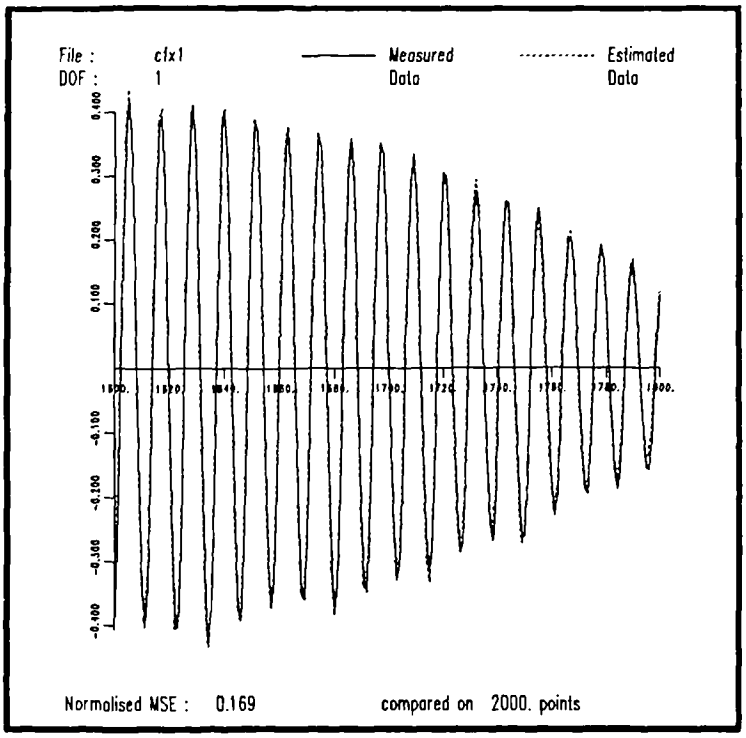

Figure 10.12 Comparison of measured data and predicted data for batch 9.

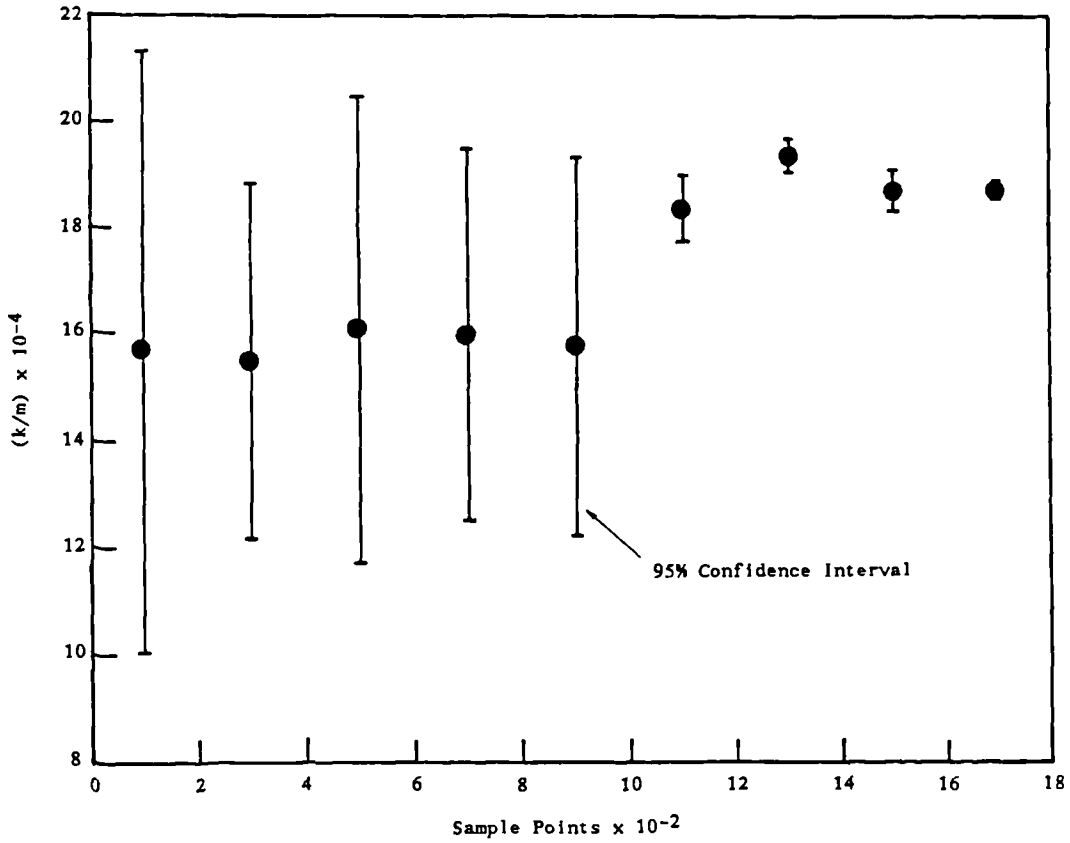

Figure 10.13 Estimated stiffnesses associated with each batch together with the 95% confidence intervals. Each stiffness is assigned to the centre point of the batch.

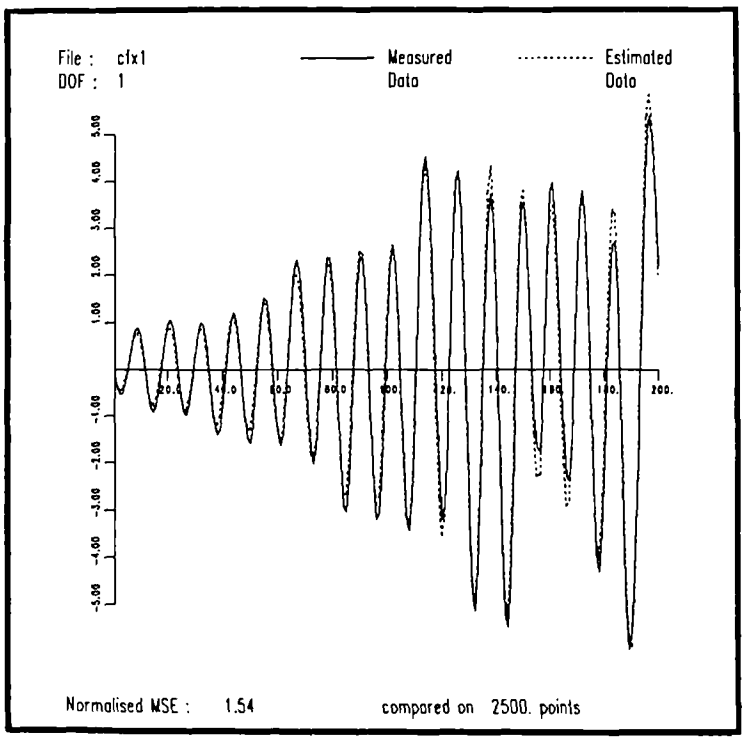

Figure 10.14 Comparison of measured data and predicted data for points 1 to 200 (100 to 300).

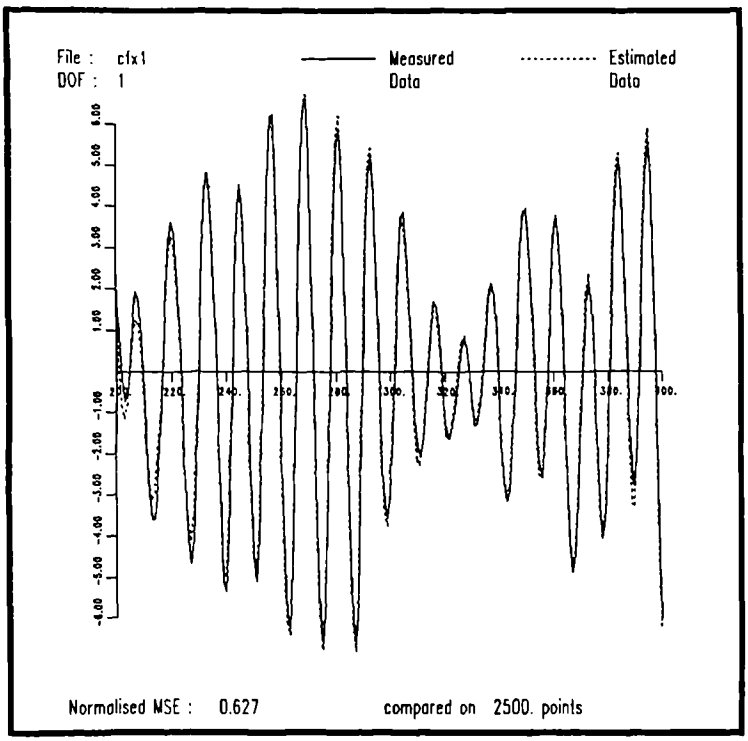

Figure 10.15 Comparison of measured data and predicted data for points 200 to 400 (300 to 500).

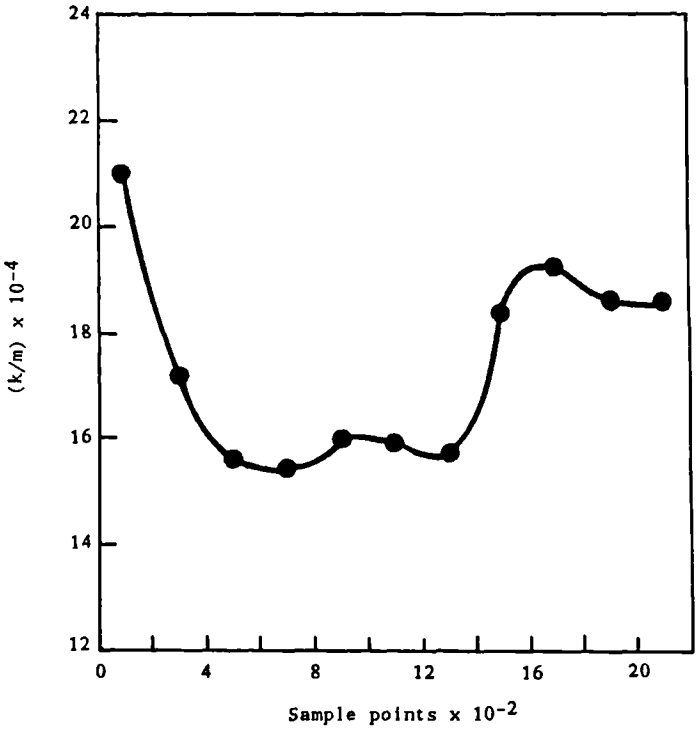

Figure 10.16. Variation in estimated stiffness over the whole data set.

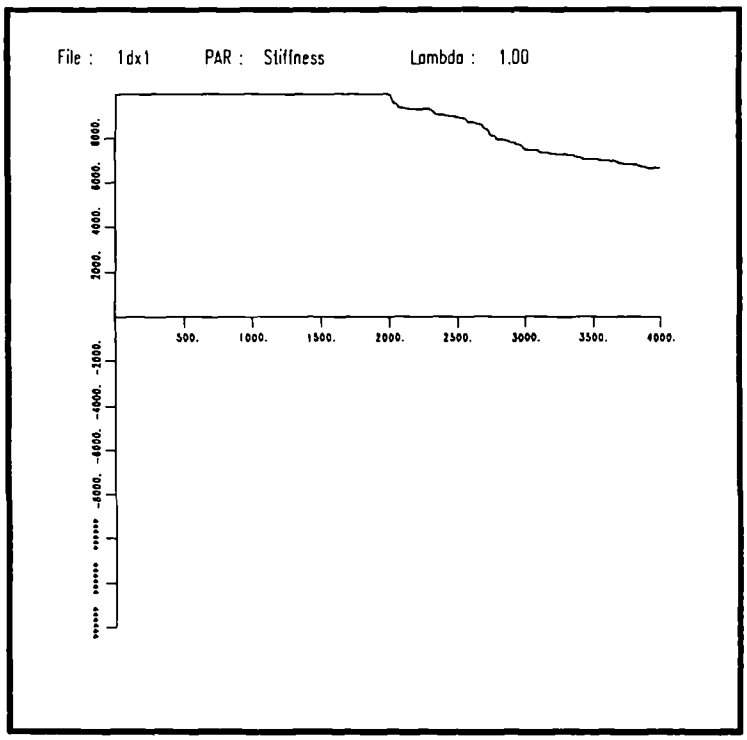

Figure 10.17 Estimated stiffness parameter for each iteration, points 1 to 4000 (t = 4 seconds to t = 8). Example (1), $\lambda = 1$.

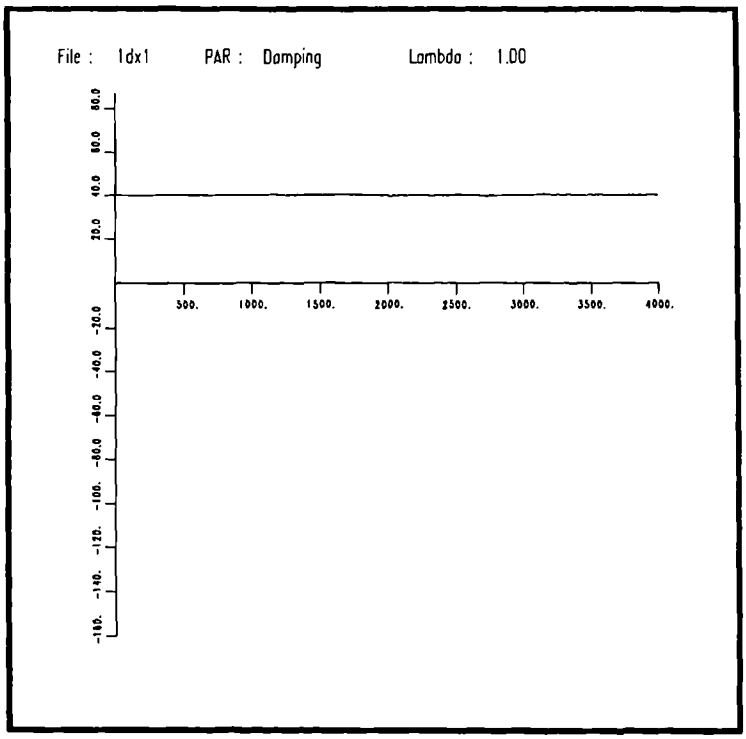

Figure 10.18 Estimated damping parameter for each iteration, points 1 to 4000 (t = 4 seconds to t = 8). Example (1), $\lambda = 1$.

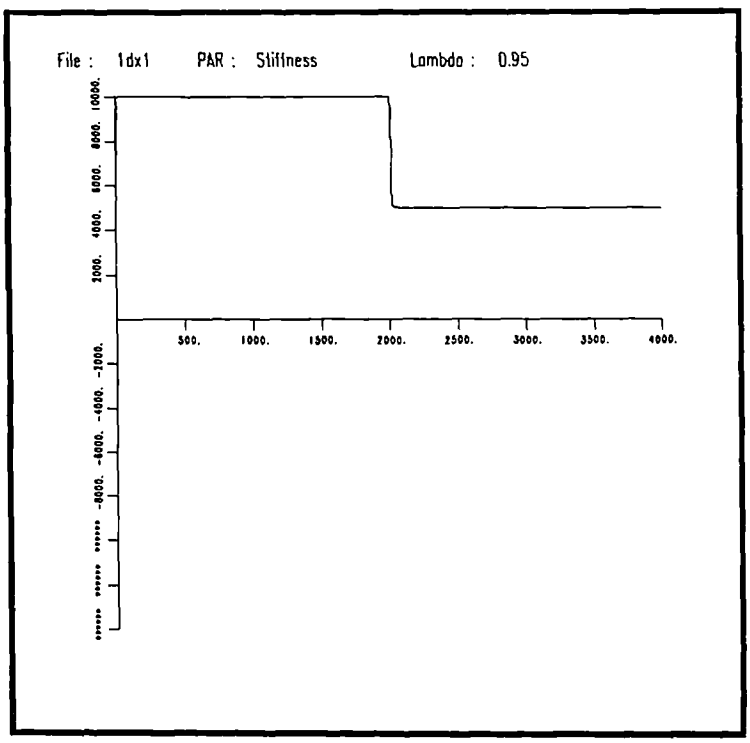

Figure 10.19 Estimated stiffness parameter for each iteration, points 1 to 4000 (t = 4 seconds to t = 8). Example (1), $\lambda = 0.95$.

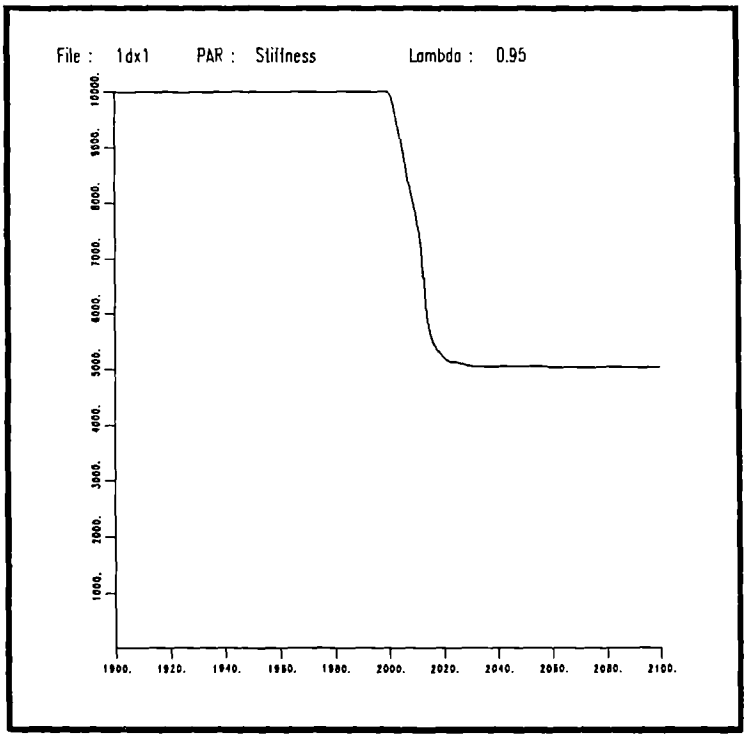

Figure 10.20 Estimated stiffness parameter for each iteration, points 1900 to 2100 (t = 5.9 seconds to t = 6.1). Example (1), $\lambda = 0.95$.

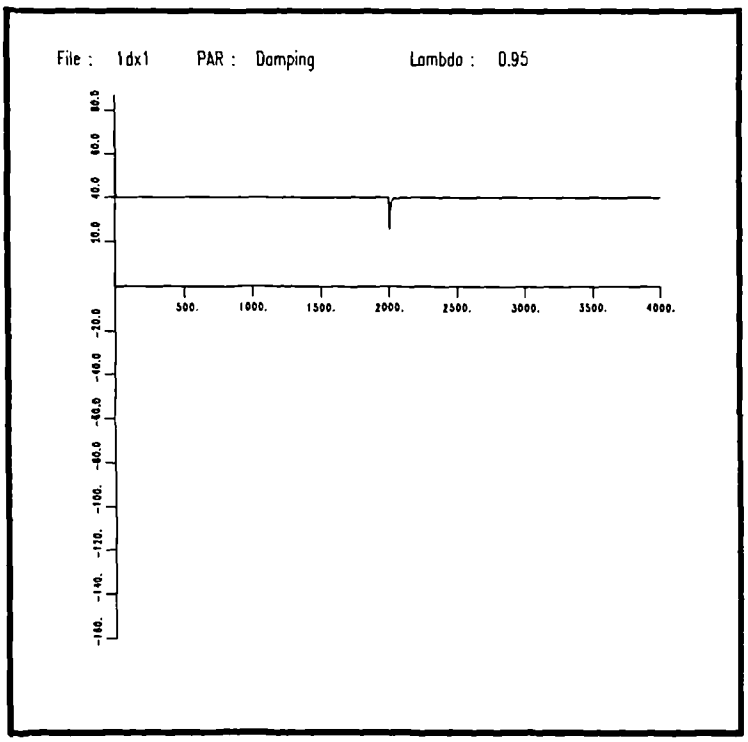

Figure 10.21 Estimated damping parameter for each iteration, points 1 to 4000 (t = 4 seconds to t = 8). Example (1), $\lambda = 0.95$.

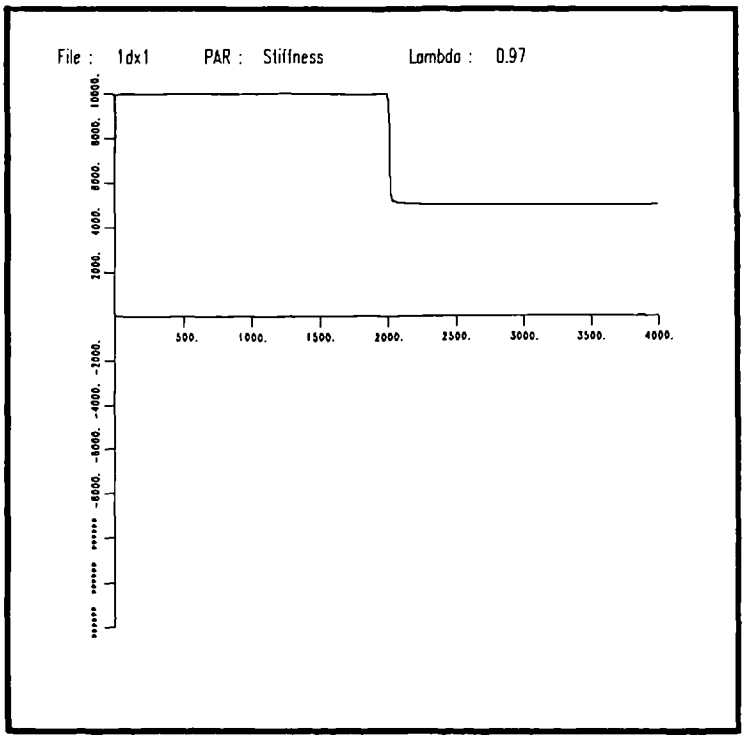

Figure 10.22 Estimated stiffness parameter for each iteration, points 1 to 4000 (t = 4 seconds to t = 8). Example (1), $\lambda = 0.97$.

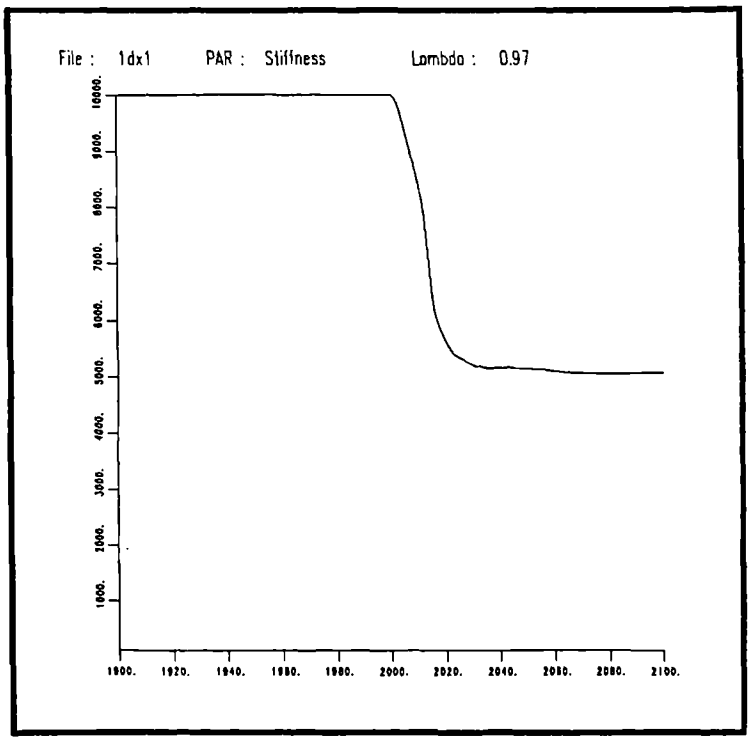

Figure 10.23 Estimated stiffness parameter for each iteration, points 1900 to 2100 (t = 5.9 seconds to t = 6.1). Example (1), $\lambda = 0.97$.

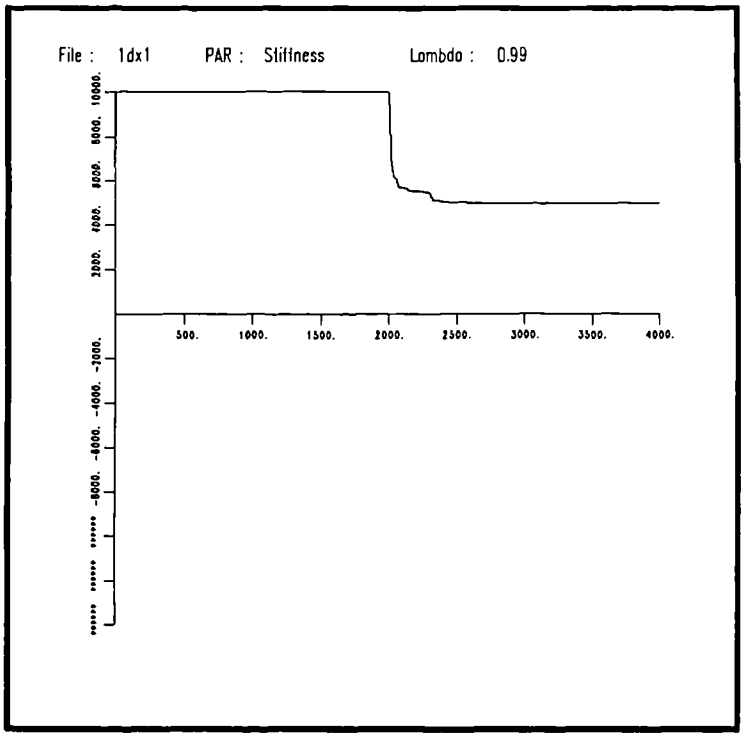

Figure 10.24 Estimated stiffness parameter for each iteration, points 1 to 4000 (t = 4 seconds to t = 8). Example (1), $\lambda = 0.99$.

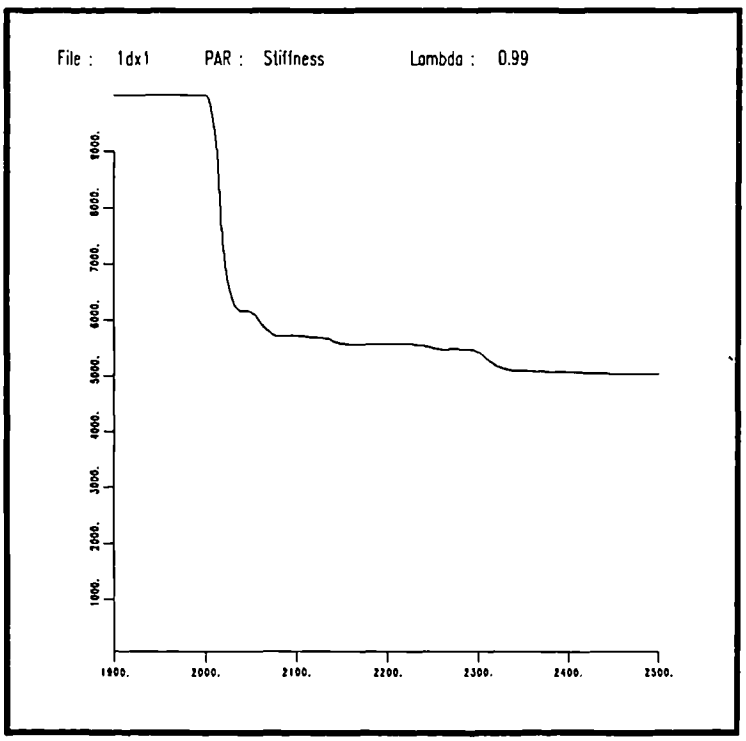

Figure 10.25 Estimated stiffness parameter for each iteration, points 1900 to 2500 (t = 5.9 seconds to t = 6.5). Example (1), $\lambda = 0.99$.

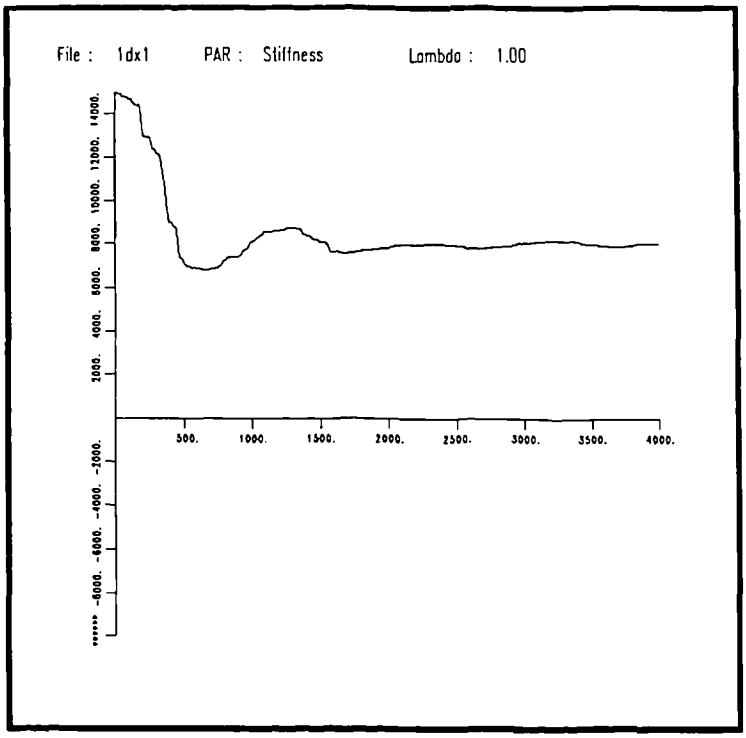

Figure 10.26 Estimated stiffness parameter for each iteration, points 1 to 4000 (t = 4 seconds to t = 8). Example (2), $\lambda = 1$.

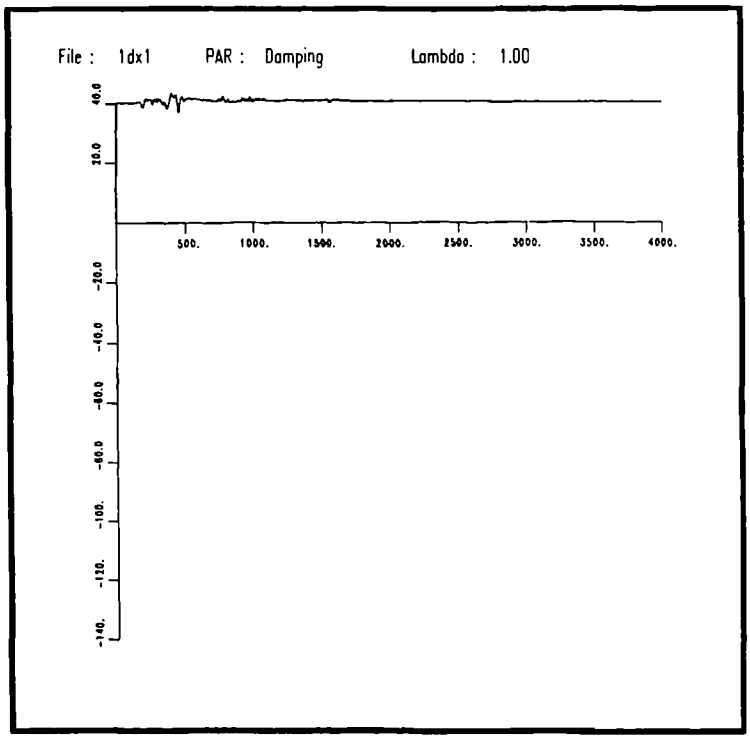

Figure 10.27 Estimated damping parameter for each iteration, points 1 to 4000 (t = 4 seconds to t = 8). Example (2), $\lambda = 1$.

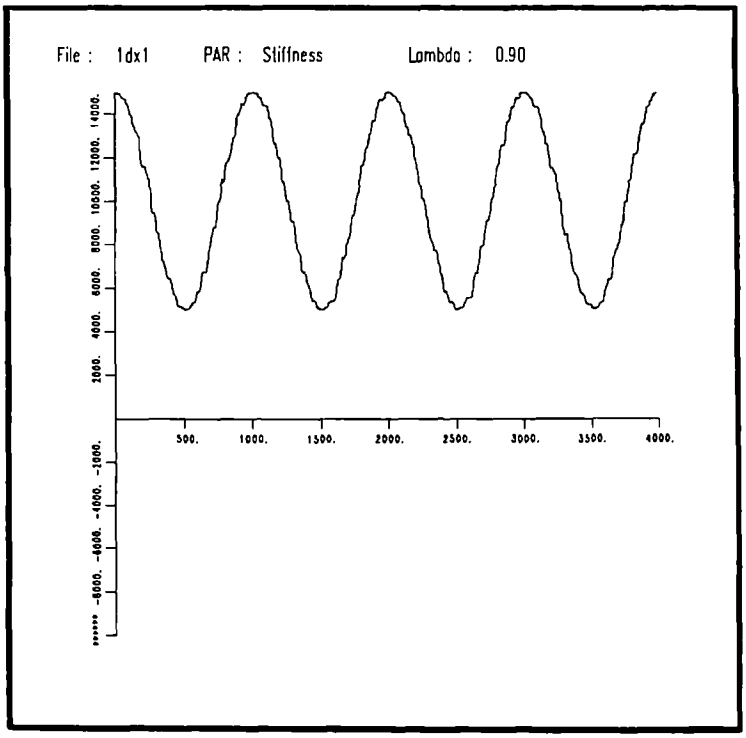

Figure 10.28 Estimated stiffness parameter for each iteration, points 1 to 4000 (t = 4 seconds to t = 8). Example (2), $\lambda = 0.90$.

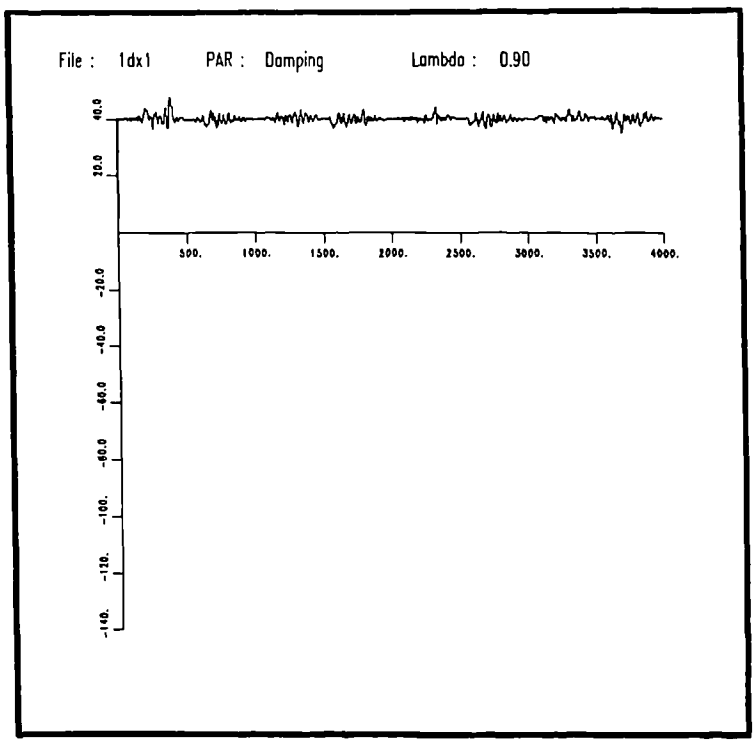

Figure 10.29 Estimated damping parameter for each iteration, points 1 to 4000 (t = 4 seconds to t = 8). Example (2), $\lambda = 0.90$.

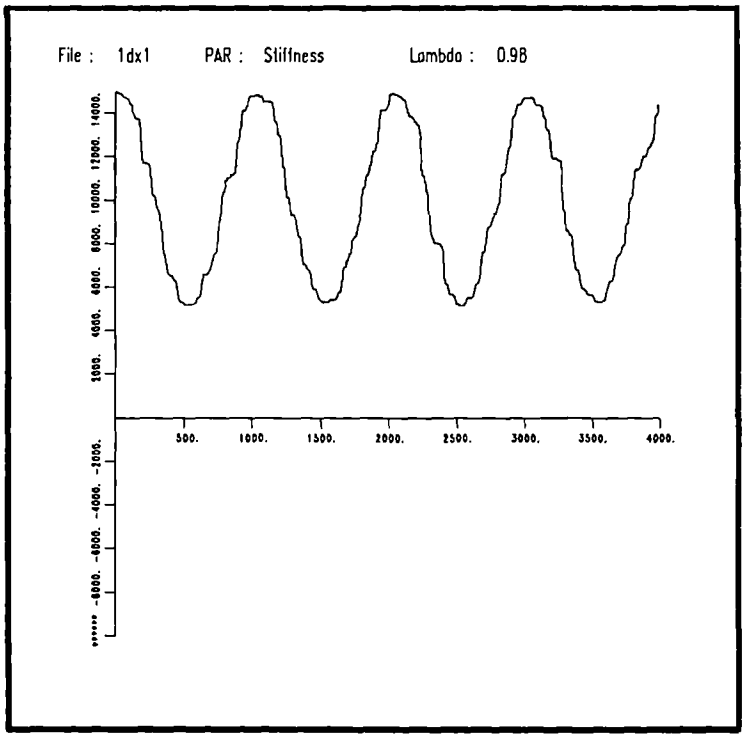

Figure 10.30 Estimated stiffness parameter for each iteration, points 1 to 4000 (t = 4 seconds to t = 8). Example (2), $\lambda = 0.975$.

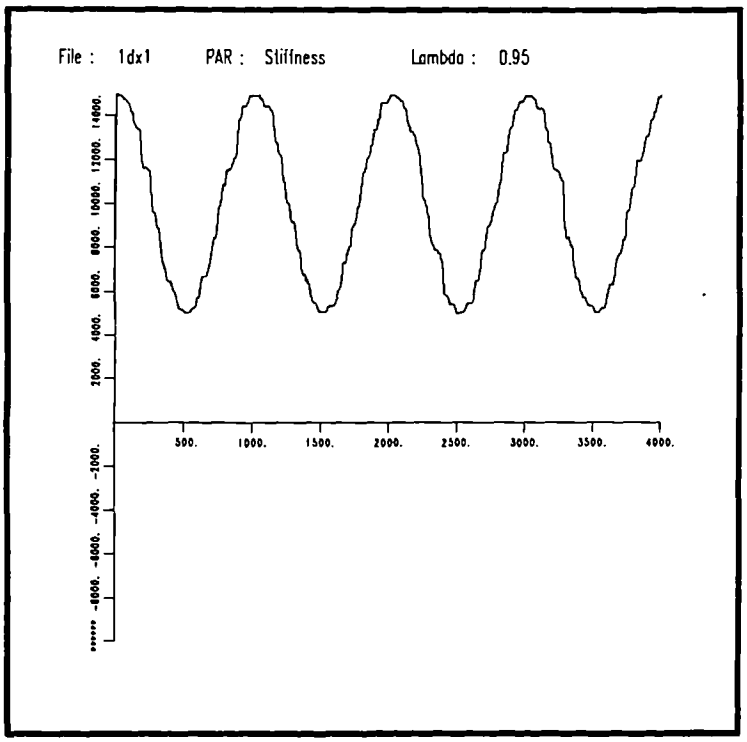

Figure 10.31 Estimated stiffness parameter for each iteration, points 1 to 4000 (t = 4 seconds to t = 8). Example (2), $\lambda = 0.95$.

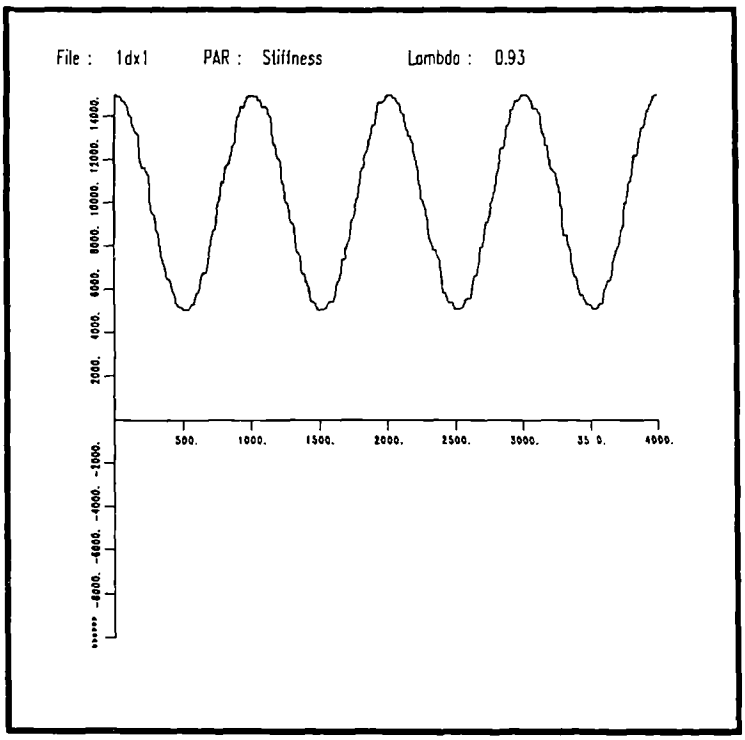

Figure 10.32 Estimated stiffness parameter for each iteration, points 1 to 4000 (t = 4 seconds to t = 8). Example (2), $\lambda = 0.925$.

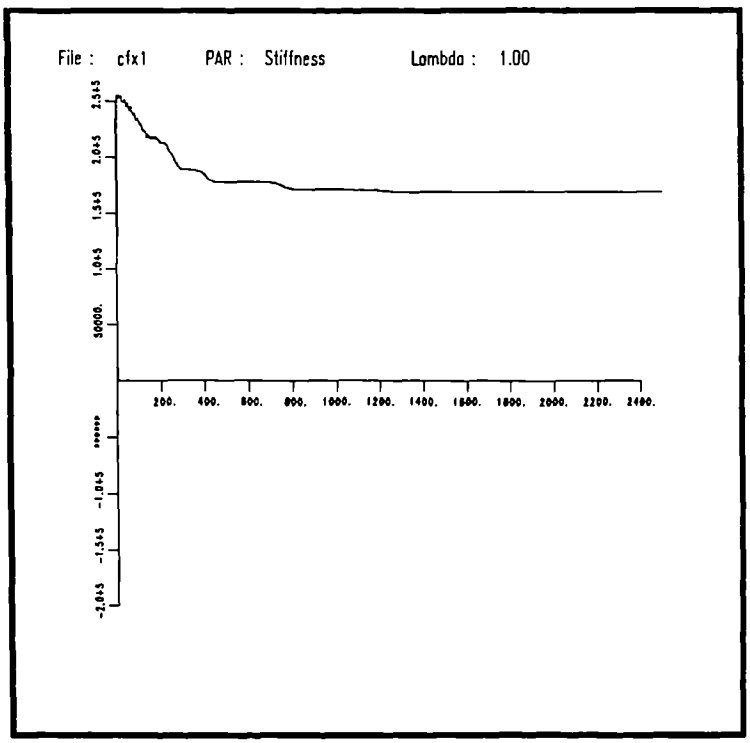

Figure 10.33 Estimated stiffness parameter for each iteration, points 100 to 2500 (t = 0.1 seconds to t = 2.5). Los Alamos data, $\lambda = 1$.

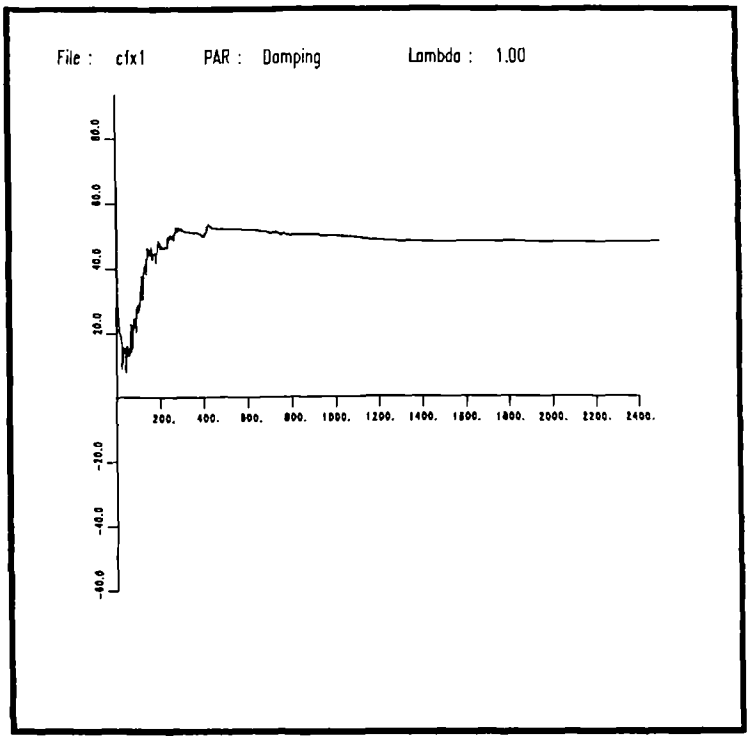

Figure 10.34 Estimated damping parameter for each iteration, points 100 to 2500 (t = 0.1 seconds to t = 2.5). Los Alamos data, $\lambda = 1$.

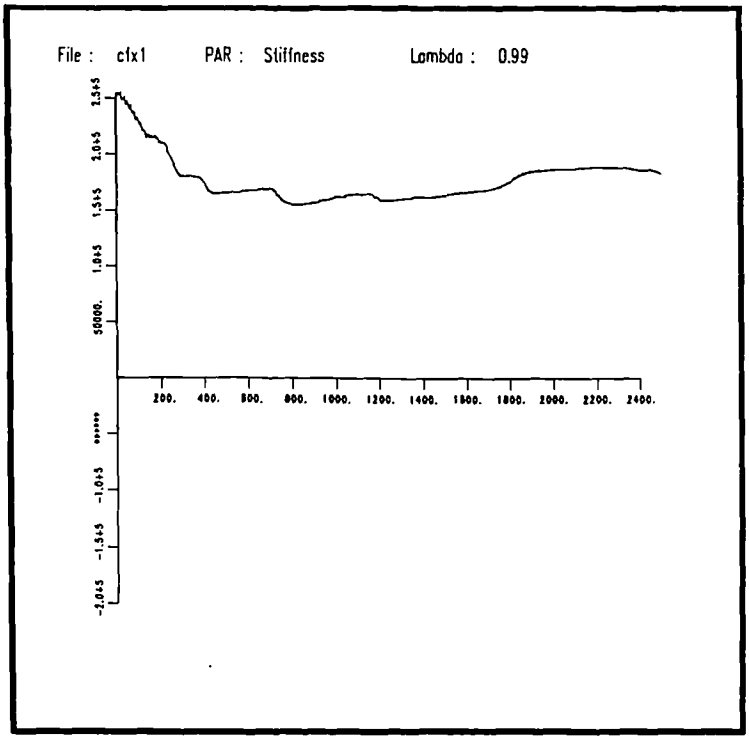

Figure 10.35 Estimated stiffness parameter for each iteration, points 100 to 2500 (t = 0.1 seconds to t = 2.5). Los Alamos data, $\lambda = 0.99$

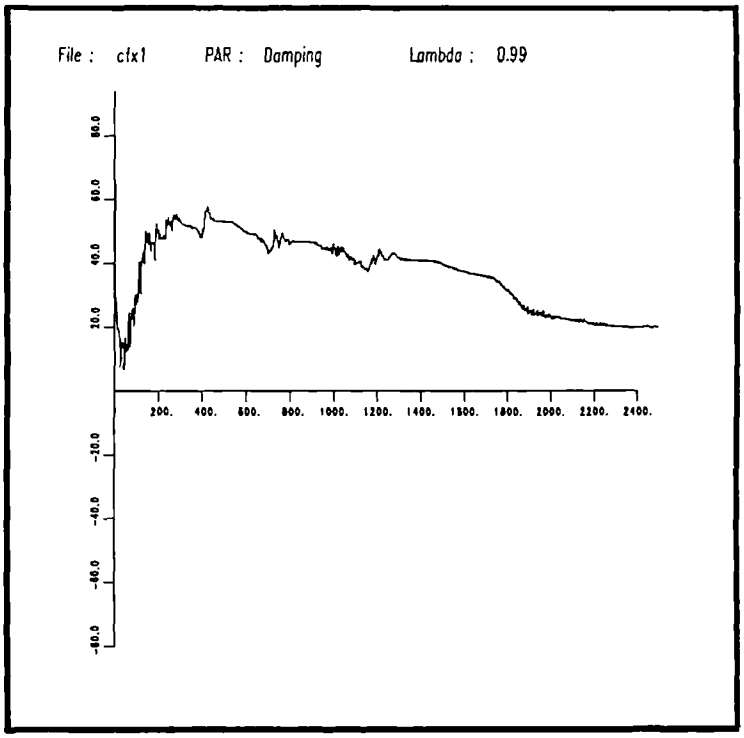

Figure 10.36 Estimated damping parameter for each iteration, points 100 to 2500 (t = 0.1 seconds to t = 2.5). Los Alamos data, $\lambda = 0.99$

CHAPTER 11

CONCLUSIONS AND FURTHER WORK

11.1. Conclusions.

1. It is shown that care is needed in the use of the Hilbert transform to detect nonlinearity if the resullts are to be interpreted unambiguously. It is important to recognise that the asymptotic structure of an FRF may be as important as it's pole structure when one is attempting to apply the Hilbert transform relations. A correction term is given which generates Hilbert transform pairs even if the FRF under investigation is not square-integrable. The Hilbert transform conventions must be tailored to the Fourier transform conventions.

2. The Masri/Caughey procedure has been implemented with an improved interpolation scheme which can generate both continuous and differentiable surfaces. The extrapolation problem is solved by operating on a reduced data set in the phase plane. The results for simulations are an improvement on those of Masri and Caughey for the types of systems they studied. The analysis is extended to systems with singular restoring forces. It is verified that hysteretic systems can be modelled in the sense that the energy loss through hysteresis is modelled by an addition to the viscous damping term. It is shown that quite high-order models are needed for systems with non-polynomial restoring forces; in addition, the models for these systems are input dependent.

3. The extension of the Masri/Caughey procedure to MDOF systems is examined. It is shown that the procedure can be very time-consuming and the parameters obtained can be biased. The effects of innaccuracies in the measured mass matrix and modal matrix are demonstrated. It is shown that a simple modification allows one to overcome the problems caused by an innaccurate modal matrix.

4. It is shown using computer simulation that direct Least-squares (LS) parameter estimation is considerably faster and more accurate than the Masri/Caughey procedure. In addition, one can estimate the mass of the system and find confidence limits for the parameters. It is shown that one can use direct LS methods to obtain Masri/Caughey type Chebyshev expansions in a fraction of the time required by the interpolation based approach. A comparitive study is made of several of the more well-known LS estimators. Singular value decomposition and orthogonal estimation are seen to provide the most foolproof estimators while orthogonal estimation and the normal equations are fastest. A comparison is made with the Masri/Caughey procedure for SDOF systems.

5. It is shown that by using transmissibility data for an SDOF system one can obtain the restoring force up to an overall scale without needing an estimate of the mass. The approach is extended to SIMO systems and it is demonstrated using simulations that one can find all parameters for an MDOF system by exciting it at one point only, as long as the system mass matrix is diagonal. The problem of linear dependence caused by off-diagonal terms in the mass matrix is identified. A comparison is made with the Masri/Caughey procedure for MDOF systems.

6. It is demonstrated that time data from simulations can be integrated simply and accurately using a computer. Differentiation is less accurate, it appears to introduce phase lags and also magnifies high-frequency noise. A comparitive study of a variety of integration and differentiation methods is made, both in the time-domain and the frequency domain. It is shown that unwanted trends in the data can be removed by a variety of methods. The trapezium rule emerges as the preferred method of integration as other methods require the data to be low-pass filtered. One concludes that the recommended experimental procedure is to measure force and acceleration and obtain the velocity and displacement data by integration.

7. It is shown using simulations that one can choose various types of input force for the restoring force method which minimise the amount of data processing required. In

almost all cases a simple trapezium rule integration followed by a linear trend removal is sufficient to produce accurate velocity and displacement data from 'measured' acceleration data. The inputs based on harmonic forcing are shown to introduce linear dependence between displacement and acceleration, this makes tham less suitable for parameter estimation than for producing a force surface. The input which appears to emerge as the most useful is a band-limited random signal. This input gives good coverage of the phase plane, producing a large expanse of force surface, allows a simple integration procedure and produces accurate parameter estimates. These conclusions apply equally well to SDOF and MDOF systems, provided the signal excites all modes of interest.

8. A number of experiments are carried out on linear and nonlinear SDOF systems, Specifically data is obtained from a set of nonlinear analogue circuits and from an impacting cantilever beam. The results for the circuits are consistent with those obtained by other methods. The parameters for the cantilever agree well with theoretical predictions. One concludes that the method can accurately identify experimental SDOF systems. It is shown that time delays in the measured data can be effectively removed by interpolation. Using simulations it is shown that the identification procedure is fairly insensitive to measurement noise as long as low frequency components are filtered out, if allowed to remain they can seriously affect the integration of the data.

9. The Direct Least-squares method is apllied to a linear three degree-of-freedom experimental system with lumped masses. Estimates of the mass and stiffness matrices are obtained which show good agreement with the theoretical predictions. The estimate of the damping matrix is innaccurate because the damping forces in the system are very small. It is shown that the mass estimates correspond to the actual physical masses in the system. The method is applied to the same system with a cubic velocity dependent force applied at one of the masses, the type and location of the nonlinearity is correctly identified by the method.

10. A sample of time data was provided from a structural test at Los Alamos National Laboratories in the U.S.A. where the structural stiffness was thought to have changed during the course of the experiment. The data was analysed using two methods which allow one to capture time variation of parameters, batch analysis and Recursive Least-Squares (RLS) analysis with an exponential forgetting factor. The conclusion was that the system stiffness dropped sharply, settled to a constant level and then rose slightly. The damping appeared to decrease steadily throughout the test. These conclusions are consistent with those of the Los Alamos group. The RLS algorithm with forgetting factor is shown to correctly track time-varying parameters in two simulated structural systems, in one the parameter change is a step function, in the other the variation is periodic.

Overall, one concludes that the restoring force methods, particularly those based on direct least-squares parameter estimation provide a powerful identification technique for nonlinear systems. In principle, one can actually obtain the equations of motion for a finite-order model of the system under test. This is beyond the capabilities of most other methods. In addition, one also has the possibility of tracking time-variation in the parameters of interest.

11.2. Suggestions for Further Work.

If the Hilbert transform is ever to be of use in identifying specific types of nonlinearity, a large amount of work remains to be done. A useful exercise would be to calculate the analytical form of the Hilbert transform for the FRF of a specific nonlinear system, where the FRF has been obtained from a harmonic balance approach. The integrals which one would have to evaluate are very difficult even for simple nonlinearities. However, if closed form expressions were available for Hilbert transforms one might see a way of extracting more detailed information about systems from the transforms.

2. The restoring force surface methods described in this work are all based on the general form of Newton's second law for a lumped-parameter structural system. A possible area of research would be to apply parameter estimation techniques to other systems where the form of the equations is known or a specific interaction term is known to be present. An extension of the approach which allowed the study of continuous or distributed parameter systems would be of interest.

3. A more careful study of hysteretic systems is required. It seems unsatisfactory to simply model hysteresis by a viscous damping term. One possible approach is to use a Bouc-Wen type model and estimate parameters. The problem with this idea is that the parameters appear in the model nonlinearly; for this reason a nonlinear least-squares estimator would be required.

4. In order to test the parameter estimation procedures experimentally it would be very useful to have a multi-degree-of-freedom system where one could control the type and location of the nonlinearity. One possibility would be to simulate an MDOF system using an analogue circuit in the same way that the ETH box simulates SDOF systems.

5. It is assumed throughout this work that any noise in the system is uncorellated and can be transferred to the input. In general, neither of these assumptions is justified. Failure to take account of this introduces bias into the estimated parameters. The way to eliminate this problem is add a nonlinear noise model during the parameter estimation stage. Another useful adjunct to the procedure would be to introduce model validity tests as used in NARMAX (nonlinear difference equation) modelling.

6. There are a number of specific situations where one can see the procedures being of use experimentally. One application which is being pursued at the moment concerns the identification of damping and stiffness coefficients for bearings. At low levels of excitation (unbalance) this simply requires one to identify a two degree-of-freedom linear system. At higher levels of excitation nonlinear effects become important;

however, the form of the nonlinear forces is known in some cases from Reynold's equation, so parameter estimation techniques could be applied. An interesting feature of this work is that the displacement of the rotor is measured using a non-contact transducer, this signal is then differentiated to produce velocity and acceleration data. This is in direct contrast to the preferred situation where the acceleration is measured. This suggests that more theoretical work should be done on the numerical differentiation of time data. In particular one would need to understand the mechanism by which phase-lags appear to be introduced into the estimated derivative.

7. One could investigate more sophisticated methods of detecting time dependence in structural parameters than recursive least-squares, e.g. random walk methods. These techniques could then be used in specific situations i.e. it has been suggested that one could study electro-rheological materials where the system stiffness varies with the applied electromagnetic field strength.

APPENDIX A

FREQUENCY DOMAIN REPRESENTATIONS OF $\delta(t)$ AND $\varepsilon(t)$

Fourier's theorem for the Fourier transform gives

$$f(t) = \frac{1}{2\pi} \int_{-\infty}^{+\infty} d\omega \; e^{i\omega t} \left\{ \int_{-\infty}^{+\infty} d\tau \; e^{-i\omega\tau} \; f(\tau) \right\}$$

i.e.

$$f(0) = \frac{1}{2\pi} \int_{-\infty}^{+\infty} d\omega \left\{ \int_{-\infty}^{+\infty} d\tau \; e^{-i\omega\tau} \; f(\tau) \right\}$$

$$= \int_{-\infty}^{+\infty} d\tau \left\{ \frac{1}{2\pi} \int_{-\infty}^{+\infty} d\omega \; e^{-i\omega\tau} \right\} f(\tau)$$

Now, the defining property of the Dirac δ-function is

$$f(0) = \int_{-\infty}^{+\infty} d\tau \; \delta(\tau) \; f(\tau)$$

So one can make the identification

$$\delta(\tau) = \frac{1}{2\pi} \int_{-\infty}^{+\infty} d\omega \; e^{-i\omega\tau}$$

or, equally well,

$$\delta(\tau) = \frac{1}{2\pi} \int_{-\infty}^{+\infty} d\omega \; e^{i\omega\tau}$$

Now, consider the integral

$$I(t) = \int_{-\infty}^{+\infty} d\omega \; \frac{e^{i\omega t}}{\omega} \qquad t > 0 \; .$$

$$= 2i \int_{0}^{+\infty} d\omega \; \frac{\sin(\omega t)}{\omega}$$

Taking the one-sided Laplace transform of both sides yields

$$L\{I(t)\} = \tilde{I}(p) = 2i \int_0^{+\infty} dt\ e^{-pt} \int_0^{+\infty} d\omega\ \frac{\sin(\omega t)}{\omega}$$

assuming that one can interchange the order of integration, one finds

$$\tilde{I}(p) = 2i \int_0^{+\infty} d\omega \left\{ \int_0^{+\infty} dt\ e^{-pt}\ \sin(\omega t) \right\} \frac{1}{\omega}$$

$$= 2i \int_0^{+\infty} d\omega\ \frac{1}{p^2 + \omega^2}$$

$$= \frac{i\pi}{p}$$

Inverse transforming gives $I(t) = i\pi$ if $t > 0$. It is obvious that a simple change of variables would give $I(t) = -i\pi$ if $t < 0$. So $I(t) = i\pi.\varepsilon(t)$ and one has the integral representation

$$\varepsilon(t) = \frac{1}{i\pi} \int_{-\infty}^{+\infty} d\omega\ \frac{e^{i\omega t}}{\omega}$$

or (in F_+)

$$\varepsilon(t) = \frac{1}{i\pi} \int_{-\infty}^{+\infty} d\omega\ \frac{e^{-i\omega t}}{\omega}$$

A simple application of the shift property for Fourier transforms gives (in F_-)

$$\frac{1}{i\pi} \int_{-\infty}^{+\infty} d\omega\ \frac{e^{i\omega t}}{\omega - \Omega} = e^{i\Omega t}\ \varepsilon(t)$$

APPENDIX B

PROPERTIES OF CHEBYSHEV POLYNOMIALS

B.1. Definitions and Orthogonality Relations.

The basic properties are now very well known (32,33). However, for the sake of completeness they are described here along with one or two perhaps less well-known properties.

The definition of the Chebyshev polynomial of order n is

$$\begin{aligned} T_n(x) &= \cos(n.\cos^{-1}(x)) && |x| \leqslant 1 \\ T_n(x) &= \cosh(n.\cosh^{-1}(x)) && |x| \geqslant 1 \end{aligned} \qquad (B.1)$$

It is not immediately obvious from this definition that $T_n(x)$ is a polynomial. However, it is a simple matter to show that this is indeed the case. For example

$$\begin{aligned} T_3(x) &= \cos(3\cos^{-1}(x)) \\ &= 4\cos^3(\cos^{-1}(x)) - 3\cos(\cos^{-1}(x)) \\ &= 4x^3 - 3x \end{aligned}$$

The Chebyshev polynomials are orthogonal on the interval [-1,1] with weighting factor $\omega(x) = (1 - x^2)^{-\frac{1}{2}}$ which means that

$$\int_{-1}^{+1} dx\ \omega(x)T_n(x)T_m(x) = \frac{\pi}{2}(1 + \delta_{n0})\delta_{nm} \qquad (B.2)$$

Again, the proof of this is simple. One makes the substitution $y = \cos^{-1}(x)$ then using the definition of the $T_n(x)$ changes the integral above to

$$\int_0^{\pi} dy \cos(my)\cos(ny)$$

This integral is easy to evaluate. It should be familiar from the theory of Fourier series. In fact expansion in a Chebyshev series is entirely equivalent to the more usual Fourier sine and cosine expansions. Returning to the integral, one has

$$\begin{aligned} \int_0^{\pi} dy \cos(my)\cos(ny) &= 0 && \text{if} \quad m \neq n \\ &= \pi && \text{if} \quad m = n = 0 \\ &= \frac{\pi}{2} && \text{if} \quad m = n \neq 0 \end{aligned}$$

With the help of the orthogonality relation (A.2) it is possible to expand any given function in terms of a summation of Chebyshev polynomials i.e.

$$f(x) = \sum_{i=0}^{N} a_i \, T_i(x) \qquad (B.3)$$

using the relation (A.2) gives for the coefficients

$$a_i = X(i) \int_{-1}^{+1} dx \, \omega(x) f(x) T_i(x)$$

where $X(i) = 1/\pi$ if $i \neq 0$ and $X(i) = 2/\pi$ if $i = 0$.

The extension to a double series is trivial. If one desires an expansion

$$f(x,y) = \sum_{i=0}^{m} \sum_{j=0}^{n} C_{ij} \, T_i(x) T_j(y)$$

$$C_{ij} = X(i)X(j) \int_{-1}^{+1} \int_{-1}^{+1} dxdy \, \omega(x)\omega(y) f(x,y) T_i(x) T_j(y)$$

One can also use the orthogonality relations to show that the Chebyshev representation of a function is unique (up to the order of the expansion). The proof is straightforward. If

$$f(x) = \sum_{i=0}^{n} a_i \, T_i(x) = \sum_{i=0}^{n} b_i \, T_i(x)$$

then multiplying by $\omega(x)T_j(x)$ and integrating over $[-1,1]$ gives

$$a_i = b_i$$

B.2. Recurrence Relations and Clenshaw's Algorithm.

Like all orthogonal polynomials, the Chebyshev polynomials satisfy a number of recursion relations. Arguably the most useful being

$$T_{n+1}(x) = 2x \, T_n(x) - T_{n-1}(x) \qquad (B.4)$$

Proof is elementary. If $y = \cos^{-1}(x)$ then

$$T_{n+1}(x) = \cos((n+1)y) = \cos(ny)\cos(y) - \sin(ny)\sin(y)$$

$$T_{n-1}(x) = \cos((n-1)y) = \cos(ny)\cos(y) - \sin(ny)\sin(y)$$

$$\therefore \quad T_{n+1}(x) + T_{n-1}(x) = 2\cos(ny)\cos(y) = 2x \, T_n(x)$$

as required.

It is clear that if one starts the recurrence with $T_0(x) = 1$ and $T_1(x) = x$, by using (A.4) one can obtain the value of $T_n(x)$ for any n. This should be the preferred means of evaluating $T_n(x)$ on a computer, where function evaluations may be much

more expensive than repeated multiplications and additions. (Obviously there is a threshold value of n beyond which one makes no saving by using the recurrence realation.)

In order to evaluate how good a Chebyshev approximation to a function is, one would compare the true function to the approximation at a number of points. This means that one would be faced with many summations of the form

$$f(x) = \sum_{i=0}^{n} a_i \, T_i(x)$$

Fortunately, there is a much more economical means of evaluating this expression than evaluating the polynomials and summing the series. One uses Clenshaw's recurrence formula. One can use this to sum a sequence composed of any type of polynomial which satisfies a recurrence relation. The version given here is specific to Chebyshev polynomials. The general result is given in (33).

First define a sequence y_i by

$$y_{n+2} = y_{n+1} = 0$$

$$y_i = 2x.y_{i-1} - y_i + a_i \qquad (B.5)$$

Then

$$f(x) = [\, y_n - 2x.y_{n+1} + y_{n+2} \,] \, T_n(x)$$

$$+ \ldots + [\, y_i - 2x.y_{i+1} + y_{i+2} \,] \, T_i(x)$$

$$+ \ldots + [\, a_0 - y_2 + y_2 \,] \, T_0(x)$$

after adding and subtracting $y_2.T_0(x)$. In the middle of this summation one has

$$\ldots + [\, y_{i+1} - 2x.y_{i+2} + y_{i+3} \,]\, T_{i+1}(x)$$

$$+ [\, y_i - 2x.y_{i+1} + y_{i+2} \,]\, T_i(x)$$

$$+ [\, y_{i-1} - 2x.y_i + y_{i+1} \,]\, T_{i-1}(x) + \cdots$$

so the coefficient of y_{i+1} is

$$T_{i+1}(x) - 2x.T_i(x) + T_{i-1}(x)$$

which vanishes as a consequence of the recurrence relation (A.4). Similarly all the coefficients vanish down to y_2, and all that remains is the end of the summation

$$\ldots + T_2(x)\,[\, y_2 - 2x.y_3 + y_4 \,]$$

$$+ T_1(x)\,[\, y_1 - 2x.y_2 + y_3 \,] = 0$$

$$+ T_0(x)\,[\, a_0 - y_2 + y_2 \,] = 0$$

$$= T_0(x)\,(\, a_0 - y_2 \,) + T_1(x)\, y_1 = 0$$

so finally

$$f(x) = a_0 + x.y_1 - y_2 \qquad (B.6)$$

Therefore, to evaluate f(x) for each x one simply passes downward through the recurrence (B.5) to obtain y_1 and y_2 and then evaluates the linear expression (B.6). Unfortunately, no obvious two-dimensional analogue of Clenshaw's result seems to exist. This means that in evaluating a double series one can only use this result if the function f(x,y) splits into single-variable functions i.e f(x,y) = g(x) + h(y). Of all the

examples considered in chapter two, only the Van der Pol oscillator of example 4 fails to satisfy this condition.

Clenshaw's recurrence can also be used algebraically in order to turn Chebyshev expansions into ordinary polynomial expansions. However one should be aware that this is not always a good idea (33).

B.3. Exact Chebyshev Coefficients for a Class of Simple Functions.

In Chapter 2, the Chebyshev expansion for the restoring force $f(y,\dot{y})$ is estimated for a number of simple systems. In order to form an opinion about the accuracy of these estimates, one needs to know the exact values of the coefficients. A function sufficiently general to include the examples of chapter 2 is

$$f(x,y) = ax^3 + bx^2 + cx + dy + ey^2 + fx^2y$$

The x and y are then subjected to a linear transformation

$$x \rightarrow \xi(x) = \bar{x} = (x - \alpha_2)/\alpha_1$$
$$y \rightarrow \dot{\xi}(y) = \bar{y} = (y - \beta_2)/\beta_1$$

where

$$\alpha_1 = \tfrac{1}{2} (x_{max} - x_{min}) \quad , \quad \alpha_2 = \tfrac{1}{2} (x_{max} + x_{min})$$
$$\beta 1 = \tfrac{1}{2} (y_{max} - y_{min}) \quad , \quad \beta_2 = \tfrac{1}{2} (y_{max} + y_{min})$$

The form of f in the $(\bar{x},\bar{y})$ coordinates is given by

$$\bar{f}(\bar{x},\bar{y}) = f(x,y) = f(\xi^{-1}(\bar{x}), \dot{\xi}^{-1}(\bar{y}))$$
$$= f(\alpha_1\bar{x} + \alpha_2, \beta_1\bar{y} + \beta_2)$$

A little algebra produces the result

$$\bar{f}(\bar{x},\bar{y}) = \bar{a}\,\bar{x}^3 + \bar{b}\,\bar{x}^2 + \bar{c}\,\bar{x} + \bar{d}\,\bar{y} + \bar{e}\,\bar{y}^2 + \bar{f}\,\bar{x}^2\bar{y} + \bar{g}\,\bar{x}\,\bar{y} + \bar{h}$$

where

$$\begin{aligned}
\bar{a} &= a\alpha_1^3 \\
\bar{b} &= 3a\alpha_1^2\alpha_2 + b\alpha_1^2 + f\alpha_1^2\beta_2 \\
\bar{c} &= 3a\alpha_1\alpha_2^2 + 2b\alpha_1\alpha_2 + 2f\alpha_1\alpha_2\beta_2 \\
\bar{d} &= d\beta_1 + 2e\beta_1\beta_2 + f\alpha_2^2\beta_1 \\
\bar{e} &= e\beta_1^2 \\
\bar{f} &= f\alpha_1^2\beta_1 \\
\bar{g} &= 2f\alpha_1\alpha_2\beta_2 \\
\bar{h} &= a\alpha_2^3 + b\alpha_2^2 + c\alpha_2 + d\beta_2 + e\beta_2^2 + f\alpha_2^2\beta_2
\end{aligned}$$

One can now expand this function as a double Chebyshev series

$$\bar{f}(\bar{x},\bar{y}) = \sum_{i=0}^{m}\sum_{j=0}^{n} C_{ij}\,T_i(\bar{x})\,T_j(\bar{y})$$

One could use the orthogonality relations to find the coefficients C_{ij}. However, it is far simpler to use direct substitution i.e. consider the $\bar{a}.\bar{x}^3$ term

$$T_3(\bar{x}) = 4\bar{x}^3 - 3\bar{x} \quad , \quad T_1(\bar{x}) = \bar{x}$$

$$\begin{aligned}
\bar{a}.\bar{x}^3 &= \tfrac{1}{4}\,\bar{a}\,(\,T_3(\bar{x}) + 3\bar{x}\,) \\
&= \frac{1}{4}\,\bar{a}\,T_3(\bar{x}) + \frac{3}{4}\,\bar{a}\,T_1(\bar{x})
\end{aligned}$$

The exact coefficients for $\bar{f}(\bar{x},\bar{y})$ are

$$\begin{aligned}
C_{00} &= \bar{h} + \tfrac{1}{2}\,(\bar{b} + \bar{e}\,) \\
C_{01} &= \bar{d} + \tfrac{1}{2}\,\bar{f} \\
C_{02} &= \tfrac{1}{2}\,\bar{e} \\
C_{10} &= \tfrac{1}{2}\,\bar{a} + \bar{c} \\
C_{11} &= \bar{g}
\end{aligned}$$

$$
\begin{aligned}
c_{12} &= 0 \\
c_{20} &= \tfrac{1}{2}\,\bar{b} \\
c_{21} &= \tfrac{1}{2}\,\bar{f} \\
c_{22} &= 0 \\
c_{30} &= \tfrac{1}{4}\,\bar{a}
\end{aligned}
$$

B.4. Least-squares and Chebyshev Series.

It has already been remarked that the Chebyshev polynomials are remarkably good approximating polynomials. In fact, fitting a Chebyshev series to data is equivalent to fitting a least-squares model. With little extra effort one can show that this is the case for any orthogonal polynomials **(70)** as follows,

let $\{ \psi_i(x),\ i = 1,\ldots\infty \}$ be a set of polynomials orthonormal on the interval [a,b] with weighting function $\omega(x)$. i.e.

$$\int_a^b dx\ \omega(x)\psi_i(x)\psi_j(x) = \delta_{ij} \qquad (B.7)$$

(The Chebyshev polynomials used in this work are not orthonormal. However the polynomials $\psi_i(x) = (2/\pi)^{\frac{1}{2}}.T_i(x)$ and $\psi_0(x) = \pi^{-\frac{1}{2}}$ are.) Suppose one wishes now to approximate a function f(x) by a summation of the form

$$\hat{f}(x) = \sum_{i=0}^{n} c_i\ \psi_i(x)$$

One can define a least-squares error functional by

$$I_n[c_i] = \int_a^b dx\ \omega(x)\ |\ f(x) - \hat{f}(x)\ |^2 \qquad (B.8)$$

$$= \int_a^b dx\ \omega(x)\ |\ f(x) - \sum_{i=0}^{n} c_i\ \psi_i(x)\ |^2$$

expanding this expression gives

$$I_n[c_i] = \int_a^b dx\ \omega(x)\ |\ f(x)\ |^2$$

$$+\ 2\sum_{i=0}^{n} c_i \int_a^b dx\ \omega(x) f(x) \psi_i(x) \qquad (B.9)$$

$$+\ c_i c_j \sum_{i=0}^{n} \sum_{j=0}^{n} \int_a^b dx\ \omega(x) \psi_i(x) \psi_j(x)$$

Now, the Fourier coefficients a_i for an expansion are defined by

$$a_i = \int_a^b dx\ \omega(x) f(x) \psi_i(x)$$

Using this definition and the orthogonality relations (B.7) gives for (B.9)

$$I_n[c_i] = \int_a^b dx\ \omega(x)\ |\ f(x)\ |^2 - 2 \sum_{i=0}^{n} a_i c_i$$

$$+ \sum_{i=0}^{n} c_i^2$$

Completing the square gives

$$I_n[c_i] = \int_a^b dx\ \omega(x)\ |\ f(x)\ |^2 - \sum_{i=0}^{n} a_i^2$$

$$+ \sum_{i=0}^{n} (\ c_i - a_i\ )^2$$

Now, the first two terms of this expression are fixed by the function f(x) and the Fourier coefficients so minimising the error functional by varying c_i is simply a matter of minimising the last term. This is only zero if $a_i = c_i$. This shows clearly that using a Fourier expansion of orthogonal functions is a least–squares procedure. The only point which needs clearing up is that the usual least–squares error functional is

$$I_n[c_i] = \int_a^b dx \mid f(x) - \hat{f}(x) \mid^2$$

For the case of Chebyshev polynomials, changing variables from x to y = cos(x) changes (B.8) from

$$I_n[c_i] = \int_{-1}^{+1} dx \, (1 - x^2)^{-\frac{1}{2}} \mid f(x) - \hat{f}(x) \mid^2$$

to

$$I_n[c_i] = \int_0^{\pi} dx \mid f(\cos^{-1}(y)) - \hat{f}(\cos^{-1}(y)) \mid^2$$

which is the required functional.

APPENDIX C

NATURAL NEIGHBOUR INTERPOLATION

The purpose of this appendix is to outline the theory behind the natural neighbour method of interpolation used in the earlier chapters. The method **(36,71)** is capable of producing a C^0 or C^1 surface (C^0 is continous, C^1 is differentiable), based on data measured at irregularly spaced points in the plane. In order to keep the theory fairly simple the theory for finding a C^0 interpolant is described. The description here roughly follows that in **(36)**.

The algorithm is based on the construction of the Dirichlet tesselation and it's associated Delaunay triangulation. The triangulation has previously been used in Engineering by practitioners of the finite element method as it can be used to generate a mesh.

Consider a set of N points { P_i, i = 1,...,N } distributed in the plane. Choosing two points from this set P_m and P_n defines three regions in the plane

(i) A_{mn} , which contains all points *in the plane* nearer to P_m than to P_n

(ii) A_{nm} , which contains all points nearer to P_n than to P_m

(iii) L_{mn} , which is a line which bounds A_{mn} and A_{nm} and contains all points equidistant from P_m and P_n.

If one now constructs the set $A_{nq} \cap A_{nm}$ (where $\cap$ represents set-theoretic intersection, in this case common area), one can immediately see that this contains all those points in the plane which are nearer to P_n than to both P_q and P_m. One

can now extend this construction to form

$$T_n := A_{n1} \cap A_{n2} \cap \ldots \cap A_N \qquad (C.1)$$

This set contains all points in the plane which have P_n as their nearest neighbour from the set of 'sample' points $\{ P_i \}$. T_n is called the *tile* (or Voronoi or Thiessen polyhedron) of P_n with respect to $\{ P_i \}$. The set of tiles $\{ T_i, i = 1,\ldots,N \}$ together with their boundaries cover the plane. This subdivision of the plane is called the Dirichlet tesselation. Equation (C.1) suggests the most direct method of constructing the tesselation. The construction is demonstrated pictorially in Figure C.1 for an example where N = 4. As one might expect, much more efficient methods of constructing the tesselation are known. Reference **(72)** outlines one such method – that used in the TILE4 package developed by R. Sibson.

If two tiles T_n and T_m have a section of boundary in common, even if this is only a single point, they are termed *contiguous*. If one now joins all pairs of points P_n and P_m by a line segment if their tiles T_n and T_m are contiguous, the network of line segments produced provides a triangulation of the plane called the Delaunay triangulation. Pairs of points with contiguous tiles are termed *natural neighbours*. A simple example of a triangulation is shown in Figure C.1.

Having constructed the tesselation for a set of points, one can then refine it by defining the *subtiles* T_{nm} which contain all the points in the plane which have P_n as their nearest neighbour from $\{ P_i \}$ and P_m as their second nearest neighbour. The subtile structure for the example in Figure C.1 is shown in Figure C.2. If one denotes the area of T_n by κ_n and that of T_{nm} by κ_{nm}, it is obvious that

$$\sum_m \kappa_{nm} = \kappa_n \qquad (C.2)$$

where the summation index m runs over the indices of all the natural neighbours of P_n. If one defines the normalised subtile area $\lambda_{nm} = \kappa_{nm}/k_n$ equation (C.2) directly

gives

$$\sum_m \lambda_{mn} = 1 \qquad (C.3)$$

It is now possible to prove a (non-trivial) result which is crucial to the interpolation.

If $\underline{x}_n$ is the position vector of the point P_n, then

$$\sum_m \lambda_{nm} \cdot \underline{x}_m = \underline{x}_n \qquad (C.4)$$

This means that if a mass equal to the area of T_{nm} was placed at each P_m then the centroid of these masses would be at P_n. Equation (C.4) means that the λ_{mn}'s provide a local coordinate system in the neighbourhood of $\underline{x}_n$. For this reason (C.4) is called the Local Coordinate Property (LCP) (71). The λ_{mn}'s are also sometimes called a *barycentric* or *centre of mass* coordinate system for obvious reasons.

As indicated, it is the LCP which allows one to construct the interpolation. Suppose a new point $P(\underline{x})$ is added at the point $\underline{x}$. One can refine the tesselation and triangulation and obtain $T(\underline{x})$, the tile of $P(\underline{x})$ and it's subtiles $T_m(\underline{x})$. The index m now runs over the indices of the natural neighbours of $P(\underline{x})$. The tile and subtile areas, $\kappa(\underline{x})$ and $\kappa_m(\underline{x})$ can now be found, along with $\lambda_m(\underline{x}) = \kappa_m(\underline{x})/\kappa(\underline{x})$. The Local Coordinate Property now gives

$$\sum_m \lambda_m(\underline{x}) \cdot \underline{x}_m = \underline{x} \qquad (C.5)$$

A consequence of this is that if f_m is the value of a function f defined at each point $\underline{x}_m$, the value of a C^0 interpolant for the function at $\underline{x}$ i.e. an estimate of $f(\underline{x})$ is given by

$$f(\underline{x}) = \sum_m \lambda_m(\underline{x}) \cdot f_m \qquad (C.6)$$

This interpolant is continuous (and differentiable except at the data sites $\underline{x}_m$). It is also possible to estimate gradients for the function f at each of the data sites, and

these can be used to construct a differentiable or C^1 interpolant.

The C^0 interpolation is exact if the function is linear, i.e. if $f(\underline{x})$ has the form

$$f(\underline{x}) = \alpha + \underline{\beta}.\underline{x} \qquad (C.7)$$

where $\underline{\beta}$ is a vector of coefficients. The proof of this follows very simply from the LCP.

$$\begin{aligned} f(\underline{x}) &= \sum_m \lambda_m(\underline{x})\ f_m \\ &= \sum_m \lambda_m(\underline{x})\ \{\ \alpha + \underline{\beta}.\underline{x}_m\ \} \\ &= \alpha \sum_m \lambda_m(\underline{x}) + \underline{\beta}.\ \{\ \sum_m \lambda_m(\underline{x})\ \underline{x}_m\ \} \\ &= \alpha + \underline{\beta}.\underline{x} \end{aligned}$$

as required. The C^1 interpolation is designed in such a way that it is exact if $f(\underline{x})$ is a spherical quadratic.

$$f(\underline{x}) = \alpha + \underline{\beta}.\underline{x} + \underline{x}.\underline{x}$$

A general quadratic would contain a term of the form $\underline{x}^t.\underline{M}.\underline{x}$ where $\underline{M}$ is a matrix of coefficients.

The results described in this appendix actually extend to an arbitrary number of dimensions because the LCP does not depend on the fact that one is working in the plane. However, interpolating a function of say three variables is considerably more difficult because the efficient construction of the Dirichlet tesselation is an open problem in three dimensions or higher.

Software which constructs the tesselation/triangulation and carries out the interpolation procedure is available in the form of the TILE4 package (73) from Professor R.Sibson of the University of Bath.

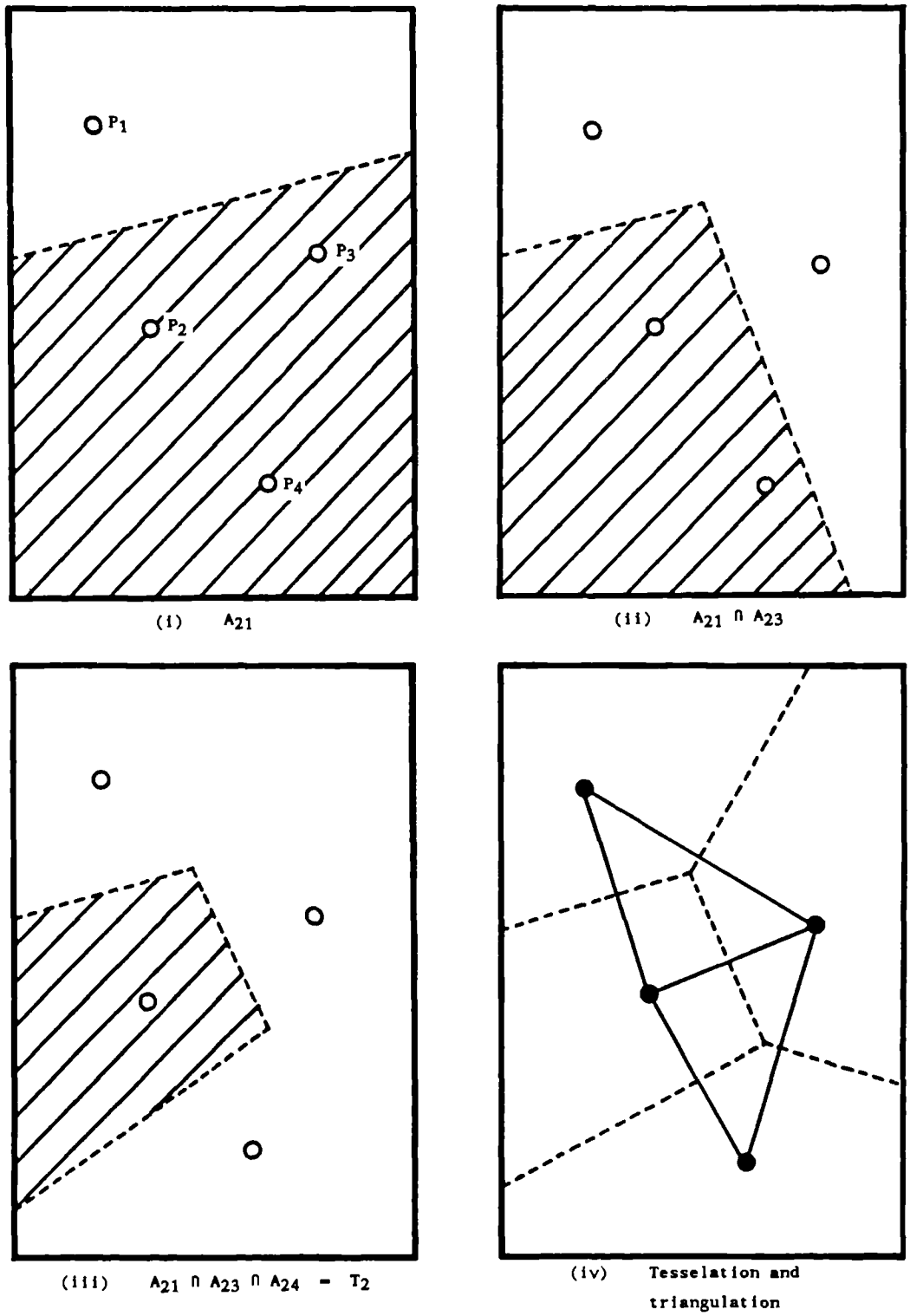

Figure C.1. The construction of the triangulation for a set of four points.

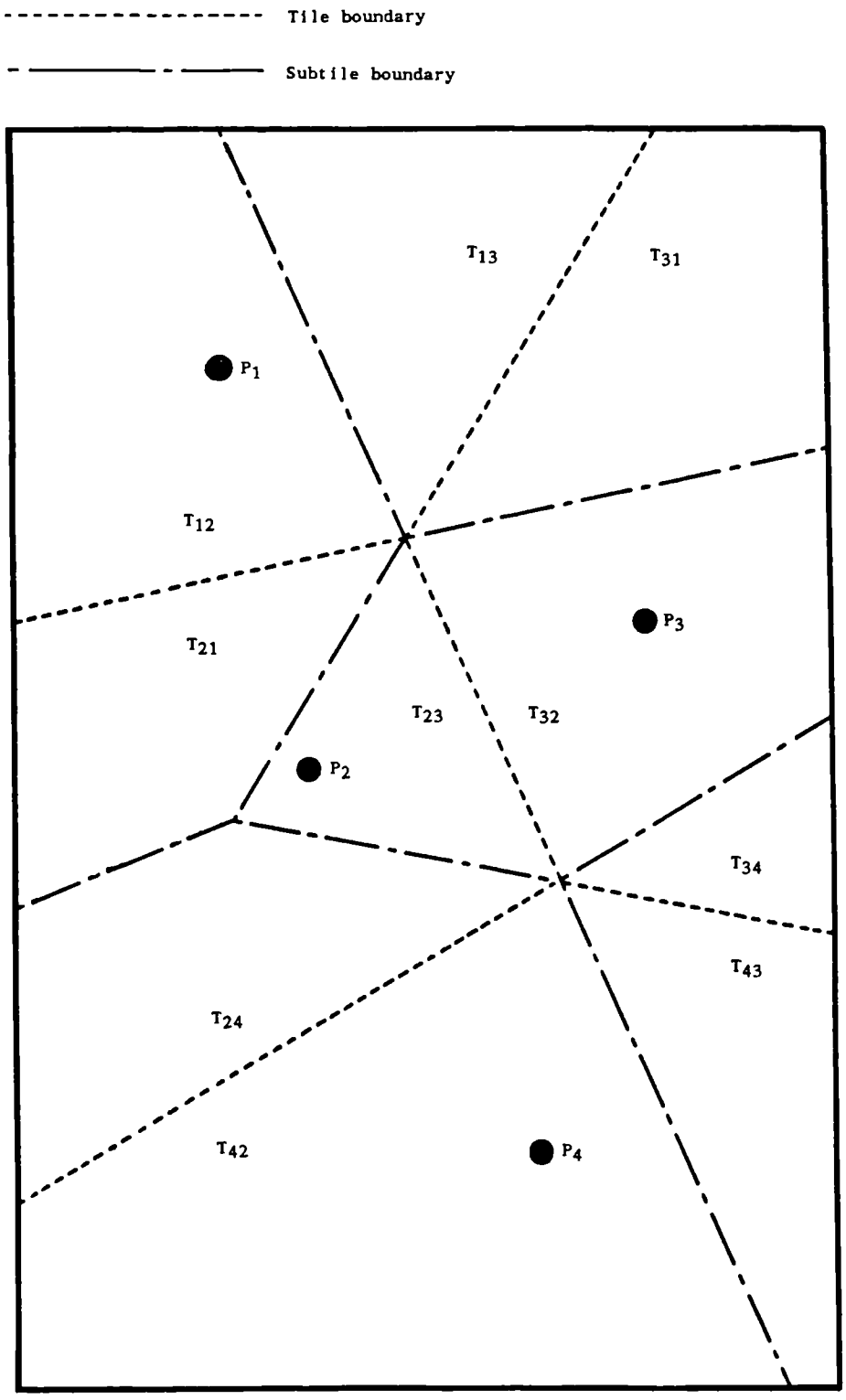

Figure C.2. Refinement of the example in Figure C.1 showing the subtile structure.

REFERENCES

1. Thompson (J.M.T.) & Stewart (H.B) 1986 *Nonlinear Dynamics and Chaos* John Wiley and Sons, London and New York.

2. Porter (B.) 1969 *Synthesis of Dynamical Systems* Nelson.

3. Low (H.S.) 1989 *Identification of Non-Linearity in Vibration Testing* B.Sc. Project, Department of Mechanical Engineering, Heriot-Watt University.

4. Simon (M.) & Tomlinson (G.R.) 1984 *Journal of Sound and Vibration* 90 pp. 275-282. Application of the Hilbert Transform in the Modal Analysis of Linear and Non-Linear Systems.

5. Ahmed (I.) 1987 *Developments in Hilbert Transform Procedures with Applications in Linear and Non-Linear Structures* Ph.D. Thesis, Department of Mechanical Engineering, University of Manchester.

6. Billings (S.A.) 1980 *IEE Proceedings* 127D pp. 272-285. Identification of Nonlinear Systems - A Survey.

7. Ewins (D.J.) 1984 *Modal Testing: Theory and Practice* Research Studies Press, Letchworth England.

8. Gifford (S.J.) 1989 *Volterra Series Analysis of Nonlinear Structures* Ph.D. Thesis. Department of Mechanical Engineering, Heriot-Watt University.

9. Tsang (K.M.) 1988 *Spectral Analysis for Nonlinear Systems* Ph.D Thesis. Department of Control Engineering, University of Sheffield.

10. Masri (S.F.) & Caughey (T.K.) 1979 *Journal of Applied Mechanics* 46 pp. 433-447. A Nonparametric Identification Technique for Nonlinear Dynamic Problems.

11. Masri (S.F.), Sassi (H.) & Caughey (T.K.) 1982 *Journal of Applied Mechanics* 49 pp. 619-627. Nonparametric Identification of Nearly Arbitrary Nonlinear Systems.

12. Masri (S.F.), MIller (R.K.), Sassi (H.) & Caughey (T.K.) 1984 *Journal of Applied Mechanics* 51 pp. 391-398. A Method for Reducing the Order of Nonlinear Dynamic Systems.

13. Masri (S.F.), Miller (R.K.), Saud (A.F.) & Caughey (T.K.) 1987 *Journal of Applied Mechanics* 54 pp. 918-929. Identification of Nonlinear Vibrating Structures: Part I - Formulation & Part II - Applications.

14. Crawley (E.F.) & Aubert (A.C.) 1986 *AIAA Journal* 24 pp. 155-162. Identification of Nonlinear Structural Elements by Force-State Mapping.

15. Crawley (E.F) & O'Donnell (K.J.) 1986 *AIAA Paper 86-1013* pp. 659-667. Identification of Nonlinear System Parameters in Joints Using the Force-State Mapping Technique.

16. Yang (Y.) & Ibrahim (S.R.) 1985 *Journal of Vibration, Acoustics, Stress and Reliability in Design* 107 pp. 60-66. A Nonparametric Identification Technique for a Variety of Discrete Nonlinear Vibrating Systems.

17. Shye (K.) & Richardson (M.) 1987 *Proceedings of the 5th International Modal Analysis Conference* pp. 756-761. Mass, Stiffness and Damping Matrix Estimates from Structural Measurements.

18. Al-Hadid (M.Ajjan) & Wright (J.R.) 1989 *Journal of Mechanical Systems and Signal Processing* 3 pp. 269-290. Developments in the Force-State Mapping Technique for Non-Linear Systems and the Extension to the Location of Non-Linear Elements in a Lumped-Parameter System.

19. Al-Hadid (M.Ajjan) & Wright (J.R.) 1989 *Paper presented at the European Forum on Aeroelasticity and Structural Dynamics, Aachen.* Application of the Force-State Mapping to the Identification of Nonlinear Systems.

20. Al-Hadid (M.Ajjan) 1989 *Identification of Non-Linear Dynamic Systems Using the Force-State Mapping Technique* Ph.D. Thesis. Department of Aeronautical Engineering, Queen Mary College, London.

21. Hammond (J.K.), Lo (H.R.) & Seager-Smith (J.) 1987 *Proceedings of the 5th International Modal Analysis Conference* pp. 1467-1473. Identification of Nonlinearities in Vibrating Systems using Optimal Control Techniques.

22. Lo (H.R.) 1988 *System Characterisation and Identification of Non-Linear Systems (with Particular Reference to Hysteretic Systems)* Ph.D. Thesis. Institute of Sound and Vibration Research, University of Southampton.

23. Lo (H.R.) & Hammond (J.K.) 1989 *Identification of a Class of Non-Linear Structures* Preprint. Institute of Sound and Vibration Research, University of Southampton.

24. Mertens (M.), Van der Auweraer (H.), Vanherck (P.) & Snoeys (R.) 1989 *Journal of Mechanical Systems and Signal Processing* 3 pp. 37-54. The Complex Stiffness Method to Detect and Identify Non-Linear Dynamic Behaviour of SDOF Systems.

25. Hunter (N.), Paez (T.) & Gregory (D.L.) 1989 *Proceedings of the 7th International Modal Analysis Conference* pp. 381-389. Force-State Mapping Using Experimental Data.

26. Mohammad (K.S.) To be submitted 1990 Ph.D. Thesis. Department of Mechanical Engineering, Heriot-Watt University.

27. Ahlfors (L.) 1966 *Complex Analysis* Second Edition, McGraw Hill.

28. Muirhead (H.) *The Physics of Elementary Particles* Pergamon Press, Oxford.

29. Goldhaber (M.) *Dispersion Relations* in *Theorie de la Particules Elementaire* Hermann, Paris.

30. Rodeman (R.) 1988 *Proceedings of the 6th International Modal Analysis Conference* pp. 37-40. Hilbert Transform Implications for Modal Analysis.

31. Goyder (H.G.D.) 1984 *Proceedings of the 2nd International Conference on Recent Advances in Structural Dynamics* Southampton, pp. 89-97. Some Theory and Applications of the Relationship Between the Real and Imaginary Parts of a Frequency Response Function Provided by the Hilbert Transform.

32. Fox (L.) & Parker (I.) 1968 *Chebyshev Polynomials in Numerical Analysis* Oxford University Press.

33. Press (W.H.), Flannery (B.P.), Teukolsky (S.A.) & Vetterling (W.T.) 1986 *Numerical Recipes - The Art of Scientific Computing* Cambridge University Press.

34. Mclain (D.M.) 1978 *The Computer Journal* 21 p.168. Two-Dimensional Interpolation from Random Data.

35. Lawson (C.L.) 1977 *Software for C^1 Surface Interpolation* in *Mathematical Software III* Academic Press.

36. Sibson (R.) 1981 *A Brief Description of Natural Neighbour Interpolation* in *Interpreting Multivariate Data* edited by V. Barnett. John Wiley and Sons, London and New York.

37. Wen (Y.K.) 1976 *Journal of the Engineering Mechanics Division* pp. 249-263. A Method for the Random Vibration of Hysteretic Systems.

38. Wright (J.R.) *Generalised Mass* Unpublished Lecture Notes, Department of Mechanical Engineering, University of Manchester.

39. Peyton-Jones (J.C.) & Billings (S.A.) 1989 *A Recursive Algorithm for Computing the Frequency Response of a Class of Nonlinear Difference Equation Models* Preprint. Department of Control Engineering, University of Sheffield.

40. Strejc (V.) 1980 *Automatica* 16 pp. 535-550. Least-Squares Parameter Estimation.

41. Leonaritis (I.J.) & Billings (S.A.) 1985 *International Journal of Control* 41 pp. 303-328. Input-Output Parametric Models for Nonlinear Systems: Part I - Deterministic Nonlinear Systems.

42. Billings (S.A.) *Parameter Estimation* Unpublished Lecture Notes. Department of Control Engineering, University of Sheffield.

43. Lawson (C.L.) & Hanson (R.J.) 1974 *Solving Least-Squares Problems* Prentice Hall Series in Automatic Computation.

44. Korenburg (M.), Billings (S.A.) & Liu (Y.P.) 1988 *An Orthogonal Estimation Routine for Nonlinear Stochastic Systems* Research Report 307. Department of Control Engineering, University of Sheffield.

45. Billings (S.A.) & Tsang (K.M.) 1988 *Spectral Analysis for Nonlinear Systems: Part I - Parametric Nonlinear Spectral Analysis* Research Report 337. Department of Control Engineering, University of Sheffield.

46. Birkhoff (G.) & Maclane (S.) 1977 *A Survey of Modern Algebra* Fourth Edition, Macmillan.

47. Forsyth (G.E.), Malcolm (M.A.) & Moler (C.B.) 1972 *Computer Methods for Mathematical Computations* Englewood Cliffs N J : Prentice Hall.

48. Proceedings SERC Summer School 1985 *Signal Processing for Control* Springer Verlag.

49. Foster (C.D.) & Mottershead (J.E.) 1989 *Parameter Estimation Techniques for Monitoring Machines and Structures* in *Modern Practice in Stress and Vibration Analysis* edited by J.E.Mottershead. Pergamon Press, Oxford.

50. Ljung (L.) & Söderström (T.) 1987 *Theory and Practice of Recursive Identification* MIT Press.

51. Leech (J.W.) 1958 *Classical Mechanics* Methuen.

52. Jackson (J.D.) 1979 *Classical Electrodynamics* Second Edition. John Wiley and Sons, London and New York.

53. Collar (A.R.) & Simpson (A.) 1987 *Matrices and Engineering Dynamics* Ellis Harwood Series in Engineering Science.

54. Stephens (J.E.) & Yao (J.T.P.) 1985 *Data Processing of Earthquake Acceleration Records* Structural Engineering Report CE-STR-85-5. Purdue University.

55. O'Donnell (K.J.) & Crawley (E.F.) 1985 *Identification of Nonlinear System Parameters on Space Structure Joints Using the Force-State Mapping Technique* Report SSL-16-85. MIT Space Systems Laboratory.

56. Hamming (R.W.) 1989 *Digital Filters* Third Edition,Prentice Hall.

57. Bert (C.W.) & Stricklin (J.D.) 1988 *Journal of Sound and Vibration* 127 pp. 221-229. Comparitive Evaluation of Six Different Integration Methods for Non-Linear Dynamic Systems.

58. Bendat (J.S.) & Piersol (A.C.) 1971 *Random Data: Analysis and Measurement Procedures* Wiley Interscience.

59. Terrell (T.J.) 1988 *Introduction to Digital Filters* Second Edition, Macmillan.

60. Pyle (I.C.) 1981 *The ADA Programming Language* Prentice Hall International Inc.

61. Burrows (C.R.) 1980 *An Appraisal of Schroeder-Phased Harmonic Signals for Bearing Identification* Paper presented at the Winter Annual Meeting of the Dynamic Systems and Control Division of the ASME.

62. *The CED 1401 Intelligent Interface Programmers's Handbook.* Cambridge Electronic Design Ltd. Science Park, Milton Road, Cambridge CB4 4FE.

63. Blevins (R.D.) 1979 *Formulas for Natural Frequency and Mode Shape* Van Nostrand Reinhold.

64. Roark (R.J.) & Young (W.C.) 1976 *Formulas for Stress and Strain* Fifth Edition, McGraw Hill.

65. Nayfeh (A.H.) & Mook (D.T.) 1979 *Nonlinear Oscillations* John Wiley and Sons, London and New York.

66. Rao (S.S.) 1986 *Mechanical Vibrations* Addison Wesley.

67. Farrar (C.R.), Dove (R.C.) & Baker (W.E.) 1989 *Preliminary Report: Simulated Seismic Testing of TRG-7 Through TRG-11* Civil Engineering Division, Los Alamos National Laboratories, U.S.A.

68. Billings (S.A.) & Voon (W.S.F.) 1983 *IEEE Proceedings* 130 pp. 193-199. Structure Detection and Model Validity Tests in the Identification of Nonlinear Systems.

69. Jefferys (E.R.) 1988 *Journal of Offshore Mechanics and Arctic Engineering* 110 pp. 245-253. Nonlinear Marine Structures Under Random Excitation.

70. Erdělyi (A.), Magnus (W.), Oberherringer (F.) & Tricomi (F.G.) 1953 *Higher Transcendental Functions: Volume II* The Bateman Manuscript Project, McGraw Hill.

71. Sibson (R.) 1980 *Mathematical Proceedings of the Cambridge Philosophical Society* 87 pp. 151-156. A Vector Identity for the Dirichlet Tesselation.

72. Green (P.J.) & Sibson (R.) 1978 *The Computer Journal* 21 pp. 168-173. Computing Dirichlet Tesselations in the Plane.

73. Sibson (R.) *Manual for the TILE4 Interpolation Package* Department of Mathematics and Statistics, University of Bath.